# Coherent Backscattering from Free-Flying Insects

## Implications for Remote Species Identification

MENG LI
DEPARTMENT OF PHYSICS | FACULTY OF ENGINEERING | LUND UNIVERSITY

# Coherent Backscattering from Free-Flying Insects

# Coherent Backscattering from Free-Flying Insects

## Implications for Remote Species Identification

Meng Li


DOCTORAL DISSERTATION

by due permission of the Faculty of Engineering, Lund University, Sweden.

To be defended at Rydbergsalen, The Department of Physics, Professorsgatan 1.

4th of October 2024 at 09.15.

*Faculty opponent*

Prof. Pete Vukusic, Department of Physics and Astronomy,

School of Physics, Exeter University, UK

**Organization:** LUND UNIVERSITY

**Document name:** DOCTORAL DISSERTATION **Date of issue:** 2024-10-04

**Author:** Meng Li **Sponsoring organization**

**Title and subtitle:** Coherent Backscattering from Free-Flying Insects

Implications for Remote Species Identification

**Abstract:** The alarming decline in global insect populations and diversity calls for improved monitoring methods with species specificity. Conventional trapping techniques are labor-intensive and fail to provide real-time *in situ* data on species composition. In response, novel remote and automated monitoring methods have emerged, offering the potential for high-resolution and efficient data collection. However, existing remote sensing techniques, which primarily focus on wingbeat frequencies or direct insect imaging, have inherent limitations. These include the overlap of wingbeat frequencies between species and image challenges of focusing on rapid-moving free-flying insects.

To address these challenges, our research group has developed an entomological lidar, using the Scheimpflug principle to acquire signals across various distances. This approach captures detailed spectroscopic and dynamic features. Lidar could be a realistic photonic solution for monitoring the state of insect populations and diversity. My Ph.D. research investigates how the unique optical properties of insects, as characterized through infrared hyperspectral imaging, can enhance their identification *in situ* through lidar with multiple spectral bands or photonic methodologies. Specifically, I'm exploring how wing reflectance, interference patterns, surface roughness, and polarimetry can improve insect species differentiation. This research also investigates promising methodologies like dual-band and hyperspectral lidar, which could identify insects in flight by their micro- and nanoscopic features.

Entomological Lidar, combined with innovative photonic techniques, could complement or transform insect monitoring. This transformation can enhance pest control strategies, strengthen biodiversity studies, and deepen our knowledge of these crucial organisms.

**Keywords:** lidar, insect, WIP, fringe, thin-film, hyperspectral, remote sensing, entomology

Classification system and/or index terms (if any) Supplementary bibliographical information

**Language:** English **ISSN and key title**: 1102-8718

**ISBN:** 978-91-8104-153-8 (Print) 978-91-8104-154-5 (PDF)

Recipient's notes **Number of pages**: 323



Signature  Date 2024-08-19

.

# Coherent Backscattering from Free-Flying Insects

## Implications for Remote Species Identification

Meng Li


LUND
UNIVERSITY

Front cover photos by Meng Li

Back cover photos by Meng Li, Hampus Månefjord, Lauro Müller, Mikkel Brydegaard



Department of Physics, Faculty of Engineering

Lund University

ISBN 978-91-8104-153-8 (Print) 978-91-8104-154-5 (PDF)

LRCP: 257

ISSN 1102-8718

ISRN: LUTFD2/TFCP-257-SE

Printed in Sweden by Media-Tryck, Lund University

Lund 2024

"It's your road and yours alone. Others may walk it with you,
but no one can walk it for you."

- Rumi
Persia, 13th century

*Credits: Harry Biggs*

# Table of Contents

# Abstract

The alarming decline in global insect populations and diversity calls for improved monitoring methods with species specificity. Conventional trapping techniques are labor-intensive and fail to provide real-time *in situ* data on species composition. In response, novel remote and automated monitoring methods have emerged, offering the potential for high-resolution and efficient data collection. However, existing remote sensing techniques, which primarily focus on wingbeat frequencies or direct insect imaging, have inherent limitations. These include the overlap of wingbeat frequencies between species and image challenges of focusing on rapid-moving free-flying insects.

To address these challenges, our research group has developed an entomological lidar, using the Scheimpflug principle to acquire signals across various distances. This approach captures detailed spectroscopic and dynamic features. Lidar could be a realistic photonic solution for monitoring the state of insect populations and diversity. My Ph.D. research investigates how the unique optical properties of insects, as characterized through infrared hyperspectral imaging, can enhance their identification *in situ* through lidar with multiple spectral bands or photonic methodologies. Specifically, I'm exploring how wing reflectance, interference patterns, surface roughness, and polarimetry can improve insect species differentiation. This research also investigates promising methodologies like dual-band and hyperspectral lidar, which could identify insects in flight by their micro- and nanoscopic features.

Entomological Lidar, combined with innovative photonic techniques, could complement or transform insect monitoring. This transformation can enhance pest control strategies, strengthen biodiversity studies, and deepen our knowledge of these crucial organisms.

# Popular Science

*Gotta Catch 'em All: A Real-Life Pokédex for Insect Identification*

Does the iconic Pokémon slogan spark a sense of adventure? What if there was a tool that could instantly identify insects like a real-world Pokédex? Scientists are working to turn this dream into reality, and it all starts with understanding the challenges we face.

Conventional methods of insect study can be time-consuming, intrusive, and impractical to scale up. That's why we need new tools to quickly identify these vital creatures without disturbing their natural behaviors. New technologies like automation, remote sensing, and machine learning are being implemented to identify insects. However, challenges exist – insects in flight are hard to track and identifying them using wingbeat frequencies alone has limitations. With millions of insect species on Earth, the task is complex!

To overcome these challenges, our team has developed a specialized tool: entomological lidar. This system uses laser light to monitor insects in flight over distances in the landscape. We can then analyze backscattered light to differentiate species and collect vast amounts of data—imagine recording up to 100,000 insect observations in a single day! This is about 1,000 times more than a standard insect trap can manage. Our technology could be used to track changes in biodiversity and understand insect migration patterns.

Despite the potential, even lidar has trouble pinpointing the exact identity of every insect. That's where my Ph.D. research comes in. I'm exploring how the unique ways in which insect wings interact with light can help with identification. Imagine each species having invisible "fingerprints" on their wings – patterns of color and reflection that hold the key to who they are. Even seemingly dull moth wings exhibit surprising colors and shine when viewed at specific wavelengths. Transparent wings, like those of a fruit fly, display vibrant, soap-bubble-like colors due to a phenomenon called thin-film interference. My research focuses on understanding how the thickness and structure of insect wing membranes scatter light. By enhancing the properties of the light reflected from insect wings, we can improve our systems' ability to detect and identify these insects even at longer ranges.

Our team is actively developing specialized lidar systems to detect these patterns. This tool could transform how we study insects, with far-reaching impacts on precision pest control and conservation efforts and, ultimately, helping us better understand and protect these essential creatures.

# Populärvetenskaplig sammanfattning på Svenska

*Måste fånga fler: En riktig Pokédex för att identifiera insekter*

Föreställ dig ett verktyg som kan identifiera levande insekter direkt i fält, precis som en Pokédex i verkligheten. Ny teknologi kan göra denna dröm till verklighet, och börjar med att förstå de utmaningar vi står inför.

Konventionella metoder för att studera insekter kan vara tidskrävande, svåra att skala upp och ger sällan realtidsinformation, ofta kräver de att vi fångar in eller till och med avlivar individer. Därför behövs nya verktyg för att snabbt identifiera dessa viktiga varelser utan att störa deras naturliga beteende. Banbrytande teknik som automatisering, och fjärranalys, samt datorseende, och maskininlärning utvecklas för att övervaka och identifiera insekter. Men utmaningar finns – insekter i flykt är svåra att fokusera på, och identifiering baserad på vingfrekvens har begränsningar. Med miljontals insektsarter på jorden är snabb bedömning av biologisk mångfald och övervakning av insekter en komplex uppgift.

För att möta behovet av mindre arbetskrävande, kostnadseffektiva, icke-invasiva och storskaliga metoder för långsiktig insektsövervakning, har vårt team utvecklat ett specialiserat verktyg: entomologisk lidar. Detta system använder en laserstråle för att räkna insekter på avstånd i luften. Vi kan sedan analysera det reflekterade ljuset för att skilja arter och samla in enorma datamängder – tänk dig att registrera 100 000 insektsobservationer på en enda dag! Det är 1 000 gånger mer än en vanlig insektsfälla klarar. Vår teknik ger en enorm fördel för att mäta förändringar i biologisk mångfald och förstå insektsmigrationsmönster.

Även lidar har svårt att exakt identifiera varje insekt. Här kommer min forskning in. Jag undersöker hur insektsvingar sprider ljus för att förbättra identifieringen. Tänk dig att varje art har osynliga "fingeravtryck" på sina vingar – mönster av färg och ljusreflektion som avslöjar deras identitet. Till och med bruna nattfjärilsvingar visar överraskande färger med skimmer vid specifika våglängder. Genomskinliga vingar, som hos bananflugor, uppvisar skiftande färger som påminner om såpbubblor på grund av tunnfilmsinterferens. Min forskning fokuserar på hur vingmembranens tjocklek påverkar dessa ljusinteraktioner. Genom att förstå vingars ljusspridning kan vi förbättra identifieringen av insekter på avstånd i fält.

Vårt team utvecklar specialiserade lidarsystem för att detektera dessa mönster. Detta verktyg kan revolutionera insektsstudier med långtgående effekter på skadedjursbekämpning, bevarandeinsatser och vår förståelse av dessa avgörande varelser.

# Popular Science in Chinese

《神奇宝贝》图鉴不再是梦：昆虫识别新科技 (科普简介)

还记得《神奇宝贝》的经典口号“Gotta Catch 'em All”吗？这激起了多少人探索大自然的热情！如果真有一款工具能像神奇宝贝图鉴那样，瞬间识别出昆虫种类，那该有多酷？科学家们正努力让这个梦想照进现实。

传统的昆虫研究费时费力，往往需要捕捉甚至杀死样本。我们需要的是既能快速识别这些小生命，又不打扰它们生活的工具。科学家们想到了自动化、遥感和机器学习等先进技术，希望能实现非接触式识别。然而，昆虫飞行轨迹难以追踪，仅凭翅膀振动频率识别种类也有局限性。地球上昆虫种类繁多，要准确识别它们绝非易事。

为了解决这些难题，我们的团队开发了昆虫激光雷达。这个系统利用激光远距离监测昆虫飞行，通过分析反射光来区分不同物种，还能收集海量数据。想象一下，它一天能记录多达 10 万次昆虫观测，是普通诱虫陷阱的 1000 多倍！这将成为追踪生物多样性变化和昆虫迁徙规律的有力工具。

尽管激光雷达很强大，但要精确识别每一种昆虫仍有难度。这时，我的博士研究就派上用场了。我研究昆虫翅膀与光的独特互动方式，希望能改进昆虫识别技术。你可以把每种昆虫的翅膀想象成拥有独特的“指纹”——那些颜色和反射光的纹理就是识别它们的线索。即使看似普通的飞蛾翅膀，在特定波长的光照下也能呈现出令人惊叹的颜色和光泽。透明的翅膀，如果蝇的翅膀，也会因“薄膜干涉”现象而呈现出类似肥皂泡的鲜艳色彩。我的研究重点关注昆虫翅膀膜的厚度和结构如何影响这种独特的光学互动。如果能增强昆虫翅膀反射光的一些特性，我们就能让昆虫识别系统更灵敏，甚至实现远距离精准探测。

我们的团队正积极开发专用激光雷达系统来检测这些特征。这必将给昆虫研究带来革命性变革，造福于精准虫害防治和益虫保护工作，最终帮助我们更好地理解和保护这些重要的小生物。

# List of Papers

*Paper I*

**M. Li**, S. Jansson, A. Runemark, J. Peterson, C. Kirkeby, A. M. Jönsson, M. Brydegaard, Bark Beetles as Lidar Targets and Prospects of photonic Surveillance, Journal of Biophotonics (2020) (Front page feature).

*Paper II*

H. Chen†, **M. Li**†, H. Månefjord, P. Travers, J. Salvador, L. Müller, D. Dreyer, J. Alison, T. T. Høye, G. Hu, E. Warrant, M. Brydegaard, Lidar as a Potential New Tool for Monitoring Migratory Insects: A Field Case Study in Sweden, iScience (2024).
† *These authors contributed equally as the first authors.*

*Paper III*

H. Månefjord, A. S. D. Yamoa, Y. A. Gbogbo, L. Müller, A. Runemark, B. K. Kouakou, R. Boateng, A. A. Huzortey, I. K. Badu, N. Wahlberg, M. Brydegaard, J. T. Zoueu, B. Anderson, **M. Li**, Stratification of Insect Diversity and Daily Activity Patterns in Taï Virgin Forest assessed by Entomological Lidar (Manuscript in preparation) (2024).

*Paper IV*

D. Bernenko, **M. Li**, H. Månefjord, S. Jansson, A. Runemark, C. Kirkeby, M. Brydegaard, Insect Diversity Estimation in Polarimetric Lidar (Submitted) (2024).

*Paper V*

D. Dreyer, **M. Li**, H. Månefjord, A. S. D. Yamoa, Y. A. Gbogbo, L. Müller, A. Runemark, B. K. Kouakou, R. Boateng, A. A. Huzortey, J. T. Zoueu, B. Anderson, M. Brydegaard, Dual-Band Lidar and Statistical Moment-Based Assessment of Insect Diversity and Abundance in the Taï Virgin Rainforest (Manuscript in preparation) (2024).

*Paper VI*

H. Månefjord, L. Müller, **M. Li**, J. Salvador, S. Blomqvist, A. Runemark, C. Kirkeby, R. Ignell, J. Bood, M. Brydegaard, 3D-Printed Fluorescence Hyperspectral Lidar for Monitoring Tagged Insects, IEEE Journal of Selected Topics in Quantum Electronics 28 1-9 (2022).

*Paper VII*

H. Månefjord, **M. Li**, C. Brackmann, N. Reistad, A. Runemark, J. Rota, B. Anderson, J. T. Zoueu, A. Merdasa, M. Brydegaard, A Biophotonic Platform for Quantitative Analysis in the Spatial, Spectral, Polarimetric, and Goniometric domains, Review of Scientific Instruments 93 (2022).

*Paper VIII*

**M. Li**, C. Seinsche, S. Jansson, J. Hernandez, J. Rota, E. Warrant, M. Brydegaard, Potential for Identification of Wild Night-flying Moths by Remote Infrared Microscopy, Journal of the Royal Society Interface (2022) (Featured by National Geographic Society and *Nature*).

*Paper IX*

**M. Li**, A. Runemark, N. Guilcher, J. Hernandez, J. Rota, M. Brydegaard, Feasibility of Insect Identification Based on Spectral Fringes Produced by Clear Wings, IEEE Journal of Selected Topics in Quantum Electronics 29 1-8 (2022).

*Paper X*

**M. Li**, A. Runemark, J. Hernandez, J. Rota. R. Bygebjerg, M. Brydegaard, Discrimination of Hover Fly Species and Sexes by Wing Interference Signals, Advanced Science (2023) (Front page feature).

*Paper XI*

H. Månefjord[†], **M. Li**[†], J. Hernandez, L. Müller, C. Brackmann, A. Merdasa, C. Kirkeby, M. D. Bulo, R. Ignell, M. Brydegaard*, The Deadliest Animals with the Thinnest Wings – Near Infrared Properties of Tropical Mosquitoes, Laser & Photonics Reviews (Submitted) (2024).

*† These authors contributed equally as the first authors.*

*Paper XII*

L. Müller, **M. Li**, H. Månefjord, J. Salvador, N. Reistad, J. Hernandez, C. Kirkeby, A. Runemark, M. Brydegaard, Remote Nanoscopy with Infrared Elastic Hyperspectral Lidar, Advanced Science (2023) (Featured by NKT).

*Paper XIII*

**M. Li**, H. Månefjord, M. Brydegaard, Resolving fast Wingbeat Flashes in situ with Entomological Lidar, IEEE IPC Proceedings (Accepted) (2024).

# Related work

*A*

M. Li, M. Tsuboi, A. Runemark, E. Svensson, M. Brydegaard, Spectral Mating Preferences in Damselfly Species with Potential Evolutionary Implications.

*B*

M. Li, V. Feng, H. Månefjord, B. K. Kouakou, R. Meier, M. Brydegaard, Integrating Lidar, Computer Vision, and Genetic sequences for Comprehensive Insect Biodiversity Monitoring.

*C*

J. Salvador, M. Li, H. Månefjord, A. Runemark, C. Kirkeby, S. Jansson, M. Brydegaard, Initial Investigation of Range Dependence of Coherent Backscatter from Free Flying Insects.

# Paper Summaries and Author's contribution

**Paper I: Bark Beetles as Lidar Targets and Prospects of Photonic Surveillance**

**M. Li**, S. Jansson, A. Runemark, J. Peterson, C. Kirkeby, A.M. Jönsson, M. Brydegaard, Journal of Biophotonics (2020) (Front page feature).

In this paper, we investigated the potential of entomological lidar for monitoring free-flying bark beetles, a destructive pest posing a significant threat to spruce forests and the timber industry. By studying light scattering characteristics, optical properties, wing thickness, and wingbeat frequency of captured beetles, we demonstrated lidar's potential for monitoring both insects and pheromone plumes in a Swedish forest. Specific polarimetric- and spectral properties for pinned bark beetles are presented.

My contributions to this paper included participation in the lidar field campaigns, preparing the samples for scanning, capturing *ex vivo* and *in vivo* data using the entomological chamber, goniometer, and hyperspectral camera, assisting in the analysis of *in situ* data, creating data visualizations, and drafting the manuscript.

**Paper II: Lidar as a Potential New Tool for Monitoring Migratory Insects: A Field Case Study in Sweden**

H. Chen†, **M. Li**†, H. Månefjord, P. Travers, J. Salvador, L. Müller, D. Dreyer, J. Alison, T. T. Høye, G. Hu, E. Warrant, M. Brydegaard, iScience (2024).

*† These authors contributed equally as the first authors.*

In this study, we evaluated the feasibility of using lidar technology to monitor migratory insects. We conducted continuous lidar observations in southern Sweden from May to July, coinciding with the insects' yearly northward migration. These observations provided detailed information on insect heights, flight directions, size, and vertical velocities. By implementing polarization bands, we could successfully differentiate moths from other insects despite the challenge of low wingbeat frequencies and short transit times. The challenges and opportunities for our lidar to study their nocturnal flight patterns near the ground are outlined.

My contributions to this paper included designing and conducting the field experiment, helping set up the lidar, developing analysis code, visualizing data, and drafting the manuscript.

**Paper III: Stratification of Insect Diversity and Daily Activity Patterns in Taï Virgin Forest assessed by Entomological Lidar**

H. Månefjord, A. S. D. Yamoa, Y. A. Gbogbo, L. Müller, A. Runemark, B. K. Kouakou, R. Boateng, A. A. Huzortey, I. K. Badu, N. Wahlberg, M. Brydegaard, J. T. Zoueu, B. Anderson, **M. Li** (Manuscript in preparation) (2024).

In this paper, we conducted a study in the Taï forest of Côte d'Ivoire to investigate the crucial role of virgin rainforests in supporting insect diversity and the effectiveness of the lidar application to assess this. We employed a lidar system and insect trapping to study the distribution and abundance of insects within the forest canopy, revealing distinct activity patterns across different layers. This approach enabled us to monitor insect populations and identify a variety of species based on their optical properties. Multiple beam elevations were employed to decouple lidar range biasing from height over ground preferences. Our findings highlight the ecological significance of undisturbed forests and lidar's potential to assess insect diversity non-intrusively in challenging conditions.

I proposed and obtained a research grant to conduct this expedition. This grant covered participation in the field experiment, instrumentation, and upgrades to the Ivorian lidar, traps, and field equipment. I was responsible for planning the field campaign, proposing several experiments, and participating in the campaign with responsibility for trap sampling, mounting, and documenting species. I calibrated, analyzed, and clustered entomological lidar data, contributed visualizations, and directed and drafted the manuscript together with the first author.

**Paper IV: Insect Diversity Estimation in Polarimetric Lidar**

D. Bernenko, **M. Li**, H. Månefjord, S. Jansson, A. Runemark, C. Kirkeby, M. Brydegaard (Submitted) (2024).

In this study, we developed an unsupervised method for estimating insect diversity using lidar observations. We applied hierarchical clustering (HCA) and Gaussian Mixture Models (GMM) to group observations based on modulation power spectra derived from retrieved entomological lidar waveforms. To estimate diversity, we propose a criterion based on HCA linkage and use instrument noise as a negative control. Additionally, we explored the potential benefits of incorporating polarization for improved specificity. We investigate to what extent distinct signals are encountered at distinct ranges and hours of the day.

My contributions to this paper included collaborating on the project's planning, participating in the field experiment, supervising an MSc student, and actively engaging in discussions and manuscript contributions.

**Paper V: Dual-Band Lidar and Statistical Moment-Based Assessment of Insect Diversity and Abundance in the Taï Virgin Rainforest**

D. Dreyer, **M. Li**, H. Månefjord, A. S. D. Yamoa, Y. A. Gbogbo, L. Müller, A. Runemark, B. K. Kouakou, R. Boateng, A. A. Huzortey, J. T. Zoueu, B. Anderson, M. Brydegaard (Manuscript in preparation) (2024).

In this study, we investigated a robust and straightforward method for interpreting lidar signals to directly reflect the biological properties of target insects. We used statistical moments to analyze the behavior and trends within lidar observations, with specific examples provided. Our study employed a dual-band lidar at 980nm and 808nm. We provide reflectance values for wild ensembles of insects, confirming that while melanization explains body reflectance, coherent scatter is necessary to explain wing scatter.

My contributions to this paper included participating in the project's planning, obtaining the grant to conduct an expedition, taking part in the field experiment, assisting with insect trapping, and contributing to manuscript development.

**Paper VI: 3D-Printed Fluorescence Hyperspectral Lidar for Monitoring Tagged Insects**

H. Månefjord, L. Müller, **M. Li**, J. Salvador, S. Blomqvist, A. Runemark, C. Kirkeby, R. Ignell, J. Bood, M. Brydegaard, IEEE Journal of Selected Topics in Quantum Electronics 28 1-9 (2022).

In this paper, we developed and field-tested a compact, inexpensive hyperspectral fluorescence lidar system designed for studying insect dispersal. Unlike coherent scatter methods, our system relies on fluorescence to identify tagged insects. Our 3D-printed system successfully identified auto-powder-tagged honeybees and free-flying mosquitoes (which had fed on fluorescent-dyed sugar water) under field conditions. This technique offers efficiency and broad applicability, allowing for parallel monitoring of multiple insect groups and facilitating novel ecological experiments.

My contributions to this paper included collaborating on project planning, participating in the field experiment, assisting with insect capture by $CO_2$ traps, handling and releasing, and contributing to the manuscript.

**Paper VII: A Biophotonic Platform for Quantitative Analysis in The Spatial, Spectral, Polarimetric, and Goniometric Domains**

H. Månefjord, **M. Li**, C. Brackmann, N. Reistad, A. Runemark, J. Rota, B. Anderson, J. T. Zoueu, A. Merdasa, M. Brydegaard, Review of Scientific Instruments 93 (2022).

In this paper, we describe the development of BIOSPACE (Biophotonics, Imaging, Optical, Spectral, Polarimetric, Angular, and Compact Equipment), a low-cost,

versatile biophotonic instrument. Designed to be accessible for hands-on learning in education and research in low-income countries, BIOSPACE uses multiplexed light-emitting diodes and a synchronized camera for high-quality quantitative analysis of biological targets. We detail the instrument's construction, calibration, evaluation, and diverse functionalities.

My contributions to this paper included participating in planning, assisting with time-of-flight measurements, and writing the manuscript.

**Paper VIII: Potential for identification of wild night-flying moths by remote infrared microscopy**

**M. Li**, C. Seinsche, S. Jansson, J. Hernandez, J. Rota, E. Warrant, M. Brydegaard, Journal of the Royal Society Interface (2022) (Featured by National Geographic Society and *Nature*).

In this paper, we investigated the specular infrared reflectance spectra of moth species using polarimetric hyperspectral imaging in the short-wave infrared region. We found that wings exhibited glossy and specular properties at longer wavelengths, revealing distinct optical signatures between species. Our comprehensive modeling and parametrization demonstrated that microscopic wing surface features could be inferred from these infrared properties. These findings hold the potential to significantly improve remote identification of free-flying moths, possibly enabling sensing over considerable distances.

My contributions to this paper include acquiring hyperspectral images during a trip to Norsk Elektro Optikk, Oslo. I also developed analysis and statistical code, visualized data, and drafted the manuscript.

**Paper IX: Feasibility of Insect Identification Based on Spectral Fringes Produced by Clear Wings**

**M. Li**, A. Runemark, N. Guilcher, J. Hernandez, J. Rota, M. Brydegaard, IEEE Journal of Selected Topics in Quantum Electronics 29 1-8 (2022).

In this paper, we explored the potential of differentiating insects based on spectral fringes, or interference signals, reflected from their clear wings. We conducted a survey study focusing on 87 common pollinator species in Skåne, Sweden. Using a hyperspectral camera to capture wing interference patterns, we accurately determined wing thickness. Our results demonstrate that distinct modulation patterns and wing thickness can significantly improve species identification using photonic sensors.

My contributions to this paper included designing and collecting hyperspectral data in Norway, visualizing data, and drafting the manuscript.

**Paper X: Discrimination of Hover Fly Species and Sexes by Wing Interference Signals**

**M. Li**, A. Runemark, J. Hernandez, J. Rota, R. Bygebjerg, M. Brydegaard, Advanced Science (2023) (Front page feature).

In this paper, we investigated the potential of spectral approaches for remote and automatic insect species identification. We analyzed unique light patterns, known as wing interference signals (WISs), generated by the wings of free-flying insects that could be used for this purpose. Our extensive study of 600 wings from 30 hoverfly species revealed that factors such as wing thickness and heterogeneity, influenced by factors like larval diet and mimicry, could differentiate between species and sexes. Using just five parameters, we achieved 91% accuracy for the differentiation of sexes and closely related species. This highlights the potential of WIS-based surveillance for enhancing our ability to identify and protect insect diversity.

My contribution to this paper included remoistening, spreading, and mounting hundreds of museum specimens. I also traveled to Oslo to acquire infrared hyperspectral data, developed the analysis code, visualized statistics, and drafted the manuscript.

**Paper XI: The Deadliest Animals with the Thinnest Wings – Near-Infrared Properties of Tropical Mosquitoes**

H. Månefjord†, **M. Li**†, J. Hernandez, L. Müller, C. Brackmann, A. Merdasa, C. Kirkeby, M. D. Bulo, R. Ignell, M. Brydegaard, Laser & Photonics Reviews (Submitted) (2024).

*† These authors contributed equally as the first authors.*

In this study, we employed photonic monitoring via hyperspectral imaging and laser multiplexing to investigate the spectroscopic properties of mosquitoes. We developed models that could deduce nanoscopic- and microscopic features like wing thickness and absorption paths of melanin and water. The investigation revealed extremely thin mosquito wings of 174 nm with high precision, which could be implemented for lidar and remote sensing of wild insects.

In this paper, my contributions included participating in the hyperspectral imaging, preparing and mounting sub-micron wings of dead mosquitoes as well as immobilizing fresh specimens for scanning. I contributed to the manuscript text and figures.

**Paper XII: Remote Nanoscopy with Infrared Elastic Hyperspectral Lidar**

L. Müller, **M. Li**, H. Månefjord, J. Salvador, N. Reistad, J. Hernandez, C. Kirkeby, A. Runemark, M. Brydegaard, Advanced Science (2023) (Featured by NKT).

In this paper, we explored the potential of infrared hyperspectral lidar, a type of laser remote sensing, for long-distance insect monitoring and species identification. We developed an infrared hyperspectral lidar system with 64 spectral bands, capable of detecting unique, species-specific wing interference patterns in free-flying insects. As a proof of principle, we successfully retrieved coherent scatter from a damselfly wing, accurately determining its membrane thickness. We also captured signals from free-flying insects, estimated their wing thickness, and detected their wingbeat frequency, demonstrating the potential of this method for differentiating insect species.

My contributions to this paper included participating in fieldwork, preparing samples for scanning, visualizing hyperspectral imaging data, and contributing to manuscript figures and text. MSc student supervision.

**Paper XIII: Resolving fast Wingbeat Flashes in situ with Entomological Lidar**

**M. Li**, H. Månefjord, M. Brydegaard, IEEE IPC Proceedings (Accepted) (2024).

In this study, we evaluated the necessary sampling frequency to accurately capture wing modulation across various insect species using a kHz entomological lidar system. By systematically increasing the sampling rate, we assessed the resolution improvements in wing modulation measurements. Additionally, we collected data on environmental factors to understand their impact on the activity patterns of each classified insect group.

My contributions to this paper included discussing the planning, setting up the field experiment, acquiring the experimental data, visualizing and illustrating the figures, and drafting the manuscript.

# Abbreviations

| | |
|---|---|
| BIOSPACE | Biophotonics, Imaging, Optical, Spectral, Polarimetric, Angular, and Compact Equipment |
| DoLP | Degree of Linear Polarization |
| eDNA | Environmental DNA |
| EHSL | Elastic Hyperspectral Scheimpflug Lidar |
| FPA | Focal Plane Array |
| HCA | Hierarchical Cluster Analysis |
| HSI | HyperSpectral Imaging |
| LED | Light-Emitting Diode |
| Lidar | Light Detection and Ranging |
| NBC | Naive Bayes Classifier |
| NIR | Near-Infrared (in this thesis: 700-1000 nm) |
| SEM | Scanning Electron Microscope |
| SWIR | Short-Wave InfraRed (in this thesis: 1000-2500 nm) |
| ToF | Time-Of-Flight |
| UV | UltraViolet (in this thesis: 200-400 nm) |
| VIS | VISible (in this thesis: 400-700 nm) |
| WBF | WingBeat Frequency |
| WIS | Wing Interference Signal |

# 1.Introduction

A single bumblebee, its fuzzy body dusted with pollen, might not seem remarkable, yet its tireless flights from flower to flower are vital for the reproduction of countless plant species. But the bumblebee is just one of millions of insect species, each playing a crucial role in the intricate dance of life. From pollinating our crops to recycling nutrients, these tiny creatures are the unsung heroes of our planet, quietly working to maintain the delicate balance of our ecosystems.

## 1.1. Insects in Ecosystems

### 1.1.1. Insects' ecological significance

Insect, known as the most abundant and diverse animals on Earth [1-3], and are often overlooked despite playing an undeniably crucial role in the ecological processes that sustain our natural world [4]. Animal pollinators, particularly insects like wild bees and hover flies, are essential for ensuring global food supply. These

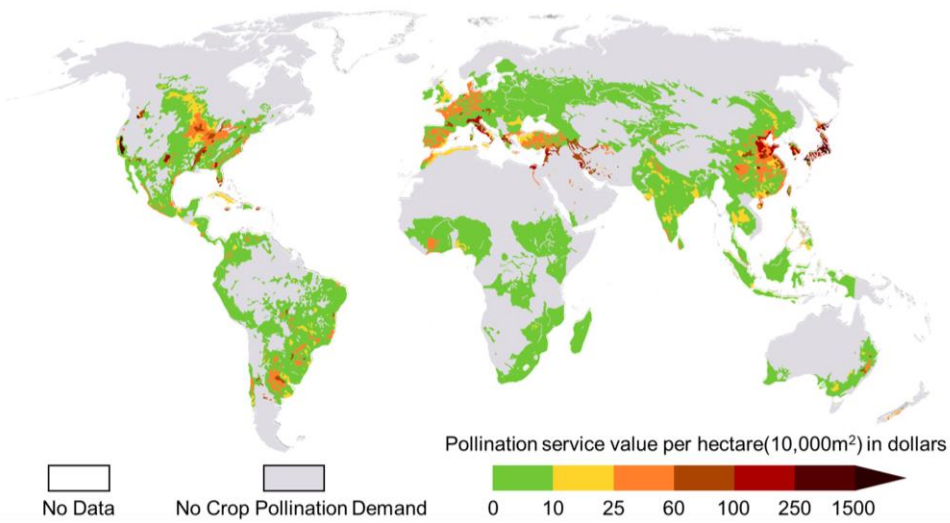


**Fig. 1.1: Global map of pollination benefits (2000).** The figure is adapted from ref [5].

pollinators underpin the reproduction of roughly 75% of the world's leading food crops [6, 7]. Among them, bees are the most vital group, visiting over 90% of the leading 107 global crop types [8]. This pollination activity has a direct impact on our diets, with 5-8% of our intake by volume being attributable to their work [9]. The global map of pollination benefits shown in Fig. 1.1 highlights the far-reaching economic stability derived from robust pollination services.

As decomposers, insects break down organic matter, which releases essential nutrients into the soil, boosting plant growth [4, 10] and forming the base of food chains [11, 12]. Additionally, many insects are natural pest control agents. Parasitoid wasps, for example, lay eggs inside other insects, controlling populations of crop-damaging pests [13].

However, the relationship between insects and humans is not always mutually beneficial. Some insects are considered serious agricultural and forestry pests, causing significant crop [14-17] or tree farm [18, 19] damage and economic hardship [20]. The spruce bark beetle (*Ips typographus*) is a major pest in European forests, capable of killing millions of trees during outbreaks. This destruction impacts both the forest ecosystem and the timber industry [21-23]. Others, like mosquitoes and disease-carrying flies, represent major public health threats. As illustrated in Fig. 1.2, where the mortality caused by insect-transmitted diseases far exceeds that caused by larger, more traditionally feared animals such as crocodiles or lions. Mosquitoes alone stand out as the world's deadliest animals due to diseases like malaria, dengue, and Zika. Malaria alone caused approximately 627,000 deaths in 2020 [24], disproportionately affecting poorer regions like Africa and Southeast Asia [24-26].

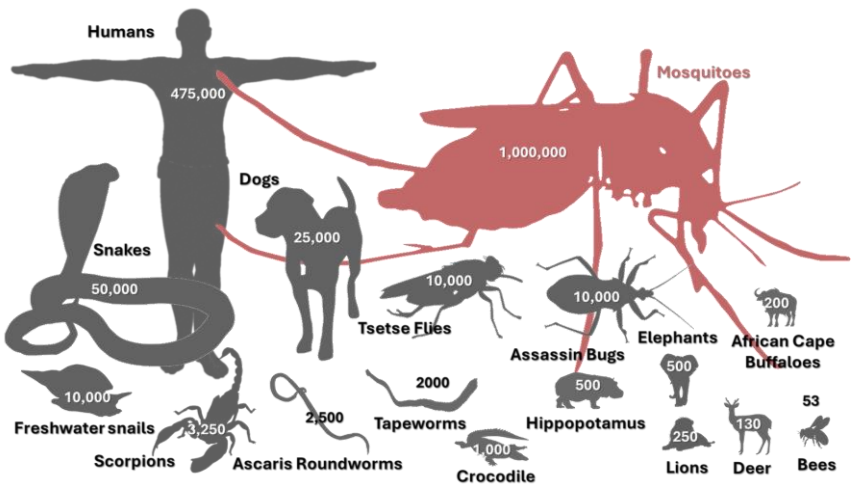


**Fig. 1.2: Top 17 of the deadliest animals in the world based on the number of human deaths as of 2016.** In the ranking of animals by annual human fatalities, the mosquito holds the grim title. Data is adapted from ref [27].

### 1.1.2. Biodiversity monitoring and conservation challenges

The monitoring of insect biodiversity is crucial for both the purposes of pest and disease vector control and pollination conservation, yet it faces numerous challenges. Insects are under-represented in general in biodiversity assessments compared with birds, mammals, and plants [29]. This is likely due to insects' small size and the high degree of knowledge necessary for identification often requiring

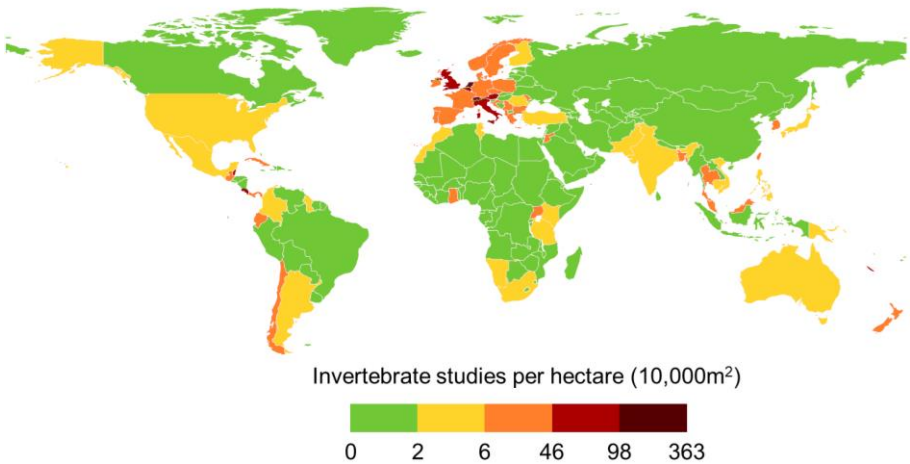


**Fig. 1.3: Global map of invertebrate studies.** The figure is adapted from ref [28].

experts with a narrow focus on a single insect order or family [30]. Flies and parasitoid wasps, for example, are often overlooked in biodiversity assessments despite their ecological importance [31, 32], simply due to the difficulty of identifying them. These challenges in accurately monitoring insect populations and diversity likely contribute to the significant lack of biodiversity data from highly biodiverse regions such as Africa and South America (as shown by the heterogeneity in research effort depicted in Fig. 1.3. A lack of comprehensive and long-term monitoring policies and methods further hinders conservation efforts [33].

## 1.2. Existing Approaches to Insect Detection and Identification

### 1.2.1. Conventional monitoring methods

Conventional methods, long considered the gold standard for monitoring and managing insect populations, often rely on various trapping systems to capture

insects under diverse environmental conditions. In our field campaigns, we utilized several conventional trapping systems to capture insects (see Fig. 1.4).

While conventional insect monitoring systems provide valuable data, they possess inherent limitations. These systems frequently result in insect mortality and offer restricted catching capacities [34]. Additionally, they necessitate specialized taxonomic knowledge for analysis, which is both time-consuming and expensive. Consider the case of a comprehensive study conducted in the San Lorenzo Forest, Panama [35-37], which sought to quantify arthropod species richness within a tropical rainforest. This collaborative effort involved 102 taxonomists and a total of 24,354 trap- (or person-) days of sampling. A total of 300,000 US$ was spent solely on fieldwork to acquire the sample. Despite substantial investment, only 23.7% of the 129,494 arthropods collected from a 0.48-hectare site could be identified to the species level after an 8-year interval, resulting in the identification of 6144 species [37]. This highlights the urgent need for more efficient collection and identification methods, as the time and cost of traditional taxonomy methods severely hinder our ability to develop timely management plans.


**Fig. 1.4: Overview of conventional insect trapping methods used in our field campaigns.** a-b) Malaise traps: a - canopy, b – ground-based. c) Sweep netting. d) Window trap with soapy water collection box. e) Pheromone trap for bark beetles. f-h) Pan traps in three colors to attract pollinators. i) UV light moth trap. j) Rotational light trap for various timeslots. k) $CO_2$ and light bait traps for catching blood-sucking insects. l-m) Mosquito traps with $CO_2$ generation from yeast l) and dry ice m).

### 1.2.2. Insect identification using wingbeat frequency

Acoustic [38] or electronic traps (E-traps) [39] offer a non-invasive way to capture and identify insects. These devices use sensors to detect and analyze the wingbeat frequencies (WBFs) of flying insects [39-42]. However, a significant challenge for both methods is their limitation in analyzing only one insect at a time, potentially causing bottlenecks in data collection. Additionally, there is considerable overlap in WBFs among different insect species, which can complicate species identification. As shown in Fig. 1.5, The 50 to 200 Hz range is crowded for WBFs, with significant overlap across various orders. This overlap is even more pronounced when considering species-level variations. Environmental factors such as temperature [43-45] and humidity [45, 46], along with biological factors like age [47, 48] and weight loading [49, 50], can also influence WBFs. Even within controlled laboratory environment, individual insects of the same species can display up to 25% variability in their WBFs [51], further complicating the analysis.

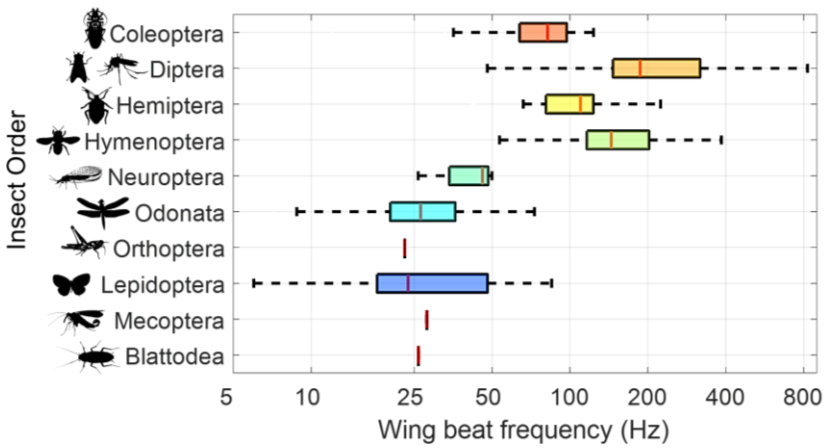


**Fig. 1.5: Distribution of WBFs across major insect orders.** This data was compiled through a massive literature review by *Noélie Guilcher*. See the accompanying Excel sheet for data sources and values [52].

### 1.2.3. Machine vision identification

Machine vision offers a practical solution to the challenges of manual insect identification. It can be a non-invasive method that captures images of insects without causing them harm. Camera traps, some equipped with light bait [53] and others without [54], are strategically placed in natural habitats to capture detailed images of insects in their environment. The images are then analyzed using a trained convolutional neural network (CNN) for accurate identification. An example of a camera trap with light bait is shown in Fig. 1.6. CNNs have shown the capability to identify insects down to the family level [55-57] and even species level [58, 59].

These systems can distinguish insects with remarkable precision. However, direct image-based machine vision systems face limitations: image clarity suffers with subject movement or focus issues, and light baits can introduce behavioral bias. These challenges underscore the need for continued refinement of detection techniques, potentially be those aimed at mitigating motion artifacts and reducing reliance on bait, to achieve accurate and unbiased insect identification.


**Fig. 1.6: Operation of a machine vision-equipped moth light trap [53].** a) Weather-resistant system with UV light ring, camera, and white sheet. b) Operated at night for optimal moth attraction. c) Attractions of many moths, demonstrating effectiveness. d) Captured high-resolution image.

### 1.2.4. Genetic methods

Genetic-based techniques are revolutionizing insect biodiversity assessment, providing researchers with powerful new tools and insights.

eDNA analysis involves detecting traces of insect DNA present in their environment [60-62], as animals naturally shed traces of DNA, by collecting samples of air, soil, or even flowers, researchers can identify related species without the need for direct observation. This non-invasive method enables efficient biodiversity surveys, cataloging a wide range of species from environmental samples [60]. However, eDNA degrades quickly [63], and its concentration does not always reflect organism abundance. Contamination risks present additional challenges.

DNA barcoding offers another approach, using a short, standardized DNA sequence from a specimen and comparing it against a reference database [64] to accurately identify the species. Metabarcoding extends this approach to identify multiple species within a mixed sample [65-67]. However, metabarcoding often lacks detailed population-level information, while individual DNA barcoding [68, 69], provides more precise abundance and diversity data while being labor-intensive.

The effectiveness of both techniques relies heavily on the availability of comprehensive and accurate reference databases [64]. Additionally, the DNA extraction process destroys part of the sample. Importantly, neither eDNA nor DNA barcoding directly measures species biomass, a crucial metric for understanding ecological dynamics, abundance, distribution, and the effects of environmental changes. Therefore, integrating these genetic techniques with other methods and continued innovation are crucial to fully utilize their potential for understanding and conserving insect populations.

### 1.2.5. Radar & Lidar

Since the mid-20th century, radar technology has been used to track the migration patterns of birds, revealing valuable insights into their movements and behaviors [70]. Decades later, this technology was adapted and applied to the study of insect migration [71]. Radar systems, such as the one illustrated in Fig. 1.7, operate by emitting radio waves and analyzing their reflections to detect and monitor large insect swarms within a range of several kilometers [71-77]. This method provides data on migration routes, swarm sizes, and the altitudinal distribution of flying insects, enriching the understanding of their ecological impact. However, traditional radar has difficulty differentiating between insect species and generally works best for larger insects with a substantial radar cross-section [78]. A newer technology, Frequency-Modulated Continuous-Wave (FMCW) radar, allows for even more detailed monitoring of insect movement at lower altitudes (between 0 and 150 m) [79, 80]. FMCW radar's potential for insect detection is promising, but its full capabilities and limitations remain to be seen, as it has not yet been widely deployed in field testing.


**Fig. 1.7: Examples of radar and lidar in field research.** a) Radar at Stensoffa field station in Sweden generates data on bird migration patterns. b) Lidar in the Tai virgin rainforest, Ivory Coast, provides insights into insect behavior and populations.

While radar technology has proven effective for tracking insect swarms, its limitations in species identification and the detection of smaller insects have spurred the development of alternative remote sensing techniques. Entomological lidar [81-86], a specialized form of Light Detection and Ranging (Lidar), offers a unique and powerful remote sensing approach for detecting insects with improved sensitivity and accuracy [87, 88]. By measuring backscattered laser light, entomological lidar gathers detailed biometric data such as WBF, wing size, and body size. This data provides valuable insights for insect identification [87, 89-91]. The Scheimpflug configuration developed for lidar systems expands their capabilities, enabling the monitoring of insects throughout diverse habitats and over long distances (see *Paper I* and reference [92]). Additionally, ongoing enhancements like polarimetric capabilities (see *Paper II-IV*) and dual-band features (see *Paper V*) are significantly improving precision, allowing us to better estimate diversity indices [92] and gain detailed biological information about the insects.

However, entomological lidar does face certain challenges. The narrow beam can limit its effectiveness for tracking large insects or their swarm migrations. Additionally, pinpointing observations down to the species level remains difficult, as insects can intersect the lidar beam at various angles (see *Papers I* and *VII*). To address this, laboratory systems are used to develop a database of reference signals from insect specimens (see *Paper I* and *VII-XI*). Studies demonstrate that insect features like melanin absorption, body size (affected by gravidity), surface roughness, and nanoscopic wing thickness can aid identification (see *Paper VII-XI* and references [93, 94]). Variables like changes in water and chitin levels reveal valuable information about an insect's state, potentially helping to determine species, sex, gravidity, and age (see *Paper XI*). Multiband lidar can differentiate between these features, and by carefully selecting the correct wavelength for a specific insect species, lidar can maximize the signal reflected from their wings.

Hyperspectral lidar offers a complementary and promising approach for advancing entomological lidar in species identification (see *Paper VI* and *XII* and reference [95]). By capturing spatial, temporal, and spectral characteristics simultaneously, this technology enables the utilization of spectral data, such as wing interference signals, for more accurate species identification of in-flight targets. In addition, ongoing exploration of higher sampling frequencies in lidar systems, as shown in *Paper XIII*, coupled with continuous advancements in hardware and analytical methods, promises to further enhance the capabilities of entomological lidar. This multifaceted approach holds the potential to unlock valuable insights into insect populations, behaviors, and their essential roles within ecosystems.

## 1.3. Thesis Outline

**Paper I** lays out the foundational techniques for using entomological lidar to track and monitor insects. It outlines the basic setup and early methodologies developed to differentiate insects based on their biometric data such as body and wing size, as well as wingbeat frequency. This paper sets the stage for subsequent enhancements and applications of lidar technology.

**Papers II-IV** focus on integrating polarimetric capabilities into entomological lidar systems. These papers explore how polarization enhances detection specificity and identification accuracy across diverse habitats and distances.

**Paper V** explores the implementation of dual-band features in lidar systems. It enhances the detection of insect biometrics by leveraging different wavelengths to maximize signal reflection from insect wings.

**Paper VI** introduces the use of fluorescence lidar for detecting specifically tagged insects, expanding the scope of lidar applications in tracking and monitoring ecological behaviors of marked targets.

**Paper VII** presents BIOSPACE, a cost-effective biophotonic instrument designed to empower research and education in low-resource settings. Demonstrate how BIOSPACE can be used to build a comprehensive insect database, directly enhancing the accuracy and capabilities of our lidar insect identification ability.

**Papers VIII-XI** explore how stable features such as melanin absorption, surface roughness, and nanoscopic wing thickness enhance species identification for lidar technique. Additionally, variable properties like changes in water and chitin provide valuable information about an insect's state, aiding in the determination of species, sex, gravidity, and age.

**Paper XII** introduces hyperspectral lidar technology, capturing spatial, temporal, and spectral data simultaneously. This paper focuses on how hyperspectral data can be utilized for detailed species identification, particularly through the analysis of wing interference patterns related to wing thickness.

**Paper XIII** extends the capabilities of lidar by incorporating high sampling frequencies, pushing the boundaries of detection and analysis of rapid and subtle changes in insect wing modulation.

# 2.Light-Insect Interactions

Light plays a crucial role in insect behavior and physiology, influencing everything from thermoregulation and signaling to camouflage and warning. When light interacts with insects, it undergoes a complex interplay of reflection, absorption, and scattering. These interactions can be categorized as either incoherent or coherent interactions. Incoherent interactions randomize light's properties, while coherent interactions preserve properties such as directionality and phase to some extent. A deep understanding of these light-insect interactions is essential for developing advanced remote sensing technologies such as entomological lidar. In this chapter, we delve into how the properties arising from the interaction between light and insects can be used to assist in the development of species-specific detection methods.

## 2.1. Incoherent Phenomena

Imagine shining a flashlight through your hand - you see a reddish glow, but not the details of your bones. This is due to incoherent light-matter interactions. As light passes through your hand, it scatters and diffuses, losing its original direction, polarization, and phase. This randomization of light properties is caused by absorption and scattering within a medium. The interplay of incoherent interactions enables the development of systems that can either reduce unwanted incoherence for improved signal strength or leverage these unique scattering characteristics for a variety of applications, such as differentiating insect species based on their water content and scattering coefficients.

### 2.1.1. Absorption

Insects are primarily defined by their exoskeleton, a crucial external structure that provides support and protection and facilitates movement [96]. This exoskeleton, composed mainly of chitin, a biopolymer, exhibits a strong absorption band around 280 nm in the ultraviolet spectrum [97, 98] (Fig 2.1a). This absorption decreases towards the visible and infrared ranges, where it becomes transparent.

In addition to chitin, melanin (eumelanin) is a key factor component influencing the varied coloration of insects. It is the predominant pigment in the animal kingdom [99] and plays a significant role in determining the colors seen in insects [100], especially within the visible spectrum. Melanin exhibits broad absorption, and it is responsible for dark coloration in animals, see Fig. 2.1b. In the case of insects, melanin is generally highly concentrated in the dark spots of the eyes, legs, or patches on the body [100]. For butterflies, melanin helps thermoregulation by absorbing solar radiation across a wide range of wavelengths [101, 102]. Melanin also provides protection against UV light to mitigate the harm it potentially does to DNA [103].

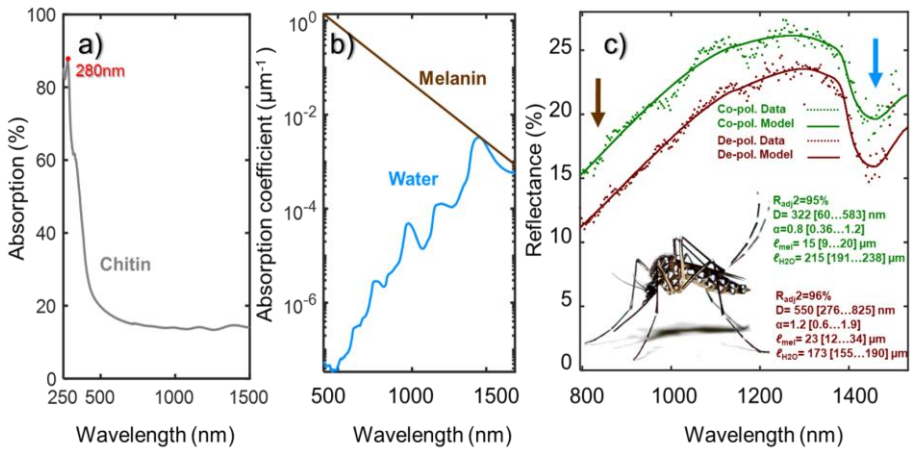


**Fig. 2.1: Optical properties of Insect**. a) Absorption spectrum of chitin, data originally from reference [98]. b) Absorption spectra of melanin (eumelanin) and water, data originally from references [104, 105]. c) Reflectance spectrum of live mosquitos measured with a hyperspectral camera, revealing strong melanin and water absorption features, highlighted by brown and blue arrows in the graph (adapted from *Paper XI*).

Another strong absorber within insects is water, which is also a dominant absorber within most biological tissues [104]. Water is a major component of the insect body, particularly concentrated in the thorax. This high water content greatly affects an insect's overall weight, as demonstrated in a study [106] where wet insects were found to be 2.1 times heavier than their dry mass. In the NIR wavelength region, water displays strong absorption bands around 1450 nm due to the vibrational modes of the water molecule [105]. This 1450 nm water absorption is evident in the hyperspectral reflectance scan of live mosquitoes, see Fig. 2.1c. The water characteristic has been used as a critical factor in remote sensing before, such as in environmental monitoring for detecting water content in leaves [107] or used in radar cross-section measurements of birds and insects to estimate their weight [108, 109]. Additionally, variations in water content can serve as indicators of different physiological states of insects, such as dehydration or feeding status [110], aiding in ecological studies and pest management strategies.

The Beer-Lambert Law, a fundamental principle in spectroscopy, quantifies the relationship between light absorption and the path length through an absorbing medium. It states that the transmitted light intensity decreases exponentially with increasing path length and concentration of the absorber,

$$I(\lambda) = \mathrm{I}_0(\lambda)\mathrm{e}^{-\mu(\lambda)\ell} \tag{2.1}$$

where $I(\lambda)$ is the intensity of the transmitted light, $I_0(\lambda)$ represents the initial light intensity, $\mu(\lambda)$ is the wavelength-dependent absorption coefficient, and $\ell$ is the effective path length. To take into consideration the absorption caused by both the water and eumelanin, the term 'Absorbance' $A(\lambda)$ was introduced into the study to describe the absorption in the insects,

$$A(\lambda) = \ell_{H_2O}\mu_{H_2O} + \ell_{mel.}\mu_{mel.} \tag{2.2}$$

where $\ell_{H2O}$ and $\ell_{\mathrm{mel}}$ are the equivalent water and melanin path lengths. $\mu_{H2O}$ and $\mu_{mel}$ is the wavelength-dependent absorption coefficients for water [111] and melanin [112].

Insects have evolved to leverage these absorption characteristics for camouflage, mating signals, and mimicry, enhancing their survival [113] and reproduction [114, 115]. Insect absorption characteristics are key to developing tools and models that quantify and predict their properties. For example, dual-band lidar systems utilizing wavelengths differentially indexing the melanin absorption (e.g., 808 nm and 980 nm) enable remote estimation of melanin content (see *Paper V*). Additionally, models can be developed to describe and estimate the effective path lengths of melanin and water within insects (Fig. 2.1 c and *Paper XI*).

### 2.1.2. Incoherent scattering

Incoherent scattering occurs when light is randomized, losing its dependence on direction, phase, and polarization prior to target interaction. When absorption is absent, this often results in a white matte appearance. This suggests that the white parts of an insect, such as the body or legs, or in the case of a gravid mosquito, the eggs within its abdomen, likely result from incoherent scattering of light (Fig. 2.2a). Polarimetric studies offer another way to investigate the origin of incoherent scattering. The image in Fig. 2.2b, showing de-polarized incoherent light signals from a pinned dried specimen, reveals that these signals predominantly originate from its veins and body.

The scattering coefficient is used to quantify the degree of scattering caused by the insect. The scattering properties of insects vary with several factors. For example, the amount of light scattered by mosquitos varies when they are gravid [94]. Additionally, insects with more water in their bodies scatter light differently than dehydrated insects. The scattering properties of insects can also change significantly

in their early development during the first few days after hatching, gradually stabilizing as the insect ages [116].

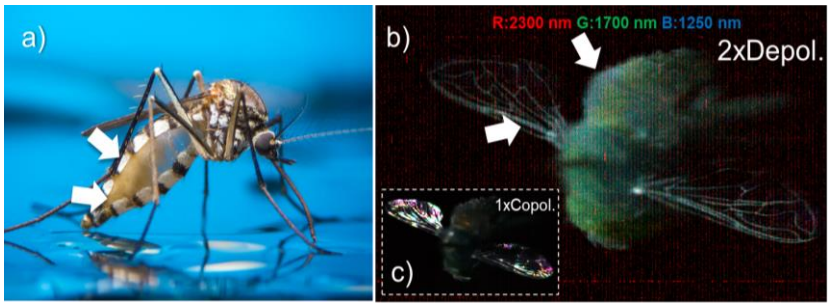


**Fig. 2.2: Examples of incoherent scattering sources.** a) An image of a pregnant mosquito, with its abdomen and setae on the body and legs displaying white colors (originally from reference [117]). b-c) False color polarimetric image of a hover fly (*Eristalis arbustorum* male), highlighting incoherent (de-polarized) signals originating from the veins and body. De-polarized component amplified 2x (1x Copol) for clarity.

To model light transport within a scattering medium like an insect body, the Kubelka-Munk theory was employed for diffuse reflectance (equation 44 from reference [118]). This theory is particularly suitable for '*thin specimens of poorly scattering material*.' In biological tissue, scattering is generally described sufficiently by a power law [119, 120]. In analogy with the term *Absorbance* the term '*Scatterance*' *S(λ)* was introduced, to represent the spectral dependent scattering:

$$S(\lambda) = \left(\frac{D_{½}}{\lambda}\right)^{\alpha} \tag{2.3}$$

Here, $D_{½}$ is the wavelength at which half of the light is reflected without absorption or transmission, acting as a gain factor for diffuse reflectance. The dimensionless parameter $\alpha$ governs the spectral shape of the scattering, allowing for adjustments in the spectral response. Based on Kubelka-Munk theory, the total diffuse reflectance from an insect can be described by the formula $R_{diff}$,

$$R_{diff}\,(\lambda) = \frac{S}{1+S+A} \tag{2.4}$$

where $A$ denotes the absorbance, as previously defined in equation 2.2. $R_{diff}$ approaches 100% as $S$ becomes very large and $R_{diff}$ approaches 0% as $A$ becomes very large. Additionally, $R_{diff}$ is 0 when $S$ is 0. This model effectively describes the spectral signal in Fig. 2.1c, with the resulting parameter values shown in the same figure.

The diffuse reflectance equation was simplified by setting $A$=0 to investigate the white spots present on the yellow fever mosquito (*Aedes aegypti*) in *Paper XI*. White coloration in thin objects is an unusual phenomenon, primarily because photons tend to escape before undergoing multiple scattering events [121-123]. Moreover,

nanostructures that strongly scatter visible light typically scatter less in the infrared range when their size is smaller than the wavelengths. Through the analysis, the reflectance characteristics of these white spots of *Aedes aegypti* can be accurately described using a short-pass filter function.

$$R_{spot(\lambda)} = \frac{1}{1+\left(\frac{\lambda}{D_{½}}\right)^{\alpha}} \tag{2.5}$$

In *Paper XI*, the parameter $D_{½}$ is found to be 1215 nm, and the parameter $\alpha$ is determined to be 4.2. This model confirms that the white spots on the *Aedes aegypti* mosquito exhibit high reflectance within the visible range (below 600 nm) and a gradual decline in reflectance at longer wavelengths.

### 2.1.3. Anisotropy factor $g$ and phase function

When considering insects as lidar targets, it is essential to analyze how an insect as a whole interacts with and scatters light. This involves determining whether more light is scattered forward (in the original direction of travel) or backward (towards the light source). The anisotropy factor $g$ is a useful parameter for quantifying the directional preference of scattered light from an object. It ranges from -1 (pure backward scattering) to 1 (pure forward scattering), with 0 indicating isotropic scattering (equal scattering in all directions). Larger objects typically exhibit forward scattering ($g > 0$), while smaller particles may show backward scattering ($g < 0$). The anisotropy factor $g$ is defined [124] as:

$$g = \int_0^{\pi} p(\theta)\cos(\theta)\mathrm{d}\theta \tag{2.6}$$

where $p(\theta)$ represents the phase function, describing the angular distribution of scattered light, and $\theta$ is the scattering angle. The anisotropy factor summarizes scattering behavior, but directly measuring the phase function is more informative. This function reveals the precise pattern of light scattering at various angles. In *Papers I* and *VII*, the phase function of examined insect species was recorded using a goniometric system.

An example of a phase function measurement is shown in Fig. 2.3. This figure illustrates how light scatters off a target insect, with the resulting patterns for co-polarized and de-polarized light indicating whether scattering is predominantly forward or backward. In this specific case, strong forward scattering is observed for co-polarized light at the given wavelength, even when wings and elytra are removed (Fig. 2.3j, k). This persistent forward scattering might be attributed to the relatively small size of the bark beetle body, resulting in fewer scattering events that would otherwise randomize the light's direction. For de-polarized light, when the insect is turned sideways, the strong forward scattered signal is reduced (Fig. 2.3l, m). Insects with strong forward or backward light scattering are best studied using experimental setups with detectors positioned accordingly. Forward scattering is suited for

extinction measurements (e.g., eBOSS system in the study [106]) while backscattering benefits from single-ended systems such as entomological lidar [125, 126]. This matched configuration maximizes signal capture while using lower-intensity light sources for eye safety.

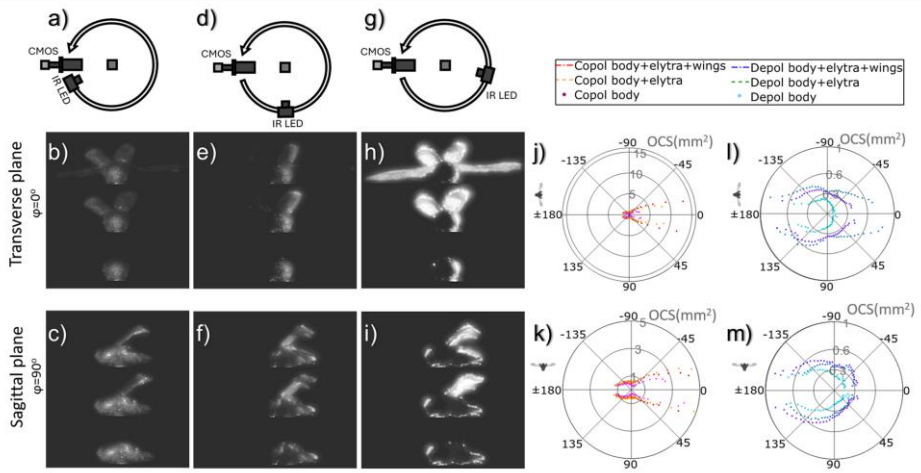


**Fig. 2.3 illustrates the scattering phase function of a bark beetle, with and without wings and elytra, under co- and de-polarized light (808 nm).** The experiment involved rotating the illumination source around the mounted sample, capturing images at various angles with the camera, including backscatter a), side scatter d), and near-extinction g). Images b, e, h) show the beetle illuminated along its transverse plane at positions a), d), and g) respectively, while images c, f, i) show illumination along the sagittal plane at the same positions. The recorded phase functions for two specimens at different anatomical planes are shown, differentiating between co-polarized j, k) and de-polarized l, m) signals. Data adapted from *Paper I*.

## 2.2. Partially Coherent Phenomena

Random organized biological tissues lack a dominant spatial frequency and thus primarily contribute to incoherent scattering [104, 124]. The organized, periodic structure of biological tissue with dominant spatial frequencies leads to contributions to coherent scattering [127-129], which can result in various optical effects depending on the symmetry and orientation of these frequencies, including iridescent [130], non-iridescent [131], grating [132], or thin-film [133, 134] patterns.

This relationship between structural organization and light scattering behavior in biological tissue is revealed through 2D Fourier analysis [135]. Fig. 2.4 illustrates this relationship between structural color and the arrangement of collagen fibers in

birds. Examples in Fig. 2.4a-d show the highly organized arrangement of fibers within green caruncles, producing a Fourier transform with distinct peaks. This frequency pattern indicates a clear, repeated structure in certain directions, demonstrating the regular spacing and alignment of the collagen fibers, see Fig. 2.4d. In contrast, less organized but still patterned fibers within light blue caruncles in Fig. 2.4e-h result in a ring-shaped transformation. Broader peaks in the 1D Fourier power spectra in Fig. 2.4h reflect this less defined structure, resulting in a spread in spatial frequency and some diffuse signal from the non-organized parts. In the case of diffuse white tissue Fig. 2.4i, lacking organized structure, the Fourier transform power spectra are characterized by a continuous distribution of spatial frequencies with a gradual decrease in power at higher frequencies. While 2D Fourier analysis is informative, this approach can be extended to 3D using electron tomography, albeit at a higher computational cost.[128].

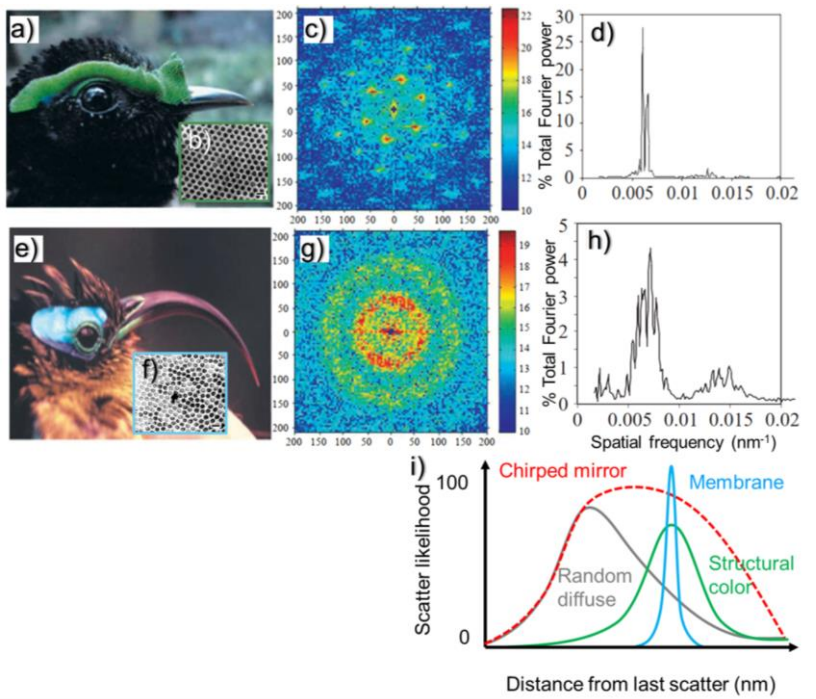


**Fig. 2.4: Structural coloration in birds, arising from the organization of collagen arrays within their caruncles.** Shown are: a,e) *Philepitta castanea* (green caruncles) and *Neodrepanis coruscans* (light blue caruncles) with their respective structurally colored caruncles; b,f) Transmission electron micrographs of color-producing collagen arrays from these caruncles; c,g) Corresponding 2D Fourier power spectra, revealing the spatial organization of the collagen; and d,h) Normalized radial averages of single quadrants of the power spectra. (All figures from a-h) adapted from reference [135]) i) Illustration of Fourier power spectra differences between organized (structural color) and unorganized (diffuse white) tissues.

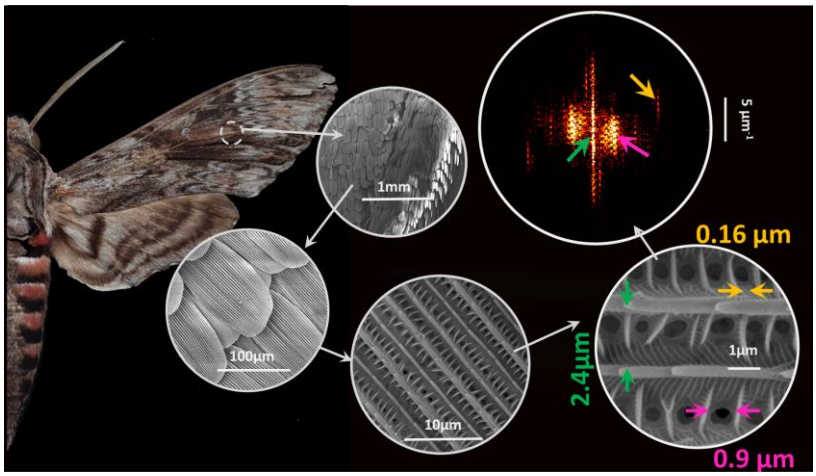


**Fig. 2.5: Scanning electron microscope (SEM) study of the surface structure of a brown moth (*Agrius convolvuli*) wing scale.** The 2D Fourier power spectrum reveals multiple periodicities across the surface, with each corresponding periodicity pattern marked.

Just as the structural organization of collagen in birds affects how it scatters light, the same principle applies to the varied colors found in insects. The composition of chitin, water, and melanin, along with the arrangement of biological structures, gives rise to both incoherent (diffuse) [122, 136] and coherent (specular) reflectance [125, 137]. In those studies (*Papers III*, *VII*, *VIII*, *X*, *XI*), BIOSPACE and a polarimetric hyperspectral camera were utilized to separate incoherent and coherent signals from insect wings. In *Paper VIII*, the repetitive patterns on rough brown moth wing scales were investigated using 2D Fourier power spectra analysis of SEM images (one example is shown in Fig. 2.5, examining the lateral, XY frequencies across the surface.). The dominant spatial frequencies identified in the Fourier transform of the SEM images were then correlated with the spectroscopic features deduced from the infrared properties of the wing scales, highlighting the relationship between surface structural arrangement and infrared reflectance properties.

### 2.2.1. Surface roughness

The wings of both clear-winged and diffuse-winged insects can exhibit a rough surface, particularly evident at visible wavelengths [138, 139]. While insect wings may appear as a thin, flat layer of chitin, their uneven surfaces arise from various factors. For instance, the clear wings of the female mosquito (*Aedes aegypti*), as shown in Fig. 2.6, have veins and hair-like structures [140] that scatter light, leading to a reduction in the specular signal [141]. Other factors contributing to the roughness of clear wings include refractive indices gradient within the membrane

[132] leading to anti-reflection. The deformation during downstrokes [142], further reduces specular scattering and enhances diffuse reflectance. In Lepidoptera, the wings are covered in scales see Fig. 2.6c, d, which are chitinous biological structures with micro and nano-scale features [139, 143, 144]. These scales can significantly increase surface roughness, leading to incoherent scattering if they lack organized structures.

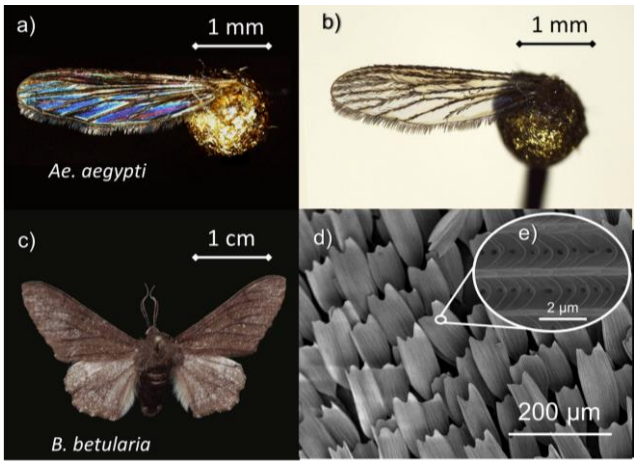


**Fig. 2.6: Both clear and diffuse wings do not have a flat, perfect membrane chitin surface.** a, b) Microscopic images of the *Aedes aegypti* female mosquito wing. A strong wing interference pattern is visible when the wing is placed against a black background. c) Photograph of a *Biston betularia*. d,e) SEM image of the microstructure on the surface of the moth wing.

The perceived roughness of insect wings can decrease as the wavelength of light used to observe them increases. If the wavelength is not short enough to resolve the lateral (XY) micro and nano-scale structures, the wings could appear specular (smooth) at certain wavelengths. Imagine illumination with a short wavelength as ping-pong balls scattering randomly off a rough surface (diffuse reflection), while longer wavelengths, like basketballs, bounce predictably (specular reflection), see Fig.2.7.

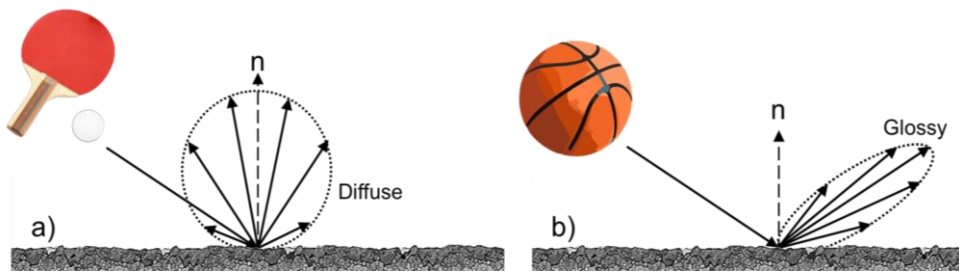


**Fig. 2.7: Wavelength influences light reflection on a rough surface.** a) short wavelengths scatter diffusely off a rough surface (like ping-pong balls bouncing off an uneven floor). b) longer wavelengths exhibit more focused, specular reflection (like basketballs maintaining a predictable trajectory on the same surface).

This wavelength-dependent scattering phenomenon has implications for lidar detection of insects, particularly those with rough wing structures like Lepidoptera.

A wing with low roughness makes a flash in lidar during wingbeat when the surface normally aligns with the beam. Therefore, smooth wings produce many harmonics. By translating lidar to mid- or long-wave infrared wavelengths, the apparent roughness of these wings can be reduced, as shown in *Paper VIII*, which can effectively mitigate the reduction in specular reflection caused by wrinkles, scales, or index gradients. This results in a stronger and more focused backscatter signal, enhancing detection capabilities and enabling species identification through the analysis of unique scattering patterns and resonant backscattering bands with lidar. This approach has been used in optical engineering and metrology since the invention of the $CO_2$ laser at 10.6 µm used to make unpolished surfaces appear specular [145, 146].

### 2.2.2. Bidirectional reflectance distribution function

The Bidirectional Reflectance Distribution Function (BRDF) was used to investigate how the perceived roughness of insect wings changes with varying wavelengths of incident light [147, 148]. The BRDF quantifies light reflection from a surface, considering incident and reflected light directions and wavelength, as the ratio of reflected radiance to incident irradiance. The BRDF has found applications in various fields, including digital imaging of heritage sites [149] and satellite imaging [150]. This function follows the principles of reciprocity and energy conservation [151],

$$R_\lambda(\theta_\mathrm{i}, \varphi_\mathrm{i}, \theta_\mathrm{r}, \varphi_\mathrm{r}) = \frac{I_\mathrm{r}(\theta_\mathrm{r},\varphi_\mathrm{r})\mathrm{d}\omega_\mathrm{r}}{I_\mathrm{i}(\theta_\mathrm{i},\varphi_\mathrm{i})\cos\,\theta_\mathrm{i}\mathrm{d}\omega_\mathrm{i}} \tag{2.7}$$

here, $I_r(\theta_r,\varphi_r)$ is the reflected light intensity within solid angle $d\omega_r$, and $I_i(\theta_i,\varphi_i)$ is the incident light intensity within solid angle $d\omega_i$, see Fig. 2.8.

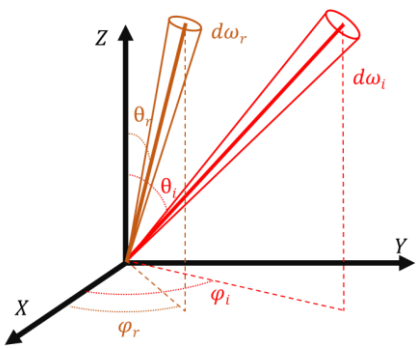


**Fig. 2.8: The relationship between the reflected light intensity $I_r(\theta_r,\varphi_r)$ and the incident light intensity $I_i(\theta_i,\varphi_i)$.** The figure is adapted from ref [151].

To model diffuse reflectance using the BRDF [149], the standard model is Lambertian scattering. In a Lambertian distribution, the BRDF, denoted as $R_\lambda(\theta_i,\phi_i,\theta_r,\phi_r)$, as the surface appears equally bright from all viewing angles. To

account for surfaces that deviate from ideal Lambertian behavior, this model can be modified with a 1/*r* term.

$$I = I_0 \cos^{\frac{1}{r}}(\theta) = I_0 \sqrt[r]{\cos\theta} \tag{2.8}$$

where *r* represents surface roughness. Here, *r* = 1 is a perfect Lambertian diffusor, and *r* = 0 is a perfect mirror. Note that conservation of brightness prevents the exponent from being less than 1, so *r* must always be between 0 and 1. The relationship between the BRDF definition of surface roughness and the angular spread of the scattered light lobes is illustrated in Fig. 2.9 with examples of different surface roughness.

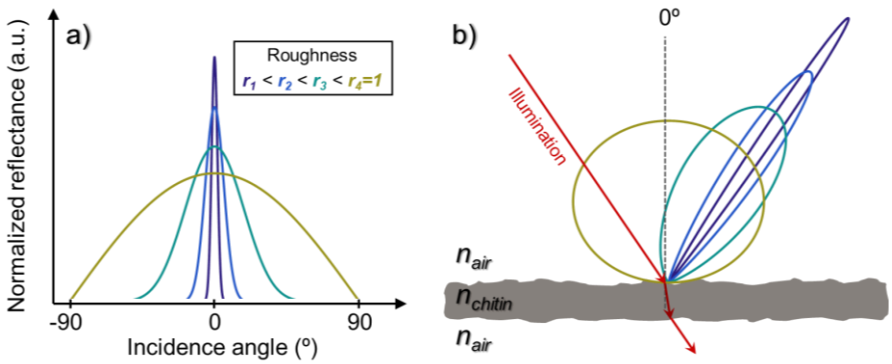


**Fig. 2.9: How the bidirectional reflectance distribution function (BRDF) defines surface roughness.** a) BRDF definition of surface roughness ($r_1 < r_2 < r_3 < r_4$), the smaller the *r* is, the less rough the surface is. b) The angular scatter lobe for different degrees of surface roughness. The figure is adapted from ref [152].

The specular reflectance model builds upon the diffuse model in equation 2.8. To capture the dependency of specular reflectance lobes on incident light, a symmetric link function, $F_{link}(\theta, \theta_0)$, with the property $F_{link}(\theta, -\theta) = 0°$ (maximum of the cosine function) was incorporated. This guarantees that incident and reflected light angles are symmetrical. Moreover, $\theta_0$ was scaled by 1 – r, ensuring that the reflectance lobe of a perfect diffuser aligns with the surface normal, thus becoming equivalent to Lambertian reflectance:

$$I(\theta, \varphi) = I_0 \left( \cos\left( F_{\text{link}}(\theta, (1-r)\theta_0) \cos\left( F_{\text{link}}(\varphi, (1-r)\varphi_0) \right) \right) \right)^{1/r} \tag{2.9}$$

$$r \in 0 \ldots 1$$

$$F_{\text{link}}(\theta, \theta_0) = 90° \left( \left( \frac{\theta + 90°}{180°} \right)^{\frac{-\log(2)}{\log\left(\frac{90° - \theta_0}{180°}\right)}} - \left( \frac{90° - \theta}{180°} \right)^{\frac{-\log(2)}{\log\left(\frac{\theta_0 + 90°}{180°}\right)}} \right) \tag{2.10}$$

$$\theta, \theta_0 \in -90° \ldots + 90°$$

$$\int_{-90^\circ}^{+90^\circ} I(\theta,\varphi)d\theta d\varphi = 1 \tag{2.11}$$

The BRDF model was used to calculate the 180° backscatter from a moth using a vertically positioned polarization lidar in *Paper VIII*. The dynamic wing roll and pitch were adopted from a previous study [153]. The backscattered reflectance during the wingbeat was multiplied by the ventral projected wing area during the wingbeat, and the optical cross-section was obtained as a function of time. The de-polarized signal is modeled with $r$ = 1. This model does not account for light diffraction and directional reflectance caused by the grating-like structures on the scales. These periodic features likely vary in alignment across the wing.

The BRDF model was also employed to investigate the surface roughness of clear wings in a recent master's project [152], to examine the relationship between the surface roughness of clear wings and the spectral fringes (calibrated as an optical cross-section in this example), see Fig. 2.10. The project revealed an inverse correlation between surface roughness and spectral fringe characteristics, specifically the intensity and spacing, especially in visible wavelengths. Wing veins were identified as the primary contributors to diffuse scattering, while wing membranes were mainly responsible for specular reflection.

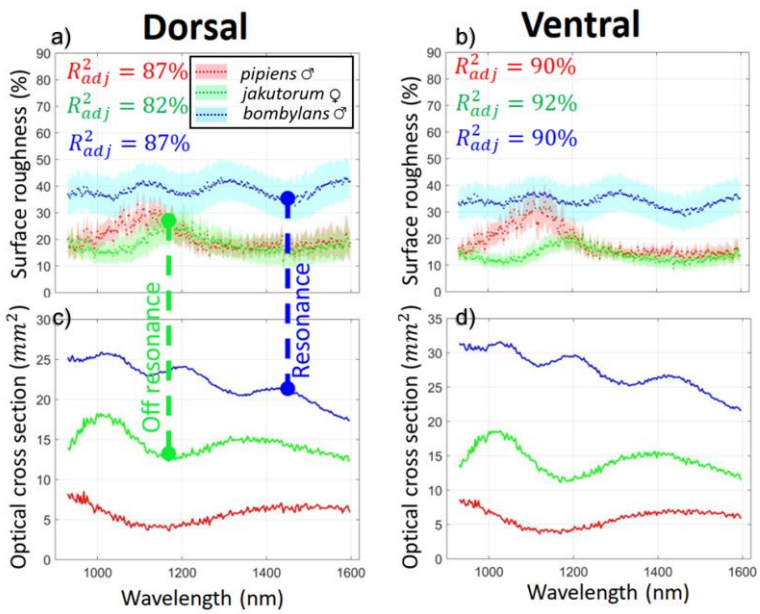


**Fig. 2.10: Relationship between the estimated surface roughness and reflectance of hover flies clear wing.** a) Estimated surface roughness on the dorsal (top) side of the wing. b) Estimated surface roughness on the ventral (bottom) side of the wing. c) Reflectance spectra from the dorsal side of the wing. d) Reflectance spectra from the ventral side of the wing. Surface roughness increases off-resonance. The figure is originally from [152].

### 2.2.3. Specular and diffuse reflection

Insect reflectance can be separated into incoherent (diffuse) reflectance, $R_{diff}$, and coherent (specular) reflectance, $R_{spec}$. Diffuse reflectance arises from light undergoing multiple scattering events within the insect's body, such as within the abdomen or eggs. Specular reflectance, on the other hand, occurs when light interacts minimally with the insect's body, as in reflections from the thin membrane wings or tiny legs. Although specular reflection from insect surfaces is rare, it can far exceed diffuse reflection when the surface normally aligns with the light source and detector. Notably, while average insect reflectance in the NIR is around 20% [137, 154], specular components can be partially collimated, enabling detection over greater distances than diffuse reflectance [98, 155]. All work included in this thesis primarily focused on the NIR and SWIR regions, where melanin [112, 156] and water [111, 157] are the main absorbers in insects.

To quantify both specular and diffuse reflectance, a Kubelka-Munk model was previously employed [118], where *Absorbance A* (equation 2.2), *Scatterance S* (equation 2.3), and total reflectance (combining specular and diffuse components) are expressed as:

$$R_{\text{spec.}} = \left| R_{\text{copol. }(\lambda)} - R_{\text{depol. }(\lambda)} \right|_{\text{median}} \tag{2.12}$$

$$\hat{R}_{\text{body}}(\lambda) = R_{\text{spec.}} + R_{\text{diff}}(\lambda) = R_{\text{spec.}} + \frac{S}{1+S+A} \tag{2.13}$$

$$\hat{R}_{\text{body}}(\lambda) = R_{\text{spec.}} + \frac{\left(\frac{D_{½}}{\lambda}\right)^{\alpha}}{1+\left(\frac{D_{½}}{\lambda}\right)^{\alpha} + \ell_{H_2O}\mu_{H_2O(\lambda)} + \ell_{\text{mel}}\,\mu_{\text{mel}\,(\lambda)}} \tag{2.14}$$

where $D_{½}$ is the wavelength of 50% reflectance, $\alpha$ adjusts the spectral shape, $\ell_{H2O}$ and $\ell_{mel}$ represent absorption in water and melanin respectively, and $\mu_{H2O(\lambda)}$ [111] and $\mu_{mel(\lambda)}$ [112] are the respective absorption coefficients, all of which were fitted to the measured diffuse reflectance using a numerical search algorithm.

### 2.2.4. Surface roughness vs lidar signal harmonics

Surface roughness determines whether reflected light is incoherent (diffuse) or coherent (specular), directly impacting the number of harmonics observed in entomological lidar signals [98, 125, 158].

The glossy wings of certain insects exhibit specular reflectance, producing bright flashes of light as their wing surface normal coincides with the source-detector midpoint. These specular flashes, captured as spikes in lidar observations, contribute to a greater number of harmonics compared to rough surfaces [87, 94, 137, 159], as illustrated in Fig. 2.11a, b. This is because spike signals contain higher frequencies, requiring more harmonics to accurately represent the waveform.

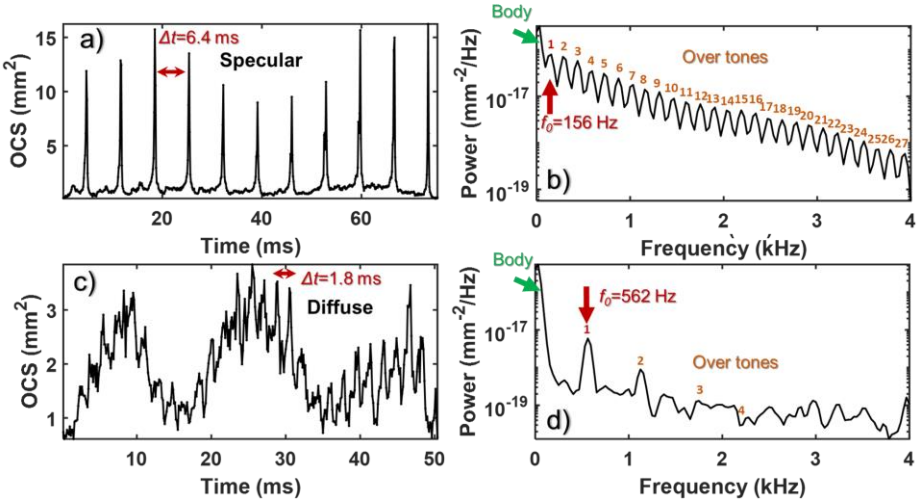


**Fig. 2.11: Comparison of lidar signals from insect wings with varying surface roughness.** a, b) Specular (glossy) wing generates a significantly larger number of harmonics compared to c, d) Diffuse (rough) wing. The laser used for these observations was an 808 nm continuous wave laser with co-polarized light.

Modulation spectra (Fig. 2.11 b and d) are composed of a non-oscillatory body contribution, a fundamental tone $f_0$, and multiple overtones. These spectra have been utilized for species recognition through modulation spectroscopy [42, 160-164]. The first few harmonics are particularly informative for identification as they relate to wing shape, dynamics, and observation aspects [165]. However, challenges arise due to the fundamental tone's variability with insect weight and temperature [43, 44, 166, 167], and its inconsistent signal strength [82, 158, 168]. To address these challenges, Scheimpflug lidar offers a promising solution. Its flexible band selection [88, 169, 170], ability to capture spectral fringes [171, 172], and integration with modulation spectroscopy [87] capture both modulation properties and spectroscopic properties. Instruments can be built with sensitivity to features such as surface roughness, wing thickness, and signal modulation. Improvements can be made to Scheimpflug lidar to reduce reliance on WBF, enabling the identification of a broader range of insect species.

### 2.2.5. Insects as polarimetric lidar target

Polarization describes the orientation of a light wave's oscillating electric field and its relationship with the magnetic field [148, 173]. This oscillation can be linear, circular, elliptical, or random, with the electric field's amplitude ($E$) indicating strength and its angle denoting direction. The relative phase between the electric and magnetic fields determines the handedness (right- or left-hand circular) of the polarization.

Polarization is used in various biomedical studies to gather detailed information about tissue [174-176]. It enhances imaging techniques, improving contrast for detailed tissue analysis [177, 178], such as separate superficial and deeper scatter contributions in biomedical imaging [176]. Animals use polarization for various functions [148, 179], including communication and vision [180-182]. Mantis shrimp possess specialized eyes that detect polarized light, aiding in hunting and social interactions [183]. Insects like field crickets [184] and dung beetles [185] use polarized light patterns for navigation [185-187]. Certain beetles reflect circularly polarized light [188-190], which enhances color and contrast, benefiting their communication and camouflage [148].

In entomological lidar studies, polarization was utilized to aid in insect identification based on the degree of polarization (DoLP) of backscattered light. Polarization lidar has previously been developed for atmospheric measurements [191]. Other research groups have also explored polarization lidar for insect studies [192, 193]. In the laboratory setting, polarization has been successfully applied to differentiate between gravid and non-gravid mosquitos [94].

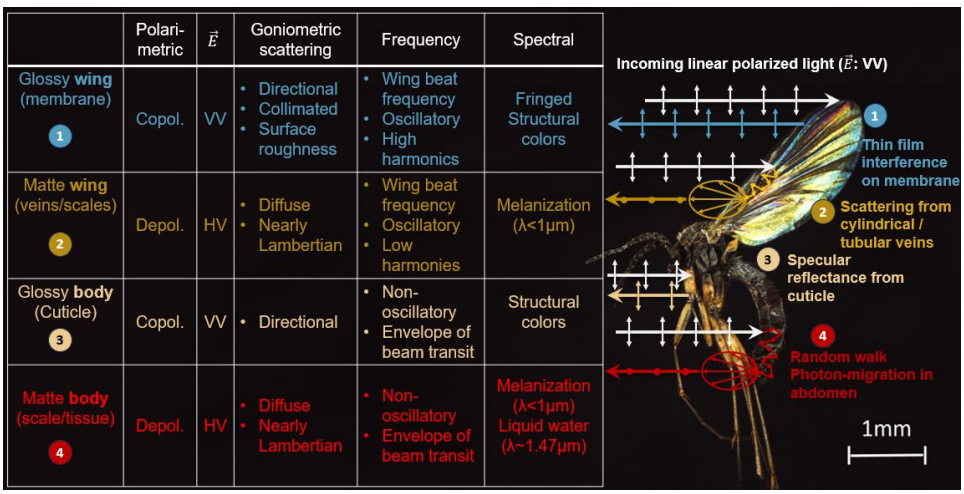


**Fig. 2.12: Contributions to backscattered polarimetric signals from insect anatomical features.** H and V represent horizontal and vertical polarization. The first letter in each combination (HV, VV) denotes the transmitted polarization, while the second letter denotes the detected polarization. The image is inspired by the reference [194].

The polarization of light reflected from various insect species was investigated in the laboratory (see references [106, 170] and *Papers I*, *III*, *VII-XII*). The experimental observations and measurements show that co-polarized and de-polarized backscatter can differentiate between coherent reflection (mainly due to thin-film interference [93, 195]) and incoherent scattering (originating from random photon migration in tissue [174, 176, 177]).

When linearly polarized light (Fig. 2.12) interacts with an insect in flight, the backscattered signal contains both co-polarized and de-polarized components. Co-polarized backscatter results from coherent specular reflections, while de-polarized backscatter arises from incoherent diffuse reflections. The lidar signal includes an oscillatory component resulting from wing flapping and a non-oscillatory component from the insect's body. The non-oscillatory signal generally resembles the lidar beam's transit envelope. Thin-film interference with insect membranes results in backscattered co-polarized light, maintaining a high DoLP. The DoLP is defined as the ratio of light maintaining its original polarization $I_{co}$ to the total light intensity $I_{co}$ + $I_{de}$, ranging from 50% (completely unpolarized) to 100% (fully linearly polarized), although instances below 50% were observed, suggesting additional de-polarization mechanisms to be detailed in the following section. The equation for DoLP is given by

$$\mathrm{DoLP} = \frac{\mathrm{I_{co}}}{\mathrm{I_{co}+I_{de}}} \tag{2.15}$$

Veins, scales, and abdomen tissue display low DoLP due to the random walk and photon migration of light entering these structures, leading to a loss of polarization, phase, and direction. Other factors like changes in scattering and absorption by melanin and water also contribute to this DoLP drop, as de-polarized photons undergoing longer migrations are more likely to be absorbed (time-of-flight phenomenon [120, 174]). The same insect can exhibit a DoLP change before and after consuming water/blood or becoming engorged with eggs [94] due to this.

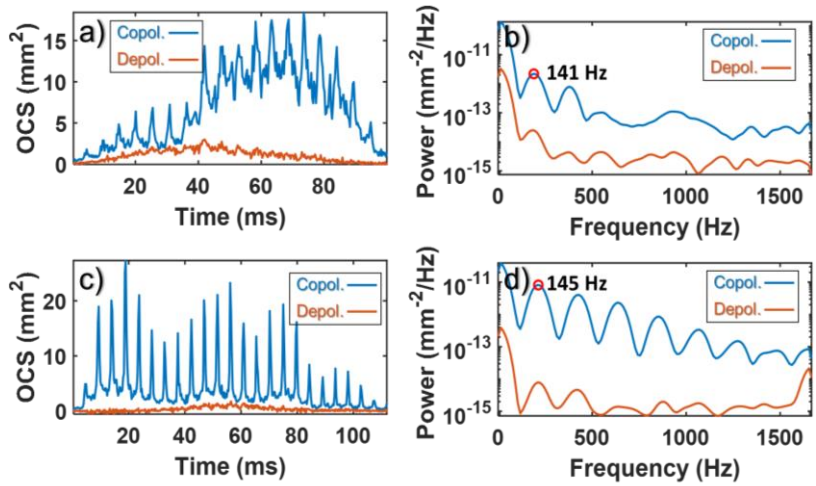


**Fig. 2.13: Example of insects displaying different specularity and polarization and their lidar signal.** a) An insect with a less specular surface and higher DoLP, and its corresponding power spectrum b). c) An insect with a more specular surface and lower DoLP, along with its power spectrum d).

Typical polarization lidar signals are shown in Fig. 2.13. The insect signal is separated into co-polarized and de-polarized components. The insect in Fig. 2.13a exhibits greater overall de-polarization and a less specular wing signal compared to the insect in Fig. 2.13c. This difference could potentially be attributed to a rough wing texture in a) and a glossy wing texture in c). The power spectra in Fig. 2.13b and d show that the rough-winged insect signal with lower overall DoLP has less pronounced overtones in the co-polarized component, consistent with rough surfaces leading to fewer harmonics. The glossy-winged insect's co-polarized signal instead shows many overtones. In both cases, the de-polarized signal in the power spectra exhibits oscillation, indicating that it contains both body signal and de-polarized wing signal, contributing to the oscillatory behavior.

### 2.2.6. Brewster angle at the air-chitin interface

The Brewster angle, calculated as $\theta_B$=56° for an air-chitin interface, assumes a step-function change in the refractive index using the formula below,

$$\theta_{\mathrm{B}} = \tan^{-1}\left(\frac{n_{chitin}}{n_{air}}\right) \tag{2.16}$$

The Fresnel equations (to be discussed in Section 2.3.3) are used to calculate the reflectance for s- and p-polarized light at this interface, as shown in Fig. 2.14, illustrating their dependence on the incidence angle. When light strikes the chitinous surface at the Brewster angle, the p-polarized component is fully transmitted into the insect's exoskeleton, while the s-polarized component is partially reflected [173]. The transmitted p-polarized light undergoes multiple scattering events within the insect, leading to de-polarization and a mixed s- and p-polarized signal upon re-emergence. Analyzing this reflected light reveals the properties of the insect's exoskeleton structures.

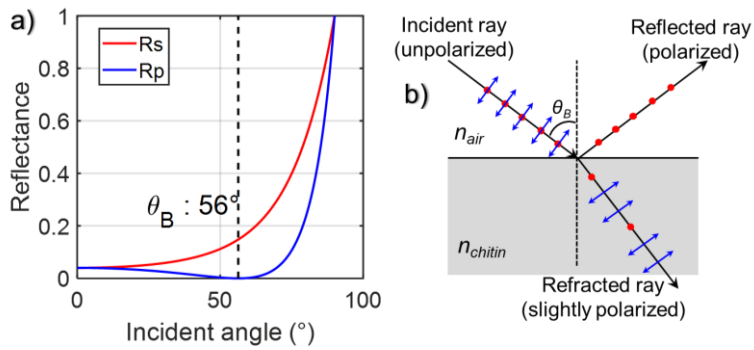


**Fig. 2.14: Fresnel reflection coefficients and Brewster angle effects at an air-chitin interface ($n_{air}$ = 1, $n_{chitin}$ = 1.53).** a) Reflectance differences for s- and p-polarized light. b) Behavior of incident light at Brewster angle (56°), no p-polarized light is reflected.

### 2.2.7. Polarization and surface roughness

Polarization has been used to study surface structure in radar [196, 197], microwave remote sensing [198], infrared [199, 200], and photometric [201]. Surface roughness influences the backscattering coefficients of electromagnetic waves, with the degree of influence depending on the incidence angle, frequency, and polarization of the waves [198, 201].

The relationship between surface roughness and polarization is most pronounced near the Brewster angle [198]. Smooth surfaces at this angle primarily reflect s-polarized light, yielding a high polarization ratio (p-polarized to s-polarized light), see Fig. 2.14. However, surface roughness disrupts this, causing increased p-polarized reflection, making the polarization ratio a sensitive indicator of even slight roughness changes.

The surface roughness of insect wings was investigated at the Brewster angle (in *Paper VIII-X*). For instance, the specular reflectance of a matte butterfly wing (illustrated in Fig. 2.15) can be modeled using a long-pass function.

$$R_{spec.} = R_{\text{long}} \frac{(\lambda/\lambda_0)^{\alpha}}{1+(\lambda/\lambda_0)^{\alpha}} \tag{2.17}$$

where $R_{long}$ represents the asymptotic maximum reflectance, $\lambda_0$ the cut-on wavelength or surface roughness, and $\alpha$ the slope steepness of the spectrum. This model is valid for specular reflectance at large incident angles. As shown in Fig. 2.15 (specular wing pixel and entire wing), specular reflectance typically increases and plateaus towards the infrared region. However, in a previous study (*Paper VIII*), it was observed some moth species with reflectance that continued increasing without reaching a plateau within the 900-2500 nm spectral range, suggesting their surfaces were too rough for accurate assessment with the SWIR hyperspectral camera with wavelength range 900-2500 nm. The wavelength-dependent polarization changes for specific regions or the entire matte wing can be expressed using the following formula:

$$\text{DoLP} = \frac{I_{\text{co}}}{I_{\text{co}}+I_{\text{de}}} = \frac{1+\text{e}^{-(\lambda_{\text{p}}/\lambda)^{\gamma}}}{2} \tag{2.18}$$

where $I_{co}$ and $I_{de}$ represent co-polarized and de-polarized reflected intensities. The wavelength at which wings become co-polarized is denoted as $\lambda_p$, and the spectral dependence of DoLP is given by $\gamma$. A higher $\lambda_p$ indicates a more diffuse wing (see the comparison between the specular and diffuse wing pixel in Fig. 2.15f), while a higher $\gamma$ means DoLP increases with wavelength more rapidly. The matte body in Fig. 2.15 exhibits a DoLP below 50%, suggesting factors beyond simple diffuse reflection. Moth scales and hairs may trap specular co-polarized light, leaving primarily de-polarized light to escape, thus lowering the observed DoLP.

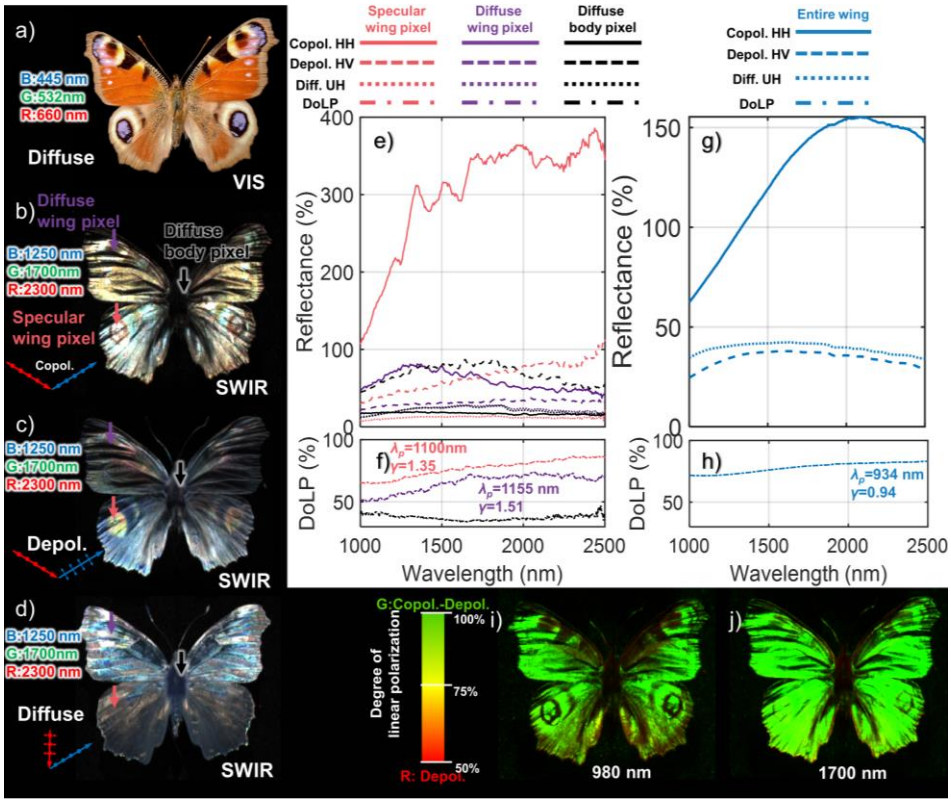


**Fig. 2.15: Example of hyperspectral polarimetric imaging used to study surface roughness in matte-winged insects.** a) A commercial camera image of a European peacock butterfly (*Aglais io*) under normal diffuse sunlight. b) Co-polarized false-color image of the same butterfly under specular illumination with Brewster angle. c) De-polarized false-color image of the butterfly under specular illumination with Brewster angle. d) False-color image under diffuse illumination. Red and blue arrows in b-d) show illumination and detection configurations. Polarization is denoted as HH, HV, or UH, with the first letter indicating transmitted and the second received polarization. e) Reflectance of selected specular wing pixel, diffuse wing pixel, and body pixel from b) under three different illumination and detection configurations (HH, HV, UH). f) DoLP calculated for all three pixels from the matte wing, showing their polarization ratio to wavelength. g) Reflectance from the entire wing under three different illumination and detection configurations (HH, HV, UH). h) DoLP of the entire wing over wavelength. i, j) DoLP images of the same butterfly at two wavelengths, showing increased linear polarization at higher wavelengths.

## 2.3. Coherent Phenomena

Coherent interactions preserve the original optical properties of light: direction, phase, and polarization. For instance, when light reflects off a thin insect membrane, which essentially acts like a mirror, it changes direction but maintains the light's initial phase and polarization.

### 2.3.1. Refractive index

The refractive index *n* of a material quantifies how light interacts with it by altering its group velocity *v* and wavelength $\lambda$ compared to a vacuum (*c* and $\lambda_0$): $v = c/n$ and $\lambda = \lambda_0/n$. The refractive index varies with wavelength, a phenomenon called dispersion, leading to the separation of different wavelengths. Materials commonly found in insect structures, such as chitin [202], melanin [203], or water [157], exhibit dispersion in the visible wavelength range, see Fig. 2.16a. The Cauchy equation models dispersion as:

$$n(\lambda) = k_0 + \frac{k_1}{\lambda^2} \tag{2.19}$$

Where $n(\lambda)$ is the refractive index at a specific wavelength $\lambda$. $k_0$ and $k_1$ are constants specific to the material. Typical values in the case of insect chitin are $k_0 = 1.517$ and $k_1 = 8800$ nm² [202]. When developing models to quantify insect microscopic features and structures, it is important to consider the changes in refractive index with wavelength, as different values could lead to varying results.

To add complexity, insect microscopic surface structures can have complex compositions resulting in a gradient refractive index. For example, when considering light interacting with a membrane as shown in Fig. 2.16b, an air-chitin-air interaction is simplified, assuming a step function change in refractive index.

However, the complex composition of the membrane, with its uneven surface and varying density, results in refractive index gradients. Calculations [132] reveal that transitioning from a step function refractive index profile to a gradient profile reduces reflectance, especially in the shorter wavelength region where photons experience a smoother gradient in relation to their wavelength (see Fig. 2.16c). Furthermore, the gradient profile flattens the spectral fringe modulation (potentially suppressing spectral fringe production in biological films). This can lead to low overall reflectance across the visible spectrum. This phenomenon is also observed in the *Papilio ulysses* butterfly, which appears "blacker than black" due to structurally enhanced blackness [151]. The cuticle spike structure in Fig. 2.16g not only efficiently scatters incident light towards the diffusely distributed pigmentation [151] but also creates a gradient surface refractive index, as illustrated in Fig. 2.16h, leading to exceptional light absorption.

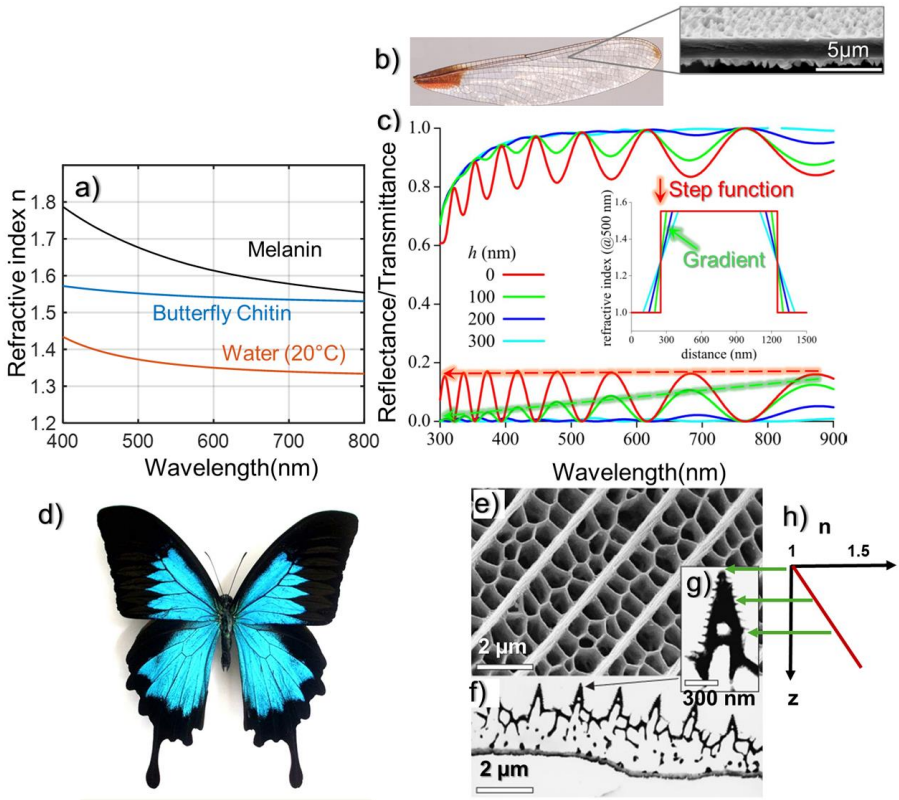


**Fig. 2.16: Refractive indices of common insect materials and the impact of structure on gradient refractive index surface.** a) Refractive index of melanin [203], chitin [202] and water [157]. Data were extracted from the corresponding references. b) Scanning electron micrograph of a section of *Hetaerina americana* damselfly wings, the photo is cited from [132]. c) Calculated transmittance and reflectance spectra for a thin film with an average thickness of 1000 nm. The refractive index was assumed to change linearly in surface layers with thicknesses h = 0, 100, 200, and 300 nm; the figure is cited from [132]. d) Image of *Papilio ulysses* butterfly. e) SEM image of the surface of a single scale from the matte black region of the butterfly shown in d). f) TEM image of the cross-section of a single scale from the matte black region of the butterfly shown in d). g) Zoomed-in view of one of the spikes shown in f). h) Sub-wavelength structures lead to a gradient refractive index surface. Images e-g) are from reference [151].

### 2.3.2. Snell's law

Snell's law describes the change in direction of light as it passes from one medium to another with a different refractive index. This change in direction, known as refraction, is caused by the mismatching of refractive indices of the two media and the angle at which the light strikes the interface. Snell's law is expressed as:

$$n_1 \sin(\theta_i) = n_2 \sin(\theta_t) \tag{2.20}$$

where $n_1$ and $n_2$ are the refractive indices of the two media, $\theta_i$ is the angle of incidence, and $\theta_t$ is the angle of refraction.

Some beetles and weevils possess intricate multilayer structures within their exoskeletons, composed of thin parallel layers of chitin with distinct refractive indices [127, 204, 205]. When light interacts with these multilayered structures, it undergoes refraction at each interface according to Snell's law. This repeated refraction, combined with subsequent interactions between the refracted light waves, can produce vibrant colors.

### 2.3.3. Fresnel equations

While Snell's Law describes how light changes direction at an interface due to refractive index mismatch, the Fresnel equations quantify the amount of light that is reflected and transmitted at this boundary [206]. For a single thin film, the analysis is simplified compared to the matrix formalism typically employed for multilayer structures [132, 207]. Importantly, the Fresnel equations distinguish between the light's polarization, whether it is p-polarized (parallel) or s-polarized (perpendicular) to the plane of incidence. The equations for a single thin film are [173]:

$$R_s = \left|\frac{n_1 cos(\theta_i) - n_2 cos(\theta_t)}{n_1 cos(\theta_i) + n_2 cos(\theta_t)}\right|^2, \quad T_s = 1 - R_s \tag{2.21}$$

$$R_p = \left|\frac{n_2 \cos(\theta_i) - n_1 \cos(\theta_t)}{n_2 \cos(\theta_i) + n_1 \cos(\theta_t)}\right|^2, T_p = 1 - R_p \tag{2.22}$$

here, $R_s$ and $R_p$ is the reflectance of s-polarized and p-polarized light, respectively, while $T_s$ and $T_p$ represent the corresponding transmittance values, $n_1$ and $n_2$ is the refractive index of the first medium (from which the light is coming), and the second medium (into which the light is going), $\theta_i$ is the angle of incidence, and $\theta_t$ is the angle of transmission, which can be found using Snell's law. In the case of lidar with normal incidence (the light beams perpendicular to the surface), the angles of incidence and refraction are zero. The Fresnel equation for an air-chitin interaction then simplifies to:

$$R_{Fresnel} = \left|\frac{n_1 - n_2}{n_1 + n_2}\right|^2 = \left|\frac{n_{air} - n_{chi.}}{n_{air} + n_{chi.}}\right|^2 \tag{2.23}$$

where $R_{Fresnel}$ represents the reflectance determined by the refractive indices of air ($n_{air}$, typically approximated as 1) and chitin $n_{chi}$. The refractive index of chitin, $n_{chi}$, is wavelength $\lambda$ dependent, as described in equation 2.19.

While the Fresnel equations provide the magnitudes of reflected and transmitted light separately, they do not directly give us the combined effect, as this depends on the complex interaction (interference) between the reflected and transmitted waves.

To account for the effective reflectance, the Fresnel equations need to be combined with thin-film equations [130], which will be discussed in a later section.

### 2.3.4. Kramers-Kronig-relation

The refractive index of a material is a complex quantity consisting of a real part $\varepsilon_1$, which determines the degree of refraction, and an imaginary part $\varepsilon_2$, which signifies absorption. The Kramers-Kronig (KK) relations [208] reveal a fundamental connection between these components: a material's absorption characteristics directly shape its refractive properties, and vice versa. This connection is rooted in causality, the principle that a material's response to light must adhere to the cause-and-effect relationship inherent in physical phenomena [209].

Mathematically, the KK relations are expressed as integral transforms, demonstrating the interdependence of the real and imaginary parts of the refractive index:

$$\varepsilon_1(\omega) = 1 + \frac{2}{\pi}\mathcal{P}\int_0^\infty \frac{\omega'\varepsilon_2(\omega')}{\omega'^2-\omega^2}d\omega' \tag{2.24}$$

$$\varepsilon_2(\omega) = -\frac{2\omega}{\pi}\mathcal{P}\int_0^\infty \frac{\varepsilon_1(\omega')-1}{\omega'^2-\omega^2}d\omega' \tag{2.25}$$

where *P* denotes the Cauchy principal value. At frequencies much higher than the material's resonance ($\omega >> \omega'$), the real part of the dielectric function ($\varepsilon_1(\omega)$) approaches 1, indicating negligible dispersion. However, at resonance ($\omega = \omega'$), the real part of the dielectric function ($\varepsilon_1(\omega)$) approaches infinity, necessitating the use of the principal value method. This signifies a strong coupling between the real ($\varepsilon_1$) and imaginary ($\varepsilon_2$) components of the dielectric function, resulting in significant absorption and pronounced changes in the refractive index, see example in Fig. 2.17. Water shows strong absorption peaks in the infrared spectrum and refractive

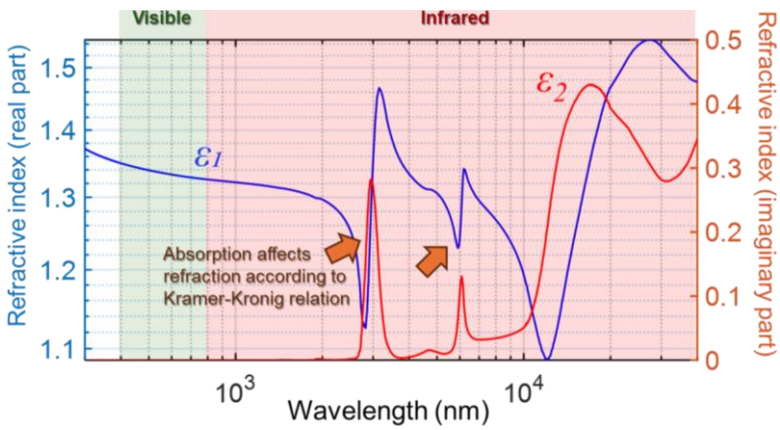


**Fig. 2.17: The complex refractive index of water.** Data from reference [111]. The figure is inspired by reference [212].

index derivation. Fig. 2.17 demonstrates that the refractive index of water remains relatively constant in the visible and NIR spectrum (before 2000 nm) due to the absence of strong water absorption lines in the range. However, significant variations in the refractive index are observed in the NIR (above 2000 nm) and SWIR regions. Applying the same logic, the refractive index of chitin is relatively flat in the NIR to SWIR range because its only absorption band peaks at 280 nm.

To maintain the cause-and-effect relationship described by the KK relations, the real and imaginary parts of a material's refractive index must be related. Dispersion, which refers to the dependence of a material's refractive index on the wavelength of light, results in changes in the phase velocity of light as it propagates through the material. This means that the speed of light varies with wavelength, leading to phenomena such as the separation of white light into its constituent wavelengths. Dispersion is crucial for comprehending the complex phenomenon of structural coloration in insects, where intricate nanoscale structures interact with light to produce vibrant colors [210, 211].

### 2.3.5. Thin film interference

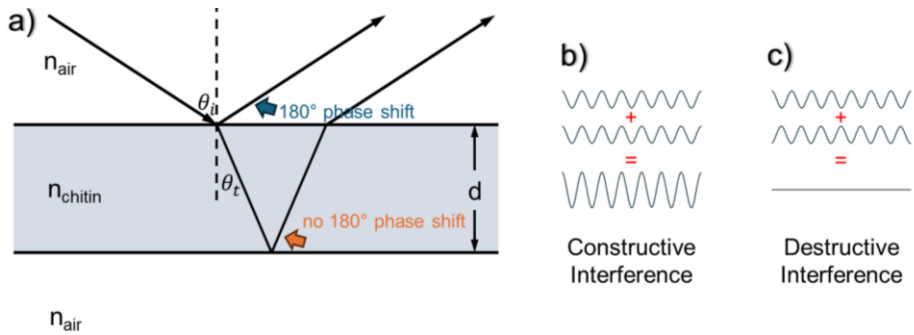


**Fig. 2.18: Illustration of thin film interference conditions of uniform thickness.** a) Showcasing angle of incidence $\theta_i$, angle of transmission $\theta_t$, refractive index of the medium $n$, and film thickness d. b-c) In constructive interference, waves with aligned phases amplify each other. In destructive interference, waves with opposite phases cancel each other out.

Thin-film interference, illustrated in Fig. 2.18, is a phenomenon arising from the interaction of light waves reflected at the upper and lower boundaries of a thin-film [173]. This interference can result in the selective amplification or attenuation of specific wavelengths, producing iridescent colors often observed in nature [132, 213, 214]. A 180° phase shift occurs when a wave reflects from a medium with a higher refractive index ($n_2 > n_1$), while no phase shift occurs with a lower refractive index ($n_2 < n_1$). The resulting colors depend on film thickness, refractive index contrast, and incident light angle.

Consider a thin chitin layer forming an insect's clear wing, surrounded by air. Since the refractive index of chitin $n_{chitin}$ is greater than that of air $n_{air}$ at the top surfaces of the wing, reflections at these boundaries induce a 180° phase shift. For constructive interference to occur, the optical path length difference (twice the wing thickness) must equal an odd multiple of half the wavelength within the chitin:

$$2dn_{chi.}\cos(\theta_t) = \left(m - \frac{1}{2}\right)\lambda_{max}, m \in \mathbb{N} \tag{2.26}$$

$$2dn_{chi.}\sqrt{1 - \frac{\sin^2(\theta_i)}{n_{\text{chi.}}^2}} = \left(m - \frac{1}{2}\right)\lambda_{max}, m \in \mathbb{N} \tag{2.27}$$

Destructive interference occurs when the optical path length difference equals an integer multiple of the wavelength within the chitin:

$$2dn_{chi.}\cos(\theta_t) = \mathrm{m}\,\lambda_{min}, m \in \mathbb{N} \tag{2.28}$$

$$2nd_{chi.}\sqrt{1 - \frac{\sin^2(\theta_i)}{n_{\text{chi.}}^2}} = m\lambda_{min}, m \in \mathbb{N} \tag{2.29}$$

where $d$ is the wing thickness, $n_{chi.}$ is the refractive index of chitin, $\lambda$ is the wavelength, $\theta_i$ is the angle of incidence, $\theta_t$ is the angle of transmission, and $m$ is an integer. For lidar measurements, the angle of incidence $\theta_i$ is zero (like the hyperspectral lidar measurement in *Paper XII*), so the entire square root factor in equations 2.27 and 2.29 can be omitted. However, for hyperspectral scan measurements performed in Papers *I*, *VIII*, *IX*, *X*, and *XII* in a laboratory, an angle of incidence is present and must be considered to adjust for the resulting spectral shift. For example, due to the increasing incidence angle, a spectral peak at 600 nm, captured at a 56° incident angle ($n$=1.53), would exhibit a blue shift to 505 nm when corrected to normal incidence. Such compensation is thus crucial to ensure comparability between laboratory hyperspectral and field lidar observations.

### 2.3.6. Fringe model

A fringe model was developed to express the spectral fringes observed in clear insect wings. This model incorporates a thin-film equation, derived from previous research on iridescence from pigeon neck feather [130], and Fresnel equations to account for the reflection and interference of light.

$$F(\lambda, d) = \frac{4R_{Fresnel}\sin^2\left(2\pi d\frac{\sqrt{{n_{chi.}}^2 - \sin^2\theta}}{\lambda}\right)}{(1-R_{Fresnel})^2 + 4R_{Fresnel}\sin^2\left(2\pi d\frac{\sqrt{{n_{chi.}}^2 - \sin^2\theta}}{\lambda}\right)} \tag{2.30}$$

where $F(\lambda,d)$ is the fringe, $\lambda$ is the wavelength of light that interacts with the wing, and $d$ is the wing's chitin layer thickness. $R_{Fresnel}$ is from equation 2.23, and the refractive index of chitin varies with wavelength, as shown in equation 2.19.

While the model $F(\lambda,d)$, incorporating thin-film interference effects, addressed scaling and material dispersion issues, it still could not account for the overall change in reflectance over varying wavelengths due to the heterogeneous nature of the wing's chitin layer thickness [132]. To address this issue, an approach (first appearing in *Paper X*) utilizes a long-pass function for amplitude and a short-pass function for bias to weigh the spectral fringe. This leads to the evaluation of spatial thickness heterogeneity across each wing by adjusting the fringe amplitude $a$ and bias $b$ relative to a specific cut-off wavelength $\lambda_0$,

$$\hat{R}_{wing(\lambda)} = \frac{aF(\lambda,d)\lambda^k + b\lambda_0^k}{\lambda_0^k + \lambda^k} \tag{2.31}$$

The exponent $k$ in these functions influences how reflectance changes with wavelength. In the hover fly study from *Paper X*, it was found that $k = e = 2.311$ to best describe all effective fringes. However, in *Paper XI*, due to thinner wings and observing only a single fringe period, $k$ could not be determined and was set to zero. The use of short- and long-pass functions is analogous to the use of electronic filters in signal processing to selectively pass specific frequency ranges [215]

For wings that do not produce fringes, the $F(\lambda, d)$ term vanishes, and the reflectance of the wing with no spectral fringe is thus described solely by the bias term of the fringe model from equation 2.31:

$$\hat{R}_{wing(\lambda)} = \frac{b}{1+\frac{\lambda}{\lambda_0}^k} \tag{2.32}$$

How the amplitude and bias terms address the increasing fringe modulation towards infrared wavelengths, and decreasing modulation towards visible wavelengths is illustrated in Fig. 2.19. It also shows examples of thick and thin wing pixel spectral fringes. The effective fringe was obtained by XY spatially integrating all wing pixel spectral profiles. The differing degrees of modulation in these fringes can be described by the modulation depth, $M$, calculated using the following equation:

$$M = \frac{\sigma_\lambda(R_\lambda)\cdot\mu_\lambda(F(\lambda,d))}{\sigma_\lambda(F(\lambda,d))\cdot\mu_\lambda(R_\lambda)} \tag{2.33}$$

where $R_\lambda$ denotes measured reflectance, $F$ denotes the computed fringe, $\lambda$ is the wavelength, $\sigma_\lambda$ denotes standard deviation in the spectral domain, and $\mu_\lambda$ is the spectral mean value.

Thicker wing regions exhibit narrower fringes, more susceptible to dephasing with neighbor regions (XY destructive interference, not XZ which is related to thickness) in the VIS spectrum due to the chirped nature of fringe periodicity. For a thin film, the periodicity of the interference fringes is constant in the frequency domain; the

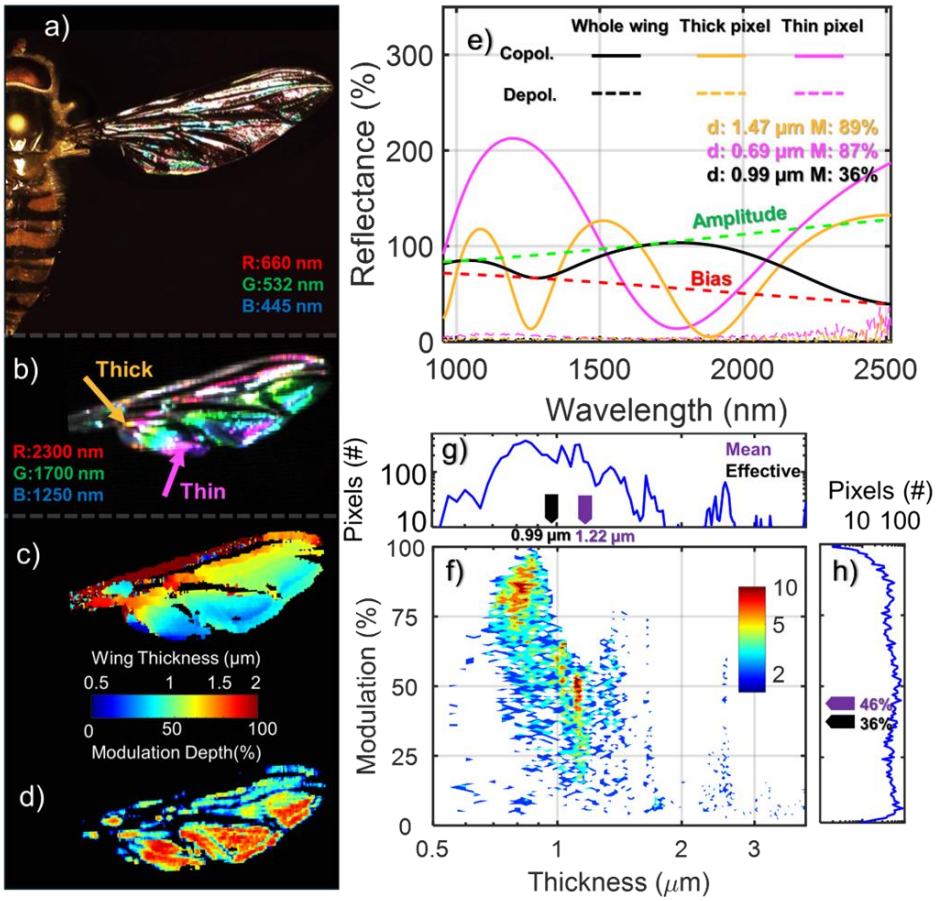


**Fig. 2.19: Characterization of structural coloration in hover fly (*Episyrphus balteatus*) wings**. a) Photograph of a hoverfly wing exhibiting structural coloration. b) False color image highlighting the wing's interference pattern. c) Wing thickness map derived from the interference signal. d) Fringe modulation depth map, revealing variations in the intensity of the interference signal at each wing pixel. e) Example of spectral fringes from thin and thick wing regions, as well as the effective fringe formed by spatially integrating the spectral profiles of all wing pixels within the SWIR hyperspectral camera detection range window. The fringe is weighted by the long and short pass functions to evaluate the heterogeneity of the wing; amplitude *a* and bias *b* are also illustrated in the same figure for the effective fringe. f) 2D histogram depicting the distribution of wing thickness and modulation depth across the wing surface. g, h) Demonstration that the resolved effective thickness and modulation depth are not simply the mean of all thickness or modulation values from the wing.

frequency *f* is directly proportional to the order *m* [132, 156]. Therefore, the fringes occur at regularly spaced frequencies, leading to non-uniform (chirped) spacing in the wavelength domain due to the inverse relationship between frequency and wavelength. As a result, fringes are more closely spaced at shorter wavelengths,

increasing the likelihood of dephasing with neighbor regions in the VIS compared to the SWIR range. Consequently, thicker wing membranes contribute less to the overall modulation of the effective fringe, as seen in Fig. 2.19c and d. While thinner wing regions exhibit higher modulation depths.

The effective fringe, formed by XY spatially integrating the spectral profiles of all wing pixels, has a final appearance determined by the interaction between spectral fringes from areas with varying thicknesses (XZ). When the wing is dominated by thin regions with high modulation fringes, their cumulative contribution results in the effective fringe converging towards the characteristic spectral patterns of these thinner regions. Notably, the effective thickness does not directly correspond to the mean of all wing thicknesses and fringe modulations due to the disproportionate influence of these thinner, highly modulating regions with different thicknesses.

Capturing spectral fringes using lidar is a promising method for performing remote nanoscopy and retrieving wing thickness characteristics from in-flight insects. Wing thickness has been shown in recent studies to be a feasible feature for identifying species, sex, and gravidity (*Papers IX, X, XI, XII*) and is more reliable than modulation spectra [40, 159, 160]. The wing interference pattern and signal are thermally stable [216], and consistent over time [93]. Lidar systems can be implemented with various laser bands. In Paper *XII*, in-flight insect fringes were successfully captured and retrieved wing thickness using hyperspectral lidar with a single flash. Spectral fringes can also be captured with passive lidar systems utilizing sunlight [158, 171, 217]. Additionally, employing several laser bands [88, 169, 170, 218] enables the extraction of biologically relevant nanoscale features, such as melanin content ratio in the body and wings, which can be used for insect identification with dual- or multi-band lidar systems (*Paper V*). If the chosen laser band is resonant with the insect wing's interference fringes, as demonstrated in *Papers I- III*, the degree of flash polarization can be utilized for insect identification. Furthermore, in *Paper XI*, the speed required to capture specular flashes was analyzed, enabling remote nanoscopy for improved insect identification.

# 3.Research Methodology

## 3.1. Hyperspectral camera

Hyperspectral imaging (HSI) is a technique where a camera collects detailed image data across a wide spectrum of light, extending beyond the capabilities of standard cameras, which capture images only in the three specular bands: red, green, and blue. HSI records hundreds of narrow spectral bands across a wide range of wavelengths, from UV [219, 220] to SWIR wavelengths [221, 222].

In remote sensing, satellites equipped with HSI sensors collect detailed spectral profiles [223], enabling the mapping of land cover, tracking changes in vegetation [224], identifying specific minerals based on their unique spectral signatures [225], and estimating water quality [226]. The ability of HSI to differentiate between materials based on their spectral characteristics is also being utilized in medical diagnostics. The spectral reflectance of skin tissues provides a non-invasive method for estimating optical parameters [227] or use as a diagnostic tool [228, 229]. In combination with lidar for tree height identification, the distinct spectral reflectance of different tree species results in accurate identification and classification using HSI [230, 231]. In the field of entomology, intricate details of wing patterns, body pigmentation, and physiological states can be captured and analyzed using HSI for accurate species identification and classification [232].

In all the studies included within this thesis, two different push-broom hyperspectral cameras: a visible-extended InGaAs camera (Norsk Elektro Optikk) with a spectral range of 900-1600 nm and a sterling-cooled HgCdTe SWIR camera (MCT) [221] (Norsk Elektro Optikk) covering 900-2500 nm were used. These cameras collect light through an objective lens, focusing it onto a narrow slit that acts as a spatial line selector. The transmitted light is then collimated and spectrally dispersed by a diffraction grating before being re-imaged onto a two-dimensional focal plane array (FPA). The FPA material determines the spectral range of each camera: for example, Si-CMOS FPAs typically cover 350-1100 nm, InGaAs FPAs cover 900-1700 nm, and HgCdTe FPAs cover 900-2500 nm. Different spectral filtering is also implemented to achieve the desired spectral ranges for specific experiments and to eliminate second-order effects. A fiber-coupled tungsten halogen lamp (Illumination Technologies model 2900) and a standard Philips tungsten bulb were used as light sources, both of which exhibit a blackbody-like spectrum.

Each hyperspectral image forms a 3D data cube, see Fig.3.1, with two spatial dimensions and one spectral dimension. Each camera exposure captures a continuous spectrum (288 spectral bands for the HgCdTe camera, 382 spectral bands for the extended InGaAs camera) for each pixel along the swath width. A complete hyperspectral image is built up over time by scanning the imaging scene. Typically, the camera is fixed in a stationary position, while the sample is placed on a motorized translation stage that moves it across the camera's field of view. This creates a hyperspectral data cube, a 3D dataset consisting of a 2D spatial image at each wavelength.

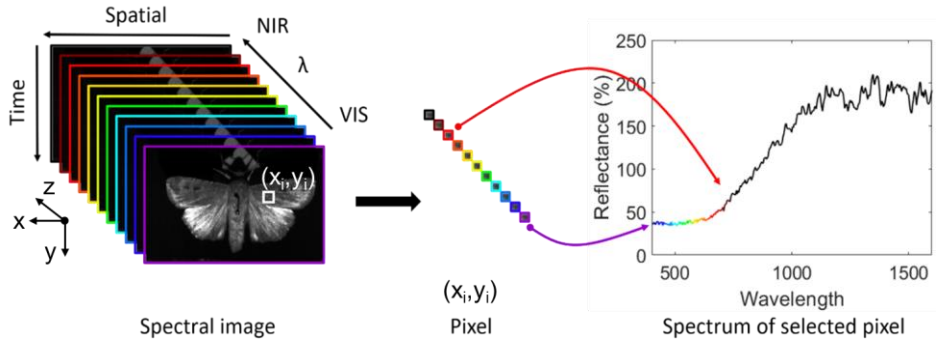


**Fig. 3.1: Detailed hyperspectral data cube of a dried Bogong moth specimen.** Data was acquired using a push-broom hyperspectral camera with an extended InGaAs sensor (450-1700 nm wavelength range). The cube's x-axis represents the spatial distribution, the y-axis represents the line-scan acquisition sequence, and the z-axis represents spectral profiles. Each pixel ($x_i$, $y_i$) contains a full spectrum across contiguous bands. Analysis of a selected pixel spectrum reveals a strong melanin presence in the wing scale, with intensity decreasing towards the infrared region.

Reflectance calibration is necessary due to the influence of factors such as the illumination source's spectral output, grating efficiency, detector quantum efficiency, and the angles of illumination and collection. This is accomplished by converting raw intensity into reflectance using a reference image. A standard Lambertian diffuse surface, typically Spectralon® with 50% diffuse reflectance, is used as the calibration target. However, the calibrated reflectance may sometimes exceed 100%. This is because a potentially specular signal is being calibrated against a Lambertian diffuse reference target, resulting in reflectance values that can exceed the expected range.

The visible-extended InGaAs camera is particularly suited for capturing features like melanin and water absorption bands, providing insights into insect body and wing melanization, thickness, and water content. The extended range into the infrared of the SWIR camera enables the investigation of surface roughness and polarization changes at longer wavelengths.

## 3.2. Polarimetric goniometry

A polarimetric goniometer is used to examine how light interacts with a target, particularly insects, by analyzing changes in light's polarization after reflection or scattering [137]. This involves precise control of illumination angles and detailed measurement of the scattered light, providing insights into the target's optical properties. Using different polarizations helps interpret how an insect's structure alters light polarization depending on the viewing angle.

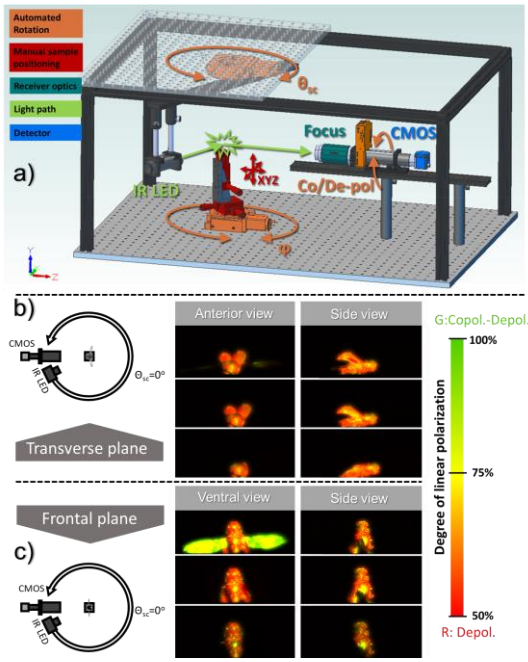


**Fig. 3.2: Polarimetric goniometry analysis of an insect sample under varying conditions.** a) CAD model of the SPOTIG system (image from reference [137]). b, c) Polarization changes in a bark beetle with progressively removed structures (wings intact, wings removed, wings and elytra removed) and viewed from different angles within anatomical planes. Due to the flat wing positioning, high polarization specular reflection is visible only in the frontal plane from ventral or dorsal views.

Two polarimetric goniometers have been developed to study the optical properties of insects. The first, SPOTIG (Spectral Polarimetric Optical Tomographic Imaging Goniometer) [137], features three motorized rotation stages, facilitating the manipulation of polarization filters, the camera, and the target specimen, see Fig. 3.2. This flexible setup provides insights into insect optical cross-sections and how anatomical features with varying optical properties influence lidar signatures. SPOTIG was notably employed to document the optical parameters of bark beetles in *Paper I* in detail, capturing backscattering and extinction cross-sections, along with the phase function, from three anatomical planes. The backscatter optical cross-sections were further parameterized using spherical harmonics to efficiently represent the target's complete features for lidar applications.

Building on SPOTIG's foundation, the BIOSPACE (Biophotonics, Imaging, Optical, Spectral, Polarimetric, Angular, and Compact Equipment) polarimetric

goniometer was created. Constructed primarily from LEGO components to facilitate adaptability and distribution for educational purposes due to its affordability, BIOSPACE boasts adjustable illumination spectral bands achieved through LED multiplexing, enabling the study of polarimetric signatures across diverse wavelengths. Its modular design, having free rotation of the polarization filter and either the insect sample or light source, enhances flexibility in measurement angles. BIOSPACE's wider spectral range and enhanced flexibility compared to SPOTIG have been instrumental in generating comprehensive reference databases of insect optical signatures, particularly through measurements of museum specimens. These findings have been presented in *Papers III, VII, and XI*.

## 3.3. Lidar

Scheimpflug lidar leverages the Scheimpflug principle, a 19$^{th}$-century photographic technique [233, 234], to achieve an extended depth of field. Unlike traditional time-of-flight (ToF) lidar, relying on pulsed lasers [235], Scheimpflug lidar employs one or more continuous wave laser diodes, often multiplexed, and a line sensor to capture backscattered light from an illuminated air volume [169, 236, 237]. Scheimpflug lidar range resolution is achieved through the Scheimpflug criterion and Hinge rule [169, 238], resulting in infinite focal depth where each sensor pixel corresponds to a specific section of the laser beam.

### 3.3.1. Light detection and ranging

Lidar, also known as laser radar, measures distances by emitting pulses of laser light toward a target and measuring the time it takes for the light to return to the sensor [235]. The conventional ToF lidar measurement calculates distances using the following formula:

$$R = \frac{tc}{2n_{medium}} \tag{3.1}$$

Where $R$ is the distance to the target, $t$ is the time difference between the transmitted and received light pulses, and $c$ is the speed of light. The resolution of a lidar system, which determines the level of detail captured in the measurements and the minimum resolvable distance between two objects (range resolution, $\Delta R$), is crucial. Higher resolution systems can distinguish between closely spaced objects and provide more accurate distance measurements [235]. It is calculated using the formula:

$$\Delta R = \frac{\tau_p c}{2n_{medium}} \tag{3.2}$$

where $\tau_p$ is the pulse duration. ToF lidar is used in environmental monitoring (forest mapping [239, 240], biomass assessment [241]), atmospheric science (aerosol

concentration [235, 242], cloud height [243]), and pollution tracking [244]. Recent research comparing ToF and Scheimpflug lidar found them comparable in performance for aerosol sensing [245], with Scheimpflug lidar offering a more cost-effective and simpler solution.

### 3.3.2. Scheimpflug principle

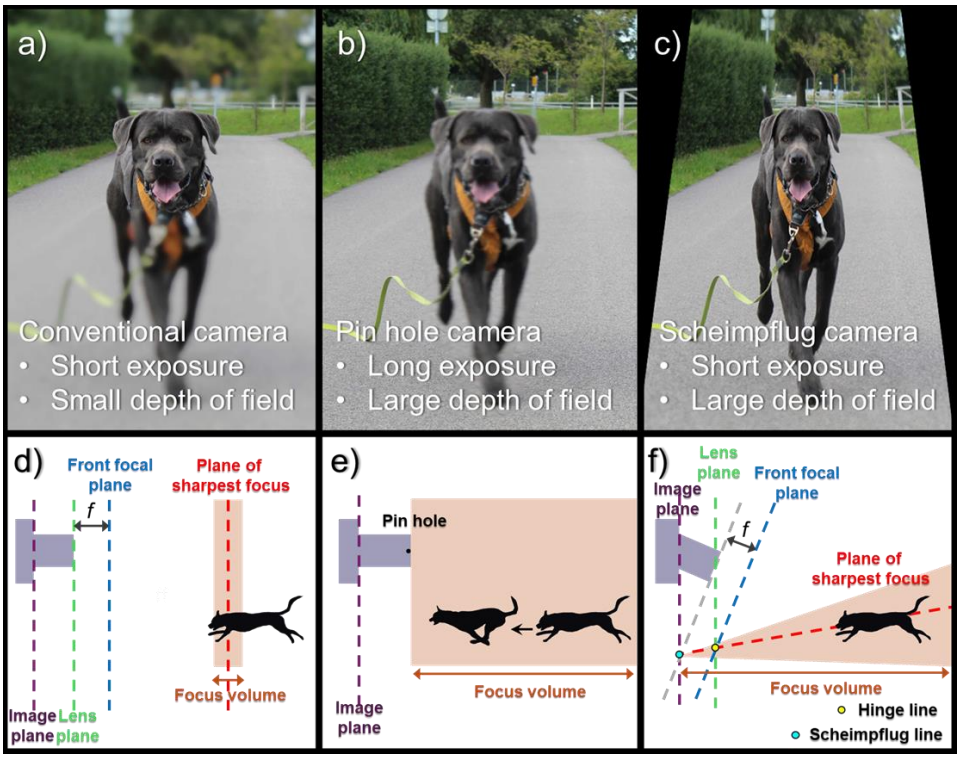


**Fig. 3.3: Comparative focus mechanisms in three different camera systems:** a, d) Conventional camera with limited depth of field; b, e) Pinhole camera with broad depth of field but motion blur; c, f) Scheimpflug camera with extended depth of field for simultaneous capture of near and far objects but with image distortion. Image inspired by work [194].

The Scheimpflug principle, popularized by Austrian Captain Theodor Scheimpflug [234] but discovered by Jules Carpentier [233], provides a unique approach to manipulating depth of field in photography. In conventional cameras, the lens and image sensor are parallel, limiting the range of sharp focus (as shown in Fig. 3.3a, d). Pinhole cameras (Fig. 3.3b, e) offer an extended depth of field due to their tiny aperture but often require long exposure times, causing motion blur. The Scheimpflug principle involves tilting the lens relative to the image sensor (Fig. 3.3c, f). This tilts the plane of focus and results in both near and far objects being in

sharp focus simultaneously. This technique offers greater control over depth of field compared to conventional photography, though it can introduce some distortion. The Scheimpflug principle finds applications in various fields, such as structural displacement monitoring [246].

### 3.3.3. Scheimpflug lidar

The application of the Scheimpflug principle to lidar systems is a relatively recent development [81, 169]. It has been used in atmospheric detection, [170, 191, 238, 247] and flame diagnostics [194], and entomology in insect study [88-91, 126, 154, 237, 248]. Fig. 3.4 illustrates the Scheimpflug condition, which requires the plane of the detector and the plane of the lens to meet at a point on the object plane. The Hinge condition further specifies that the tilted lens plane parallel to the detector, also intersects the front focal plane of the lens at this same point on the object plane. The range $r$ to a target, can be approximated by considering the chip-normalized pixel positions ($p_r$ and $p_\lambda$), the baseline length ($\ell_{BL}$ = 0.814m), the slant angle between the optical axes ($\Phi_{slant}$), and the receiver field of view ($\theta_{FoV}$):

$$\hat{r}(p_r, p_\lambda) = \ell_{\mathrm{BL}} \cot\left(\Phi_{\mathrm{slant}} + \theta_{\mathrm{FoV}} p_r\right) \tag{3.3}$$

This formula is originally from *Paper XII*. For a basic entomological lidar system, such as the one used in *Paper I*, one wavelength band is used and multiplexed to capture both background and laser signal reflections from in-flight insect targets,

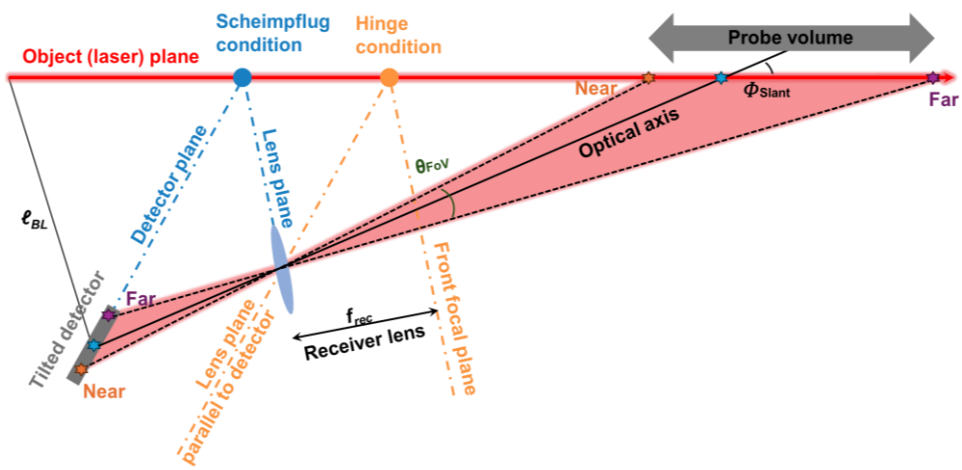


**Fig. 3.4: Scheimpflug and Hinge configuration in an entomological lidar system.** Varying observations along the laser beam are detected at distinct locations on the tilted detector, with each pixel corresponding to a unique distance from the lidar. The figure is based on references [86, 249] with minor modifications.

it measures the backscattered intensity as a function of range and time. This type of lidar data contains information on insect time of detection, range, optical cross-section (in $mm^2$), and apparent size (in mm) [125]. The optical cross-section is calibrated using a fixed target of known distance and reflectance. Typically, a neoprene flat board serves as the lidar termination and is also used for calibration. The insect signal is then calibrated to optical cross-sections based on the neoprene reference. Apparent size, derived from the pixel footprint and telescope magnification, provides an estimate of the insect's dimensions (see detailed explanation in *Paper II*). Captured lidar time series data generally reveal wingbeats of in-flight insects. Power spectral analysis via Welch's method of these modulations provides wingbeat frequency, characteristics, and surface roughness at the illumination wavelength. Depending on the insect body's orientation, the fundamental frequency may not be the strongest signal in the power spectrum [158]. For a detailed discussion of calibration and sizing calculations, see a recent study [89].

### 3.3.4. Backward-lasing with Scheimpflug lidar

Backward propagating lasers in lidar are desirable to circumvent the range attenuation of the signal. This can be accomplished through atmospheric lasing and filamentation. Atmospheric lasing manipulates the atmosphere itself to amplify the returning light signal, offering increased signal strength and longer detection ranges, but requires specific conditions and sophisticated systems [250-255]. Filamentation, using high-intensity femtosecond laser pulses, creates a waveguide in the atmosphere, enhancing sensitivity and probe volumes, but also necessitates complex and expensive technology [256-258]. By capturing the specular reflections from flat membranes, it is possible to achieve "backward-lasing" from atmospheric insects. The lasing approach based on optical breakdown in the medium is not feasible for insect monitoring as it is destructive. The use of flat targets presents a simpler and more practical approach to backward-lasing. This method involves directly reflecting the outgoing laser beam backward off a flat surface, maintaining its collimation, polarization, and phase while propagating in the backward direction [98, 259, 260]. This approach has found applications in gas sensing [261] and has been instrumental in achieving the longest lidar-ranging distances [262]. Snowflakes [259, 263] and insect wings [247] are naturally occurring structures that act as flat targets for lidar. The reflective properties of insect wings can be optimized by selecting a laser wavelength that resonates with the wing thickness or aligns with a specific infrared spectral band where the wing surface is most specular and reflective. This approach enhances insect wings' reflectivity for lidar systems, leveraging their natural flatness for coherent backscatter and polarization analysis. This enables specularity estimation, remote nanoscopy via thin-film interference, see *Paper XII*, and enhanced flatness in the infrared.

### 3.3.5. Polarization lidar

Polarization lidar was first developed for atmospheric studies utilizing a linearly polarized pulsed laser to distinguish between ice and water clouds [264]. Due to their spherical shape, liquid water drops preserve the polarization of backscattered light, only changing its propagation direction. In contrast, non-spherical ice crystals induce a change in the polarization of the backscattered light through multiple scattering events. By analyzing the polarization of the backscattered light, the lidar can thus effectively differentiate between ice and water clouds [265]. This technology has since found further applications in atmospheric research [191, 263, 266] and ecological studies [192, 193, 267].

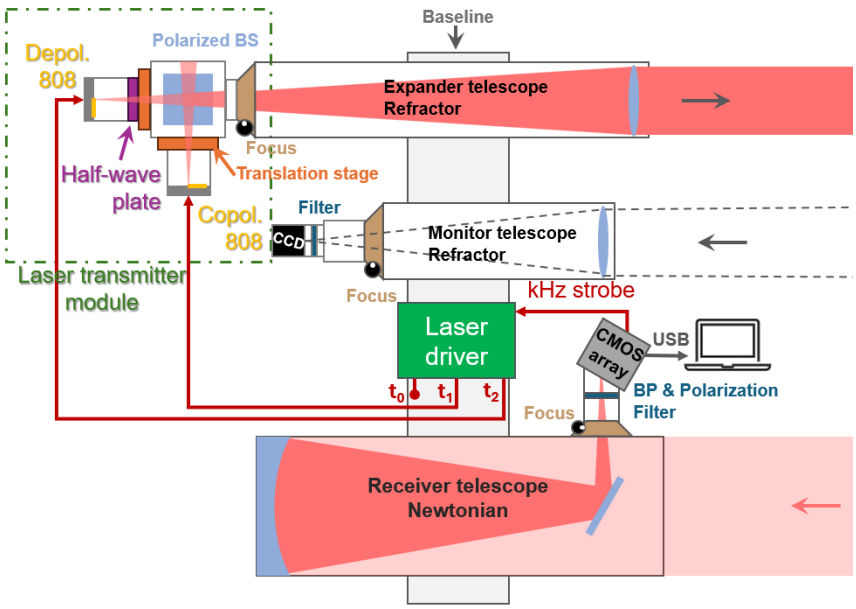


**Fig. 3.5: Schematic of a polarization lidar, showcasing the key components and their function.** The laser transmitter itself is integrated with two 3W TE-polarized 808 nm laser diodes. One of these laser beams is then rotated 90 ° using a wide-angle polymer half-wave plate. A polarization beam splitter combines these beams for transmission. Backscattered light is collected and passed through a polarization analyzer, separating the orthogonal components for detection and subsequent analysis of the target's de-polarization characteristics. Figure inspired by lecture slide from Biophotonics course and reference [194].

Polarization lidar for insect study (an example of the schematic is shown in Fig. 3.5) utilizes a laser module with two polarized laser diodes multiplexed into de-polarized, co-polarized, and background bands. The receiver telescope projects the collected light through a linear polarizer onto a linear detector array, enabling analysis of the backscattered light's polarization. As previously discussed, the DoLP observed in the backscattered signal from insect is influenced by several factors,

including the location of light scattering on the insect [98, 137], absorption of light by melanin, blood, or water [120, 174], and scattering effects related to the insect's body size and the influence of gravidity [94]. The differences in polarization signatures in lidar observations are effective in separating glossy wing and diffuse wing signals, as shown in *Paper II-IV*, the dependence of signal range on flash coherence and the frequency content of specular flashes was investigated, knowing that de-polarized incoherent scatter attenuates by the squared range. The findings demonstrate that the glossiness of an insect's wings directly impacts how easily it can be detected using lidar. The most detailed information about wing glossiness is obtained by analyzing the harmonic content within the co-polarized power spectra.

The polarization characteristics observed in lidar signals can be compared to a reference library of polarization signatures associated with specific insect species. This library, as demonstrated in *Papers III*, *VII*, and *XI*, can be generated using BIOSPACE scans by analyzing the varying scattering profiles produced when wavelengths and polarization are adjusted. By comparing lidar signals to this established reference library, it is possible to identify insect species in the field. This database should store quantitative data in SI units to ensure compatibility and enable meaningful comparisons across different instruments and research groups. This approach fosters an accurate understanding of light scattering from insects and allows retrieval of quantitative measures in metric units, ultimately aiding in insect species identification.

### 3.3.6. Dual-band lidar

Previous research has demonstrated the feasibility of retrieving kHz modulation wingbeat from free-flying insects and simultaneously retrieving dual-band signals [159]. This has enabled the separation of mosquito species and sex based on dual-band signatures. Other optical sensors using dual wavelengths have also proven effective in separating insect species [51, 162, 163]. Building upon this concept, dual-band lidar was developed and has proven valuable in various fields, including atmospheric [170, 268] and ecological research [88].

A typical dual-band lidar system, similar in configuration to polarization lidar but with a modified laser transmitter module [88], transmits superimposed laser beams at 808 nm and 980 nm with multiplexing (Fig. 3.6). Dual-band illumination enables estimation of insect melanization and wing thickness. By analyzing differences in backscattered light due to both differential absorption and thin-film interference, increased diffuse reflectance at the longer wavelength is correlated with a higher

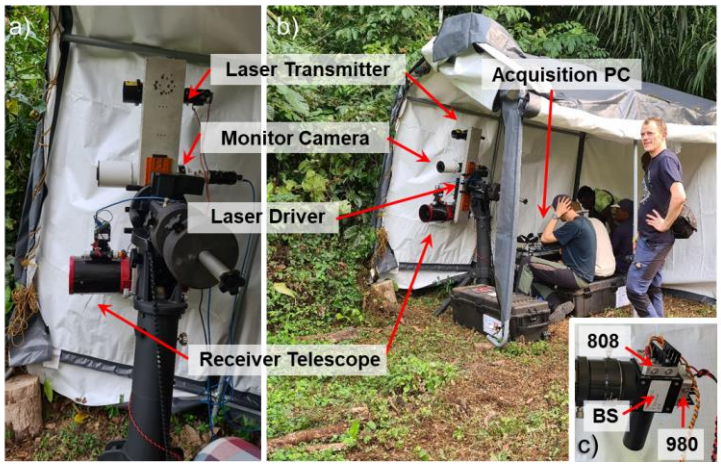


**Fig. 3.6: Photos of a dual-band lidar.** a-b) Lidar system and its components. c) Laser transmitter module; in this instance, there is no half-wave plate since no altering the polarization plane. Instead, combining a 980 nm and 808 nm laser beam together. BS: beam splitter.

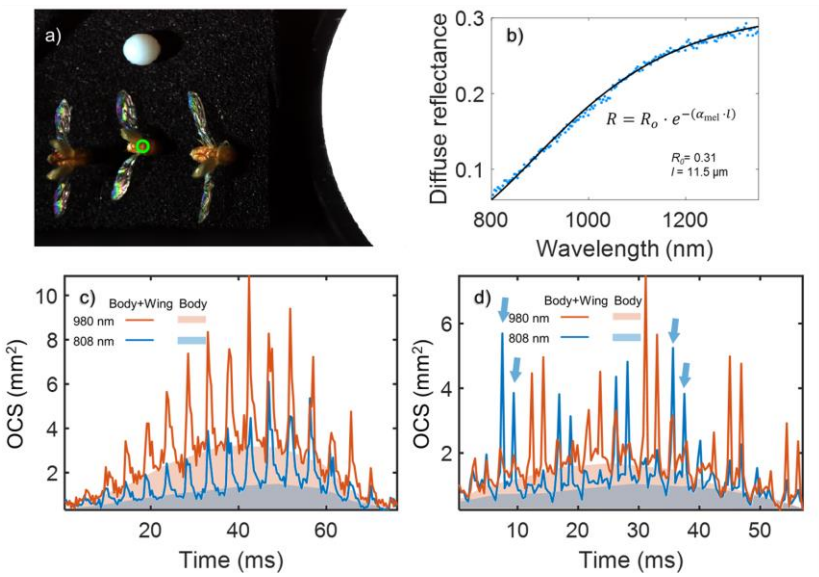


**Fig. 3.7: Diffuse reflectance from a dried bark beetle abdomen, showcasing variations in wavelengths and their impact on insect specificity.** a-b) Reflectance dips before 1200 nm indicate melanin presence, with a model provided to show melanin path length at the chosen pixel. c) Generally observation using dual-band LiDAR demonstrates that 980 nm is less affected by melanin, thus providing a stronger signal for body and wing analysis compared to 808 nm. d) Specific instances where the 808 nm wing signal exceeds that of 980 nm during certain wingbeats, indicating wing membrane resonance with 808 nm, a crucial clue to insect specificity.

degree of melanization [104], and wavelength-dependent variations in the intensity of specular flashes provide insights into the insect's wing thickness. An example of Dual-band lidar observations (Fig. 3.7) reveals that the 980 nm wavelength, being less absorbed by melanin, generally results in a stronger lidar signal from both the insect's body and wings compared to 808 nm. However, Fig. 3.7d shows that during certain wingbeats, the 808 nm wing signal surpasses that of 980 nm, suggesting that the wing membrane resonates more with the 808 nm wavelength at specific roll pitches. The varying response between 808 and 980 nm during different wingbeats highlights how wing structure, such as wing thickness, influences wavelength-specific interactions, potentially enabling more accurate species-specific identification.

### 3.3.7. Hyperspectral lidar

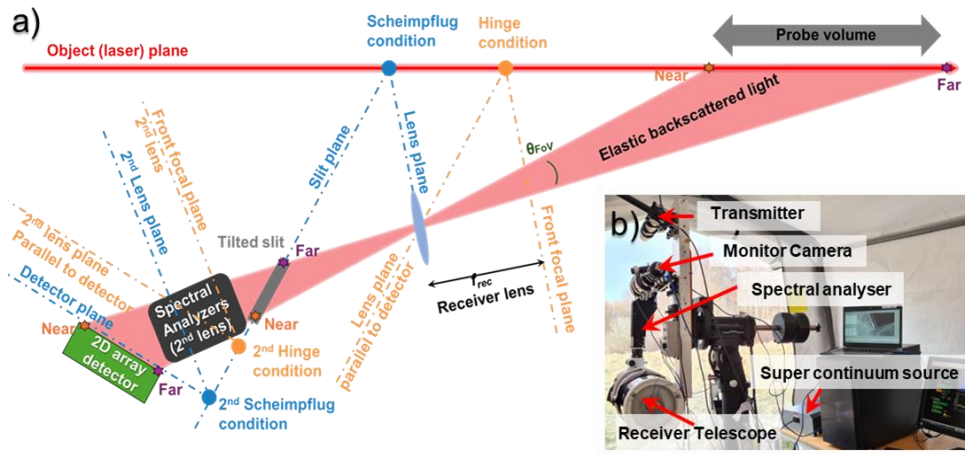


**Fig. 3.8: Example of Elastic Hyperspectral Scheimpflug Lidar (EHSL).** a) Scheimpflug and hinge conditions were applied twice on a hyperspectral lidar. The figure is based on references [86, 249] with minor modifications. b) Photo of the EHSL setup.

Hyperspectral lidar offers detailed spectral profiles across numerous narrow bands. With the capability to operate across various wavelength ranges, including visible (VIS) [172, 230, 269], NIR [231], and SWIR [231], hyperspectral lidar has found diverse applications. In environmental monitoring, for instance, hyperspectral lidar has been utilized for remote sensing of vegetation or forests [230, 231, 270]. Additionally, it is also used to differentiate rock in geological studies and mining operations [271, 272]. Beyond terrestrial applications, hyperspectral lidar has also extended its reach to aquatic studies [172]. Other promising applications involve monitoring powder-tagged insects, where the fluorescence of an applied powder is measured [273], and induced fluorescence [274-276].

Existing hyperspectral lidar systems typically offer around 8 spectral bands and a detection range of 20 to 30 meters [270, 272], providing valuable insights into the composition of objects and environments. A new hyperspectral lidar system (*Paper XII*) has been developed that utilizes 64 bands and achieves a detection range of up to 100 meters. The 100 meters range limitation is due to the test site meadow size, not the lidar system itself. *Paper XII*'s hyperspectral lidar system (Fig. 3.8) achieves spectral dispersion and maintains focus across scene depth and the SWIR spectral range by applying Scheimpflug and hinge conditions twice. The object plane is projected onto a tilted entrance slit, then dispersed light is projected onto a tilted 2D array detector. The system uses a supercontinuum light source with a long-pass filter to minimize insect disturbance. This unique combination of lidar and hyperspectral imaging enables the collection of detailed spectral reflectance and interference signals (Fig. 3.9) from insects, showing the potential for remote identification of insect species and advancing entomological research through remote insect studies.

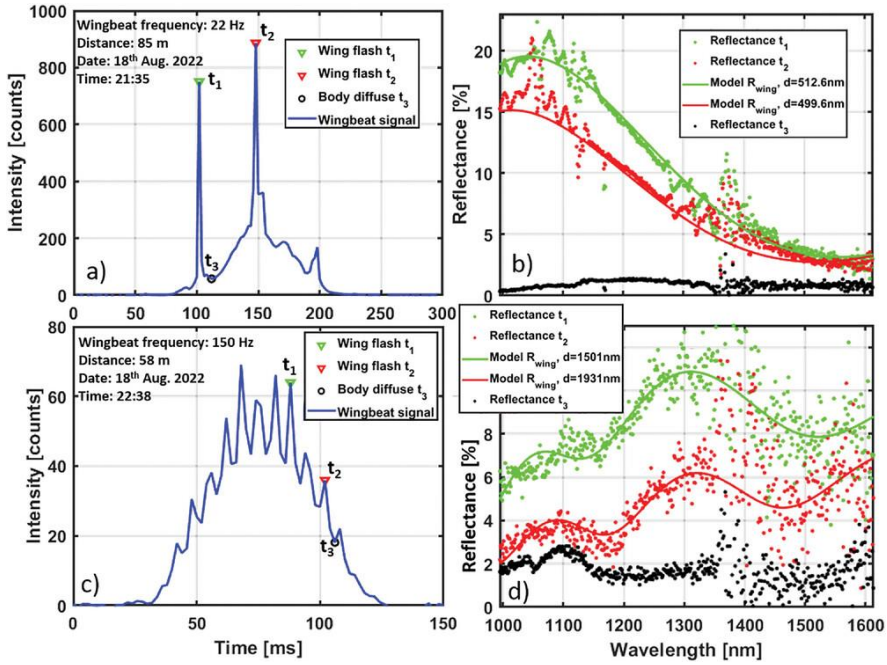


**Fig. 3.9: Hyperspectral lidar signals from free-flying insects (figure originally from *Paper XII*).** a) Large insect (85m): spiky waveforms, glossy wings, precise fringe model fit. b) Spectral reflectance with fringe model fit. c) Smaller insect (58m): less precise fringe model fit. d) 430 nm fringe difference.

# 4.Computational data processing

## 4.1. Scheimpflug lidar data analysis

### 4.1.1. Raw data visualization and initial signal identification

Entomological lidar offers flexibility for various upgrades or adjustments. It can be adapted to operate in various modes, including polarimetric, dual-band, multi-band, fluorescence, or hyperspectral. To illustrate lidar data processing, this section is focused on polarization lidar data only. Note that lidar settings are also highly customizable, the camera exposure, lines of exposure, offset, and laser module choice can all be adjusted [88, 169, 170, 236-238, 245]. Therefore, it is important to maintain careful documentation of these settings.

In polarization lidar, the laser alternates between de-polarization, co-polarization, and background modes. The lidar was set to capture 30,000 exposure lines per file. Each file takes approximately 4 seconds to record and reaches 120MB in size (sampling frequency at 9kHz). Continuous 24-hour data collection would generate approximately 2.47 TB of data. Given this volume, an initial overview of the data is crucial to monitor data quality. To create this overview, plots are generated that color-code the maximum de-polarized, co-polarized, and background readings within each file. These plots offer insights into temporal and spatial variations in insect presence (appearing as bright green dots) while also revealing atmospheric changes, such as increased cloud echoes under humid conditions.

Consider frame 3991, recorded on June 6, 2022, at 22:46:08 (Fig. 4.1a). Zooming in on this timeframe (Fig. 4.1b) shows distinct signals (later classified as insects) along with persistent aerosol plumes (clouds). Fig. 4.1c details intensity counts for this frame, including pixel-wise median and maximum values. Insect signals are isolated using a threshold defined as the median plus five times the interquartile range (IQR), or SNR=5. This SNR ratio is configurable, but it has proven effective for visually highlighting insect observations while suppressing cloud/mist signals. Fig. 4.1d illustrates how the threshold adapts based on each pixel's median and IQR, for separation of rare, localized events (insects) from continuous aerosol signals.

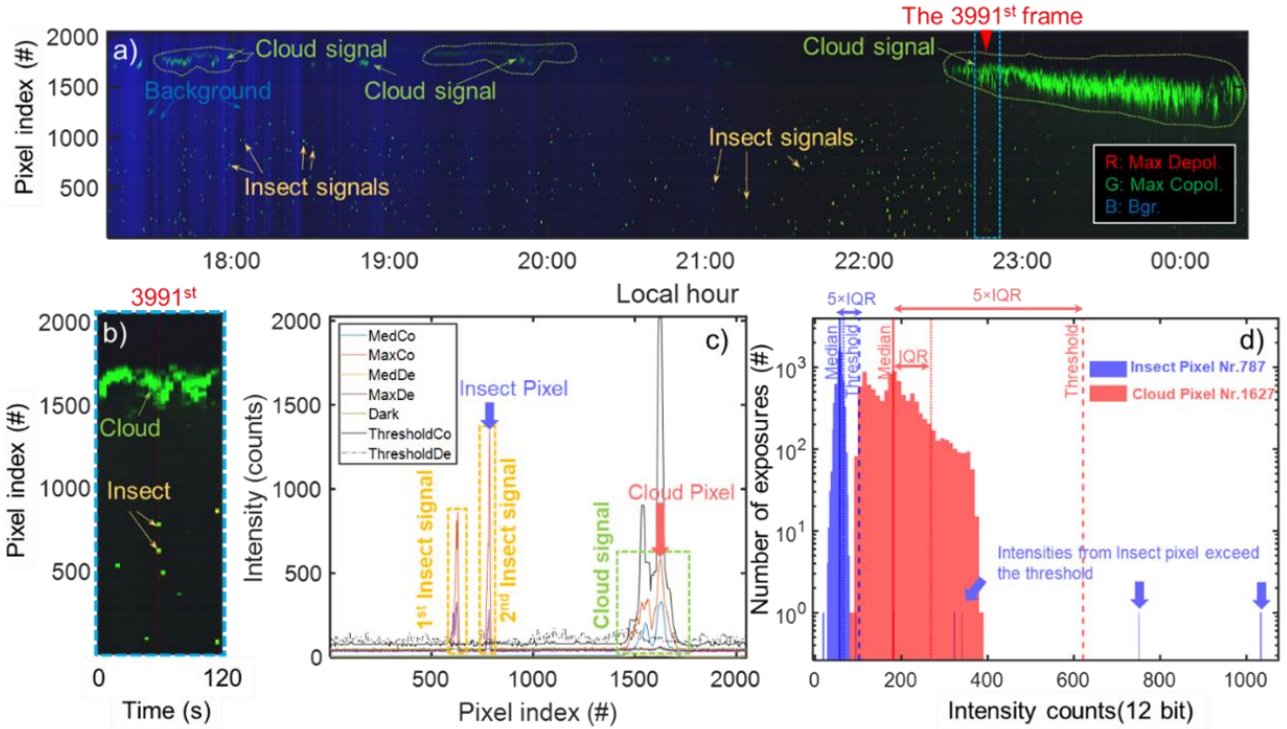


**Fig. 4.1: Time-range overview map of the evening of June 6, 202.** The map is color-coded to represent the maximum values of de-polarized signal, co-polarized signal, and background for each pixel in 4-second intervals. A zoomed view focuses on the time range around frame 3991. The intensity distribution on frame 3991 reveals two insect signals exceeding the SNR=5 threshold (5 times the IQR of the histogram), distinguishing them from cloud signals and leading to their exclusion. Finally, one insect pixel and one cloud pixel from frame 3991 illustrate the recorded values and demonstrate the thresholding process.

### 4.1.2. Observation extraction

When visualizing frame 3991 around one of these observations (Fig. 4.2a), the raw data reveals stripes due to the lidar laser's multiplexed operation. This cycling of de-polarized, co-polarized, and background modes is illustrated in Fig. 4.2b. The data was extracted for each band. The insect observation appears as shown in Fig. 4.2c-e for the different bands. After acquisition, background subtraction was performed on both the co-polarized and de-polarized signals (Fig. 4.2c, d). To isolate insect signals from noise, a detection threshold was applied, retaining only signals with an SNR of 5 or higher (Fig. 4.1d and 4.2f). Finally, the insect signals were isolated and cropped using methods detailed in previous work [125].

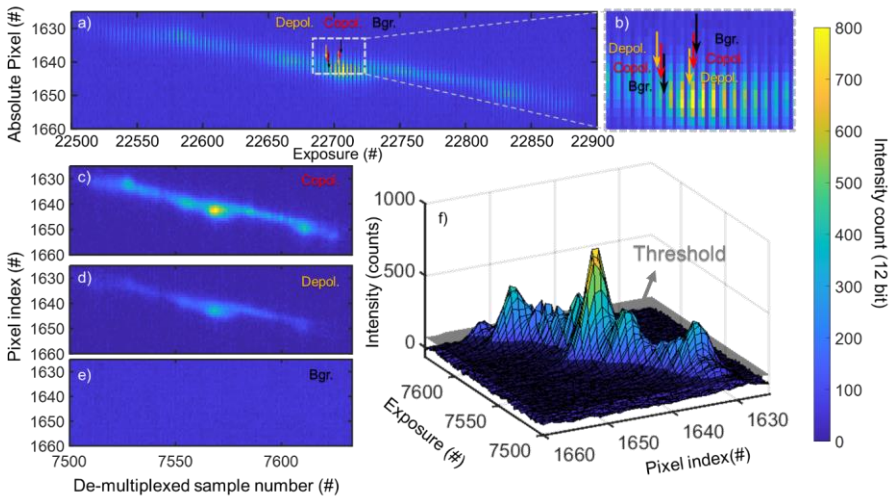


**Fig. 4.2: Illustration of raw data acquisition and processing.** a) and b) show the raw data captured with the laser multiplexed to de-polarized, co-polarized, and background bands. c) and d) depict the subtraction of de-polarized and co-polarized signals from the raw data, respectively. f) shows the detection mask applied to retain only signals exceeding a defined threshold of SNR=5, effectively isolating insect signals from background noise.

The data shown in Fig. 4.2f is presented as a 2D false-color image in Fig. 4.3a. This visualization employs color coding to differentiate signals: red represents de-polarization, green signifies co-polarization, and blue indicates background. This approach enables the observation of the insect's movement and heading direction within the brief period captured by the lidar. The height and apparent size of the insect were derived using lidar processing methodologies established in previous work [89, 125]. Fig. 4.3c sums all intensity pixels from Fig. 4.3a, revealing the insect's wingbeat pattern. For further calibration of the optical cross-section ($mm^2$), a reference target range and its corresponding optical cross-section is required. A

base calibration method involves placing a flat neoprene board in the lidar beam to serve as a reference target and termination.

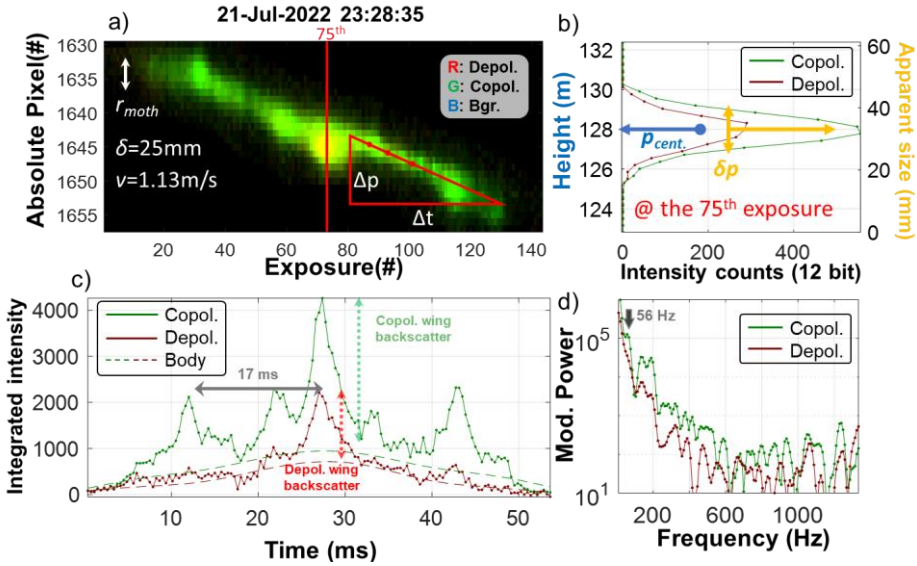


**Fig. 4.3: An example of an insect observation obtained using polarization lidar technology (figure originally from *Paper II*).** a) A false-color spatiotemporal display showcases the insect's presence. b) A single-camera exposure highlights the insect echo. c) The time series for both polarization bands reveal an oscillatory component due to wing movement, along with a biased envelope caused by the insect's body. d) The corresponding power spectrum identifies the fundamental frequency as the highest tone in this specific observation.

### 4.1.3. Hierarchical clustering & biodiversity assessment

Entomological lidar, while highly effective at quantifying insects passing through its laser beam [87, 89, 125, 277], faces challenges in associating these echoes with specific, verified taxa. This difficulty is similar to the challenge of identifying insects exclusively by their WBFs, as various factors can influence an insect's flight orientation and WBF. Both environmental conditions (temperature [43-45], humidity [45, 46]) and individual insect characteristics (age [47, 48], weight loading [49, 50]) can influence WBFs. These variations can lead to misidentification, as different insects may exhibit similar oscillatory signals and be grouped together, or the same insect may be identified as a different species due to changes in its WBF in response to environmental factors.

Despite these limitations, field data analysis using unsupervised hierarchical cluster analysis (HCA) reveals numerous distinct signal types [51, 87, 92, 277]. It is

anticipated that a diverse insect assemblage would exhibit a similarly diverse range of signals, whereas a less diverse group would display fewer distinct signals. This deterministic approach, previously applied to photonic sensors and lidar [51, 87, 93, 287], has successfully grouped observations into many groups of clusters. Some of these clusters have been associated with specific insects, like male and female mosquitoes [87, 277]. While a perfect match between the number of clusters (NoC) and species richness is unlikely, an increase in NoC is generally expected as species richness increases. A study [51] found a 67% correlation between photonic-sensed insect signals and insect families identified in Malaise traps, and the algorithm estimated higher insect diversity than was revealed by family-level trap identifications. However, malaise trap catches vary significantly depending on deployment location and time, potentially capturing vastly different species and resulting in poor correlation between individual deployments [34], suggesting that the limitations of the Malaise trap itself may be hindering a more accurate assessment of insect biodiversity.

HCA is well-suited for lidar data due to its ability to handle inconsistencies and group data points based on relative similarities rather than absolute distances or predefined labels [278]. By analyzing the power modulation spectra and calculating pairwise similarities using Euclidean distances [279], HCA organizes observations into a hierarchical structure ($Z$). This structure serves as a foundation for deriving clusters by setting distance thresholds or specifying the desired number of clusters. This approach enables the exploration of natural groupings within the data, aiding in the determination of distinct signal types representing different species based on their unique power modulation spectra.

An example of how this method was applied is described below. The data used in the following examples is from an unpublished study related to dual-band lidar signals (*Related Work B*). In this experiment, a dual-band lidar system was deployed to measure the population and diversity of a Swedish meadow over three consecutive days. To minimize bias and provide a negative control for biodiversity assessment, background noise captured by the lidar system was processed in the same manner as the lidar signals themselves, see Fig. 4.4. Both the lidar data and noise were normalized and compensated for slope using the data processing pipeline described in [92]. The number of compensated clusters exceeding the threshold provides an estimate of the number of species/clusters. To calculate compensated clustering, we employ a multi-step process involving the Pwelch method, logged Euclidean distances, and median slope detrending. The detailed formula and implementation can be found in the reference [92]:

$$NoC = \sum_{p}^{N-1} \left[ Z_{\text{comp.(p)}} > \left( \left| Z_{\text{comp.(p)}} \right|_{\text{median}} + \left| Z_{\text{comp.}(p)} \right|_{IQR} \right) \right] \qquad (4.1)$$

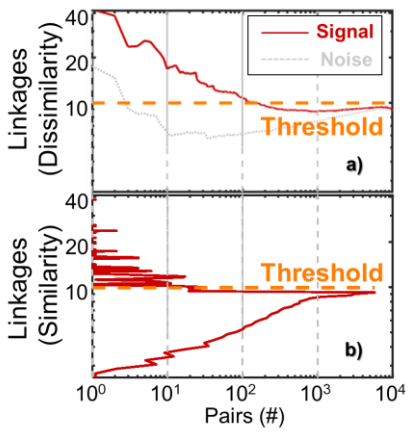


**Fig. 4.4: Determination of optimal linkage threshold for biodiversity search**. a) The relationship between the number of sample pairs and their corresponding compensated linkage distances, with an emphasis on dissimilarity. b) Histogram depicting the frequency distribution of linkage Z values. The vertical threshold line highlights the cutoff for significant Z values.

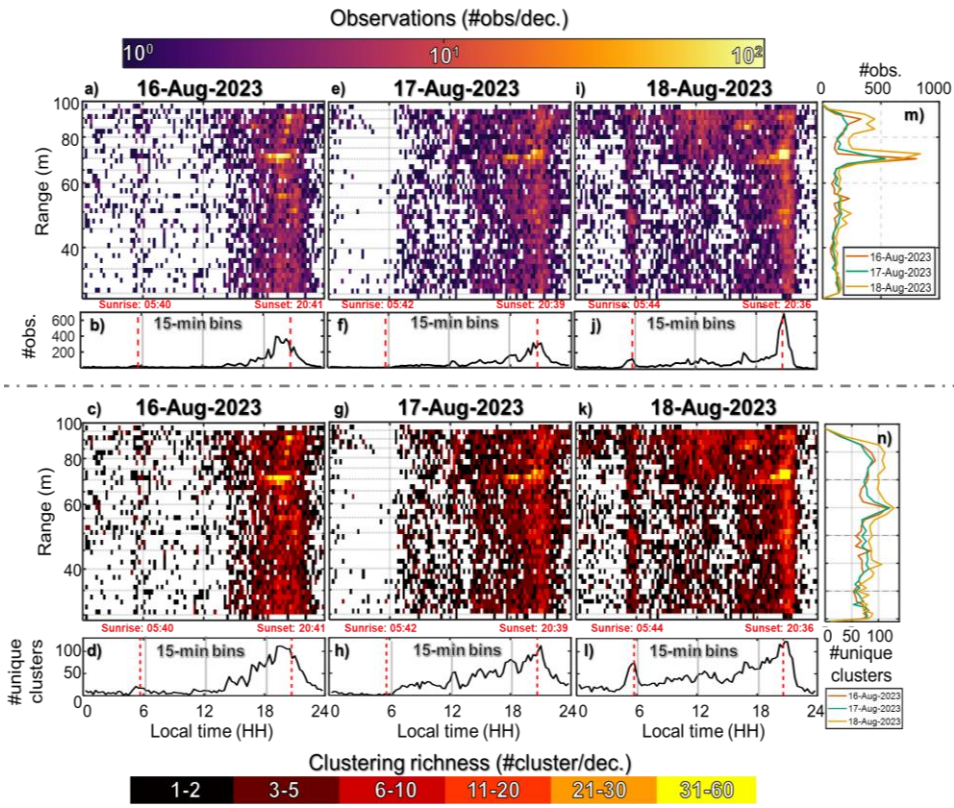


**Fig. 4.5: Spatiotemporal patterns of insect activity and biodiversity across the experimental period.** Heatmaps a, e, i) illustrate the spatial and temporal distribution of insect activity based on lidar observations for each experimental day, with brighter colors indicating higher activity levels within 15-minute intervals. Line graphs b, f, j) depict the overall temporal pattern of insect activity throughout each day. Heatmaps c, g, k) reveal

the variation in insect biodiversity across the three experimental days, with each decade representing the number of unique insect clustering groups within specific time and range intervals. Line graphs d, h, l) illustrate the overall temporal variation in biodiversity throughout each day. A combined line graph m) displays the total lidar-detected insect counts across the entire transect for each day, highlighting areas of higher abundance. Finally, a line graph n) shows the variation in biodiversity across the entire transect for each day, illustrating differences in group activity with respect to range.

The analysis of insect biodiversity in a Swedish meadow over three consecutive days reveals intriguing patterns in insect activity, species richness, and spatial distribution. Utilizing equation 4.1, a total of 153 unique insect species was estimated to present across the three days of observation. Heatmaps (Fig. 4.5) illustrate distinct patterns in insect activity and diversity distribution throughout the day and across different spatial zones within the meadow. Notably, the 60-100 meter range consistently demonstrated high insect activity, suggesting this area may offer favorable conditions or resources for insect populations.

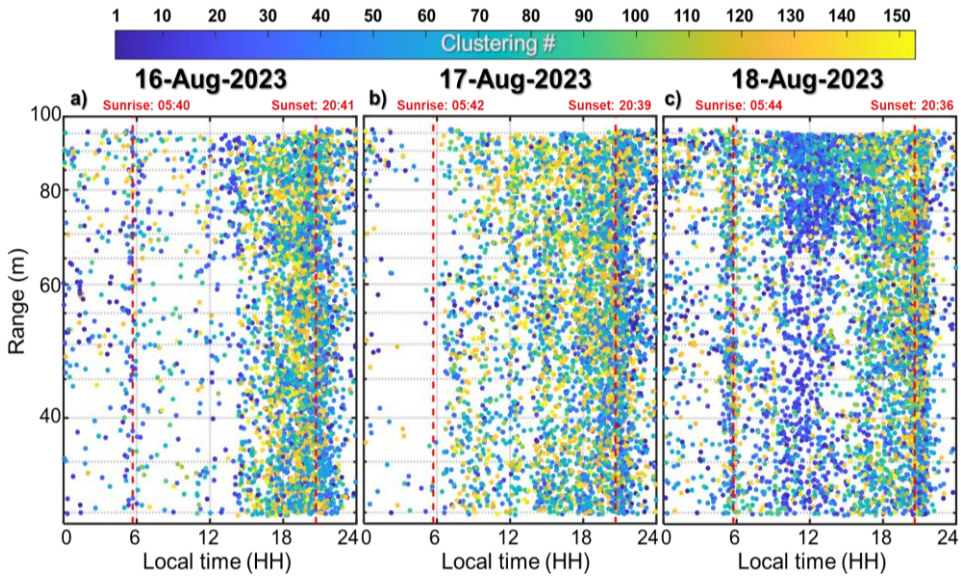


**Fig. 4.6: Temporal and spatial distribution of clustering groups.** Different colors represent distinct clusters

Additionally, specific clustering groups exhibited unique preferences for particular time intervals and spatial ranges, with some groups exclusively active in the late afternoon and evening, see Fig. 4.6. These findings highlight the complex dynamics of biodiversity within ecosystems and emphasize the value of advanced remote sensing techniques to visualize population and diversity distribution, enabling the possibility to correlate species distribution with habitat characteristics, activity patterns, and resource availability.

## 4.2. Hyperspectral data analysis

### 4.2.1. Reflectance calibration of hyperspectral image

The unprocessed spectral data acquired by a hyperspectral system is influenced by several instrumental factors. These encompass the spectral irradiance of the illumination source, the diffraction efficiency of the grating, the quantum efficiency of the detector, and the specific geometries of illumination and collection. Calibration using known reference standards is required to compensate for these effects. Reflectance calibration is performed using an equation derived from measurements of the sample, dark current, and a white reference. The dark current, measured in the absence of light, is important for subtracting electronic noise. In hyperspectral cameras with integrated shutters, the equation often simplifies to (Fig. 4.7):

$$R_{(y,\lambda)} = \frac{I_{S_{(y,\lambda)}}}{I_{W_{(y,\lambda)}}} \tag{4.2}$$

The choice of reference material is important. Both Teflon (approximately 99% reflectance) and a Lambertian gray Spectralon® references are good options. Note that calibrating a specular surface against a diffuse reference can result in reflectance values exceeding 100%.


**Fig. 4.7: Hyperspectral scan scenario where the sample and reference are placed on the same plane.** This configuration ensures close pixel-by-pixel matching between the camera's Y pixels and the reference.

### 4.2.2. Effective fringe and membrane thickness

Earlier discussions established that clear insect wings produce fringes due to thin-film interference. This phenomenon was elaborated upon using equations introduced in chapter 2; resonance backscatter conditions were addressed by equation 2.27, and non-resonance conditions by equation 2.29. Furthermore, each

fringe was described through equation 2.30 in conjunction with the Fresnel equations (equation 2.23) and the refractive index of chitin (equation 2.19). The method of modulation for each fringe was characterized by a formula where $R$ represents measured reflectance, $F$ signifies the computed fringe, $\lambda$ is the wavelength, $\sigma_\lambda$ denotes the standard deviation in the spectral domain, and $\mu_\lambda$ is the spectral mean value,

The model in equation 2.30, $F\ (\lambda,\ d_{pix})$ was used to calculate fringes based on membrane thickness $d_{pix}$. Fringe modulation was estimated using equations 2.31 and 2.33 (see equation 2.19 for examples from thick, thin, and effective thicknesses). To do this, 1000 fringes with realistic membrane thicknesses (ranging from 350 nm to 4000 nm as used in *Paper X*) were computed to ensure accurate numerical fitting within the limits of the hyperspectral camera's spectral range (950 nm to 2500 nm as used in *Paper X*). To model fringes across entire wings (including those with single thickness, $d_{wing}$, the function $F\ (\lambda,\ d_{pix})$ from equation 2.30 was expanded into equation 4.3. The measured fringes, $R_\lambda$, were compared with computed fringes, $F\ (\lambda,\ d_{pix})$, using the correlation coefficient $C$ and quality parameter $Q$. Taking derivatives of Q helped disregard slopes and squared factors that could introduce calculation complexities. Finally, this model was applied to each wing pixel to determine membrane thicknesses and modulation depths, for example fringes.

$$C(R,F) = \frac{\int_{0.95}^{2.5}\left(F_{\lambda,d_{pix}} - \mu_\lambda\left(F_{\lambda,d_{pix}}\right)\right)\left(R_\lambda - \mu_\lambda(R_\lambda)\right)}{\sqrt[2]{\int_{0.95}^{2.5}\left(F_{\lambda,d_{pix}} - \mu_\lambda\left(F_{\lambda,d_{pix}}\right)\right)^2 \partial\lambda \int_{0.95}^{2.5}\left(R_\lambda - \mu_\lambda(R_\lambda)\right)^2 \partial\lambda}} \tag{4.3}$$

$$\mathrm{Q}\left(d_{\mathrm{pix}}\right) = C(R,F)\left(C\left(\frac{\partial R}{\partial\lambda},\frac{\partial F}{\partial\lambda}\right)\right)^2 \tag{4.4}$$

This enhanced model accounts for fringe modulation behavior, which increases with infrared wavelengths and decreases with visible wavelengths. Long-pass and short-pass functions were used to model modulation amplitude and bias. Parameters such as amplitude $\alpha$, bias $\beta$, and heterogeneity $\lambda_0$ were fitted numerically across all recordings, ultimately parameterizing the fringe into just four values.

# 5.Conclusions and Outlook

This study builds upon advancements made during campaigns at the HySpex hyperspectral camera lab. We have conducted several field campaigns using entomological Scheimpflug lidar, progressively enhancing the system's capabilities with each endeavor. The development and validation of the polarimetric kHz lidar system enhances measurement specificity while preserving lidar's inherent ability to provide precise temporal and spatial information on detected insects. The introduction of dual-band lidar has proven invaluable in assisting with insect identification, leveraging the relationship between backscatter signals with insect membrane thickness and degree of melanization. Furthermore, the recent advancement in hyperspectral lidar technology has enabled detailed spectral analysis of insect membrane characteristics. This technology also captures detailed temporal and spatial data while still allowing for the detection of wingbeat patterns.

After examining thousands of specimens, we discovered that features such as membrane thickness, surface roughness, and polarization hold the potential for accurately identifying species and sex across diverse insect groups. Moreover, variations in melanin, chitin, and water content were found to enhance the capabilities of photonics-based systems to distinguish between gender, species, and life stages of insects.

Building upon these findings, we developed a novel, unsupervised biodiversity assessment algorithm that utilizes lidar data. Similar to acoustic indices used in ecological research, this algorithm clusters signals based on similarity, eliminating the need for a training dataset. This innovative approach enables rapid, large-scale biodiversity assessment and provides preliminary estimates of species richness without the need for time-consuming species identification. However, the accuracy of these estimations is contingent upon the algorithm and lidar instrument's ability to differentiate between the expected number of groups within a given habitat. If this criterion is not met, the accuracy of the richness estimation will be limited by the capabilities of either the algorithm or the instrument itself. The prerequisite for species differentiation is that differences in physical properties exceed within-species variation. We have established this to be true and have successfully extracted multiple quantitative micro-features from free-flying insects. This confirms that this approach can accurately and efficiently assess biodiversity using lidar technology.

Our work on the 'Farfetched Flatness' of rough-surfaced wing insects like brown moths has demonstrated the capability of longer wavelengths to enhance backscatter signal strength, effectively minimizing the loss of specular reflection caused by surface features like wrinkles, scales, and refractive gradient, potentially broadening the use of long wavelengths in ecological studies for insect detection. The future could benefit from a much larger database that utilizes tools like BIOSCAPE to augment lidar observations with scanned species data based on spectral and polarization properties. This could be achieved through parallelization, citizen science initiatives, and engaging high schools in data collection [280]. The collection of quantitative optical properties data of insects in standardized metric units is essential for building universally applicable and interpretable entomological databases.

Advancements in entomological lidar, combined with spectroscopy and polarimetry, offer transformative potential for insect identification and monitoring. This technology provides detailed insights into insect behavior and ecology, leading to improved strategies for pest control, pollination, and disease prevention. Ultimately, gaining a deeper understanding of insect populations and their interactions with the environment promises a more sustainable future.

Looking ahead, several promising directions for this research are evident. One such direction is to enhance the lidar system's capabilities by exploring the use of carefully selected laser bands to resolve insect wing thickness, potentially eliminating the need for complex setups like supercontinuum light sources. Furthermore, incorporating DNA sampling [65-67] along the lidar beam path could validate the lidar index monitor changes in insect abundance and diversity and be more cost-effective. This will enable the assessment of the correlation between captured insect species richness and lidar data, providing valuable insights into ecological dynamics. Additionally, integrating lidar with machine learning algorithms [55, 281, 282] has the potential to expand its applications in long-term ecosystem monitoring.

In the field of sustainable agriculture, lidar technology could prove invaluable. By assessing biodiversity changes under different farming systems, it could revolutionize landscape management practices. Similarly, in forestry, lidar could be utilized to monitor pest populations and their ecological impact, leading to more effective management strategies.

The future of entomological research lies in advancing these monitoring technologies and integrating them into broader ecological frameworks. A critical challenge remains in making these technologies accessible. By making lidar technology affordable and user-friendly, global biodiversity assessment can be empowered, ensuring its reach on a worldwide scale. As knowledge expands, a path is charted toward a more informed and sustainable coexistence with the natural world.

# Acknowledgment

I'm extremely grateful to my tremendously revolutionary fantastic supervisor, *Mikkel Brydegaard*, for this incredible Ph.D. journey. Your dedication and passion are an inspiration. No matter the hour or the place, you've always made yourself available to answer our questions, even interrupting your holiday or evenings. I really appreciate your willingness to open up your network and help us build our own paths in the academic world. Your understanding and support during challenging moments have meant a lot to me. Thank you for everything!

I want to say a big thank you to my friend and colleague, *Hampus Månefjord*. He is extraordinarily intelligent – truly one of the smartest people I know – and always carries himself with kindness and gentlemanly grace. I have no doubt that he will achieve anything he sets his mind to because he is just that incredible. I am thankful for all the times he provided insights that helped me overcome challenges.

I am very happy and thankful for my friend and colleague, *Dolores Bernenko*. It has been super nice to share an office with you for the past half-year. You are not just incredibly kind but also a beacon of support. You listen with such care, making me feel valued and heard in ways I never have before. Whenever I'm stuck or have a question, you never hesitate to dive deep and help find the best solution, showing your dedication and kindness. Your intelligence shines in your work, matched only by your hard work and commitment.

I would like to extend my sincere thanks to my friend, colleague, and old-officemate, *Lauro Müller*. I've truly enjoyed sharing an office with you! Your knack for decorating our shared workspace made it feel like a second home. Your intelligence, handiness, and multilingual abilities are truly impressive. I still remember the day when you sent out three applications and ended up with seven job offers – a testament to your incredible value in the professional world!

I would like to extend my heartfelt gratitude to my friend and former colleague, *Samuel Jansson*. When I first joined the group, you were already deep into your Ph.D. with Mikkel. You've been an incredible mentor – always dependable, patient, and friendly. Your unique style and dedication to interesting projects and hobbies have truly inspired us all.

I'd like to express my gratitude to *Elin Malmqvist*. Even though we didn't work directly together, your cool and kind approach has always stood out. Your guidance,

especially with lidar coding, has been invaluable. As a fellow dog lover, I also deeply appreciate your passion for animals.

I am deeply grateful for my friend and former colleague, *Jonathan Peterson*. You were the one who patiently sat down with me at the start of my PhD and guided me through the complexities of lidar coding. Your kindness, patience, and willingness to share your knowledge have been invaluable to me.

A huge thanks to David Dreyer for his unwavering support, delicious treats, and infectious positivity. His dedication and kindness make him an invaluable member of our team.

My deep gratitude goes out to my co-supervisors, *Christian Brackmann* and *Jadranka Rota*. Christian, your kindness, patience, and stellar teaching have profoundly shaped my academic journey. I'm thankful for the role you've played in my development. Jadranka, your dedication, passion, and support have been a source of inspiration and comfort during challenging times. Together, you've been the bedrock of my support, offering essential help, guidance, and encouragement. The difference you've both made in my life, personally and academically, is immeasurable.

I truly appreciate your guidance, *Anna Runemark*, my career mentor. Your dedication and passion for your work are inspirational, and you stand as a role model for me. Beyond your kindness and caring nature, you openly share your ideas and experiences with us juniors. The lunches where you share your academic career journey are incredibly helpful as we navigate this world. Your success in the field, combined with your genuine kindness, makes you a treasure in academia. I'm deeply grateful for your mentorship.

I'd like to take this opportunity to thank the rest of the strategy lunch members: *Hanna Thosteman*, *Sofie Nilén*, *Erica Winslott*, and *Emma Kärrnäs*. Each of you is truly amazing, and your passion for your work is both motivating and inspiring. I feel privileged to have shared this time with you. I wish you all the very best in your research careers and hope we can continue our lunch gatherings even after I complete my Ph.D.

I want to extend a special word of thanks to *Nina Reistad*. From the moment we met at the atomic division, your kindness and support have been unwavering. Your gentle and friendly nature always encourages me to dream big, reminding me that anything is possible. Your generous offer to teach me how to drive is just one example of your caring spirit. Nina, you're an extraordinary person, and I hold a great deal of admiration for you.

My sincerest thanks go to *Jacobo Salvador*. Your care and concern during each field campaign ensured our safety and well-being. As a friend, your kindness and compassionate nature have been a source of great comfort. Jacobo, your presence was invaluable, and I am grateful to you. Your selflessness and unwavering support

have been a beacon during challenging times. Thank you for being an extraordinary person and friend.

I must extend my sincere appreciation to my colleague and friend, *Vivian Feng*. Even though we only worked together for a week, it surprisingly felt like we'd known each other forever. Vivian, your friendly character made it so easy to bond with you, and I'm extremely thankful for our friendship. Your love for bubble tea is adorable, and your interest in Swedish paper bags always brings a smile to my face. Additionally, your enthusiasm for your work and remarkable work ethic truly inspires all of us.

*Julio Hernandez*, I cannot thank you enough for generously allowing me to use your setup so frequently. Your friendliness and warm welcome every time we are in Oslo mean a lot, especially considering how busy you are. I know it's challenging to plan time with you, but you always make a genuine effort.

I would like to express my heartfelt gratitude to *Klas Rydhmer* and *Carsten Kirkeby*. Working with both of you has been an enjoyable experience. Klas, your warm and cheerful nature has always brought comfort to those around you. Your passion for your work and career is remarkable, along with your ambition to create a biodiversity world map. Carsten, your friendly and patient explanations have been invaluable. Your love for your career shines through, and I particularly cherish the moments when we all exchange awkward glances at Mikkel's dad's jokes. Thank you both for creating such a pleasant atmosphere during each field campaign.

I want to express my sincere appreciation to *Malin Malmsjö*, *Aboma Merdasa*, *Nils Gustafsson*, and *Sheikh Rafi* from the eye clinic for their support and generosity in lending us the hyperspectral camera. I also appreciate *Magnus Cinthio* and *Tobias Erlöv* from the ultrasound group for introducing us to the photoacoustic tomography system. Additionally, I'm grateful to my ultrasound course teacher, *Monica Almqvist*. Your inspiring teaching style makes you one of the best lecturers I've had during my time at the university. Thank you for an unforgettable learning experience.

I'm truly grateful to our department's incredible team: *Emelie Niléhn*, *Cecilia Bille*, *Minna Ramkull*, *Charlotta Åberg*, and *Igor Buzuk*. Emelie, your kindness and gentle demeanor brighten every day. Cecilia, I greatly appreciate your warmth, kindness, and immense patience. Minna, your friendly and lively spirit always brings joy to our workspace. Charlotta, thank you for always being so kind, friendly, and welcoming. Your patience and understanding are truly appreciated. Igor, your kindness is a beacon of light, and your problem-solving abilities are legendary. I deeply appreciate each of you. It's always a pleasure to see you all – you are the heart of the department, and your friendliness, care, and genuine warmth are unmatched.

I want to express my deepest thanks to *Per-Erik Bengtsson*. Your extraordinary kindness, support, and ability to notice when someone needs help, even before they realize it, speaks volumes about your care for those around you. When I was unwell, your prompt support and understanding were incredibly reassuring. I feel fortunate to be part of a division with such considerate and supportive leadership.

My heartfelt thanks go to *Joakim Bood* and *Sven-Inge Möller* for their exceptional kindness, care, and support. You have both shown incredible supportiveness, always available to discuss any matter. Your guidance and empathetic approach have enriched our division immensely.

My thanks also go to *Dina Hot* and *Xin Liu*. Their warm welcome to the department was a great comfort. When they graduated, their absence created a significant void that we all deeply felt. I would be remiss if I did not also mention *Jundie Chen*, *Emma Axebrink*, and *Yue Qiu*. It always makes me so happy to see you all; you are welcoming, kind, and always willing to listen. Yue, your constant cheerfulness is a joy to behold and uplifts everyone around you.

I must express my heartfelt admiration for *Yupan Bao* and *Emma Simpson*. You two have been a constant source of inspiration, and I can confidently say that you both are forever my idols. Your dedication, passion, and positive attitude toward everything you do are truly motivating. I am profoundly grateful for your influence on my life and for the example you set for me and others.

I would like to extend my heartfelt thanks to *Hui Chen*. It was a pleasure to work with you. I must say, it was the first time I encountered a biologist who understood our lidar so thoroughly. Your friendliness, intelligence, and hard work make you an exceptional colleague and valued friend.

To all the Bachelor's and Master's students I've had the chance to work with, thank you for the valuable time we spent together. I'm particularly grateful to *Ebba von Wachenfeldt*, whose dedication during the Stensoffa 2020 campaign was remarkable, keeping our system going even in the hottest weather. I want to extend my thanks to *Andrés Andrés* for the great companionship during the fieldwork at Nyteboda and for teaching me how to carve a spork. Special thanks go to *Noélie Guilcher* for organizing a vast amount of insect literature and to *Clara Seinsche* for her strong work ethic – your future in research looks bright! I also appreciate *Paul Travers* for his commitment in 2022, his help with the moths, and the impressive data he gathered. A huge thanks to *Zhicheng Xu* – your initiative and hard work are truly admirable, and you are such a caring, kind, sweet, and cute person. Also, a big shout-out to *Isa Hendriks*. Your dedication, and friendly vibe are amazing. It's great to see you diving into work you're passionate about (And thank you so much for feeding me cookies)! I would also like to express my sincere gratitude to *Emmanuel Kotu Robertson* for his incredible work ethic, independent spirit, and invaluable contributions. Your ability to create such beautiful and inspiring figures is truly remarkable.

I want to take a moment to express my heartfelt thanks to all my current and former colleagues and friends in our division and department. Your support and friendliness have been fundamental to my experience here. Although I can't mention each of you by name, please know that your contributions have been deeply appreciated. Thank you for being such a crucial part of my journey. And a special thanks to *Trivselgruppen* – you all do a wonderful job making our division feel friendly and supportive. Your dedication is really appreciated!

To our collaborators. I am deeply grateful to *Jérémie T. Zoueu*, *Edoukoua Jean Michel Konin*, and *Benoit Kouassi Kouakou* for their warm welcome and being a great host to the Côte d'Ivoire. I would also like to express my gratitude to the wonderful friends and colleagues who provided invaluable support and made our time in the jungle an enjoyable experience: *Assoumou Saint-Doria Yamoa*, *Yatana Adolphe Gbogbo*, *Rabbi Boateng*, and *Andrew Atiogbe Huzortey*. Your constant support and companionship made the impossible possible. Un grand merci à *Doria* pour m'avoir constamment nourri. Ta nourriture est très bonne.

I want to express my deep gratitude to *Tidiane Ouattara*. In the dense jungle, you were like our 'Dad', the one who could miraculously fix everything and extinguish any challenges. We faced a couple of daunting situations, but your skills and knowledge helped us navigate through them all. Without you, I genuinely doubt we could have completed the experiment in the jungle successfully. Your contributions were critical to our success, and for that, I am profoundly grateful. Je souhaite remercier *Tidiane Ouattara* pour son aide dans la jungle. Il était notre mentor et savait toujours comment résoudre les problèmes. Son expertise a été essentielle à notre succès et je lui suis profondément reconnaissant(e).

I want to say a huge thank you to *Sofia Mouchard*, my high school teacher from IHGR. When I first came to Sweden, I was lost in a world of new languages and cultures. But you were there for me, not just as a teacher, but as a friend. You showed me patience and kindness and believed in me when I was unsure of myself. You never made me feel like a burden but always treated me as someone who could reach their goals. You helped me to believe in myself and gave me the courage to chase my dream. Your influence on my life has been so important, and I carry that confidence you gave me every day. Thank you from the bottom of my heart.

I want to extend a big thank you to my Bachelor's and master's thesis supervisors, *Stefan Andersson-Engels* and *Stefan Kröll*. Your knowledge and professional attitude have truly inspired me. Your passion and dedication towards photonics have revealed its beauty and excitement to me, compelling me to pursue a path in Biophotonics. I genuinely appreciate the time I spent working under your guidance. Thank you for your mentorship and for inspiring me to continue in this fascinating field.

I want to express my deepest thanks to all my friends. Honestly, I can't imagine trying to fit all my gratitude for you all into this text – we'd end up with more pages

of acknowledgments than the thesis itself! I apologize in advance if I've inadvertently missed anyone on this list, as so many of you have touched my life in meaningful ways. So, let's catch up soon and celebrate together. Special thanks to *Alsu Zubairova, Armand Dominguez, Bonnie Wu, Daniel Dannymannen Cheveyo, Daniel Nastasijevic, David Sanned, Friederike Koerting, Hafsa Syed, Hang Yin, Harry Biggs, Hasti Yavari, Isabelle John, James Harkonnen, Josefin Lindström Månefjord, Justine Le Douaron, Kerstin Bergentz, Khanh Trinh, Lisa Rämisch, Madeleine Burheim, Martin Guvå, Megha Prakash, Meena Raveesh, Mohammed Μοχαμεντ Ghanem, Qiaoyin He, Sabrina Gericke, Senfeng Li, Stelios Στέλιος Gakis, Timothy Lewis, Timothé Ramboazanaka, Tina Lorentzon, Vanessa Skällenäs, Vibha Kumra Ahnlide, Vidar Flodgren, Yamin Zhang, Yanhong Cai, Yoana Ilarionova,* and *Yousef Namazi*. Your companionship, laughter, assistance, and support have been incredibly vital to me, providing comfort and resilience during challenging times. I may not have been able to spend as much time with you all lately due to other obligations, but each moment we share is treasured and reminds me of the warmth and support our friendships provide. To all my friends, named here or not, thank you for being such a significant part of my life and my journey. You've enriched my experiences in countless ways, and for that, I am eternally grateful. <3

I would like to express my sincere admiration for *Selma Flodgren*, undoubtedly the best artist in the world. Your professionalism, kindness, efficiency, and exceptional skill are truly inspiring. I deeply appreciate your assistance with my front cover designs.

I wish to take a moment to extend my deepest appreciation and gratitude to my old gaming family from *Final Fantasy 14*, our beloved group, the Meme Raiders. I hold each and every one of you in high regard – *Jen Jen*, *Lin*, *Saro*, *Zel*, *MB*, *Mazee*, *Aphelios*, *Seth*, and our honorary raider, *Coach*, *Kumen*, Saudi Princess *Uleena*, and Saudi Prince *Fahad*. I'm sorry I couldn't play games with you as much due to my busy schedule, but I truly cherish every moment we've shared – gaming, singing, or simply chatting. A special thank you to Saro: When Karl found himself stranded in England, you went above and beyond the call of friendship. Driving for hours to rescue him in the middle of the night showed incredible kindness, and we are eternally grateful. You're a beacon of light, and we couldn't ask for a better friend. We love you, man; thank you so much!

I am deeply grateful for the love and support from my second family, *Marketa Adamek Bastos*, *Adriano Bastos*, *Marina Bastos*, *Jana Wettermark*, and *Gunnar Wettermark*. Your encouragement means so much to me. Jag är så tacksam för all kärlek och stöd jag fått från Marketa Adamek Bastos, Adriano Bastos, Marina Bastos, Jana Wettermark och Gunnar Wettermark. Era uppmuntrande ord betyder jättemycket för mig.

I want to express my deepest gratitude to my family - Mom, Dad, Grandma, Grandpa, Niuniu, Uncle, and Aunt. Your love and support are the most precious

gifts in my life. Mom, your hard work and selfless dedication have touched me deeply. You not only gave me life but also taught me wisdom and courage. Your diligence, optimism, and resilience are my eternal role models, and you have shown me that with effort, women can also achieve great success in their careers. Dad, you are the most important male figure in my life. You have always been there for me, guiding and supporting me. Your love has provided me with the safest harbor and your dedication has taught me the profound meaning of fatherly love, which is a solid foundation for my growth. Grandpa, you taught me how to treat others with kindness and patience. I have benefited greatly from your words and deeds, and I will pass on these valuable qualities. Grandma, you are my mentor in life. You have watched over my growth with love and companionship. Your wisdom and strength are my lifelong role models, and your kind smile and warm embrace are my most cherished childhood memories. Niuniu, you little cheeky, you've grown up so much! Your company, tenderness, and support have always warmed my heart. Thank you, caring boy. Uncle and Aunt, thank you for your care and concern. Your love and support are also indispensable to my growth. Thank you all, you are the most important people in my life. You have taught me to love and be loved, and have shaped me into the person I am today.我想要深深感谢我的家人们 - 妈妈、爸爸、姥姥、姥爷、牛牛、舅舅、舅妈。你们的爱和支持是我生命中最宝贵的礼物。妈妈，您的辛勤付出和无私奉献令我永生难忘和感激。您不仅给予我生命，更教会我生活的智慧与勇气。您的勤劳、乐观和坚韧是我永远的榜样，也让我明白，只要努力，女性同样可以在事业上大放异彩。爸爸，您是我生命中最重要的男性角色。您总是陪伴我、教导我，您的爱让我拥有了最安全的港湾，您的付出让我明白，父爱如山，厚重而深沉，是我成长路上坚实的依靠。姥爷，您教导我如何待人接物，让我学会了善良和耐心。您的言传身教让我受益匪浅，我也会将这份珍贵的品质传承下去。姥姥，您是我人生的导师，您用爱和陪伴守护着我成长。您的智慧和坚强，是我一生学习的榜样，您用慈祥的笑容和温暖的怀抱守护着我，您是我童年最美好的回忆。牛牛，你这个小机灵鬼，不知不觉中你都长这么大了。这些年来，你的陪伴、温柔和支持也一直温暖着我。谢谢你，小暖男。舅舅、舅妈，感谢你们一直以来对我的关心和照顾。你们的爱和支持也是我成长路上不可或缺的力量。感谢你们，你们是我生命中最重要的人，你们教会我爱与被爱，让我成为今天的自己。

My deepest gratitude goes to the most important person in my life, my love, *Karl Bastos*. We've been together a long time, and every day, you shower me with care and support. From late-night pizza deliveries during my bachelor's thesis to ice cream runs after 4 am lab sessions for my master's degree, you've always been there. When I had to drive 2 hours at midnight to some middle-of-nowhere place for field work, I was very scared, but you would come with me and sleep on the floor of the Lumbo while I was operating the lidar. Whether I'm abroad or in the field, you take over at home, making sure everything runs smoothly and caring for Ace. You tell me you love me constantly, and while I playfully try to quiet you sometimes, it never

stops you from expressing your affection. You have an uncanny ability to sense my emotions, always offering solutions when I'm down and a safe haven during storms, literally and figuratively. Your strength and caring nature are a constant source of comfort. I apologize for neglecting you and Ace at times when I was consumed by work. Thanks to you, I've learned the true importance of family, especially during Ace's illness. You're my rock, my ADC, tank, and healer in games – roles you effortlessly fulfill in real life. You shield me from worries, mend my sadness, and always give your all. Karl, your unwavering support is my pillar of strength. You've made countless sacrifices to ensure my well-being, and I'm eternally grateful. Your love is my guiding light, leading me through dark times and towards a brighter future. Your kindness, compassion, and dedication are unmatched. I am beyond lucky to have you by my side. Thank you for everything, my love.

In the end, to the memory of *Jens Rydell*. You were a brilliant scientist and a truly wonderful person. Thank you for inspiring me.

# Funding

European Research Council (ERC) under the European Union's Horizon 2020 research and innovation program (Grant Agreement No. 2019-850463 Bug-Flash).

Grant holder Mikkel Brydegaard

The Royal Physiographic Society of Lund. (Grant Agreement No. 151277 - Kungl Fysiogr-22 Ivorian Lidar)

Grant holder Meng Li

The African Spectral Imaging Network (AFSIN) is funded by the International Science Program (ISP, Uppsala University) by the Swedish Development Agency (SIDA).

Grant holders Jeremie Zoueu & Carla Puglia

FORMAS. (Grant Agreement No. 2018-01061)

Grant holder Mikkel Brydegaard

# References


[1] C. W. Sabrosky, "How many insects are there?," *Systematic Zoology,* vol. 2, no. 1, pp. 31-36, 1953.

[2] A. D. Chapman, "Numbers of living species in Australia and the world," 2009.

[3] N. E. Stork, "How many species of insects and other terrestrial arthropods are there on Earth?," *Annual review of entomology,* vol. 63, pp. 31-45, 2018.

[4] E. O. Wilson, "The little things that run the world (the importance and conservation of invertebrates)," ed: JSTOR, 1987, pp. 344-346.

[5] S. Lautenbach, R. Seppelt, J. Liebscher, and C. F. Dormann, "Spatial and temporal trends of global pollination benefit," *PloS one,* vol. 7, no. 4, p. e35954, 2012.

[6] S. G. Potts *et al.*, "Safeguarding pollinators and their values to human well-being," *Nature,* vol. 540, no. 7632, pp. 220-229, 2016/12/01 2016, doi: 10.1038/nature20588.

[7] A.-M. Klein *et al.*, "Importance of pollinators in changing landscapes for world crops," *Proceedings of the royal society B: biological sciences,* vol. 274, no. 1608, pp. 303-313, 2007.

[8] R. PRESCOTT‐ALLEN and C. PRESCOTT‐ALLEN, "How many plants feed the world?," *Conservation Biology,* vol. 4, no. 4, pp. 365-374, 1990.

[9] M. A. Aizen, L. A. Garibaldi, S. A. Cunningham, and A. M. Klein, "How much does agriculture depend on pollinators? Lessons from long-term trends in crop production," *Annals of botany,* vol. 103, no. 9, pp. 1579-1588, 2009.

[10] K. Y. Barragán-Fonseca *et al.*, "Insect frass and exuviae to promote plant growth and health," *Trends in Plant Science,* vol. 27, no. 7, pp. 646-654, 2022.

[11] L. H. Yang and C. Gratton, "Insects as drivers of ecosystem processes," *Current Opinion in Insect Science,* vol. 2, pp. 26-32, 2014.

[12] P. S. Barton, C. Strong, M. J. Evans, A. Higgins, and M.-M. Quaggiotto, "Nutrient and moisture transfer to insect consumers and soil during vertebrate decomposition," *Food Webs,* vol. 18, p. e00110, 2019.

[13] M. A. Jervis, G. E. Heimpel, P. N. Ferns, J. A. Harvey, and N. A. C. Kidd, "Life-history strategies in parasitoid wasps: a comparative analysis of 'ovigeny'," *Journal of Animal Ecology,* vol. 70, no. 3, pp. 442-458, 2001, doi: https://doi.org/10.1046/j.1365-2656.2001.00507.x.

[14] S. Sharma, R. Kooner, and R. Arora, "Insect pests and crop losses," *Breeding insect resistant crops for sustainable agriculture,* pp. 45-66, 2017.

[15] H. E. Tonnang, B. M. Sokame, E. M. Abdel-Rahman, and T. Dubois, "Measuring and modelling crop yield losses due to invasive insect pests under climate change," *Current Opinion in Insect Science,* vol. 50, p. 100873, 2022.

[16] G. Biswas, "Insect pests of soybean (Glycine max L.), their nature of damage and succession with the crop stages," *Journal of the Asiatic Society of Bangladesh, Science*, vol. 39, no. 1, pp. 1-8, 2013.
[17] G. Dhaliwal, V. Jindal, and A. Dhawan, "Insect pest problems and crop losses: changing trends," *Indian Journal of Ecology*, vol. 37, no. 1, pp. 1-7, 2010.
[18] L. Ji, Z. Wang, X. Wang, and L. An, "Forest insect pest management and forest management in China: an overview," *Environmental Management*, vol. 48, pp. 1107-1121, 2011.
[19] K. R. Day and S. R. Leather, "Threats to forestry by insect pests in Europe," *Forests and insects*, pp. 177-205, 1997.
[20] E. D. Ivantsova, A. I. Pyzhev, and E. V. Zander, "Economic consequences of insect pests outbreaks in boreal forests: A literature review," *Журнал Сибирского федерального университета. Гуманитарные науки,* vol. 12, no. 4, pp. 627-642, 2019.
[21] H. Eidmann, "Impact of bark beetles on forests and forestry in Sweden 1," *Journal of Applied Entomology*, vol. 114, no. 1 - 5, pp. 193-200, 1992.
[22] R. Seidl, W. Rammer, D. Jäger, and M. J. Lexer, "Impact of bark beetle (Ips typographus L.) disturbance on timber production and carbon sequestration in different management strategies under climate change," *Forest Ecology and Management*, vol. 256, no. 3, pp. 209-220, 2008.
[23] E. Christiansen and A. Bakke, *The spruce bark beetle of Eurasia* (Dynamics of forest insect populations). Springer, 1988, pp. 479-503.
[24] I. Statista. "Deadliest Animals Globally by Annual Number of Human Deaths 2022." In Statista. https://www.statista.com/statistics/448169/deadliest-creatures-in-the-world-by-number-of-human-deaths/ (accessed 2024-03-12.
[25] A. R. Magalhães, C. T. Codeço, J.-C. Svenning, L. E. Escobar, P. Van de Vuurst, and T. Gonçalves-Souza, "Neglected tropical diseases risk correlates with poverty and early ecosystem destruction," *Infectious Diseases of Poverty*, vol. 12, no. 1, p. 32, 2023/04/10 2023, doi: 10.1186/s40249-023-01084-1.
[26] A. Nigusie, Z. Gizaw, M. Gebrehiwot, and B. Destaw, "Vector-Borne Diseases and Associated Factors in the Rural Communities of Northwest Ethiopia: A Community-Based Cross-Sectional Study," (in eng), *Environ Health Insights*, vol. 15, p. 11786302211043049, 2021, doi: 10.1177/11786302211043049.
[27] J. Learish. "The 24 deadliest animals on Earth, ranked." https://www.cnet.com/pictures/the-24-deadliest-animals-on-earth-ranked/ (accessed Retrieved March 24, 2019, CNET. Archived from the original on March 24, 2019).
[28] M. A. Titley, J. L. Snaddon, and E. C. Turner, "Scientific research on animal biodiversity is systematically biased towards vertebrates and temperate regions," *PLOS ONE*, vol. 12, no. 12, p. e0189577, 2017, doi: 10.1371/journal.pone.0189577.
[29] H. Moersberger *et al.*, "Europa Biodiversity Observation Network: User and Policy Needs Assessment," *ARPHA Preprints*, vol. 3, 2022, doi: 10.3897/arphapreprints.e84517.

[30] A. Petrović, "Sizing the Knowledge Gap in Taxonomy: The Last Dozen Years of Aphidiinae Research," *Insects*, vol. 13, no. 2, p. 170, 2022. [Online]. Available: https://www.mdpi.com/2075-4450/13/2/170.

[31] G. Pérez-Lachaud and J.-P. Lachaud, "Hidden biodiversity in entomological collections: The overlooked co-occurrence of dipteran and hymenopteran ant parasitoids in stored biological material," *PLoS One*, vol. 12, no. 9, p. e0184614, 2017.

[32] J. T. Huber, "Biodiversity of hymenoptera," *Insect biodiversity: science and society*, pp. 419-461, 2017.

[33] S. Köthe *et al.*, "Recommendations for effective insect conservation in nature protected areas based on a transdisciplinary project in Germany," *Environmental Sciences Europe*, vol. 35, no. 1, p. 102, 2023/11/19 2023, doi: 10.1186/s12302-023-00813-5.

[34] G. A. Montgomery, M. W. Belitz, R. P. Guralnick, and M. W. Tingley, "Standards and Best Practices for Monitoring and Benchmarking Insects," (in English), *Frontiers in Ecology and Evolution*, Review vol. 8, 2021-January-15 2021, doi: 10.3389/fevo.2020.579193.

[35] Y. Basset *et al.*, "IBISCA-Panama, a large-scale study of arthropod beta-diversity and vertical stratification in a lowland rainforest: rationale, study sites and field protocols," *Bulletin de L'Institut Royal des Sciences Naturelles de Belgique Entomologie*, 2007.

[36] Y. Basset *et al.*, "Arthropod Distribution in a Tropical Rainforest: Tackling a Four Dimensional Puzzle," *PLOS ONE*, vol. 10, no. 12, p. e0144110, 2015, doi: 10.1371/journal.pone.0144110.

[37] Y. Basset *et al.*, "Arthropod Diversity in a Tropical Forest," *Science*, vol. 338, no. 6113, pp. 1481-1484, 2012, doi: doi:10.1126/science.1226727.

[38] K. M. Staunton, L. Usher, T. Prachar, S. A. Ritchie, N. Snoad, and B. J. Johnson, "A Novel Methodology For Recording Wing Beat Frequencies of Untethered Male and Female Aedes aegypti," *Journal of the American Mosquito Control Association*, vol. 35, no. 3, pp. 169-177, 2019, doi: 10.2987/18-6799.1.

[39] I. Potamitis, I. Rigakis, and K. Fysarakis, "The electronic McPhail trap," *Sensors*, vol. 14, no. 12, pp. 22285-22299, 2014. [Online]. Available: https://res.mdpi.com/d_attachment/sensors/sensors-14-22285/article_deploy/sensors-14-22285-v3.pdf.

[40] I. Potamitis, I. Rigakis, and K. Fysarakis, "Insect biometrics: Optoacoustic signal processing and its applications to remote monitoring of McPhail type traps," *PloS one*, vol. 10, no. 11, p. e0140474, 2015. [Online]. Available: https://www.ncbi.nlm.nih.gov/pmc/articles/PMC4636391/pdf/pone.0140474.pdf.

[41] I. Potamitis and I. Rigakis, "Measuring the fundamental frequency and the harmonic properties of the wingbeat of a large number of mosquitoes in flight using 2D optoacoustic sensors," *Applied Acoustics*, vol. 109, pp. 54-60, 2016.

[42] I. Potamitis, I. Rigakis, and N.-A. Tatlas, "Automated surveillance of fruit flies," *Sensors*, vol. 17, no. 1, p. 110, 2017.

[43] D. M. UNWIN and S. A. CORBET, "Wingbeat frequency, temperature and body size in bees and flies," *Physiological Entomology*, vol. 9, no. 1, pp. 115-121, 1984, doi: https://doi.org/10.1111/j.1365-3032.1984.tb00687.x.
[44] J. Oertli, "Relationship of wing beat frequency and temperature during take-off flight in temperate-zone beetles," *Journal of experimental biology*, vol. 145, no. 1, pp. 321-338, 1989.
[45] A. R. S. Parmezan, V. M. A. Souza, I. Žliobaitė, and G. E. A. P. A. Batista, "Changes in the wing-beat frequency of bees and wasps depending on environmental conditions: a study with optical sensors," *Apidologie*, vol. 52, no. 4, pp. 731-748, 2021/08/01 2021, doi: 10.1007/s13592-021-00860-y.
[46] M. Wang, J. Wang, P. Liang, and K. Wu, "Nutritional Status, Sex, and Ambient Temperature Modulate the Wingbeat Frequency of the Diamondback Moth Plutella xylostella," *Insects*, vol. 15, no. 2, p. 138, 2024. [Online]. Available: https://www.mdpi.com/2075-4450/15/2/138.
[47] J. Huang, G. Zhang, and Y. Wang, "Effects of age, ambient temperature and reproductive status on wing beat frequency of the rice leafroller Cnaphalocrocis medinalis (Guenée) (Lepidoptera: Crambidae)," *Applied Entomology and Zoology*, vol. 48, no. 4, pp. 499-505, 2013/11/01 2013, doi: 10.1007/s13355-013-0209-z.
[48] R.-B. Xu, S.-S. Ge, W.-H. Yu, X.-K. Li, and K.-M. Wu, "Physiological and Environmental Influences on Wingbeat Frequency of Oriental Armyworm, Mythimna separata (Lepidoptera: Noctuidae)," *Environmental Entomology*, vol. 52, no. 1, pp. 1-8, 2022, doi: 10.1093/ee/nvac101.
[49] D. N. Byrne, S. L. BUCHMANN, and H. G. SPANGLER, "Relationship between wing loading, wingbeat frequency and body mass in homopterous insects," *Journal of Experimental Biology*, vol. 135, no. 1, pp. 9-23, 1988.
[50] E. Feuerbacher, J. H. Fewell, S. P. Roberts, E. F. Smith, and J. F. Harrison, "Effects of load type (pollen or nectar) and load mass on hovering metabolic rate and mechanical power output in the honey bee Apis mellifera," *Journal of Experimental Biology*, vol. 206, no. 11, pp. 1855-1865, 2003, doi: 10.1242/jeb.00347.
[51] K. Rydhmer *et al.*, "Photonic sensors reflect variation in insect abundance and diversity across habitats," *Ecological Indicators*, vol. 158, p. 111483, 2024/01/01/ 2024, doi: https://doi.org/10.1016/j.ecolind.2023.111483.
[52] N. Guilcher. "Supplementary: Study of the variation of wing thickness among species of clear winged insect." https://github.com/BioBeamMeng/InsectWBF/blob/main/InsectWingProjectData.xls (accessed 16 April 2024).
[53] B. Kim, N. Jakob Bonde, S. Martin Videbæk, H.-N. Flemming, and H. Toke Thomas, "A light trap and computer vision system to detect and classify live moths (Lepidoptera) using tracking and deep learning," *bioRxiv*, p. 2020.03.18.996447, 2020, doi: 10.1101/2020.03.18.996447.
[54] K. Bjerge, J. Alison, M. Dyrmann, C. E. Frigaard, H. M. R. Mann, and T. T. Høye, "Accurate detection and identification of insects from camera trap images

with deep learning," *PLOS Sustainability and Transformation*, vol. 2, no. 3, p. e0000051, 2023, doi: 10.1371/journal.pstr.0000051.

[55] L. Wührl *et al.*, "DiversityScanner: Robotic handling of small invertebrates with machine learning methods," *Molecular ecology resources*, vol. 22, no. 4, pp. 1626-1638, 2022. [Online]. Available: https://onlinelibrary.wiley.com/doi/pdfdirect/10.1111/1755-0998.13567?download=true.

[56] K. Thenmozhi and U. S. Reddy, "Crop pest classification based on deep convolutional neural network and transfer learning," *Computers and Electronics in Agriculture*, vol. 164, p. 104906, 2019.

[57] D. Xia, P. Chen, B. Wang, J. Zhang, and C. Xie, "Insect detection and classification based on an improved convolutional neural network," *Sensors*, vol. 18, no. 12, p. 4169, 2018.

[58] O. L. P. Hansen *et al.*, "Species-level image classification with convolutional neural network enables insect identification from habitus images," *Ecology and Evolution*, vol. 10, no. 2, pp. 737-747, 2020, doi: https://doi.org/10.1002/ece3.5921.

[59] J. Ärje *et al.*, "Automatic image‐based identification and biomass estimation of invertebrates," *Methods in Ecology and Evolution*, vol. 11, no. 8, pp. 922-931, 2020.

[60] Y. Milián-García, C. Pyne, K. Lindsay, A. Romero, and R. H. Hanner, "Unveiling invasive insect threats to plant biodiversity: Leveraging eDNA metabarcoding and saturated salt trap solutions for biosurveillance," *PLOS ONE*, vol. 18, no. 8, p. e0290036, 2023, doi: 10.1371/journal.pone.0290036.

[61] Y. Milián‐García, R. Young, M. Madden, E. Bullas‐Appleton, and R. H. Hanner, "Optimization and validation of a cost‐effective protocol for biosurveillance of invasive alien species," *Ecology and Evolution*, vol. 11, no. 5, pp. 1999-2014, 2021.

[62] J. P. Newton *et al.*, "Monitoring the birds and the bees: Environmental DNA metabarcoding of flowers detects plant–animal interactions," *Environmental DNA*, vol. 5, no. 3, pp. 488-502, 2023, doi: https://doi.org/10.1002/edn3.399.

[63] T. Saito and H. Doi, "A Model and Simulation of the Influence of Temperature and Amplicon Length on Environmental DNA Degradation Rates: A Meta-Analysis Approach," (in English), *Frontiers in Ecology and Evolution*, Original Research vol. 9, 2021-March-19 2021, doi: 10.3389/fevo.2021.623831.

[64] "GBIF | Global Biodiversity Information Facility." https://www.gbif.org/ (accessed 17th April 2024).

[65] A. Bush *et al.*, "Studying ecosystems with DNA metabarcoding: Lessons from biomonitoring of aquatic macroinvertebrates," *Frontiers in Ecology and Evolution*, vol. 7, p. 434, 2019.

[66] A. Kirse, S. J. Bourlat, K. Langen, and V. G. Fonseca, "Metabarcoding Malaise traps and soil eDNA reveals seasonal and local arthropod diversity shifts," *Scientific reports*, vol. 11, no. 1, p. 10498, 2021.

[67] C. S. Svenningsen *et al.*, "Detecting flying insects using car nets and DNA metabarcoding," *Biology Letters*, vol. 17, no. 3, p. 20200833, 2021.

[68] A. Srivathsan *et al.*, "Rapid, large-scale species discovery in hyperdiverse taxa using 1D MinION sequencing," *BMC biology*, vol. 17, pp. 1-20, 2019.
[69] A. Srivathsan *et al.*, "ONTbarcoder and MinION barcodes aid biodiversity discovery and identification by everyone, for everyone," *BMC biology*, vol. 19, pp. 1-21, 2021.
[70] B. Bruderer, "The Study of Bird Migration by Radar," *Naturwissenschaften*, vol. 84, pp. 45-54, 02/01 1997, doi: 10.1007/s001140050348.
[71] V. A. Drake and D. R. Reynolds, *Radar entomology: observing insect flight and migration*. Cabi, 2012.
[72] J. Riley, P. Valeur, A. Smith, D. Reynolds, G. Poppy, and C. Löfstedt, "Harmonic radar as a means of tracking the pheromone-finding and pheromone-following flight of male moths," *Journal of Insect Behavior*, vol. 11, no. 2, pp. 287-296, 1998.
[73] A. Smith, D. Reynolds, and J. Riley, "The use of vertical-looking radar to continuously monitor the insect fauna flying at altitude over southern England," *Bulletin of Entomological Research*, vol. 90, no. 3, pp. 265-277, 2000.
[74] J. W. Chapman, D. R. Reynolds, and A. D. Smith, "Vertical-looking radar: a new tool for monitoring high-altitude insect migration," *Bioscience*, vol. 53, no. 5, pp. 503-511, 2003.
[75] O. Ovaskainen *et al.*, "Tracking butterfly movements with harmonic radar reveals an effect of population age on movement distance," *Proceedings of the National Academy of Sciences*, vol. 105, no. 49, pp. 19090-19095, 2008, doi: 10.1073/pnas.0802066105.
[76] J. W. Chapman, V. A. Drake, and D. R. Reynolds, "Recent insights from radar studies of insect flight," *Annual review of entomology*, vol. 56, pp. 337-356, 2011.
[77] V. A. Drake and H. Wang, "Ascent and descent rates of high-flying insect migrants determined with a non-coherent vertical-beam entomological radar," *International Journal of Remote Sensing*, pp. 1-22, 2018, doi: 10.1080/01431161.2018.1519283.
[78] J. R. Riley, "Radar cross section of insects," *Proceedings of the IEEE*, vol. 73, no. 2, pp. 228-232, 1985, doi: 10.1109/PROC.1985.13135.
[79] A. Noskov, S. Achilles, and J. Bendix, "Presence and biomass information extraction from highly uncertain data of an experimental low-range insect radar setup," *Diversity*, vol. 13, no. 9, p. 452, 2021.
[80] A. Noskov, J. Bendix, and N. Friess, "A review of insect monitoring approaches with special reference to radar techniques," *Sensors*, vol. 21, no. 4, p. 1474, 2021.
[81] M. Brydegaard, A. Gebru, and S. Svanberg, "Super resolution laser radar with blinking atmospheric particles----Application to interacting flying insects," *Progress In Electromagnetics Research*, vol. 147, pp. 141-151, 2014.
[82] M. Brydegaard, "Towards quantitative optical cross sections in entomological laser radar–potential of temporal and spherical parameterizations for identifying atmospheric fauna," *PLoS One*, vol. 10, no. 8, p. e0135231, 2015. [Online]. Available: https://www.ncbi.nlm.nih.gov/pmc/articles/PMC4546581/pdf/pone.0135231.pdf.

[83] E. Malmqvist, S. Jansson, S. Török, and M. Brydegaard, "Effective parameterization of laser radar observations of atmospheric fauna," *IEEE Journal of Selected Topics in Quantum Electronics,* vol. 22, no. 3, pp. 327-334, 2015.
[84] M. Brydegaard and S. Jansson, "Advances in Entomological Laser Radar," presented at the IET Intenstional Radar Cenference, Nanjing, China, 2018.
[85] M. Brydegaard and S. Svanberg, "Photonic Monitoring of Atmospheric and Aquatic Fauna," *Laser & Photonics Reviews,* vol. 12, no. 12, p. 1800135, 2018, doi: 10.1002/lpor.201800135.
[86] H. Månefjord, "Toward Accessible Biophotonics: Instrumentation for Insect and Vegetation Applications," Ph.D. Thesis, 2024.
[87] S. Jansson *et al.*, "Real-time dispersal of malaria vectors in rural Africa monitored with lidar," *PLOS ONE,* vol. 16, no. 3, p. e0247803, 2021, doi: 10.1371/journal.pone.0247803.
[88] V. Santos *et al.*, "Dual-Band Infrared Scheimpflug Lidar Reveals Insect Activity in a Tropical Cloud Forest," *Applied Spectroscopy,* vol. 77, no. 6, pp. 593-602, 2023, doi: 10.1177/00037028231169302.
[89] M. Brydegaard, B. Kouakou, S. Jansson, J. Rydell, and J. Zoueu, "High Dynamic Range in Entomological Scheimpflug Lidars," *IEEE Journal of Selected Topics in Quantum Electronics,* 2021, doi: 10.1109/JSTQE.2021.3062088.
[90] K. Rydhmer *et al.*, "Scheimpflug lidar range profiling of bee activity patterns and spatial distributions," *Animal Biotelemetry,* vol. 10, no. 1, p. 14, 2022/04/19 2022, doi: 10.1186/s40317-022-00285-z.
[91] Z. Song *et al.*, "Application of lidar remote sensing of insects in agricultural entomology on the Chinese scene," *Journal of Applied Entomology,* vol. 144, no. 3, pp. 161-169, 2020, doi: 10.1111/jen.12714.
[92] A. S.-D. Yamoa *et al.*, "Comparative lidar assessment of insect diversity at four Ivorian habitats," *(Draft),* 2024.
[93] E. Shevtsova, C. Hansson, D. H. Janzen, and J. Kjaerandsen, "Stable structural color patterns displayed on transparent insect wings," (in eng), *PNAS,* Research Support, Non-U.S. Gov't

Research Support, U.S. Gov't, Non-P.H.S. vol. 108, no. 2, pp. 668-73, Jan 11 2011, doi: 10.1073/pnas.1017393108.
[94] A. Genoud, Y. Gao, G. Williams, and B. Thomas, "Identification of gravid mosquitoes from changes in spectral and polarimetric backscatter cross-sections," *Journal of Biophotonics,* vol. 12, p. e201900123, 06/18 2019, doi: 10.1002/jbio.201900123.
[95] H. Månefjord *et al.*, "Hyperspectral lidar for monitoring high-resolution activity patterns of African stingless bee species," *Animal Biotelemetry,* vol. 12, no. 1, p. 15, 2024/05/29 2024, doi: 10.1186/s40317-024-00372-3.
[96] S. Gunderson and R. Schiavone, "The insect exoskeleton: A natural structural composite," *JOM,* vol. 41, no. 11, pp. 60-63, 1989/11/01 1989, doi: 10.1007/BF03220386.
[97] E. Cohen, "Chitin Biochemistry: Synthesis and Inhibition," *Annual Review of Entomology,* vol. 32, no. Volume 32, 1987, pp. 71-93, 1987, doi: https://doi.org/10.1146/annurev.en.32.010187.000443.

[98] M. Brydegaard, S. Jansson, M. Schulz, and A. Runemark, "Can the narrow red bands of dragonflies be used to perceive wing interference patterns?," *Ecology and evolution*, vol. 8, no. 11, pp. 5369-5384, 2018. [Online]. Available: https://www.ncbi.nlm.nih.gov/pmc/articles/PMC6010746/pdf/ECE3-8-5369.pdf.

[99] W. Song *et al.*, "Melanin: insights into structure, analysis, and biological activities for future development," *Journal of Materials Chemistry B*, 10.1039/D3TB01132A vol. 11, no. 32, pp. 7528-7543, 2023, doi: 10.1039/D3TB01132A.

[100] M. M. A. Whitten and C. J. Coates, "Re-evaluation of insect melanogenesis research: Views from the dark side," *Pigment Cell & Melanoma Research*, vol. 30, no. 4, pp. 386-401, 2017, doi: https://doi.org/10.1111/pcmr.12590.

[101] W. B. Watt, "ADAPTIVE SIGNIFICANCE OF PIGMENT POLYMORPHISMS IN COLIAS BUTTERFLIES. I. VARIATION OF MELANIN PIGMENT IN RELATION TO THERMOREGULATION1," *Evolution*, vol. 22, no. 3, pp. 437-458, 1968, doi: 10.1111/j.1558-5646.1968.tb03985.x.

[102] J. G. Kingsolver and D. C. Wiernasz, "Seasonal Polyphenism in Wing-Melanin Pattern and Thermoregulatory Adaptation in Pieris Butterflies," *The American Naturalist*, vol. 137, no. 6, pp. 816-830, 1991, doi: 10.1086/285195.

[103] M. Brenner and V. J. Hearing, "The protective role of melanin against UV damage in human skin," (in eng), *Photochem Photobiol*, vol. 84, no. 3, pp. 539-49, May-Jun 2008, doi: 10.1111/j.1751-1097.2007.00226.x.

[104] S. Jacques, "Optical Properties of Biological Tissues: A Review," *Physics in medicine and biology*, vol. 58, pp. R37-R61, 05/10 2013, doi: 10.1088/0031-9155/58/11/R37.

[105] omlc. "Optical Absorption of Water Compendium." https://omlc.org/spectra/water/abs/index.html (accessed July, 2024.

[106] A. P. Genoud, T. Saha, G. M. Williams, and B. P. Thomas, "Insect biomass density: measurement of seasonal and daily variations using an entomological optical sensor," *Applied Physics B*, vol. 129, no. 2, p. 26, 2023/01/17 2023, doi: 10.1007/s00340-023-07973-5.

[107] T. S. Le, R. Harper, and B. Dell, "Application of Remote Sensing in Detecting and Monitoring Water Stress in Forests," *Remote Sensing*, vol. 15, no. 13, p. 3360, 2023. [Online]. Available: https://www.mdpi.com/2072-4292/15/13/3360.

[108] V. Alistair Drake, D. Mirkovic, and M. J. Steinbauer, "Insects as radar targets: size, form, density and permittivity," *International Journal of Remote Sensing*, vol. 45, no. 9, pp. 2985-3002, 2024.

[109] C. R. Vaughn, "Birds and insects as radar targets: A review," *Proceedings of the IEEE*, vol. 73, no. 2, pp. 205-227, 1985, doi: 10.1109/PROC.1985.13134.

[110] M. J. O'Donnell, "A perspective on insect water balance," *Journal of Experimental Biology*, vol. 225, no. 7, 2022, doi: 10.1242/jeb.242358.

[111] D. J. Segelstein, "The complex refractive index of water," University of Missouri--Kansas City, 1981.

[112] D. G. Stavenga, H. L. Leertouwer, T. Hariyama, H. A. De Raedt, and B. D. Wilts, "Sexual dichromatism of the damselfly Calopteryx japonica caused by a melanin-chitin multilayer in the male wing veins," *PloS one*, vol. 7, no. 11, p. e49743,

2012. [Online]. Available: https://www.ncbi.nlm.nih.gov/pmc/articles/PMC3502265/pdf/pone.0049743.pdf.
[113] C. E. Pinheiro, A. V. Freitas, V. C. Campos, P. J. DeVries, and C. M. Penz, "Both Palatable and Unpalatable Butterflies Use Bright Colors to Signal Difficulty of Capture to Predators," (in eng), *Neotrop Entomol*, vol. 45, no. 2, pp. 107-13, Apr 2016, doi: 10.1007/s13744-015-0359-5.
[114] D. G. Stavenga, A. Matsushita, and K. Arikawa, "Combined pigmentary and structural effects tune wing scale coloration to color vision in the swallowtail butterfly Papilio xuthus," *Zoological Letters*, vol. 1, no. 1, p. 14, 2015/04/24 2015, doi: 10.1186/s40851-015-0015-2.
[115] T. E. White, J. Zeil, and D. J. Kemp, "Signal design and courtship presentation coincide for highly biased delivery of an iridescent butterfly mating signal," *Evolution*, vol. 69, no. 1, pp. 14-25, 2015, doi: 10.1111/evo.12551.
[116] C. W. Mason, "Structural colors in insects. II," *The Journal of Physical Chemistry*, vol. 31, no. 3, pp. 321-354, 2002.
[117] R. INSIGHTS. https://summitchemical.com/mosquitoes-lay-their-eggs-in-standing-water/ (accessed 2024-07-11.
[118] P. Kubelka, "New Contributions to the Optics of Intensely Light-Scattering Materials. Part I," *J. Opt. Soc. Am.*, vol. 38, no. 5, pp. 448-457, 1948/05/01 1948, doi: 10.1364/JOSA.38.000448.
[119] J. Qin and R. Lu, "Measurement of the optical properties of fruits and vegetables using spatially resolved hyperspectral diffuse reflectance imaging technique," *Postharvest Biology and Technology*, vol. 49, no. 3, pp. 355-365, 2008/09/01/ 2008, doi: https://doi.org/10.1016/j.postharvbio.2008.03.010.
[120] T. Svensson, E. Alerstam, D. Khoptyar, J. Johansson, S. Folestad, and S. Andersson-Engels, "Near-infrared photon time-of-flight spectroscopy of turbid materials up to 1400 nm," *Review of Scientific Instruments*, vol. 80, no. 6, 2009, doi: 10.1063/1.3156047.
[121] P. Vukusic, B. Hallam, and J. Noyes, "Brilliant Whiteness in Ultrathin Beetle Scales," *Science*, vol. 315, no. 5810, pp. 348-348, 2007, doi: doi:10.1126/science.1134666.
[122] M. Burresi *et al.*, "Bright-White Beetle Scales Optimise Multiple Scattering of Light," *Scientific Reports*, vol. 4, no. 1, p. 6075, 2014/08/15 2014, doi: 10.1038/srep06075.
[123] M. Rebora, G. Salerno, S. Piersanti, A. Kovalev, and S. N. Gorb, "The origin of black and white coloration of the Asian tiger mosquito Aedes albopictus (Diptera: Culicidae)," (in eng), *Beilstein J Nanotechnol*, vol. 14, pp. 496-508, 2023, doi: 10.3762/bjnano.14.41.
[124] D. Fukutomi, K. Ishii, and K. Awazu, "Determination of the scattering coefficient of biological tissue considering the wavelength and absorption dependence of the anisotropy factor," *Optical Review*, vol. 23, no. 2, pp. 291-298, 2016/04/01 2016, doi: 10.1007/s10043-015-0161-y.
[125] S. Jansson, "Entomological Lidar : Target Characterization and Field Applications," PhD Thesis, Department of Physics, Lund University, Lund University, Lund University, 2020.

[126] B. K. Kouakou, S. Jansson, M. Brydegaard, and J. T. Zoueu, "Entomological Scheimpflug lidar for estimating unique insect classes in-situ field test from Ivory Coast," *OSA Continuum,* vol. 3, no. 9, 07/22 2020, doi: 10.1364/osac.387727.
[127] S. Kinoshita, S. Yoshioka, and J. Miyazaki, "Physics of structural colors," *Reports on Progress in Physics,* vol. 71, no. 7, p. 076401, 2008.
[128] M. D. Shawkey *et al.*, "Electron tomography, three-dimensional Fourier analysis and colour prediction of a three-dimensional amorphous biophotonic nanostructure," *Journal of the Royal Society Interface,* vol. 6, no. suppl_2, pp. S213-S220, 2009.
[129] J. Walther *et al.*, "Optical coherence tomography in biomedical research," *Analytical and bioanalytical chemistry,* vol. 400, pp. 2721-2743, 2011.
[130] H. Yin *et al.*, "Iridescence in the neck feathers of domestic pigeons," *Physical Review E,* vol. 74, no. 5, p. 051916, 11/22/ 2006, doi: 10.1103/PhysRevE.74.051916.
[131] R. O. Prum and R. Torres, "Structural colouration of avian skin: convergent evolution of coherently scattering dermal collagen arrays," *Journal of Experimental Biology,* vol. 206, no. 14, pp. 2409-2429, 2003, doi: 10.1242/jeb.00431.
[132] D. G. Stavenga, "Thin film and multilayer optics cause structural colors of many insects and birds," *Materials Today: Proceedings,* vol. 1, pp. 109-121, 2014.
[133] E. Shevtsova and C. Hansson, "Species recognition through wing interference patterns (WIPs) in Achrysocharoides Girault (Hymenoptera, Eulophidae) including two new species," *Zookeys,* no. 154, p. 9, 2011.
[134] M. F. Hawkes *et al.*, "Sexual selection drives the evolution of male wing interference patterns," *Proceedings of the Royal Society B: Biological Sciences,* vol. 286, no. 1903, p. 20182850, 2019, doi: doi:10.1098/rspb.2018.2850.
[135] R. O. Prum, R. Torres, C. Kovach, S. Williamson, and S. M. Goodman, "Coherent light scattering by nanostructured collagen arrays in the caruncles of the malagasy asities (Eurylaimidae: aves)," *Journal of Experimental Biology,* vol. 202, no. 24, pp. 3507-3522, 1999, doi: 10.1242/jeb.202.24.3507.
[136] A. P. Genoud, R. Basistyy, G. M. Williams, and B. P. Thomas, "Optical remote sensing for monitoring flying mosquitoes, gender identification and discussion on species identification," *Applied Physics B,* vol. 124, no. 3, pp. 1-11, 2018.
[137] S. Jansson, P. Atkinson, R. Ignell, and M. Brydegaard, "First polarimetric investigation of malaria mosquitoes as lidar targets," *IEEE Journal of Selected Topics in Quantum Electronics,* vol. 25, no. 1, pp. 1-8, 2018.
[138] A. Yoshida, M. Motoyama, A. Kosaku, and K. Miyamoto, "Antireflective nanoprotuberance array in the transparent wing of a hawkmoth, Cephonodes hylas," *Zoological science,* vol. 14, no. 5, pp. 737-741, 1997.
[139] D. G. Stavenga, J. R. Wallace, and E. J. Warrant, "Bogong Moths Are Well Camouflaged by Effectively Decolourized Wing Scales," *Frontiers in physiology,* vol. 11, p. 95, 2020. [Online]. Available: https://www.ncbi.nlm.nih.gov/pmc/articles/PMC7026391/pdf/fphys-11-00095.pdf.

[140] P. O. Vidal and L. Suesdek, "Comparison of wing geometry data and genetic data for assessing the population structure of Aedes aegypti," *Infection, Genetics and Evolution*, vol. 12, no. 3, pp. 591-596, 2012/04/01/ 2012, doi: https://doi.org/10.1016/j.meegid.2011.11.013.
[141] M. Nixon, A. Orr, and P. Vukusic, "Wrinkles enhance the diffuse reflection from the dragonfly Rhyothemis resplendens," *Journal of the Royal Society Interface*, vol. 12, no. 103, p. 20140749, 2015.
[142] S. A. Combes and T. L. Daniel, "Flexural stiffness in insect wings I. Scaling and the influence of wing venation," *Journal of experimental biology*, vol. 206, no. 17, pp. 2979-2987, 2003.
[143] T. R. Neil, Z. Shen, D. Robert, B. W. Drinkwater, and M. W. Holderied, "Moth wings are acoustic metamaterials," *Proceedings of the National Academy of Sciences*, vol. 117, no. 49, pp. 31134-31141, 2020. [Online]. Available: https://www.pnas.org/content/pnas/117/49/31134.full.pdf.
[144] X. Wang, Q. Cong, J. Zhang, and Y. Wan, "Multivariate coupling mechanism of NOCTUIDAE moth wings' surface superhydrophobicity," *Chinese Science Bulletin*, vol. 54, no. 4, pp. 569-575, 2009/02/01 2009, doi: 10.1007/s11434-009-0071-0.
[145] C. Munnerlyn and M. Latta, "Rough surface interferometry using a $CO_2$ laser source," *Applied Optics*, vol. 7, no. 9, pp. 1858-1859, 1968.
[146] O. Kwon, J. Wyant, and C. Hayslett, "Rough surface interferometry at 10.6 μm," *Applied optics*, vol. 19, no. 11, pp. 1862-1869, 1980.
[147] R. Basistyy, A. Genoud, and B. Thomas, "Backscattering properties of topographic targets in the visible, shortwave infrared, and mid-infrared spectral ranges for hard-target lidars," *Applied optics*, vol. 57, no. 24, pp. 6990-6997, 2018.
[148] S. Berthier, *Iridescence*. Springer, 2007.
[149] F. Stanco, S. Battiato, and G. Gallo, *Digital imaging for cultural heritage preservation: Analysis, restoration, and reconstruction of ancient artworks*. CRC Press, 2017.
[150] J. Shell, "Bidirectional reflectance: An overview with remote sensing applications & measurement," 2004.
[151] P. Vukusic, J. Sambles, and C. Lawrence, "Structurally assisted blackness in butterfly scales," *Proceedings of the Royal Society of London. Series B: Biological Sciences*, vol. 271, no. suppl_4, pp. S237-S239, 2004.
[152] E. K. Robertson, "Goniometric investigation of scattering from insect wings in near infrared," 2024.
[153] A. P. Willmott and C. P. Ellington, "The mechanics of flight in the hawkmoth Manduca sexta. I. Kinematics of hovering and forward flight," *Journal of experimental Biology*, vol. 200, no. 21, pp. 2705-2722, 1997, doi: 10.1242/jeb.200.21.2705.
[154] E. Malmqvist *et al.*, "The bat–bird–bug battle: daily flight activity of insects and their predators over a rice field revealed by high-resolution Scheimpflug Lidar," *Royal Society open science*, vol. 5, no. 4, p. 172303, 2018, doi: 10.1098/rsos.172303.

[155] T. D. Schultz and O. M. Fincke, "Structural colours create a flashing cue for sexual recognition and male quality in a Neotropical giant damselfly," *Functional Ecology*, vol. 23, no. 4, pp. 724-732, 2009.
[156] H. Cong and W. Cao, "Thin film interference of colloidal thin films," *Langmuir*, vol. 20, no. 19, pp. 8049-8053, 2004.
[157] A. N. Bashkatov and E. A. Genina, "Water refractive index in dependence on temperature and wavelength: a simple approximation," in *Saratov Fall Meeting 2002: Optical Technologies in Biophysics and Medicine IV*, 2003, vol. 5068: SPIE, pp. 393-395.
[158] S. Jansson and M. Brydegaard, "Passive kHz lidar for the quantification of insect activity and dispersal," *Animal Biotelemetry*, vol. 6, no. 1, p. 6, 2018/05/30 2018, doi: 10.1186/s40317-018-0151-5.
[159] A. Gebru, S. Jansson, R. Ignell, C. Kirkeby, J. Prangsma, and M. Brydegaard, "Multiband modulation spectroscopy for determination of sex and species of mosquitoes in flight," *J. Biophotonics*, vol. 11, no. 8, 2018.
[160] A. Moore and R. H. Miller, "Automated Identification of Optically Sensed Aphid (Homoptera: Aphidae) Wingbeat Waveforms," *Annals of the Entomological Society of America*, vol. 95, no. 1, pp. 1-8, 2002, doi: 10.1603/0013-8746(2002)095[0001:Aioosa]2.0.Co;2.
[161] K. Bjerge, J. B. Nielsen, M. V. Sepstrup, F. Helsing-Nielsen, and T. T. Høye, "An automated light trap to monitor moths (Lepidoptera) using computer vision-based tracking and deep learning," *bioRxiv*, p. 2020.03.18.996447, 2020, doi: 10.1101/2020.03.18.996447.
[162] C. Kirkeby *et al.*, "Advances in automatic identification of flying insects using optical sensors and machine learning," *Scientific Reports*, vol. 11, no. 1, p. 1555, 2021/01/15 2021, doi: 10.1038/s41598-021-81005-0.
[163] K. Rydhmer *et al.*, "Automating insect monitoring using unsupervised near-infrared sensors," *Scientific Reports*, vol. 12, no. 1, pp. 1-11, 2022.
[164] M. E. Sinka *et al.*, "HumBug–An Acoustic Mosquito Monitoring Tool for use on budget smartphones," *Methods in Ecology and Evolution*, vol. 12, no. 10, pp. 1848-1859, 2021.
[165] R. J. Bomphrey, T. Nakata, N. Phillips, and S. M. Walker, "Smart wing rotation and trailing-edge vortices enable high frequency mosquito flight," *Nature*, vol. 544, no. 7648, pp. 92-95, 2017/04/01 2017, doi: 10.1038/nature21727.
[166] M. L. May, "Wingstroke frequency of dragonflies (Odonata: Anisoptera) in relation of temperature and body size," *Journal of comparative physiology*, vol. 144, no. 2, pp. 229-240, 1981.
[167] T. Saha, A. P. Genoud, J. H. Park, and B. P. Thomas, "Temperature Dependency of Insect's Wingbeat Frequencies: An Empirical Approach to Temperature Correction," *Insects*, vol. 15, no. 5, p. 342, 2024. [Online]. Available: https://www.mdpi.com/2075-4450/15/5/342.
[168] V. Drake, "Distinguishing target classes in observations from vertically pointing entomological radars," *International Journal of Remote Sensing*, vol. 37, no. 16, pp. 3811-3835, 2016.

[169] M. Brydegaard, E. Malmqvist, S. Jansson, J. Larsson, S. Török, and G. Zhao, "The Scheimpflug lidar method," *Lidar Remote Sensing for Environmental Monitoring 2017*, vol. 10406, p. 104060I, 2017, doi: 10.1117/12.2295982.
[170] M. Brydegaard *et al.*, "Short-wave infrared atmospheric Scheimpflug lidar," in *EPJ Web of Conferences*, 2018, vol. 176: EDP Sciences, p. 01012.
[171] A. Runemark, M. Wellenreuther, H. H. Jayaweera, S. Svanberg, and M. Brydegaard, "Rare events in remote dark-field spectroscopy: an ecological case study of insects," *IEEE Journal of Selected Topics in Quantum Electronics*, vol. 18, no. 5, pp. 1573-1582, 2012.
[172] G. Zhao *et al.*, "Inelastic Hyperspectral Lidar for Profiling Aquatic Ecosystems," *Laser & Photonics Reviews*, vol. 10, no. 5, pp. 807–813, 2016.
[173] B. E. Saleh and M. C. Teich, *Fundamentals of photonics*. john Wiley & sons, 2019.
[174] V. V. Tuchin, "Tissue optics and photonics: light-tissue interaction," *Journal of Biomedical Photonics & Engineering*, vol. 1, no. 2, pp. 98-134, 2015.
[175] V. V. Tuchin, "Polarized light interaction with tissues," *Journal of biomedical optics*, vol. 21, no. 7, pp. 071114-071114, 2016.
[176] S. L. Jacques and J. C. Ramella-Roman, "Polarized light imaging of tissues," *Lasers and Current Optical Techniques in Biology*, vol. 4, pp. 591-607, 2004.
[177] S. L. Jacques, J. R. Roman, and K. Lee, "Imaging superficial tissues with polarized light," *Lasers in Surgery and Medicine: The Official Journal of the American Society for Laser Medicine and Surgery*, vol. 26, no. 2, pp. 119-129, 2000.
[178] S. L. Jacques, J. C. Ramella-Roman, and K. Lee, "Imaging skin pathology with polarized light," *Journal of biomedical optics*, vol. 7, no. 3, pp. 329-340, 2002.
[179] K. Järrendahl and H. Arwin, "Polarizing Natural Nanostructures," *Ellipsometry of Functional Organic Surfaces and Films*, pp. 247-268, 2018.
[180] N. Shashar, R. Hagan, J. G. Boal, and R. T. Hanlon, "Cuttlefish use polarization sensitivity in predation on silvery fish," *Vision research*, vol. 40, no. 1, pp. 71-75, 2000.
[181] V. Pignatelli, S. E. Temple, T.-H. Chiou, N. W. Roberts, S. P. Collin, and N. J. Marshall, "Behavioural relevance of polarization sensitivity as a target detection mechanism in cephalopods and fishes," *Philosophical Transactions of the Royal Society B: Biological Sciences*, vol. 366, no. 1565, pp. 734-741, 2011.
[182] C. W. Hawryshyn, "Mechanisms of ultraviolet polarization vision in fishes," *Sensory processing in aquatic environments*, pp. 252-265, 2003.
[183] F. Lou *et al.*, "How mantis shrimp compound eye recognizes circularly polarized light," *Authorea Preprints*, 2023.
[184] D. BRUNNER and T. LABHART, "Behavioural evidence for polarization vision in crickets," *Physiological entomology*, vol. 12, no. 1, pp. 1-10, 1987.
[185] M. Dacke, D.-E. Nilsson, C. H. Scholtz, M. Byrne, and E. J. Warrant, "Insect orientation to polarized moonlight," *Nature*, vol. 424, no. 6944, pp. 33-33, 2003.
[186] M. Dacke, "Polarized light orientation in ball-rolling dung beetles," in *Polarized Light and Polarization Vision in Animal Sciences*: Springer, 2014, pp. 27-39.

[187] B. el Jundi, J. Smolka, E. Baird, M. J. Byrne, and M. Dacke, "Diurnal dung beetles use the intensity gradient and the polarization pattern of the sky for orientation," *Journal of experimental biology*, vol. 217, no. 13, pp. 2422-2429, 2014.
[188] S. A. Jewell, P. Vukusic, and N. W. Roberts, "Circularly polarized colour reflection from helicoidal structures in the beetle Plusiotis boucardi," *New Journal of Physics*, vol. 9, no. 4, p. 99, 2007/04/23 2007, doi: 10.1088/1367-2630/9/4/099.
[189] H. Arwin, R. Magnusson, J. Landin, and K. Järrendahl, "Chirality-induced polarization effects in the cuticle of scarab beetles: 100 years after Michelson," *Philosophical Magazine*, vol. 92, no. 12, pp. 1583-1599, 2012.
[190] P. Brady and M. Cummings, "Differential response to circularly polarized light by the jewel scarab beetle Chrysina gloriosa," *The American Naturalist*, vol. 175, no. 5, pp. 614-620, 2010.
[191] L. Mei and P. Guan, "Development of an atmospheric polarization Scheimpflug lidar system based on a time-division multiplexing scheme," *Optics letters*, vol. 42, no. 18, pp. 3562-3565, 2017, doi: 10.1364/OL.42.003562.
[192] S. Zhu *et al.*, "Insect abundance over Chinese rice fields in relation to environmental parameters, studied with a polarization-sensitive CW near-IR lidar system," *Applied Physics B*, vol. 123, no. 7, p. 211, 2017/07/10 2017, doi: 10.1007/s00340-017-6784-x.
[193] S. Zhu *et al.*, "Insect remote sensing using a polarization sensitive cw lidar system in chinese rice fields," *EPJ Web of Conferences*, vol. 176, p. 07001, 01/01 2018, doi: 10.1051/epjconf/201817607001.
[194] E. Malmqvist, "From Fauna to Flames."
[195] N. J. Butterworth, T. E. White, P. G. Byrne, and J. F. Wallman, "Love at first flight: wing interference patterns are species‐specific and sexually dimorphic in blowflies (Diptera: Calliphoridae)," *Journal of Evolutionary Biology*, vol. 34, no. 3, pp. 558-570, 2021. [Online]. Available: https://onlinelibrary.wiley.com/doi/pdfdirect/10.1111/jeb.13759?download=true.
[196] F. Mattia *et al.*, "The effect of surface roughness on multifrequency polarimetric SAR data," *IEEE Transactions on Geoscience and Remote Sensing*, vol. 35, no. 4, pp. 954-966, 1997.
[197] D. Kasilingam, D. Schuler, and J.-S. Lee, "The depolarization of radar backscatter from rough surfaces due to surface roughness and slopes," in *IGARSS 2001. Scanning the Present and Resolving the Future. Proceedings. IEEE 2001 International Geoscience and Remote Sensing Symposium (Cat. No. 01CH37217)*, 2001, vol. 2: IEEE, pp. 925-927.
[198] S. Hong, "Surface roughness and polarization ratio in microwave remote sensing," *International Journal of Remote Sensing*, vol. 31, no. 10, pp. 2709-2716, 2010.
[199] U. Persson, "Measurement of surface roughness using infrared scattering," *Measurement*, vol. 18, no. 2, pp. 109-116, 1996/06/01/ 1996, doi: https://doi.org/10.1016/S0263-2241(96)00047-4.

[200] C. J. Tay, S. H. Wang, C. Quan, and H. M. Shang, "In situ surface roughness measurement using a laser scattering method," *Optics Communications*, vol. 218, no. 1, pp. 1-10, 2003/03/15/ 2003, doi: https://doi.org/10.1016/S0030-4018(03)01102-7.
[201] W. G. Egan, "Polarization and surface roughness," in *Scattering and Surface Roughness II*, 1998, vol. 3426: SPIE, pp. 144-152.
[202] H. L. Leertouwer, B. D. Wilts, and D. G. Stavenga, "Refractive index and dispersion of butterfly chitin and bird keratin measured by polarizing interference microscopy," *Optics Express*, vol. 19, no. 24, pp. 24061-24066, 2011/11/21 2011, doi: 10.1364/OE.19.024061.
[203] D. G. Stavenga, H. L. Leertouwer, D. C. Osorio, and B. D. Wilts, "High refractive index of melanin in shiny occipital feathers of a bird of paradise," *Light: Science & Applications*, vol. 4, no. 1, pp. e243-e243, 2015/01/01 2015, doi: 10.1038/lsa.2015.16.
[204] A. R. Parker, D. R. Mckenzie, and M. C. Large, "Multilayer reflectors in animals using green and gold beetles as contrasting examples," *Journal of experimental biology*, vol. 201, no. 9, pp. 1307-1313, 1998.
[205] J. A. Noyes, P. Vukusic, and I. R. Hooper, "Experimental method for reliably establishing the refractive index of buprestid beetle exocuticle," *Optics express*, vol. 15, no. 7, pp. 4351-4358, 2007.
[206] A. I. Lvovsky, "Fresnel equations," *Encyclopedia of Optical Engineering*, vol. 27, pp. 1-6, 2013.
[207] M. Born and E. Wolf, *Principles of optics: electromagnetic theory of propagation, interference and diffraction of light*. Elsevier, 2013.
[208] V. Lucarini, J. J. Saarinen, K.-E. Peiponen, and E. M. Vartiainen, *Kramers-Kronig relations in optical materials research*. Springer Science & Business Media, 2005.
[209] J. S. Toll, "Causality and the Dispersion Relation: Logical Foundations," *Physical Review*, vol. 104, no. 6, pp. 1760-1770, 12/15/ 1956, doi: 10.1103/PhysRev.104.1760.
[210] T. Sai, M. Saba, E. R. Dufresne, U. Steiner, and B. D. Wilts, "Designing refractive index fluids using the Kramers–Kronig relations," *Faraday Discussions*, 10.1039/D0FD00027B vol. 223, no. 0, pp. 136-144, 2020, doi: 10.1039/D0FD00027B.
[211] V. Lucarini, J. Saarinen, K. Peiponen, and E. Vartiainen, "Kramers-Kronig Relations in Optical Materials Research," *Kramers-Kronig Relations in Optical Materials Research, by V. Lucarini, J. Saarinen, K. Peiponen, and E. Vartiainen. X, 162 p. 37 illus. 3-540-23673-2. Berlin: Springer, 2005.*, vol. 110, 01/01 2005, doi: 10.1007/b138913.
[212] A. Paar. "Basics of refractometry." https://wiki.anton-paar.com/de-de/grundlagen-der-refraktometrie/ (accessed.
[213] D. G. Stavenga, H. L. Leertouwer, and B. D. Wilts, "Coloration principles of nymphaline butterflies–thin films, melanin, ommochromes and wing scale stacking," *Journal of Experimental Biology*, vol. 217, no. 12, pp. 2171-2180, 2014.

[214] M. Giraldo and D. Stavenga, "Brilliant iridescence of Morpho butterfly wing scales is due to both a thin film lower lamina and a multilayered upper lamina," *Journal of Comparative Physiology A*, vol. 202, no. 5, pp. 381-388, 2016. [Online]. Available: https://www.ncbi.nlm.nih.gov/pmc/articles/PMC4841846/pdf/359_2016_Article_1084.pdf.

[215] M. Khan, M. Alam, M. Masud, and A. Amin, "Importance of high order high pass and low pass filters," *World Applied Sciences Journal*, vol. 34, no. 9, pp. 1261-1268, 2016.

[216] S. M. Villarreal, O. Winokur, and L. Harrington, "The impact of temperature and body size on fundamental flight tone variation in the mosquito vector Aedes aegypti (Diptera: Culicidae): implications for acoustic lures," *Journal of medical entomology*, vol. 54, no. 5, pp. 1116-1121, 2017. [Online]. Available: https://www.ncbi.nlm.nih.gov/pmc/articles/PMC5850351/pdf/tjx079.pdf.

[217] I. E. Hendriks, "Spectrally resolved insect flashes by sunlight," 2024 2024.

[218] G. Zhao *et al.*, "Dual-band continuous-wave lidar system employed for particle classification," *To appear*, 2017.

[219] M. Zucco, V. Caricato, A. Egidi, and M. Pisani, "A hyperspectral camera in the UVA band," *IEEE Transactions on Instrumentation and Measurement*, vol. 64, no. 6, pp. 1425-1430, 2015.

[220] J. Yang, Q. Xue, J. Li, B. Han, Y. Wang, and H. Bai, "Deep ultraviolet high-resolution microscopic hyperspectral imager and its biological tissue detection," *Applied Optics*, vol. 62, no. 13, pp. 3310-3319, 2023.

[221] HySpex. "HySpex Classic SWIR-384." https://www.hyspex.com/hyspex-products/hyspex-classic/hyspex-swir-384/ (accessed 07 Jun, 2021).

[222] M. Li *et al.*, "Potential for identification of wild night-flying moths by remote infrared microscopy," *Journal of The Royal Society Interface*, vol. 19, no. 191, p. 20220256, 2022, doi: doi:10.1098/rsif.2022.0256.

[223] S.-E. Qian, "Hyperspectral satellites, evolution, and development history," *IEEE Journal of Selected Topics in Applied Earth Observations and Remote Sensing*, vol. 14, pp. 7032-7056, 2021.

[224] M. Govender, K. Chetty, V. Naiken, and H. Bulcock, "A comparison of satellite hyperspectral and multispectral remote sensing imagery for improved classification and mapping of vegetation," *Water sa*, vol. 34, no. 2, pp. 147-154, 2008.

[225] E. Bedini, "The use of hyperspectral remote sensing for mineral exploration: A review," *Journal of Hyperspectral Remote Sensing*, vol. 7, no. 4, pp. 189-211, 2017.

[226] V. E. Brando and A. G. Dekker, "Satellite hyperspectral remote sensing for estimating estuarine and coastal water quality," *IEEE transactions on geoscience and remote sensing*, vol. 41, no. 6, pp. 1378-1387, 2003.

[227] A. Bjorgan, M. Milanic, and L. L. Randeberg, "Estimation of skin optical parameters for real-time hyperspectral imaging applications," *Journal of biomedical optics*, vol. 19, no. 6, pp. 066003-066003, 2014.

[228] M. Denstedt, B. S. Pukstad, L. A. Paluchowski, J. E. Hernandez-Palacios, and L. L. Randeberg, "Hyperspectral imaging as a diagnostic tool for chronic skin ulcers," in *Photonic Therapeutics and Diagnostics IX*, 2013, vol. 8565: SPIE, pp. 71-84.

[229] L. L. Randeberg, "Hyperspectral characterization of tissue in the SWIR spectral range: a road to new insight?," in *Optical Biopsy XVII: Toward Real-Time Spectroscopic Imaging and Diagnosis*, 2019, vol. 10873: SPIE, pp. 125-140.

[230] H. P. La, Y. D. Eo, A. Chang, and C. Kim, "Extraction of individual tree crown using hyperspectral image and LiDAR data," *KSCE Journal of Civil Engineering*, vol. 19, pp. 1078-1087, 2015.

[231] Y. Shi *et al.*, "Tree species classification using plant functional traits from LiDAR and hyperspectral data," *International Journal of Applied Earth Observation and Geoinformation*, vol. 73, pp. 207-219, 2018.

[232] J. M. Medina, S. M. C. Nascimento, and P. Vukusic, "Hyperspectral optical imaging of two different species of lepidoptera," *Nanoscale research letters*, vol. 6, pp. 1-5, 2011.

[233] J. Carpenter, "Improvements in enlarging or like cameras, 1901," *British patent GB*, vol. 1139, 1901.

[234] T. Scheimpflug, "Improved method and apparatus for the systematic alteration or distortion of plane pictures and images by means of lenses and mirrors for photography and for other purposes," *GB patent*, vol. 1196, 1904.

[235] S. Svanberg, *Atomic and molecular spectroscopy: basic aspects and practical applications*. Springer Science & Business Media, 2012.

[236] E. Malmqvist, M. Brydegaard, M. Aldén, and J. Bood, "Scheimpflug Lidar for combustion diagnostics," *Optics Express*, vol. 26, no. 12, pp. 14842-14858, 2018/06/11 2018, doi: 10.1364/OE.26.014842.

[237] S. Jansson, E. Malmqvist, M. Brydegaard, S. Akesson, and J. Rydell, "A Scheimpflug lidar used to observe insect swarming at a wind turbine," *Ecological Indicators*, vol. 117, p. 106578, 10/01 2020, doi: 10.1016/j.ecolind.2020.106578.

[238] L. Mei and M. Brydegaard, "Development of a Scheimpflug lidar system for atmospheric aerosol monitoring," in *EPJ Web of Conferences*, 2016, vol. 119: EDP Sciences, p. 27005.

[239] R. Clawges, K. Vierling, L. Vierling, and E. Rowell, "The use of airborne lidar to assess avian species diversity, density, and occurrence in a pine/aspen forest," *Remote sensing of environment*, vol. 112, no. 5, pp. 2064-2073, 2008.

[240] J. Müller and R. Brandl, "Assessing biodiversity by remote sensing in mountainous terrain: the potential of LiDAR to predict forest beetle assemblages," *Journal of Applied Ecology*, vol. 46, no. 4, pp. 897-905, 2009.

[241] G. Sun, K. J. Ranson, Z. Guo, Z. Zhang, P. Montesano, and D. Kimes, "Forest biomass mapping from lidar and radar synergies," *Remote sensing of environment*, vol. 115, no. 11, pp. 2906-2916, 2011.

[242] A. Ansmann and D. Müller, "Lidar and atmospheric aerosol particles," in *Lidar: range-resolved optical remote sensing of the atmosphere*: Springer, 2005, pp. 105-141.

[243] S. R. Pal, W. Steinbrecht, and A. I. Carswell, "Automated method for lidar determination of cloud-base height and vertical extent," *Applied optics*, vol. 31, no. 10, pp. 1488-1494, 1992.
[244] A. Piroli, V. Dallabetta, M. Walessa, D. Meissner, J. Kopp, and K. Dietmayer, "Detection of Condensed Vehicle Gas Exhaust in LiDAR Point Clouds," in *2022 IEEE 25th International Conference on Intelligent Transportation Systems (ITSC)*, 8-12 Oct. 2022 2022, pp. 600-606, doi: 10.1109/ITSC55140.2022.9922475.
[245] L. Mei, T. Ma, Z. Kong, Z. Gong, and H. Li, "Comparison studies of the Scheimpflug lidar technique and the pulsed lidar technique for atmospheric aerosol sensing," *Applied Optics*, vol. 58, no. 32, pp. 8981-8992, 2019/11/10 2019, doi: 10.1364/AO.58.008981.
[246] L. Xing, W. Dai, and Y. Zhang, "Scheimpflug camera-based technique for multi-point displacement monitoring of bridges," *Sensors*, vol. 22, no. 11, p. 4093, 2022.
[247] J. Larsson *et al.*, "Atmospheric CO2 sensing using Scheimpflug-lidar based on a 1.57um fiber source," *Optics Express*, vol. 27, no. 12, pp. 17348-17358, 2019/06/10 2019, doi: 10.1364/OE.27.017348.
[248] Y. Li, K. Wang, R. Quintero-Torres, R. Brick, A. V. Sokolov, and M. O. Scully, "Insect flight velocity measurement with a CW near-IR Scheimpflug lidar system," *Optics Express*, vol. 28, no. 15, pp. 21891-21902, 2020/07/20 2020, doi: 10.1364/OE.394992.
[249] L. Müller, "Elastic hyperspectral lidar for detecting coherent backscatter from insects," Master Thesis, 2022.
[250] P. R. Hemmer *et al.*, "Standoff spectroscopy via remote generation of a backward-propagating laser beam," *Proceedings of the National Academy of Sciences*, vol. 108, no. 8, pp. 3130-3134, 2011.
[251] A. Dogariu, J. B. Michael, M. O. Scully, and R. B. Miles, "High-gain backward lasing in air," *Science*, vol. 331, no. 6016, pp. 442-445, 2011.
[252] V. Letokhov and S. Johansson, *Astrophysical Lasers* Oxford University Press, 2009, p. 304.
[253] P. Polynkin and Y. Cheng, "Air Lasing," ed: Springer, 2018.
[254] U. Westblom, S. Agrup, M. Aldén, H. Hertz, and J. Goldsmith, "Properties of laser-induced stimulated emission for diagnostic purposes," *Applied Physics B*, vol. 50, no. 6, pp. 487-497, 1990.
[255] P. Ding, M. Ruchkina, Y. Liu, M. Alden, and J. Bood, "Femtosecond two-photon-excited backward lasing of atomic hydrogen in a flame," *Opt. Lett.*, vol. 43, no. 5, pp. 1183-1186, 2018.
[256] J. Kasparian *et al.*, "White-Light Filaments for Atmospheric Analysis," *Science*, vol. 301, no. 5629, pp. 61-64, July 4, 2003 2003, doi: 10.1126/science.1085020.
[257] J. Kasparian and J.-P. Wolf, "Physics and applications of atmospheric nonlinear optics and filamentation," *Opt. Express*, vol. 16, no. 1, pp. 466-493, 2008.
[258] J.-P. Wolf, "Short-pulse lasers for weather control," *Reports on Progress in Physics*, vol. 81, no. 2, p. 026001, 2017.

[259] M. Goerke *et al.*, "Characterizing ice particles using two-dimensional reflections of a lidar beam," *Applied optics*, vol. 56, no. 19, pp. G188-G196, 2017.
[260] M. Vollmer and J. A. Shaw, "Brilliant colours from a white snow cover," *Physics Education*, vol. 48, no. 3, p. 322, 2013.
[261] U. Platt and J. Stutz, "Differential absorption spectroscopy," in *Differential Optical Absorption Spectroscopy*. Berlin, Heidelberg: Springer, 2008, pp. 135-174.
[262] M. T. Zuber *et al.*, "The Lunar Reconnaissance Orbiter Laser Ranging Investigation," *Space Science Reviews*, vol. 150, no. 1-4, pp. 63-80, 2009, doi: 10.1007/s11214-009-9511-z.
[263] R. R. Neely *et al.*, "Properties of horizontally oriented ice crystals observed by polarization lidar over summit, Greenland," in *EPJ Web of Conferences*, 2018, vol. 176: EDP Sciences, p. 05007.
[264] R. M. Schotland, K. Sassen, and R. Stone, "Observations by lidar of linear depolarization ratios for hydrometeors," *Journal of Applied Meteorology and Climatology*, vol. 10, no. 5, pp. 1011-1017, 1971.
[265] A. Tsekeri *et al.*, "Polarization lidar for detecting dust orientation: system design and calibration," *Atmos. Meas. Tech.*, vol. 14, no. 12, pp. 7453-7474, 2021, doi: 10.5194/amt-14-7453-2021.
[266] G. David *et al.*, "UV polarization lidar for remote sensing new particles formation in the atmosphere," *Optics Express*, vol. 22, no. 103, pp. A1009-A1022, 2014.
[267] J. A. Shaw *et al.*, "Polarization lidar measurements of honey bees in flight for locating land mines," *Optics express*, vol. 13, no. 15, pp. 5853-5863, 2005. [Online]. Available: https://www.osapublishing.org/oe/fulltext.cfm?uri=oe-13-15-5853&id=85242.
[268] G. Zhao *et al.*, "Particle profiling and classification by a dual-band continuous-wave lidar system," *Applied Optics*, vol. 57, no. 35, pp. 10164-10171, 2018/12/10 2018, doi: 10.1364/AO.57.010164.
[269] J. Sun *et al.*, "Evaluation of hyperspectral LiDAR for monitoring rice leaf nitrogen by comparison with multispectral LiDAR and passive spectrometer," *Scientific Reports*, vol. 7, no. 1, p. 40362, 2017.
[270] T. Hakala, J. Suomalainen, S. Kaasalainen, and Y. Chen, "Full waveform hyperspectral LiDAR for terrestrial laser scanning," *Optics express*, vol. 20, no. 7, pp. 7119-7127, 2012.
[271] Y. Chen *et al.*, "Feasibility Study of Ore Classification Using Active Hyperspectral LiDAR," *IEEE Geoscience and Remote Sensing Letters*, vol. 15, pp. 1-5, 07/31 2018, doi: 10.1109/LGRS.2018.2854358.
[272] T. Malkamäki, S. Kaasalainen, and J. Ilinca, "Portable hyperspectral lidar utilizing 5 GHz multichannel full waveform digitization," *Optics express*, vol. 27, no. 8, pp. A468-A480, 2019.
[273] H. Månefjord *et al.*, "3D-Printed Fluorescence Hyperspectral Lidar for Monitoring Tagged Insects," *IEEE Journal of Selected Topics in Quantum Electronics*, vol. 28, no. 5, pp. 1-9, 2022, doi: 10.1109/JSTQE.2022.3162417.
[274] X. Wang, Z. Duan, M. Brydegaard, S. Svanberg, and G. Zhao, "Drone-based area scanning of vegetation fluorescence height profiles using a miniaturized

hyperspectral lidar system," *Applied Physics B*, journal article vol. 124, no. 11, p. 207, October 09 2018, doi: 10.1007/s00340-018-7078-7.
[275] O. Shoshanim and A. Baratz, "Daytime measurements of bioaerosol simulants using a hyperspectral laser-induced fluorescence LIDAR for biosphere research," *Journal of Environmental Chemical Engineering*, vol. 8, no. 5, p. 104392, 2020.
[276] R. Boateng *et al.*, "Remote Vegetation Diagnostics in Ghana with a Hyperspectral Fluorescence Lidar," *IEEE Journal of Selected Topics in Quantum Electronics*, vol. 29, no. 4: Biophotonics, pp. 1-7, 2023 2023, doi: 10.1109/JSTQE.2023.3234022.
[277] M. Brydegaard *et al.*, "Lidar reveals activity anomaly of malaria vectors during pan-African eclipse," *Science Advances*, vol. 6, 05/13 2020, doi: 10.1126/sciadv.aay5487.
[278] F. Murtagh and P. Contreras, "Algorithms for hierarchical clustering: an overview," *Wiley Interdisciplinary Reviews: Data Mining and Knowledge Discovery*, vol. 2, no. 1, pp. 86-97, 2012.
[279] I. Dokmanic, R. Parhizkar, J. Ranieri, and M. Vetterli, "Euclidean distance matrices: essential theory, algorithms, and applications," *IEEE Signal Processing Magazine*, vol. 32, no. 6, pp. 12-30, 2015.
[280] M. Brydegaard *et al.*, "Towards global insect biomonitoring with frugal methods," *Philosophical Transactions of the Royal Society B: Biological Sciences*, vol. 379, no. 1904, p. 20230103, 2024, doi: doi:10.1098/rstb.2023.0103.
[281] K. Dyba *et al.*, *How Spectral Properties and Machine Learning Can Categorize Twin Species - Based on Diachrysia Genus*. 2021.
[282] T. T. Høye *et al.*, "Deep learning and computer vision will transform entomology," *Proceedings of the National Academy of Sciences*, vol. 118, no. 2, 2021.

# Appendix

## Guide to pinning insects for optical scanning

Here's a detailed guide on how to pin insects for the BIOSPACE scan. Remember, we need the wings flattened out to get the best normal incidence reflection when scanned at the right angle. For more visual help, we have a lot of videos on insect pinning and lidar assembly on our group YouTube channel, *@biophotonicslund653*. To the new Ph.D. and PostDoc of the lidar group, please help keep this channel alive after we leave. If you need the logins, contact me.

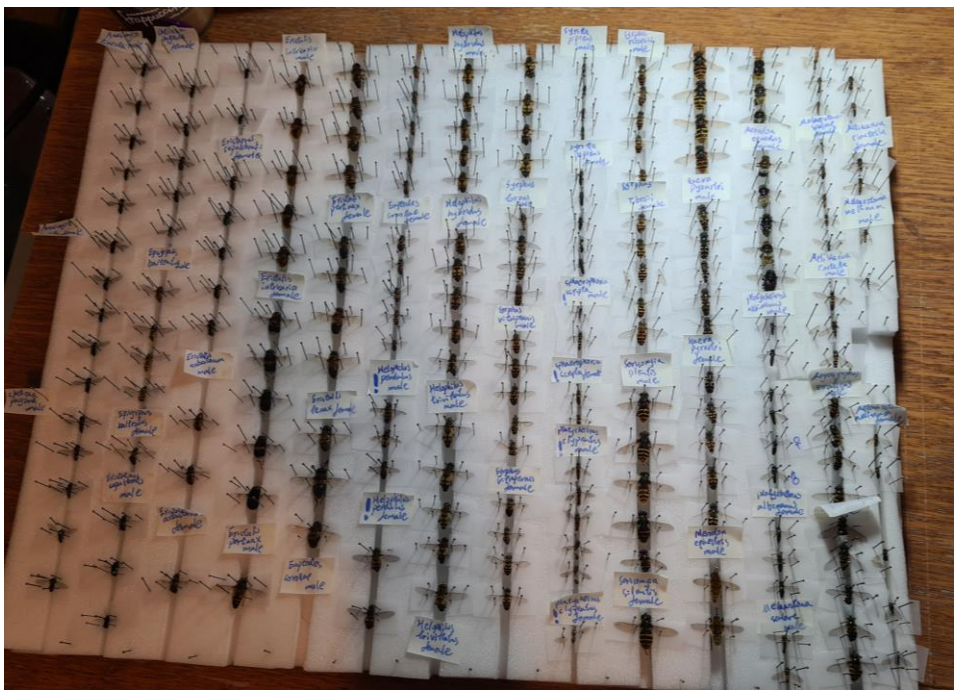

**Fig. S1: Example of a finished pinning board.** When borrowing samples from a museum, it is important to carefully track which individual specimen is which.

***Acquisition:***

Obtain insect specimens from museums, or catch them yourself, or acquire them from insect breeders. If your specimens are dry, you need to soften them in a wet chamber first.

***Preparation of a Wet Chamber:***

1. Build a wet chamber using a box with a lid, wet tissue paper, plastazote foam, pins, scissors, and a knife.
2. Add water to the box and place tissue paper inside. Pin the specimen onto the plastazote foam, and place the insect and flastazote foam in the box, ensuring it does not touch the water of the wet tissue paper. Close the lid and let it sit for a day.

***Softening the Specimen:***

After a day, check the specimen's flexibility. If it has been moistened sufficiently, the specimen will be flexible enough for further handling.

***Building a Pinning Board:***

1. Cut two long rectangles from plastazote foam and place them parallel to each other on a larger piece of foam.
2. Position the specimen between these rectangles, leaving a gap approximately the width of the insect's body.
3. Fix the two long rectangles with insect pins, and then push the specimen into the gap and leave the wing outside the gap and on the same plane as the two rectangle boards upper surface.

***Pinning the Wings:***

1. Use wing-setting tape (preferably made from baking paper) at least double or triple the size of the wing area.
2. Gently move the wings onto the side of the rectangle board and secure them with the wing-setting tape and pins. Ensure the pins do not pierce the wings themselves.

***Drying:***

Place the board in a dry, stable location away from direct sunlight. Allow at least two days for the specimen to dry in the desired position. This drying period ensures the wings remain in the desired configuration permanently.

***Handling Beetles with Elytra:***

1. Place beetles in a wet chamber for a day. No direct touch of water or wet tissue.

2. Use a needle or tweezers to gently open the elytra (hardened wing covers) to expose the wings underneath.
3. Follow the same wing-pinning procedure as with other insects.
4. When pinning beetle wings, extra care is needed due to the complex folding within the elytra, requiring patience to avoid damaging the wings.

***Re-pinning for Different Scans:***

1. For most museum specimen collection, the pin is through the specimen's thorax.
2. For scans requiring the frontal plane view, remove the pin from the thorax and re-pin the specimen through its anteroposterior.

***Handling Fresh Specimens:***

1. Freeze fresh or live insects for at least half a day.
2. After freezing, place them on dry tissue to prevent moisture absorption.
3. Since these specimens do not require a wet chamber, proceed with pinning directly.

# Paper I

4/2021

# JOURNAL OF BIOPHOTONICS

www.biophotonics-journal.org

**Bark beetles as lidar targets and prospects of photonic surveillance**
*Meng Li, Samuel Jansson, Anna Runemark, Jonathan Peterson, Carsten Thure Kirkeby, Anna Maria Jönsson, Mikkel Brydegaard*

WILEY-VCH

Received: 19 October 2020 | Revised: 20 November 2020 | Accepted: 26 November 2020

DOI: 10.1002/jbio.202000420

FULL ARTICLE

JOURNAL OF BIOPHOTONICS

# Bark beetles as lidar targets and prospects of photonic surveillance

**Meng Li[1*] | Samuel Jansson[1,2] | Anna Runemark[2] | Jonathan Peterson[1] | Carsten Thure Kirkeby[4] | Anna Maria Jönsson[3] | Mikkel Brydegaard[1,2,5]**

[1]Department of Physics, Lund University, Lund, Sweden

[2]Department of Biology, Lund University, Lund, Sweden

[3]Department of Physical Geography and Ecosystem Science, Lund University, Lund, Sweden

[4]Animal Welfare and Disease Control, Copenhagen University, Frederiksberg C, Denmark

[5]Norsk Elektro Optikk AS, Prost Stabels vei 22, Skedsmokorset, Norway

***Correspondence**
Meng Li, Department of Physics, Lund University, Sölvegatan 14, SE-223 62 Lund, Sweden.
Email: meng.li@forbrf.lth.se

**Funding information**
European Research council, Grant/Award Number: 2019-850463; Svenska Forskningsrådet Formas, Grant/Award Number: 2018-01061

## Abstract

Forestry is raising concern about the outbreaks of European spruce bark beetle, *Ips typographus*, causing extensive damage to the spruce forest and timber values. Precise monitoring of these beetles is a necessary step towards preventing outbreaks. Current commercial monitoring methods are catch-based and lack in both temporal and spatial resolution. In this work, light scattering from beetles is characterized, and the feasibility of entomological lidar as a tool for long-term monitoring of bark beetles is explored. Laboratory optical properties, wing thickness, and wingbeat frequency of bark beetles are reported, and these parameters can infer target identity in lidar data. Lidar results from a Swedish forest with controlled bark beetle release event are presented. The capability of lidar to simultaneously monitor both insects and a pheromone plume mixed with chemical smoke governing the dispersal of many insects is demonstrated. In conclusion, entomological lidar is a promising tool for monitoring bark beetles.

**KEYWORDS**

bark beetle, coherent scattering, entomological lidar, environmental monitoring, *Ips typographus*, target characterization, thin films

**Abbreviations:** DoLP, degree of linear polarization; FoV, field of view; IQR, interquartile range; NIR, near infrared; OCS, optical cross-section; SWIR, short-wave infrared; WBF, wing beat frequency; WIP, wing interference pattern.

Precise monitoring of European spruce bark beetle *Ips typographus* is necessary for fighting bark beetle infestation early. In this work optical properties wing thickness and WBF of bark beetles are reported and these parameters infer target identity in lidar data. Lidar results from a Swedish forest with a controlled bark beetle release event are presented. We concluded that our entomological lidar is a promising tool for remote monitoring bark beetles

## 1 | INTRODUCTION

The spruce bark beetle (*Ips typographus*) is one of the most severe insect pests in European forests, capable of killing millions of spruce trees in large outbreaks [1]. During normal conditions, the adult insects mainly attack trees that are already dead. Storm damage or severe drought stress, however, lead to ample availability of brood material for the beetles. Rapid population increases have then been observed, resulting in outbreaks during which healthy trees are attacked and killed [2]. Spruce bark beetles communicate via pheromones to form aggregated attacks, which overcome the defense capacity of living trees [3]. Whereas most attacks occur within a distance of 500 m from a previous attack [4], the spruce bark beetle can disperse several kilometers [5]. Both the flight activity and the development from egg to mature bark beetle are temperature-dependent. The flight mainly occurs during days with a temperature above 16–20°C [6]. A new generation of bark beetles is initiated by overwintering adults in May and June, and maturity is reached in July to August. In central Europe and Denmark, the first generation commonly initiates a second generation peaking during late summer [7]. In Sweden, this has been rare historically, but the likelihood of two generations per year increases due to climate change [8] and it has been observed that there is a second generation emerging beetles in the south of Sweden in July [9].

A common countermeasure against bark beetles outbreaks is the timely sanitary cutting of recently attacked trees. Pheromone traps are used for monitoring flying beetles, and when there are a large number of beetles in the trap, it indicates a high risk of attacks. Traps are usually emptied weekly during the swarming season. The Swedish Forest Agency (Skogsstyrelsen), in 2020, continuously operates traps in 60 locations throughout the country [10]. Even though the traps are emptied weekly, it is still laborious to collect the trap catches, and the trap catches are therefore also limited in time resolution. They do not show the population dispersal and cannot be used to infer how the weather changes throughout the week affect bark beetle activity. The catch efficiency is also highly location-dependent, and trapped rotten insects can deter the beetles away from traps [11].

The efficiency of outbreak control depends on knowing the time, location, and magnitude of infestations. Therefore, surveillance of the population density of beetles is crucial. Several methods have been used by researchers to access the population dynamic of insects, such as e-traps [12, 13], entomological radar [14, 15], and lidar [16–22]. Existing aerial topographic lidar has primarily been used for damage assessment [23]. E-trap provides a limited assessment of insects fluxes and no dispersal estimation, and radar is unable to monitor untagged insects imbedded in the forest due to ground clutter. To overcome the limitations of those photonic surveillance methods, our group developed a kHz entomological lidar for non-intrusive remote sensing [17, 19, 22, 24, 25]. It provides optical oscillatory and microstructure information of the in-flight target, based on the retrieved spectral and polarization information.

This study aims to evaluate the feasibility of entomological lidar as a tool for long-term monitoring of bark beetles. For this reason, we characterized ex-vivo bark beetle with hyperspectral imaging and goniometry, and we recorded in-vivo dynamic scattering of beetles in a flight chamber. We investigated the relationship between the acquired optical properties and lidar measurement in-situ. In addition, we demonstrated the ability of lidar in visualizing and monitoring an otherwise unperceivable plume of pheromones together with insect activity simultaneously. In summary, this study provides improved knowledge for surveillance and identification of bark beetles. We concluded that our entomological lidar is a promising tool for remote monitoring of bark beetle population density, allowing for fighting bark beetle infestation early.

## 2 | MATERIALS AND METHODS

Several laboratory instruments were used to characterize bark beetles optically. Hyperspectral push-broom imaging was carried out to assess spectral features from the body, elytra, and wings. An imaging polarimetric goniometer system was used to study the scattering cross-section and de-polarization of anatomical features of beetles from various aspects of observation. A dual-band polarimetric setup was used to investigate the dynamic scattering properties and wingbeat frequency (WBF) of free-flying beetles in a flight chamber. Finally, the laboratory recordings were compared to in-field lidar measurements of released beetles.

### 2.1 | Field collection

Beetles were captured by using pheromone traps [26] during a lidar in-field campaign in April and May 2019 in the vicinity of Nytebodaskogen, Sweden (56°20′04.0”N 14°22′59.3″E). Beetles were preserved by freezing or drying. For the mounting purpose, specimens were re-moisture, and the softened beetles were pinned vertically through the thorax with small stainless steel insect pins (size 100 μm). The elytra were opened up, and the hind wings extended and positioned horizontally to the body.

The body sizes and wingspans of 30 randomly selected beetles were measured with a caliper.

## 2.2 | Hyperspectral imaging (ex-vivo)

We carried out hyperspectral push-broom scans with an instrument similar to previous studies [27]. The source was a halogen-tungsten lamp, which delivered light from a ø8 mm fiber bundle from an 80 mm distance (5.7° light cone). The light source and camera were arranged in a specular condition of ±22° to the bark beetle wing surface. The specimens were mounted on a black neoprene sheet with pins to minimize the background reflectance. The hyperspectral camera is based on a visible extended InGaAs imager (Hyspex, Norsk Elektro Optikk, Norway) with a spectral coverage of 600 nm to 1600 nm filter settings in this study. The camera was operated with a microscope objective yielding a swat width of 40 mm with a resolution of 62.5 μm per pixel and 3 nm per spectral bands. The objective had an aperture of ø 16 mm and a working distance of 80 mm, and the collected light cone was 11°. The recorded hyperspectral images were calibrated to diffuse reflectance using a Lambertian gray reference with a 50% diffuse reflectance (Spectralon®). Note that the objective only captures 3.0% of the Lambertian distribution, calibrate a reflected signal from a specular surface to a diffuse reference could produce up to ~3400% times stronger reflectance signal than from a diffuse object.

## 2.3 | Imaging Polarimetric Goniometry (ex-vivo)

Studies have shown that the body and wings of insects display distinct degrees of linear polarization (DoLP) from various aspects and scattering angles [28–30]. We use the definition of DoLP:

$$\mathrm{DoLP} = \frac{I_{co}}{I_{co} + I_{de}}. \quad (1)$$

where $I_{co}$ is the intensity of measured co-polarized reflected light and $I_{de}$ is the intensity of de-polarized reflected light (the dark current and background are assumed subtracted).

A spectral polarimetric optical tomographic imaging goniometer system (SPOTIG, see details in [30]) was used to study the DoLP contributed from anatomical features of the beetles. Such a system has been previously used in 3D reconstruction of insects [31, 32], and a similar technique has been used for optical tomography with a light sheet [33]. SPOTIG uses an LED as the light source (680 mW, 810 nm), and the light is horizontally polarized and collimated into an ø 25 mm beam. A sample is mounted on another rotational stage in order to investigate different projection aspects, and the light source can be rotated around the sample to change the scattering angle. The light scattered from the sample is collected by a horizontal microscope (f100mm, ø25mm, WD 20 cm). A linear polarization analyzer on a third rotation stage allows retrieval of both co- and de-polarization measurements (HH and HV, respectively). The camera used is a 12 bit, USB3 CMOS imager, with 1240 × 980, 4.8 × 4.8 μm pixels (Basler Ace acA2500-60 um USB3 Mono). The strobe modulated light source for automatic background subtraction.

Backscattering is recorded by placing the light source on the same side of the sample as the camera. Forward scattering/extinction can be recorded by rotating the light source to the opposite side of the sample. Flat-field calibration is done by setting the system in different illumination configurations and acquire an image of a homogeneous calibration target. The backscattering ($\theta_{sc} = 165°$) and forward scattering ($\theta_{sc} = 14°$) properties of beetles were studied in all anatomical planes, which was done by mounting each specimen in the corresponding plane and rotating the aspect stage 360° in steps of 5° (aspect angle is presented by φ). The same procedure was repeated for a beetle specimen with removed wings and specimens with removed wings and elytra in co- and de-polarization. In extinction mode ($\theta_{sc} = 0°$), the same experimental procedure as in backscattering mode was used.

The scattering phase function of beetles was also studied. Each specimen was mounted on the aspect stage, and the light source was rotated around the specimen to scan the scatter angle between $-164° < \theta_{sc} < -14°$ and $14° < \theta_{sc} < 164°$ with a step size of 5°. The same procedure was repeated for the beetle specimen without wings and specimen without wings and elytra. The phase function measurement was done in both co- and de-polarized modes.

## 2.4 | Entomological flight chamber measurement (in-vivo)

Dual-band backscattering properties of beetles in free flight were studied in our entomological chamber, see details of the setup in [29]. A dichroic beamsplitter was used to combine an 808 nm NIR laser beam (5 W) and a 1550 nm SWIR laser beam (3 W). The superimposed NIR/SWIR beam was horizontally polarized and collimated with an ø 50.8 mm lens. Detection optics (another

ø 50.8 mm lens) was placed adjacent to the light source, and the field of view (FoV) of the detector was overlapped with the NIR/SWIR laser beam to form the probe volume. A long-pass filter (RG780) was used to remove ambient LED light. A polarizing beamsplitter was used to separate the received backscattered light into co- and depolarized components. Each polarization was measured by a Si/InGaAs sandwiched photodiode (K3413-09, Hamamatsu, Japan), with a trans-impedance amplifier (TIA, OPA404) with 47 MΩ transimpedance and ~ 4 kHz bandwidth. Both NIR/SWIR laser beam and detection optics FoV were terminated in separate dark cones of neoprene. An enclosed chamber was built around the probe volume without blocking the beam or detectors [29]. White diffuse (Lambertian 100%) Teflon balls (ø 6.35 mm) was dropped through the probe volume to calibrate the backscattered light signals in all 4 channels from volts to optical cross-sections ($mm^2$) [18, 34, 35]. Beetles were released inside the chamber, and the modulated signals were measured with a sampling rate of 20 kHz in both wavelength- and polarization bands (DAQ-USB6012, National Instruments, USA).

## 2.5 | Lidar at field site measurement (in-vivo and in-situ)

A lidar in-field campaign was undertaken in Nytebodaskogen, Sweden (56°20′04.0"N 14°22′59.3″E) on May 13th - 17th, 2019, see Figure 1. The lidar system was set up on a small hill next to a barn. The lidar transect was about 120 meters long and 4 meters above the ground. The transect stretched over a clearing in a valley and terminated on a termination board covered with black neoprene (1.8% diffuse reflectance at wavelength 808 nm). A pheromone trap was positioned at mid-distance of the lidar transect and right underneath the lidar beam to lure the bark beetles, and a weather station was set next to the pheromone trap. The lidar was running 24 hours every day except the times when hard drives were replaced to enable gathering more data. On May 16th, 2019, we carried out a controlled bark beetle release event and a smoke release event separately right next to the pheromone trap. The smoke is a chemical mixture of hydrochloric acid and ammonia. The release was used to visualize the movement of pheromone plume from the trap, and the controlled bark beetle released was to obtain reference measurement of bark beetles in-situ.

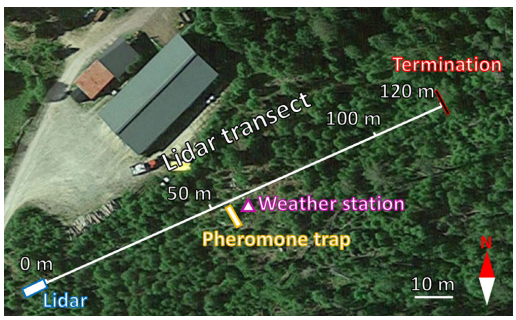


**FIGURE 1** Aerial view of the lidar site in Nyteboda. The entomological lidar was set on a small hill, and it was monitoring over a small clearing in a valley. The lidar beam was terminated by a black neoprene board. A pheromone trap and a weather station were placed halfway of the lidar transect path

We used a kHz entomological Scheimpflug lidar at 808 nm, resembling previous work [36, 37]. It was a single band lidar system, and it transmitted a 3.2 W laser beam. The beam was expanded and collimated by a refractor telescope (ø 76 mm, f = 200 mm). The backscattered light was collected by a Newtonian telescope (ø 205 mm, f = 800 mm) and focused onto a CMOS sensor array with 2048 pixels and 16-bit dynamic count. An RG780 long-pass filter and a bandpass filter (808 nm, FWHM: 3 nm) were used to block background light. The baseline of expander and collector are separated by 814 mm, and the CMOS array was tilted 45° in Scheimpflug configuration to achieve infinite focal depth [17, 18, 22, 35–38]. The laser and the CMOS camera were connected to a multiplexer and a laser driver, and the laser was controlled by a strobe signal sent from the CMOS sensor to switch on and off alternately, the sensor line rate was 3.5 kHz, and the sampling rate for both backscattered signal and background were 1.75 kHz [37]. Each acquired data file is 10 seconds long and contains 35 000 lines exposures.

# 3 | RESULTS AND DISCUSSION

Here, we report on a successful characterization of the spectral property of bark beetles from both in-vivo and ex-vivo experiments. Using the hyperspectral camera, we studied membrane thickness and its variance within and between individuals. Soap-bubble color patterns found on beetle wings in Figure 2 are caused by the thin-film effect, a typical example of coherent and incoherent light interference. Cross-section and polarization of scattered light from beetles were studied with goniometer from various observation angles. Several beetles were released

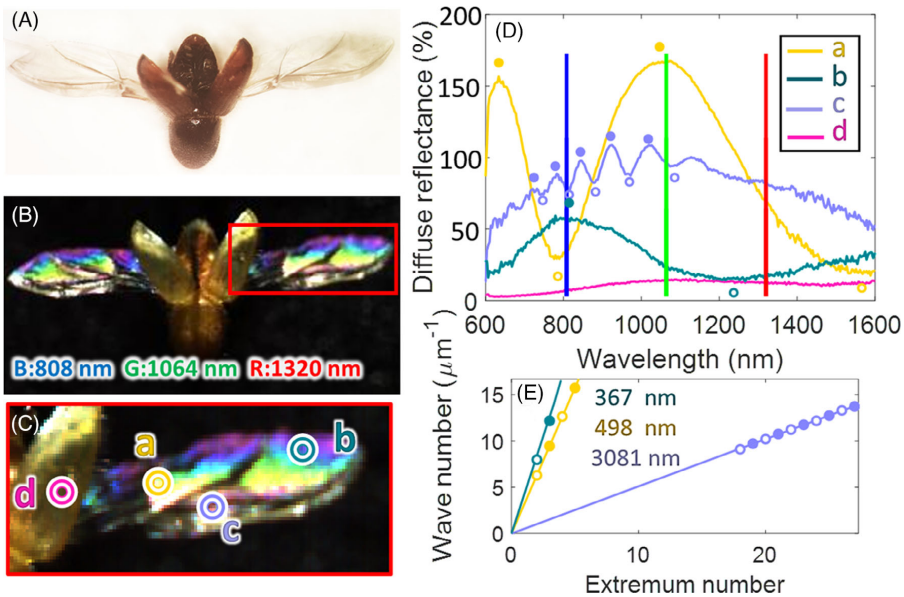


**FIGURE 2** Thin-film properties of a beetle wing. A, A true-color image of a bark beetle specimen under the diffuse lighting. B, C, False-color hyperspectral image of the same specimen in the NIR wavelength range, distinct interference color patterns are shown in the wing. The area highlighted by a red rectangle in B, is magnified and presented in C. D, The diffuse reflectance spectra of three specular pixels were selected from the hyperspectral image C. E, Reflectance maxima (closed circles) and minima (open circles) from D, for each selected pixel are fitted with a linear function with an extremum number to calculate the corresponding membrane thickness

in the dual-band polarimetric flight chamber to determine the WBF and dynamic properties of flying beetles. When laser light interacts with free-flying bark beetles, the recorded signal can be decomposed into a non-oscillatory and oscillatory scatter contribution [21, 22, 24, 25]. The oscillatory signal is contributed from the wing throughout many wingbeats, and the non-oscillatory scattered signal is contributed from the body and elytra. Both frequency components of the signals can be further decomposed into coherent ($I_{co}$-$I_{de}$) and incoherent scattering ($I_{de}$). The light interaction with the body and elytra is primarily diffuse [39], with the dominant chromophores being melanin acting as a gain factor on the reflectance (~$\lambda^{-3.48}$) [40] and for the body also liquid water scaling with the interaction path length.

## 3.1 | Hyperspectral imaging (ex-vivo)

Beetles captured in-situ from Nyteboda, Sweden, were measured according to Section 2.1 and had a median body length of 4.8 mm (IQR: 0.25 mm), median body width of 1.9 mm (IQR: 0.16 mm), and a median wing length of 6.7 mm (IQR: 0.40 mm).

Beetle wings appear transparent in the diffuse angle of light incidence (Figure 2A) but can display structural colored patterns at the specular light condition. A false-color image was formed from the hyperspectral images in Figure 2B, C. Three bands (1320, 1064, and 808 nm) coinciding with commercial laser diode wavelengths are displayed in red, green, and blue lines. The reflectance spectra of three specular pixels are shown in Figure 2D, exhibiting strong spectral fringes. Thicker wing sections display narrow spectral fringes. The extreme wave numbers (indicated with closed and open circles in Figure 2D) were used to calculate the wing.

membrane thickness by a linear fitting method [41]. We also present the spectrum of the elytra, which is sloped due to the melanization of the insect carapace and is approximately by,

$$R_{Elytra} = 13.6 \times \exp\left(-8.65 \times 10^{19} (\lambda)^{-6.83}\right) + 2.92. \quad (2)$$

where $R_{Elytra}$ is in percentage and λ is in unit of nm. Parameter 13.6 corresponding to 13.6% of diffused light from elytra was collected, parameter $8.65 \times 10^{19}$ is for scaling the fitting equation and parameter 2.92

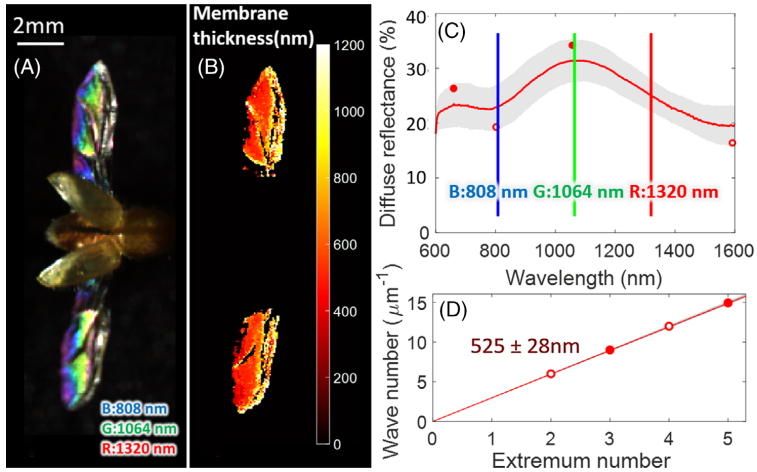


**FIGURE 3** Visual representation of the bark beetle membrane thickness among the whole wings. A, A false-color hyperspectral image of a beetle specimen. B, A color map of the membrane thickness distribution of the same specimen. C, The diffuse reflectance contributed from the whole wing, the gray background shows the spectra variations from 10 random selected beetle specimens and the red curve is the median curve of the 10 measurements. D, Reflectance maxima (closed circles) and minima (open circles) from C, are fitted with a linear function with an extremum number to calculate the corresponding membrane thickness

corresponding to the reflectance offset due to refractive index. The melanization gain factor value from our fitting is 6.83 which is larger than the one provided by the reference, 3.48 [40].

The wing interference pattern (WIP) can roughly map out the wing membrane thickness distribution, see Figure 3A,B. Specular pixels were selected with an intensity threshold, enabling calculation of the membrane thickness distribution of the insect wings [42]. The thickness of the membranes decreases from the anterior wing margin to the posterior wing margin, as the veins confined to the anterior wing margin thicken the membrane to support the vein-free structure near the posterior wing margin.

Fringes shown in Figure 2D only provide wing thickness information of the selected pixels. It is like perform a point measurement on the membrane with a spectrometer. But for the purpose of remote sensing, it is more likely for the lidar to retrieve a strong backscattered specular signal reflected from the whole wing, rather than a small section of the membrane. Therefore, we spatially integrated all spectral fringes for all specular pixels and the result effective fringe is shown in Figure 3C. If such fringes survived a spatial integration into an effective fringe from the entire wing, it would enable us to retrieve the nanoscopic wing thickness remotely, which could be highly species-specific. Note that spatially integrated fringe magnitude is more moderate than the ones from individual pixels in Figure 2D. The same measurements were carried out on 10 randomly chosen beetles to estimate the variation among individuals. The obtained effective wing membrane thickness of the entire wings of beetles was thereby calculated to 525 ± 28 nm. This biological variance of just 5% is exceptional by itself, considering that the variance of wingbeat-measurement displays at least five times higher relative spread (>25%).

All wavelengths of effective fringe were corrected for the angle of incidence of 22°, and the fringe maxima and minima from Figure 3C have wavelength values of 1592 nm, 1063 nm, 802 nm, and 646 nm under normal incidence. Three commercial laser diode wavelengths were also displayed in Figure 3C, where laser bands 808 nm and 1064 nm are very close to the destructive and constructive wavelength of 802 nm and 1063 nm.

## 3.2 | Imaging Polarimetric Goniometry, DoLP (ex-vivo)

Using a goniometer, we investigated the DoLP of beetles in different anatomical planes in backscatter- and forward scatter configurations. DoLP results are presented in Figure 4-5.

In backscattering configuration, see Figure 4, lights scattered from the beetle body and elytra are highly depolarized regardless of the aspect angles. Small features

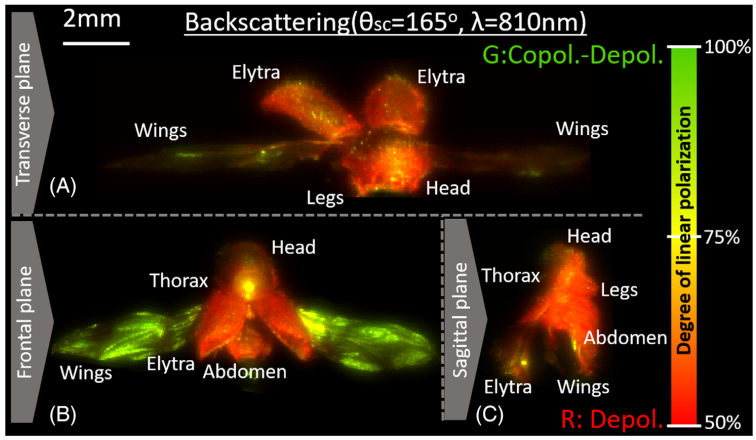


**FIGURE 4** De-polarization images of a bark beetle from different anatomical planes in backscattering. The difference between co- and de-polarized features is presented in green color, and the de-polarized features are represented in red

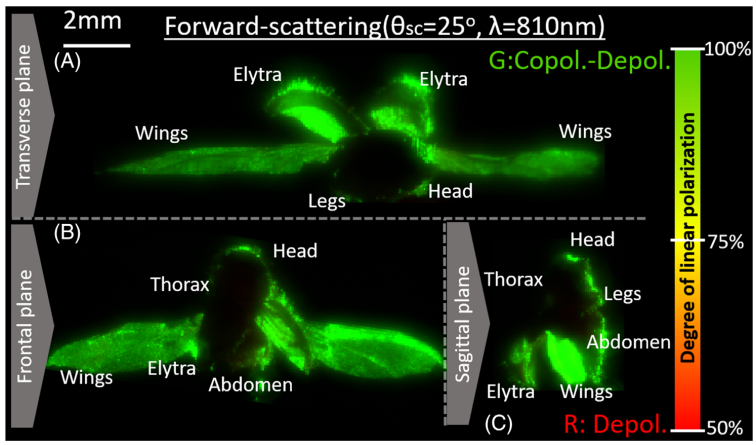


**FIGURE 5** De-polarization images of a bark beetle from different anatomical planes in forward scattering. The difference between co- and de-polarized features is presented in green color, and the de-polarized features are represented in red

such as hair on the beetle maintain a high DoLP due to light undergoes less scattering events within small features. Beetle wing exhibits minimal de-polarization when the light impinges in specular condition (±8°), as shown in Figure 4B. However, the DoLP of the wing changes when the observer moved away from the specular condition, see Figure 4A,C. Hence, when the beetle wing is in a normal incidence with the lidar probe beam, we will receive the strongest co-polarized backscattered signal.

In forward-scattering mode (see Figure 5), the impinging light maintains a high degree of polarization. It could be due to the forward scattered light undergoes a single or few scattering events through the thin body structure, such as wings and elytra. Since light did not penetrate through the thicker body part of the beetle, the polarization features of those areas could not be determined in the forward scattering configuration.

### 3.3 | Imaging Polarimetric Goniometry, OCSs and phase function (ex-vivo)

The goniometer was also used to study the optical cross-sections (OCSs) and phase function of ex-vivo beetles. The measured OCS (in $mm^2$) of a beetle is presented in Figure 6 in all anatomical planes for co- and de-polarization. Anatomical terms in the figure are used to describe the beetle positioning to the camera. In both extinction and backscattering modes, the largest OCS value is observed when measuring the beetle from ventral (belly) or dorsal (back). According to Figures 4 and 5, a beetle has the largest projection if the beetle is observed from the dorsal/ventral side, due to the positioning of wings and elytra corresponding to a large cross-section area.

Figure 4 shown that the wing membrane retains a high degree of polarization in backscattering mode. The

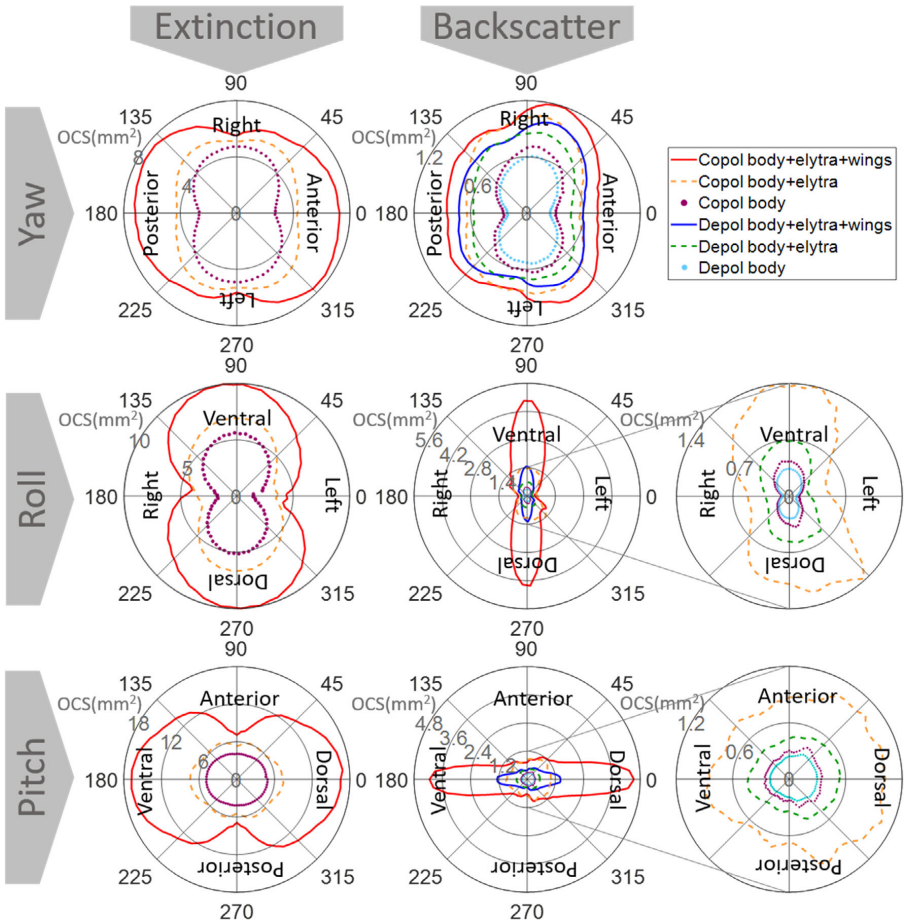


**FIGURE 6** OCSs of beetles in all anatomical planes for both polarizations. High symmetry in OCS is displayed around anatomical planes, as the beetle itself is approximately bilaterally symmetrical. Remove wings and elytra from the beetle changes the symmetry and OCS values

de-polarized signals in backscatter-roll and backscatter-pitch diagrams in Figure 6 indicate that light undergoes multiple scattering in the membrane, which could be from the thicker sections of the wing, such as the veins.

In the backscattering mode, the backscattered signal intensity is related to the reflectance of the target and how much light was collected by the camera. Therefore, the OCS values in extinction mode are way larger than the backscattered OCSs. The contribution of wings or elytra to the co- and the de-polarized signal can be observed in Figure 6 in each diagram by comparing the OCS values before and after removing wings and elytra. With the OCS values provided in Figure 6, we can calculate the DoLP of beetle with Equation (1) from different aspects. For the frontal aspect, the beetle body+wing+elytra has a DoLP of 56%, beetle body+elytra has a DoLP of 55%, and beetle body has a DoLP of 55%, which is in good agreement with the DoLP visualization result in Figure 4A. The DoLP was calculated for the dorsal aspect, where beetle body+wing+elytra has a DoLP of 76%, beetle body+elytra has a DoLP of 65%, and a beetle body has a DoLP of 55%.

The backscattering OCSs of beetle is parameterized into a set of spherical harmonics with scaling and axial flipping [34]. Furthermore, spherical harmonic coefficients were then obtained through regression. The coefficients are presented in Table 1, where the unit sphere has a radius of 1 and center at the coordinate's origin.

**TABLE 1** Parameterized table values of a set of harmonics bases used to generate the backscattering OCS in 3D. The corresponding images are presented in Figure 7

| | Backscattering | | | | | |
|---|---|---|---|---|---|---|
| | Body + elytra + wings | | Body + elytra | | Body | |
| | Copol. ($mm^2$) | Depol. ($mm^2$) | Copol. ($mm^2$) | Depol. ($mm^2$) | Copol. ($mm^2$) | Depol. ($mm^2$\|) |
| $Y_{00}$ | 0.67 | 0.71 | 0.50 | 0.42 | 0.24 | 0.19 |
| $Y_{21}$ | - | - | 0.27 | 0.21 | 0.30 | 0.26 |
| $Y_{22}$ | −0.35 | −0.19 | −0.17 | −0.14 | −0.05 | −0.05 |
| $Y_{30}$ | 3.11 | 0.72 | 0.43 | 0.13 | 0.03 | 0.03 |
| $Y_{31}$ | 0.16 | 0.12 | 0.33 | 0.03 | - | - |

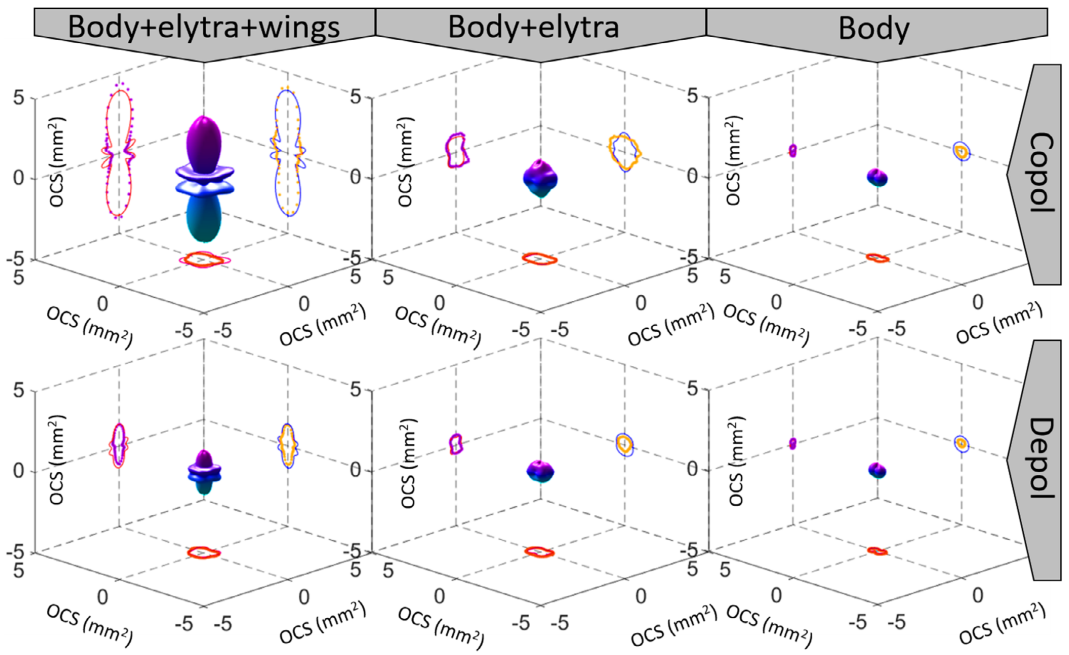


**FIGURE 7** Backscattering OCS of a beetle from three anatomical planes are parameterized by a set of spherical harmonics. Dots represent measured values, and lines are projections of harmonic fits. The color coding is blue to purple shading by height

Spherical harmonics have two indices, where $l$ is the degree, and $m$ is the order. The values of the real part of spherical harmonic were stored for all $l$ and $m$ (degree up to $l = 3$) and sum up to real cross-section values (in the unit of $mm^2$), see Figure 7. Such table values in Table 1 can confirm or disconfirm a given field observation could be a bark beetle observed from an arbitrary direction. The ratio between co- and de-polarized signals from the spherical harmonics in Table 1 can be used to identify possible angular dependence of DoLP or melanization.

The phase function of a beetle at two observation aspects was investigated with the goniometer. The scattering pattern was measured by rotating the light source in a circle and illuminate the beetle from different scattering angle $\theta_{sc}$.

When the beetle is facing the camera (Figure 8C), the angular distribution of scattered light intensity shows a

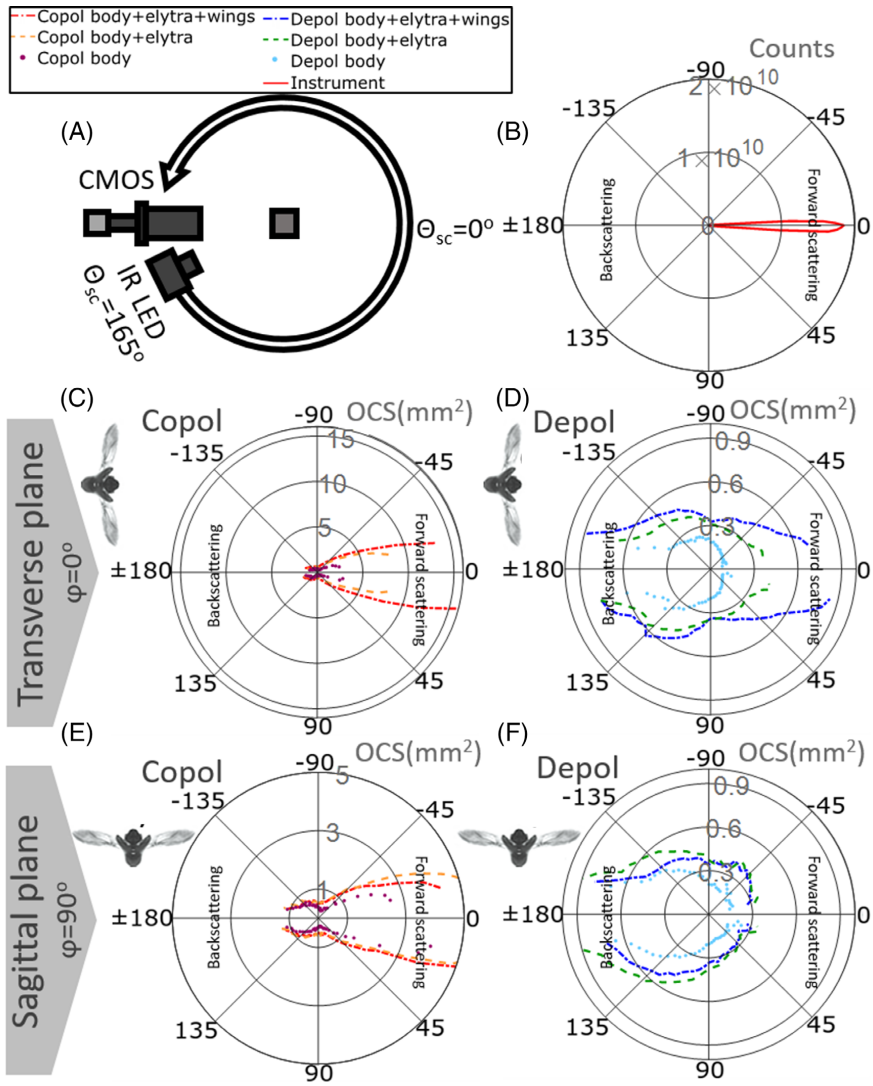


**FIGURE 8** Scattering phase function of beetle with and without wings and elytra in both co- and de-polarizations. A, A schematic of the experimental setup. B, The FWHM of the instrument sensitivity loop is 5°. C, D, Copolarized and de-polarized phase function of the beetle while the beetle is facing the camera. E-F, Copolarized and de-polarized phase function while the side of the beetle is facing the camera

strong forward scattering feature for co-polarized light at the given wavelength, where its intensity is roughly 20 times stronger than the de-polarized signal in the forward direction (Figure 8D). Even when wings and elytra were removed, the body of the beetle is still strongly forward scattered, which could be due to the body size of a beetle is small, so the light undergoes fewer scattering events. Lidar probe and detect a small amount of backscattered light from in-flight insects, other sensors such as E-trap [43] could, in principle, capture forward scattered light. For insects that are highly forward scattering, a forward detection configuration will require less probe intensity and still acquire strong forward scattered signals.

When the side of the beetle is facing the camera (Figure 8E), it also shows a strong forward scattering feature in the phase function. However, its scattered light intensity is 3 times weaker comparing to Figure 8C when wings and elytra are still attached to the beetle. This magnitude difference is due to changing the observation aspect of the beetle has changed the size of projection area from the wings, see the difference in Figure 5B,C, and this magnitude difference is diminished when the wings are removed from the beetle, see the difference in Figure 8C,E. Changing aspects of the beetle do not seem to have a strong impact on changing the de-polarized signal magnitude in Figure 8D,F for backscattering. This could be due mainly to that, the body and elytra are the main contributors to the de-polarized backscattered signal, and that there are no big projected area changes when the beetle is turned around from the front to the side. The big intensity changes for the de-polarized forward scattering signal when the beetle was turned could be due to the scattered light from the left-wing were blocked by the beetle body.

### 3.4 | Entomological chamber (in-vivo)

Roughly, 200 beetles were released inside the entomological flight chamber to study the dynamic properties of wingbeats of free-flying beetles. However, not all the beetles were flying within the probe volume, and the same beetle could have entered the probe volume more than once. We also discarded observations that do not contain at least three clear wingbeats, as we cannot resolve a WBF if it is less than three wingbeats in the time series are available, and we discard signals that contain significant changes in body orientation, as we could not apply our parameterization method when the body signal is not consistent. Therefore, the amount of observations we presented does not correspond to the number of beetles recorded. Their backscattered signals were recorded for two laser bands in co- and de-polarization. Suppose we assume all the beetles have a similar flight speed and mostly fly horizontally. In that case, we expect a long observation recording from a beetle when it is flying along the beam and a short observation when it is flying perpendicularly to the beam. Examples of long and short transit observations of flying beetles are presented in Figure 9. A short observation should contain at least three clear wingbeat signals. In the bark beetle case, a short observation with at least three clear wingbeats is roughly 30 to 40 ms long in time. And a long observation for bark beetle typically contains more than six clear wingbeats, and its corresponding transit time is roughly longer than 70 ms.

The backscattered signal rises and drops throughout many wingbeat cycles, as seen in Figure 9A,C. The oscillatory signal components are contributed from the wing during the wingbeat, and the non-oscillatory component is contributed from the body elytra. The WBFs of 68 bark beetle signals were acquired in the entomological flight chamber, and bark beetles have a median of a WBF of 104 Hz with an IQR of 26 Hz.

A parameterization method [24, 34] was used to project the observation data onto a set of discrete harmonics, which can then estimate in a unit of contributions to the cross-section ($mm^2$). The strength of the fundamental tone appears different in respect to the second harmonic tone for long and short transit observations, which could relate to the orientation and wing dynamic of the flying beetle [34, 44]. Brydegaard and collaborators [34] suggested an insect wing dynamic model, when an insect is observed from the side with lidar, will result in a strong first overtone in the power spectrum. When the insect is observed from the front, or back it yields a strong fundamental tone.

InGaAs co-polarized signal (at 1550 nm) in Figure 9, the difference between the fundamental tones to the first overtone is large in the short transit and small in the long transit observation is in disagreement with the model [34]. However, the diffuse signal from Figure 9 is in agreement with the proposed model. For example, the Si de-polarized signal (at 808 nm) has a large tone difference between the fundamental tone to the first overtone in the long transit, and such difference becomes smaller for short transit. Jansson and collaborators [44] also provided several results that argue that the model in [34] only applies to the diffused signal instead of specular.

### 3.5 | Lidar (in-vivo, in-situ)

To achieve the most effective management of damage control of bark beetles, we need to monitor their distribution to determine the active measures. Bark beetles release pheromones to attract other beetles for breeding or initiating an attack on healthy trees [3, 45]. This released pheromone is invisible to human eyes and cannot be easily monitored. We employed our entomological lidar system in a field together with pheromones mixed with aerosols to illustrate that our lidar can simultaneously monitor the pheromone plume and insects attraction. The measurement result is presented in Figure 10.

As presented in Figure 10, our lidar system has successfully monitored both aerosols smoke and insects within the same time-range map. Insect observations are shown as intensity snippets in the map instead of a

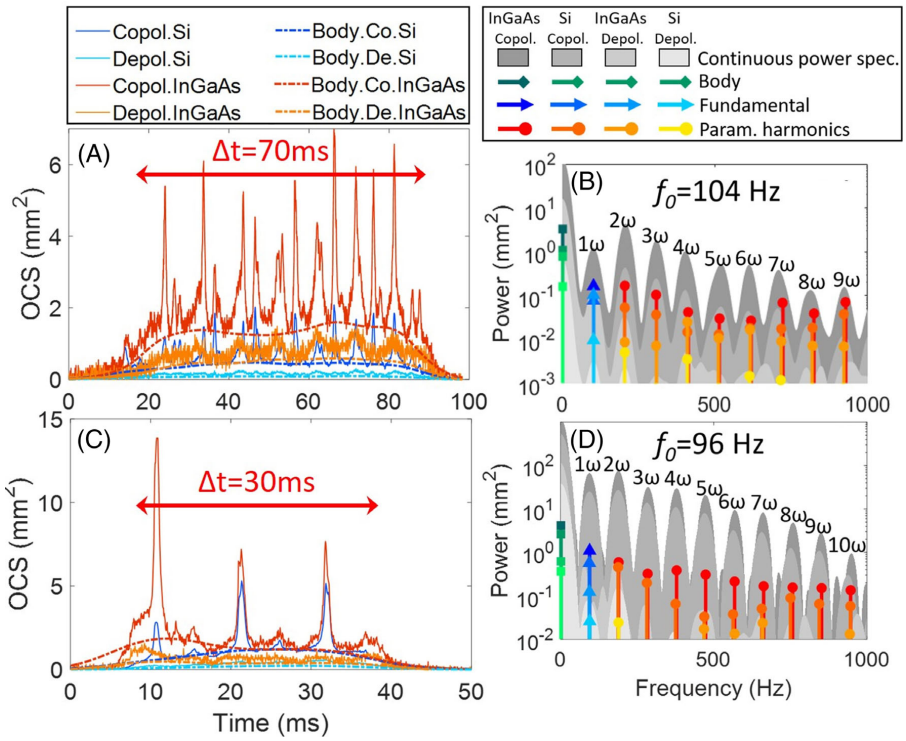


**FIGURE 9** Dual-band polarimetric modulated signal acquired from the entomological chamber for beetles. A, C, The backscattered signal in time series from in-flight beetle for long and short transit time observation. B, D, The corresponding power spectrum for each transit time and time series were parameterized by a set of discrete harmonics weighted with the body contribution

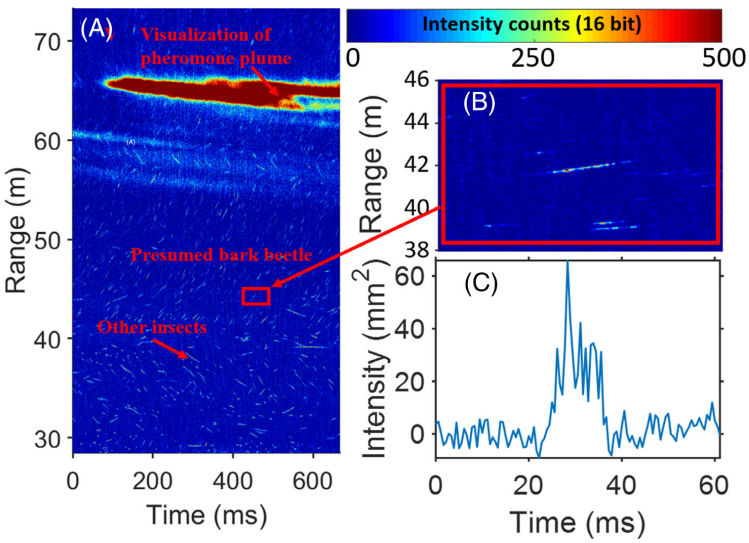


**FIGURE 10** An example of lidar observation. A, Time range map of insect and smoke release event. B, A small section of the time range map is zoomed in and presented. C, The time series of the observation in B

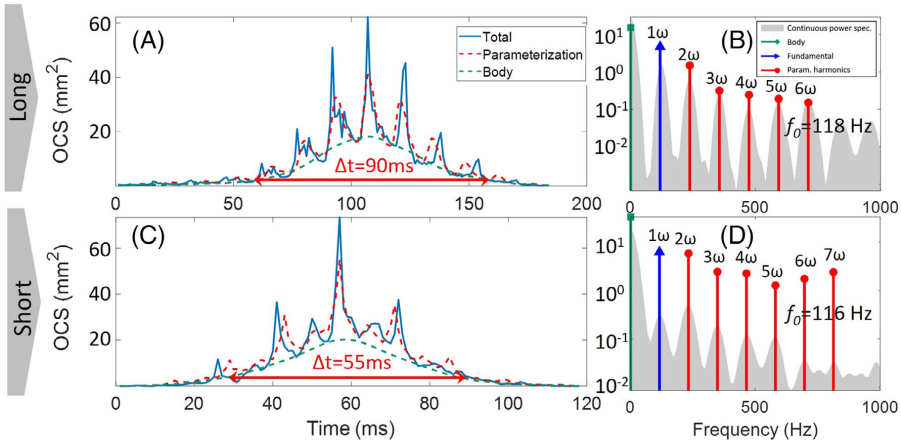


**FIGURE 11** Representative example of insect long and short detection event observed in the field measurement. A, C, Time series of observations with different transit times. B, D, Observations in time series were parameterized by a set of discrete harmonics weighted with the body contribution

continuous intensity distribution as the smoke. A presumed bark beetle observation is highlighted in Figure 10B,C based on the event distance and release time. A long and short lidar transit observation are presented in Figure 11. Both are presumed to be bark beetles based on the release location and time. Their recorded WBFs are also within the bark beetle WBFs span measured from the flight chamber (a median of 104 Hz and IQR of 26 Hz).

The parameterization method was used to retrieve the strength of the body and harmonic tones from the lidar observations. The interpretation of the signals is important when the body to fundamental tone ratios are close. The relation between the fundamental tones to the first overtone of the lidar measurement is similar to what we observed in the flight chamber in Figure 9. When the transit is long, the fundamental tone is stronger than the first overtone. When the transit is short, the difference in tone strength decreases.

Then we investigated if the ratio between body and fundamental tone from the lidar measurement in Figure 11 is comparable to the flight chamber recordings in Figure 9. Unlike the flight chamber, lidar only had one laser band at 808 nm, and it records the sum of both co- and de-polarization. The body to fundamental tone ratio is calculated for lidar by dividing the body signal strength by the fundamental tone strength in Figure 11B,D. The long observation gives a ratio of 3.2, and the short observation gives a ratio of 5.3. The body to fundamental tone ratio is calculated for the flight chamber by dividing the sum of the co- and de-polarized body signal with the sum of co- and de-polarized fundamental tone signal in Figure 9B,D for Si measurements only. Six long observations from the flight chamber within time interval 70 to 100 ms were randomly selected, and they gave a median value of 10.6 (IQR:4.4) for the body-to-fundamental-tone ratio, where 6 short observations within time interval 30 to 40 ms gave a median of 5.5 (IQR:1.2). The body to fundamental tone ratio is nearly the same for both lidar and flight chamber short transit measurement. However, their values were fairly different for the long observation, which could be due to a long transit time means the beetle could have several orientation changes within the same recording, while for a short transit beetle is most likely just flying perpendicular through the beam without big adjustments to its heading. Changes of orientation within the same recording could lead to erroneous strength estimations for body and harmonic tones.

We also looked into if the lidar measured OCS values are comparable to the flight chamber and goniometer measurements. Our lidar measured OCS value for a presumed bark beetle is a factor 10 times larger than the lab measurement. Lidar does face the challenge of calibrating the signal intensity into absolute OCS precisely. Unlike the goniometer and flight chamber that allows the placement of calibration targets in the detection path, lidar is commonly placed in a complex environment and monitoring a long distance (>100 m). Most of the time, the monitoring environment does not allow the placement of a calibration target. Lidar uses its beam size on the termination board to mathematically convert the lidar signals into OCS ($mm^2$). Some of the beam widths are imaged

outside of the lidar linear array at a short range, leading to a wrong OCS estimation for observations. The lidar transect in Nyteboda had a range of 120 m, but the beetles were released halfway, at 60 m, which is considered a short range for the lidar system.

## 4 | CONCLUSION AND OUTLOOK

This paper evaluated the feasibility and characterized optical scattering from bark beetles as lidar target, ex-vivo, in-vivo, and in-situ. We explored various optical domains such as imaging of anatomical features, spectral content, polarization properties, goniometric scatter analysis, modulation properties, and remote sensing. We applied hyperspectral imaging, polarimetric imaging and goniometry, multiband modulation spectrometry, and laser radar.

The body melanization and thickness across bark beetles wings in the range of 600–1600 nm was measured. It was showed that wing interference patterns survive spatial integration over the entire wing producing an effective spectral fringe that can be exploited for remote sensing. By determining this effective fringe from numerous specimens, we discovered an extraordinary small variance of wing thickness less than one magnitude lower than the variance of WBFs. This not only raises questions of fundamental nature in biology, but such small variance also has great implications for differentiating insect species remotely should this be a generally occurring feature across species. Further studies are needed to validate this feature for remote identification of insects.

Anatomical features responsible for the de-polarization of backscatter light were pinpointed. Beetle wings maintain a high degree of co-polarization even when the wavelength is not in condition for resonant backscatter. We also demonstrated that both the body and elytra almost randomizes the polarization entirely. This is noteworthy because both body and elytra are melanized (a feature normally increasing DoLP) and elytra are thin, providing a limited optical path length for multiple scattering and de-polarization.

Analyzing forward scattered light, we concluded that the body is mainly opaque for near-infrared light (in the tissue window) despite being a small organism of a few mm size. From the highly co-polarized light transmitted through both wings and elytra, we concluded that the transmitted light experiences a shorter interaction path length compared to the reflected light. This is counter-intuitive compared to classical medial optics but compatible with similar findings in mosquitoes [30].

Quantitative optical backscatter cross-sections from all anatomical projections for both co- and de-polarized laser light are presented as well as extinction coefficients. These estimated values are useful for designing field monitoring instrumentation and interpreting entomological lidar data, such as determining plausible bark beetle targets in an ensemble of insects. We concluded that the DoLP is invariant with heading and observation angle, and such it could be a feature for identification. This finding is similar to earlier findings for mosquitoes [29, 30].

By repeated scans and relieving the beetles from wings and elytra, we could attribute different fractions of the cross-section to different anatomical parts. This is interesting because entomological lidar is capable of isolating oscillatory scattered light from wings from the non-oscillatory light scattered of the body and therefore provides a stronger foundation for remote detection. We also notice that the angular dependence of cross-sections and (consequently, the circular and spherical harmonics required to explain them) are three folded symmetrical for both the body and wings. However, this is not the case for the contribution from the elytra, and beetles can thus be expected to display asymmetric cross-section depending on the observation aspect.

By identifying symmetries, we provided spherical functions of cross-sections using a limited set of spherical harmonics. Thus scattering by an insect target from an arbitrary observation aspect can be given with quantitative values in a table. This paves the way for establishing a library for cross-section for insect species of key importance such as pests, disease vectors, or pollinators.

With goniometric scatter analysis, we demonstrated dominant co-polarized forward scattering. The scattering phase function can be understood as a product of the cross-section from the illumination and observed aspect in conjunction with an intrinsic Henyey-Greenstein scattering function. The retrieved phase function helps us understand the light interaction with such small biological samples. It could also have implications for field detection schemes where the strong forward scattering is exploited to ease laser power requirements.

By polarimetric dual-band modulation spectroscopy on free-flying bark beetles, we have identified the range of WBFs. We applied parameterization and demonstrate quantitative cross sections values for a high number of overtones. The proposed wing dynamic model from [34] apply to diffuse signal observation. The DoLP of long transit observation is in agreement with the goniometry measurement.

We contributed a solution to monitor an invisible pheromone released by bark beetle by employing our lidar system in the field and mixing aerosols with pheromones. We successfully observed the bark beetle signals and pheromones smoke plumes simultaneously. Moreover, they both have distinguishable characters in the lidar time and range map, so it is easy to tell them apart.

We compared the lidar observations to the flight chamber measurements to prove the feasibility of having the lidar as a tool for monitoring the bark beetles. We had some challenges with absolute cross-section calibration, but there are plenty of other features to identify the beetles. Firstly, both lidar and flight chamber measurements showed the same relative tone strength relation for long and short transit observations. Secondly, the WBF measured by lidar is within the WBF span measured by the flight chamber. Thirdly, the body to fundamental tone ratio is nearly the same for short transit observation in both lidar and flight chamber measurements.

With clues provided from this work, we can distinguish bark beetle observations from in-situ lidar or other sensors measurements. Our methodology can be applied to other key insect species and enable developing a specific monitoring system. Future studies should focus on developing an insect outbreak index system to indicate the risk by employing several lidar systems at various locations.

## ACKNOWLEDGMENTS

This study was supported by the Swedish Research Council – FORMAS(2018-01061) and European Research Council – ERC (2019-850463). We thank Bengt Hansson for his support in acquiring the FORMAS grant. We thank Bengt Augustsson for his kind permission to operate the experiment on his property. We very much appreciate the support and kindly lending the lidar instrument from Eric Warrant. We highly appreciate the help of Aboma Merdasa and Julio Hernandez for using the hyperspectral camera.

## CONFLICTS OF INTEREST

The authors declare that there is no financial or commercial conflict of interest.

## DATA AVAILABILITY STATEMENT

Data is available by contacting the correspondence author upon a reasonable request.

## ORCID

*Meng Li* https://orcid.org/0000-0003-4931-5647
*Mikkel Brydegaard* https://orcid.org/0000-0003-0586-664X

## REFERENCES

[1] E. Christiansen, A. Bakke, *The Spruce Bark Beetle of Eurasia*, Springer, Norway, **1988**.
[2] A. Komonen, L. Schroeder, J. Weslien, *J. Appl. Entomol.* **2011**, *135*, 132.
[3] P. Baier, *J. Appl. Entomol.* **1996**, *120*, 587.
[4] L. Wichmann, H. P. Ravn, *For. Ecol. Manage.* **2001**, *148*, 31.
[5] J. A. Byers, Q.-H. Zhang, G. Birgersson, *Naturwissenschaften* **2000**, *87*, 503.
[6] G. Lobinger, *Anzeiger für Schädlingskunde, Pflanzenschutz, Umweltschutz.* **1994**, *67*, 14.
[7] A. M. Jönsson, G. Appelberg, S. Harding, L. Bärring, *Glob. Chang. Biol.* **2009**, *15*, 486.
[8] A. M. Jönsson, S. Harding, L. Bärring, H. P. Ravn, *Agric. For. Meteorol.* **2007**, *146*, 70.
[9] P. Öhrn, *Seasonal Flight Patterns of the Spruce Bark Beetle (Ips Typographus) in Sweden*, Sveriges lantbruksuniv, Sweden, **2012**.
[10] Skogsstyrelsen, Bekämpning av granbarkborre, https://www.skogsstyrelsen.se/bruka-skog/skogsskador/insekter/granbarkborre/bekampning-av-granbarkborre (accessed: July 08,2020).
[11] Skogsstyrelsen, Feromonfällor med eller utan insekticider, https://www.skogsstyrelsen.se/bruka-skog/skogsskador/insekter/granbarkborre/bekampning-av-granbarkborre/feromonfallor-med-eller-utan-insekticider (accessed: July 08,2020).
[12] A. Moore, R. H. Miller, *Ann. Entomol. Soc. Am.* **2002**, *95*, 1.
[13] D. F. Silva, M. A. Souza, D. P. W. Ellis, E. J. Keogh, G. E. A. P. A. Batista, *J. Intelligent Robotic Sys.* **2015**, *80*, 313.
[14] V. A. Drake, D. R. Reynolds, *Cabi* **2015**, 13.
[15] W. Daniel Kissling, D. E. Pattemore, M. Hagen, *Biol. Rev.* **2014**, *89*, 511.
[16] K. S. Repasky, J. A. Shaw, R. Scheppele, C. Melton, J. L. Carsten, L. H. Spangler, *Appl. Optics* **2006**, *45*, 1839.
[17] M. Brydegaard, A. Gebru, S. Svanberg, *Progress Electromag. Res.* **2014**, *147*, 141.
[18] M. Brydegaard, A. Merdasa, A. Gebru, H. Jayaweera, S. Svanberg, *Appl. Spectrosc.* **2016**, *70*, 372.
[19] M. Brydegaard, E. Malmqvist, S. Jansson, J. Larsson, S. Török, G. Zhao, *Int. Soc. Opt. Photon.* **2017**, 10406, 104060I.
[20] S. Zhu, E. Malmqvist, W. Li, S. Jansson, Y. Li, Z. Duan, K. Svanberg, H. Feng, Z. Song, G. Zhao, M. Brydegaard, S. Svanberg, *Applied Physics B.* **2017**, *123*, 211.
[21] M. Brydegaard, S. Svanberg, *Laser Photon. Rev.* **2018**, *12*, 1800135.
[22] M. Brydegaard, S. Jansson, E. Malmqvist, Y. Mlacha, A. Gebru, F. Okumu, G. Killeen, C. Kirkeby, *Sci. Adv.* **2020**, *6*, eaay5487.
[23] S. Solberg, E. Næsset, K. H. Hanssen, E. Christiansen, *Remote Sens. Environ.* **2006**, *102*, 364.
[24] E. Malmqvist, S. Jansson, S. Török, M. Brydegaard, *IEEE J. Selected Topics Quantum Electron.* **2015**, *22*, 327.
[25] S. Jansson, PhD Thesis, Lund University, **2020**.
[26] F. Schlyter, J. A. Byers, J. Löfqvist, *J. Chem. Ecol.* **1987**, *13*, 1503.
[27] J. Hernandez-Palacios, L. Randeberg, *SPIE BiOS*, SPIE, San Francisco, CA, United States, **2012**.
[28] A. Genoud, Y. Gao, G. Williams, B. Thomas, *J. Biophotonics* **2019**, *12*, e201900123.
[29] A. Gebru, S. Jansson, R. Ignell, C. Kirkeby, J. C. Prangsma, M. Brydegaard, *J. Biophotonics* **2018**, *11*, e201800014.
[30] S. Jansson, P. Atkinson, R. Ignell, M. Brydegaard, *IEEE J. Selected Topics Quantum Electron.* **2018**, *25*, 1.
[31] B. Ströbel, S. Schmelzle, N. Blüthgen, M. Heethoff, *ZooKeys.* **2018**, *759*, 1.
[32] C. V. Nguyen, D. R. Lovell, M. Adcock, J. La Salle, *PloS one.* **2014**, *9*, e94346.

[33] O. E. Olarte, J. Andilla, D. Artigas, P. Loza-Alvarez, *Optica.* **2015**, *2*, 702.
[34] M. Brydegaard, *PLoS One.* **2015**, *10*, e0135231.
[35] M. Brydegaard, A. Gebru, C. Kirkeby, S. Åkesson, H. Smith, *EDP Sciences* **2016**, 119, 22004.
[36] S. Jansson, E. Malmqvist, M. Brydegaard, S. Akesson, J. Rydell, *Ecol. Indic.* **2020**, *117*, 106578.
[37] K. Kouassi Benoit, S. Jansson, M. Brydegaard, J. Zoueu, *OSA Continuum.* **2020**, 3, 2362.
[38] L. Mei, M. Brydegaard, *Laser Photon. Rev.* **2015**, *9*, 629.
[39] S. Jacques, B. Pogue, *J. Biomed. Opt.* **2008**, *13*, 041302.
[40] S. Jacques, R. Glickman, J. Schwartz, *Photonics West '96*, SPIE, San Jose, CA, United States **1996**.
[41] D. G. Stavenga, *Mater. Today: Proc.* **2014**, *1*, 109.
[42] M. Brydegaard, S. Jansson, M. Schulz, A. Runemark, *Ecol. Evol.* **2018**, *8*, 5369.
[43] I. Potamitis, I. Rigakis, K. Fysarakis, *Sensors.* **2014**, *14*, 22285.
[44] S. Jansson, M. Brydegaard, *Animal Biotelemetry.* **2018**, *6*, 6.
[45] F. Lieutier, K. R. Day, A. Battisti, J.-C. Gregoire, H. F. Evans, *Bark and Wood Boring Insects in Living Trees in Europe: A Synthesis*, Springer, Netherlands, **2004**.

**How to cite this article:** Li M, Jansson S, Runemark A, et al. Bark beetles as lidar targets and prospects of photonic surveillance. *J. Biophotonics*. 2021;14:e202000420. https://doi.org/10.1002/jbio.202000420

# Paper II

iScience

CellPress
OPEN ACCESS

Article

# Lidar as a potential tool for monitoring migratory insects

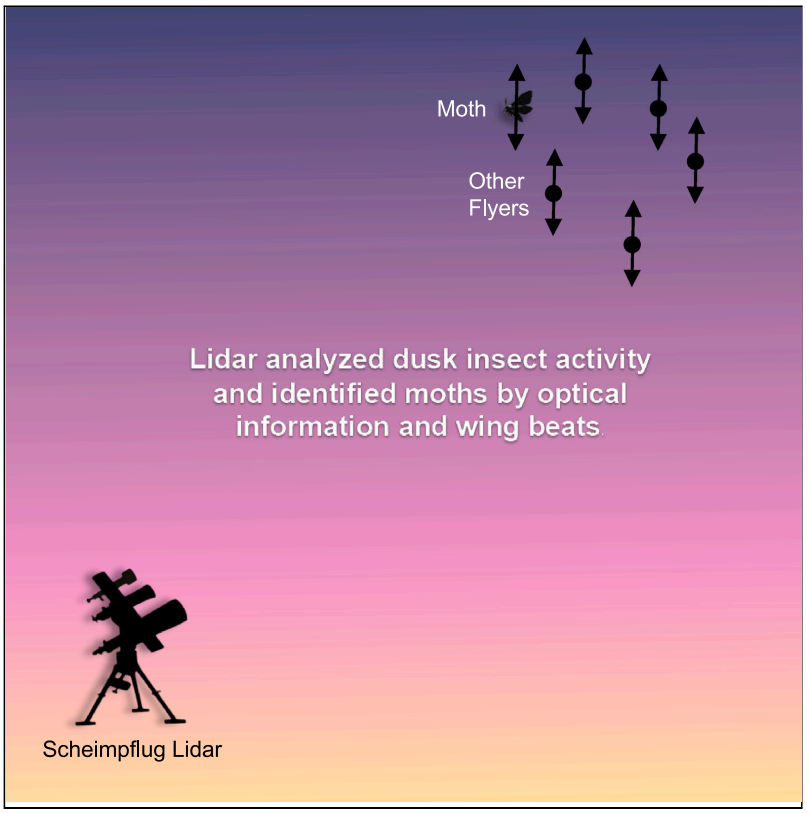


Hui Chen, Meng Li, Hampus Månefjord, ..., Gao Hu, Eric Warrant, Mikkel Brydegaard

hui.chen@njau.edu.cn (H.C.)
meng.li@fysik.lu.se (M.L.)
mikkel.brydegaard@fysik.lu.se (M.B.)

## Highlights

Lidar to elucidate the low-height dusk movements and detailed information of insects

Moths were filtered based on optical information and wing beat frequency by lidar

Chen et al., iScience 27, 109588
May 17, 2024 
https://doi.org/10.1016/j.isci.2024.109588

iScience

CellPress
OPEN ACCESS

Article

# Lidar as a potential tool for monitoring migratory insects

Hui Chen,[1,4,10,*] Meng Li,[2,10,*] Hampus Månefjord,[2] Paul Travers,[3] Jacobo Salvador,[2] Lauro Müller,[2] David Dreyer,[4] Jamie Alison,[6] Toke T. Høye,[6,7] Gao Hu,[1] Eric Warrant,[4] and Mikkel Brydegaard[2,5,8,9,11,*]

## SUMMARY

**The seasonal migrations of insects involve a substantial displacement of biomass with significant ecological and economic consequences for regions of departure and arrival. Remote sensors have played a pivotal role in revealing the magnitude and general direction of bioflows above 150 m. Nevertheless, the takeoff and descent activity of insects below this height is poorly understood. Our lidar observations elucidate the low-height dusk movements and detailed information of insects in southern Sweden from May to July, during the yearly northward migration period. Importantly, by filtering out moths from other insects based on optical information and wingbeat frequency, we have introduced a promising new method to monitor the flight activities of nocturnal moths near the ground, many of which participate in migration through the area. Lidar thus holds the potential to enhance the scientific understanding of insect migratory behavior and improve pest control strategies.**

## INTRODUCTION

Insect migrations displace vast quantities of individuals, biomass, and nutrients across the earth's surface, with profound implications for both agriculture and biodiversity.[1–3] Transitioning to the nocturnal aspect, the night sky is a less explored avenue in insect migration studies. The cover of darkness offers a different set of environmental conditions and challenges, prompting distinct behavioral adaptations among migrating insects. Most of the large nocturnal migrants are moths,[4] which commonly migrate at significant heights above the ground (as high as 1 km), taking advantage of seasonally favorable winds.[5] Many migratory moth species provide beneficial ecosystem functions, such as pollination,[6] but many are also economically significant pests or vectors of plant-disease viruses.[7–9] The detection, quantification, and characterization of moth migratory movements are therefore of great value to insect ecologists and ethologists for improving our understanding of the drivers and consequences of migration.

A major challenge in insect migration research is to understand where and when migrating insects take off and descend.[10,11] This is particularly crucial to aid agriculturists in predicting the timing and location of migration events, helping to mitigate damaging pest outbreaks.[12,13] Vertical-looking entomological radar (VLR) has proven pivotal for producing accurate estimates of both the horizontal and vertical components of the flight vectors of target insects at heights above roughly 150 m,[4,14,15] but its inherent noise interference below 150 m has prohibited the study of insect migration close to the ground.[11,16–19] Scanning radar can detect the targets by adopting different angles with scanning mode, which has been utilized for monitoring the agricultural pest[9]; it hardly provides flight detailed information of migratory insects. While frequency-modulated continuous-wave (FMCW) radar has demonstrated its capability to surmount inherent noise challenges, thereby presenting itself as a promising tool for monitoring insect migrants,[20–22] its practical application in field monitoring of migratory insects has not been realized to date. Furthermore, while harmonic radar can detect low-altitude insect migratory behavior with high-resolution positional data, the need for tagging renders this method unsuitable for the comprehensive monitoring of migratory insects. Building upon previous work, entomological lidar (laser radar[23]), with lower inherent noise interference, can be further employed and is an extra option for efficient insect monitoring below 150 m for both tagged[24] and untagged[25] insects, potentially unraveling the remaining mysteries of insect migration at low heights.[25]

[1]Department of Entomology, Nanjing Agricultural University, Nanjing 210095, China
[2]Department Physics, Lund University, Sölvegatan 14c, 22363 Lund, Sweden
[3]Department Biological Engineering, Polytech Clermont, 2 Av. Blaise Pascal, 63100 Aubière, France
[4]Lund Vision Group, Department Of Biology, Lund University, Sölvegatan 35, 22362 Lund, Sweden
[5]Department Biology, Lund University, Sölvegatan 35, 22362 Lund, Sweden
[6]Department Ecoscience, Aarhus University, C. F. Møllers Allé 8, 8000 Aarhus C, Denmark
[7]Arctic Research Centre, Aarhus University, Ole Worms Allé 1, 8000 Aarhus C, Denmark
[8]FaunaPhotonics, Støberigade 14, 2450 Copenhagen, Denmark
[9]Norsk Elektro Optikk, Østensjøveien 34, 0667 Oslo, Norway
[10]These authors contributed equally
[11]Lead contact
*Correspondence: hui.chen@njau.edu.cn (H.C.), meng.li@fysik.lu.se (M.L.), mikkel.brydegaard@fysik.lu.se (M.B.)
https://doi.org/10.1016/j.isci.2024.109588

Extending existing applications of Lidar, it has been successfully applied in different kinds of insect monitoring with the advantage of detection sensitivity and specificity.[26–28] Such specificity can be achieved with multiband lidars that can quantify molecular absorption by melanin,[29] nanoscopic wing thicknesses,[30] or microstructural information such as surface roughness.[29] The widely diverse detection distances and the rapid movements of free-flying insects pose challenges to focusing and classification of insect species.[31] However, wing interference phenomena and wingbeat modulation are unaffected by focus blur and show potential for insect classification based on lidar observations.[26,28,32–34] Lidar may also provide an accurate description of flight parameters, such as flight velocity and speed, which are scarcely documented for moths. This lack of documentation hinders understanding of moth migration and hampers the development of effective conservation and pest control strategies.

In this study, we further explore the utility of lidar for insect surveillance at low heights by collecting real-time, *in situ*, spatially profiled observations during two months of the insect migration season. The study was conducted in a rural area in southern Sweden within a healthy ecosystem (including pasture, forests, and wetlands) with minimal light pollution. Southern Sweden is positioned along the migratory path from southern Europe to the Scandinavian Peninsula and serves as a vital stopover for migratory insects.[2,35] During the northward migration period from May to July, nightly migratory insect takeoff and landing behaviors occur in this region.[2,35]We used lidar to derive flight parameters for moths and other insects, such as vertical velocity and height, recorded around dusk when migration activity normally begins. Moreover, through the optical information and wing beat captured by our refined lidar methods, we have demonstrated in this paper the potential to distinguish moth signals from those of other insects. Our study enhances the methodology for insect surveillance and, by distinguishing moths, lays the groundwork for deeper analysis of migratory moth activity patterns. Our pioneering research introduces a promising tool for remote monitoring, poised to significantly contribute to the development of innovative and more effective conservation and pest control strategies.

## RESULTS

Our field campaign was executed at Stensoffa Field Station (55°41′44″N 13°26′50″E) between 25$^{th}$ May and 21$^{st}$ July, 2022. The operation of the lidar system was conditional on favorable atmospheric conditions, specifically excluding instances of rain and strong winds. The schedule for data recording varied. Full-day recording was executed on certain days, whereas, on others, recording was constrained to a time window from 18:00 to 24:00 (sunset occurred between 20:52 and 21:21 during the measurement period). Our results are later controlled for observation hours.

The lidar system was oriented northwards (Figures 1A and 1B) and aimed skyward with an elevation angle of 30° (Figure 1C). Although the Scheimpflug lidar operates to infinity, the furthest insect in this study was detected at roughly 700 m distance, corresponding to a height of 400 m. In our previous study[32] the lidar transect was conducted at ground level, closer to vegetation where insects emerge and are more abundant, achieving a detection range of up to ∼2 km. However, the lidar's 30° elevation angle and near limit of 35 m (approximately 18 m in height) restrict observations to above 18 m. The experimental site's lack of tall trees and average tree height (15–20 m, based on Global Ecosystem Dynamics Investigation tree height maps) support the assumption that the observed signals are not from plant debris or plankton. See Figure 1 for an image of the surrounding vegetation.

The lidar system was oriented skyward to observe insect migration at elevated altitudes. Given the anticipated lower insect density at heights hundreds of meters above the ground, the furthest detection at 400 m elevation is within expectations. The 30° elevation angle was chosen over a vertical (zenith) configuration for two reasons: firstly, to attempt to prolong the transit time of insects through the lidar beam, thereby facilitating better data capture, and, secondly, to permit housing the instrument within a protective garage tent (Figures 1A and 1B), thereby reducing the need for constant supervision. At a 30° elevation, the lidar's trajectory passed above varied vegetation, including an assortment of tree species (Figure 1D). Throughout the campaign, we gathered lidar data for a total of 18 days, yielding 17,254 insect observations.

Our lidar measurements recorded insect activity patterns with high spatial and temporal resolution throughout the day and at various heights (Figure 2). It is pertinent to note that the alignment of the beam and receiver, which first intersect at a height of 20 m above the ground, substantially reduces the chances of detecting dispersal flights emanating from the vegetation below. Our observations demonstrate prominent insect activity during the late afternoon and evening hours (until around just before midnight), in contrast to a significantly reduced activity observed from then until just after sunrise. Insect activity again peaks around mid-morning before declining later in the morning and during the early afternoon. The campaign was conducted in the south of Sweden, with short summer nights close to midsummer, typically experiencing sunrise as early as 04:21 and sunset nearing 21:54, on average (there is 17:30 h of daylight; 19:30 h also include twilight, and light levels exceed astronomical twilight limits throughout the day (https://www.timeanddate.com/sun/).

Interestingly, despite the lengthy daylight periods, most insect activity at higher heights (over 100 m) was observed during the late afternoon and evening, with most observations made after 21:00 and before midnight. This might be due to the fact that crepuscular or nocturnal insects are typically more tolerant to colder temperatures, which are commonly experienced during the night and at higher altitudes. The notable decrease in activity at altitudes above approximately 50 m just before midnight could be attributed to high-altitude insects, potentially migratory ones, having landed by this time.

By implementing a previously described method[36] (see also quantification and statistical analysis), we determined the velocities of observed insects, as well as their vertical movement directions and speeds (that is, whether they were ascending or descending). This could be achieved by initially setting the lidar system at a vertical beamline position and then tilting the system to a 30° elevation angle. (Figure 1A).

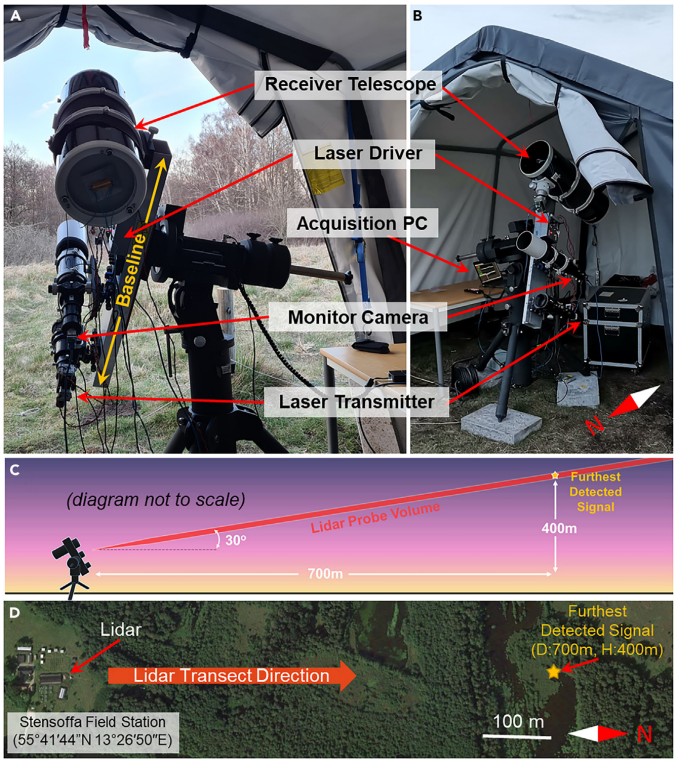


**Figure 1. The experimental setting at Stensoffa ecological field station, southern Sweden, in 2022**

(A–C) The lidar instrument setup with 30° elevation angle, optimized to observe migratory insect patterns.

(D) A satellite image pinpointing the location of the experimental site.

The same method was previously employed by another group using a horizontal baseline that yielded lateral east-west movements.[36] Ranging uncertainty in Scheimpflug lidar arises from the beam beam width.[37] This uncertainty is approximately 3%–5% of the range but also allows to estimate size[26] and coarse assessment of transverse velocity.[36]

Previous radar studies have demonstrated evening ascents and descents,[11] and studies on foraging insects using quadrant photodiodes concluded that movement was predominantly lateral during the day and close to the ground.[38] Figure 3A shows the total movement direction and speed of all detected insects over an entire day or summed across all insect sizes and detectable heights. Insect size was approximated using apparent size, which is derived from the pixel footprint from the camera and telescope magnification, providing an estimate of the insect's dimensions (this calculation is presented in the STAR methods section). It is crucial to underscore that the apparent size of an insect is fundamentally a representation of its projection onto the camera sensor. This measurement can be markedly influenced by the insect's body orientation during flight: when an insect is projected sideways compared to a projection from its posterior or anterior onto the camera sensor, the apparent size is observed to be larger from the sideways projection. The variation in apparent size can be noticeable, depending on the angle or position of the insect. Therefore, while the apparent size data offer a close estimate, it may not always directly reflect the precise physical dimensions of an insect.

By sub-sectioning the data into different height intervals (Figures 3A–3D), we noticed a decrease with height in the number of observations and a shift in the overall movement direction from predominantly upward (ascending) to equally upward and downward (descending). Similar patterns were noted in Figures 3E–3H: as for late hours, movement became more even in both directions. Moreover, insects with smaller size estimates, such as those under 10 mm, typically exhibit relatively slower movement speeds, and the central tendency (median) is at zero for heading direction (Figures 3A and 3I–3L). As the size increases, larger insects seem to trend toward an upward heading and demonstrate increased flight speeds. When we examine insects of larger proportions, specifically those exceeding 40 mm, these occasionally exhibit higher speeds, yet their overall heading distribution appears to be evenly divided between ascending and descending individuals. There

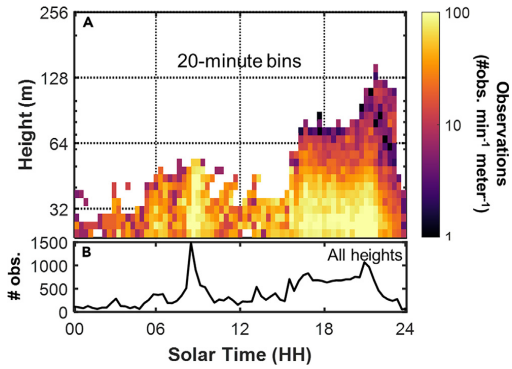


**Figure 2. Diel insect variation over the course of 18 days, all types of insects are included**

(A) Insect activity across various heights throughout the day, which was compensated for observation hours for a period of 18 days.

(B) Overall number of detected flights regardless of height. All insect activity data have been post-compensated to correct for biases due to inconsistencies in observational hours.

was a strong tendency for insects to ascend rather than descend (Figure 3A), suggesting that our study area was a strong population source[39] for many insect species during data collection.

Additionally, two distinct patterns of change were observed. One pattern indicates that the central tendency shifts from upwards to no directional change with increasing height and hour after sunset. The other pattern reveals the disappearance of the bimodal distribution. This latter observation implies that there is an increasing randomness in the directions of the insects as the night progresses and at higher altitudes, whereas, around dusk and at lower heights, insects predominantly move either up or down. This observation further complements the findings of the study, reinforcing the notion that the movement patterns of insects vary significantly based on the time of day and their altitude.

These findings offer the potential for future advancements in monitoring the ascending and descending behaviors of migratory insects, as well as studies related to predation, such as between birds, bats, and insects. Such studies would significantly benefit from the ability to accurately distinguish migratory moth signals from those of other insects. If such a distinction could be made, we can delve deeper into understanding the intricacies of moth behavior and their contribution to overall insect ecology.

Finally, we showcase an instance (Figure 4) where we successfully singled out a moth observation from those of other insects, an accomplishment achieved due to a long transit time and wing stroke signal. This observation, however, does not typify the majority of our recorded data in this study. To increase our chances of such successful identifications, we attempted to extend the transit time by reducing the lidar beam's elevation angles. Unfortunately, this approach proved insufficient as most observations remained too short to accurately identify wing beats and wing strokes. Despite this challenge, we can nonetheless demonstrate, with a clear capture of wing strokes, that we can indeed distinguish moths from other insects according to moth's high wing depolarization ratios. In Figure 4A, we offer an illustrative example of a lidar signal: the flight trajectory of a moth at an elevated height. Here, the distance can be inferred from the absolute pixel numbers and the heading and sizing can be inferred from the differential pixel numbers. The camera exposures over time represent the passage of time, and the false color scheme is indicative of light intensity and its polarization state. In the generated false color image, specific light characteristics are mapped to distinct RGB color layers: depolarized light intensity is encoded as red, co-polarized light intensity as green, and the background is attributed to blue (negligible). This RGB mapping creates a composite visualization where combined intensities lead to observed colors. Specifically, when both depolarized (red) and co-polarized (green) light intensities are present in a region, their superposition yields a yellow hue in accordance with the principles of additive color mixing, whereas greenish shades indicate co-polarized backscatter.

Whereas Figure 4A provides a comprehensive visualization of the lidar signal through sequential camera exposures, Figure 4B displays the intensity distribution observed at a single exposure, thereby delineating a particular temporal instance within observation. This observation exhibits a strong signal in co-polarization. It also displays a weaker, albeit significant, depolarized signal. The pixel number covered by a single insect transit, also known as the pixel footprint in Figure 4A, is calibrated to height and apparent size in Figure 4B, where the apparent size provides an estimate of the insect's dimensions, as discussed earlier. The height above ground where the signal was detected was calculated based on the Scheimpflug configuration. In the case of triangulating lidar, the primary source of range inaccuracy comes from the beam width, which typically yields around 3%–5% variation.[37] Figure 4B shows a change in range of 8 m at a height of 128 m. If the object being measured is flying at a constant height in an east-west direction, then this translates to a precision of about 6% (Δ8m/128m). This seems to align well with the expected precision of the lidar system. For this observation, the moth appeared to have a length of 35 mm and was heading downward at a speed of ~1.1 m/s. Figure 4C illustrates the time series of both polarization bands showing the higher-frequency oscillations of the wings

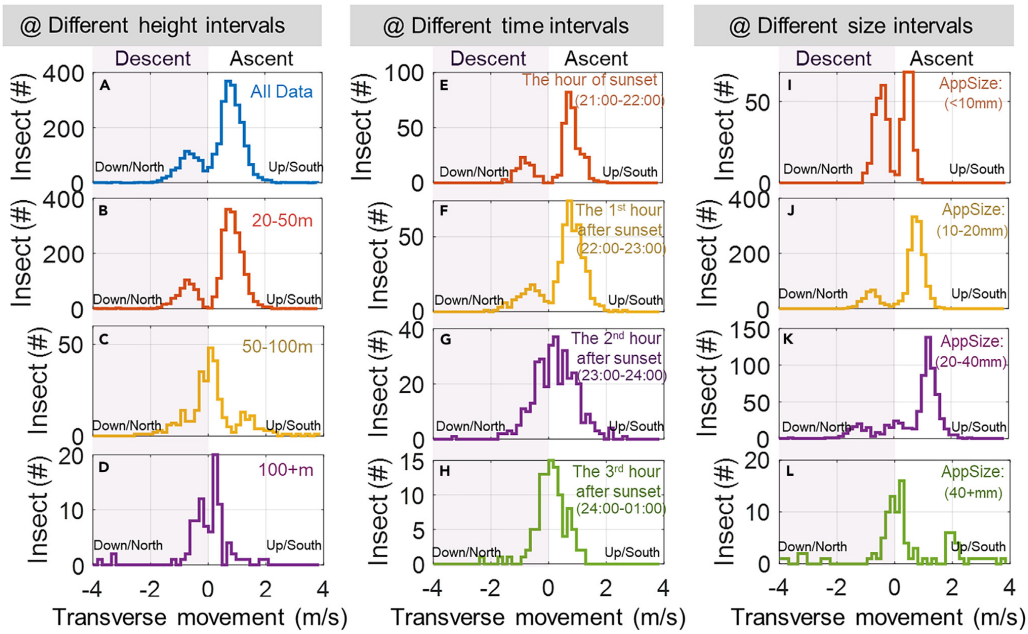


**Figure 3. Variation in insect flight direction and speed based on height (A–D), time (A, E–H), and insect size (A, I–L) intervals, all types of insects included**

AppSize is short for apparent size. Positive values indicate upward (ascending) flights, while negative values indicate downward (descending) flights.

(A) An overview of the overall distribution observed throughout the entire day and over all heights and sizes.

(A–D) The variation in insect speed and heading at different height intervals summed across the entire day.

(A and E–H) The temporal changes in flight speed and heading direction at specific time intervals following sunset (at ~22:00), all heights included.

(A and I–L) Variances in flight direction and velocity, for different insect size intervals summed across the entire day.

superimposed on a bias envelope arising from the moth's body. With polarimetric information, we can confidently deduce that this signal is from a moth due to its high depolarization in the wing signal; such signals are observed in Lepidoptera (butterflies or moths) with diffuse wings.[27] In contrast, clear-winged insects, such as wasps or hoverflies, display negligible wing depolarization effects due to their ultra-thin wing membranes.[40,41] Figure 4D presents the corresponding power spectrum. The fundamental frequency could only be estimated for the co-polarized signal and was found to be 56 Hz. This low wingbeat frequency is another indicator that this signal originated from a moth.[42–44] Our methodology thus has the potential to allow the differentiation of moths from other insects by leveraging the unique characteristics of wingbeat frequency and polarization. To achieve higher taxonomic precision in our identification process, we foresee the integration of additional wavelengths into our lidar system.[29] Alternatively, the construction of a lookup database with the help of a goniometric polarimetric system,[45] linking specific lidar signals with corresponding moth species, may also prove feasible in the future.

## DISCUSSION

Lidar allowed detailed monitoring of the daily activity patterns of insects at low heights (20–200 m) and has also provided robust measures of flying insect density, size, ascents, and descents at different times, heights, and size intervals. This information could be vital for studies of insect migratory behavior since migrations are a large-scale phenomenon, and the impacts of migration (e.g., nutrient flows, herbivory, pollination) are felt locally through emigrations and colonization occurring at low heights. For example, many insects initiate takeoff within 1 h after sunset, exhibiting a nearly equal number of ascents and descents thereafter in our station. This observation suggests that our study area may serve as a population source or transit zone for migratory insects.[39] Moreover, lidar observations, via its successful calculation of apparent size and wingbeat frequency, could allow a deeper and more efficient examination of the individual category and recognization in the future, which is greatly helpful for understanding the adaptions and strategies of small migrants at the low heights.

Since the development of VLR-based tracking methods for diurnal and nocturnal flying vectors,[17,46] a wealth of fascinating phenomena related to insect migration above 150 m have been uncovered.[1,5,13] These discoveries have greatly deepened our understanding of the intricate behavioral patterns (e.g., flight orientations) exhibited by high-flying migratory insects.[1,5] Besides, FMCW radar appears subsequently

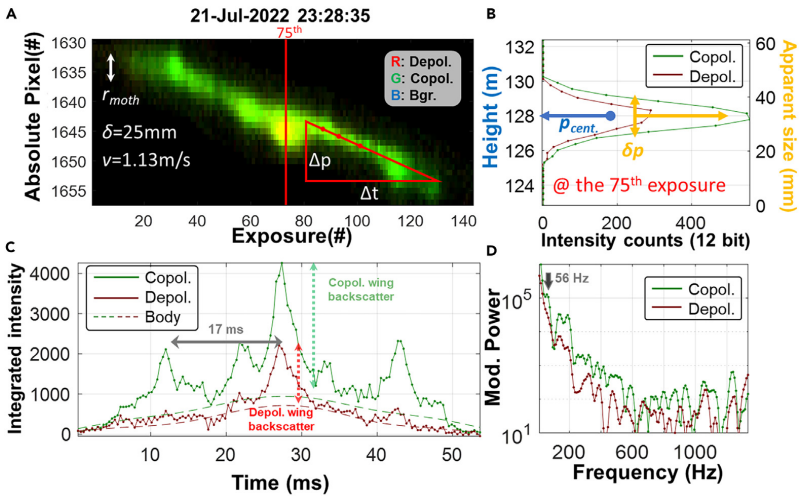


**Figure 4. An example of a single moth observation obtained using polarization lidar technology**

(A) A spatiotemporal display demonstrating an observation of a single slow oscillatory insect presented as a false color image.

(B) The echo from a single camera exposure of a moth.

(C) Time series of both polarization bands, featuring an oscillatory part from the wing movements and a bias envelope from the insect's body.

(D) Corresponding power spectrum where the fundamental frequency emerges as the highest tone in this specific observation.

with several advancements (lower inherent interference, lower cost, more flexible), to fill the crucial niche of insect migration monitoring below 150 m, which becomes promising remote sensors for tiny migrants nowadays.[20–22] However, the potential of lidar as a complementary technique to VLR or FMCW radar is underappreciated, despite its ability to provide valuable information on horizontal velocities at heights below 200 m. Integrating all of these remote sensors, light traps, and pheromone traps would significantly enhance our ability to unravel the complexities of insect migration and could provide a more complete picture of these dynamics.[1,5]

Although the lidar system has emerged as a complement to radar providing information about the timing, location, size, and wingbeat frequency of individual moths, species classification has proven elusive due to the limitations imposed by the typical beam widths of lidar systems. In this study the average moth transit time measured by the lidar was only around 15 ms, and, for successfully identifying slow-flying moths that have a wingbeat frequency of around 20 Hz, a transit time at least 3 times longer would be required. It is realistic to imagine a dedicated moth-monitoring lidar with an expander providing a 3-times wider beam, although the beam intensity would thereby be diluted by a factor of 9. This is achievable given the laser used in this study was relatively weak, and stronger laser diodes are available at little added cost. In turn, by appropriately changing the beam width, we anticipate that the classification of nocturnal moths can become possible, even at greater heights, from lidars pointed vertically. By using an expanded lidar beam to retrieve optical signals from migrating moths, we would have the potential to classify moth species based on the inherent microstructural differences between them, something that is not possible with VLR. Moreover, other studies have demonstrated the feasibility of remotely classifying moths, further supporting the potential for successful species identification in our research.[27,29,41] Additionally, due to the lidar's near limit, insect activity was not detectable below a range of 20 m, effectively hiding any insect activity within this range. This problem is only worsened by the lidar's narrow beam. These factors also contribute to reducing the likelihood of detecting moths that choose to fly at varying heights or distances from the lidar beam. Another shortcoming of our study is the relatively brief monitoring period we used (18 days), which might have limited our ability to capture longer-term or seasonal behavioral patterns of migratory moths. Future studies can address this issue by establishing a stationary setup and implementing an improved data pipeline, enabling automated and extended collection and analysis of the data.[47]

While we have observed wing depolarization in Lepidoptera, alternative data sources, such as the smooth waveforms in the time domain or sparse harmonics in the frequency domain, could also yield this information. Therefore, exploring alternative technologies, such as a dual-wavelength system, like the one used in Ecuador,[27] could provide more in-depth information. Such systems might prove beneficial considering the differing levels of melanization in the body and wings of Lepidoptera,[29] potentially leading to more detailed observational information.

As we plan the future direction of this research, we believe that our study has established initial signal expectations which now allow us to explore the possibility of developing dedicated systems with increased beam width and power. We are committed to enhancing our understanding of the behavior and ecology of these remarkable nocturnal migrants, and we are confident that future advancements in lidar technology and methodology will continue to play a crucial role in this field.

### Limitations of the study

Even though our lidar methods have successfully recorded the flight behaviors of insects, much still needs to be addressed regarding identification of these moths at a species' level. Specifically, our attempts to capture the wing strokes of moths having low wingbeat frequencies was challenging due to the relatively narrow width of the lidar beam. Furthermore, given the oblique angle of the lidar beam, our calculation of apparent vertical velocity of insects, based on transverse velocity, assumes that insect movements are unbiased along the north-south axis. Still, as we plan the future direction of this research, we believe that our study has established initial signal expectations which now allow us to explore the possibility of developing dedicated systems with increased beam width and power in the future.

## STAR★METHODS

Detailed methods are provided in the online version of this paper and include the following:

- KEY RESOURCES TABLE
- RESOURCE AVAILABILITY
  - Lead contact
  - Materials availability
  - Data and code availability
- EXPERIMENTAL MODEL AND SUBJECT DETIALS
  - Scheimpflug lidar
  - Laser light multiplexing for polarization data analysis
  - Compensation for observation hours
  - Signal projections on camera chip and movement direction estimation
- QUANTIFICATION AND STATISTICAL ANALYSIS
  - Apparent size calculation
  - Insect velocity calculation

## SUPPLEMENTAL INFORMATION

Supplemental information can be found online at https://doi.org/10.1016/j.isci.2024.109588.

## ACKNOWLEDGMENTS

This project has received funding from the European Research Council (ERC) under the European Union's Horizon 2020 research and innovation program (grant agreement no. 850463 Bug-Flash and 741298 Magnetic Moth) and from FORMAS the Swedish Research Council (grants 2018-01061 and 2021-04917). We thank Dr. Rachel Muheim (University of Lund), the Director of the Stensoffa Ecological Field Station, for logistical support.

## AUTHOR CONTRIBUTIONS

Conceptualization: M.B., E.W., M.L., J.S., P.T., T.T.H. Methodology: M.B., E.W., J.S. Investigation: P.T., J.S., L.M., H.M., M.B., M.L., H.C., D.D., J.A., T.T.H. Visualization: M.B., M.L., H.C. Funding acquisition: M.B., E.W. Project administration: M.B., E.W. Supervision: M.B., E.W. Writing – original draft: H.C., M.L., M.B. Writing – review and editing: H.C., M.L., P.T., J.S., L.M., H.M., D.D., G.H., E.W., M.B., J.A., T.T.H.

## DECLARATION OF INTERESTS

The authors declare no competing interests.

Received: September 15, 2023
Revised: January 29, 2024
Accepted: March 25, 2024
Published: March 27, 2024

## REFERENCES

1. Hu, G., Lim, K.S., Horvitz, N., Clark, S.J., Reynolds, D.R., Sapir, N., and Chapman, J.W. (2016). Mass seasonal bioflows of high-flying insect migrants. Science *354*, 1584–1587. https://doi.org/10.1126/science.aah4379.
2. Chapman, J.W., Bell, J.R., Burgin, L.E., Reynolds, D.R., Pettersson, L.B., Hill, J.K., Bonsall, M.B., and Thomas, J.A. (2012). Seasonal migration to high latitudes results in major reproductive benefits in an insect. Proc. Natl. Acad. Sci. USA *109*, 14924–14929. https://doi.org/10.1073/pnas.1207255109.
3. Hawkes, W.L.S., Walliker, E., Gao, B., Forster, O., Lacey, K., Doyle, T., Massy, R., Roberts, N.W., Reynolds, D.R., Özden, Ö., et al. (2022). Huge spring migrations of insects from the Middle East to Europe: quantifying the migratory assemblage and ecosystem services. Ecography *2022*. https://doi.org/10.1111/ecog.06288.
4. Wood, C.R., Reynolds, D.R., Wells, P.M., Barlow, J.F., Woiwod, I.P., and Chapman, J.W. (2009). Flight periodicity and the vertical distribution of high-altitude moth migration over southern Britain. Bull. Entomol. Res. *99*,

525–535. https://doi.org/10.1017/S0007485308006548.

5. Chapman, J.W., Reynolds, D.R., Mouritsen, H., Hill, J.K., Riley, J.R., Sivell, D., Smith, A.D., and Woiwod, I.P. (2008). Wind selection and drift compensation optimize migratory pathways in a high-flying moth. Curr. Biol. *18*, 514–518. https://doi.org/10.1016/j.cub.2008.02.080.
6. Alison, J., Alexander, J.M., Diaz Zeugin, N., Dupont, Y.L., Iseli, E., Mann, H.M.R., and Høye, T.T. (2022). Moths complement bumblebee pollination of red clover: a case for day-and-night insect surveillance. Biol. Lett. *18*, 20220187. https://doi.org/10.1098/rsbl.2022.0187.
7. Reynolds, D.R., Chapman, J.W., and Harrington, R. (2006). The migration of insect vectors of plant and animal viruses. Adv. Virus Res. *67*, 453–517. https://doi.org/10.1016/S0065-3527(06)67012-7.
8. Jones, C.M., Parry, H., Tay, W.T., Reynolds, D.R., and Chapman, J.W. (2019). Movement ecology of pest helicoverpa: implications for ongoing spread. Annu. Rev. Entomol. *64*, 277–295. https://doi.org/10.1146/annurev-ento-011118-111959.
9. Riley, J.R., Xia-nian, C., Xiao-xi, Z., Reynolds, D.R., Guo-min, X., Smith, A.D., Ji-yi, C., Ai-dong, B., and Bao-ping, Z. (1991). The long-distance migration of *Nilaparvata lugens* (Stål) (Delphacidae) in China: radar observations of mass return flight in the autumn. Ecol. Entomol. *16*, 471–489. https://doi.org/10.1111/j.1365-2311.1991.tb00240.x.
10. Li, X.J., Wu, M.F., Ma, J., Gao, B.Y., Wu, Q.L., Chen, A.D., Liu, J., Jiang, Y.Y., Zhai, B.P., Early, R., et al. (2020). Prediction of migratory routes of the invasive fall armyworm in eastern China using a trajectory analytical approach. Pest Manag. Sci. *76*, 454–463. https://doi.org/10.1002/ps.5530.
11. Drake, V.A., and Wang, H. (2018). Ascent and descent rates of high-flying insect migrants determined with a non-coherent vertical-beam entomological radar. Int. J. Rem. Sens. *40*, 883–904. https://doi.org/10.1080/01431161.2018.1519283.
12. Drake, V.A., and Wang, H. (2013). Recognition and characterization of migratory movements of Australian plague locusts, *Chortoicetes terminifera*, with an insect monitoring radar. J. Appl. Remote Sens. *7*, 075095. https://doi.org/10.1117/1.Jrs.7.075095.
13. Wotton, K.R., Gao, B., Menz, M.H.M., Morris, R.K.A., Ball, S.G., Lim, K.S., Reynolds, D.R., Hu, G., and Chapman, J.W. (2019). Mass seasonal migrations of hoverflies provide extensive pollination and crop protection services. Curr. Biol. *29*, 2167–2173.e5. https://doi.org/10.1016/j.cub.2019.05.036.
14. Aralimarad, P., Reynolds, A.M., Lim, K.S., Reynolds, D.R., and Chapman, J.W. (2011). Flight altitude selection increases orientation performance in high-flying nocturnal insect migrants. Anim. Behav. *82*, 1221–1225. https://doi.org/10.1016/j.anbehav.2011.09.013.
15. Drake, V.A. (2016). Distinguishing target classes in observations from vertically pointing entomological radars. Int. J. Rem. Sens. *37*, 3811–3835. https://doi.org/10.1080/01431161.2016.1204028.
16. Drake, V.A., Hatty, S., Symons, C., and Wang, H. (2020). Insect monitoring radar: maximizing performance and utility. Remote Sens. Basel *12*, 596. https://doi.org/10.3390/rs12040596.
17. Riley, J.R. (1989). Remote sensing in entomology. Annu. Rev. Entomol. *34*, 247–271. https://doi.org/10.1146/annurev.en.34.010189.001335.
18. Chapman, J.W., Reynolds, D.R., and Smith, A.D. (2003). Vertical-looking radar: a new tool for monitoring high-altitude insect migration. Bioscience *53*, 503–511. https://doi.org/10.1641/0006-3568(2003)053[0503:Vrantf]2.0.Co;2.
19. Feng, H.Q., Zhao, X.C., Wu, X.F., Wu, B., Wu, K.M., Cheng, D.F., and Guo, Y.Y. (2008). Autumn migration of *Mythimna separata* (Lepidoptera: Noctuidae) over the Bohai Sea in Northern China. Environ. Entomol. *37*, 774–781. https://doi.org/10.1093/ee/37.3.774.
20. Noskov, A., Achilles, S., and Bendix, J. (2021). Presence and Biomass Information Extraction from Highly Uncertain Data of an Experimental Low-Range Insect Radar Setup. Diversity *13*, 452. https://doi.org/10.3390/d13090452.
21. Noskov, A., Bendix, J., and Friess, N. (2021). A Review of Insect Monitoring Approaches with Special Reference to Radar Techniques. Sensors *21*, 1474. https://doi.org/10.3390/s21041474.
22. Noskov, A., Achilles, S., and Bendix, J. (2023). Toward forest dynamics' systematic knowledge: concept study of a multi-sensor visually tracked rover including a new insect radar for high-accuracy robotic monitoring. Front. Ecol. Evol. *11*. https://doi.org/10.3389/fevo.2023.1214419.
23. Brydegaard, M., and Svanberg, S. (2018). Photonic monitoring of atmospheric and aquatic fauna. Laser Photon. Rev. *12*, 1800135. https://doi.org/10.1002/lpor.201800135.
24. Månefjord, H., Müller, L., Li, M., Salvador, J., Blomqvist, S., Runemark, A., Kirkeby, C., Ignell, R., Bood, J., and Brydegaard, M. (2022). 3D-Printed fluorescence hyperspectral lidar for monitoring tagged insects. IEEE J. Sel. Top. Quant. *28*, 1–9. https://doi.org/10.1109/JSTQE.2022.3162417.
25. Song, Z., Zhang, B., Feng, H., Zhu, S., Hu, L., Brydegaard, M., Li, Y., Jansson, S., Malmqvist, E., Svanberg, K., et al. (2020). Application of lidar remote sensing of insects in agricultural entomology on the Chinese scene. J. Appl. Entomol. *144*, 161–169. https://doi.org/10.1111/jen.12714.
26. Jansson, S., Malmqvist, E., Mlacha, Y., Ignell, R., Okumu, F., Killeen, G., Kirkeby, C., and Brydegaard, M. (2021). Real-time dispersal of malaria vectors in rural Africa monitored with lidar. PLoS One *16*, e0247803. https://doi.org/10.1371/journal.pone.0247803.
27. Santos, V., Costa-Vera, C., Rivera-Parra, P., Burneo, S., Molina, J., Encalada, D., Salvador, J., and Brydegaard, M. (2023). Dual-band infrared Scheimpflug lidar reveals insect activity in a tropical cloud forest. Appl. Spectrosc. *77*, 593–602. https://doi.org/10.1177/00037028231169302.
28. Li, M., Jansson, S., Runemark, A., Peterson, J., Kirkeby, C.T., Jönsson, A.M., and Brydegaard, M. (2021). Bark beetles as lidar targets and prospects of photonic surveillance. J. Biophot. *14*, e202000420. https://doi.org/10.1002/jbio.202000420.
29. Li, M., Seinsche, C., Jansson, S., Hernandez, J., Rota, J., Warrant, E., and Brydegaard, M. (2022). Potential for identification of wild night-flying moths by remote infrared microscopy. J. R. Soc. Interface *19*, 20220256. https://doi.org/10.1098/rsif.2022.0256.
30. Li, M., Runemark, A., Hernandez, J., Rota, J., Bygebjerg, R., and Brydegaard, M. (2023). Discrimination of hover fly species and sexes by wing interference signals. Adv. Sci. *10*. https://doi.org/10.1002/advs.202370232.
31. Li, Y.Y., Zhang, H., Duan, Z., Lian, M., Zhao, G.Y., Sun, X.H., Hu, J.D., Gao, L.N., Feng, H.Q., and Svanberg, S. (2016). Optical characterization of agricultural pest insects: a methodological study in the spectral and time domains. Appl. Phys. B *122*, 213. https://doi.org/10.1007/s00340-016-6485-x.
32. Brydegaard, M., Kouakou, B., Jansson, S., Rydell, J., and Zoueu, J. (2021). High dynamic range in entomological scheimpflug lidars. IEEE J. Sel. Top. Quant *27*, 1–11. https://doi.org/10.1109/JSTQE.2021.3062088.
33. Rydhmer, K., Prangsma, J., Brydegaard, M., Smith, H.G., Kirkeby, C., Kappel Schmidt, I., and Boelt, B. (2022). Scheimpflug lidar range profiling of bee activity patterns and spatial distributions. Anim. Biotelemetry *10*, 14. https://doi.org/10.1186/s40317-022-00285-z.
34. Brydegaard, M., Jansson, S., Malmqvist, E., Mlacha, Y.P., Gebru, A., Okumu, F., Killeen, G.F., and Kirkeby, C. (2020). Lidar reveals activity anomaly of malaria vectors during pan-African eclipse. Sci. Adv. *6*, eaay5487. https://doi.org/10.1126/sciadv.aay5487.
35. Wiktelius, S. (1984). Long range migration of aphids into Sweden. Int. J. Biometeorol. *28*, 185–200. https://doi.org/10.1007/BF02187959.
36. Li, Y., Wang, K., Quintero-Torres, R., Brick, R., Sokolov, A.V., and Scully, M.O. (2020). Insect flight velocity measurement with a CW near-IR Scheimpflug lidar system. Opt Express *28*, 21891–21902. https://doi.org/10.1364/OE.394992.
37. Malmqvist, E., Brydegaard, M., Aldén, M., and Bood, J. (2018). Scheimpflug Lidar for combustion diagnostics. Opt Express *26*, 14842–14858. https://doi.org/10.1364/OE.26.014842.
38. Jansson, S., and Brydegaard, M. (2018). Passive kHz lidar for the quantification of insect activity and dispersal. Anim. Biotelemetry *6*, 6. https://doi.org/10.1186/s40317-018-0151-5.
39. Rydhmer, K., Jansson, S., Still, L., Beck, B.D., Chatzaki, V., Olsen, K., Van Hoff, B., Grønne, C., Meier, J.K., Montoro, M., et al. (2024). Photonic sensors reflect variation in insect abundance and diversity across habitats. Ecol. Indicat. *158*, 111483. https://doi.org/10.1016/j.ecolind.2023.111483.
40. Müller, L., Li, M., Månefjord, H., Salvador, J., Reistad, N., Hernandez, J., Kirkeby, C., Runemark, A., and Brydegaard, M. (2023). Remote nanoscopy with infrared elastic hyperspectral lidar. Adv. Sci. *10*, 2207110. https://doi.org/10.1002/advs.202207110.
41. Li, M., Runemark, A., Guilcher, N., Hernandez, J., Rota, J., and Brydegaard, M. (2023). Feasibility of insect identification based on spectral fringes produced by clear wings. IEEE J. Sel. Top. Quant. *29*, 1–8. https://doi.org/10.1109/JSTQE.2022.3218218.
42. Willmott, A.P., and Ellington, C.P. (1997). The mechanics of flight in the hawkmoth *Manduca sexta*. I. Kinematics of hovering and forward flight. J. Exp. Biol. *200*, 2705–2722. https://doi.org/10.1242/jeb.200.21.2705.
43. Warfvinge, K., Johansson, L.C., and Hedenström, A. (2021). Hovering flight in hummingbird hawkmoths: kinematics, wake dynamics and aerodynamic power. J. Exp. Biol. *224*, jeb230920. https://doi.org/10.1242/jeb.230920.

44. Huang, J.l., Qiu, M., and Ma, L.l. (2013). Effects of age, ambient temperature and reproductive status on wing beat frequency of the rice leafroller *Cnaphalocrocis medinalis* (Guenée) (Lepidoptera: Crambidae). Appl. Entomol. Zool. *45*, 499–503. https://doi.org/10.1007/s13355-013-0209-z.

45. Månefjord, H., Li, M., Brackmann, C., Reistad, N., Runemark, A., Rota, J., Anderson, B., Zoueu, J.T., Merdasa, A., and Brydegaard, M. (2022). A biophotonic platform for quantitative analysis in the spatial, spectral, polarimetric, and goniometric domains. Rev. Sci. Instrum. *93*, 113709. https://doi.org/10.1063/5.0095133.

46. Dwivedi, M., Shadab, M.H., and Santosh, V.R. (2020). Insect pest detection, migration and monitoring using radar and LiDAR systems. In Innovative Pest Management Approaches for the 21st Century: Harnessing Automated Unmanned Technologies, pp. 61–76. https://doi.org/10.1007/978-981-15-0794-6_4.

47. Lukach, M., Dally, T., Evans, W., Hassall, C., Duncan, E.J., Bennett, L., Addison, F.I., Kunin, W.E., Chapman, J.W., and Neely, R.R., 3rd (2022). The development of an unsupervised hierarchical clustering analysis of dual-polarization weather surveillance radar observations to assess nocturnal insect abundance and diversity. Remote Sens. Ecol. Conserv. *8*, 698–716. https://doi.org/10.1002/rse2.270.

48. Jansson, S., Malmqvist, E., Brydegaard, M., Åkesson, S., and Rydell, J. (2020). A Scheimpflug lidar used to observe insect swarming at a wind turbine. Ecol. Indicat. *117*, 106578. https://doi.org/10.1016/j.ecolind.2020.106578.

49. Kouakou, B.K., Jansson, S., Brydegaard, M., and Zoueu, J.T. (2020). Entomological Scheimpflug lidar for estimating unique insect classes in-situ field test from Ivory Coast. OSA Continuum *3*, 2362. https://doi.org/10.1364/osac.387727.

50. Spie, P.o., Malmqvist, E., Jansson, S., Larsson, J., Török, S., and Zhao, G. (2017). The Scheimpflug lidar method. Lidar Remote Sensing for Environmental Monitoring *10406*, 104060I. https://doi.org/10.1117/12.2295982.

51. Mei, L., and Guan, P. (2017). Development of an atmospheric polarization Scheimpflug lidar system based on a time-division multiplexing scheme. Opt. Lett. *42*, 3562–3565. https://doi.org/10.1364/OL.42.003562.

52. Zhao, G., Malmqvist, E., Török, S., Bengtsson, P.-E., Svanberg, S., Bood, J., and Brydegaard, M. (2018). Particle profiling and classification by a dual-band continuous-wave lidar system. Appl. Opt. *57*, 10164–10171. https://doi.org/10.1364/AO.57.010164.

53. Jansson, S. (2020). Entomological lidar: target characterization and field applications. PhD Thesis (Lund University). https://lup.lub.lu.se/search/publication/0a1b0d54-552d-4a3f-805a-c848932d1de2.

## STAR★METHODS

### KEY RESOURCES TABLE

| REAGENT or RESOURCE | SOURCE | IDENTIFIER |
|---|---|---|
| Deposited data | | |
| Raw data files | Meng Li, Mikkel Brydegaard, Lund University, Sweden | https://lu.box.com/s/c7a1jxneh8owxuyh0r725ocbzi0bjcqh |
| Analyzed data files | This paper | Figures 1, 2, 3, and 4 |
| Software and algorithms | | |
| LabVIEW 2022 | National Instruments | https://www.ni.com/en/support/downloads.html |
| Custom made LabView code for Scheimpflug Lidar data acquisition | This paper; Hampus Månefjord, Lund University, Sweden | https://github.com/BioBeamMeng/LidarMoth |
| MATLAB 2022 | MathWorks | https://se.mathworks.com/ |
| Custom Matlab-script was used for data and figure analysis | This paper; Meng Li, Mikkel Brydegaard, Lund University, Sweden | https://github.com/BioBeamMeng/LidarMoth |

### RESOURCE AVAILABILITY

#### Lead contact

Further information and requests for resources should be directed to and will be fulfilled by the Lead Contact, Mikkel Brydegaard (mikkel.brydegaard@fysik.lth.se).

#### Materials availability

This study did not generate new unique reagents.

#### Data and code availability

- All data reported in this paper have been deposited at GitHub, and are publicly available as of the date of publication, as detailed in the key resources table.
- This paper does not report original code.
- Any additional information required to reanalyze the data reported in this paper is available form the lead contact upon request.

### EXPERIMENTAL MODEL AND SUBJECT DETIALS

#### Scheimpflug lidar

Our lidar system was based on the Scheimpflug lidar principle,[26–28,32,48,49] which allows us to focus on flying insects over varying distances simultaneously. This lidar system is mounted on an 814 mm long baseline with a transmitting and a receiving telescope, as depicted in Figure 1A. For stabilization, we utilized a tripod (EQ8, SkyWatcher, China).

The transmitting telescope, integrated with two 3W TE-polarized 980 nm laser diodes, has an aperture of 75 mm and a focal length of 300 mm. The 980 nm wavelength is near-infrared, invisible and do not disturb air traffic. Eye-safe levels were obtained beyond 30 m range and 15 m altitude. The beam is inaccessible. The polarization from one laser diode is altered by 90° using a wide-angle polymer half-wave plate and superimposed with the other laser beam via a polarization beam splitter, then transmitted.

The receiving telescope is a Ø200 mm, f800 mm Newton reflector (Quattro, SkyWatcher, China) equipped with a CMOS detector (OctoPlus, Teledyne e2v, USA) at its eyepiece to collect signal data. This CMOS detector consists of 2048 pixels, each measuring 10 μm × 200 μm. In line with the Scheimpflug principle and the hinge rule,[49,50] the camera is tilted at a 45° angle relative to the optical axis within the transmitter module.

The lidar system, employing a polarimetric configuration, operated at an 8 kHz sampling rate, with co-polarized, de-polarized, and background signals being sampled at approximately 2.66 kHz each after de-multiplexing.[51,52] Each lidar file contained a 4-s length of observation data with 30,000 exposure lines. Each file was around 120 MB in size, and throughout the campaign, more than 20 TB of raw data was acquired. In the process of data acquisition, the polarization of the laser light was multiplexed, allowing for the sequential capture of depolarized,

co-polarized, and background light. Subsequent processing steps involved the subtraction of the depolarized, co-polarized, and background signals from the raw data, and cropping out the insect observation signal following the data processing pipeline.[53] As most of the data were empty, the data size was reduced to less than 1% of the original size. In total, we acquired lidar signals for 18 days. Operating at a fast-sampling rate of 8 kHz (equivalent to a short exposure time of 125 μs), our lidar system efficiently distinguishes insect signals from atmospheric particles and aerosols with a threshold SNR of 5. Typically, achieving a reliable signal from air particles or aerosols would necessitate longer exposure times. For example, capturing air signals would require an exposure setting of 620 μs, in addition to doubling the gain and preamplification when using our lidar system.

The typical cost for the construction of these lidar systems ranges from 15 to 20 kEuro, which includes travel boxes, and other associated expenses. A dozen systems have been assembled within this budget. The timeline for this process involves three months for ordering components and assembling the system, followed by an additional three months for alignment and mastering the analysis code.

### Laser light multiplexing for polarization data analysis

For a comprehensive view of each measurement day, we generate overview plots (like the example shown in Figure S1). These plots color-code the maximum depolarized, copolarized, and background values within each file. This visualization reveals temporal and spatial shifts in maximum values and emphasizes rare events (e.g., insects appear as bright green dots). Cloud echoes are also evident, with higher atmospheric scatter coefficients and humidity causing clouds to descend during evening hours.

To demonstrate how we use a threshold to pick out insect observations, frame 3991 (recorded at 06-Jun-2022 22:46:08 and marked in Figure S1A) is examined. Figure S1B zooms in on this time frame, highlighting distinct signals (later classified as insects) alongside persistent aerosol plumes (clouds). Intensity counts for frame 3991, including pixel-wise median and maximum values, are shown in Figure S1C. A threshold based on each pixel's intensity distribution isolates insect signals from aerosols (e.g., clouds). This threshold is the median plus five times the interquartile range (IQR), or SNR = 5. The SNR ratio is configurable; we employed SNR = 5 to visually confirm the threshold appropriately suppressed cloud/mist signals while preserving insects. Higher or lower SNRs may be suitable depending on observational conditions (e.g., dense fog). Figure S1D illustrates how the threshold varies with a pixel's median and IQR; the insect pixel retains some values above the threshold, while all cloud pixel values are eliminated due to its broader IQR and higher median. This demonstrates the threshold's (Figure S1C) effectiveness in selecting rare events (insects, with lower median and IQR) over continuous aerosol signals.

During the data acquisition process, the laser light was multiplexed, enabling it to sequentially illuminate in depolarized, co-polarized, and background modes. This multiplexing sequence is represented in Figures S2A and S1B, where the strips of signals in the captured data change as the laser light transitions between its modes. After acquisition, the background signals were subtracted from both the co-polarized and depolarized signals, as depicted in Figures S2C and S1D. To distinguish insect signals from background noise, a threshold was applied, with Figure S2E showing the use of a detection mask that retains only those signals exceeding an SNR of 5. Further procedures to isolate and crop the insect signals are described in detail in previous study.[53]

### Compensation for observation hours

As mentioned earlier, the lidar system was not operated continuously, resulting in a bias in the observations. There were more observations recorded between 18:00 and 24:00 compared to full-day recordings, leading to a false insect activity pattern as shown in Figure S3A. In Figure S3B, it is evident that there is a higher accumulation of files recorded during the 18:00 to 24:00 time period, indicating the bias caused by the uneven lidar operation hours. To address this bias, the insect activity pattern was compensated using Figure S3B, resulting in Figure S3C, which removes the effect of lidar operation hours. With the compensation, a higher insect activity is now reported during the daytime as well, but overall, there is still a greater insect activity observed during the evening at higher heights.

### Signal projections on camera chip and movement direction estimation

Expounding upon the technique of insect signal detection, an extended illustration from Figure 1C is provided in Figure S4A. Initially, the lidar is set at an elevation angle of 30°, with the beam and the receiver's field of view converging around a distance of 35 m afar (20 m in height). Given the orientation of the camera chip, pixel number $p_{2048}$ captures the observational scene at an elevation angle $\Phi = 30^{\circ}$, whereas pixel $p_1$ captures at an elevation angle $\Phi + \varphi$, with $\varphi = 1.27^{\circ}$.

Delving into the dynamics of signal detection, the range is ascertained using Equation 3, considering the absolute center pixel location, $p_{cent}$. For instance, in the scenario depicted in Figure S4B, $p_{cent}$ would be $p_{1641}$ at time $t_0$ and at time $t_1$, the signal is captured onto pixel $p_{1642}$. The traversed distance by the center pixel, denoted as $\Delta p$ is the signal displacement. By dividing $\Delta p$ by the time difference $\Delta t$, the velocity is then calculated. Additionally, in Figure S4B, the spread of the signal on the chip is denoted as $\delta p$. The apparent size can be calculated utilizing the magnification from the camera and telescope, which in turn, is employed to approximate the insect size.

With the Lidar system positioned facing north at an elevation angle of 30°, a positive velocity value, as derived from Equation 2, denotes movement either upwards or toward the south. Figure S4B illustrates the relative camera chip positioning in accordance to the north, south, upward, and downward directions. The differential $\Delta p/\Delta t$, contingent on the value of $\Delta p$, registers as positive only when the detected target's movement is directed either upwards or southward. Given the configuration of the Lidar system, it exhibits a greater efficacy in capturing movements directed upwards compared to those directed southward.

## QUANTIFICATION AND STATISTICAL ANALYSIS

### Apparent size calculation

To determine the apparent size of the insects, symbolized as $\delta_{insect}$, we implemented a formula based on the methodology from a previous study which also used the Scheimpflug lidar configuration,[32]

$$\delta_{\text{insect }(t)} = 4\sqrt{2\log(2)}\,\frac{r\cos(\theta)\,W}{F_{rec}}\sqrt{\frac{\sum_{\text{mask}} I_{\text{insect}}(p,t)\left(p - p_{\text{cent.}}\right)^2}{\sum_{\text{mask}} I_{\text{insect}}(p,t)}} \quad \text{(Equation 1)}$$

where $r$ is the range to the observed insect, $W$ is pixel pitch, the distance from the center of one pixel to the center of the next on the camera, which was 10 $\mu$m/pix, $\theta$ is the tilt angle of the sensor in the Scheimpflug configuration, set at 45° between the camera and optical axis within the transmitter module. $F_{rec}$ is the focal length of the receiver, which was 0.8 m. The central pixel in our analysis, symbolized as $p_{cent}$, is calculated using the first statistical moment or the Center of Mass (CoM) calculation. $I$ represents the lidar intensity count as a function of pixels, $p$, and time, $t$. The term *mask* denotes the pixels and exposures that exceed a noise level. The right hand square-root term is the second statistical moment (standard deviation) of the range echo to gauge the pixel spread. The left hand scalar term $4(2\log(2))^{½}$ translates the standard deviation into twice the full-with-half-max (FWHM), whereby the value better reflects the whole physical extension of the insect size. Note that the FWHM term is not present in our previous study.[32] All statistical analysis and graphical plotting were conducted in MATLAB R2021a.

### Insect velocity calculation

To measure the vertical heading velocity of the insects observed, we employed a formula derived from a previous study.[36] In Scheimpflug lidar, ranging is accomplished by triangulation and thus the range accuracy is limited by the beam width. This uncertainly can be exploited for estimating target sizes[32] and movements perpendicular to the beam.[36] Insect transverse velocity was calculated as

$$v_{\text{up / south}} = \frac{F_{\text{rec}}\,W\,\frac{\Delta p}{\Delta t}\cos(\theta)}{r} \quad \text{(Equation 2)}$$

where $v$ (m/s) represents the velocity component of the insect as it moves perpendicular to the optical path of the receiving telescope, a positive value meaning upwards/south (ascending) flight and a negative value meaning downwards (descending) flight. $\Delta p/\Delta t$ (pix/s) is the number of pixels per unit time, which is itself obtained from a linear fit of the insect signal trajectory in a time-pixel map. Finally, $F_{rec}$ and $r$ refer to the object and image distances, respectively, with the relationship between these two factors specifying the specific magnification for pixel $x$. $W$ and $\theta$ are constants set to 10 μm/pix and 45°, respectively. The estimated range $r$ is calculated by

$$\hat{r}(p_r) = \ell_{\text{BL}}\cot\left(\Gamma_{\text{slant}} + \varphi p_{cent}\right) \quad \text{(Equation 3)}$$

The normalized pixel positions are represented by $p_r$ which range from 0 to 1. $\ell_{BL}$ denotes the baseline length, set at 0.814 m $\Gamma_{slant}$ is the angle between the optical axis of the beam expander and the receiver. The receiver's field of view is given by $\varphi$. The center pixel, $p_{cent}$, is determined using the center of mass formula, or CoM. All statistical analysis and graphical plotting were conducted in MATLAB R2021a.

# Paper III

# Stratification of Insect Diversity and Daily Activity Patterns in Taï Virgin Forest assessed by Entomological Lidar

Hampus Månefjord[1*], Assoumou saint-doria Yamoa[2], Yatana Adolphe Gbogbo[2], Lauro Müller[1], Anna Runemark[3], Benoit Kouassi Kouakou[4], Rabbi Boateng[5], Andrew Atiogbe Huzortey[5], Isaac Kwame Badu[6], Niklas Wahlberg[7], Mikkel Brydegaard[1,2,8], Jérémie T. Zoueu[4], Benjamin Anderson[5], Meng Li[1]

[1] Dept. Physics, Lund University, Sölvegatan 14c, 22363 Lund, Sweden
[2] Institut National Polytechnique Félix Houphouët-Boigny de Yamoussoukro, Côte d'Ivoire
[3] Dept. Biology, Lund University, Sölvegatan 35, 22362 Lund, Sweden
[4] Dept. Physics, University of San-Pedro, BP 1800 San-Pedro - Côte d'Ivoire
[5] Fibre Optics Centre (LAFOC) at the Univeristy of Cape Coast (UCC), Cape Coast, Ghana
[6] Dept. Conservation Biology and Entomology, University of Cape Coast (UCC), Cape Coast, Ghana
[7] Biological Museum, Department of Biology, Lund University, Sölvegatan 37, 22362 Lund, Sweden
[8] Norsk Elektro Optikk, Østensjøveien 34, 0667 Oslo, Norway

* Correspondence: Hampus Månefjord, Department of Physics, Lund University, Sölvegatan 14, 22362 Lund, Sweden.

Email: hampus.manefjord@fysik.lu.se

**Abstract:**
Lidar technology was utilized to non-destructively explore the diverse insect life in the Taï virgin forest of Côte d'Ivoire. This study combined entomological Lidar with traditional insect trapping to investigate the composition and spatial-temporal distribution of insects across the forest canopy. We detected stratified patterns of insect activity at various canopy heights, revealing differences in composition of optical signals reflecting divergent species composition with height and time of the day, indicative of high and sampling height dependent insect biodiversity. The optical properties of captured insects, including wing specularity and polarimetric response, were analyzed and correlated with Lidar signals, revealing distinct insect clusters and activity patterns at different canopy heights. These findings show the potential of using Lidar to non-invasively assess insect diversity continuously across complex canopies to uncover species composition in ecosystems with high species diversity.

**One-Sentence Summary:**
Lidar profiling revealed that insect community composition varies with sampling time and height in canopy in the Taï forest, suggesting Lidar as a promising tool for estimating local- and temporal variation in species richness.

## Introduction

Tropical virgin forests stand as some of the world's richest reservoirs of biodiversity, yet they also rank among the most threatened biomes. To conserve the species richness in these regions, it is crucial to understand the distribution and predictors of biodiversity [1-3], especially for insects, which are not only the most species-rich taxa but also among the most threatened [4-6]. Recent reports have highlighted alarming declines in insect assemblages and biomass, with estimates suggesting that terrestrial insects are declining at an average rate of 11% per decade globally [7, 8]. Despite their significance, our understanding of insect populations in tropical rainforests, in particular in sub-Saharan Africa, lags behind that of regions like Europe and North America [9, 10]. One challenge in identifying the habitats that are key to maintain insect diversity is the non-uniform distribution of insects within tropical canopies, making vertical stratification a key aspect to assess [11, 12]. Understanding and preserving insect biodiversity in tropical forests is key component for avoiding insect mass extinction.

Traditional methods for insect monitoring, incluing malaise- and baited traps[13] and tree-branch beating[14] offer limited spatial and temporal resolution (REFS). These methods also have inherent biases [15-17] and are weather-dependent species composition in catches[18]. The employment, operation and taxonomical [19] or DNA [20] based identification of catches of trap- and tree branch beat catches are both time-consuming and costly and require skill and equipment that is not accessible to all. Importantly, these methods often require sacrificing captured insects, posing ethical concerns, especially in areas harboring endangered species [21].

The limitations of traditional methods call for innovative, non-invasive approaches to monitor insect diversity within complex ecosystems. High spatial and temporal resolution with retained ability to differentiate species is key for capturing the true diversity. While techniques such as image- and sound recognition [22-24] and digital holography [25] show great potential, their field of view is often limited. Radars show promise for monitoring high-altitude insect migration on a large scale[26-29] but can generally not be operated within forest canopies due to ground clutter noise [30]. Moreover, their capacity to distinguish between species is often restricted [31]. While low-altitude insects can be tracked with harmonic radar [32] such methods require a catch-mark and release scheme, limiting the scope of species that can be investigated.

In this study, we address the challenge of monitoring insects in stratified environments and representing the full composition of species that are active over the day by employing entomological Lidar. We have previously demonstrated the potential of Lidar to provide detailed information on insect abundance[33], distribution [34], flight characteristics[35, 36], species richness [37], powder-tagged monitoring [38, 39] and features such as wing thickness [40], have been previously established. We expand on this work by using a near-infrared (NIR) polarization Lidar [41] to achieve unprecedented spatial (centimeter-scale) and temporal (millisecond)

resolution in mapping insect activity within a virgin rainforest canopy. This study establishes a baseline for investigating the intricate patterns of insect distribution within forests, with strong potential to improve our understanding of insect diversity in stratified forests.

## Results

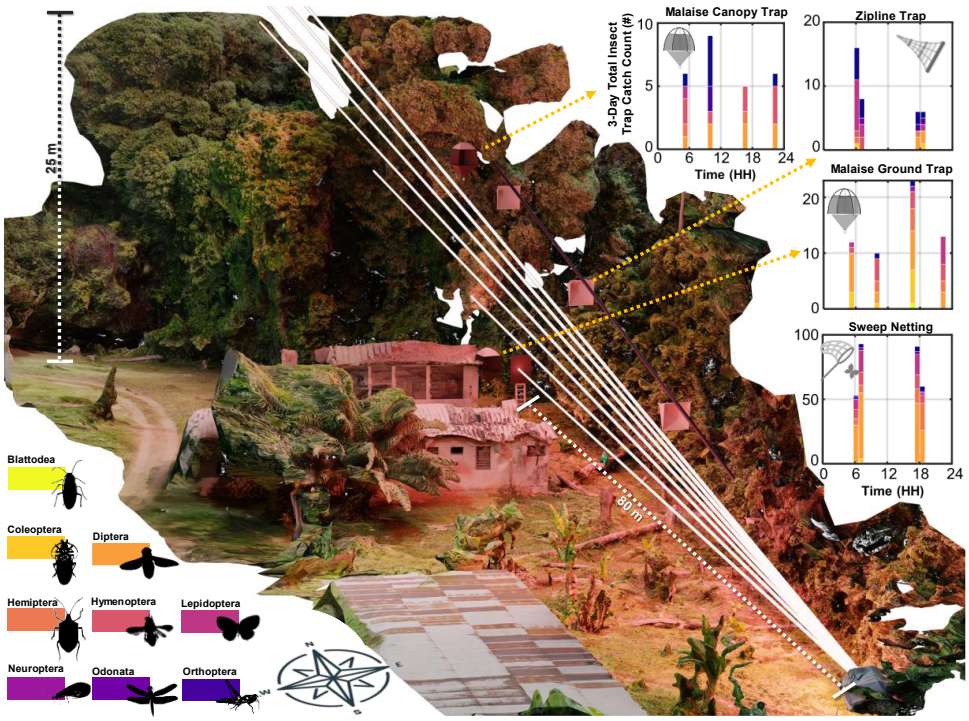


**Figure 1. A 3D-rendered representation of the Taï virgin forest experimental site derived from 600 drone-acquired images.** The illustration delineates Lidar measurements taken at seven distinct elevation angles, ranging from 0˚ to 20˚. The locations of the malaise and zipline traps are marked. Data of the capture counts for each trap, accumulated over a three-day measurement interval, is presented on the right. The 80 m ground Lidar transect was oriented to 34˚N, and the canopy reached a height of 25 m at this specific site.

The study was conducted in Taï rainforest (Parc National de Taï), Côte d'Ivoire (5°49'59.5"N 7°20'32.8"W), from January 12th to 14th 2023, with measurements recorded throughout the day. Insect activity was measured through manual trapping techniques and Lidar observations, see Fig. 1. Manual trapping yielded 290 catches over the three-day measurement period. Our initial observations indicate substantial variation in the species caught by the three different trapping methods employed; malaise, zipline, and manual sweep netting. The variation was larger between

the catching methods compared to the probed height, e.g., the malaise trap positioned 1 m above the ground level had similar catches as the 20 m malaise trap. Diptera was the majority of catches in all traps. The zipline stood out however, being the only trap to capture Odonata and Orthoptera, except for a few manual sweep netting catches. The temporal resolution of all traps was four times per 24 hour period. Both malaise traps and the manual sweep netting resulted in higher catches during evening hours consistent with higher levels of activity during these hours, while the zipline trap instead results in higher catches during morning hours.

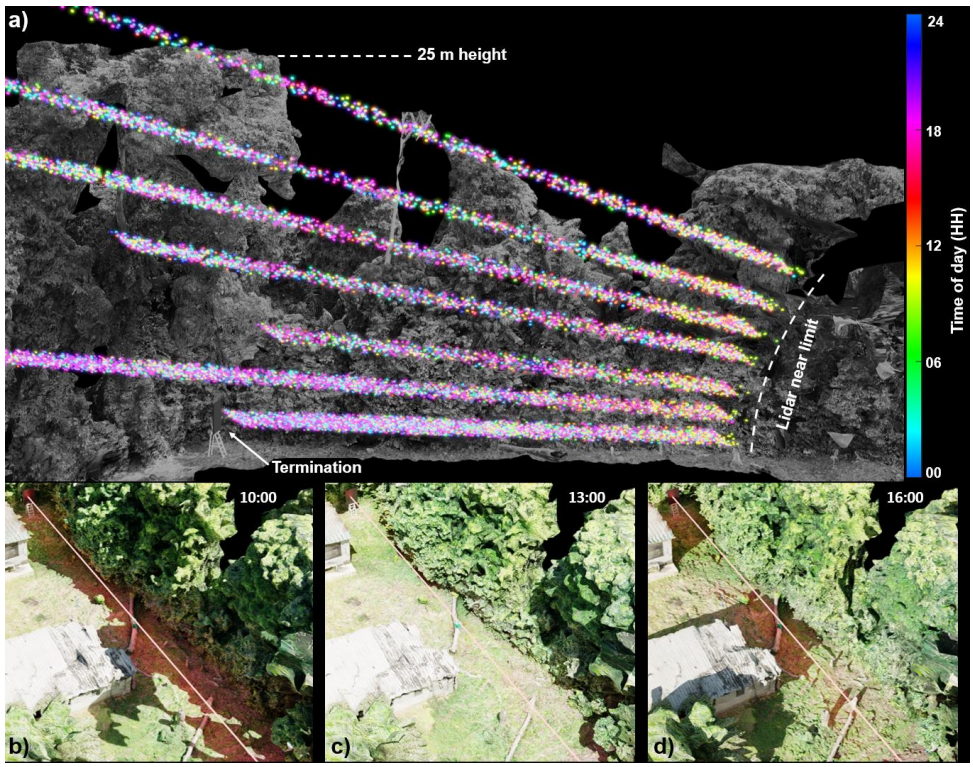


**Figure 2: Illustration of insect activity at multiple distances and canopy levels.** a) Insect scatter points are color-coded according to the time of day. b-d) display the laser beam's position and shaded areas at different times of day.

The lidar system detected 19,369 insects over three days, exceeding the approximately 290 catches obtained with manual traps with orders of magnitude. For in-depth analysis, we focused on 6,962 lidar observations with signal durations exceeding 25 milliseconds. This selection criterion ensured sufficient wingbeat information within the signal for reliable estimation of modulation power spectra. Constraints arose from the slow-moving tripod motor, which necessitated frequent pauses for canopy scanning adjustments. As a result, the Lidar was operational for only 12% of the total measurement duration, leading to a reduced number of insect observations compared to previous studies [34, 42].

Sunlight exposure and canopy stricture significantly affected insect prevalence and species composition.. Lidar insect signals are recorded throughout the day, here illustrated with color-coding indicating the time of observation (Fig. 2a). The shaded and sunlit areas changes across the transect during the daily cycle (Fig. 2b-d). We reveal a higher insect signal density within the shade of the large canopy compared to the open area at closer range when interrogating data from elevation angles 5 and 6 in Fig. 2a. This difference in density cannot be explained by the lidar beam's characteristics, suggesting that factors such as direct sunlight exposure may be influencing insect distribution patterns. Additionally, closer-range observations show an increase in activity near a vegetation wall around 10 AM (Fig. 2a; indicated by yellow points). This observation adds to the evidence that many insects are active in the shade, particularly smaller insect species that might be more susceptible to desiccation from direct sunlight.

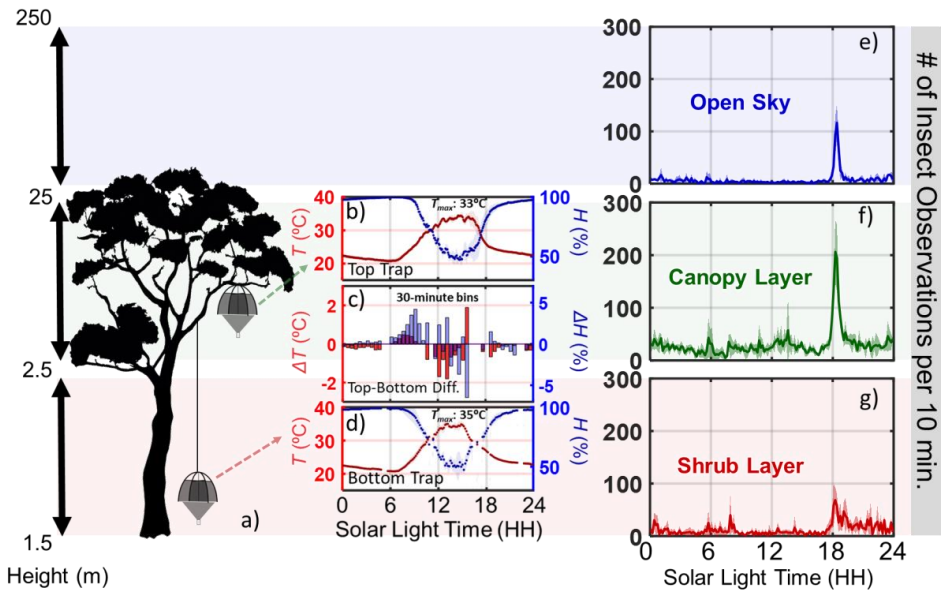


**Figure 3: A representation of insect activity across the varied layers of the forest canopy.** a) The position of the Malaise traps on a tree, differentiating tree heights into the shrub layer (1.5-2.5 m), the canopy layers (2.5 m - 25 m), and open sky (25 m and above). Note that the depiction is not to scale. b) and d) Temperature and humidity measurements from the two Malaise traps over a three-day period, with lines marking mean values and shaded regions indicating variation over the 3-day span. c) Variance in temperature and humidity between the top and bottom traps. e-g) Insect activity patterns at the different canopy levels, with lines showing mean values and shaded portions reflecting standard deviation variations over the 3-day measurement interval.

We documented insect activity and diversity at three heights: the Shrub layer (1.5 to 2.5m), the Canopy layer (2.5 to 25m), and the Open Sky layer (above 25m) to identify variation in species composition and activity patterns across these zones. Temperature and humidity were recorded at

1m and 20m heights to assess environmental conditions within the Shrub and Canopy layers, revealing that the Shrub layer is 2°C warmer during peak hours (12:00-16:00). There is also a notable difference in morning humidity, with the Canopy layer having 5 percentage points higher humidity than the Shrub layer.

The Open Sky layer (above 25m) exhibited a prominent activity peak between 18:00-20:00 (38% of the observations for the layer). In contrast, the Canopy layer showed both a similar evening activity peak (25%) and sustained activity throughout daylight hours (9:00-17:00, 73% of observations). There is also some nocturnal activity and an early morning surge in the Canopy layer, which thus is the layer showing the most consistent insect activity. The Shrub layer displayed an evening peak (18:00 - 20:00, 26% of layer observations), significant nocturnal activity (20:00-2:00, 32% of layer observations), and morning activity (05:00-9:00, 15% of layer observations), with minimal activity during warmer daylight hours (9:00-17:00).

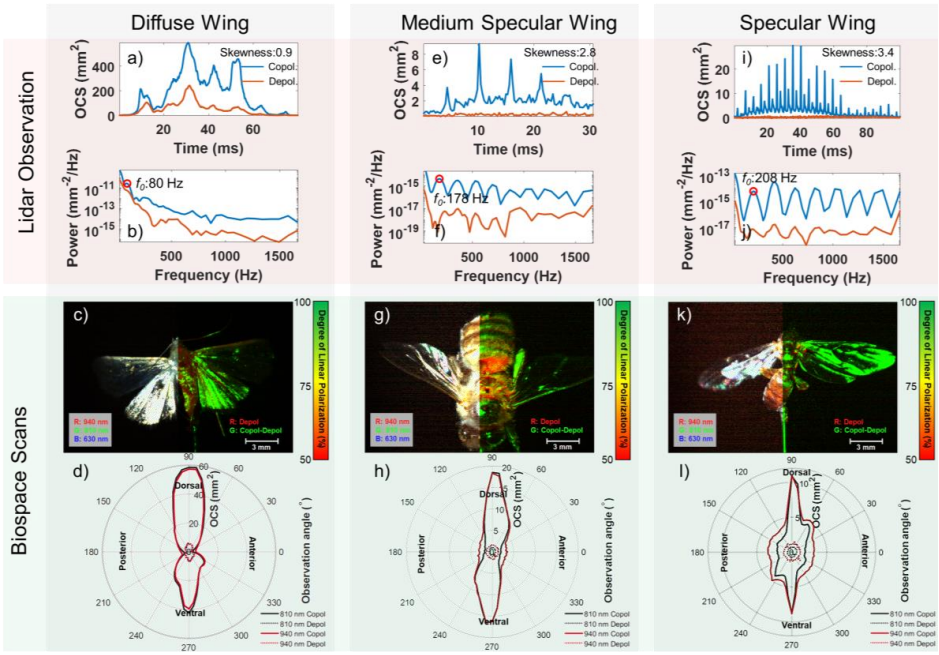


**Figure 4: A comparative representation of data from two interconnected systems, in-flight insect Lidar observation and goniometric insect specimen scan.** The upper section provides a comprehensive display of Lidar-derived insect signals. Specifically, a, e, and i) and b, f, and j) present the time series and power spectra respectively. c, g, and k) depict the near infrared and polarization color images of three captured specimens, a Lepidoptera, an Apis and a Diptera, measured with an instrument called BIOSPACE (Biophotonics, Imaging, Optical, Spectral, Polarimetric, Angular, and Compact Equipment). The lower section, d, h, and l), showcases the angular reflection at different angles for flashy, medium flashy, and diffuse wings, also measured with BIOSPACE at the jungle field station.

The retrieved lidar signals characteristics correlate with the degree of insect wing specularity [30]. To illustrate how lidar signal varies depending on characteristics of the observed insect, three insect specimens with diffuse, moderately specular, and highly specular were selected for in depth signal analysis. Importantly, these specimens are not the exact individuals detected by the lidar but demonstrate the effect of wing specularity on lidar signals. To determine the relationship between physical traits, angle and signal, the specimens differing in wing specularity quantified through angular reflectance measurements obtained using a separate goniometric instrument, BIOSPACE (Biophotonics, Imaging, Optical, Spectral, Polarimetric, Angular, and Compact Equipment) [43, 44]. Whereas diffuse wings produce broader peaks (Fig. 4a) compared to sharper peaks observed with moderate (Fig. 4e) and high specularity (Fig. 4i). Corresponding differences are observed in the power spectra, with higher specularity leading to more pronounced overtones (Fig. 4c, 4g, 4k). Sharper dorsal peaks in the polar plots (Fig. 4d, 4h, 4l) indicate increasing specularity.

In addition to specularity, the degree of linear polarization on insect bodies and wings is an optical property that can be used to classify insects. Both BIOSPACE and the lidar measure this degree of polarization, illustrated across all panels in Fig. 4 for the three BIOSPACE scanned insects and the lidar observations. Finally, wingbeat frequency is a well established parameter for insect classification [37]. The lidar's high sampling rate independently facilitates the detection of insects' wingbeat frequencies, and the variation in wing beat frequency is illustrated in Figures 4b, 4f, and 4j, representing 80 Hz, 178 Hz, and 208 Hz, respectively.

Hierarchical clustering was used to analyze modulation power spectra derived from the 6.962 insect observations. This analysis incorporated both insect wing specularity, the degree of linear polarization, and wingbeat frequency. This analysis identified 129 distinct clusters which varied in cluster sizes, with the largest cluster containing 153 observations. The distribution the clusters differs among the canopy, shrub and open sky layer as visualized in a ternary plot (Fig. 5a). Here, dot position indicates relative proportional representation, with dot size corresponding to the cluster's observation count. The relative frequency of the different clusters also vary across time, as illustrated by a similar ternary plot (Fig. 5b) depicting the temporal distribution (crepuscular, diurnal, nocturnal). Six clusters with distinct wing beat frequencies were selected for to be highlighted in the paper (Fig. 5), while the remainder are available as supplementary figures (S4-S6). From each group we show average power spectra (Fig. 5c, f, i, l, o, r), time series data (Fig. 5d, g, j, m, p, s), and scatterplots depicting observation times and heights (Fig. 5e, h, k, n, q, t). Logarithmic frequency binning was used for power spectra calculations to accommodate at least 25% intraspecific variation in wingbeat frequencies. The number of lidar clusters retrieved has been demonstrated to be strongly correlated with observed insect diversity, even if correlating clusters to specific species is not possible in general. The 25% variation in wingbeat frequency that is known to arise due to variation with temperature, sex and body sizes of insects was incorporated into the clustering analysis to mitigate classification errors.

Our analysis demonstrates the potential to distinguish and group insects based on lidar signal characteristics, even when direct species identification is challenging. We find that power spectra composition varies, time series, temporal activity patterns, and vertical distribution along the canopy were observed. Moreover, classification to broader taxonomic groups can be made based on the extensive studies of group specific characteristics (REFS). The examples in Fig. 5c-k suggest a predominance of Diptera species, supported by distinct wingbeat frequencies, specular wing signals, and significant linear polarization. Certain clusters have distinct charactersitics that

allow for further taxonomic inferences. For instance, Fig. 5l-n likely represent mosquitoes based on their higher wingbeat frequencies and dusk, crepuscular, and nocturnal activity. Observations in Fig 5o-q could represent Odonata species, based on intense time series signals, specular wing signals, and them primarily being observed in the open sky. Fig. 5r-t might represent butterflies (Lepidoptera), suggested by their high polarization signals and diurnal activity.

It is important to note that clusters may contain multiple species with similar characteristics. The mosquito cluster in Fig. 5l exhibits predominantly dusk, crepuscular, and nocturnal activity, concentrated at the canopy level (see inset pie chart). Comprehensive information for all 129 clusters is provided in the supplementary material.

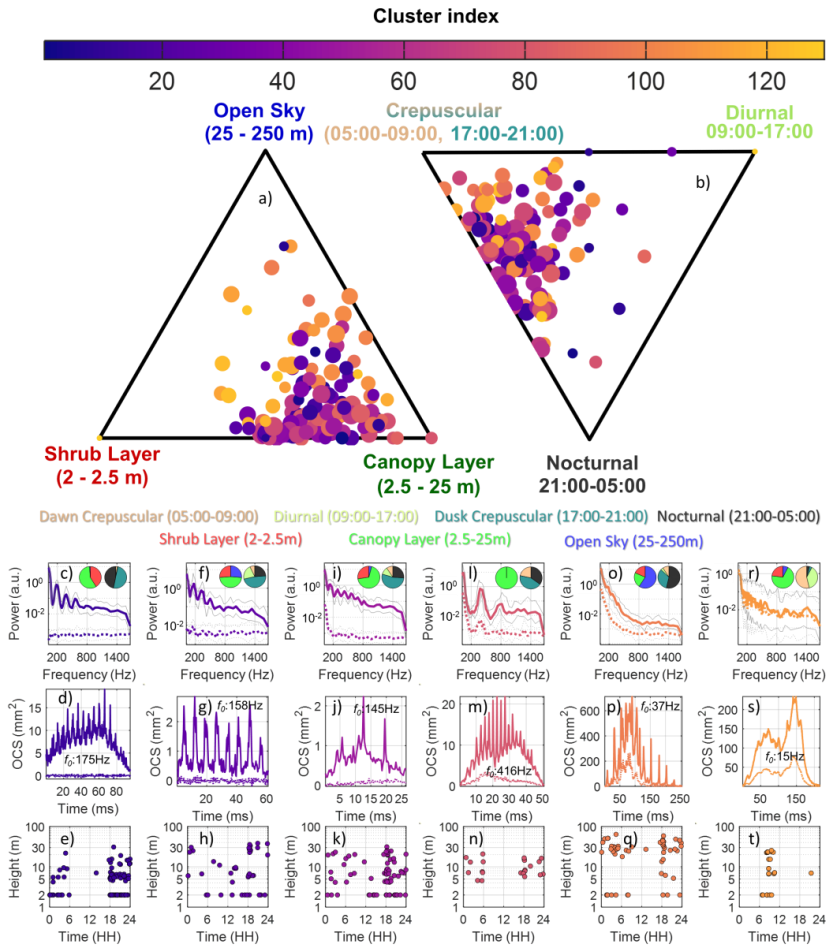

**Figure 5: The spatial and temporal distributions of 129 clusters from Lidar observations, with 6 specific cases selected for in-depth examination**. a) The ternary plot depicts the 129 clusters' ratios of distribution across the tree layers. b) Temporal distribution of cluster activity illustrating the main activity time for the cluster dawn and dusk (crepuscular), diurnal, and nocturnal. The scatter dot sizes within these plots are proportional to each cluster's observations' square root. The cluster number is indicated by the color of the dots. Six clusters were selected to be representative of different insect groups. The selected clusters' modulation spectra and polarization are detailed in panels c, f, i, l, o, and r). Accompanying pie charts reveal the frequency distribution of these clusters across various times and tree height intervals. Panels d, g, j, m, p, and s) present representative time series Lidar signals for each of the highlighted clusters, while panels e, h, k, n, q, t) map out their spatial height and temporal distribution across a three-day measurement period.

Cluster counts reflect a representation of biodiversity. Throughout the three-day study, the number of observations within the shrub, canopy, and open sky layer remained relatively consistent (Fig. 6). However, the number of clusters per layer varied more strongly, potentially suggesting that this metric is a more sensitive measurement of biodiversity than insect abundance. The canopy layer consistently had the highest number of both observations and clusters throughout the study, highlighting the importance of height specific insect trapping for estimating diversity.

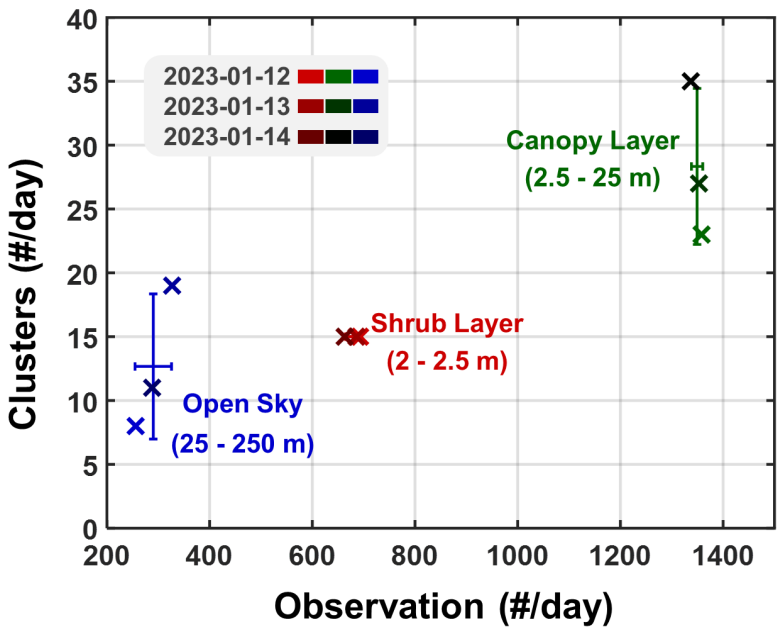


**Figure 6: Biodiversity estimates for distinct tree height intervals, color-coded by date.** Consistency is depicted across a three-day measurement period. Error bars are derived from mean and standard deviation calculations.

## Discussion

Our study explores the spatial distribution and activity patterns of insects across vegetation layers, revealing significant variation in insect activity and species composition across space and time. The lidar technique employed may facilitate future assessment of diversity of flying insects, as we have demonstrated that it is possible to retrieve data enabling comparisons, revealing significant and consistent differences across sites separated merely by a few height meters.

We show that the lidar observations outnumber the trapping methods by a factor of ~70, while simultaneously being less labor-intensive and less prone to biases. Its ability to provide high-resolution temporal and spatial data gave us a detailed insight into insect dynamics in ways otherwise unattainable. Based on the lidar data, we identified distinct activity patterns across the canopy layers. The open sky layer had its major peak during the late afternoon, while the shrub and canopy layers both also had significant morning peaks. The activity patterns are greatly influenced by microclimatic conditions, with sun exposure, humidity, and temperature differences across the canopy influencing insect activity. For example, higher temperatures coincide with a significantly reduced insect activity in the shrub layer. Rainforests, known for their intricate canopy stratification, are known to host different insect species in the different canopy layers, as these layers provide divergent niches. Our findings add to this evidence, highlighting that documenting insect diversity across different microhabitats in complex rainforest canopies is crucial to assess the full importance of a site for insect diversity.

Our manual trapping methods, malaise traps, sweep nets, and zipline traps, proved to be labor-intensive and each came with its limitations. Malaise traps, while effective, missed capturing certain species like grasshoppers and dragonflies. Sweep nets were predominantly effective for ground-level captures, and zipline traps, designed to mimic the Lidar beam path, had speed constraints that affected their overall capture rates. A significant limitation was our inability to extend insect identification to the species level due to constraints in resources, time, and manpower. The lack of electricity and appropriate conditions for preserving insects limited the possibilities to preserve captured specimens for classification to species.

An interesting approach towards closing the gap between lidar observations and individual species is provided by the approach implemented in BIOSPACE. We documented both scatter phase functions for wings of different reflectivity types and polarimetric goniometric optical information for specimens. This sheds light on the specific dynamics of three distinct types of wings, with wings having diffuse, medium specular and specular reflectance, respectively. Although we can use this to identify the broader taxonomic groups of the clusters retrieved by the Lidar time series, enabling correlation of Lidar data with insect biophotonics characterization, linking individual Lidar observation to a specific species characterized by BIOSPACE remains a goal for future research.

In conclusion, our study offers insights into insect temporal activity patterns, spatial distribution and vertical stratification in forest canopies. It demonstrates how Lidar technology can overcomes many traditional monitoring challenges, offering a comprehensive view of insect diversity patterns across space and time. The findings of consistent and significant differences in insect abundance, composition and temporal activity on small spatial scales and with factors as subtle as shade regime have profound implications for insect monitoring aimed at identifying areas key for conservation of insect diversity in face of the threat of mass extinction. In addition, non-invasive nature of lidar data collection provides an ethical approach for studying sensitive populations or protected areas.

The Scheimpflug lidar techniques hold promise for efficient monitoring in habitats beyond forests, including for plantations, farms and urban habitats, and has the potential to revolutionize insect monitoring.

## Materials and methods

*Lidar System and Scanning Procedure*

The Lidar system was deployed at a forest edge in the Taï rainforest (5°49'59.5"N 7°20'32.8"W). The transmitter and receiver telescopes were positioned on an 814 mm baseline, supported by a tripod (EQ8, SkyWatcher, China). The lidar used the Scheimpflug configuration with an angled transmitter, receiving lens, and sensor to measure high-resolution ranging up to 500 meters.

The transmitter telescope expanded two 3W TE-polarized 808 nm laser diodes. The polarization of one of the laser beams was rotated by 90˚ using a wide-angle polymer half-wave plate and was combined with the other laser beam using a polarization beam combiner. The transmitter telescope had a diameter of Ø 102 mm and a focal length of 500 mm. The receiver module was a Ø150 mm diameter and an f600 mm focal Newton reflector (TeleskopService, Germany). Its eyepiece was connected to a CMOS line sensor (OctoPlus, Teledyne e2v, USA) comprising 2048 pixels, each with dimensions of 10x200 $\mu m^2$. According to the Scheimpflug condition and the hinge rule, the CMOS sensor was tilted at a 37° angle relative to the optical axis of the Newton receiver telescope.

The system operated at a 10 kHz sampling rate, with a 100 µs line rate and 80 µs exposure time. Each data file, capturing 3 seconds of observations, contained approximately 30,000 exposure lines, with an average file size of around 120 MB. A custom LabVIEW script was employed for continuous Lidar data acquisition and file organization.

Over a two-week period, various measurements were conducted in the rainforest. The data analyzed in this paper originates from a continuous 3-day Lidar measurement. During these 3 days, a total of 6 terabytes of raw data was collected. However, after filtering for relevant observations, the dataset was reduced to 180 gigabytes, 3% of its original size.

The Lidar system was programmed to periodically adjust its elevation angles, cycling through 0, 3, 6, 10, 13, 16, and 20 degrees. At 0 degrees, the beam terminated at the board covered with neoprene positioned approximately 80 meters away. At 3, 6, and 10 degrees, it targeted different canopy layers. At 13, 16, and 20 degrees, the beam extended beyond the treetops into the sky. Due to the necessary pauses and adjustments for canopy scanning, the Lidar was operational for 12% of the total measurement duration.

*Lidar observation calibration*

Conducting experiments in the jungle presented challenges, primarily due to the lack of a direct power supply for the Lidar system. The system was powered by a generator (Champion Inverterelverk 2200W, Sweden), which required periodic refueling (~7 minutes, 4 times a day), resulting in temporary gaps in data collection when the generator was powered off for refueling. The bias in the data collection introduced by refueling breaks was however correctable. Importantly, these biases did not significantly impact the overall conclusions, as they were

effectively addressed during data analysis and interpretation. The compensation method for observation hours was demonstrated in a previous study [45].

*Signal diversity estimation*

Observational data revealed a consistent trend in insect distribution versus transition time across all three segmented tree heights on different dates (see Fig. S1 a-d). Longer transition observations were more prevalent in the canopy and shrub layers. To analyze the species diversity at different heights and days, we implemented a hierarchical clustering analysis on the power spectra derived from Lidar signals and environmental noises. The analysis was initiated with a linkage procedure to calculate cluster distances, based on the pairwise similarity of observations. To minimize potential biases, we processed instrument noise through the same data pipeline as used for the Lidar signals, functioning as a negative control. This approach facilitated the calculation of excess linkage, which involved dividing the signal linkage by the noise linkage[46], as shown in Fig. S1 e-g. Importantly, the linkage curve for the noise (illustrated with grey dash lines in the same figure panels) was significantly less intense than that for the Lidar signals (illustrated with colored solid lines) across time intervals and layers (refer to Figure S1 e-g).

Based on these findings, an analytical model was formulated to estimate the cluster count accurately. This model entailed calculating the median and interquartile range (IQR) of the excess linkage curve. Subsequently, a threshold function $Z$, derived from the median plus the IQR, was applied to all excess linkage curves for the three segments and various time intervals:

$$Z_0 = \frac{L_{\text{insects}}}{L_{\text{noise}}} \tag{1}$$

$$Z = \widetilde{Z_0} + \left(Q_3(Z_0) - Q_1(Z_0)\right) \tag{2}$$

where $L$ denotes the Lidar signal and noise, $Z_0$ denotes the excess linkage, and $(Q_3(Z_0)-Q_1(Z_0))$ symbolizes the interquartile range, which is the difference between the third quartile ($Q_3$) and the first quartile ($Q_1$) of $Z_0$. The threshold, as illustrated in Fig. S1 h-j, was determined using this methodology. This approach revealed that the canopy level exhibited the highest diversity of clusters.

*Conventional Trapping Configuration*

To manually sample the insect fauna at different locations and canopy heights, various types of traps were utilized, each selected based on their advantages and limitations. The traps were emptied and cleaned at specified times of the day.

**Malaise Traps:**
Two Malaise traps were employed different altitudes – ground level (~1 m) and canopy top (~20 m). These traps were emptied four times a day, specifically at 5 am, 10 am, 5 pm, and 10 pm. These timings were selected to maximize insect capture before and after their peak activity periods (dawn, dusk crepuscular). The Malaise trap, typically exhibiting the least bias compared to bait and light traps, aimed to capture a diverse distribution of fauna at both the ground and canopy levels. However, it was observed that larger insects such as grasshoppers and dragonflies were

often not captured. We used dry collection bottles, potentially enabling some insect groups to escape.

**Zipline Traps:**
Zipline traps were utilized and emptied four times a day: at 6:30 am, 7:30 am, 5:30 pm, and 6:30 pm. The primary objective of the zipline trap was to capture insects that followed a path similar to the Lidar beam, representing the insects observed in the Lidar signal. However, due to the system's slow movement (about 1 m/s travel speed), many in-flight insects often evaded the net. This limitation indicated the potential benefit of a motorized zipline system with a faster speed, around 10 m/s for increased catches.

**Active Sweep Netting:**
Parallel to the zip line trapping, active sweep netting was conducted four times a day, at 6:30 am, 7:30 am, 5:30 pm, and 6:30 pm. This method was executed with care, sweeping only just above the grass level to try to avoid provoking grass-dwelling insects into jumping into the net. This precaution was taken to prevent the potential overrepresentation of these species in the data. The aim was to ensure that the insects captured were in-flight during collection. The selected times ensured adequate sunlight for safe movement, given the jungle's lack of electricity, while also targeting insects before and after dusk and dawn.

*Insect Handling, Documenting and Selection*

**Insect Documenting:** Insects were euthanized and placed in individual bags labeled with the time, location, and method of capture. Insects were identified to at least the order level, and their counts and size classes were recorded. Photographs of all catches were taken using both cellphones and microscopes, with a scale marker included for reference (Fig. S8).

**Insect Selection for BIOSPACE Study:** Insects that were frequently captured and that fit the size criteria for BIOSPACE imaging, typically those with a wingspan of 0.5 to 1.5 cm, were chosen for further examination. The wings of these selected insects were spread and photographed using higher-quality cameras. Samples with minimal damage and either diffused or clear wings were specifically selected for scanning. For beetles, their elytra (wing covers) were carefully opened, and their wings were spread to enhance wing signal acquisition. Insect specimens were identified to the order level for general taxonomic categorization.

**Scanning with BIOSPACE:** The selected insects were mounted in BIOSPACE and scanned with different rotation angles. For each angle, images with different spectral (eight wavelength bands from 365 nm to 940 nm) and polarization information were captured. The same procedure was conducted with the removed wings of the insects, to measure their specularity. The measurements were conducted on-site with the portable BIOSPACE, placed in a dark box to minimize the ambient signal.

**Acknowledgments:**

We want to thank Tidiane Ouattara and Gaege Toh Arsene for their invaluable help during the field campaign.

**Funding:**

This project has received funding from The Royal Physiographic Society of Lund (Fysiografen): the Märta and Eric Holmberg Endowment, and the European Research Council (ERC) under the European Union's Horizon 2020 research and innovation program (grant agreement No. 850463) and partially funded by the Swedish International Development Agency (SIDA) through the International Science Program (ISP, Uppsala) by a grant to the African Spectral Imaging Network (AFSIN).

**Author contributions:**

Conceptualization: MB, ML, HM, LM, AR, JZ, BK, BA, NW

Methodology: MB, HM, LM, ML, AR, JZ, BK

Investigation: HM, AY, YG, LM, AR, BK, RB, IB, AH, MB, JZ, ML, NW

Visualization: HM, AY, YG, RB, AH, ML

Funding acquisition: MB, ML

Project administration: MB, AR, JB, BK, BA

Supervision: MB, JZ, ML

Writing – original draft: HM, ML, MB, AY, YG, RB, AH

Writing – review & editing: HM, AY, YG, LM, AR, BK, RB, AH, IB, MB, JZ, BA, ML, NW

**Competing interests:** Authors declare that they have no competing interests.

**Data and materials availability:** All data are available in the main text or the supplementary materials

**References**


1. Gibson, L., T.M. Lee, L.P. Koh, B.W. Brook, T.A. Gardner, J. Barlow, C.A. Peres, C.J. Bradshaw, W.F. Laurance, and T.E. Lovejoy, *Primary forests are irreplaceable for sustaining tropical biodiversity.* Nature, 2011. **478**(7369): p. 378-381.
2. Gardner, T.A., J. Barlow, R. Chazdon, R.M. Ewers, C.A. Harvey, C.A. Peres, and N.S. Sodhi, *Prospects for tropical forest biodiversity in a human-modified world.* Ecology letters, 2009. **12**(6): p. 561-582.
3. Barlow, J., G.D. Lennox, J. Ferreira, E. Berenguer, A.C. Lees, R.M. Nally, J.R. Thomson, S.F.d.B. Ferraz, J. Louzada, and V.H.F. Oliveira, *Anthropogenic disturbance in tropical forests can double biodiversity loss from deforestation.* Nature, 2016. **535**(7610): p. 144-147.
4. Forister, M.L., E.M. Pelton, and S.H. Black, *Declines in insect abundance and diversity: We know enough to act now*. Conservation Science and Practice, 2019. **1**(8): p. e80.
5. Srivathsan, A., Y. Ang, J.M. Heraty, W.S. Hwang, W.F.A. Jusoh, S.N. Kutty, J. Puniamoorthy, D. Yeo, T. Roslin, and R. Meier, *Convergence of dominance and neglect in flying insect diversity.* Nature Ecology & Evolution, 2023.
6. Miller, J.C., *Insect natural history, multi-species interactions and biodiversity in ecosystems.* Biodiversity & Conservation, 1993. **2**(3): p. 233-241.
7. Wagner, D.L., E.M. Grames, M.L. Forister, M.R. Berenbaum, and D. Stopak, *Insect decline in the Anthropocene: Death by a thousand cuts.* Proceedings of the National Academy of Sciences, 2021. **118**(2): p. e2023989118.
8. Van Klink, R., D.E. Bowler, K.B. Gongalsky, A.B. Swengel, A. Gentile, and J.M. Chase, *Meta-analysis reveals declines in terrestrial but increases in freshwater insect abundances.* Science, 2020. **368**(6489): p. 417-420.
9. Hughes, A.C., K.Z. Than, K.C. Tanalgo, A.P. Agung, T. Alexander, Y. Kane, S. Bhadra, A. Chornelia, T. Sritongchuay, and P. Simla, *Who is publishing in ecology and evolution? the underrepresentation of women and the Global South.* Frontiers in Environmental Science, 2023. **11**: p. 1211211.
10. Balmford, A., K.J. Gaston, and A. James, *Integrating costs of conservation into international priority setting.* Conservation Biology, 2000. **14**(3): p. 597-605.
11. de Souza Amorim, D., B.V. Brown, D. Boscolo, R. Ale-Rocha, D.M. Alvarez-Garcia, M.I.P. Balbi, A. de Marco Barbosa, R.S. Capellari, C.J.B. de Carvalho, and M.S. Couri, *Vertical stratification of insect abundance and species richness in an Amazonian tropical forest.* Scientific reports, 2022. **12**(1): p. 1734.
12. McCaig, T., L. Sam, A. Nakamura, and N.E. Stork, *Is insect vertical distribution in rainforests better explained by distance from the canopy top or distance from the ground?* Biodiversity and Conservation, 2020. **29**(3): p. 1081-1103.
13. Preisser, E., D.C. Smith, and M.D. Lowman, *Canopy and ground level insect distribution in a temperate forest.* Selbyana, 1998: p. 141-146.

14. Neves, F.S., C.F. Sperber, R.I. Campos, J.P. Soares, and S.P. Ribeiro, *Contrasting effects of sampling scale on insect herbivores distribution in response to canopy structure.* Revista de Biologia Tropical, 2013. **61**(1): p. 125-137.

15. Missa, O., Y. Basset, A. Alonso, S.E. Miller, G. Curletti, M. De Meyer, C. Eardley, M.W. Mansell, and T. Wagner, *Monitoring arthropods in a tropical landscape: relative effects of sampling methods and habitat types on trap catches.* Journal of Insect conservation, 2009. **13**: p. 103-118.

16. Muirhead-Thompson, R., *Trap responses of flying insects: the influence of trap design on capture efficiency.* 2012.

17. Baum, K.A. and K.E. Wallen, *Potential bias in pan trapping as a function of floral abundance.* Journal of the Kansas entomological society, 2011. **84**(2): p. 155-159.

18. Csóka, G., A. Hirka, L. Szőcs, N. Móricz, E. Rasztovits, and Z. Pödör, *Weather-dependent fl uctuations in the abundance of the oak processionary moth, Thaumetopoea processionea (Lepidoptera: Notodontidae).* European Journal of Entomology, 2018. **115**: p. 249-255.

19. Lenat, D.R. and V.H. Resh, *Taxonomy and stream ecology—the benefits of genus-and species-level identifications.* Journal of the North American Benthological Society, 2001. **20**(2): p. 287-298.

20. Chua, P.Y., S.J. Bourlat, C. Ferguson, P. Korlevic, L. Zhao, T. Ekrem, R. Meier, and M.K. Lawniczak, *Future of DNA-based insect monitoring.* Trends in Genetics, 2023.

21. Fischer, B. and B.M. Larson, *Collecting insects to conserve them: a call for ethical caution.* Insect Conservation and Diversity, 2019. **12**(3): p. 173-182.

22. Tosa, M.I., E.H. Dziedzic, C.L. Appel, J. Urbina, A. Massey, J. Ruprecht, C.E. Eriksson, J.E. Dolliver, D.B. Lesmeister, and M.G. Betts, *The rapid rise of next-generation natural history.* Frontiers in Ecology and Evolution, 2021. **9**: p. 698131.

23. Bjerge, K., H.M. Mann, and T.T. Høye, *Real-time insect tracking and monitoring with computer vision and deep learning.* Remote Sensing in Ecology and Conservation, 2022. **8**(3): p. 315-327.

24. Walter, T., J. Degen, K. Pfeiffer, A. Stöckl, S. Montenegro, and T. Degen, *A new innovative real-time tracking method for flying insects applicable under natural conditions.* BMC zoology, 2021. **6**: p. 1-11.

25. Hall, M.L., K. Gleave, A. Hughes, P. McCall, C.E. Towers, and D.P. Towers, *The application of digital holography for accurate three-dimensional localisation of mosquito-bednet interaction.* Light: Advanced Manufacturing, 2022. **3**(1): p. e20.

26. Hu, G., K.S. Lim, N. Horvitz, S.J. Clark, D.R. Reynolds, N. Sapir, and J.W. Chapman, *Mass seasonal bioflows of high-flying insect migrants.* Science, 2016. **354**(6319): p. 1584-1587.

27. Drake, V.A. and H. Wang, *Ascent and descent rates of high-flying insect migrants determined with a non-coherent vertical-beam entomological radar.* International Journal of Remote Sensing, 2018: p. 1-22.

28. Tauc, M.J., K.M. Fristrup, K.S. Repasky, and J.A. Shaw, *Field demonstration of a wing-beat modulation lidar for the 3D mapping of flying insects.* OSA Continuum, 2019. **2**(2): p. 332-348.

29. D.R.Reynolds, J.R.R., *Remote-sensing, telemetric and computer-based technologies for investigating insect movement: a survey of existing and potential techniques.* Computers and Electronics in Agriculture, 2002.

30. Brydegaard, M., B. Kouakou, S. Jansson, J. Rydell, and J. Zoueu, *High Dynamic Range in Entomological Scheimpflug Lidars.* IEEE Journal of Selected Topics in Quantum Electronics, 2021. **27**(4): p. 1-11.

31. Drake, V., J. Chapman, K. Lim, D. Reynolds, J. Riley, and A. Smith, *Ventral-aspect radar cross sections and polarization patterns of insects at X band and their relation to size and form.* International Journal of Remote Sensing, 2017. **38**(18): p. 5022-5044.

32. Riley, J. and A. Smith, *Design considerations for an harmonic radar to investigate the flight of insects at low altitude.* Computers and Electronics in Agriculture, 2002. **35**(2-3): p. 151-169.

33. Zhu, S., E. Malmqvist, W. Li, S. Jansson, Y. Li, Z. Duan, K. Svanberg, H. Feng, Z. Song, and G. Zhao, *Insect abundance over Chinese rice fields in relation to environmental parameters, studied with a polarization-sensitive CW near-IR lidar system.* Applied Physics B, 2017. **123**: p. 1-11.

34. Jansson, S., E. Malmqvist, Y. Mlacha, R. Ignell, F. Okumu, G. Killeen, C. Kirkeby, and M. Brydegaard, *Real-time dispersal of malaria vectors in rural Africa monitored with lidar.* PLOS ONE, 2021. **16**(3): p. e0247803.

35. Brydegaard, M., *Towards quantitative optical cross sections in entomological laser radar–potential of temporal and spherical parameterizations for identifying atmospheric fauna.* PLoS One, 2015. **10**(8): p. e0135231.

36. Li, Y., K. Wang, R. Quintero-Torres, R. Brick, A.V. Sokolov, and M.O. Scully, *Insect flight velocity measurement with a CW near-IR Scheimpflug lidar system.* Opt Express, 2020. **28**(15): p. 21891-21902.

37. Kouakou, B.K., S. Jansson, M. Brydegaard, and J.T. Zoueu, *Entomological Scheimpflug lidar for estimating unique insect classes in-situ field test from Ivory Coast.* OSA Continuum, 2020. **3**(9).

38. Månefjord, H., L. Müller, M. Li, J. Salvador, S. Blomqvist, A. Runemark, C. Kirkeby, R. Ignell, J. Bood, and M. Brydegaard, *3D-Printed Fluorescence Hyperspectral Lidar for Monitoring Tagged Insects.* IEEE Journal of Selected Topics in Quantum Electronics, 2022. **28**(5): p. 1-9.

39. Månefjord, H., A.A. Huzortey, R. Boateng, Y.A. Gbogbo, A.D. Yamoa, J.T. Zoueu, P.K. Kwapong, B. Anderson, and M. Brydegaard, *Hyperspectral lidar for monitoring high-resolution activity patterns of African stingless bee species.* Animal Biotelemetry, 2024. **12**(1): p. 15.

40. Müller, L., M. Li, H. Månefjord, J. Salvador, N. Reistad, J. Hernandez, C. Kirkeby, A. Runemark, and M. Brydegaard, *Remote Nanoscopy with Infrared Elastic Hyperspectral Lidar*. Advanced Science, 2023. **10**(15): p. 2207110.

41. Jansson, S., P. Atkinson, R. Ignell, and M. Brydegaard, *First Polarimetric Investigation of Malaria Mosquitoes as Lidar Targets.* IEEE Journal of Selected Topics in Quantum Electronics, 2019. **25**(1): p. 1-8.

42. Brydegaard, M., S. Jansson, E. Malmqvist, Y. Mlacha, A. Gebru, F. Okumu, G. Killeen, and C. Kirkeby, *Lidar reveals activity anomaly of malaria vectors during pan-African eclipse.* Science Advances, 2020. **6**.

43. Månefjord, H., M. Li, C. Brackmann, N. Reistad, A. Runemark, J. Rota, B. Anderson, J.T. Zoueu, A. Merdasa, and M. Brydegaard, *A biophotonic platform for quantitative analysis in the spatial, spectral, polarimetric, and goniometric domains.* Review of Scientific Instruments, 2022. **93**(11).

44. Månefjord, H., M. Li, C. Brackmann, N. Reistad, A. Merdasa, and M. Brydegaard, *BIOSPACE – A low-cost platform for problem- based learning in biophotonics.* 2021: Conference on Teaching and Learning - Proceedings, 2021. **11**.

45. Chen, H., M. Li, H. Månefjord, P. Travers, J. Salvador, L. Müller, D. Dreyer, J. Alison, T.T. Høye, and G. Hu, *Lidar as a potential tool for monitoring migratory insects.* Iscience, 2024. **27**(5).

46. Xu, Z., *Insect Diversity Estimation in Entomological Lidar*, in *Department of Biology*. 2022, Lund univeristy: LUP. p. 32.

**Supplementary Materials**

Materials and Methods

Figs. S1 to S8

Figures and Tables:

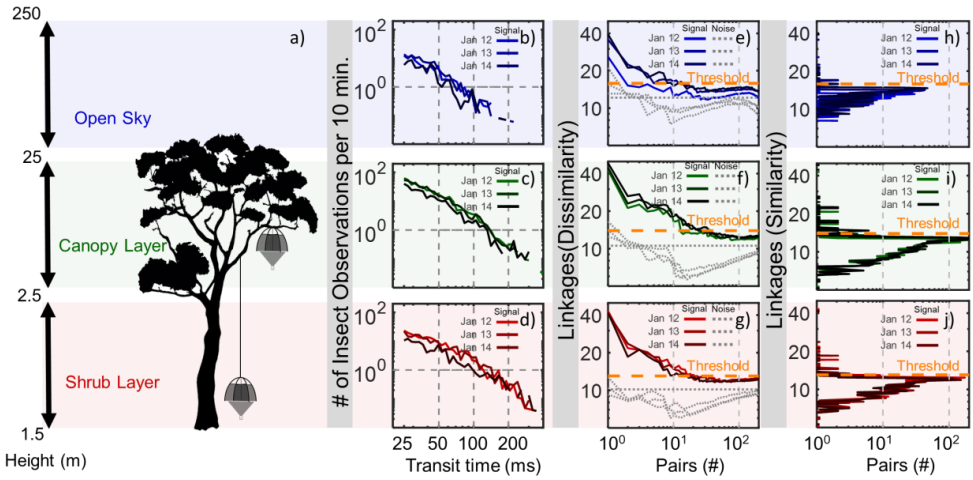


**Figure S1:** a) A schematic representation details the placement of two Malaise traps on a tree, segmenting tree heights into the shrub layer (0-2.5 m), the canopy layers (2.5 m - 25 m), and the open sky (25 m and above). Note: This depiction is not to scale. b, c, d) Histograms display transit time distributions for observations, differentiated by date and height intervals. e, f, g) Linkages, based on dissimilarity values, are plotted against the number of pairs. h, i, j) Demonstrations of linkages, emphasizing similarity, are related to the number of pairs.

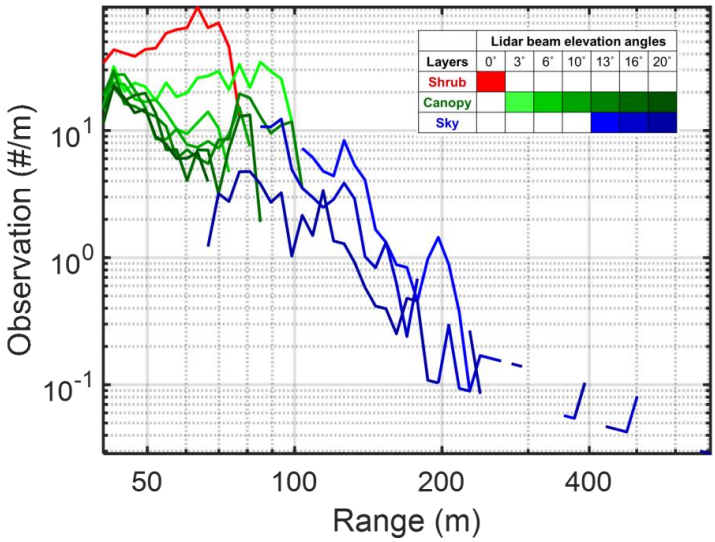


**Figure S2:** This graph illustrates the observation range in relation to the number of observations for different beam elevation angles.

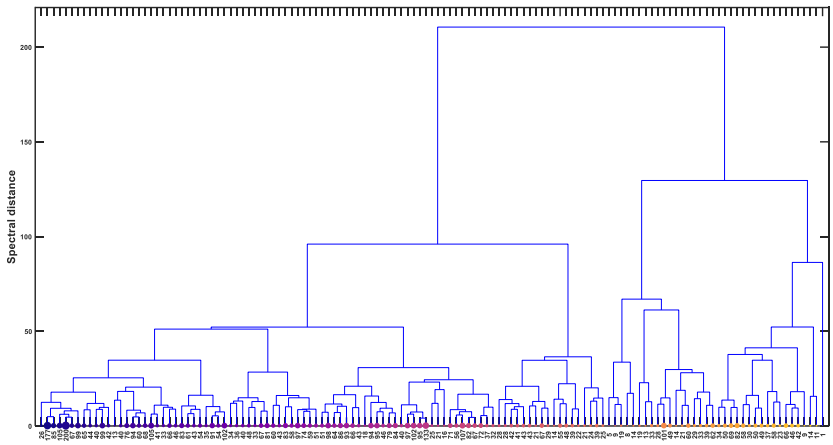


**Figure S3:** We clustered 6,962 LIDAR observations into 129 unique clustering groups, and this dendrogram illustrates the hierarchical arrangement of these clusters.


**Figure S4:** The modulation spectra of clustering groups numbered from 1 to 50 among the 129 clusters. Accompanying pie charts provide insights into the frequency distribution of these clusters across different times of the day and tree height intervals.


**Figure S5:** The modulation spectra of clustering groups numbered from 51 to 100 among the 129 clusters. Accompanying pie charts provide insights into the frequency distribution of these clusters across different times of the day and tree height intervals.

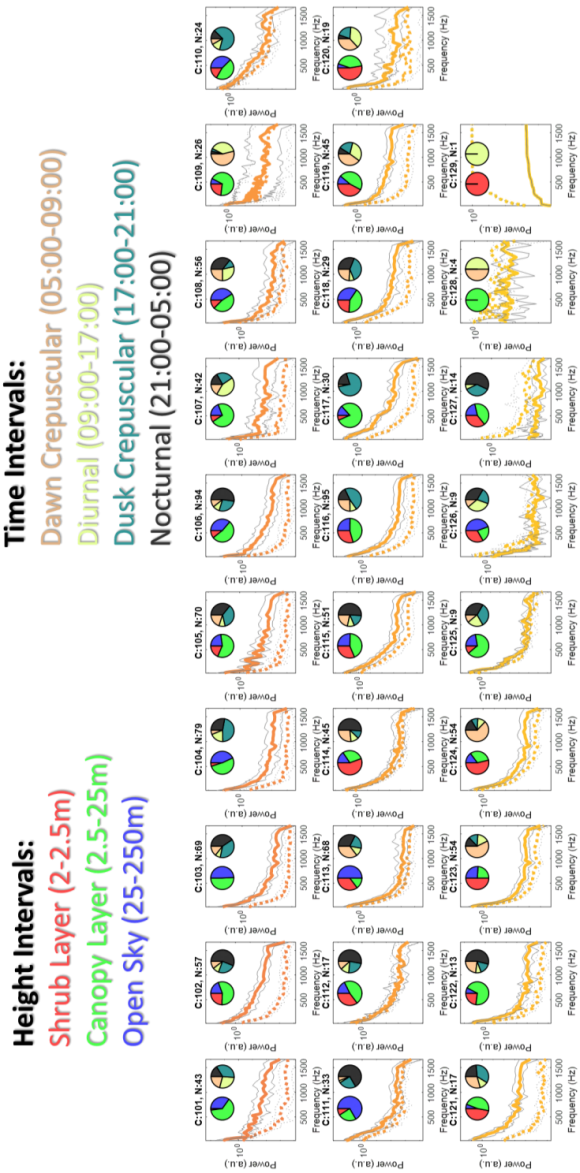


**Figure S6:** The modulation spectra of clustering groups numbered from 101 to 129 among the 129 clusters. Accompanying pie charts provide insights into the frequency distribution of these clusters across different times of the day and tree height intervals.

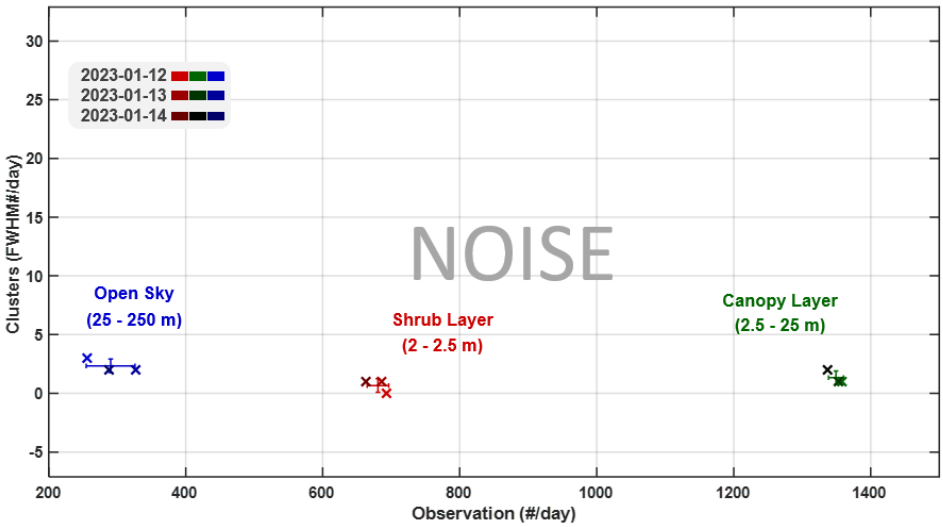


**Figure S7:** Validation of Biodiversity in Lidar Signals Against Noise - This figure demonstrates the analysis conducted to confirm that the biodiversity detected in the Lidar signals is not due to random noise. Noise levels were clustered within the shrub, canopy, and open sky layers, revealing no significant diversity or difference in clustering between these ecological layers.


**Figure S8:** A comprehensive overview of the field operations conducted in the Tai Virgin Forest to enable Lidar measurements and subsequent BIOSPACE scanning. a) Searching for a suitable experimental site, b) Setting up the Lidar system with elevation scanning feature, c) Deploying ground and canopy malaise traps, d&e) Zipline trap in action, f) Utilizing sweep netting to capture insects, g) Meticulous insect sorting, counting, identification, and documentation, h) Insect pinning and wing spreading, i) Employing grid paper as a scale reference during insect photography, j) Preparing pinned insects with wing spread for BIOSPACE scanning, k&l) Capturing higher resolution images of pinned individuals using a better camera setup, m) Repositioning insects for different orientation scanning with BIOSPACE, n) Conducting BIOSPACE scanning with the collected insects.

# Paper IV

# Insect Diversity Estimation in Polarimetric Lidar

**Dolores Bernenko[1*], Meng Li[1], Hampus Månefjord[1], Samuel Jansson[1], Anna Runemark[2], Carsten Kirkeby[3,4], Mikkel Brydegaard [1,2,4,5]**

[1] Dept. Physics, Lund University, Sölvegatan 14c, 22363 Lund, Sweden

[2] Dept. Biology, Lund University, Sölvegatan 35, 22363 Lund, Sweden

[3] Dept. of Veterinary and Animal Sciences, University of Copenhagen, Copenhagen, Denmark.

[4] FaunaPhotonics, Støberigade 14, 2450 Copenhagen, Denmark

[5] Norsk Elektro Optikk, Østensjøveien 34, 0667 Oslo, Norway

* Corresponding author:

Email: dolores.bernenko@fysik.lu.se

# Abstract

Identification of insects in flight is a particular challenge for ecologists in several settings with no other method able to count and classify insects at the pace of entomological lidar. Thus, it can play a unique role as a non-intrusive diagnostic tool to assess insect biodiversity, inform planning, and evaluate mitigation efforts aimed at tackling declines in insect abundance and diversity. While species richness of co-existing insects could reach tens of thousands, to date, photonic sensors and lidars can differentiate roughly one hundred signal types. This taxonomic specificity or number of discernible signal types is currently limited by instrumentation and algorithm sophistication. In this study we report 32,533 observations of wild flying insects along a 500-meter transect. We report the benefits of lidar polarization bands for differentiating species and compare the performance of two unsupervised clustering algorithms, namely Hierarchical Cluster Analysis and Gaussian Mixture Model. We demonstrate that polarimetric properties could be partially predicted even with unpolarized light, thus polarimetric lidar bands provide only a minor improvement in specificity. Finally, we use physical properties of the clustered observation, such as wing beat frequency, daily activity patterns, and spatial distribution, to establish a lower bound for the number of species represented by the differentiated signal types.

# Introduction

Abundance and diversity of insects is in decline (1–4) especially in regions with industrialized agriculture (5). This loss of biomass and ecological functions can imply serious consequences for food chains in ecosystems (6) and pollination services of our crops (7). Rapid changes for conservation require rapid diagnostic tools to assess insect abundance and diversity. Photonic approaches (8) such as photonic sensors (9,10) and entomological lidars (11,12) have the potential to count and classify free-flying insects *in situ* continuously with close to no running costs. To date, entomological lidar can detect more than $10^5$ insects daily (13) and differentiate more than a dozen groups (11,12). While the count rate is superior to sweepnetting (14), traps (15) and robotic analysis (16), the taxonomic specificity is inferior to classification by e.g. machine vision (17) and genetic approaches (14). The non-intrusive nature of photonic approaches excludes post examination of the identified specimens. On the other hand, photonic *in situ* observations of insects provide complementary information which could not be obtained otherwise. For example, daily activity patterns (12), preferences for topographic features (18), or information on the species abundance distributions (19).

The number of insect species that can be identified by lidar or photonic sensors may be constrained by: a) the performance of the data clustering approach, b) the number of spectral (20,21) or polarization (22–24) bands of the instrument, or, in the ideal case, c) the number of present species in the habitat. The latter can reach more than tens of thousands co-existing species (25) out of the approximately ten million estimated insect species worldwide, amounting to an overall higher number of groups constituted by sexes, phenotypic variation, and appearance changing with the age of the specimens.

Most proposed photonic clustering of insects is based on assessing the wingbeat frequencies (WBF) (9,26). Insect WBFs range from approximately 10 Hz to 1000 Hz, however, the relative spread for a single species and sex under constant environmental conditions is generally 25%, which only leaves room for 18 distinct WBFs within this range. Wingbeat harmonics can provide additional information on wing dynamics (27) and specularity of the wings (28,29), thus improving specificity. Multiple studies have exploited wingbeat harmonics to differentiate insect groups (30). Even sexes from a single species can produce distinct harmonic content depending on observation aspect (22,24,31), with females generally being larger and having slower WBFs (32). WBFs are also influenced by temperature (32–34). However, in many cases, closely related species could

produce similar signals indistinguishable for the instrument and setup. Nevertheless, species-rich insect ensembles will generally produce more diverse ensemble of signals (9).

Multiple studies have highlighted how multiple wavelengths could aid the differentiation of closely related species (22,28,35,36). In particular, specular flashes can be expected to be highly sensitive to the ratio of laser wavelength to wing membrane. Also, wing membrane thicknesses are frequently highly species-specific (28).

To what extent polarimetric information could improve specificity is less well-characterized. Generally, light loses its original polarization by multiple scattering in biological tissue (37). Consequently, near-infrared (NIR) light depolarizes when interacting with larger probe volumes in insect bodies on the scale of millimeters (22,31,38), whereas polarization is maintained when light probes thin insect wings on the order of a micron (28,39). Factors increasing the degree of linear polarization (DoLP) include absorption by melanin and water, which primarily punish photons with longer interaction path lengths that are more prone to depolarization. Factors reducing DoLP include wing scales of moth and butterflies (29) and even eggs inside the abdomen (40), which increase multiple scattering. However, it remains unknown to what extent polarimetrics could aid species differentiation.

In this paper, therefore, we investigate the benefits of polarimetric information for clustering of free-flying wild ensembles of insects. We report 32,533 insect polarimetric lidar observations, in a 500 m long transect over a lake. We use two unsupervised clustering methods to estimate signal diversity with and without polarimetric information. We attempt to assess to what extent diverse signals derive from a single species by analyzing the similarity of daily activity patterns and spatial distributions.

# Data Collection

## Field site

Field work was conducted on June 14th, 2020, at Stensoffa ecological field station, Sweden (55°41'44"N 13°26'50"E). The field site includes a forest, graze land, pond and a swamp (41), with low level of light pollution and high species richness. Within this site, we placed the experimental setup over a 500 m long, homogeneous, artificially created peat pond. A Scheimpflug lidar was positioned on one shore with the termination point on the opposing shore. Both the lidar and termination point maintained a constant height over the pond throughout the transect, with mostly the same distance to the shore on both sides of the transect.

By selecting a rectangular pond, we aimed to minimize the influence of topological differences on insects flying across the laser beam, for example, due to differences in vegetation or flight distance between shores. However, some parts of the beam were visited by insects more frequently due to the presence of patches of reeds and floating water plants.

## Instrument

The design of the Scheimpflug lidar system is described in (42). It is based on kHz time-multiplexing, comprising two TE polarized 3W, 980 nm laser diodes (MLD-980-3000, CNI lasers, China). The laser apertures are 95µm and fast-axis-collimators (FACs) are glued to diodes reducing their divergence to 8° in both axes. A NIR wavelength was chosen to avoid disturbing the insects, as they are insensitive to this light. Furthermore, backscattering is increased at this wavelength because insect melanization absorbs less NIR light.

To retrieve polarimetric lidar data, we illuminate the targets with laser beams of alternating orthogonal linear polarization. To achieve this, we rotate the polarization state of one of the laser sources by 90° using a half-wave plate (WPQ10E-980, Thorlabs, USA), then co-align the two beams using a polarizing cube beam splitter (PBS203+B4CRP/M, Thorlabs, USA). The radiation is collimated by a Ø75 mm, f = 300 mm achromatic doublet (#88-597, Edmund Optics, UK) in a focus mechanism (Monorail, Teleskop-Service, Germany). The lidar overlap is controlled by a tangential mount (Stronghold, Baader planetarium, Germany). The receiving telescope is a Ø200 mm, f = 800 mm Newton reflector (Quattro, SkyWatcher, China). The received light passes a 10nm FWHM filter at 980 nm (#65-247, Edmund Optics, UK) and a NIR linear polarizer (LPNIRE200-B, Thorlabs, USA) before

it is imaged onto a linear CMOS detector, which is tilted 45° according to the Scheimpflug condition and hinge rule. The linear array detector (OctoPlus, Teledyne e2v, USA) has 2048 pixels of 10x200 µm each. It can read out 80 kLines/s at 12 bits, but in this experiment, it was operated at 6 kHz.

Our system achieves kHz-rate separation of co-polarized and de-polarized light components by multiplexing two orthogonal laser sources (43,44). We sequentially illuminate the target with a three-timeslot cycle: timeslot 1, laser I is ON; timeslot 2, laser II is ON; timeslot 3, both lasers are OFF (used for real time subtraction of the background from the first two exposures). This effectively provides a 2 kHz sample rate with a maximum observable modulation frequency of 1 kHz due to the Nyquist criterion (45). The lowest achievable frequency and resolution depend on the insect's transit time through the laser beam.

## Lidar observations

We conducted continuous lidar recordings throughout June 14, 2020, accumulating ~2.5 terabytes of raw data. To isolate insect observations, we implemented a thresholding technique, selecting data exceeding the median intensity of backscattered light plus five times the interquartile range (IQR) within each 5-second data file (~30,000 exposures), see (13,46,47) for detailed accounts of the preprocessing. We further refined the dataset to include only observations exceeding 40 ms transit time, corresponding to a minimum detectable WBF of 25 Hz. This criterion yielded a total of 32,533 observations. A typical insect observation manifests as a modulation of backscattered light intensity over both time (exposure number) and space (pixel number), as illustrated in **Fig 1a**.

We analyzed the lidar signal in several ways. First, projecting the signal into the spatial domain provides lidar echo intensity across pixels. This information can be used in two ways: 1) by transforming absolute pixel numbers to determine the distance to a target (left y-axis in **Fig 1b**), and 2) by transforming differential pixel numbers to estimate the apparent insect size (right y-axis in **Fig 1b**).

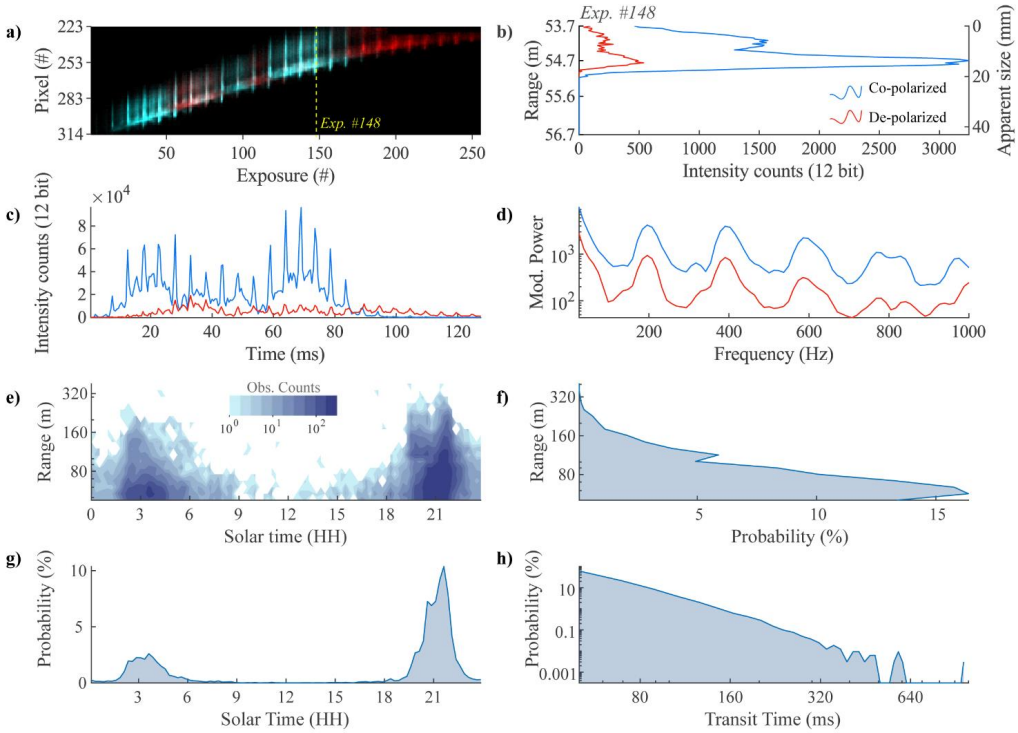


**Fig 1. Lidar insect observations**. (a) Modulation of backscattered light intensity from a single insect across exposures (time domain) and pixels (space domain). Co-polarized (cyan) and de-polarized (magenta) components shown. (b) Instantaneous echo in the range domain (@ exposure #148), with range and insect size deduced from absolute and differential pixels respectively. (c) Signal waveform showing intensity modulation over time. (d) Power spectra. (e) Distribution of observations by solar time (15-minute bins with bin centers from 00:07 and ending at 23:53) and range (20 logarithmically spaced bins between 48 m and 427 m). Time is reported in true solar time. (f) Range distribution of insect observations. (g) Time distribution of insect observations. (h) Distribution of insects' transit times >40 ms. In (b-d), co-polarized components are in red, de-polarized in blue, see legend in (b).

Second, analyzing the signal from the co-polarized and de-polarized channels in the time domain generates two waveforms (**Fig 1c**). Comparing these waveforms, we observe that co-polarized backscatter from glossy wings manifests as a series of brief, specular flashes. In contrast, the de-polarized backscatter lacks these distinct flashes and instead presents less intense, smoother waveform with the same periodicity, caused by broader scattering lobes by the de-polarizing wing features such as the veins and scales. The relative intensities of co-polarized and de-polarized light are also informative. For example, nearly equal intensity in the co-polarized and

de-polarized waveforms suggests that most of the backscattered light has a randomized polarization state (thus an equal chance to detect co-pol. and de-pol. signals), while a dominant co-polarized signal indicates a higher degree of glossiness.

We also explored the temporal and spatial distributions of the observations. **Fig 1e** visualizes a 2D histogram illustrating the count distribution, while **Figs 1f** and **1g** show the probability of observations based on range and solar time. Notably, few observations are detected close to noon, and it is more likely to detect an insect closer to the detector. Additionally, we present a transit time histogram (**Fig 1h**) displaying the distribution of transit times for all observations exceeding the 40 ms threshold.

By combining spatial, temporal, and polarimetric information, we can characterize each insect observation and identify broader patterns within groups. For example, in the waveforms, periodic bright reflections correspond to the insect's WBF, while the duration of these flashes can indicate wing specularity. By comparing the intensity of co-polarized and de-polarized backscatter, we can quantify the DoLP. This combined analysis allows us to differentiate insects with similar WBF but distinct polarization signatures. Additionally, we can determine the detection range and time of day for each observation, or analyze these distributions for a group, revealing time activity patterns and spatial preferences for groups of insects.

## Estimation of oscillatory power spectra

Despite waveforms being highly informative, directly comparing them for insect clustering is challenging. Variations in waveform shape can arise from external factors, such as the insect's time spent within the lidar beam, and the independent phases of wingbeat and lidar sampling. To address this, we calculate the oscillatory power spectra for each observation (**Fig 1d**), which represent the signal in frequency domain as a distribution of power across normalized frequency bins. The resulting power spectra reveal the insect's fundamental WBF and its harmonic overtones, providing a more robust basis for clustering and comparison.

To estimate the power spectral density, we use Welch’s method, implemented in MATLAB Signal Processing Toolbox. We define the observable frequency range spanning between 25 Hz (reciprocal of minimal transit time) and 1000 Hz (the Nyquist frequency), and the number of linearly spaced frequency bins as 80 (the number of time samples in 40 ms-long observation at 2000 Hz sampling frequency). We also define a Gaussian time window with a FWHM of half the number of time samples. We set the number of overlapping samples in the

sliding Welch power estimate to 79, the maximum possible overlap constituting the heaviest computations operation.

# Power spectra preprocessing

While power spectra capture an insect's wingbeats in a fundamental peak and wing glossiness as the number of harmonic overtones, we hypothesize that incorporating polarimetric data may reveal additional distinctions based on wings' DoLP. To test this hypothesis, we generated three datasets representing different data acquisition scenarios: with and without polarimetric data.

**Non-polarimetric data acquisition (unpolarized dataset)**

This dataset simulates a scenario when a signal is acquired without polarimetry. We achieve this by summing up both co- and de-polarized power spectra and then normalizing the area under the merged curve to unity (**Eq. 1**).

$$P_{unpol}(f) = \frac{P_{co}(f) + P_{de}(f)}{\sum[P_{co}(f) + P_{de}(f)]} \quad (1)$$

Here, $P_{unpol}(f)$ is the unpolarized power spectrum, $P_{co}(f)$ and $P_{de}(f)$ are the co-polarized and de-polarized power spectra, respectively.

We show the resulting power spectrum in **Figs 2a** (specular case) and **2d** (diffuse case). By color-coding the proportion of the de-polarized signal, we illustrate the similarity between the unpolarized (total) signal and the de-polarized signal. We observe that in a specular case, de-polarized light improves the certainty of the peak at ~250 Hz, however, and has little influence on other frequency peaks. Whereas, in diffuse case, de-polarized light is the main contribution to powers.

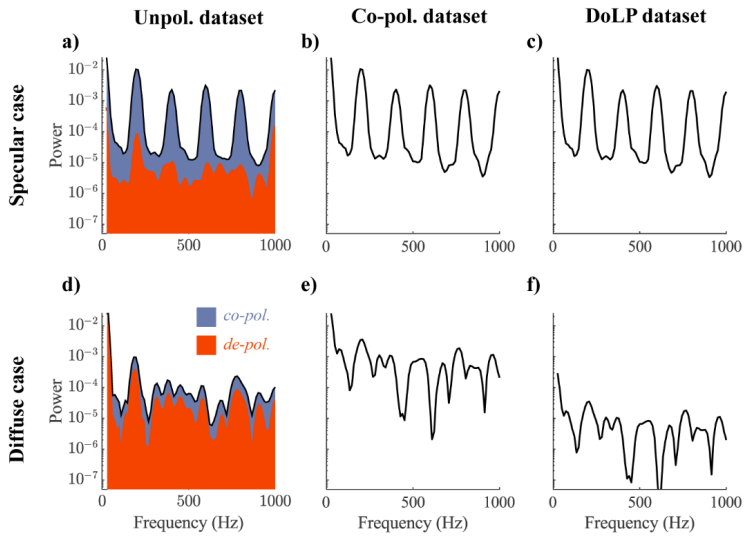


**Fig 2. Three datasets with varying polarimetric information for a specular (top row) and a diffuse observation (bottom row)** (a, d) Unpolarized data is shown as black solid line, whereas blue shade shows contribution from the co-polarized channel, and orange – from de-polarized; (b, e) Co-polarized dataset. (c, f) DoLP dataset.

**Coherently backscattered light acquisition (co-pol. dataset)**

To obtain the co-polarized dataset, we take only the co-polarized component and normalize it to unity (**Eq. 2**). This represents an acquisition scenario, when targets are illuminated using linearly polarized light, and measurements made in the same polarization state (**Figs 2b, 2e**).

$$P_{co}^{*}(f) = \frac{P_{co}(f)}{\sum P_{co}(f)} \tag{2}$$

**Polarimetric data acquisition with Degree of Linear polarization (DoLP dataset)**

The DoLP dataset (**Figs 2c, 2f**) is a scaled version of the co-polarized dataset. In this dataset, the area under the co-polarized power spectrum represents the DoLP information for the oscillatory part of the signal, excluding the 0-25 Hz range (**Eq. 3**).

$$P_{DoLP}(f) = \frac{P_{co}(f)}{\sum[P_{co}(f) + P_{de}(f)]} \tag{3}$$

Importantly, when normalizing the areas under all power spectra, we ensured that the relative strength of frequency components within each spectrum remains consistent regardless of the distance at which the insect was observed. This approach addresses a potential source of bias in our analysis—namely, the signal intensity attenuation with distance.

# Results and discussion

## Cluster count and agreement analysis: HCA vs. GMM

Unsupervised clustering is a valuable tool for rapidly assessing insect diversity from lidar observations. Unlike classification, which requires labeled data that is often scarce and costly to obtain, clustering groups insect observations based on inherent similarities in their characteristics. This study focuses on characteristics embedded into power spectra of observations, specifically the frequency content (WBF and harmonic overtones) and the DoLP (when using the DoLP dataset).

However, these features may not sufficiently distinguish among insect species, as WBF can be common across multiple species and exhibit significant variability even within the same species. This feature overlap can cause multiple species to merge into clusters or a single species to split into multiple clusters, affecting our conclusions on insect diversity estimates. Additionally, diversity estimates could be biased due to different clustering algorithms producing different solutions, that vary in the number and size of identified clusters.

In this section, we explore the differences between clustering solutions by employing two contrasting methods. One is Hierarchical Clustering Analysis (HCA), a deterministic approach previously employed to group observations from photonic sensors and lidar (9,11,12,19) (see **Methods: HCA**), and Gaussian Mixture Model (GMM), a stochastic approach (see **Methods: GMM**). Comparing HCA and GMM clustering results, we observed that these methods clustered lidar observations with varying granularity. HCA yielded 803 (unpolarized), 245 (co-polarized), and 256 (DoLP) clusters, while GMM produced fewer: 80 (unpolarized), 86 (co-polarized), and 89 (DoLP).

To determine if these methods produce consistent results despite the varying granularity, with HCA offering a more fine-grained view, we assessed the agreement between their clusterings using two metrics: Adjusted Mutual Information (AMI) and Homogeneity score. AMI ranges from 0 to 1, with higher values indicating that

the same observations are grouped into the same clusters across both methods, after adjusting for chance. The Homogeneity score, also ranging from 0 to 1, evaluates whether each cluster from one method contains observations primary from a single cluster in the other method. A high Homogeneity score indicates that one method's clusters are subsets of the other's. We explain both metrics in detail in Section **Methods: Evaluating clustering agreement**.

We observed moderate agreement between the methods, with AMI scores ranging from 0.47 to 0.55 (**S1a Fig**). However, the Homogeneity score was higher, ranging from 0.66 to 0.74 (**S1b Fig, the upper triangle**). This result suggests that there is a difference in the underlying composition of clusters, and that the methods did not merely identify the same clusters at different resolutions. Despite these differences in the number and composition of clusters, most clusters in both solutions exhibited discernible frequency content (see median power spectra for clusters in **S2-S3 Figs**). In the absence of ground truth for optimal partitioning, we then evaluated clustering results based on DoLP homogeneity, distinction in activity time patterns, and spatial distribution.

## Degree of linear polarization for clusters

In this section, we investigate whether wings' polarimetric characteristics (from glossy to diffuse) can be predicted using unpolarized data alone, and how this prediction is improved by including polarimetric data. To quantify the differences between datasets, we measure the clusters' DoLP homogeneity as detailed in **Methods: Bootstrapping to evaluate confidence intervals.** We report the clusters' homogeneity as the mean DoLP and its 95% confidence interval (CI) ($2.5^{th}$ and $97.5^{th}$ percentiles). To determine the significance of the observed results, we compared the CIs of a mean DoLP for found clusters against those derived from randomly assembled clusters of the same size. We also divided clusters into four groups based on DoLP quartiles (from $Q_1$, most glossy, to $Q_4$, most diffuse).

We find that most of clusters from the glossy group ($Q_1$) and some from the diffuse group ($Q_4$) are significantly different from random ones (CIs of found and random clusters do not overlap), see **Fig 3** (DoLP dataset) and **S4-S5 Figs** (unpol. and co-pol. datasets). The clusters' DoLP uncertainty is largest for the HCA applied to the unpolarized dataset (**S4a Fig**), however, this dataset returns smaller clusters. The major difference between the three datasets is that including polarimetric information improves isolation of low-DoLP observations into distinct clusters. Notably, HCA shows greater sensitivity in finding clusters with lower DoLP compared to GMM.

Intriguingly, both methods identified clusters with anomalously low DoLP (~1-2%), suggesting a less than random polarization state for the backscattered light. Potential explanations include scattering from extremely small, fluffy insects where polarized light escapes on the backside before having the chance to scatter 180°. It could also be measurement outliers due to imperfect beam overlap.

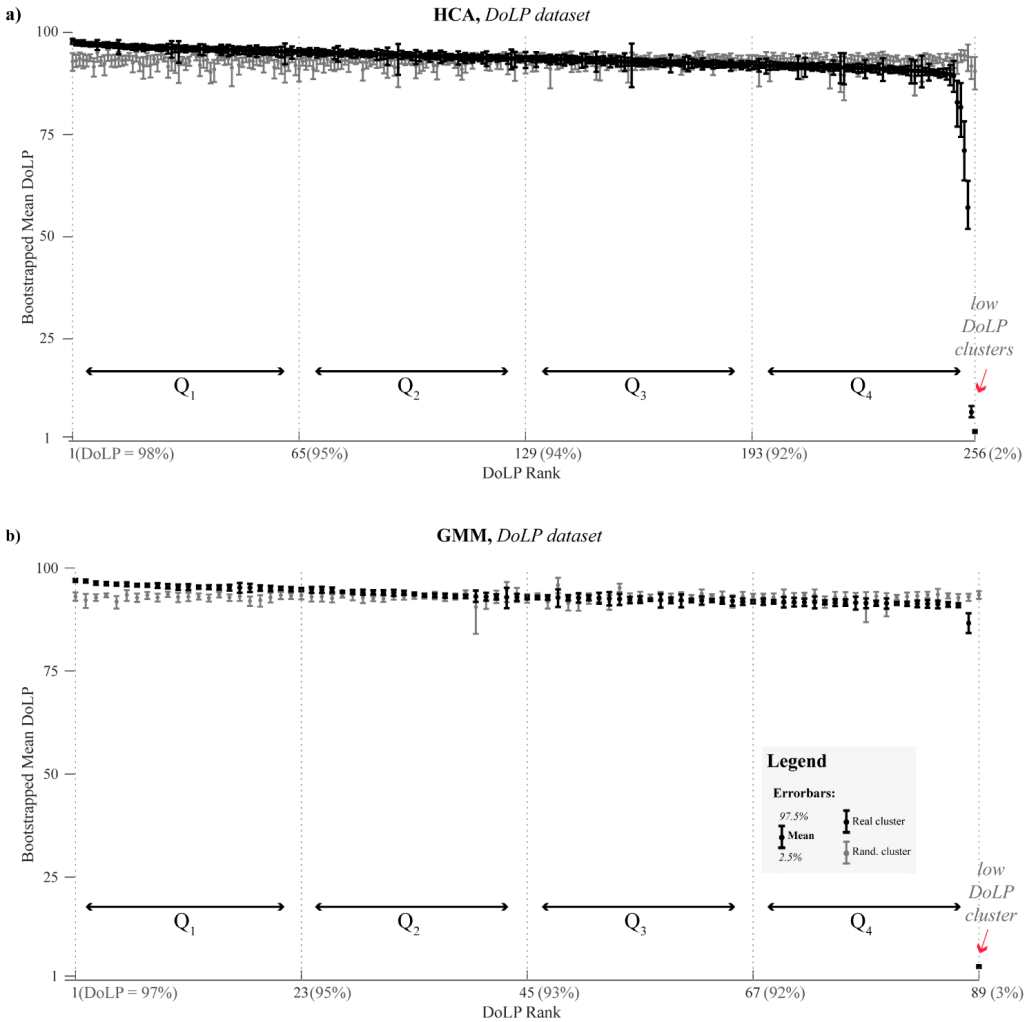


**Fig 3. DoLP characterization of clustering results.** (a) HCA and (b) GMM show comparisons of cluster DoLP distributions for found clusters (black error bars) and randomly generated clusters of the same size (gray error bars). Error bars represent the bootstrapped mean DoLP and its 95% CI for each cluster. Found clusters are ranked by decreasing mean DoLP (x-axis). Vertical lines denote DoLP quartile boundaries ($Q_1$-$Q_4$).

To further examine the impact of polarimetric information on clustering results, we visualized the rearrangement of observations across different DoLP quartiles **(Fig 4**). We aggregated observations based on the DoLP of their assigned cluster and represented these rearrangements using flow lines. Our analysis shows that the $Q_1$ quartile produces the most consistent results, with 26% of $Q_1$ observations being shared across the three datasets in HCA and 37% in GMM. Significant rearrangements between unpol. and DoLP datasets predominantly occur between adjacent quartiles, though 9% (HCA) or 12% (GMM) observations are reassigned across non-adjacent quartiles (e.g., from $Q_1$ to $Q_4$). We conclude that even without polarimetric information, clustering algorithms can identify highly glossy wings. However, polarimetric data is particularly beneficial for co-clustering together low-DoLP observations.

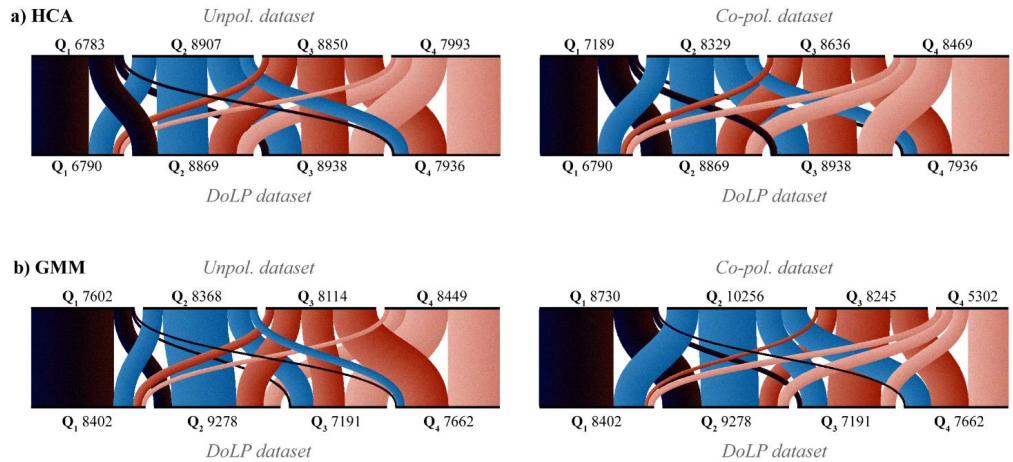


**Fig 4. Rearrangement of observations between cluster's DoLP quartiles**. (a) HCA clusters. (b) GMM clusters. Left panels show rearrangements between the unpolarized and the DoLP datasets, and right panels illustrate differences between co-polarized and DoLP datasets. Each quartile ($Q_1$—$Q_4$) is labeled with the number of observations. The flows (lines) between quartiles indicate the fraction of observations, with line width proportional to the number of observations. To plot the alluvial diagrams we use RAWGraphs (48).

To evaluate if HCA and GMM agree on the content of the top five glossy clusters, we next compare their median power spectra (DoLP dataset, **S6-S7 Figs**). Despite both returning similar power spectra for rank 1 and 2 clusters, GMM aggregates more observations per cluster (e.g., rank 1: 123 observations in GMM vs. 23 in HCA). This indicates that GMM generalizes power spectral patterns more broadly, leading to larger clusters, while

HCA maintains a stricter similarity criterion. The conclusion is thus the same when based on similarity of top two glossy clusters as when based on the homogeneity score.

## Time and range communities

Distinct species are likely to exploit distinct niches in time and space. This could be a matter of crepuscular species adapted to a certain ambient light level or bumble bees adapted to forage earlier in the colder mornings. In terms of range, preferences for topographic features such as vegetation or reeds along the transect could differ. It could also be biased by the resolution of the instrument since larger, brighter, or glossier species could be detected over further ranges.

To further assess the biological relevance of clustering, we investigated whether distinct daily activity patterns and range profiles could define communities – groups of clusters that are more similar within a group than between (see Section **Methods: Time and range communities**). Comparing two clustering approaches, we find that GMM method most clearly recovers community structure, whereas HCA performs worse. We quantify it using a modularity metric (M). It ranges from 0 (random structure), to 1 (well-defined structure), or to -1 (less optimal than random). In HCA, modularity increased with the addition of polarimetric information (unpol. < co-pol. < DoLP). This trend was evident in both time communities ($M_{unpol.}$ = 0.07, $M_{co\text{-}pol.}$ = 0.15, $M_{DoLP}$ = 0.16) and range communities ($M_{unpol.}$ = 0.08, $M_{co\text{-}pol.}$ = 0.13, $M_{DoLP}$ = 0.14). In contrast, clusters identified by GMM show relatively strong community structure across all datasets, with modularity remaining consistent for both time ($M_{unpol.}$ = 0.26, $M_{co\text{-}pol.}$ = 0.27, $M_{DoLP}$ = 0.25) and range communities ($M_{unpol.}$ = 0.12, $M_{co\text{-}pol.}$ = 0.09, $M_{DoLP}$ = 0.11). The presence of community structure indicates that the time and range profiles of the clusters diverge from the average pattern, suggesting ecologically distinct groups. However, the moderate modularity scores imply these patterns are not discrete but rather overlapping, with some clusters exhibiting similarity to multiple communities. This is visualized in **Fig 5**, a heatmap of cluster-to-cluster similarity, where communities appear as bright squares along the diagonal, but some clusters show high similarity across communities.

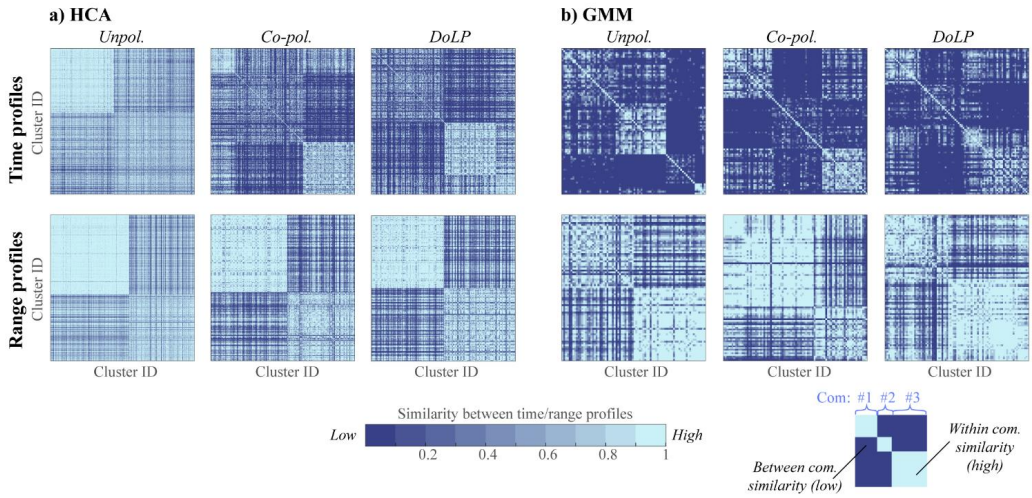


**Fig 5. Community structure analysis for HCA and GMM clustering results based on time and range profiles.** Each symmetric matrix displays similarity of time (top panels) and range (bottom panels) profiles across cluster pairs, with darker pixels indicating greater dissimilarity. The heatmaps are organized to place rows/columns adjacently if clusters are from the same community, thus making communities to appear as bright squares along the matrix diagonal manifesting greater similarity within a community then between them (see the bottom-right schematic).

Next, we characterized both time and range communities by plotting communities' probability distributions across time and range bins (**Figs 6** and **S8**). To illustrate clusters' variability, we employed bootstrapping (see **Methods: Bootstrapping to evaluate confidence intervals**). We observe that time communities primary differentiate based on variation in evening activity patterns (**Fig 6 I-III**), whereas range communities are characterized by a decaying probability of an observation with a different detectability cut-off: with some clusters detected at mid-ranges, <160 m (**Fig 6A)** and others primarily at long ranges, <255 m (**Fig 6B**).

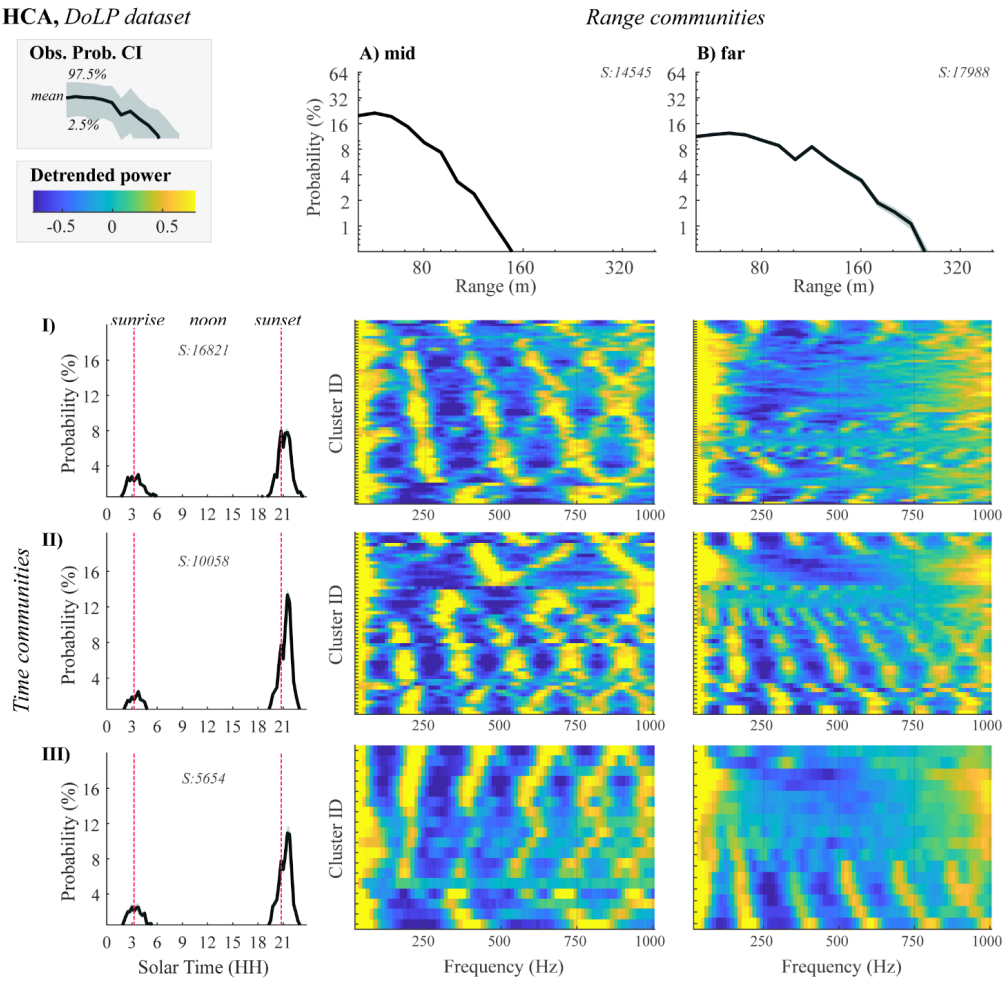


**Fig 6. Characterization of time and range communities.** CIs of observation probability for (A, B) range and (I-II-III) time communities (see legend). At the top of each panel, we show the size of a community. Heatmaps at the AB and I-III intersection display median power spectra for a corresponding time-range community. The y-axis segments heatmaps into stripes, one for each cluster. Variation of colors within a stipe indicates power magnitude at corresponding frequencies (x-axis). The powers are shown after normalization, logarithmic transformation, and detrending. The color-bar encompasses 5$^{th}$ to 95$^{th}$ percentiles of all range of power values.

We hypothesize, the variation in spatiotemporal profiles may be related to the frequency content of the lidar signal. To visualize this, we plot clusters' median power spectra after detrending (see **Methods: Detrending of power spectra**) showing them as heatmaps at the intersection of (A, B) and (I-II-III) probability plots (**Fig 6B**).

Here, we observe that insects detected at long ranges (group B) tend to have a first peak in their frequency spectrum below 250 Hz. This peak could correspond to the fundamental frequency of a wingbeat, suggesting that larger insects, which have lower WBFs, are more likely to be detected at greater distances (for example, predating dragonflies with up to 14 cm wingspan).

## Range dependence of co-polarized backscatter

To further explore the factors influencing long-range detectability, we investigated the impact of wing glossiness. We hypothesize that insects with glossy and clear wings scatter laser light coherently, with a narrow lobe and rapid angular speeds, resulting in improved transmission over distances. To test this hypothesis, we subdivided insects from the range communities (A: mid; B: far) into four quartiles based on their DoLP ($Q_1$-$Q_4$, representing decreasing glossiness, see **Fig 3**). Creating these subsets of clusters allows us to compare range profiles of, for example, highly glossy insects detectable at far ranges ($Q_1$-B subset of clusters) with diffusive insects detectable at the mid-range ($Q_4$-A). Next, for each subset, we calculated the mean probability of detection at each range bin, along with the 2.5$^{th}$ and 97.5$^{th}$ percentiles (CIs), as described in section **Methods: Bootstrapping to evaluate confidence intervals**.

Comparing range profiles for different DoLP groups, we observe a striking feature in the far-range community: a peak at ~120m in an otherwise decaying with distance probability of observation (**Fig 7** and **S9 Fig**). This peak is most prominent for glossy insects ($Q_2$). Visualizing the laser beam path over the pond (**Fig 7**, bottom), we note that this peak coincides with the proximity of a landmass, marked with a red dot. This suggests differences in insect communities based on proximity to land. Acknowledging the noise introduced by assuming that observations from all DoLP groups ($Q_1$-$Q_4$) have an equal probability of being present at this landmass, we hypothesize that the lack of a peak at 120 m in the low-DoLP distributions (particularly $Q_4$) implies that glossiness significantly affects detectability at this distance.

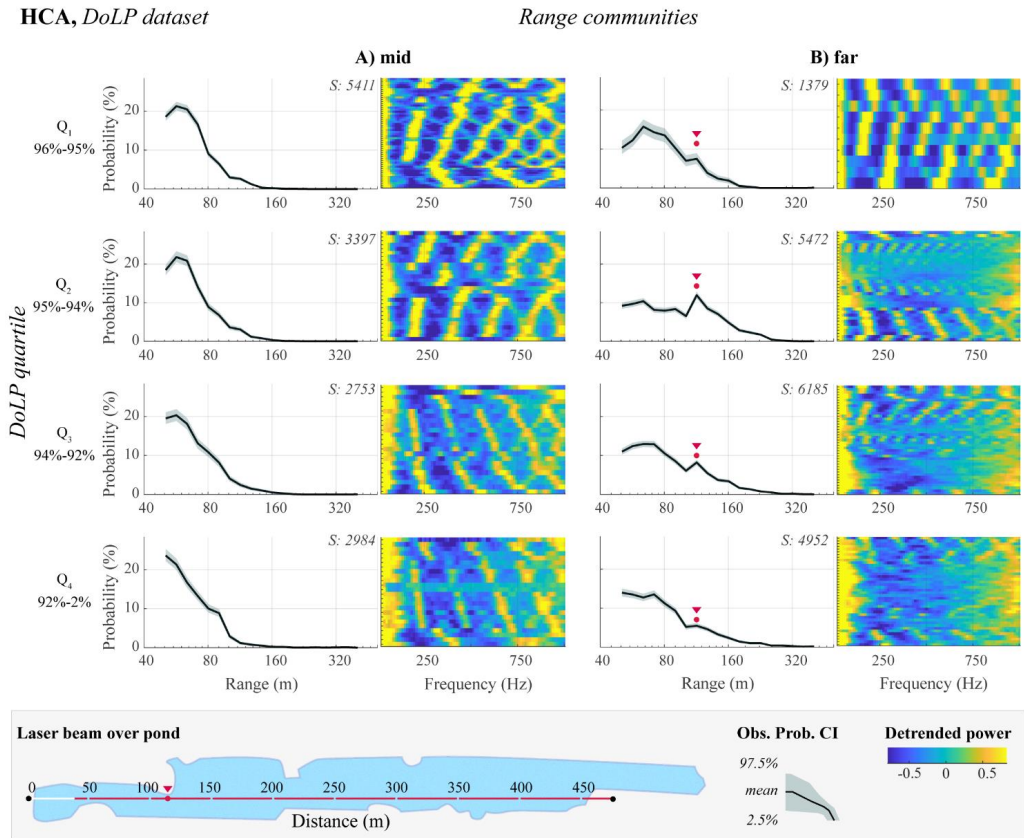


**Fig 7. Range dependence of co-polarized backscatter**. CIs of probability distributions show the likelihood of observing an insect within a DoLP quartile ($Q_1$-$Q_4$: glossy to diffuse) and range community (A: mid-range, B: far-range). In the top-right corner of probability distributions, we show the number of observations. In B-plots, we show with the red dot the spike in the probability of observing an insect, potentially linked to a nearby landmass (see bottom panel). Heatmaps depict median power spectra for clusters within corresponding DoLP-range subsets (as in **Fig 6**).

These findings indicate that the clusters reflect spatial preferences of insects and thus could be seen as a meaningful coarse-grained representation of lidar observations. This representation can be further employed to describe insects' activity patterns and spatial preferences, for example, due to changes in vegetation over seasons, or to provide a means for evaluating the attraction range of conventional insect traps.

Our findings also highlight some limitations of the current lidar setup in assessing biodiversity. Specifically, there are biases in determining the abundance and richness of insects. For example, some morphological

features make certain insects easier to detect, leading to overestimation of their presence. These features could be size, brightness, and glossiness, and depend on how wing thickness resonates with the lidar wavelength. This observation suggests a direction for improving lidar technology by using longer wavelengths to enhance specularity and detection range. Longer (infrared) wavelength have proven efficient in clustering moths (29,49).

## Lidar based diversity indices

We hypothesized that integrating polarimetric information into lidar signals would enhance discrimination between insect taxa, leading to a rearrangement of observations into clusters based on both the frequency content of power spectra and the similarity of polarimetric properties of insect wings and bodies towards low frequencies. However, clusters' count and composition depend not only on the instrument but also on the choice of clustering algorithm, influencing conclusions about the diversity at the monitored site. To evaluate the impact of clustering approaches on diversity estimates, we compared the results of HCA and GMM clustering, focusing on the number and relative size of the identified clusters.

To illustrate cluster count and their relative size, we plotted the Ranked Abundance Distribution (RAD), depicting cluster sizes in descending order (**Fig 8**). We further characterized clustering results using Hill numbers, a family of diversity metrics (see **Methods: Lidar based diversity indices**). Specifically, $H_0$ represents the total cluster count, providing an overall estimate of diversity; $H_1$ represents the effective number of clusters, accounting for relative abundance; and $H_2$ represents the dominant number of clusters, highlighting the most prevalent clusters.

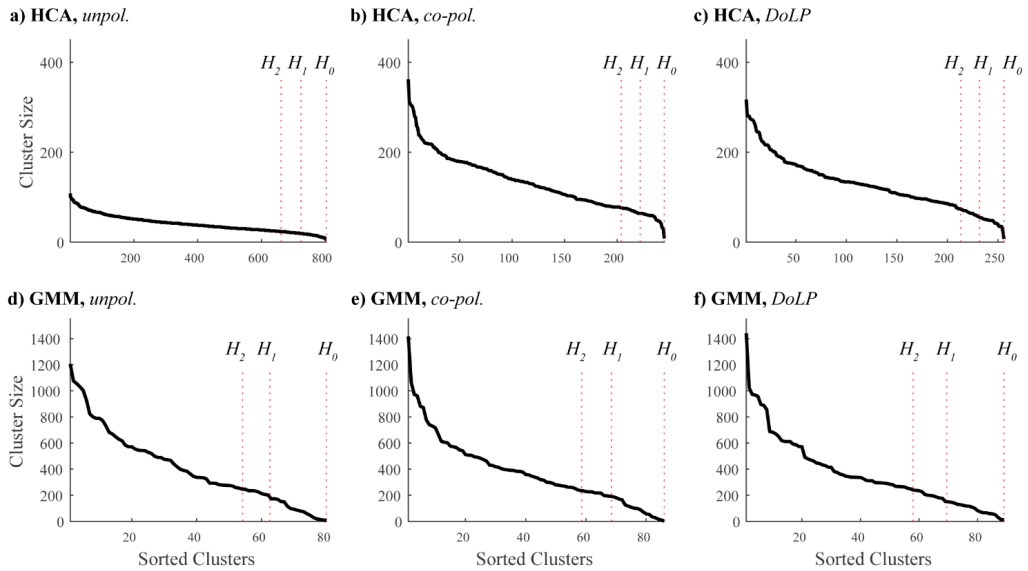


**Fig 8. Clusters' size distribution.** (a—c) HCA clustering on three datasets; (d—f) GMM clustering on three datasets. The solid line shows the number of observations per cluster for clusters sorted from largest to smallest. Vertical lines mark Hill numbers.

Our analysis revealed a consistent trend of HCA producing a higher number of clusters compared to GMM (~250 vs. ~85), particularly evident in the unpolarized dataset (~800 vs. ~80) as illustrated in **Fig 8** and **Table 1**. This suggests that HCA clusters are generally more diverse than GMM clusters. However, the high homogeneity score (~0.7, **S1b Fig**) between the two clustering solutions indicates that larger GMM clusters are often fragmented into smaller HCA clusters. Thus, the higher diversity estimates obtained through HCA likely reflect a finer resolution level at which the data is partitioned.

**Table 1. Characterization of clustering results with Hill numbers.** NoC is a number of clusters.

| | **Dataset** | $H_0$ (NoC) | $H'$ (Shannon Index) | $H_1$ (Effective NoC) | $H_2$ (Dominant NoC) |
|---|---|---|---|---|---|
| **HCA** | unpol. | 803 | 6.58 | 724 | 662 |
| | co-pol. | 245 | 5.40 | 222 | 204 |
| | DoLP | 256 | 5.45 | 232 | 213 |

| | | | | | |
|---|---|---|---|---|---|
| **GMM** | unpol. | 80 | 4.14 | 63 | 54 |
| | co-pol. | 86 | 4.23 | 68 | 59 |
| | DoLP | 89 | 4.24 | 69 | 58 |

To address the potential disproportionate influence of rare clusters on cluster richness ($H_0$), we further evaluated the cluster size distribution using the effective number of clusters ($H_1$). HCA consistently yielded a larger effective number of clusters than GMM relative to the total number of clusters, suggesting a more balanced distribution of cluster sizes. Moreover, HCA identified a substantially larger proportion of dominant clusters ($H_2$) compared to GMM (~90% vs. ~65%) (**Fig 8**), indicating that our diversity estimates were not significantly inflated by rare clusters.

Hill numbers reveal that each method can lead to distinct conclusions, particularly regarding the proportion of dominant clusters within the total cluster count. These discrepancies are largely due to HCA and GMM exhibiting different levels of tolerance for variation within clusters. HCA favors similarly sized, spherical clusters because of the Ward linkage criterion, which defines a "good" cluster as one where all observations are relatively close to the cluster centroid. In contrast, GMM identifies clusters based on the probability of an observation belonging to a specific Gaussian distribution, allowing for the identification of elliptical clusters. Consequently, these differences impact the number and size distribution of clusters, and subsequently, the estimated diversity indices. Therefore, when interpreting insect diversity estimates derived from lidar data, it's crucial to carefully consider the inherent biases and assumptions of different clustering algorithms.

To move beyond the limitations of single clustering solutions and ensure more robust lidar-based diversity assessments, future research would benefit from evaluating the robustness of these indices through a more comprehensive approach. One promising avenue involves using stochastic algorithms to analyze an ensemble of clustering solutions, rather than relying on a single outcome (50,51). This would allow us to report a range of values for each Hill number, gaining valuable insights into the sensitivity of these metrics in detecting changes within the monitored site (see additional analysis for GMM results in **S1 Text**). Additionally, focusing on observations that consistently co-cluster together across multiple solutions could provide a more reliable basis for diversity estimates, as these observations represent a stronger signal compared to those that are grouped inconsistently and may introduce unpredictable variability.

# Conclusions

Estimating insect diversity has traditionally been labor-intensive, relying on manual capture and classification (52). However, researchers have sought to automate this process (53) using technologies like radar (54) and lidar. In this study, we use polarimetric lidar to detect free-flying insects and investigate whether polarimetry improves diversity estimates. We hypothesized that diversity estimates would vary depending on the amount of polarimetric information included in lidar observations.

We initially focused on the total cluster count produced by each clustering method. We observed a distinct difference in resolution, with GMM yielding ~85 clusters and HCA ~250. However, when interpreting this value as an estimate of insect diversity, it's important to recognize that neither algorithm intrinsically determines the optimal number of clusters. In HCA, increasing the significance threshold for compensated linkage would lower the cluster count, while in GMM, minimizing the AIC instead of the BIC would increase it, yielding ~300 clusters per dataset. Therefore, this value should be seen as a lidar-based diversity index rather than a direct measure of insect diversity.

Regardless of clustering resolution, we aimed to determine which lidar signal (unpolarized, co-polarized, or DoLP) results in greater diversity estimates when comparing results within the same clustering approach. This analysis yielded conflicting results. GMM yielded fewer clusters for the unpolarized dataset than for DoLP (80 vs. 89), while HCA produced a significantly higher number (803 vs. 256).

To investigate whether HCA's higher cluster count in the unpolarized dataset truly indicates greater insect diversity, we analyzed the time/range community structure. Our hypothesis was that higher species specificity would correspond to a richer time/range community structure. However, our findings revealed that the HCA-derived community structure was weaker, particularly in the time dimension (**Fig 5**). This suggests that HCA's additional clusters may not correspond to distinct insect species but rather to over-sensitivity to variations in power spectra.

This over-sensitivity likely arises from the inherent differences in how HCA and GMM generalize power spectra patterns. HCA, being sensitive to variations in the relative powers of frequency peaks (55), may focus on differences between the powers of the fundamental frequency and its overtones. These differences can be due

to varying observation aspects and could be accentuated for the fundamental peaks and a few harmonic overtones after averaging co-polarized and de-polarized signals.

In contrast, the GMM approach was applied not to the power spectra directly but to their UMAP-reduced representations. This transformed the 81-dimensional power spectra into a three-dimensional representation that aims to preserve the global structure and relationships between observations rather than focusing on specific frequencies and powers. Consequently, this makes GMM clustering less prone to overfitting and reduces sensitivity to individual spectral components.

Despite observing different granularity at which datasets are partitioned, we argue that the total cluster count remains a valid proxy for diversity, provided that the same approach is consistently used in comparative studies and reliably scales the number of clusters with actual insect diversity. This has been demonstrated in previous research using photonic sensors coupled with HCA clustering (9). Therefore, to evaluate the performance of polarimetric lidar, we shift our focus from analyzing cluster count to analyzing clusters' polarimetric properties.

Our comparative analysis of clusters retrieved from unpolarized and DoLP datasets reveals that the unpolarized approach struggles to co-cluster observations with low DoLP values. However, its clusters exhibit significant DoLP differentiation from random ones within the glossiest ($Q_1$) and most diffuse ($Q_4$) DoLP quartiles (compare **Figs 3** and **S4**). Moreover, incorporating polarimetric information only minimally rearranges observations (~10%) across non-adjacent DoLP quartiles (**Fig 4**). This suggests that unpolarized backscatter retains sufficient information on wing glossiness to effectively co-cluster the majority of DoLP-similar observations.

Furthermore, our comparison of results from co-polarized and DoLP datasets indicates that they yield similar diversity estimates. Also, both HCA and GMM produce DoLP-homogeneous clusters (**Fig 3** and **S4-5 Figs**), with the strongest agreement observed within the top glossy clusters ($Q_1$ group) (**Fig 4**). This suggests that most information on wing glossiness is derived from the harmonic content of co-polarized power spectra, while DoLP quantification remains valuable for identifying rare low-DoLP cases.

Our findings underscore the interplay between instrument sensitivity to insect morphology and the chosen clustering methodology. We find that while polarimetric lidar provides additional information, much of the relevant information is also present in unpolarized data, suggesting a need to balance instrument complexity with research goals. Furthermore, our findings highlight the importance of understanding the biases inherent to different clustering algorithms, as these can significantly influence diversity estimates.

# Methods

## HCA

We conducted Hierarchical Cluster Analysis (HCA) on area-normalized, log-transformed power spectra using MATLAB's **linkage** function, with **'ward'** specified as the method and **'euclidean'** as the metric. This method employs Euclidean distance to cluster power spectra based on similarity, accommodating minor variations in Wing Beat Frequencies (WBFs), a phenomenon frequently observed within the same species (9). Furthermore, this metric is sensitive to changes in the Degree of Linear Polarization (DoLP), including variations in the number of harmonic overtones and how power spectra scale with DoLP. We selected Ward's linkage criterion (56) to minimize the variance within newly formed clusters, thereby ensuring that observations within each cluster closely resemble the cluster's centroid.

To determine the optimal number of clusters, we analyze the changes in linkage rates, identifying significant deviations from the expected values due to random variations in power spectra. **Fig 9** illustrates our method. Panel **a** presents the linkage values in reverse order (from largest to smallest). By displaying these values on a logarithmic scale, we linearize the decrease in linkage values. From this plot, we calculate the linkage rates (slopes) at each step of the HCA and determine the median slope ($\gamma = -0.357$), which is depicted in **Fig 9a** as a solid line. This slope represents the expected decrease in linkage under conditions of random spectral variation.

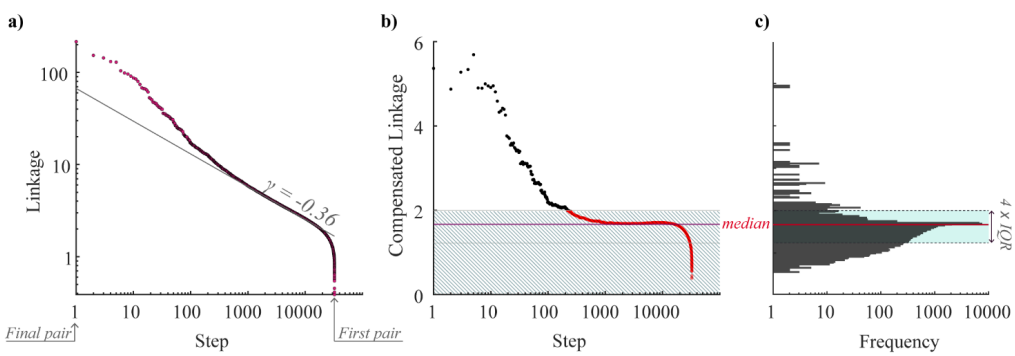


**Fig 9. Identifying optimal cluster numbers in hierarchical cluster analysis.** (a) Reverse-ordered linkage values on a logarithmic scale. The median slope (γ, solid line) represents the expected linkage decrease. (b) Compensated linkage

values. Shaded area highlights the expected linkage. (c) Distribution of compensated linkage values with median (red line) and outlier boundaries ($Q_1 - 1.5 \cdot IQR$, $Q_3 + 1.5 \cdot IQR$, blue shaded area).

Next, to identify significant linkages, we calculate compensated linkage values using the formula $\boldsymbol{L_i^* = (i/N)^\gamma \cdot L_i}$, where $\boldsymbol{L_i^*}$ represents the compensated linkage, $\boldsymbol{L_i}$ is the reversed linkage (from largest to smallest), $\gamma$ is the median slope, and $\boldsymbol{i}$ ranges from 1 to the total number of steps, $\boldsymbol{N}$. This transformation effectively modifies the linkage plot from **Fig 9a** to **Fig 9b**. Subsequently, we analyze the distribution of these compensated linkage values (**Fig 9c**) and identify significant linkages (outliers) using the 1.5xIQR rule (57). Specifically, we select those linkage values that exceed $Q_3 + 1.5 \cdot IQR$. The optimal number of clusters is then determined by the count of these outliers, as illustrated above the shaded area in **Fig 9b**.

# GMM

Prior to clustering lidar observations using GMM, we reduced the dimensionality of area-normalized, log-transformed power spectra using Uniform Manifold Approximation and Projection (UMAP) (58), MATLAB implementation (59). UMAP parameters were **n_components = 3, dmin = 0.01, n_neighbours = 199**, and **metric= 'euclidean'**. The **dmin** parameter is chosen to achieve tighter grouping of similar observations, while **n_neighbours** balanced algorithm between focusing on local and global structure of the data. We chose the maximal **n_neighbours** value allowed by the UMAP library. Reducing the data from 81 features (frequencies) to three (UMAP-coordinates) increased data point density, aiding a density-based GMM algorithm to identify clusters.

Next, we fit a Gaussian mixture distribution (60) to the UMAP-embedded data using MATLAB's **fitgmdist** function (Statistics and Machine Learning Toolbox). To determine the optimal number of clusters, we scanned the **n_components** parameter (range: 55 – 555) and selected the solution minimizing the Bayesian Information Criterion (BIC). BIC is calculated as $BIC = ln(n)k - 2ln(L)$, where $n$ is the number of observations, $k$ is the number of estimated parameters, and $L$ is the maximum value of the likelihood function for the model. Other **fitgmdist** parameters were: **RegularizationValue = 1e-6, CovarianceType = 'full', SharedCovariance = 'false', Replicates = 1**, and **Options= statset (MaxIter = 100, TolFun = 1e-3)**.

Another approach to finding the optimal number of clusters would be to use Akaike Information Criterion (AIC) calculated as $AIC = 2k - 2ln(L)$. Both AIC and BIC criteria favor models that fit data well (large $L$) and have

fewer parameters (small $k$), however BIC tends to impose a stronger penalty on the number of parameters, resulting in favoring simpler models than AIC.

## Evaluating clustering agreement

Next, we evaluate how well clustering algorithms agree about the optimal partitioning of the data. To compare solutions, we leverage two metrics from the scikit-learn library in Python (61): Adjusted Mutual Information Score (AMI) and Homogeneity Score. AMI (62) is a variation of Mutual Information (MI) that accounts for a chance for two solutions to agree, especially when we compare clusterings of different sizes or with different numbers of clusters. AMI scores range from 0 to 1, with 1 indicating perfect agreement and score of 0 indicating agreement no better than random chance.

We also employ a Homogeneity score (63), a metric that reflects the internal consistency of solutions, for example, if larger clusters in one solution are split into many in another. A homogeneity score of 0 indicates that clusters of one solution have random observations compared to another solution. A score of 1 indicates perfect homogeneity, with each cluster in one solution containing observations of the same cluster in another.

## Time and range communities

We analyze the time and range profiles associated with clusters by extracting the time and range stamps of assigned observations. For each cluster, we calculate the probability of observing a member at specific time and range bins (as in **Figs 1f** and **1g**). To compare clusters' time and range distributions, we employ the two-sample Kolmogorov-Smirnov (K-S) test (64), implemented in MATLAB, Statistics and Machine Learning Toolbox. The K-S test assesses whether two empirical distributions originated from the same parent distribution, providing a distance metric and p-value. Using K-S p-values measured between cluster pairs, we construct two similarity matrices: one for time and another for range.

We construct similarity matrices to understand how clusters naturally group into communities. These communities are characterized by greater internal similarity compared to their similarity with clusters outside the group. To identify these communities, we first calculate a modularity matrix (65) using **modularity_f(A, gamma)**, implemented in an external MATLAB library (66), where:

1. **A:** The similarity matrix (K-S p-values) that contains K-S p-values between all cluster pairs.
2. **gamma (γ):** The resolution parameter controlling the granularity of the community structure. Lower values ($\gamma < 1$) tend to produce fewer communities, while higher values ($\gamma > 1$) result in more communities. In our analysis, we use the default value of $\gamma = 1$.

GenLouvain algorithm (66), with deterministic output and default parameters, is then applied to the modularity matrix. This yields a community assignment for each cluster, effectively partitioning the clusters into time and range communities.

Additionally, based on this cluster-to-community mapping, we calculate a modularity score ($M$), which quantifies the strength of the identified community structure. Modularity values range from 0 (indicating a random structure) to 1 (signifying a well-defined structure), or even -1 (suggesting a structure less optimal than random).

# Lidar based diversity indices

To quantify and compare clustering results across experiments, we employed Hill numbers (67), a family of diversity metrics that allows us to emphasize different aspects of diversity by adjusting a single parameter, $\alpha$ (68). Hill numbers are expressed by the following equation (**Eq. 4**):

$$H_\alpha = \left[\sum_{j=1}^{S} p_j^\alpha\right]^{\frac{1}{1-\alpha}} \quad (4)$$

, where $S$ is a set of all clusters, $p_j$ is a relative size of cluster $j$ (cluster $j \in S$) calculated as the number of observations in cluster $j$ divided by the total observations, and $\alpha$ is an integer value ranging from $\pm\infty$.

Varying $\alpha$, we land at three diversity indices:

**Total number of clusters.** The $H_0$ metric ($\alpha = 0$) reflects the total number of clusters (species) $S$, giving a high importance to rare clusters (**eq. 5**):

$$H_0 = \sum_{i=1}^{S} p_i^0 = S \quad (5)$$

**Effective number of clusters.** The $H_1$ ($\alpha = 1$), also known as Shannon diversity of order 1, weighs both rare and abundant clusters (69), providing an estimate of how many equally-sized clusters would yield the same Shannon Entropy (**Eq. 6, 7**). This is analogous to the number of effective choices in a prediction model.

$$H_1 = exp(H') \quad (6)$$

$$H' = -\sum_{i=1}^{S} p_i ln(p_i) \quad (7)$$

**The number of dominant clusters.** The $H_2$ metric ($\alpha = 2$) emphasizes dominant clusters, indicating a more even spread of diversity across clusters (**Eq. 8**).

$$H_2 = 1/\sum_{i=1}^{S} p_i^2 \quad (8)$$

## Detrending of power spectra

For visualization purposes, we detrended the power spectra by fitting a line (trend) to area-normalized and log-transformed power spectra and then subtracting it. The resulting positive and negative values indicate power above and below the trend. This approach, applied for heatmap visualization with a diverging colormap, allows us to highlight even subtle oscillations. However, it is important to note that we do not use the detrended power spectra in any analysis.

## Bootstrapping to evaluate confidence intervals

To assess the variability of our metrics, we employed a bootstrapping technique (70), a resampling-based method well-suited for scenarios with limited day-to-day data. This approach involves generating N = 1000 synthetic datasets by randomly sampling observations with replacement from the original dataset. Each original observation has an equal probability of being included in a synthetic dataset, and some may be included multiple times. The original dataset can be observations from the same cluster, community, or any other relevant subset.

For each synthetic sample, we calculate the metric of interest, resulting in N = 1000 variants depending on the drawn observations. From this distribution, we empirically estimate the mean of the metric and its 95% confidence intervals (CIs) using the $2.5^{th}$ and $97.5^{th}$ percentiles. This provides a range within which we are 95% confident that the true value of the metric lies, accounting for sampling variability.

In our study, we applied bootstrapping to estimate confidence intervals (CIs) for several key metrics:

1. **Clusters' mean DoLP:** To assess the DoLP for both found and random clusters, we generated N = 1000 synthetic samples for each cluster by randomly drawing observations with replacement from the evaluated cluster. For each synthetic sample, we calculated the mean DoLP. By retrieving N values of mean DoLP, we then evaluated this distribution to obtain the mean and CIs for the cluster's DoLP.
2. **Time and Range Profiles:** For each time/range community or range-DoLP subset, we generated N = 1000 synthetic samples by randomly drawing observations with replacement. For each synthetic sample, we determined the probability of an observation in time (or range). To quantify the variability of these probabilities, we analyzed the N values obtained at each time (or range) bin, reporting the mean probability and its 95% CIs.

# Acknowledgments

The lidar instrumentation were in part, kindly provided by Norsk Elektro Optikk A/S, Norway. We thank Ebba von Wachenfeldt, Zachary Nolen, Magne Friberg, Jadranka Rota and in particular, Jens Rydell for assistance in field work, may he rest in peace. We thank Rachel Muheim for receiving us at the Stensoffa ecological field station. We thank Zhicheng Xu and Jacobo Salvador for discussion and initial data analysis.

# References


1. van Klink R, Bowler D, Gongalsky K, Shen M, Swengel S, Chase J. Disproportionate declines of formerly abundant species underlie insect loss. Nature. 2023 Dec 20;628:1–6.

2. Hallmann CA, Sorg M, Jongejans E, Siepel H, Hofland N, Schwan H, et al. More than 75 percent decline over 27 years in total flying insect biomass in protected areas. PLOS ONE. 2017 Oct 18;12(10):e0185809.

3. Goulson D. The insect apocalypse, and why it matters. Curr Biol. 2019 Oct 7;29(19):R967–71.

4. Møller AP. Parallel declines in abundance of insects and insectivorous birds in Denmark over 22 years. Ecol Evol. 2019;9(11):6581–7.

5. van Klink R, Bowler DE, Gongalsky KB, Swengel AB, Gentile A, Chase JM. Meta-analysis reveals declines in terrestrial but increases in freshwater insect abundances. Science. 2020 Apr 24;368(6489):417–20.

6. Moreno-Mateos D, Power ME, Comín FA, Yockteng R. Structural and Functional Loss in Restored Wetland Ecosystems. PLOS Biol. 2012 Jan 24;10(1):e1001247.

7. Potts SG, Biesmeijer JC, Kremen C, Neumann P, Schweiger O, Kunin WE. Global pollinator declines: trends, impacts and drivers. Trends Ecol Evol. 2010 Jun 1;25(6):345–53.

8. Brydegaard M, Svanberg S. Photonic Monitoring of Atmospheric and Aquatic Fauna. Laser Photonics Rev. 2018;12(12):1800135.

9. Rydhmer K, Jansson S, Still L, Beck BD, Chatzaki V, Olsen K, et al. Photonic sensors reflect variation in insect abundance and diversity across habitats. Ecol Indic. 2024;158(111483).

10. Saha T, Genoud AP, Williams GM, Thomas BP. Monitoring the abundance of flying insects and atmospheric conditions during a 9-month campaign using an entomological optical sensor. Sci Rep. 2023 Sep 20;13(1):15606.

11. Kouakou BK, Jansson S, Brydegaard M, Zoueu JT. Entomological Scheimpflug lidar for estimating unique insect classes in-situ field test from Ivory Coast. OSA Contin. 2020;3(9):2362–71.

12. Brydegaard M, Jansson S, Malmqvist E, Mlacha YP, Gebru A, Okumu F, et al. Lidar reveals activity anomaly of malaria vectors during pan-African eclipse. Sci Adv. 2020 May 13;6(20):eaay5487.

13. Jansson S, Malmqvist E, Mlacha Y, Ignell R, Okumu F, Killeen G, et al. Real-time dispersal of malaria vectors in rural Africa monitored with lidar. PLOS ONE. 2021 Mar 4;16(3):e0247803.

14. Svenningsen CS, Frøslev TG, Bladt J, Pedersen LB, Larsen JC, Ejrnæs R, et al. Detecting flying insects using car nets and DNA metabarcoding. Biol Lett [Internet]. 2021 Mar [cited 2024 May 8];17(3). Available from: http://www.scopus.com/inward/record.url?scp=85103683350&partnerID=8YFLogxK

15. Diserud OH, Stur E, Aagaard K. How reliable are Malaise traps for biomonitoring? – A bivariate species abundance model evaluation using alpine Chironomidae (Diptera). Insect Conserv Divers. 2013;6(5):561–71.

16. Wührl L, Pylatiuk C, Giersch M, Lapp F, von Rintelen T, Balke M, et al. DiversityScanner: Robotic handling of small invertebrates with machine learning methods. Mol Ecol Resour. 2022;22(4):1626–38.

17. Bjerge K, Geissmann Q, Alison J, Mann HMR, Høye TT, Dyrmann M, et al. Hierarchical classification of insects with multitask learning and anomaly detection. Ecol Inform. 2023 Nov 1;77:102278.

18. Jansson S, Malmqvist E, Brydegaard M, Åkesson S, Rydell J. A Scheimpflug lidar used to observe insect swarming at a wind turbine. Ecol Indic. 2020 Oct 1;117:106578.

19. Assoumou S. Doria Yamoa, Benoit K. Kouakou, Adolphe Y. Gbogbo, Anna Runemark, Roel van Klink, Jeremie T. Zoueu, et al. Comparative lidar assessment of insect diversity at four Ivorian habitats. Unpublished. 2024 May;

20. Santos V, Costa-Vera C, Rivera-Parra P, Burneo S, Molina J, Encalada D, et al. Dual-Band Infrared Scheimpflug Lidar Reveals Insect Activity in a Tropical Cloud Forest. Appl Spectrosc. 2023 Jun 1;77(6):593–602.

21. Müller L, Li M, Månefjord H, Salvador J, Reistad N, Hernandez J, et al. Remote Nanoscopy with Infrared Elastic Hyperspectral Lidar. Adv Sci. 2023;10(15):2207110.

22. Gebru A, Jansson S, Ignell R, Kirkeby C, Prangsma JC, Brydegaard M. Multiband modulation spectroscopy for the determination of sex and species of mosquitoes in flight. J Biophotonics. 2018;11(8):e201800014.

23. Genoud AP, Basistyy R, Williams GM, Thomas BP. Optical remote sensing for monitoring flying mosquitoes, gender identification and discussion on species identification. Appl Phys B. 2018 Feb 17;124(3):46.

24. Li Y, Han Z, Nessler R, Yi Z, Hemmer P, Brick R, et al. Optical multiband polarimetric modulation sensing for gender and species identification of flying native solitary pollinators. iScience. 2023 Nov 17;26(11):108265.

25. Basset Y, Cizek L, Cuénoud P, Didham RK, Guilhaumon F, Missa O, et al. Arthropod Diversity in a Tropical Forest. Science. 2012 Dec 14;338(6113):1481–4.

26. Potamitis I, Rigakis I. Measuring the fundamental frequency and the harmonic properties of the wingbeat of a large number of mosquitoes in flight using 2D optoacoustic sensors. Appl Acoust. 2016 Aug 1;109:54–60.

27. Bomphrey RJ, Nakata T, Phillips N, Walker SM. Smart wing rotation and trailing-edge vortices enable high frequency mosquito flight. Nature. 2017 Apr;544(7648):92–5.

28. Li M, Runemark A, Hernandez J, Rota J, Bygebjerg R, Brydegaard M. Discrimination of Hover Fly Species and Sexes by Wing Interference Signals. Adv Sci. 2023;10(34):2304657.

29. Li M, Seinsche C, Jansson S, Hernandez J, Rota J, Warrant E, et al. Potential for identification of wild night-flying moths by remote infrared microscopy. J R Soc Interface. 2022 Jun 22;19(191):20220256.

30. Moore A, Miller RH. Automated Identification of Optically Sensed Aphid (Homoptera: Aphidae) Wingbeat Waveforms. Ann Entomol Soc Am. 2002 Jan 1;95(1):1–8.

31. Li M, Jansson S, Runemark A, Peterson J, Kirkeby CT, Jönsson AM, et al. Bark beetles as lidar targets and prospects of photonic surveillance. J Biophotonics. 2021;14(4):e202000420.

32. Wang M, Wang J, Liang P, Wu K. Nutritional Status, Sex, and Ambient Temperature Modulate the Wingbeat Frequency of the Diamondback Moth Plutella xylostella. Insects. 2024 Feb;15(2):138.

33. Unwin DM, Corbet SA. Wingbeat frequency, temperature and body size in bees and flies. Physiol Entomol. 1984;9(1):115–21.

34. Saha T, Genoud AP, Park JH, Thomas BP. Temperature Dependency of Insect's Wingbeat Frequencies: An Empirical Approach to Temperature Correction. Insects. 2024 May;15(5):342.

35. Shevtsova E, Hansson C. Species recognition through wing interference patterns (WIPs) in Achrysocharoides Girault (Hymenoptera, Eulophidae) including two new species. ZooKeys. 2011 Dec 12;154:9–30.

36. Shevtsova E, Hansson C, Janzen DH, Kjærandsen J. Stable structural color patterns displayed on transparent insect wings. Proc Natl Acad Sci. 2011 Jan 11;108(2):668–73.

37. Jacques SL, Ramella-Roman JC, Lee K. Imaging skin pathology with polarized light. J Biomed Opt. 2002 Jul;7(3):329–40.

38. Jansson S, Atkinson P, Ignell R, Brydegaard M. First Polarimetric Investigation of Malaria Mosquitoes as Lidar Targets. IEEE J Sel Top Quantum Electron. 2019 Jan;25(1):1–8.

39. Li M, Runemark A, Guilcher N, Hernandez J, Rota J, Brydegaard M. Feasibility of Insect Identification Based on Spectral Fringes Produced by Clear Wings. IEEE J Sel Top Quantum Electron. 2023 Jul;29(4: Biophotonics):1–8.

40. Genoud AP, Gao Y, Williams GM, Thomas BP. Identification of gravid mosquitoes from changes in spectral and polarimetric backscatter cross sections. J Biophotonics. 2019 Oct;12(10):e201900123.

41. Tuva [Internet]. [cited 2024 May 30]. Available from: https://etjanst.sjv.se/tuvaut/

42. Zhu S, Malmqvist E, Li W, Jansson S, Li Y, Duan Z, et al. Insect abundance over Chinese rice fields in relation to environmental parameters, studied with a polarization-sensitive CW near-IR lidar system. Appl Phys B. 2017 Jul 10;123(7):211.

43. Zhao G, Malmqvist E, Török S, Bengtsson PE, Svanberg S, Bood J, et al. Particle profiling and classification by a dual-band continuous-wave lidar system. Appl Opt. 2018 Dec 10;57(35):10164–71.

44. Mei L, Guan P. Development of an atmospheric polarization Scheimpflug lidar system based on a time-division multiplexing scheme. Opt Lett. 2017 Sep 15;42(18):3562.

45. Nyquist H. Certain Topics in Telegraph Transmission Theory. Trans Am Inst Electr Eng. 1928 Apr;47(2):617–44.

46. Chen H, Li M, Månefjord H, Travers P, Salvador J, Müller L, et al. Lidar as a potential tool for monitoring migratory insects. iScience [Internet]. 2024 May 17 [cited 2024 Apr 27];27(5). Available from: https://www.cell.com/iscience/abstract/S2589-0042(24)00810-1

47. Brydegaard M, Kouakou B, Jansson S, Rydell J, Zoueu J. High Dynamic Range in Entomological Scheimpflug Lidars. IEEE J Sel Top Quantum Electron. 2021 Jul;27(4):1–11.

48. Mauri M, Elli T, Caviglia G, Uboldi G, Azzi M. RAWGraphs: A Visualisation Platform to Create Open Outputs. In: Proceedings of the 12th Biannual Conference on Italian SIGCHI Chapter [Internet]. New York, NY, USA: Association for Computing Machinery; 2017 [cited 2022 Jun 1]. p. 1–5. (CHItaly '17). Available from: https://doi.org/10.1145/3125571.3125585

49. Basistyy R, Genoud A, Thomas B. Backscattering properties of topographic targets in the visible, shortwave infrared, and mid-infrared spectral ranges for hard-target lidars. Appl Opt. 2018 Aug 20;57(24):6990–7.

50. Lee D, Lee SH, Kim BJ, Kim H. Consistency landscape of network communities. Phys Rev E. 2021 May 11;103(5):052306.

51. Calatayud J, Bernardo-Madrid R, Neuman M, Rojas A, Rosvall M. Exploring the solution landscape enables more reliable network community detection. Phys Rev E. 2019 Nov 21;100(5):052308.

52. Montgomery GA, Belitz MW, Guralnick RP, Tingley MW. Standards and Best Practices for Monitoring and Benchmarking Insects. Front Ecol Evol [Internet]. 2021 Jan 15 [cited 2024 May 21];8. Available from: https://www.frontiersin.org/articles/10.3389/fevo.2020.579193

53. van Klink R, Sheard JK, Høye TT, Roslin T, Do Nascimento LA, Bauer S. Towards a toolkit for global insect biodiversity monitoring. Philos Trans R Soc B Biol Sci. 2024 May 6;379(1904):20230101.

54. Drake VA. Distinguishing target classes in observations from vertically pointing entomological radars. Int J Remote Sens. 2016 Aug 17;37(16):3811–35.

55. Xu Z. Insect Diversity Estimation in Entomological Lidar. 2022 [cited 2024 May 23]; Available from: http://lup.lub.lu.se/student-papers/record/9102879

56. Ward Jr. JH. Hierarchical Grouping to Optimize an Objective Function. J Am Stat Assoc. 1963 Mar 1;58(301):236–44.

57. Páez A, Boisjoly G. Exploratory Data Analysis. In: Discrete Choice Analysis with R [Internet]. Cham: Springer International Publishing; 2022 [cited 2024 May 6]. p. 25–64. (Use R!). Available from: https://link.springer.com/10.1007/978-3-031-20719-8_2

58. McInnes L, Healy J, Melville J. UMAP: Uniform Manifold Approximation and Projection for Dimension Reduction [Internet]. arXiv; 2020 [cited 2024 Apr 19]. Available from: http://arxiv.org/abs/1802.03426

59. Connor Meehan, Jonathan Ebrahimian, Wayne Moore, and Stephen Meehan. Uniform Manifold Approximation and Projection (UMAP) - File Exchange - MATLAB Central [Internet]. 2022 [cited 2024 Apr 19]. Available from: https://se.mathworks.com/matlabcentral/fileexchange/71902-uniform-manifold-approximation-and-projection-umap

60. Reynolds DA, others. Gaussian mixture models. Encycl Biom. 2009;741(659–663).

61. Pedregosa F, Varoquaux G, Gramfort A, Michel V, Thirion B, Grisel O, et al. Scikit-learn: Machine Learning in Python. J Mach Learn Res. 2011;12:2825–30.

62. Vinh NX, Epps J, Bailey J. Information Theoretic Measures for Clusterings Comparison: Variants, Properties, Normalization and Correction for Chance.

63. Rosenberg A, Hirschberg J. V-Measure: A Conditional Entropy-Based External Cluster Evaluation Measure. In: Eisner J, editor. Proceedings of the 2007 Joint Conference on Empirical Methods in Natural

Language Processing and Computational Natural Language Learning (EMNLP-CoNLL) [Internet]. Prague, Czech Republic: Association for Computational Linguistics; 2007 [cited 2024 May 14]. p. 410–20. Available from: https://aclanthology.org/D07-1043

64. Massey Jr. FJ. The Kolmogorov-Smirnov Test for Goodness of Fit. J Am Stat Assoc. 1951 Mar;46(253):68–78.

65. Newman MEJ. Modularity and community structure in networks. Proc Natl Acad Sci. 2006 Jun 6;103(23):8577–82.

66. Lucas G. S. Jeub, Marya Bazzi, Inderjit S. Jutla, and Peter J. Mucha. GenLouvain/GenLouvain [Internet]. GenLouvain; 2024 [cited 2024 Apr 22]. Available from: https://github.com/GenLouvain/GenLouvain

67. Hill MO. Diversity and Evenness: A Unifying Notation and Its Consequences. Ecology. 1973;54(2):427–32.

68. Cazzolla Gatti R, Amoroso N, Monaco A. Estimating and comparing biodiversity with a single universal metric. Ecol Model. 2020 May 15;424:109020.

69. Morris EK, Caruso T, Buscot F, Fischer M, Hancock C, Maier TS, et al. Choosing and using diversity indices: insights for ecological applications from the German Biodiversity Exploratories. Ecol Evol. 2014;4(18):3514–24.

70. Efron B. Bootstrap Methods: Another Look at the Jackknife. Ann Stat. 1979 Jan;7(1):1–26.

# Supporting information

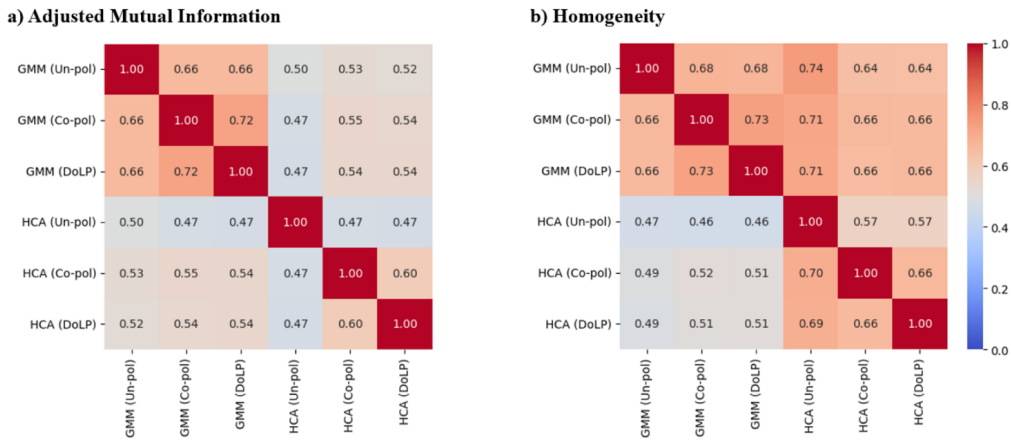


**S1 Fig. AMI and homogeneity scores between HCA and GMM clusters.**

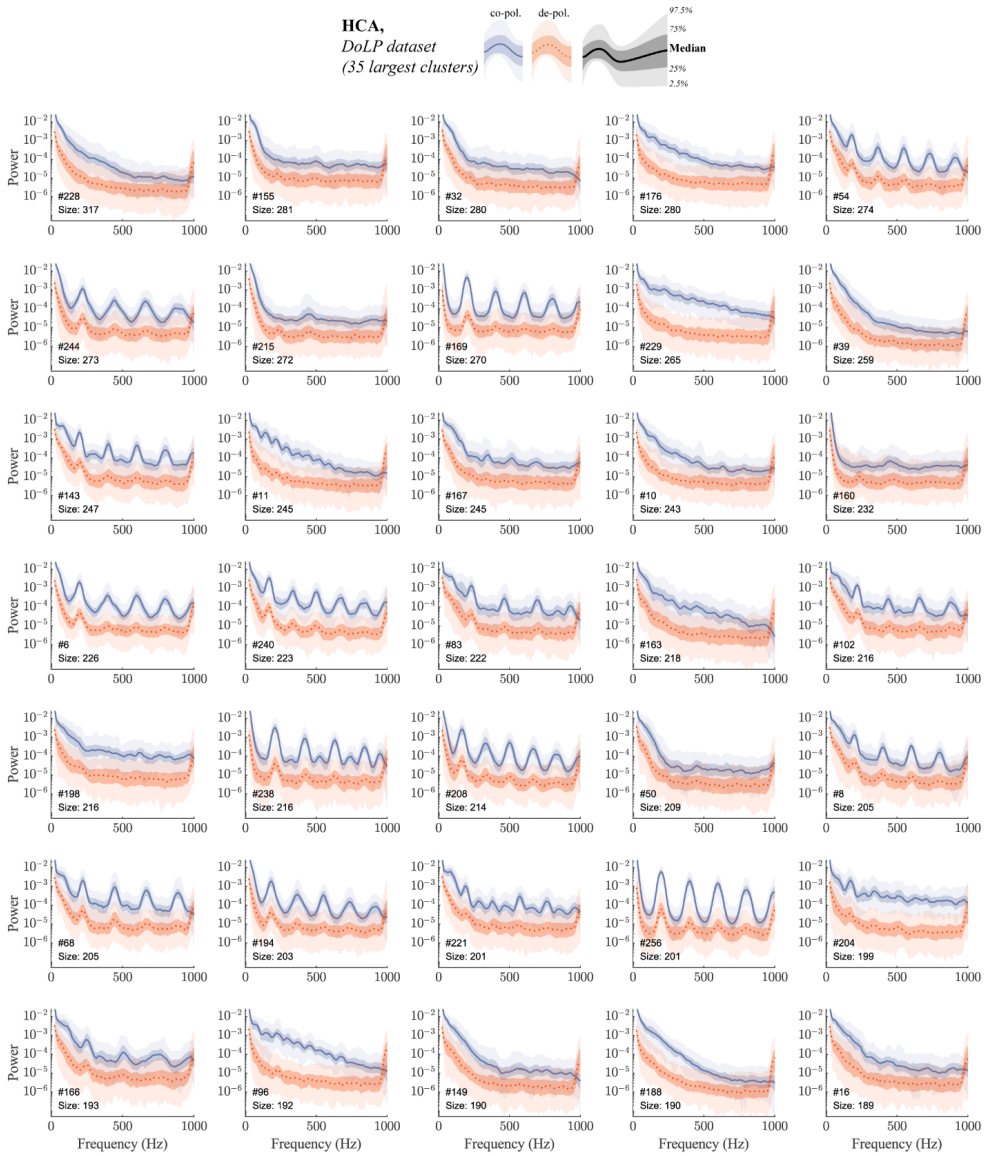


**S2 Fig. 35 largest clusters (HCA, DoLP dataset)**

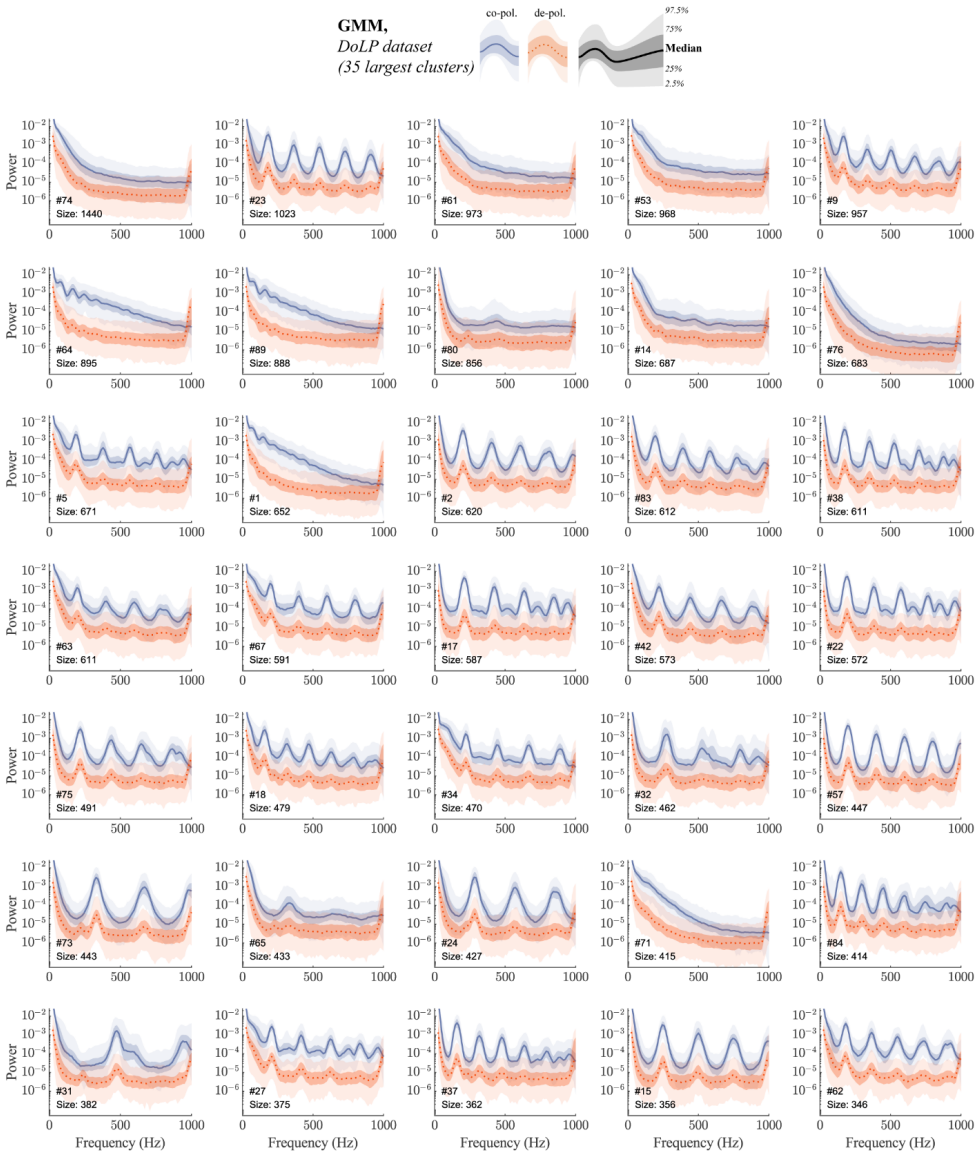


**S3 Fig. 35 largest clusters (GMM, DoLP dataset)**

## S1 Text. Diversity indices variability due to random UMAP/GMM initialization

We also investigated the impact of random initialization of the UMAP and GMM algorithms on clustering results. Given they are stochastic, each algorithms' execution can yield different labeling solutions, potentially affecting the consistency of derived diversity indices.

To quantify variability of diversity indices, we perform 100 runs of UMAP embedding followed by GMM clustering. Each run, we change the random seed for both algorithms, while maintaining other parameters as described in Section **Methods: GMM**. Specifically, we keep the same value for the number of components, as was found to be optimal when using BIC score (see **S1 Table**). We summarize the results of these 100 UMAP/GMM runs in **S2 Table**, presenting the mean diversity indices in bold, along with their corresponding confidence intervals in italics ($2.5^{th}$ and $97.5^{th}$ percentiles).

**S1 Table. Optimal solutions from UMAP and GMM algorithms initialized with 'random seed' = 42 (result reported in the main text).**

| | Dataset | Number of components (GMM model) | Number of clusters found, *NoC, ($H_0$)* | BIC (for optimal solution) |
|---|---|---|---|---|
| GMM | un-pol | 80 | 80 | 2.091e+05 |
| | co-pol | 87 | 86 | 2.040e+05 |
| | DoLP | 89 | 89 | 2.020e+05 |

**S2 Table. Variations in diversity indices resulting from 100 random initializations of UMAP and GMM.**

| | Dataset | $H_0$, $N_{cl}$ | $H'$ | $H_1$ | $H_2$ | BIC |
|---|---|---|---|---|---|---|
| GMM | un-pol | **79.34**<br>*77...80* | **4.13**<br>*4.05...4.19* | **62**<br>57.17...66.02 | **54.25**<br>*47.85...59.22* | **2.108e+05**<br>*2.082e+05...2.136e+05* |
| | co-pol | **85.44**<br>*82...87* | **4.18**<br>*4.10...4.24* | **65.16**<br>*60.14...69.29* | **56.51**<br>*50.24...61.63* | **2.059e+05**<br>*2.034+05...2.088e+05* |
| | DoLP | **87.34**<br>*84...89* | **4.19**<br>*4.11...4.27* | **66.02**<br>*60.81...71.51* | **56.43**<br>*51.22...62.21* | **2.050e+05**<br>*2.023e+05...2.081e+05* |

We observed that the number of found clusters ($H_0$) varied by up to ±2 across all three datasets, with significantly fewer clusters found in the unpolarized dataset compared to the co-polarized and DoLP datasets. Despite these minor fluctuations in $H_0$, random initialization introduced variability of approximately ±5 cluster for the effective ($H_1$) and dominant ($H_2$) cluster numbers. These results show that the unpolarized and DoLP datasets differ significantly in the number of clusters ($H_0$), and therefore, the DoLP dataset shows a higher richness of signal. However, the variability of other indices is too high to confidently determine if these diversity estimates are significantly different between datasets.

By considering both optimal and suboptimal clustering solutions (as indicated by the BIC variability in **S2 Table**), this analysis provided insights into the stability and robustness of diversity indices in the presence of stochastic algorithms. Furthermore, it allowed us to assess whether the three datasets exhibited distinct diversity profiles, irrespective of the specific clustering solution obtained in each run.

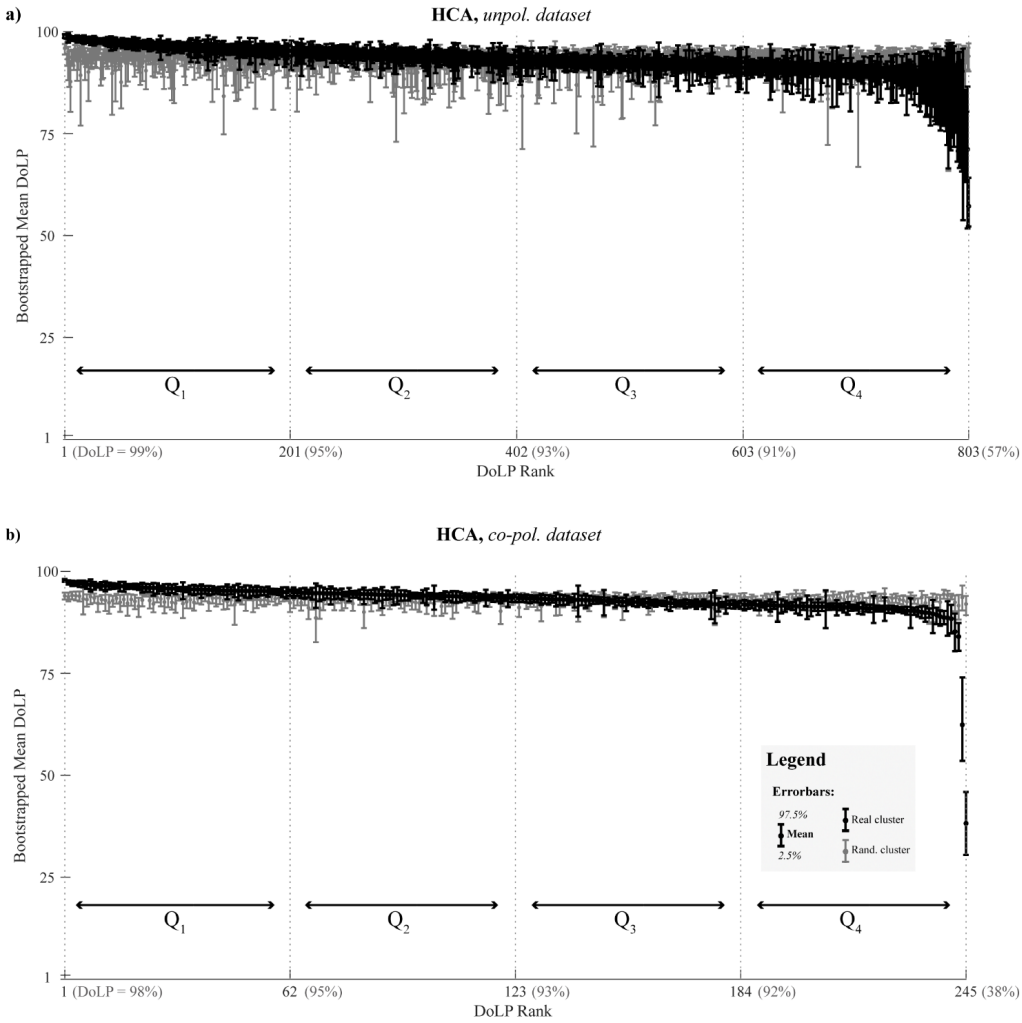


**S4 Fig. DoLP characterization of clustering results (HCA, un-pol. and co-pol. datasets).** Comparison of HCA clustering results (black) with random clustering (gray).

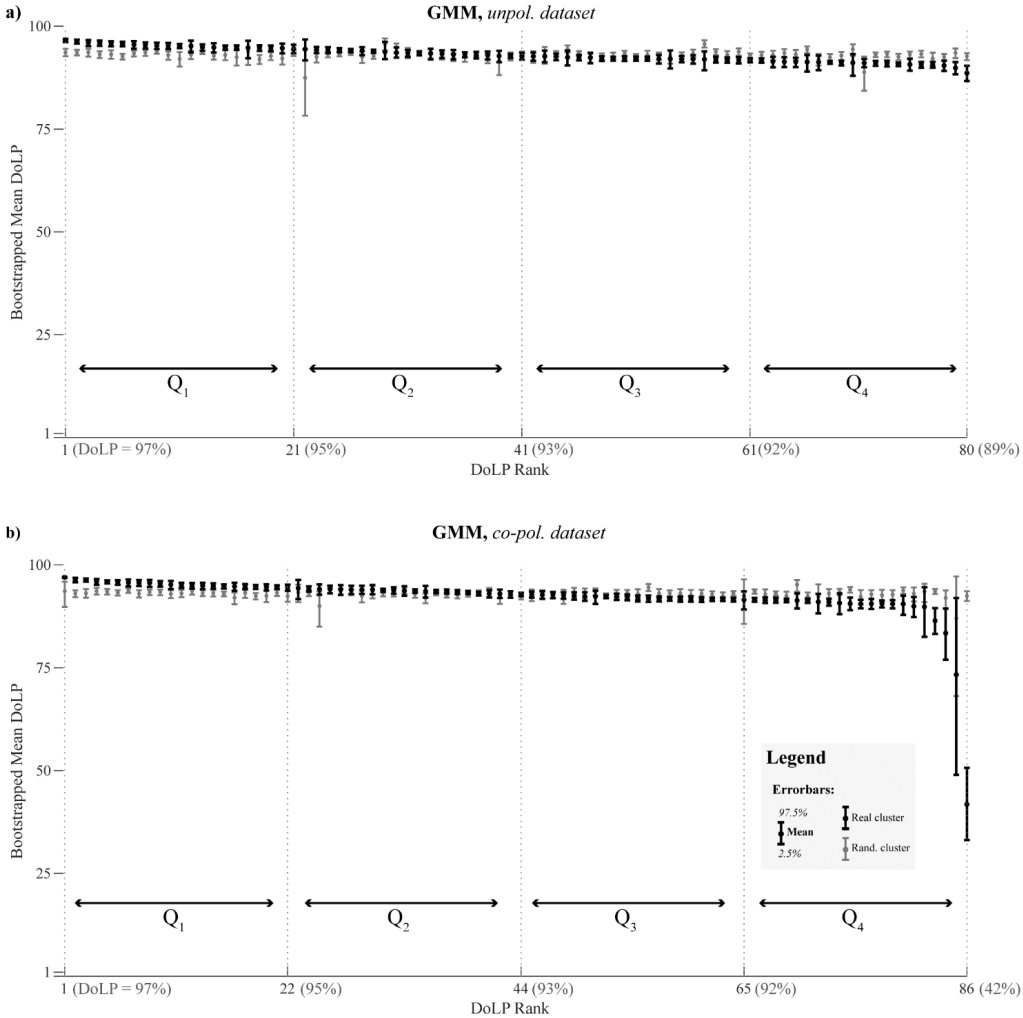


**S5 Fig. DoLP characterization of clustering results (GMM, un-pol. and co-pol. datasets).** Comparison of DoLP clustering results (black) with random clustering (gray).

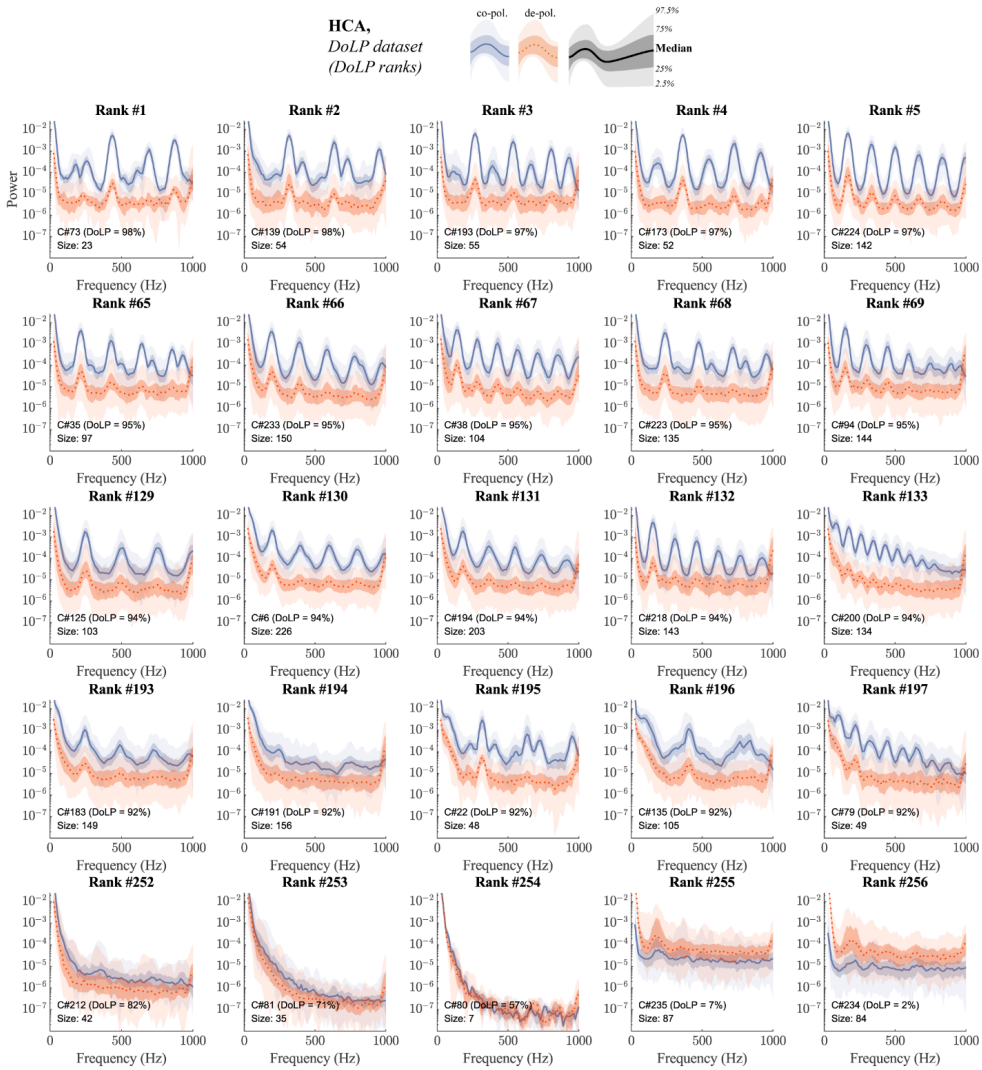


**S6 Fig. Median power spectra of clusters that belong to various DoLP ranks (HCA, DoLP dataset).**

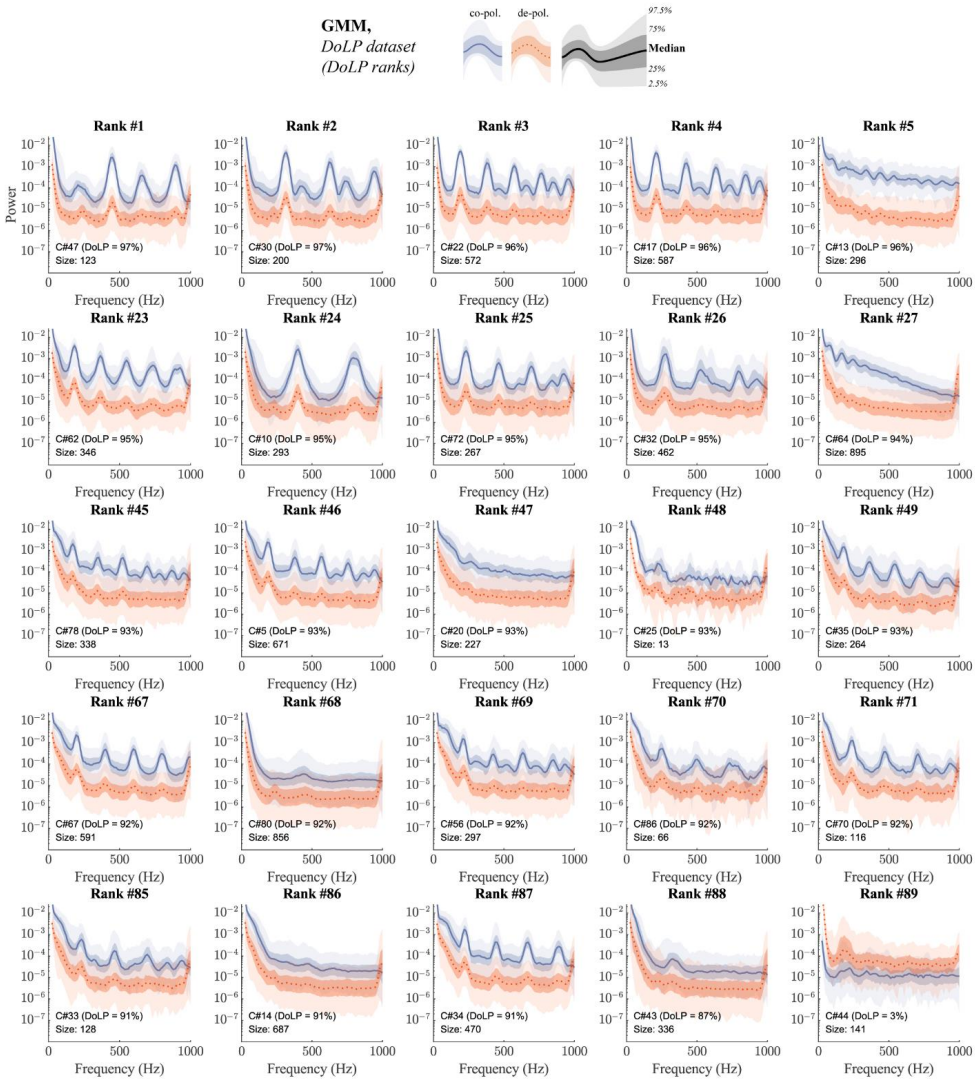


**S7 Fig. Median power spectra of clusters that belong to various DoLP ranks (GMM, DoLP dataset).**

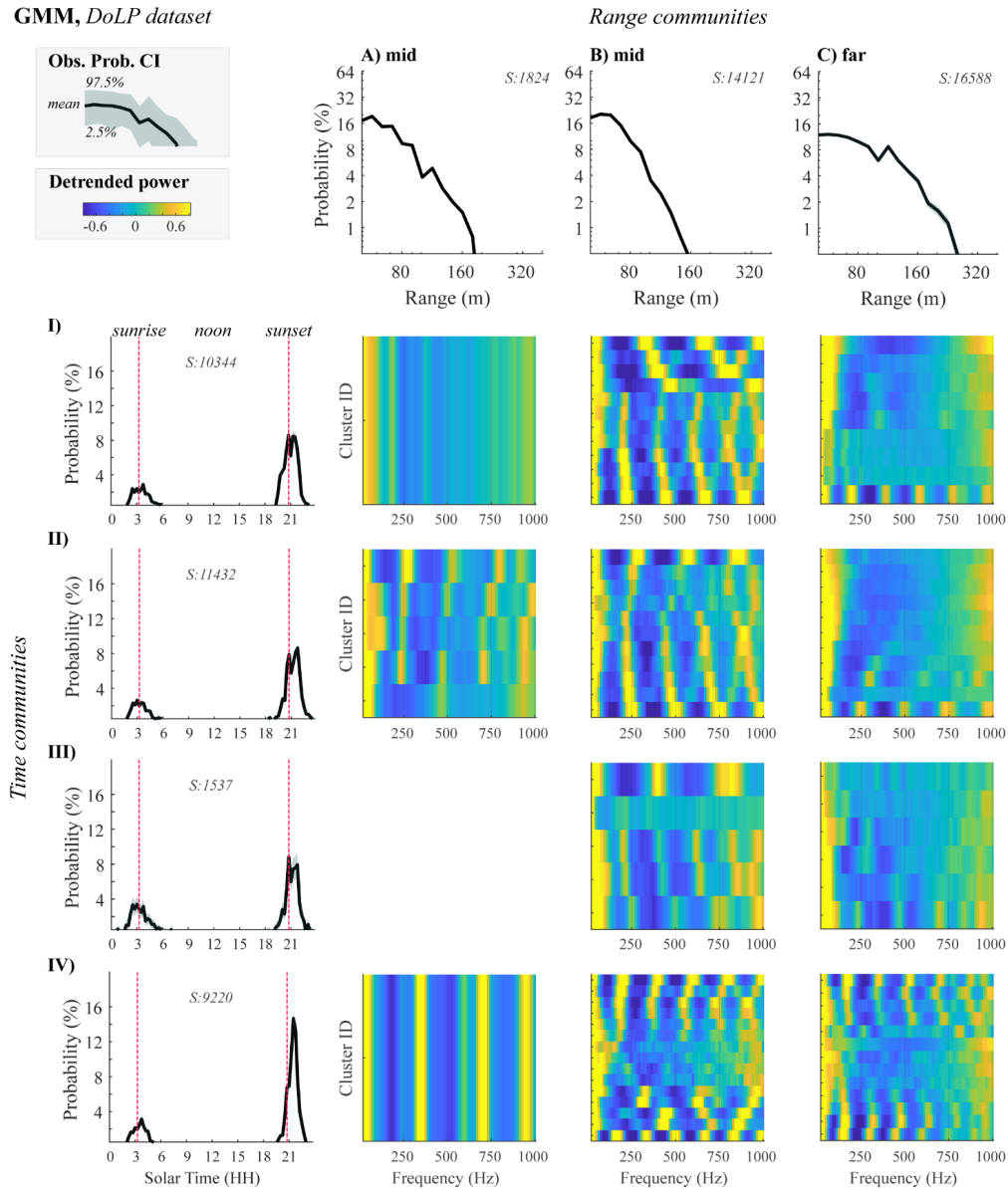


**S8 Fig. Characterization of time and range communities.** Probability distributions for range (**ABC**) and time (**I-II-III**) communities. **Heatmaps at the ABC and I-II-III intersection** display median power spectra for each time-range community.

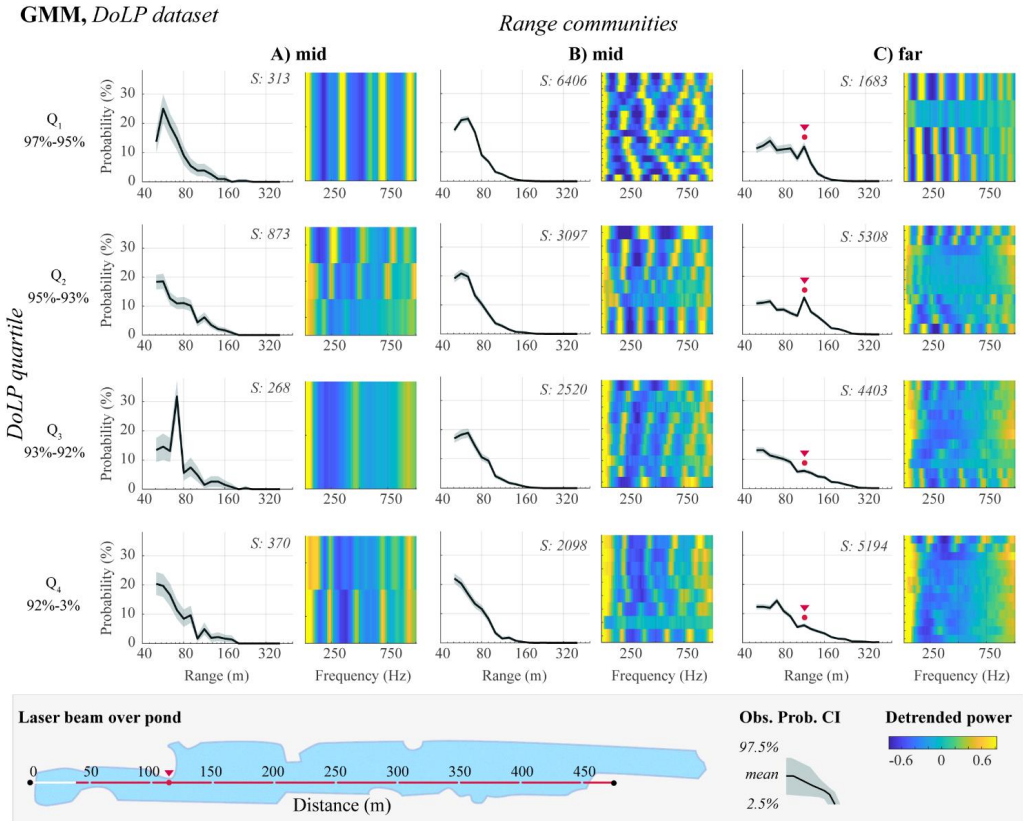


**S9 Fig. Range dependence of co-polarized backscatter.** Probability distributions show the likelihood of observations within range communities (A, B, C) and DoLP quartiles (Q1-Q4), with heatmaps of corresponding power spectra. Note the probability spike in C-plots (red dot) co-occurred with the land piece left of the laser beam over the pond.

# Paper V

**Title:** Dual-Band Lidar and Statistical Moment-Based Assessment of Insect Diversity and Abundance in the Taï Virgin Rainforest

Authors: David Dreyer[1*], Meng Li[1], Hampus Månefjord[1], Assoumou saint-doria Yamoa[2], Yatana Adolphe Gbogbo[2], Lauro Müller[1], Anna Runemark[3], Benoit Kouassi Kouakou[4], Rabbi Boateng[5], Andrew Atiogbe Huzortey[5], Jérémie T. Zoueu[4], Benjamin Anderson[5], Mikkel Brydegaard[1,2,6]

**Affiliations:**
[1] Dept. Physics, Lund University, Sölvegatan 14c, 22363 Lund, Sweden
[2] Institut National Polytechnique Félix Houphouët-Boigny de Yamoussoukro, Côte d'Ivoire
[3] Dept. Biology, Lund University, Sölvegatan 35, 22362 Lund, Sweden
[4] Dept. Physics, University of San-Pedro, BP 1800 San-Pedro - Côte d'Ivoire
[5] Fibre Optics Centre (LAFOC) at the Univeristy of Cape Coast (UCC), Cape Coast, Ghana
[6] Norsk Elektro Optikk, Østensjøveien 34, 0667 Oslo, Norway

* Correspondence: David Dreyer, Department of Physics, Lund University, Sölvegatan 14, 22362 Lund, Sweden.

Email: david.dreyer@biol.lu.se

**Keywords:** Statistical Moment, Lidar, Insect,

**Summary**
Insects are fundamentally important for every terrestrial food web. They constitute a major food source for numerous animal groups and perform as indispensable pollinators and nutrient recyclers. Many terrestrial ecosystems and freshwater ecosystems will collapse without insects (Goulson 2019). On the other hand, certain insect species spread diseases in both humans and livestock, ravage crops and food stocks, damage forests and destroy infrastructures (e.g., termites). In a world with a warming climate, phenomena such as the overall decline of insect biodiversity and biomass, the turnover in species composition or seasonal mass infestations of pest-insects could cause a serious long-term threat to human well-being (Outhwaite et al., 2022). This is why affordable, precise, non-invasive and unadministered long term *in situ* observation techniques are needed to monitor changes in insect activity and species composition as a part of insect biodiversity monitoring (Van Klink et al., 2024). To this day, insect monitoring is often done using work-intensive methods including nets or insect traps. Other concepts, such as entomological radar systems (Noskov et al., 2021) are heavy, large (trailer and vehicle needed), produced in small numbers and relatively expensive. Promising new results have been reported using simple camera techniques in combination with machine learning analysis as well (Wallace et al., 2023). The Entomological Scheimpflug-Lidar (ESL) technique has been tested in several countries and habitats as varied as Swedish forests (Li et al., 2020), African rainforests (Kouakou et al., 2020) or the Australian alpine regions. It is a well-established technique, which allows the detection of high and low flying insects alike, featuring a superb temporal and spatial resolution, in terrestrial as well as aquatic environments (Brydegaard & Svanberg, 2018; Brydegaard & Jansson, 2019). In the past, automated monitoring systems have targeted particularly the wing beat frequency of individual insects in flight as diagnostic tool for species identification (Rydhmer et al., 2022; Wallace et al., 2023). However, most insect species feature context and sex specific ranges of wing beat frequencies (Gibson & Russell

2006; Tercel et al., 2018) which can in addition be relatively similar from species to species. Additional information for species detection is needed.
Here, we showcase ecologically relevant information utilizing basic statistical moments for species selection which can be extracted from recorded ESL-datasets, based on a full observation report of insects detected in the Taï National Park (Parc National de Taï, Côte d'Ivoire, a primary rainforest in West Africa) using a dual-band Lidar system (DB-ESL; Santos et al., 2023).

**Introduction**
Insect flight activity is the driver of various ecological processes like predator-prey dynamics, plant-insect interactions, or organic matter decomposition, which influence ecosystem stability and resilience (Crespo-Pérez et al., 2020). Especially many nocturnal insects play crucial roles in ecosystem functioning, including pollination (Macgregor & Scott-Brown 2020). Moths and nocturnal bees are common nocturnal fliers of the tropics, facilitating the reproduction of flowering plants, including many crops (Buxton et al., 2022).

Monitoring the abundance and diversity of insect communities in different habitats has been established as a measure for the status of a habitat's overall biodiversity (Landmann et al., 2023). It has been shown that agriculture and global warming have negative effects on the species richness and abundance on certain insect communities (Outhwaite et al., 2022). To validate conservational measures and to quantify anthropogenic impact on the biodiversity of a respective habitat, field surveys with respect to the abundance and diversity of insect species, therefore seems an excellent tool. To establish the first steps of baseline measurements of insect biodiversity in the Tai National Park, we deployed a dual-band ESL (DB-ESL, 808 and 980 nm lasers) within the boundaries of the national park.

The Tai National Park hosts a 3,300 km^2 patch of pristine tropical, moist broadleaf forest, which is part of the Upper Guinean Forest system of Western Africa. Over the last decades, logging and extensive agriculture have threatened the existence of this "biodiversity hotspot" (Arcilla et al., 2015), creating a pattern of secluded patches of woodland.

Insect abundance and species diversity exhibits seasonal patterns in tropical environments, which are linked to climatic changes such as rainfall, temperature, and humidity (Wolda, 1978; Denlinger, 1980). The rainfalls during wet seasons may stimulate increased insect activity due to breeding opportunities and resource availability (Grøtan et al., 2012), peaking at the beginning of dry season followed by a decline at the end of dry season and the beginning of the following wet season (Valtonen et al., 2013). The dry season in Ivory Coast usually begins around November as the Inter-Tropical Convergence Zone (ITCZ) shifts southward, taking the rain-bearing weather systems away from the region. Rainfall decreases significantly during this period, marking the transition from the wet season to the dry season. The peak of the dry season is typically experienced between December and February. During these months, Ivory Coast experiences its driest and hottest weather conditions. Rainfall is minimal, if any, and humidity levels decrease. Clear skies and sunny weather are common during the day, with cool temperatures at night in some areas. The dry season persists throughout December, January, and February, with little rainfall recorded in most parts of the country (Le Houérou 2009).

Besides the relatively light equipment, ELS offers cost-efficient long-term monitoring of insect activity featuring the capacity of hundreds of thousands insect observations per day and a temporal (multi-kHz sampling rates) and spatial resolution (ranging precision < 1m) which

is unachieved by classic monitoring techniques using e.g. malaise traps. Even though the setup, calibration and operation of an ELS system requires some technical expertise and experience, ELS systems, with their 2 main components, a laser unit, and a receiving unit, stand out when it comes to conceptual simplicity. The ELS method was extensively described elsewhere (Brydegaard & Jansson, 2019). In very simplistic terms, the concept is based on a collimated Laser beam (multiband or single band, up to several hundred meters long, 50-70mm in diameter) which is usually pointed at a termination target (a black neoprene surface) for calibration purposes. The beam can be oriented horizontally, parallel to the ground or vertically, pointing at the sky, as well as any desired angle in between. Once an insect enters the cross section of the laser beam while in flight, light will be scattered from the body and/or the wings of the insect, which is then collected by the receiving unit (usually a Newton telescope) and focused on a CMOS sensor. The Scheimpflug configuration (Brydegaard et al., 2017) of the detector allows to record optically sharp images of these backscattered light events, or observations, over several hundred meters simultaneously, since signals from different ranges are focused on different pixels of the sensor.

Hence the receiving unit can operate at sampling frequencies up to several kHz, hundreds or thousands of exposures of the same insect can be recorded before the respective insect leaves the beam. A typical insect observation lasts several milliseconds and contains hundreds of exposures, featuring oscillatory modulations of the wings and non-oscillatory information of the body. This allows us to reliably determine the wing beat frequency, as well as body- and wing-size ratios, which are relevant for target classification. Naturally, the gathered wing beat frequencies can be further analyzed in e.g. un-administered clustering procedures (Bernenko et al., in preparation) in combination with machine learning (Wallace et al., 2023), which in turn bears the potential for automated detection of individual species.

The motivation to deploy a dual-band system is that by comparison of the light-signal, which is backscattered by the insects' body, predictions about the degree of the corresponding melanization of the respective insect can be made. The darkish or brownish body coloration of insects is strongly influenced by the interaction of certain regulatory and effector genes, concerting the production of the pigment melanin all over the insects' body (Popadić & Tsitlakidou, 2021), which can be remarkably diverse, even between closely related species (True et al., 2003). The expectation is that a higher degree of melanization means a higher diffuse reflectance of the longer wavelength (980nm) in comparison to the lower wavelength (808nm), and that the resulting ratio of the backscattered signal's intensity can be used for species identification (Gebru et al., 2017). The recorded datasets include ecologically relevant information which allows us to determine overall insect activity patterns in time and space, insect species abundance and thereby insect biodiversity.

## Materials and methods:

*Deployment and Configuration of the LiDAR System*

A dual-band entomological laser system (ELS) was established at the edge of the Tai rainforest to investigate insect diversity and abundance. The ELS system was designed according to the Scheimpflug principle, which ensures high-resolution imaging over extended distances. This was achieved by precisely aligning the transmitter and receiver telescopes, mounted on a tripod (EQ8, SkyWatcher, China), with a baseline separation of 814 mm. The transmitter telescope, a Ø 102 mm instrument with a 500 mm focal length, housed the core of

the ELS system – a module containing two 3W TE-polarized laser diodes, one emitting at 808 nm and the other at 980 nm. The 808 nm laser beam was combined with the second 980 nm beam using a beam combiner to achieve the system's dual-band capability. The receiver module comprised a Newton reflector telescope (TeleskopService, Germany) with a Ø 150 mm diameter and 600 mm focal length. A CMOS camera (OctoPlus, Teledyne e2v, USA), featuring 2048 pixels (10x200 μm² each), was attached to the eyepiece of the receiver. The angles between the instruments and slit orientation were meticulously adjusted to adhere to the Scheimpflug condition, further enhancing image quality. Importantly, the CMOS sensor was tilted at 37° relative to the optical axis of the Newton telescope to ensure optimal alignment with the Scheimpflug principle and facilitate smooth hinge dynamics.

The LiDAR beam, emitted from the transmitter, was directed across the top of the rainforest edge canopy at an elevation angle of 13 degrees. Due to pauses required for canopy scanning and elevation adjustments, the LiDAR actively recorded data for 12% of the total flight duration. During operation, the system maintained a 10 kHz pulse repetition frequency, 100 μs scan line rate, and 80 μs pulse duration. Each 3-second data file, composed of approximately 30,000 scan lines, averaged 120 MB in size. A custom LabVIEW script continuously logged the LiDAR observations and structured the data into organized files for subsequent analysis and interpretation. Over the night of the measurement, a total of 1.1 TB of raw data was acquired. After excluding irrelevant data (e.g., background noise, non-insect echoes), the dataset was reduced to approximately 300 MB, which is less than 30% of its original size.

**Results:**

General observations:
During the night of the 7th to the 8th of January 2023, our system recorded over 14310 observations of insects at various heights. The rate of observations peaked at 21:00 and began to gradually decline from around 23:00 onwards until it fell below the mean observation rate (255 observations /15min. bin) at around 4:00. This pattern was interrupted by a narrow peak after sunrise between 7:00 and 8:00 in the morning.
The mean flight altitude of the detected insects was 19.2m (SD: 8.7), while the highest detected observation was at an altitude of about 405 m. The peak flight activity took place right under the canopy (~25m) at an altitude between 20-25m during the first half of the night.

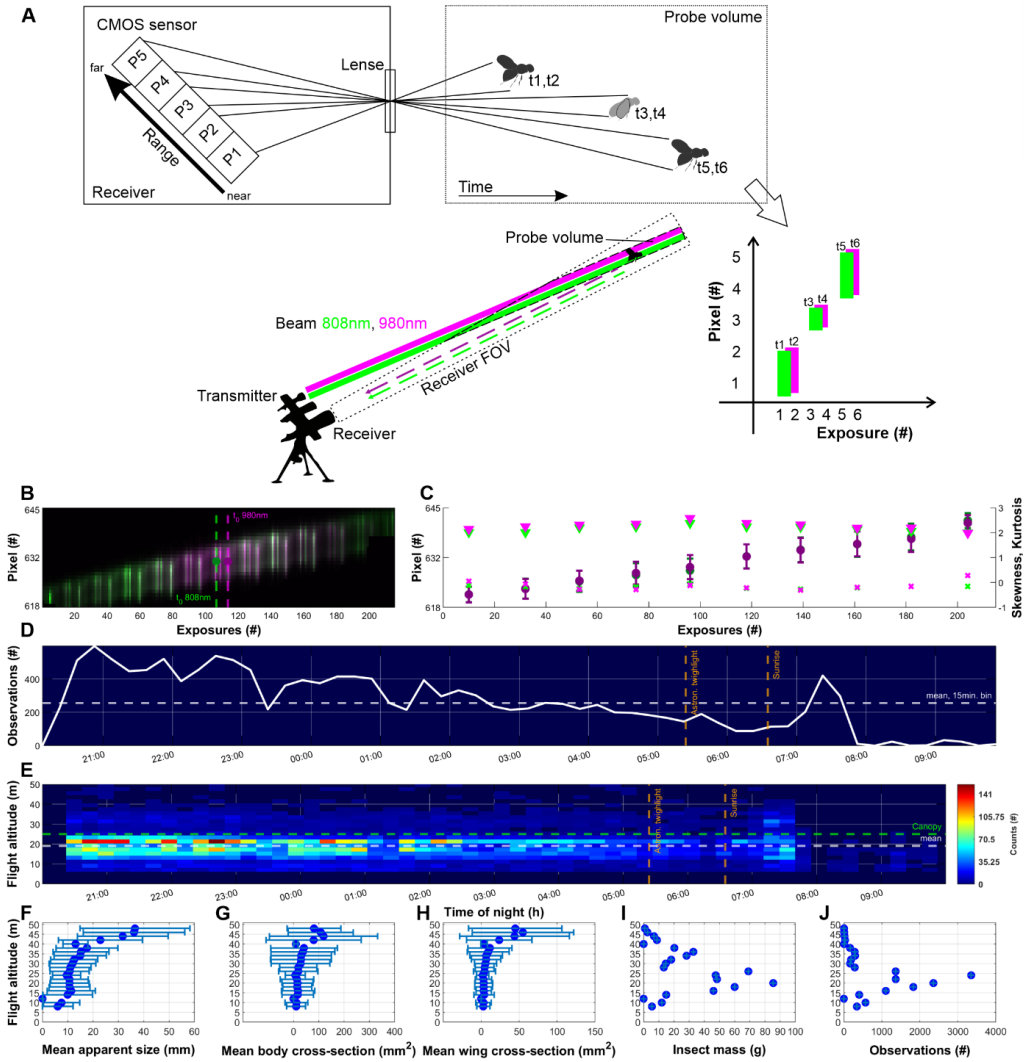


**Fig 1.: (A) The scheme shows the general setup and principle of our dual band LiDAR system. The overlapping region of the laser beam and of the field of view of the receiver form the probe volume. Any insect which crosses the beam in flight will generate a signal of backscattered light which is detected by the receiver. In this example an insect crosses the probe volume of the LiDAR and is registered in 6 samples or exposures with the timestamps t1 to t6. The signal is focused on different pixels of the CMOS-sensor, allowing us to determine the range of the respective signal. The Pixel number can be plotted as a function of the respective exposure, revealing the dual-band signal. Note that the samples t3 and t4 leave a weaker signal than t1, t2 and t5 and t6 since the signal was captured while the wings of the insect and the body were at the same line of sight of the receiver, resulting in a smaller signal. This repetitive pattern allows the analysis of the wingbeat frequency of a respective insect observation. (B) A false color coded 2D map of a single insect observation. The signal strength is encoded at 12-bit resolution as overlay of the dual-band signal (green: 808nm, magenta: 980nm). The dashed lines encode the time of the calculated center of mass of the signal ($t_0$) for both signal bands. (C) The plot displays some statistical moments which can be extracted from a respective exposure (data only shown for every 20th exposure). The filled circles encode the center of mass of the intensity distribution of the respective exposure (left y-axis) over the respective pixels, including the spread of the intensity (vertical error bars). The crosses and triangles depict the corresponding skewness (crosses) and kurtosis (triangles) of the respective intensity distribution. D: The plot shows the number of observations plotted as a function of time (15min. bins). The vertical dashed lines indicate the beginning of Astronomical twilight and the time of sunrise. Note the negative trend of detections as night progresses. All relevant graphs: green: 808nm, magenta: 980nm. E: 2D histogram depicting the flight altitude of the observations vs the time of night. The vertical dashed lines indicate the beginning of Astronomical twilight and the time of sunrise. The horizontal dashed lines indicate the height of the canopy (25m) and the mean flight altitude (19.2m). F-J: The flight altitude was binned (2m bin) on the y-axis and plotted as a function of the mean apparent size (F), the mean body (G) and wing (H) cross-sections, the mean mass (I) and number of observations, per respective bin from 0 to 50m. Note that the LiDAR was set up with the beam pointing in the sky at an angle of 10° relative to ground level, which is why we could not recorded insects flying lower than 7m. Insects in B; Observation #: 1975. Time: 21:18:47. Apparent size: 2.53mm. Flight altitude: 10m. Wing beat frequency: 148 Hz.**

Cross-sections:

Using the sum of the calculated body cross-sections (~0.23m$^2$), we utilized coefficients suggested by Genoud et al., (2023) to estimate the total mass of detected insects of ~ 0.58 kg. As expected, the cross-sections in the 980nm are larger than the cross-sections of the 808nm signal-band in most recordings. The opposite is the case for only ~20% of observations for the body cross-sections and ~30% for the wing cross-sections (see Fig 3.I). Our recordings suggest that our observations show a mean body cross-section of 16.3 (SD: 70.2; 808nm) and 18.2mm$^2$ (SD: 89.7; 980nm). The mean wing cross-sections are 3.9 (SD: 14.3; 808nm) and 6.12mm$^2$ (SD: 27.1; 980nm).

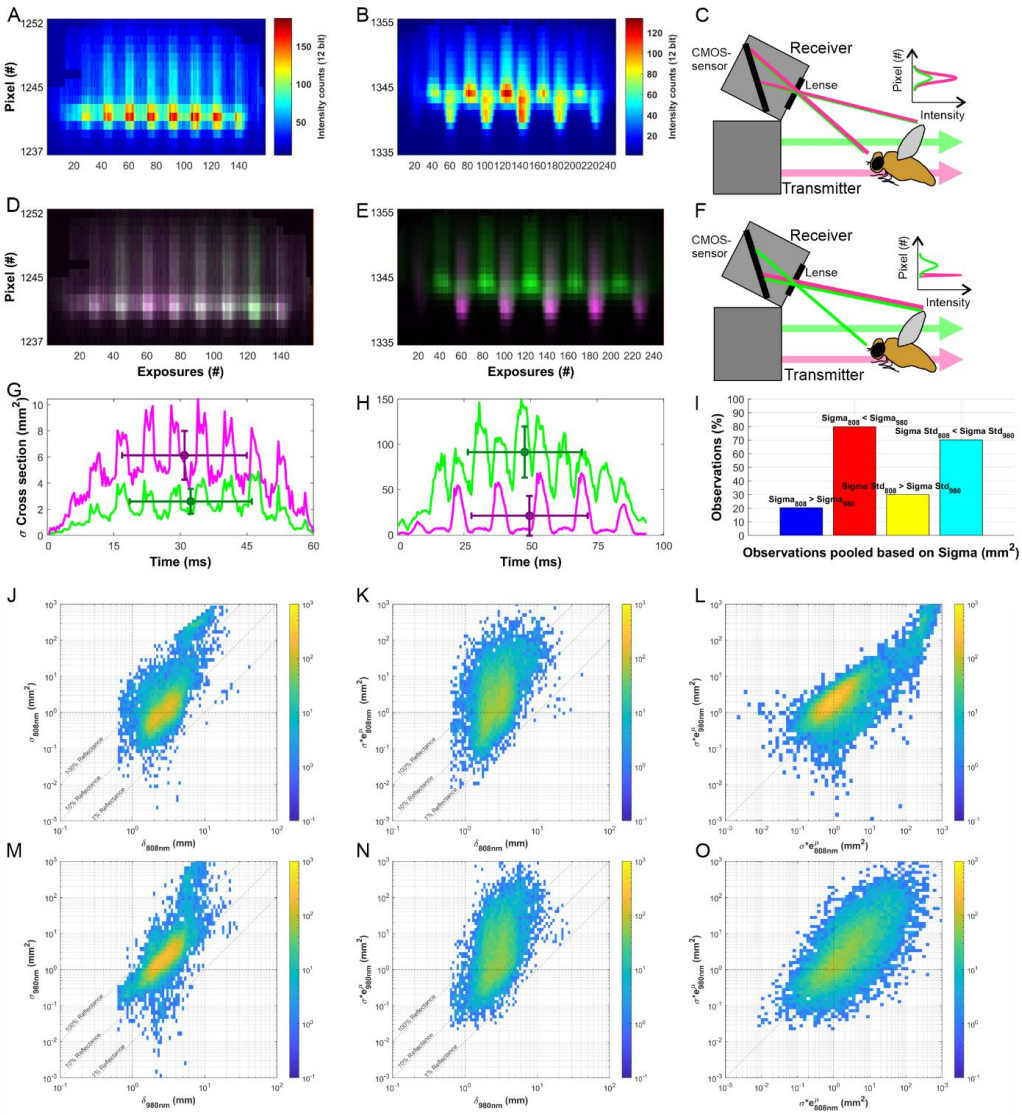


**Fig 2.: Comparison of insect cross-sections of body and wings using both signal-bands. A, B: Time-range maps of two insects recorded (time and height). C, F: The schemes illustrate the concept underlying the cross-section comparison. In C, a given insect creates a LiDAR signal by flying through the probe volume of the beam. While the diffuse reflection of the insect is stronger for the 980nm band (illustrated by thick lines in magenta) as it is the case in (G), the signal of the 808nm is considerably weaker (illustrated**

**by thin green lines). In F, due to the spectral characteristics of the given insect, an entire body part leaves little to no signature within the signal of one of the respective bands, as it is the case for (H). G, H: The cross section of the recorded signal plotted as a function of time. The filled circles represent the bias (mean of the cross section within deltat, horizontal error bars), while the vertical error bars depict the standard deviation of the cross section (within deltat). We used the standard deviation to determine the cross section of the wings (oscillatory part and the mean of the bias for the cross section of the insect's body (envelope) for the body to wing-ratio. Note that the 808nm signal (green) is considerably weaker in G, but higher than the 980nm signal in H. I: The bar diagram illustrates the composition of observations featuring a bigger cross section of the body and the wings in the two different bands. J, M: The 2D histograms show the cross sections of the bodies of all observations plotted as a function of the corresponding apparent sizes for both bands, 808nm in J and 980nm in M. Note that the signal in M is about double as strong as in J, reporting a higher degree of diffuse reflectance within the signal of the 980nm band. K, N: Same as in J and M but for the cross section of the wings. L, O: Direct comparison of the body cross sections of both bands in L and the cross sections of the wings in O. Insects in A and B; observations #: 219, 4189. Times: 20:29:28, 22:31:55. Apparent sizes: 5, 6 mm. Flight altitudes: 18, 21m. Wing beat frequencies: 166, 64 Hz.**

Size:

There seems to be a weak trend that larger insects may fly at higher altitudes (compare Fig.1, F; Fig.3, H). We did not detect any obvious trends regarding the time of flight and the apparent size of the insects. (Fig.3, G). The mean apparent size of our observations is 3.12mm (SD: 3.7) for the 808nm and 3.19 (SD: 8.2) for the 980nm signal-band.

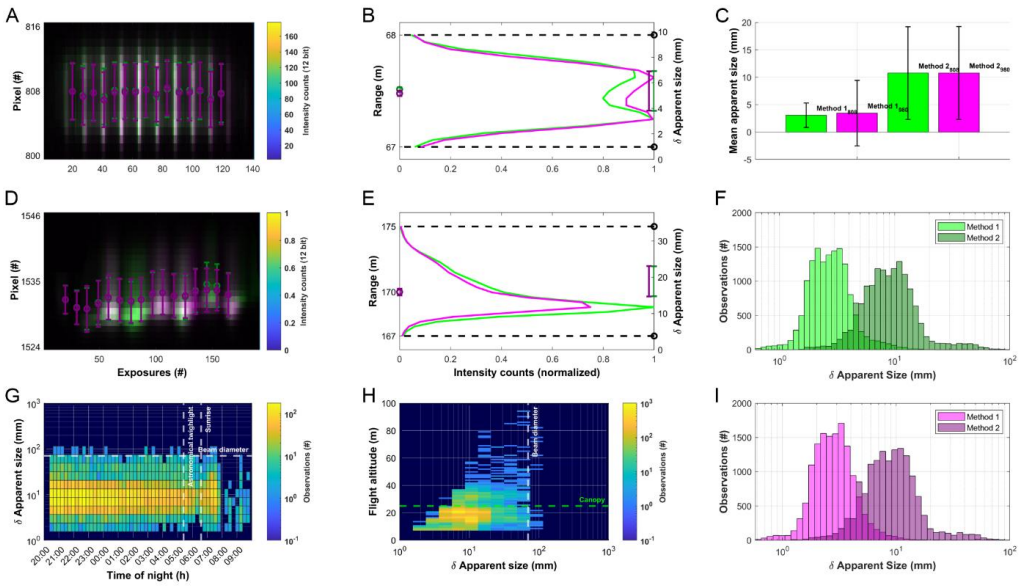


**Fig 3.: Apparent size and range. A, D: Time-range map of the dual-band signal with both respective signal bands plotted in false colors (green: 808nm, magenta: 980nm). The dashed lines encode the exposure number which is closest to the calculated center of mass of the signal (t0) for both signals. B, E: The apparent size and range of the same insects as in (A), (D). The curves show the intensity distributions of both signals plotted over the respective range of the signal. The open circles on the left y-axes show the mean range of the respective observation (between 67 and 68m for B and about 170m for E). The apparent size can be calculated using two different calculations (see methods). The conventional method (method 1, size depicted as distance of respective error bars on the right y-axis) utilizes the spread over the respective pixels over all exposures, while the other method (method 2) basically thresholds the pixels which contain signal at $t_0$ and projects the apparent size on a previously calculated scale (distance between stippled lines on right y-axis). While method 1 seems to deliver a more conservative impression of the estimated apparent sizes, it tends to underestimate the apparent size of the individual observations. (C) Mean apparent sizes calculated for all observations for boths bands using both methods (method 1 on the left, method 2 on the right). The error bars encode the standard deviation. F, I: Apparent sizes calculated using both methods plotted as histograms for both bands (F, for 808nm and I, for 980nm). Note that the distribution of method 2 is shifted towards a larger apparent size, in both bands. G: To check for possible trends in size distribution over the course of the night, the apparent size (method 1) was plotted vs the Time of night in a 2D histogram. H: 2D histogram depicting the flight altitude vs the apparent size. Bigger insects seem to fly at higher altitudes in general (compare Fig.1 F). Insects in A and D; observations #: 13, 1581. Times: 20:22:25, 21:06:28. Apparent sizes: 3, 8 mm. Flight altitudes: 11, 29m. Wing beat frequencies: 225, 75 Hz.**

Skewness:

In some insect species, the ventral side of the wings (Fig.4, A, B) seemingly shows a higher degree of reflection and vice versa (Fig.4, D, E). The result is that the individual exposures show the animals' signal during the downstroke (Fig.4, L, left) or the upstroke (Fig.4, L, right) of the wingbeat cycle. Since the signal from the body of an insect is usually stronger than the signal from its wings, the distribution of the signal's intensity usually shows some degree of skewness in both signal bands, which can be negative (Fig.4, C; $skewness_{808}$:-0.6, $skewness_{980}$: -0.6), positive (Fig.4, F; $skewness_{808}$: 0.6, $skewness_{980}$: 0.6) or in some cases even both (Fig.4, I; $skewness_{808}$: 0.1, $skewness_{980}$: -0.02). The signal's skewness in our observations is positive on average and slightly lower for the 808nm band (mean: 0.2, SD: 2.7) as the 980nm band (mean: 0.3, SD: 3.4).

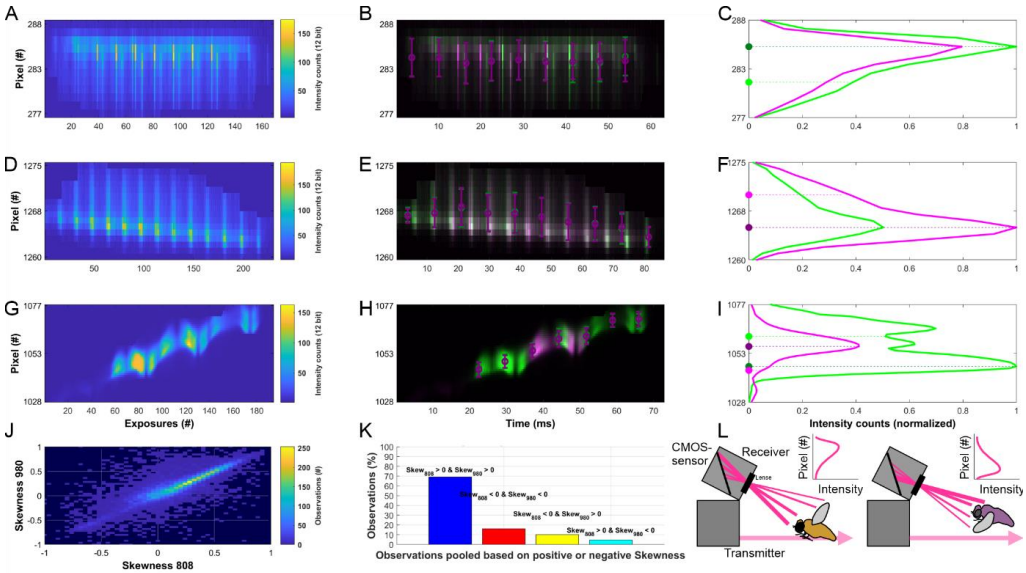


**Fig 4.: A comparison of the Skewness. A, D, G: Time-range maps of two insects recorded (time and height). B, E, H: Time-range map of the dual-band signal of the same observations as in A, D and G but respective signal bands plotted separately (green: 808nm, magenta: 980nm). The filled circles encode the center of mass of the intensity distribution of the respective exposure (left y-axis) over the respective pixels, including the spread of the intensity (vertical error bars). C, F, I: The intensity distribution (normalized) of the corresponding insects signal in B, E and H for both bands. Note that the detected signal is considerably skewed negatively in both bands (green: 808nm and magenta: 980nm) in C, while the distribution shows a positive skewness in F. I shows both, a positive skewness for the 808nm band and a positive skewness for the 980nm band. The filled circles and the stipulated lines indicate the mode (dark green, dark purple) and the mean (bright green, bright purple) of the respective curves, indicating a negative or positive skewness respectively. J: The 2D histogram shows the skewness of the 808 vs the 980-band intensity distribution of all observations. K: The diagram displays the composition of skewness combinations of the intensity distribution of the two bands. L: The scheme depicts how the signal-skewness can be used to make assumptions of the characteristics of the insect-species, particularly of the reflectiveness of the wings of a respective species: The body of an insect usually shows a higher degree of diffuse reflection if compared to the wings. This leads to a negatively skewed distribution of the intensity distribution if the wings do reflect light during the downstroke (left) or a positively skewed distribution during the upstroke (right) of the wings. Insects in A, D and G; observations #: 2882, 5109, 36. Times: 21:49:40, 22:57:55, 20:22:58. Apparent sizes: 1, 4, 4 mm. Flight altitudes: 8, 19, 15m. Wing beat frequencies: 188, 161, 122 Hz.**

Kurtosis:

Some insect species have a larger reflective body surface relative to their overall mass than others. Mosquitos for instance spread out their legs while in flight, which makes their cross-section much larger relative to the actual diameter of thorax and abdomen (Fig 5. I, right). Moths on the other hand tuck their legs close to their abdomen while in flight, creating a smaller cross-section relative to the mass of the insect. This leads to varying kurtosis values of the intensity distribution of the signal (Fig 5. C, F). Interestingly, the kurtosis value of the

respective signal bands can vary considerably as it is the case for the observations in Fig. 5, C (kurtosis808: 2.1, kurtosis980: -35.3) and Fig. 5, F (kurtosis808: 0.6, kurtosis980: 2.3).

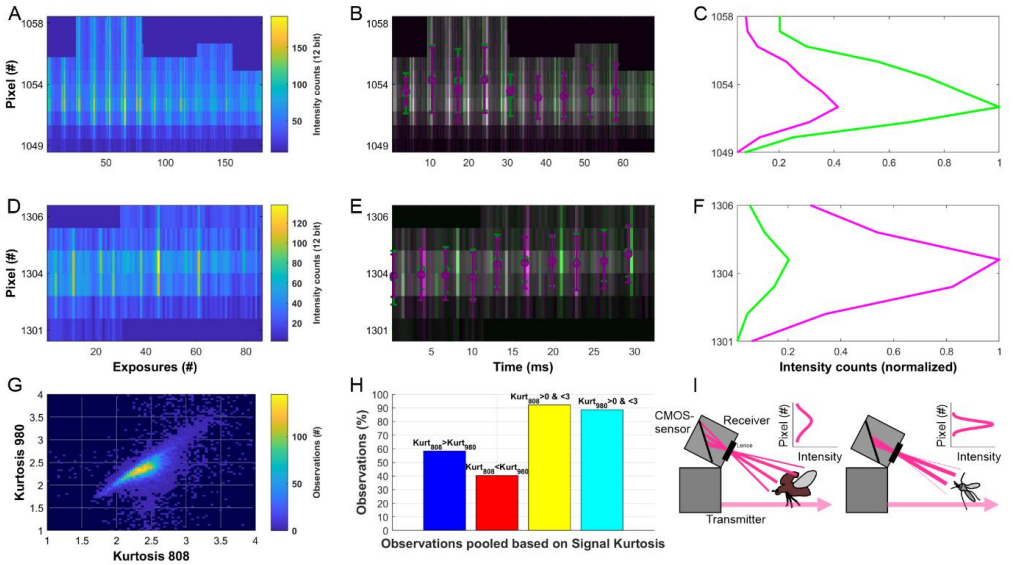


**Fig 5.: A comparison of the signal kurtosis. A, D: Time-range maps of two insects recorded (time and height). B, E: Time-range map of the dual-band signal of the same observations as in A, D and G but respective signal bands plotted separately (green: 808nm, magenta: 980nm). The filled circles encode the center of mass of the intensity distribution of the respective exposure (left y-axis) over the respective pixels, including the spread of the intensity (vertical error bars). C, F: The intensity distribution (normalized) of the corresponding insects signal in B and E for both bands. Note that the intensity distribution of the detected signals of both bands (green: 808nm and magenta: 980nm) show considerably different forms of kurtosis. While the distribution of the 980 band shows a more compressed, low kurtosis in C, the distribution of the same band seems high in F. The intensity distribution of the 808 signal shows the opposite configuration. I shows both, a positive skewness for the 808nm band and a positive skewness for the 980nm band. The filled circles and the stipulated lines indicate the mode (dark green, dark purple) and the mean (bright green, bright purple) of the respective curves, indicating a negative or positive skewness respectively. G: The 2D histogram shows the kurtosis of the 808 vs the 980-band intensity distribution of all observations. H: The diagram displays the composition of kurtosis combinations of the intensity distribution of the two bands. I: The scheme illustrates how the signal-kurtosis can be used to make assumptions of the characteristics of the insect-species, particularly of the different reflectiveness of the entire insect: The body of an insect usually shows a higher degree of diffuse reflection if compared to the wings or legs. This leads to a high kurtosis of the intensity distribution of the overall signal, if the thorax and abdomen of an insect are small if compared to the overall less melanized surface (like in a mosquito on the right) or if thorax and abdomen are big and highly melanized like in e.g. a beetle (left). Insects in A and D; observations #: 226, 2857. Times: 20:29:47, 21:48:43. Apparent sizes: 5, 5 mm. Flight altitudes: 15, 20 m. Wing beat frequencies: 212, 137 Hz.**

## Discussion:

This report is complementary to previous measurements conducted in Ecuador (Santos et al., 2023), which aimed to monitor insects in a coastal rainforest and dense fog under natural conditions. Due to technical difficulties, the start of the measurement was delayed to around 20:00 after sunset (07. January 2023, 18:20 local time) which was well within astronomical darkness at the recording site. Our laser beam did penetrate the canopy, pointing at the nightly sky, enabling us to detect insects flying beyond and above the canopy. Interestingly, most observations were recorded at a flight altitude less than 25m, directly beneath the canopy. At this stage, we cannot make any assumptions about the exact species of insects that we have recorded, but we noticed a remarkable abundance of epiphytes in the trees next to the camp. Many epiphyte orchids native to Western Africa are members of the genus *Angraecum* and *Bulbophyllum.* These orchids are known to be visited by nocturnally pollinating insects, such as moths, nocturnal bees and even crickets, but also usually diurnal and crepuscular active

species such as flies (Raguso, 2020; Micheneau et al., 2010). At least in Thailand, members of the group *Phoridae* are known *Bulbophyllum* pollinators (Pakum et al., 2019), and certain *Phoridae* are known to exhibit distinct nocturnal activity (Bostock et al., 2017). It might be the case that a considerable proportion of the insects which were detected by our system were visiting epiphytes and were therefore flying just below the canopy.

The benefit of a dual-band LiDAR configuration is that the gathered complementary information of both bands can be used for species discrimination if the wing beat frequency, or other features do not deliver enough certainty for a precise species identification. Let's assume two individuals of two closely related insect species, or male and female of the same species are detected by a LiDAR system: The wing beat frequencies or the apparent size and cross-sections of body and wings of both species (or both sexes of the same species) are nearly identical, except the coloration, as it is the case for e.g. certain members of the families *Coccinellidae*, *Acrididae* or *Libellulidae* (and many more). A different coloration, especially a difference in darkish/brownish color patterns would naturally mean a difference in the absorption/diffuse reflection characteristics in the two signal bands at 808nm and 980nm. A difference in the ratio of both bands would mean that both observations mentioned above would be in fact members of different species (or members of the same species but different sex). Observation number 4189 (see Fig. 2, B, E, H) represents an extraordinarily interesting specimen when it comes to the comparison of both signal bands. In this case, the 808nm signal (green) is considerably stronger than the 980nm signal. Moreover, due to the shifted pattern of the 2 signals (Fig. 2, H), we can deduce that the observation was an insect with 2 pairs of wings. The 808nm band in Fig. 2, H features about double as many peaks as the 980nm band. Most interestingly, the missing peak in the 980nm band of Fig. 2, H allows us to deduce further that the ventral side of one pair of the wings has different reflective characteristics than the ventral side of the other pair of wings. An alternative explanation would be that the single peak in Fig. 2, H represents the signal of a beetle's elytron which did not perform the full upstroke/downstroke amplitude during the wingbeat cycle (https://youtu.be/1Wnd6c42w7w?si=JSQzbA6Tk3Pe8f8n 3:56)

As already mentioned in the results, there is a weak trend of larger insects being recorded at higher altitudes. This might be simply since the system naturally is prone to detect larger insects at higher distances at a higher rate due to the stronger signal they create in contrast to smaller insects. In this report, we demonstrate that the dual-band LiDAR method in combination with a few simple calculations of e.g. the skewness and the kurtosis offer an addition to the toolkit of species identification. In addition, insect group specific cross-section ratios of the 808nm and the 980nm signal will make it easy to perform rough insect group analysis to determine insect group compositions even without time and labor-intensive machine learning procedures. The simple comparison of features like the cross-sections, skewness and kurtosis of both signal-bands in combination with e.g. the calculation of the apparent size might even lead to family or even species specific signal signatures which can be filtered for in the recorded datasets.

**Acknowledgments:**

We gratefully acknowledge the invaluable contributions of Tidiane Ouattara, whose driving skills and mechanical expertise, particularly in the challenging conditions of the rainforest interior, were essential to the success of this research. We also thank forest ranger Gaege Toh Arsene for his professionalism and diligence in ensuring our safety during fieldwork.

**Competing interests:**

The authors declare that they have no competing interests.

**Author contributions:**

Conceptualization: MB, DD, ML, HM, LM, AR, JZ, BK, BA

Methodology: MB, HM, LM, ML, AR, JZ, BK

Investigation: DD, HM, AY, YG, LM, AR, BK, RB, AH, MB, JZ, ML

Resources: MB, JZ, BK, BA

Formal analysis: DD, MB

Visualization: DD, MB

Writing – original draft: DD, MB

Writing – review & editing: DD, ML, HM, AY, YG, LM, AR, BK, RB, AH, JZ, BA, MB

Supervision: MB, JZ, ML

Funding acquisition: MB, ML, JZ, BA

**Funding:**

This project has received funding from The Royal Physiographic Society of Lund (Fysiografen): the Märta and Eric Holmberg Endowment, and the European Research Council (ERC) under the European Union's Horizon 2020 research and innovation program (grant agreement No. 850463) and partially funded by the Swedish International development Agency (SIDA) through the International Science Program (ISP, Uppsala) by a grant to the African Spectral Imaging Network (AFSIN).

**Data and materials availability:**

All data are available in the main text or the supplementary materials

**References**

Genoud, A. P., Saha, T., Williams, G. M., & Thomas, B. P. (2023). Insect biomass density: measurement of seasonal and daily variations using an entomological optical sensor. In Applied Physics B (Vol. 129, Issue 2). Springer Science and Business Media LLC. https://doi.org/10.1007/s00340-023-07973-5

Gebru, A., Brydegaard, M., Rohwer, E., & Neethling, P. (2017). Probing insect backscatter cross section and melanization using kHz optical remote detection system. In Journal of Applied Remote Sensing (Vol. 11, Issue 1, p. 016015). SPIE-Intl Soc Optical Eng. https://doi.org/10.1117/1.jrs.11.016015

Popadić, A., & Tsitlakidou, D. (2021). Regional patterning and regulation of melanin pigmentation in insects. In Current Opinion in Genetics & Development (Vol. 69, pp. 163–170). Elsevier BV. https://doi.org/10.1016/j.gde.2021.05.004

True, J. R. (2003). Insect melanism: the molecules matter. In Trends in Ecology & Evolution (Vol. 18, Issue 12, pp. 640–647). Elsevier BV. https://doi.org/10.1016/j.tree.2003.09.006

Santos, V., Costa-Vera, C., Rivera-Parra, P., Burneo, S., Molina, J., Encalada, D., Salvador, J., & Brydegaard, M. (2023). Dual-Band Infrared Scheimpflug Lidar Reveals Insect Activity in a Tropical Cloud Forest. In Applied Spectroscopy (Vol. 77, Issue 6, pp. 593–602). SAGE Publications. https://doi.org/10.1177/00037028231169302

Gibson, G., & Russell, I. (2006). Flying in Tune: Sexual Recognition in Mosquitoes. In Current Biology (Vol. 16, Issue 13, pp. 1311–1316). Elsevier BV. https://doi.org/10.1016/j.cub.2006.05.053

Rydhmer, K., Bick, E., Still, L., Strand, A., Luciano, R., Helmreich, S., Beck, B. D., Grønne, C., Malmros, L., Poulsen, K., Elbæk, F., Brydegaard, M., Lemmich, J., & Nikolajsen, T. (2022). Automating insect monitoring using unsupervised near-infrared sensors. In Scientific Reports (Vol. 12, Issue 1). Springer Science and Business Media LLC. https://doi.org/10.1038/s41598-022-06439-6

Tercel, M. P. T. G., Veronesi, F., & Pope, T. W. (2018). Phylogenetic clustering of wingbeat frequency and flight-associated morphometrics across insect orders. In Physiological Entomology (Vol. 43, Issue 2, pp. 149–157). Wiley. https://doi.org/10.1111/phen.12240

Goulson, D. (2019). The insect apocalypse, and why it matters. In Current Biology (Vol. 29, Issue 19, pp. R967–R971). Elsevier BV. https://doi.org/10.1016/j.cub.2019.06.069

Outhwaite, C. L., McCann, P., & Newbold, T. (2022). Agriculture and climate change are reshaping insect biodiversity worldwide. In Nature (Vol. 605, Issue 7908, pp. 97–102). Springer Science and Business Media LLC. https://doi.org/10.1038/s41586-022-04644-x

van Klink, R., Sheard, J. K., Høye, T. T., Roslin, T., Do Nascimento, L. A., & Bauer, S. (2024). Towards a toolkit for global insect biodiversity monitoring. *Philosophical Transactions of the Royal Society of London. Series B, Biological Sciences*, *379*(1904). https://doi.org/10.1098/rstb.2023.0101

Kouakou, B. K., Jansson, S., Brydegaard, M., & Zoueu, J. T. (2020). Entomological Scheimpflug lidar for estimating unique insect classes in-situ field test from Ivory Coast. In OSA Continuum (Vol. 3, Issue 9, p. 2362). Optica Publishing Group. https://doi.org/10.1364/osac.387727

Li, M., Jansson, S., Runemark, A., Peterson, J., Kirkeby, C. T., Jönsson, A. M., & Brydegaard, M. (2020). Bark beetles as lidar targets and prospects of photonic surveillance. In Journal of Biophotonics (Vol. 14, Issue 4). Wiley. https://doi.org/10.1002/jbio.202000420

Brydegaard, M., & Jansson, S. (2019). Advances in entomological laser radar. In The Journal of Engineering (Vol. 2019, Issue 21, pp. 7542–7545). Institution of Engineering and Technology (IET). https://doi.org/10.1049/joe.2019.0598

Brydegaard, M., & Svanberg, S. (2018). Photonic Monitoring of Atmospheric and Aquatic Fauna. In Laser & Photonics Reviews (Vol. 12, Issue 12). Wiley. https://doi.org/10.1002/lpor.201800135

Arcilla, N., Holbech, L. H., & O'Donnell, S. (2015). Severe declines of understory birds follow illegal logging in Upper Guinea forests of Ghana, West Africa. In Biological Conservation (Vol. 188, pp. 41–49). Elsevier BV. https://doi.org/10.1016/j.biocon.2015.02.010

Wolda, H. (1978). Fluctuations in Abundance of Tropical Insects. In The American Naturalist (Vol. 112, Issue 988, pp. 1017–1045). University of Chicago Press. https://doi.org/10.1086/283344

Denlinger, D. L. (1980). Seasonal and Annual Variation of Insect Abundance in the Nairobi National Park, Kenya. In Biotropica (Vol. 12, Issue 2, p. 100). JSTOR. https://doi.org/10.2307/2387725

Grøtan, V., Lande, R., Engen, S., Sæther, B., & DeVries, P. J. (2012). Seasonal cycles of species diversity and similarity in a tropical butterfly community. In Journal of Animal Ecology (Vol. 81, Issue 3, pp. 714–723). Wiley. https://doi.org/10.1111/j.1365-2656.2011.01950.x

Valtonen, A., Molleman, F., Chapman, C. A., Carey, J. R., Ayres, M. P., & Roininen, H. (2013). Tropical phenology: bi-annual rhythms and interannual variation in an Afrotropical butterfly assemblage. In Ecosphere (Vol. 4, Issue 3, pp. 1–28). Wiley. https://doi.org/10.1890/es12-00338.1

Crespo-Pérez, V., Kazakou, E., Roubik, D. W., & Cárdenas, R. E. (2020). The importance of insects on land and in water: a tropical view. In Current Opinion in Insect Science (Vol. 40, pp. 31–38). Elsevier BV. https://doi.org/10.1016/j.cois.2020.05.016

Macgregor, C. J., & Scott-Brown, A. S. (2020). Nocturnal pollination: an overlooked ecosystem service vulnerable to environmental change. In A. Scott-Brown & H. Koch (Eds.), Emerging Topics in Life Sciences (Vol. 4, Issue 1, pp. 19–32). Portland Press Ltd. https://doi.org/10.1042/etls20190134

Buxton, M. N., Gaskett, A. C., Lord, J. M., & Pattemore, D. E. (2022). A global review demonstrating the importance of nocturnal pollinators for crop plants. In Journal of Applied Ecology (Vol. 59, Issue 12, pp. 2890–2901). Wiley. https://doi.org/10.1111/1365-2664.14284

Landmann, T., Schmitt, M., Ekim, B., Villinger, J., Ashiono, F., Habel, J. C., & Tonnang, H. E. Z. (2023). Insect diversity is a good indicator of biodiversity status in Africa. In Communications Earth & Environment (Vol. 4, Issue 1). Springer Science and Business Media LLC. https://doi.org/10.1038/s43247-023-00896-1

Noskov, A., Bendix, J., & Friess, N. (2021). A Review of Insect Monitoring Approaches with Special Reference to Radar Techniques. In Sensors (Vol. 21, Issue 4, p. 1474). MDPI AG. https://doi.org/10.3390/s21041474

Brydegaard, M., Malmqvist, E., Jansson, S., Zhao, G., Larsson, J., & Török, S. (2017). The Scheimpflug lidar method. In U. N. Singh (Ed.), Lidar Remote Sensing for Environmental Monitoring 2017. SPIE. https://doi.org/10.1117/12.2272939

Wallace, J. R. A., Reber, T. M. J., Dreyer, D., Beaton, B., Zeil, J., & Warrant, E. (2023). Camera-based automated monitoring of flying insects (Camfi). I. Field and computational methods. In Frontiers in Insect Science (Vol. 3). Frontiers Media SA. https://doi.org/10.3389/finsc.2023.1240400

Le Houérou, H. N. (2009). Bioclimatology and Biogeography of Africa. Springer Berlin Heidelberg. https://doi.org/10.1007/978-3-540-85192-9

Raguso, R. A. (2020). Don’t forget the flies: dipteran diversity and its consequences for floral ecology and evolution. In Applied Entomology and Zoology (Vol. 55, Issue 1, pp. 1–7). Springer Science and Business Media LLC. https://doi.org/10.1007/s13355-020-00668-9

Micheneau, C., Fournel, J., Warren, B. H., Hugel, S., Gauvin-Bialecki, A., Pailler, T., Strasberg, D., & Chase, M. W. (2010). Orthoptera, a new order of pollinator. In Annals of Botany (Vol. 105, Issue 3, pp. 355–364). Oxford University Press (OUP). https://doi.org/10.1093/aob/mcp299

Pakum, W., Kongbangkerd, A., Srimuang, K.-O., Gale, S. W., & Watthana, S. (2019). Reproductive biology of a rare, fly-pollinated orchid, Bulbophyllum nipondhii Seidenf., in Thailand. In Flora (Vol. 260, p. 151467). Elsevier BV. https://doi.org/10.1016/j.flora.2019.151467

Bostock, E., Green, E. W., Kyriacou, C. P., & Vanin, S. (2017). Chronobiological studies on body search, oviposition and emergence of Megaselia scalaris (Diptera, Phoridae) in controlled conditions. In Forensic Science International (Vol. 275, pp. 155–159). Elsevier BV. https://doi.org/10.1016/j.forsciint.2017.03.002

# Paper VI

# 3D-Printed Fluorescence Hyperspectral Lidar for Monitoring Tagged Insects

Hampus Månefjord, Lauro Müller, Meng Li, Jacobo Salvador, Sofia Blomqvist, Anna Runemark, Carsten Kirkeby, Rickard Ignell, Joakim Bood, and Mikkel Brydegaard

***Abstract*—Insects play crucial roles in ecosystems, and how they disperse within their habitat has significant implications for our daily life. Examples include foraging ranges for pollinators, as well as the spread of disease vectors and pests. Despite technological advances with radio tags, isotopes, and genetic sequencing, insect dispersal and migration range remain challenging to study. The gold standard method of mark-recapture is tedious and inefficient. This paper demonstrates the construction of a compact, inexpensive hyperspectral fluorescence lidar. The system is based on off-the-shelf components and 3D printing. After evaluating the performance of the instrument in the laboratory, we demonstrate its efficient range-resolved fluorescence spectra in situ. We present daytime remote ranging and fluorescent identification of auto-powder-tagged honey bees. We also showcase range-, temporally- and spectrally-resolved free-flying mosquitoes, which were tagged through feeding on fluorescent-dyed sugar water. We conclude that violet light can efficiently excite administered sugar meals imbibed by flying insects. Our field experiences provide realistic expectations of signal-to-noise levels, which can be used in future studies. The technique is generally applicable and can efficiently monitor several tagged insect groups in parallel for comparative ecological analysis. This technique opens up a range of ecological experiments, which were previously unfeasible.**

***Index Terms*—Laser radar, fluorescence, hyperspectral sensors, remote sensing, environmental monitoring, instrumentation, ecology, pollination, disease vectors.**

## I. Introduction and Motivation

POWDER tagging can be what ring marking is for ornithology, what staining is for microscopy, or what isotopic labelling is for tomography, but for ecological entomology. The ability to mark insects significantly increases detection certainty and specificity compared to classification by intrinsic properties[1], [2], such as cross sections, spectral- or polarimetric properties, and wing beat modulation. In addition, marking allows for the detection of specific individuals, enabling assessment of insect lifetimes[3], population densities[4], and dispersal in the landscape[5], approaches, which have been the cornerstones in numerous entomological studies. Moreover, marking and detecting insects is crucial for monitoring the dispersal and survival of biological control agents in different habitats. In particular, marking and detecting insects have been used to investigate the interaction between predators and parasitoids, as understanding their movement is important for crop management[6]. Powder tagging also enables interaction experiments, involving cross contaminations between, *e.g.,* pollinators and flowers, or as indicators of mating[7]. Except for a few larger species[8], [9], most insects are too small to carry harmonic tags, GPS, or radio devices. Remote sensing, such as radar[10], [11] and lidar[12], [13], can potentially measure insect fluxes in the landscape, but specificity is limited, and flux assessment does not provide information on the migration or dispersal range, or tracking of individuals. Lastly, marking and detection procedures may be used to estimate the population size of insects in a given area.

Lidar is a particularly interesting and efficient active approach to monitor insects[14]. As opposed to sonar, atmospheric attenuation, $\mu_{att.}$, of light can be less than a $km^{-1}$, and as opposed to radar, the outgoing lidar beam can be collimated. The collimated lidar beam implies that signal loss is dominated by the omnidirectional backscattering, and the attenuation is dependent on the squared return distance, whereas radar typically attenuates by the distance to the fourth power (round trip). The simultaneous ranging and intensity measures of lidar allow the estimation of the fraction of light reaching the aperture and, thus, enable quantification of scattering and fluorescence to some extent[15].

The collimated beam and tunnel vision of lidar systems allow illumination and high detection sensitivity of large probe volumes, even with limited laser power. This is due to the fact that the same light transverses the probed air transect and, thus, light is recycled meter by meter, unless attenuated by an object in the transect. Consequently, entomological lidar[16] yields more observations over time compared to, *e.g.*, sensors or E-traps[17], [18] with a limited probe volume.

Early work demonstrated fluorescence detection of marked insects using lidar [19], but the instrumentation was inefficient in terms of observation counts, and the system was excessively bulky, preventing widespread replication and usage. Over the last decade, topographical lidar technology has undergone

Manuscript received December 13, 2021; revised March 9, 2022; accepted March 22, 2022. Date of publication March 25, 2022; date of current version April 21, 2022. This work was supported by the Swedish Research Council and FORMAS. *(Corresponding author: Hampus Månefjord.)*

Hampus Månefjord, Lauro Müller, Meng Li, Jacobo Salvador, Sofia Blomqvist, Anna Runemark, and Joakim Bood are with the Department of Physics and Department of Biology, Lund University, SE-221 00 Lund, Sweden (e-mail: hampus.manefjord@forbrf.lth.se; lauro.mueller@hotmail.com; meng.li@forbrf.lth.se; jacobo.salvador@forbrf.lth.se; sofia.blomqvist@biol.lu.se; anna.runemark@biol.lu.se; joakim.bood@forbrf.lth.se).

Carsten Kirkeby is with the Copenhagen University, 1165 København, Denmark (e-mail: ckir@sund.ku.dk).

Rickard Ignell is with the Swedish Agricultural University, 23053 Alnarp, Sweden (e-mail: rickard.ignell@slu.se).

Mikkel Brydegaard is with the Department of Physics and Biology, Lund University, SE-221 00 Lund, Sweden, and also with the Norsk Elektro Optikk A/S, 0667 Oslo, Norway (e-mail: mikkel.brydegaard@fysik.lth.se).

Color versions of one or more figures in this article are available at https://doi.org/10.1109/JSTQE.2022.3162417.

Digital Object Identifier 10.1109/JSTQE.2022.3162417

tremendous development and miniaturization. This has offered many novel ecological applications for profiling vegetation structure[20], which affects the abundance and composition of the fauna[21], and can now be used to assess insect defoliation[22]. The depth information gained from airborne lidars yields complementary information to hyperspectral imaging, discriminating molecular compositions. Examples are today well-established on satellites, airplanes, and drones[23], [24].

The need for improved specificity has spurred the development of multiband lidar[*e.g.*, 25, 26], and extensive efforts for combining data from vegetation lidar and hyperspectral imaging have been conducted[*e.g.*, 27]. The method of fusing lidar and hyperspectral imaging signals is challenging, since the harmonic pulses of the lidar at distinct ranges are difficult to match to individual pixels of the hyperspectral image. Advanced multiband lidar concepts, including fluorescence lidar have been presented over the last two decades[28]–[32]. These time-of-flight systems are based on pulsed solid-state lasers and ultraviolet harmonics through gated-imagers, spectrometers, or multi-anode PMT arrays. None of these concepts provide at the same time: a) full-waveforms range echo, b) hyperspectral signatures, and c) continuous time series.

Full waveform hyperspectral short-range time-of-flight lidars have been reported based on super-continuum sources[33], [34]. Such fiber lasers are, however, limited to low peak powers and high repetition rates, and the approach can therefore not be scaled up to long-range remote sensing, because the maximum unambiguous range is the speed of light over twice the repetition rate. This limitation does not exist for continuous-wave Scheimpflug lidars[35]. Scheimpflug lidars can be rescaled to cover both short[36] and long ranges[37]. The Scheimpflug method can be extended to full waveform real-time hyperspectral lidar based on image sensors and laser diode devices[38], [39]. Applications have included aquatic profiling[40] and vegetation profiling from drones[41].

In this work, we further develop the design principles of fluorescence hyperspectral Scheimpflug lidar, and demonstrate a compact, low-cost instrument built with off-the-shelf components and 3D printing. Compared to previous aquatic work based on blue 445 nm lasers and shorter ranges, this instrument is based on violet laser at 401 nm and working distance up to 100 m in air. We show that fluorescence can simultaneously be resolved in range, time, and photon energy (wavelength) from free-flying tagged insects in full sunlight. Furthermore, we demonstrate the feasibility of detecting insects fed by a fluorescent sugar solution.

## II. Instrument Design

Here, we present the initial design considerations, raytracing optimization, and the fabrication with 3D printed parts. The complete system overview is provided in Table I.

### A. First-Order Design

The fluorescence hyperspectral lidar derives from earlier projects of Scheimpflug lidar[36], [42], [43], and its hyperspectral variety[44], [45], as well as the geometry and design details have been thoroughly revised[35], [46], [47]. Hyperspectral Scheimpflug lidar is based on the combination of Scheimpflug lidar and hyperspectral push-broom imaging[48].

TABLE I
System Specifications of the Fluorescence Hyperspectral Lidar

| Parameter | Symbol | Quantity | Unit |
|---|---|---|---|
| **Transmitter** | | | |
| Transmitted wavelength | $\lambda_{ex}$ | 401 | nm |
| Lidar power | $P$ | 1 | W |
| Expander diameter | $Ø_{exp}$ | 25 | mm |
| Expander focal length | $F_{exp}$ | 75 | mm |
| Slant angle | $\varphi$ | 0..3 | ° |
| Laser chip size | | 3x50 | µm |
| Beam divergence (transversal) | | 0.4 | mrad |
| Beam convergence (baseline axis) | | 0.15 | mrad |
| **Receiver** | | | |
| Receiver diameter | $Ø_{rec}$ | 75 | mm |
| Receiver focal length | $F_{rec}$ | 300 | mm |
| Field-of-View | $FoV$ | 0.7x57 | mrad |
| Range | $r$ | 5..100 | m |
| Range resolution | $\Delta_r/r$ | 5..10 | % |
| Range of half overlap | $r_0$ | 11 | m |
| Shape factor | $\gamma$ | 7 | |
| **Spectral analyzer** | | | |
| Spectral range | $\lambda$ | 400..800 | nm |
| Spectral resolution | $\Delta\lambda$ | ~6.7 | nm |
| Slit-imager magnification | M | 2:1 | |
| Number of effective bands | | 71 | # |
| Slit width | | 200 | µm |
| **Imager** | | | |
| Pixel pitch | $\ell_{pix}$ | 5.89 | µm |
| Number of pixels | $N_{pix}$ | 1920x1200 | # |
| Max sample rate | $f_s$ | 124 | Hz |
| Signal-noise ratios demonstrated | $SNR$ | 22..950 | |
| Dynamic range | | 12 | bits |
| **System** | | | |
| Baseline separation | $D$ | 324 | mm |
| Slit tilt | $\alpha$ | 39.5 | ° |
| Power consumption (not PC) | $P_{tot}$ | 11 | W |
| System footprint (not PC) | | 30x50x9 | cm |
| Weight (not PC) | | ~3 | Kg |
| Bill of materials (not PC) | | ~2715 | € |

Briefly, the Scheimpflug principle[49] allows sharp focusing across wide ranges despite using a large aperture. This is accomplished by letting the object plane, the lens plane, and the image plane intersect. For a Scheimpflug lidar, the object plane is comprised of an air transect illuminated by a laser beam (see Fig. 1a). In addition to the Scheimpflug condition, which does not consider focal lengths, the so-called hinge rule relates the focal plane of the optics to the object- and image planes (see Fig. 1a).

As a rule of thumb, a larger tilt of the detector (here slit) -plane implies a decreased triangulation resolution. A benefit, however, is a shorter lidar baseline, and, thus, a more compact system. We designed our lidar to cover a range from 5 m to 100 m, which was accomplished by an f300 mm, ø75 mm receiver achromat, a transmitter-receiver baseline separation, $D$, of 32.4 mm, a slit tilt angle, $\alpha$, of 39.5°, and a slant angle, $\varphi$, of 2° (the angle between the optical axis of the transmitter and receiver).

Spectral dispersion of received light is accomplished perpendicularly to the ranging axis (see spectral analyzer sketch in Fig. 1b). We employed the prism-grating-prism (PGP) method[48], with an ensemble of an f100 mm achromat, a 6° wedge, a 300 groove/mm transmission grating, a 4° wedge, and an f50 mm achromat. The purpose of the two wedges is

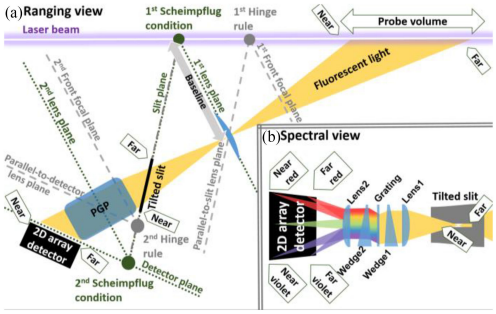


Fig. 1. a) First-order design approach to hyperspectral lidar using two consecutive sets of Scheimpflug conditions and hinge rules. The first Scheimpflug condition relates the violet laser beam to the receiver lens- and slit-plane, whereas the second Scheimpflug condition relates the slit-plane to the spectrometer- and detector-plane. Note that the angle between the receiver and the laser axes is exaggerated in this drawing. In reality, it is approximately 2°, which elongates the probe volume. b) Orthogonal sketch showing the dispersion of photon energies by a prism-grating-prism method (PGP).

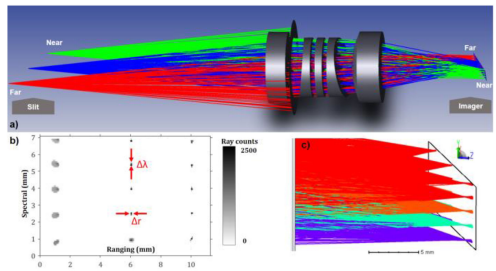


Fig. 2. Screenshots from raytracing simulation and optimizations of the spectral analyzer. a) From left; polychromatic light-cone point sources at three positions along the tilted slit propagate through the prism-grating-prism assembly and form a range-photon energy image on the imager. The colors of the rays represent the different source points along the slit b) Point spread functions of the ray bundles across the imager. c) Close-up of beam waists or ray bundles, the focus for closer ranges was down-prioritized since the triangulation principle of bistatic lidars counteract this effect. The colors of the bundles represent [as opposed to in (a)] the wavelength of the light.

to get the optimal incidence angle of the light onto the blazed grating, while keeping the optical path coaxial.

The f-number of the spectrometer optics needs to be smaller than the f-number of the collecting optics to capture the light cone across the slit efficiently. Systems covering one octave (*e.g.*, 400-800 nm), such as the one presented here, require gratings with the lowest available groove per millimeter. In order to fit the entire spectral range onto our imager (Sony IMX174 CMOS in a Basler acA1920-155 um camera), the setup required a slit-to-imager magnification of 2:1. This suggests a detector tilt of 39.5°/2 ≈ 20°. Since the area of the imager is 11.3 mm x 7.1 mm, the magnification implies that 22.6 mm of the slit is imaged onto the imager. To accomplish a decent signal strength at fast sample rates, we chose a moderate spectral resolution with a slit width of 200 µm. Considering the magnification of the spectral analyzer, this potentially provides 2·7.1 mm/200 µm = 71 effective spectral bands across the imager.

### B. Raytracing

The Scheimpflug condition and hinge rule are similar to the first order reciprocal truncation, the thin lens formula. In practice, the achromats, wedges, and grating account for several cm of glass with different refractive indices. Consequently, the optimal design deviates substantially from thin lens approximations. Raytracing was implemented in OpticStudio (Zemax, USA) to model the light through the spectral analyzer. The initial setup was based on the Scheimpflug- and hinge rules, as described in the previous section. The raytracing used three F/4 light cones sources from the near, middle, and far end of the slit as sources. Each source consisted of five wavelengths, 400, 480, 560, 640, 720, and 800 nm. In total 15 ray bundles impinged on the imager, three along the ranging axis, and five along the spectral axis (Fig. 2).

The distance and the tilt of the imager were adjusted to minimize the point spread function of all 15 ray bundles ($\Delta\lambda$ and $\Delta r$ in Fig. 2b). In practice, the point solutions are convoluted by the imaged slit width (100 µm). Thus, the spot size should ideally match this size in the spectral domain. Since Scheimpflug lidar is based on the triangulation principle, range resolution deteriorates with range. Therefore, focusing in the ranging domain should be prioritized for the far end of the imager (Fig. 2b and 2c). Stray light, ghost reflections, and the $0^{th}$ diffraction order from the grating could also be traced. This was, however, not pursued in this initial test.

### C. 3D Printed Spectral Analyzer

The spectral analyzer is comprised of five optical elements of various shapes, with minimal spacing. Mounting them with conventional photonic lab supplies would be both challenging and costly. Furthermore, precise alignment of the pieces would not be guaranteed. Instead, we proceeded with the optimized parameters from the raytracing and designed a sandwich structure for additive filament 3D printing. The sandwich concept implies cutting the envisioned optical design into two similar blocks, in which the optical path and slots for the optical components were removed.

3D printing offers numerous simplifications over conventional optical design approaches, such as CNC milling. Considerations, such as the effects of the size of the milling tool, and the problem of milling right-angle corners are not present in the additive manufacturing. Precise baffles, matching the light cones, were added along the optical path in order to prevent forward scattered light.

The sandwich structure was printed in black PLA (PLA-DF02, Dremel, USA), with a fill factor of 100% on a commercial 3D printer (Dremel 3D45, USA) with 200 µm layer height. The used filament was opaque but glossy. We learned that a limited number of baffles, spaced along the light pipe, was optimal for suppressing stray light. In addition, maximal internal fill factor was not required. The structural integrity was ensured by steel rods through the assembly, see Fig. 3. Carbonized and antistatic alternative filaments, which could reduce the glossiness are available at a higher cost.

After the initial 3D-printing trials, dimensions for screw- and rod holes, and the slots for optical elements, had to be adjusted

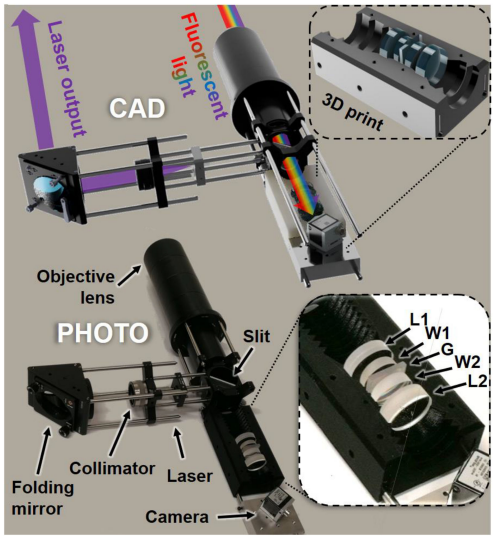


Fig. 3. CAD drawing and photograph of the complete hyperspectral lidar, partly made from a commercial optical cage system, with precision kinetic mechanisms for aligning beam field of view overlap and divergence, as well as slit positioning. The 3D-printed sandwich structure (seen in the two insets) had its top part removed to reveal the lenses L1 and L2, wedge prisms W1 and W2 and the transmission grating G. .

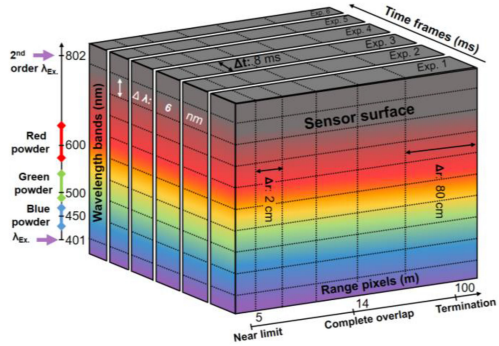


Fig. 4. The data acquired by the hyperspectral lidar contains information about range and wavelength, which are imaged onto the horizontal and vertical direction of the imager. Time is resolved by stacking camera exposures. The resolution and range in the three dimensions are indicated in the figure. Specific system values are indicated, such as the wavelength of the laser and the fluorescent powders used, the near limit, the range of complete overlap, and the position of the termination board.

with a margin for the nozzle width of the 3D printer. The precision, structural stability, and rigidness of the spectral analyzer sandwich structure were satisfactory. Long-term degradation seems unlikely because a steel rod cage system was embedded along the optical path, and steel bolts clamped the two sandwich parts together. Fig. 3 displays the 3D model, and the prototype of the entire lidar, including the bottom part of the spectral analyzer, revealing the internal optical elements.

## III. Calibration and Performance

The hyperspectral lidar acquires backscattering and fluorescence intensity counts (12 bit), as a function of time, distance, and photon energy (see Fig. 4). The spectral range covers the excitation wavelength, the fluorescence spectra of different powder dyes, and the entire visible range. The spectral range also includes the second-order diffraction of the excitation wavelength, which may be used as spectral calibration. The time-domain information is acquired as a sequence of images, and the frame rate is limited by the exposure time and the USB3 transfer speed.

Our customized acquisition program was made in LabVIEW (National Instruments, USA). The program acquires a sequence of images, with parameters, such as the number of images, their binning, exposure time, and gain, being real-time customizable. The collected sequence of images, in the form of a data cube (see Fig. 4), is visualized in the interface of the program. The mean image, averaged over time, the lidar echo (intensity *vs*. range) of selected spectral bands, the average spectrum of a selected range region, and a time-range map are all visualized, while the system acquires the lidar signal. The image cubes are then continuously saved as raw files, with time-stamped filenames.

### A. Spectral Calibration

A spectral calibration procedure investigated the mapping from pixel number to wavelength, in nanometer, along the spectral dimension. The spectral analyzer was removed from the lidar system, and the slit was directed towards an ø200 mm integration sphere coated with $BaSO_4$ (Oriel, USA). Light from a spectral cadmium (Cd) lamp, with known spectral lines, was injected into the sphere through another port. The sphere provides a homogenous Lambertian light field. The resulting intensity image on the imager can be seen in Fig. 5a. Four atomic cadmium spectral lines are observed with wavelengths of 467.8, 480.0, 508.6, and 643.8 nm (Fig. 5d). The full width at half maximum (FWHM) of the 5s5p-5s6s transition (508.6 nm) was measured satisfactory at the far- and mid-range of the slit to 5.5 and 7.6 nm. However, in the near range, the spectral resolution deteriorated to 30 nm.

For the same atomic line, the shift of the spectral registration along the range axis was studied, by finding the center of mass (CoM) and the standard deviation (SD) of the signal (Fig. 5c). The CoM and SD account for the first two statistical moments, and are used to quantify spectral misregistration effects, such as keystone and smile[50]. The pixel-to-wavelength mapping could best be described by first-order polynomials. The first coefficient varied from 348 to 338 nm from the near to the far end of the imager, and the second polynomial coefficient varied from 0.369 to 0.385 nm/pixel. This change in the polynomial coefficients quantifies the keystone effect. The coefficients varied linearly across the range, thus, no smile was detected. Correcting the artifact by image transformation, and wrapping, induces interpolation errors. Another approach would be to use range-dependent spectral calibration.

*In situ*, the lidar provided an auto-calibration feature; both the elastic (401 nm) backscattering from the atmosphere, and its

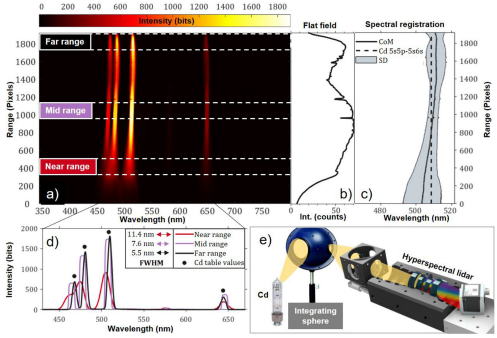


Fig. 5. Laboratory calibration and performance tests. a) Light distribution on the CMOS image chip when the spectral analyzer was presented with a homogeneous light-field of a cadmium (Cd) spectral lamp. b) The mean intensity along the ranging direction of the hyperspectral lidar was obtained by averaging over the complete spectral range. The intensity goes down in the extreme ends of the range, and its shape changes slightly with the positioning of the spectral analyzer relative to the integrating sphere port. c) The spectral registration of light from the 508.6 nm atomic line (the Cd 5s5p-5s6s transition) is described with the center of mass (CoM) and standard deviation (SD) of intensity on the imager. d) The spectrum of the spectral cadmium lamp is shown for the far, mid, and near range as indicated in (a). A shift in the peak wavelength and the smearing of the 467.8 and 480.0 nm lines can be seen for the near range, and smearing increases further at the extreme near range. e) The experimental configuration included a Cd spectral lamp illuminating an integrating sphere, and the spectral analyzer was directed toward another port of the sphere.

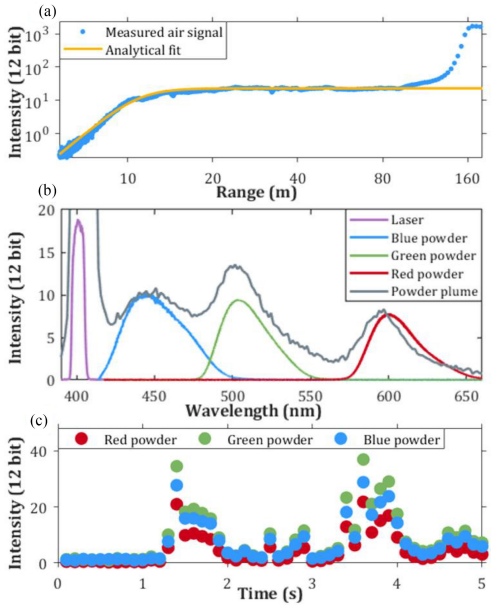


Fig. 6. a) Elastic backscattering lidar signal from the air. The lidar transect is terminated at a board 166 m away. The analytical function (1) is fitted to the air signal with $r_0 = 11$ m and $\gamma = 7$. b) Remotely retrieved spectrum for the powder plume containing elastic backscattering, and fluorescence from released plume of all three powders; the axis indicates lidar intensity counts. The individual spectra of the laser, and each powder, as measured with a compact spectrometer in the lab. c) The average intensity of the recorded fluorescence of each powder over time near the release point of the plume.

second-order diffraction (fake 802 nm light), was observable as two narrowband signals. Spectral calibration was thus always available as an interpolation between these lines.

### *B. White Calibration*

The spectral response of the instrument is primarily governed by the spectral sensitivity of the CMOS imager, and the efficiency curve of the grating. Light from a halogen tungsten filament was injected into the integrating sphere. The source spectrum was assumed to be a 3000 K Planck black body distribution. The measured peak response was identified in the 500-600 nm region, but sensitivity extended over the full spectral range. The response was ∼25% of the peak value in the extremes at 400 nm and 800 nm. This suppression was somewhat beneficial, since no suppression filter for the elastic excitation light was used, which is desirable when capturing elastic and fluorescence light within the same dynamic range. A steep spectral response will have the effect of shifting observed fluorescence features towards the center if not compensated for. In our case, however, this effect was minimal.

### *C. Flat Field Calibration, Lidar Form Factor, and Cross-Sections*

The homogeneous light field from the integrating sphere measurements provides the intensity along the slit (Fig. 5b). A partial shielding of the light cones, at the extremes of the slit, resulted in an attenuation of the response at the outermost near and far ends. The effect could be addressed by lowering the f-number of the spectral analyzer or by reducing the slit-detector magnification. We noted from Fig. 5b that at least 85% of the imager could be used in the ranging domain.

The actual range response of the lidar in the field was a combined effect of the aforementioned flat-field calibration and the beam-FoV overlap. The curve can be expressed analytically[51], although the gold standard[52] is to use the tabulated Raman cross-section of a bulk signal of, *e.g.*, $N_2$, $O_2$ (or $H_2O$ in aquatic lidar). Instead, we used a previously described analytical model for Scheimpflug lidars[53],

$$G_{overlap(r)} = \frac{1}{1 + \left(\frac{r_0}{r}\right)^{\gamma}} \tag{1}$$

Here, $r_0$ is the range of half overlap, and $\gamma$ is a shape factor. In the field, the lidar provides an intrinsic form-factor calibration, since the homogenous and static air signal will continuously report the system-range sensitivity curve. We used this elastic air signal from the field experiment (see Fig. 6a), and identified $r_0 = 11$ m and $\gamma = 7$. The intensity counts of the measured air signal at 50 m range averaged 21 counts, while the noise (SD over time) was 0.96 counts. This gives a signal-to-noise ratio (SNR) of 22.

Whereas the air signal can be flat beyond complete overlap (as seen in Fig. 6a), fluorescent echoes from solid targets will decrease by $r^2$. It is possible to compensate for the $r^2$ decrease to

some extent by the increasing slope of Eq. 1. However, the field of quantitative fluorescence cross-sections is poorly developed, possibly due to the scarce availability of fluorescence lidars. More details on elastic lidar cross-sections can be found in[53].

### D. Range Calibration

The Scheimpflug range calibration relies on precise geometric information about the system. A position along the slit is converted into an observation angle with the receiver lens as a pivot. The range can then be estimated by triangulation, given that the baseline separation and the observation angle are known. The range for each pixel, $r_{pix,}$ is described by

$$r_{pix(n)} = D\frac{F_{rec} + nM\ell_{pix}\left(\sin\alpha - \cos\alpha\cot\varphi\right)}{F_{rec}\cot\varphi + nM\ell_{pix}\left(\sin\alpha\cot\varphi + \cos\alpha\right)} \quad (2)$$

in which $D$, $F_{rec}$, $M$, $\ell_{pix}$, $\alpha$, and $\varphi$ are system parameters found in Table I, and $n$ is a running index from 1 to $N_{pix}$. The details and derivation of Eq. 2 are found in[47]. The pixel-to-range mapping can, however, also accurately be approximated by a squared relation[46]. The ranging accuracy deteriorates with range. However, ranging precision can be improved at far ranges, at the expense of range precision in the short range, by choosing an adequate beam expander aperture and a convergent beam[35], [54]. Consequently, the range resolution can deteriorate linearly. We estimate the ranging accuracy to approximately 6% for the present system.

## IV. Examples of Field Applications

Several field applications were investigated at Stensoffa Field Station located in southern Sweden. The fluorescence hyperspectral lidar was mounted on an astronomical tripod (EQ8, SkyWatcher, Canada) placed in a carport tent for weather protection.

### A. Powder Plume Releases

Plume-release experiments are often performed within different variations of lidar research. Such experiments can have several different purposes, *e.g.,* characterizing a lidar system or examining the measurement possibilities for a specific lidar. Other possibilities include fundamental research, *e.g.*, in studies of biological aerosols or to detect biological warfare agents [see, e.g., 31 and references therein]. Measurements in plumes of different particles and smoke have also been performed with Scheimpflug lidar to investigate the potential for particle classification and sizing[55], [56].

In the present work, as an initial proof-of-concept study, released plumes of mixed fluorescent powders were investigated with the Scheimpflug-lidar system. An equal mixture of red, green, and blue fluorescent powder (UV Holi powder, Paint-Glow, U.K.) was released in the vicinity of the lidar transect. The imager was set to 100 ms exposure time, a gain of 24 and 2x4 binning (4 along the spectral axis). The spectral intensity profile of the powder mixture was captured at the range of release 50 m from the lidar at a single exposure (Fig. 6b). The intensity variation at the release point over time was recorded (Fig. 6c).

### B. Powder Tagged Bees for Foraging Range Assessment

Pollination is an ecosystem service, which is crucial for food production[57]. By marking bees from known hives and tracking them over fields, we can gain fundamental insights into their ecology, facilitating the use of beehives as pollination services. Moreover, in the face of insect decline[58]–[61], a solid understanding of how honey bees impact wild pollinators is crucial for maintaining pollination services from wild insects. Powder tagging provides a powerful tool to study interactions between bees from specific hives and untagged wild insects. Several hives could also be distinguished by tagging with spectrally distinct fluorescent powder to study how spatial distributions from hives perturb each other. This approach, hence opens up novel research questions on species interactions.

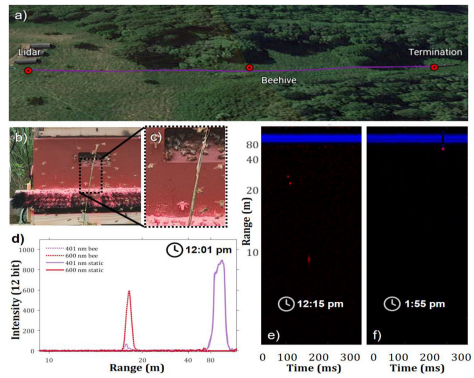


Fig. 7 a) The lidar transect over a meadow at Stensoffa field station. The beam was terminated 100 m from the lidar. Forest surrounds the transect, but no trees are in the vicinity of the beam. A beehive with a fluorescent marking tray was located at 55 m from the lidar at the ground, 1 m below the beam. b) The beehive with the attached powder tray and a broom. c) Several powdered bees are flying around the hive. d) The signal acquired by the hyperspectral lidar shown as an echo for a time during which a bee is in the beam, and a static time during which nothing is obstructing the beam before the termination. For both instances, the elastic signal (397-406 nm) and the red fluorescent signal (585-615 nm) are shown in violet and red, respectively. The SNR of the fluorescent signal was 177 compared to 20 of the elastic. e,f) Two selected occurrences of marked bees entering the beam during full daylight. The intensities of the red and elastic spectral band are shown as the red and blue channels of the RGB image, in which the axes represent time and range. A reduction of the elastic termination signal is seen at the same time of the bee occurrence in e), which is caused by the extinction cross-section of the bee in the beam.

In this work, a powder-marked bee monitoring experiment was conducted. The lidar transect spanned a meadow of varying vegetation, before reaching a laser beam termination screen 100 m away. A beehive was situated at 55 m along the lidar transect (Fig. 7a).

Auto-marking of the bees was accomplished by attaching a tray with red dye powder under the entrance of a beehive; similar methods have been applied in previous work[62]. In our implementation, a powdered broom was mounted above the entrance to ensure automatic marking of bees as they departed from the hive (Fig. 7b and 7c).

The experiment was conducted over three days, and the powder tray was refilled each morning at 7:30 am. Subsequently, the hyperspectral lidar was started. The lidar collected data during the day until 8 pm, at which time no more honey bees were active. Several marked bees were observed with the lidar, corresponding to registered occurrences in time-range plots (Fig. 7e and 7f), or

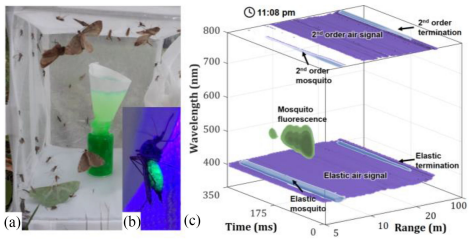


Fig. 8. a) Insects collected from a $CO_2$ trap were moved to a cage with a dyed sugar solution. b) A mosquito fed with fluorescent sugar water, lit by a violet torch. c) A released marked mosquito entered the lidar beam. The resulting signal is presented as colored iso-surfaces in time, range and wavelength, which is the full data cube collected by the lidar (compare to Fig. 4).

echoes in range-intensity diagrams (Fig. 7d). The imager was set to 124 Hz framerate, 7 ms exposures, 24 gain, and 4x4 binning. The fluorescence signal from the bee corresponding to the echo shown in Fig. 7d peaked at 595 intensity counts, averaged over a red spectral window from 585 nm to 615 nm. The noise (SD) of this window was 3.4 counts, which gives an SNR of 177. From the insignificant reduction of the termination echo, we understand that this individual bee intersects the beam peripherally.

### C. Sugar Feeding With Fluorescence Dyes

Previous studies have used sugar feeding to mark insects, *e.g.*, to monitor the proportion of released sterile mosquitoes, both with radioactive isotopes[63], fluorescent markers[64], of which some can even mark the seminal fluid of males, facilitating monitoring of mosquito mating behavior, and non-fluorescent markers[65]. Sugar feeding has also been used to kill insects with toxic baits[66].

One of the most valuable aspects of marking insects alive, and then releasing and detecting them again, is to estimate the population size in a habitat[6]. This method can provide insight into the effectiveness of control measures, such as bed nets and the removal of breeding sites for specific species of mosquitoes.

In our work, a combined light- and $CO_2$-trap (Model 1212, John W. Hock Company, USA) was operated near a lakeshore inside the forest at Stensoffa, approximately 100 m from the lidar beam, shielded by trees. The trap was baited with $CO_2$, from dry ice, and set overnight 6:00 pm, 9$^{th}$ August 2021. The live catch was emptied into a cage the following day at 8:00 am. The catch contained predominantly mosquito species, but also moths and blackflies (Fig. 8a). The species were kept in the cage over the day along with a vial of 10% sugar solution with a dissolved green fluorescence marker pen (Q-connect, Belgium), and a coffee filter, allowing the insects to land and feed on the solution (Fig. 8a). Using a violet (405 nm) LED torch, we could verify that both mosquitoes and moths had fed from the sugar solution, by the green fluorescence in their abdomen (see Fig. 8b).

At 11:00 pm the fluorescent sugar-fed specimens were carefully released one by one under the beam at 15 m distance from the lidar. The specimens were detected directly upon their release, and at later instances when transiting the beam again. Fig. 8c displays one case of a free-flying sugar-fed mosquito entering the beam. The visualization displays registered light intensity as a function of time, range, and wavelength (photon energy). Semi-transparent iso-surfaces at 500, 1000, 1500, and 2000 counts encircles the green fluorescence at 12 m, the elastic backscattering from the mosquito, the elastic air scatter, and the termination at 100 m distance. The imager was operated at 124 Hz frame rate, 7 ms exposures, 24 gain, 4x2 binning (4 in the spectral axis). The fluorescence peak signal was at 3794 intensity counts in a single spectral band, and the noise amplitude with the same settings was 1.3 counts. Thus, the SNR was 3015 at 12 m distance. Considering the form factor, and the $1/r^2$ attenuation, we estimate that we could detect such signals at 458 m with an SNR of 2:1. This is, however, beyond the design range of our system.

## V. Conclusion and Outlook

In this work, a hyperspectral lidar has been presented with a detailed discussion on its design and assembly. The material costs amounted to ∼2715 € and the weight ∼3 kg (excluding acquisition computer and tripod). For comparison, fluorescence lidars reported a decade ago had material costs of more than a million euros and weights of several tons[19], [31]. Since then, smaller systems were reported[30], still with a solid-state laser of around one hundred kg. A previously reported pulsed lidar[19] operated at 10 Hz (100 ms between pulses), and since insect transit times can be expected to be less than 10 ms the insect count was low. The low price of the present system opens up possibilities for, *e.g.,* larger-scale future comparative studies using multiple lidar systems or *in situ* implementation in low-income countries. The portability of the system enables not only placement on astronomical tripods, but also mounting on drones[45], vehicles, or in hiking backpacks could be envisioned.

The performance of the hyperspectral lidar was tested in the field for multiple fluorescence applications with excellent SNR even during full daylight, which is generally a challenge even for pulsed fluorescence lidars. Usage of our lidar in ecological studies has the potential to reduce the labor-intensive mark-recapture studies of insects. We have demonstrated that multiple methods of fluorescent marking (exterior-powder-tagging and ingestion) are feasible with the lidar, which could yield complementary ecological information. Possible biases of this technique include affecting the behavior of the studied insects by the tagging powder. This also applies in non-lidar-based marking studies. Still, a higher amount of powder yields a stronger lidar echo but could affect the insects more severely. The mass powder tagging lifetime of bees was previously estimated to 4 days [67], compared to our study bees retag themselves multiple times per day and laser induced fluorescence is expected to be more sensitive than the naked eye. Another challenge is that the violet 401 nm light from the laser is visible to most insects and could imply a bias in nocturnal monitoring.

Other inelastic applications such as autofluorescence of chlorophyll in vegetation or Raman scattering for various uses could be envisioned for the instrument without modifications. CAD drawings, a component list, driver circuit, and acquisition software can be provided upon request from the corresponding author.

## References

[1] A. P. Genoud *et al.*, "Identification of gravid mosquitoes from changes in spectral and polarimetric backscatter cross-sections," *J. Biophoton.*, 2019, Art. no. e201900123.

[2] M. Li *et al.*, "Bark beetles as lidar targets and prospects of photonic surveillance," *J. Biophoton.*, vol. 14, no. 4, 2021, Art. no. e202000420.

[3] M. Sielezniew, A. Kostro-Ambroziak, and Á. Kőrösi, "Sexual differences in age-dependent survival and life span of adults in a natural butterfly population," *Sci. Rep.s.*, vol. 10, no. 1, pp. 1–10, 2020.

[4] L. M. Torres-Vila *et al.*, "Assessing mass trapping efficiency and population density of Cerambyx Welensii Küster by mark-recapture in dehesa open woodlands," *Eur. J. Forest Res.*, vol. 131, no. 4, 2012, pp. 1103–1116.

[5] C. Kirkeby *et al.*, "Quantifying dispersal of european culicoides (Diptera: Ceratopogonidae) vectors between farms using a novel mark-release-recapture technique," *PloS One*, vol. 8, no. 4, 2013, Art. no. e61269.

[6] B. Lavandero, S. Wratten, J. Hagler, and M. Jervis, "The need for effective marking and tracking techniques for monitoring the movements of insect predators and parasitoids," *Int. J. Pest Manage.*, vol. 50, no. 3, pp. 147–151, 2004, doi: 10.1080/09670870410001731853.

[7] J. W. Crenshaw Jr, "The life history of the southern spiny lizard, sceloporus undulatus undulatus latreille," *Amer. Midland Naturalist*, 1955, pp. 257–298.

[8] R. S. Pasquet *et al.*, "Long-distance pollen flow assessment through evaluation of pollinator foraging range suggests transgene escape distances," *PNAS*, vol. 105, no. 36, pp. 13456–13461, 2008.

[9] O. Ovaskainen *et al.*, "Tracking butterfly movements with harmonic radar reveals an effect of population age on movement distance," *PNAS*, vol. 105, no. 49, pp. 19090–19095, 2008.

[10] G. Hu *et al.*, "Mass seasonal bioflows of high-flying insect migrants," *Science*, vol. 354, no. 6319, pp. 1584–1587, 2016.

[11] V. A. Drake and H. Wang, "Ascent and descent rates of high-flying insect migrants determined with a non-coherent vertical-beam entomological radar," *Int. J. Remote Sens.*, vol. 40, no. 3, pp. 883–904, 2019.

[12] Y. Li *et al.*, "Insect flight velocity measurement with a CW near-IR scheimpflug lidar system," *Opt. Exp.*, vol. 28, no. 15, pp. 21891–21902, 2020.

[13] S. Jansson *et al.*, "Real-time dispersal of malaria vectors in rural africa monitored with lidar," *PLoS One*, vol. 16, no. 3, 2021, Art. no. e0247803.

[14] M. Brydegaard and S. Svanberg, "Photonic monitoring of atmospheric and aquatic fauna," *Laser Photon. Rev.*, 2018, vol. 12, Art. no. 1800135.

[15] V. A. Kovalev and W. E. Eichinger, *Elastic Lidar: Theory, Practice, and Analysis Methods*. Hoboken, NJ, USA: Wiley, 2004.

[16] M. Brydegaard *et al.*, "Lidar reveals activity anomaly of malaria vectors during pan-African eclipse," *Sci. Adv.*, vol. 6, no. 20, 2020, Art. no. eaay5487.

[17] K. Rydhmer *et al.*, "Automating insect monitoring using unsupervised near-infrared sensors," 2021, *arXiv:2108.05435*.

[18] I. I. Rigakis *et al.*, "The e-funnel trap: Automatic monitoring of lepidoptera; a case study of tomato leaf miner," *Comput. Electron. Agriculture*, vol. 185, 2021, Art. no. 106154.

[19] Z. Guan *et al.*, "Insect monitoring with fluorescence lidar techniques: Field experiments," *Appl. Opt.*, vol. 49, no. 29, pp. 1–11, 2010.

[20] M. A. Wulder *et al.*, "Lidar sampling for large-area forest characterization: A review," *Remote Sens. Environ.*, vol. 121, pp. 196–209, 2012.

[21] X. Guo *et al.*, "Regional mapping of vegetation structure for biodiversity monitoring using airborne lidar data," *Ecological Inform.*, vol. 38, pp. 50–61, 2017.

[22] R. Meng *et al.*, "Mapping canopy defoliation by herbivorous insects at the individual tree level using bi-temporal airborne imaging spectroscopy and LiDAR measurements," *Remote Sens. Environ.*, vol. 215, pp. 170–183, 2018.

[23] P. S. Thenkabail and J. G. Lyon, *Hyperspectral Remote Sensing of Vegetation*. Boca Raton, FL, USA: CRC, 2016.

[24] J. P. Arroyo-Mora *et al.*, "Assessing the impact of illumination on UAV pushbroom hyperspectral imagery collected under various cloud cover conditions," *Remote Sens. Environ.*, vol. 258, 2021, Art. no. 112396.

[25] N. Ekhtari, C. Glennie, and J. C. Fernandez-Diaz, "Classification of airborne multispectral lidar point clouds for land cover mapping," *IEEE J. Sel. Topics Appl. Earth Observ. Remote Sens.*, vol. 11, no. 6, pp. 2068–2078, Jun. 2018.

[26] S. Kaasalainen, "Multispectral terrestrial lidar: State of the art and challenges," *Laser Scanning*, vol. 14, pp. 5–18, 2019.

[27] T. Sankey *et al.*, "UAV lidar and hyperspectral fusion for forest monitoring in the southwestern USA," *Remote Sens. Environ.*, vol. 195, pp. 30–43, 2017.

[28] S. Svanberg, *Fluorescence Spectroscopy and Imaging of Lidar Targets*. in L. R. Sensing, T. Fujii, and T. Fukuchi, Eds. Boca Raton, FL, USA: CRC, 2005, pp. 433–467.

[29] V. Raimondi *et al.*, "The fluorescence lidar technique for the remote sensing of photoautotrophic biodeteriogens in the outdoor cultural heritage: A decade of in situ experiments," *Int. Biodeterioration Biodegradation*, vol. 63, no. 7, 2009, pp. 823–835.

[30] V. Raimondi, C. Conti, D. Lognoli, and L. Palombi, "Latest advancements in fluorescence hyperspectral lidar imaging of the cultural heritage," in *Fundamentals of Laser-Assisted Micro-And Nanotechnologies*, vol. 9065, Bellingham, WA, USA: SPIE, Nov. 2013, pp. 274–284.

[31] NATO, *Laser Based Stand-Off Detection of Biological Agents*. Washington, DC, USA: North Atlantic Treaty Organisation, 2010.

[32] M. Sasano, *et al.*, "Development of a regional coral observation method by a fluorescence imaging LIDAR installed in a towable buoy," *Remote Sens.*, vol. 8, no. 1, 2016, Art. no. 48.

[33] T. Malkamäki, S. Kaasalainen, and J. Ilinca, "Portable hyperspectral lidar utilizing 5 GHz multichannel full waveform digitization," *Opt. Exp.*, vol. 27, no. 8, pp. A468–A480, 2019.

[34] T. Hakala *et al.*, "Full waveform hyperspectral LiDAR for terrestrial laser scanning," *Opt. Exp.*, vol. 20, no. 7, pp. 7119–7127, 2012.

[35] M. Brydegaard *et al.*, "The scheimpflug lidar method. SPIE lidar remote sensing for environmental monitoring," 2017, Art. no. 10406.

[36] E. Malmqvist, M. Brydegaard, M. Aldén, and J. Bood, "Scheimpflug lidar for combustion diagnostics," *Opt. Exp.*, vol. 26, no. 12, pp. 14842–14858, 2018.

[37] Z. Liu *et al.*, "Preliminary studies on atmospheric monitoring by employing a portable unmanned Mie-scattering scheimpflug lidar system," *Remote Sens.*, vol. 11(7), 2019, Art. no. 837.

[38] S. Nakamura, "Background story of the invention of efficient InGaN blue-light-emitting diodes (Nobel lecture)," *Angewandte Chemie Int. Ed.*, vol. 54, no. 27, 2015, pp. 7770–7788.

[39] G. E. Smith, "Nobel lecture: The invention and early history of the CCD," *Rev. Modern Phys.*, vol. 82, no. 3, 2010, Art. no. 2307.

[40] G. Zhao *et al.*, "Inelastic hyperspectral lidar for profiling aquatic ecosystems," *Laser Photon. Rev.*, vol. 10, no. 5, pp. 807–813, 2016.

[41] X. Wang *et al.*, "Drone-based area scanning of vegetation fluorescence height profiles using a miniaturized hyperspectral lidar system," *Appl. Phys. B*, vol. 124, no. 11, 2018, Art. no. 207.

[42] M. Brydegaard, A. Gebru, and S. Svanberg, "Super resolution laser radar with blinking atmospheric particles – application to interacting flying insects," *Prog. Electromagn. Res.*, vol. 147, pp. 141–151, 2014.

[43] L. Mei and M. Brydegaard, "Continuous-wave differential absorption lidar," *Laser Photon. Rev.*, vol. 9, no. 6, pp. 629–636, 2015.

[44] G. Zhao *et al.*, "Inelastic hyperspectral lidar for profiling aquatic ecosystems," *Laser Photon. Rev.*, vol. 10, no. 5, pp. 807–813, 2016.

[45] X. Wang *et al.*, "Drone-based area scanning of vegetation fluorescence height profiles using a miniaturized hyperspectral lidar system," *Appl. Phys. B*, vol. 124, no. 11, pp. 1–5, 2018.

[46] L. Mei and M. Brydegaard, "Atmospheric aerosol monitoring by an elastic scheimpflug lidar system," *Opt. Exp.*, vol. 23, no. 24, pp. A1613–A1628, 2015.

[47] E. Malmqvist, *From Fauna to Flames: Remote Sensing With Scheimpflug Lidar*. Lund, Sweden: Lund University, 2019.

[48] M. Aikio, "Hyperspectral prism-grating-prism imaging spectrograph," 2001.

[49] J. Erdkamp and J. Marriage, "Theodor scheimpflug - The life and work of the man who gave us that rule," *Photograph. World*, vol. 3, no. 3, pp. 29–38, 2012.

[50] G. Høye, T. Løke, and A. Fridman, "Method for quantifying image quality in push-broom hyperspectral cameras," *Opt. Eng.*, vol. 54, no. 5, 2015.

[51] K. Stelmaszczyk *et al.*, "Analytical function for lidar geometrical compression form-factor calculations," *Appl. Opt.*, vol. 44, no. 7, pp. 1323–1331, 2005.

[52] H. Baars *et al.*, "An overview of the first decade of polly NET: An emerging network of automated Raman-polarization lidars for continuous aerosol profiling," *Atmospheric Chem. Phys.*, vol. 16, no. 8, pp. 5111–5137, 2016.

[53] M. Brydegaard *et al.*, "High dynamic range in entomological scheimpflug lidars," *IEEE J. Sel. Topics Quantum Electron.*, vol. 27, no. 4, Jul./Aug. 2021, Art. no. 6900711.

[54] E. Malmqvist *et al.*, "CW-Laser radar for combustion diagnostics," in *Imaging and Applied Optics*. Heidelberg, Germany: Optical Society of America, 2016.

[55] G. Zhao *et al.*, "Particle profiling and classification by a dual-band continuous-wave lidar system," *Appl. Opt.*, vol. 57, no. 35, pp. 10164–10171, 2018.

[56] M. Brydegaard *et al.*, "Short-wave infrared atmospheric scheimpflug lidar," *EDP Sci.*, vol. 176, 2018, Art. no. 4.

[57] T. Tscharntke *et al.*, "Landscape moderation of biodiversity patterns and processes-eight hypotheses," *Biol. Rev.*, vol. 87, no. 3, pp. 661–685, 2012.

[58] J. C. Habel *et al.*, "Butterfly community shifts over two centuries," *Conservation Biol.*, vol. 30, no. 4, pp. 754–762, 2016.

[59] J. C. Biesmeijer *et al.*, "Parallel declines in pollinators and insect-pollinated plants in Britain and The Netherlands," *Sci.*,, vol. 313, no. 5785, pp. 351–354, 2006.
[60] G. D. Powney *et al.*, "Widespread losses of pollinating insects in britain," *Nature Commun.*, vol. 10, no. 1, pp. 1–6, 2019.
[61] E. Mathieu-Bégné *et al.*, "Demographic and genetic collapses in spatially structured populations: Insights from a long-term survey in wild fish metapopulations," *Oikos*, vol. 128, no. 2, pp. 196–207, 2019.
[62] J. Hagler *et al.*, "A method for distinctly marking honey bees, apis mellifera, originating from multiple apiary locations," *J. Insect Sci.*, vol. 11, no. 1, 2011.
[63] R. Hood-Nowotny, L. Mayr, and B. G. Knols, "Use of carbon-13 as a population marker for anopheles arabiensis in a sterile insect technique (SIT) context," *Malaria J.*, vol. 5, no. 1, pp. 1–8, 2006.
[64] E. I. Aviles *et al.*, "Fluorescent markers rhodamine b and uranine for anopheles gambiae adults and matings," *Malaria J.*, vol. 19, no. 1, pp. 1–9, 2020.
[65] T. Mascari and L. Foil, "Laboratory evaluation of the efficacy of fluorescent biomarkers for sugar-feeding sand flies (Diptera: Psychodidae)," *J. Med. Entomol.*, vol. 47, no. 4, pp. 664–669, 2010.
[66] K. Khallaayoune *et al.*, "Attractive toxic sugar baits: Control of mosquitoes with the low-risk active ingredient dinotefuran and potential impacts on nontarget organisms in Morocco," *Environ. Entomol.*, vol. 42, no. 5, pp. 1040–1045, 2013.
[67] D. Howpage, R. Spooner-Hart, and J. Sheehy, "A successful method of mass marking honey bees, apis mellifera, at the hive entrance for field experiments," *J. Apicultural Res.*, vol. 37, no. 2, pp. 91s–997.

**Hampus Månefjord** was born in Lekeryd, Sweden, in 1992. He received the M.Sc. degree in physics engineering from Lund University, Lund, Sweden, in 2018. The part of his master's education was taken with Nanyang Technological University, Singapore. He is currently working toward the Ph.D. degree in 3D-printed optical instrumentation and biophotonics with the Department of Physics, Lund University.

**Lauro Müller** was born in Bern, Switzerland, in 1990. He received the B.Sc. degree in micro-and medical technology from the Bern University of Applied Sciences, Bern, Switzerland. He is currently working toward the master's degree in photonics with Lund University, Lund, Sweden. He is also working on his master's Thesis in hyperspectral lidar applications with the Division of Combustion Physics, Lund University.

**Meng Li** was born Kunming, China, in 1993. She received the M.Sc. degree in photonics in 2018 from Lund University, Lundm, Sweden, where she is currently working toward the Doctoral degree (second-year). Her research focuses on specular reflexes backlasing from insects' flat wings, which report on the membrane thickness for target identification.

**Jacobo Salvador** was born in Buenos Aires, Argentina, in 1976. He received the Electronic Engineering degree and the Ph.D. degree in image and signal processing from National Technological University, Buenos Aires, Argentina, in 2007 and 2011, respectively. He specialized in embedded system with Buenos Aires University, Buenos Aires, Argentina, in 2020.

**Sofia Blomqvist** was born in Ronneby, Southern Sweden, in 1992. She received the M.Sc. degree in conservation biology with Lund University, Lund, Sweden. She is currently working toward the Ph.D. degree in environmental science with the Centre for Environmental and Climate Science, Lund, with focus on pollinating insects in road verges.

**Anna Runemark** was born in Karlskrona, Sweden, in 1982. She received the M.Sc. degree in biology from Uppsala University, Uppsala, Sweden, in 2007, and the Ph.D. degree in evolutionary ecology from Lund University, Lund, Sweden, in 2012. She completed the Postdoctoral studies from the Centre for Ecological and Evolutionary Synthesis, University of Oslo, Oslo, Norway. She is currently an Associate Senior with the Department of Biology, Lund University.

**Carsten Kirkeby** was born Køge, Denmark, in 1980. He received the M.Sc. degree in biology from the University of Copenhagen, Copenhagen, Denmark, in 2007, and the Ph.D. degree in epidemiology of *Culicoides* from the Technical University of Denmark, Denmark, in 2013.

**Rickard Ignell** was born in Dalby, Sweden, in 1969. He received the M.Sc. degree in animal ecology and the Ph.D. degree in chemical ecology from Lund University, Lund, Sweden. He is currently the PI of the Disease Vector Group, Swedish University of Agricultural Sciences, Uppsala, Sweden, which focuses on the ecology, particularly the chemical ecology, of disease transmitting mosquitoes.

**Joakim Bood** was born in Norrköping, Sweden, in 1967. He received the M.Sc. and Ph.D. degree in physics from Lund University, Lund, Sweden, in 1995 and 2000, respectively. From 2001 to 2003, he was a Postdoc with Sandia National Laboratories, Albuquerque, NM, USA. Since 2017, he has been a Full Professor with Lund University, where he is running a research program focused on short-pulse (ps/fs) spectroscopy, applied molecular spectroscopy, and remote sensing.

**Mikkel Brydegaard** was born in Copenhagen, Denmark, in 1980. He received the M.Sc. degree in electrical engineering, and the Ph.D. degree in atomic physics, biophotonics, and remote sensing from Lund University, Lund, Sweden, in 2007 and 2012, respectively. He is/was a Postdoctoral Research with Stellenbosch University, Stellenbosch, South Africa and Norsk Elektro Optikk, Oslo, Norway. He was the recipient of the Inaba prize 2014, Docent 2016, and ERC awardee 2018. Since 2021, he has been a Senior lecturer with Lund University. He is/was the Co-founder of the African Spectral Imaging Network and Fauna Photonics, Denmark.

# Paper VII

Review of Scientific Instruments

RESEARCH ARTICLE | NOVEMBER 18 2022

# A biophotonic platform for quantitative analysis in the spatial, spectral, polarimetric, and goniometric domains

Hampus Månefjord ; Meng Li; Christian Brackmann; Nina Reistad ; Anna Runemark; Jadranka Rota; Benjamin Anderson ; Jeremie T. Zoueu ; Aboma Merdasa; Mikkel Brydegaard



*Rev. Sci. Instrum.* 93, 113709 (2022)
https://doi.org/10.1063/5.0095133





AIP Publishing

Review of Scientific Instruments ARTICLE scitation.org/journal/rsi

# A biophotonic platform for quantitative analysis in the spatial, spectral, polarimetric, and goniometric domains

Cite as: Rev. Sci. Instrum. 93, 113709 (2022); doi: 10.1063/5.0095133
Submitted: 8 April 2022 • Accepted: 21 October 2022 •
Published Online: 18 November 2022



Hampus Månefjord,[1,a)] Meng Li,[1] Christian Brackmann,[1] Nina Reistad,[1,2] Anna Runemark,[3] Jadranka Rota,[4] Benjamin Anderson,[5] Jeremie T. Zoueu,[6] Aboma Merdasa,[1,7] and Mikkel Brydegaard[1,3,8,9]

## AFFILIATIONS

[1] Department of Physics, Lund University, Sölvegatan 14, SE-223 62 Lund, Sweden
[2] Centre for Environmental and Climate Science, Lund University, Sölvegatan 37, SE-223 62 Lund, Sweden
[3] Department of Biology, Lund University, Sölvegatan 35, SE-223 63 Lund, Sweden
[4] Biological Museum, Department of Biology, Lund University, Sölvegatan 37, SE-223 62 Lund, Sweden
[5] Department of Physics, University of Cape Coast, Cape Coast, Ghana
[6] Laboratoire d'Instrumentation, Image et Spectroscopie, INP-HB, BP 1093 Yamoussoukro, Côte d'Ivoire
[7] Department of Clinical Sciences, Lund University, Skåne University Hospital, Lund, Sweden
[8] Norsk Elektro Optikk A/S, Østensjøveien 34, 0667 Oslo, Norway
[9] FaunaPhotonics A/S, Støberigade 14, 2450 Copenhagen, Denmark

[a)] **Author to whom correspondence should be addressed:** hampus.manefjord@forbrf.lth.se

## ABSTRACT

Advanced instrumentation and versatile setups are needed for understanding light interaction with biological targets. Such instruments include (1) microscopes and 3D scanners for detailed spatial analysis, (2) spectral instruments for deducing molecular composition, (3) polarimeters for assessing structural properties, and (4) goniometers probing the scattering phase function of, e.g., tissue slabs. While a large selection of commercial biophotonic instruments and laboratory equipment are available, they are often bulky and expensive. Therefore, they remain inaccessible for secondary education, hobbyists, and research groups in low-income countries. This lack of equipment impedes hands-on proficiency with basic biophotonic principles and the ability to solve local problems with applied physics. We have designed, prototyped, and evaluated the low-cost Biophotonics, Imaging, Optical, Spectral, Polarimetric, Angular, and Compact Equipment (BIOSPACE) for high-quality quantitative analysis. BIOSPACE uses multiplexed light-emitting diodes with emission wavelengths from ultraviolet to near-infrared, captured by a synchronized camera. The angles of the light source, the target, and the polarization filters are automated by low-cost mechanics and a microcomputer. This enables multi-dimensional scatter analysis of centimeter-sized biological targets. We present the construction, calibration, and evaluation of BIOSPACE. The diverse functions of BIOSPACE include small animal spectral imaging, measuring the nanometer thickness of a bark-beetle wing, acquiring the scattering phase function of a blood smear and estimating the anisotropic scattering and the extinction coefficients, and contrasting muscle fibers using polarization. We provide blueprints, component list, and software for replication by enthusiasts and educators to simplify the hands-on investigation of fundamental optical properties in biological samples.

## I. INTRODUCTION

Biophotonics is the discipline of using light for the diagnosis and treatment of biological tissue.[1–3] The field of biophotonics has developed rapidly since the emergence of optoelectronics half a century ago. In particular, thanks to devices such as the light emitting diode (LED), semiconductor lasers, and image sensors. Over the decades, a myriad of approaches, specialized instruments, and applications have emerged within, e.g., medicine,[4] environmental monitoring,[5,6] and organic products.[7–10] In the following sections, we discuss how biophotonic approaches can address these disciplines in various domains covered by our Biophotonics, Imaging, Optical, Spectral, Polarimetric, Angular, and Compact Equipment (BIOSPACE).

### A. Spatial domain

Biological insights have been gained by analyzing the spatial features in tissue through optical imaging[11] on macroscopic and microscopic scales.[12,13] The latest advances allow the study of subcellular structures.[14] Imaging concepts have also been extended to three dimensions with techniques such as photoacoustics,[15,16] optical coherence tomography,[17] structured illumination and light-sheets microscopy,[18] diffuse optical tomography,[19] and optical projection tomography.[20,21]

### B. Spectral domain

Although molecules are too tiny to be resolved spatially, spectroscopy provides the means to quantify the chemical composition of tissues; such techniques are known as molecular imaging or tissue spectroscopy.[22,23] The strategies to acquire multispectral images range from red-green-blue (RGB) imaging, filter wheels, and tunable liquid crystal filters,[24] which all collect a limited number of spectral bands. In contrast, hyperspectral imaging by push-broom imaging[8,25] or interferometry[26–28] captures hundreds of bands. Multispectral imaging can also be accomplished by controlling and multiplexing the light source.[29–33] Such multiplexing can be implemented inexpensively and efficiently uses the produced light.

### C. Polarimetric domain

Polarimetry is a viable technique for acquiring molecular contrast that also has the benefit of assessing microstructural features. In polarimetry, coherently scattered photons recalling their initial propagation, phase, and polarization state can be distinguished from incoherent photons resulting from multiple scattering and photon migration in the tissue.[34,35] Polarimetric imaging can be accomplished by arranging a linear polarizer on the illumination and a rotating analyzer on the collecting optics. Approaches for snapshot polarization imaging have also been developed.[36,37]

### D. Goniometric domain

The most common microscopy and imaging geometries comprise reflectance and transmittance. In fact, these geometries assess different light scattering angles. The imaging contrast can differ significantly between geometries depending on the type of sample.[38] This concept can be extended to include modes such as total transmittance, ballistic transmittance,[39] total diffuse reflectance, and specular reflectance. In particular, dark-field forward scattering can improve contrast in microscopy.[40] In analogy to extending a handful of bands in multispectral imaging to hundreds of bands in hyperspectral imaging, the angular scattering modes can be extended from a few modes such as reflectance, transmittance, and dark-field[31] to cover a continuous angular range from zero to π. In the specular domain, as well as the angular domain, this dramatically increases the gathered information and conclusions that one can draw. For angular analysis, such an extended measurement is called goniometry.[41,42] Although uncommon, goniometry can also be implemented in imaging mode.[43,44]

### E. Optical properties

As understood, there are multiple types of both reflectance and transmittance modes, e.g., co- and de-polarized, and ballistic and diffuse. In general, the quantities reported from such studies are subject to the specific measurement geometry, e.g., the numerical apertures of illumination and objectives. Therefore, results are challenging to relate across different studies, laboratories, and instruments. The proposed solution is to convert such measurands into quantitative optical properties. Optical properties include the absorption-, scatter- and de-polarization coefficients—$\mu_a$, $\mu_s$, and $\mu_{LP}$, respectively—in units of $cm^{-1}$. Also, the dimensionless refractive index $n$ and the scatter anisotropic factor $g$ govern the radiative transport. The use of optical properties permits the inter-comparison of values between research groups.[45]

The task of disentangling optical properties from measurands is not trivial,[46] and it constitutes a long-standing fundamental problem in biophotonics. For example, reflectance and transmittance from a blood sample are governed by $\mu_a$, $\mu_s$, $n$, and $g$ for any wavelength. Furthermore, $n$ is coupled to $\mu_a$ via the Kramer–Kronig relations, and in turn, $\mu_s$ and $g$ are determined by deviations of $n$ from the surrounding medium.[47]

In general, the solution to the disentangling challenge is to acquire more measurands than the number of optical properties varying within the study. An early approach measures multiple angular scatter lobes by using integrating spheres in total transmittance, total reflectance, ballistic transmittance, and specular reflectance modes.[39] A modern approach acquires multiple measurands as a function of time-of-flight using mode-locked lasers and single-photon counting.[48–50] Similar results can also be accomplished by frequency sweeps.[51] For steady-state solutions, the number of measurands can instead be increased in the spatial domain by multiple injection or detection points, which yield a plurality of interrogation path lengths.[9,52,53] Such concepts constitute the cornerstones in diffuse optical tomography.[54]

### F. Biophotonic instrumentation

While the ideas, instruments, and insights of modern biophotonics are fascinating, the aforementioned implementations are inaccessible for research groups in lower-income regions, secondary education students, and hobbyists. This fact limits hands-on learning opportunities for light–tissue interaction at early stages and prevents applied research teams from tackling local issues, for instance, in the tropics. Several initiatives for realistic or low-cost instrumentation have emerged. Such concepts include an ultra-low-cost microscope based on a cardboard origami

structure;[55] accessible optical instruments such as 3D-printed holographic microscopes,[56] smartphone-based spectrometers,[57,58] LEGO®-based fluorometers;[59] and advanced instruments such as Raman spectrometers,[60] Brewster angle microscopes,[61] and Michelson interferometers.[62] In particular, recent progress in widely available 3D printers has facilitated projects in open-source hardware,[63,64] biophotonic objects impossible to produce conventionally,[65] and general-purpose toolboxes for 3D-printed optomechanical components.[66,67] While these advances report on low-cost and more adaptive photonic instrumentation, in general, they are also considered inferior in quality as compared to milled counterparts or commercial photonic lab supplies.

In contrast, here, we report a low-cost biophotonic platform of such complexity and modularity beyond what is available commercially. Furthermore, the multiaxis mechanisms would be highly challenging to design with conventional off-the-shelf photonic laboratory components. The structure of BIOSPACE is made of LEGO technic and 3D-printed adaptors for optical elements, making it modular and adaptive for studies of diverse samples. The instrument captures multispectral images with polarization and light scatter angle information of a biological target, rotated around two axes. This yields measurands of high dimensionality, allowing disentanglement of quantitative optical properties.

## II. INSTRUMENT DESIGN AND CONFIGURATION

The biophotonic instrument BIOSPACE is inspired by simpler earlier work[31,44] but now covers more measurement domains. The structure is made with LEGO-technic, which significantly reduces the cost. The instrument consists of three modules: an illuminator, a target rotation stage, and a receiver unit. Four servomotors control the angles of the parts: the illuminator can rotate around the target to achieve a goniometric scan; the target can rotate around two axes to project it from all viewing angles; and a linear polarizer on the receiver unit can be rotated to yield polarimetric information. In Fig. 1, the optical arrangement of BIOSPACE's illuminator and receiver unit are illustrated, along with the dimensions of the placement of components. The schematic in Fig. 1 is drawn for a goniometric scatter angle of zero (ballistic transmittance mode). The rotation axes of the motors and the data flows are also indicated.

### A. Optical arrangement

The optical arrangement of BIOSPACE is illustrated in Fig. 1 for ballistic transmittance, and the specific optical components are listed in supplementary material Table S1. The illuminator is seen as an exploded-view drawing in Fig. 2(a), and its mounting on BIOSPACE is shown in Fig. 2(b). It has eight LEDs with individual emission wavelengths ranging from 365 to 940 nm, mounted on a multiplexing printed circuit board (PCB). The LEDs are lit sequentially and synchronized with a strobe input. The LED light is injected into a white diffuse cavity and guided out through a homogenizing light pipe. The light is polarized by a linear polarization filter and collimated by a lens before it impinges on the biological target. The scattered light is collected by an achromatic objective lens. A motorized polarization analyzer can select, e.g., co- or de-polarized light. After this, the scattered light is imaged onto a camera.

### B. Mechanics and materials

The BIOSPACE mechanical construction is made of LEGO-technic plastic parts as shown in Fig. 2(b). The necessary parts can be acquired from a single LEGO-technic kit (Bucket Wheel Excavator, LEGO, Denmark). The target rotation stage consists of three motorized axes inside each other, where the inner controls the roll- and yaw-angle of the sample and the outer supports the illuminator and controls the scatter angle. The roll- and yaw-axes of rotation are tilted 45° with respect to each other, allowing full goniometric scans without obscuration. The rotation axes are shown in Fig. 2(b). These axes are controlled by servo motors (EV3 Medium Servo Motors, LEGO, Denmark). The size of the BIOSPACE is 300 × 500 × 300 mm$^3$ and the weight is 1 kg. The detailed assembly instructions of BIOSPACE are provided as supplementary material (S2).

The 3D-printed parts connect the illuminator, the optical components, and the camera to the LEGO structure. Individual lenses are secured with O-rings. The 3D-printing material used for connecting optical components and shielding for glare and stray light

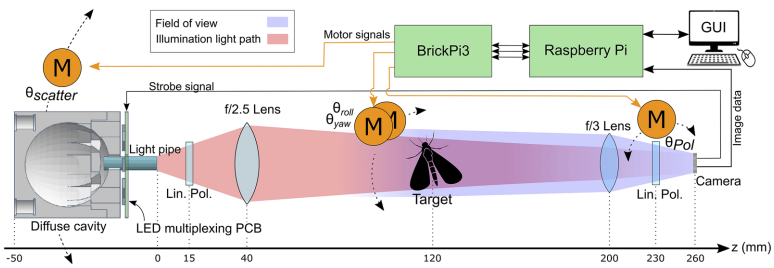


**FIG. 1.** BIOSPACE's components, optical arrangement, and diagram of the data flow of a measurement. The orange M-circles indicate rotating motors, while the orange arrows imply the control signals for the motors. The black arrows indicate other data communication such as image data. The green boxes are circuit boards. The red cone represents the light produced by the illuminator, and the blue cone represents the field of view (FoV) of the camera. The placement of optical components is indicated in mm on the *z* axis.

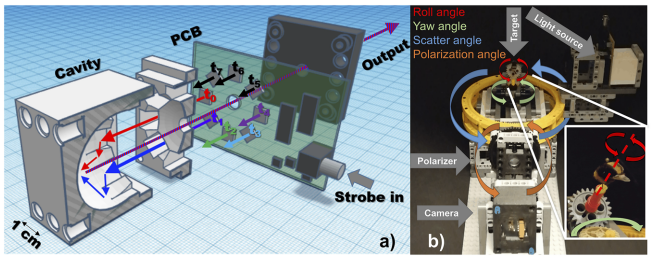


**FIG. 2.** (a): Exploded view of the illuminator. The components of the illuminator include an LED-multiplexer PCB, a white diffusive cavity, and a connector piece compatible with LEGO-technic. The arrows illustrate the light path of the different LEDs of the illuminator. (b) Photograph of the mechanical construction of BIOSPACE. The placement of different parts is indicated with arrows. The motorized degrees of freedom include scatter-, polarization-, roll- and yaw-angle.

is black ABS (acrylonitrile butadiene styrene) plastic. The LEGO-optical adaptor CAD (computer-aided design) files are available as supplementary material (S3).

The white diffuse cavity, an integral part of the illuminator, is 3D printed with white ABS filament with 100% infill and coated with Barium Sulfate ($BaSO_4$) applied with a brush. Common filament types for 3D printing were evaluated [see Fig. 3(a)]. The ABS material was selected as it exhibits maximal scattering, minimal absorption, and no fluorescence for the relevant wavelength range (365–940 nm). Each of the evaluated 3D-printed materials suffered from low reflectance in the UV region, and thus, the highly reflective $BaSO_4$ coating was applied.

If milling or hot-wire subtractive methods remained viable options, materials such as PTFE (polytetrafluoroethylene) or polystyrene foam would be well-suited options due to their broad high reflectance. The evaluation was performed using spectroscopy with a bifurcated fiber connected to a tungsten deuterium lamp (SLS204, Thorlabs, USA) and a compact spectrometer (USB4000, OceanOptics, USA). A Spectralon™ white standard (Labsphere, Inc., North Sutton, USA) with specified 99% reflectance was used as a reference.

Further investigation of the materials' quantitative scattering coefficients was made by photon time-of-flight spectroscopy (PToFS).[48] The absorption and reduced scattering coefficients of ABS for wavelengths of 630, 810, and 940 nm were found to be $\mu_a$ = 0.014, 0.0090, and 0.015 $cm^{-1}$, and the reduced scattering coefficients $\mu_s'$ = 46, 47, and 48 $cm^{-1}$, respectively. The mean photon path length within the coated cavity (3 cm diameter) with a time-correlated single-photon counting (TCSPC) instrument was found to be 27 cm for 630 nm [see Fig. 3(b)]. The TCSPC setup[48] measures the time delay of light traveling between two fiber probes. Slabs of 5, 10, and 15 mm thickness of the different materials were placed in the

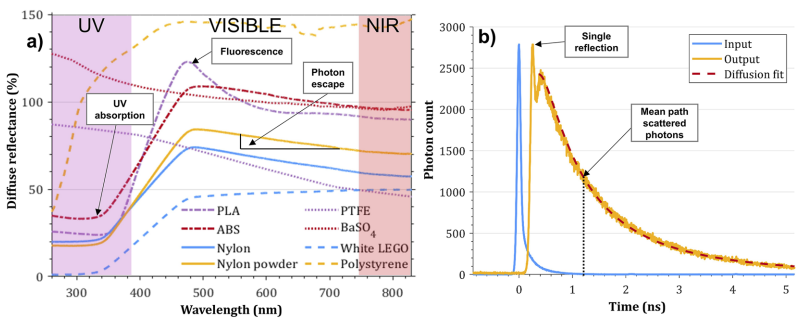


**FIG. 3.** (a) Diffuse reflectance from candidate materials for manufacturing a white diffuse cavity, a high diffuse reflection from 365 to 940 is desired. A strong UV and violet absorption is clearly seen for all 3D-printing filaments (PLA, ABS, and nylon). The PTFE, polystyrene foam, and $BaSO_4$ all show excellent reflectance over the relevant range, and the latters' reflectance exceeding 100% is explained by their scatter coefficient being greater than the Spectralon standard. A fluorescence peak can be observed at 470 nm for PLA, which makes it unsuitable for LED spectroscopy. The downward slope from 500 nm and onward is explained by photon escape as a consequence of the measurement geometry rather than absorption in the material. (b) The PToFS histogram of 630 nm light inside the cavity shows a histogram of the times each photon takes before leaving the cavity. From this, the material with the highest scattering can be found. The path length of the single reflected peak is 7.6 cm, which corresponds to the shortest path the light can take within the cavity, i.e., a single reflection. The mean path length for all light leaving the cavity is 27 cm.

setup. The absorption and reduced scattering coefficients of the different materials were found by solving the inverse diffusion equation for the slabs.[65]

### C. Electronics and data flow

BIOSPACE uses several components for performing and controlling a measurement, including parts for data acquisition, motor control, and user input/output. BIOSPACE is controlled by an open-source single-board computer (Raspberry Pi 4, Raspberry Pi Foundation, Cambridge, UK). The computer runs the Linux operating system and has ports for connecting the display, mouse, and keyboard for user input and output, as well as a USB3 port for connecting an external hard drive for storing the acquired measurement data. The computer communicates with the motors through an add-on board (BrickPi3, Dexter Industries, Washington DC, United States). The add-on board has four Ethernet ports for setting and reading positions of the servo motors. The measurement images are captured with an industrial camera (acA1920-155um, Basler AG, Ahrensburg, Germany), with a silicon CMOS chip. It records 2-megapixel images with a 12-bit dynamic range; it has a global shutter and can be binned up to four times on both rows and columns. Important for our implementation is that it has a strobe out-port, which gives a high value when there is an active exposure of the camera. Finally, for multiplexing the light, a custom-designed and manufactured LED-multiplexing printed circuit board (PCB) is used (see Fig. 4).

The multiplexing PCB consists of a coaxial input (BNC), which is connected to a strobe-out from the camera. The strobe signal is amplified and connected to a (not-)enable port of a decimal counter. A transistor array drives one of the eight LEDs sequentially. There is also one dark time slot used for background subtraction. All LEDs are driven with currents of 100 mA except for the 365 and 940 nm LEDs, which have a current of 500 mA. This equalizes the spectral response of the silicon image chip and allows all bands to be captured within the dynamical range using the same exposure time.[31]

### D. Data acquisition and user interface

BIOSPACE has an open-source application that is available for download.[68] The program is built in the free-to-use programming language, Python (Python Software Foundation, Delaware, United States), and uses various open-source software libraries. The graphical user interface is built with a library called Tkinter (Python Software Foundation, Delaware, United States).[69] Tkinter is the standard Python binding of an open-source, cross-platform widget toolkit called Tk. Camera communication is implemented with a library called PyPylon.[70] PyPylon is the official Python wrapper for the Basler Pylon Camera Software Suite (Basler AG, Ahrensburg, Germany). For controlling the servo motors, the BrickPi3 (Dexter Industries, Washington DC, United States) repository is used.[71]

The application controls the standard camera parameters such as exposure time and gain. A calibration view is presented before a measurement is started with the press of a button. A complete measurement is then performed according to a spreadsheet measurement protocol file, where the relevant scatter-, roll-, yaw, and polarization-angles are listed. These angles can then be associated with every multispectral image. The motors of BIOSPACE are moved to the relevant positions and a non-compressed .tiff image is captured for each spectral band. Each image is background-subtracted with an ambient image, ensuring that measurements can be run regardless of the light in the room. However, a minimization of ambient light is recommended to maximize the dynamic range of the measurement.

Image analysis can be performed in any suitable software since the source images are saved as non-compressed image files. Matlab (Mathworks) was used for the image analysis in this paper, and scripts for importing and calibrating images to a white reference are available for download.[68]

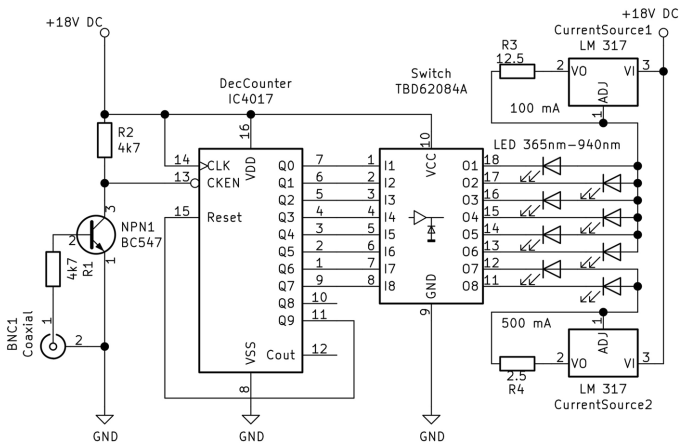


**FIG. 4.** Circuit diagram of the LED multiplexing PCB. Here, the LEDs are fed with constant-current sources of 500 and 100 mA, respectively. Each LED is lit sequentially and synchronized with the camera strobe connected to the coaxial input.

## III. SYSTEM PERFORMANCE AND CALIBRATION

A BIOSPACE measurement results in a seven-dimensional intensity tensor, $I(x, y, b, scatter, roll, yaw, pol)$, where $x$, $y$, $b$, $scatter$, $roll$, $yaw$, and $pol$ are integer indices of the vectors $\ell_x$, $\ell_y$, $\lambda_b$, $\theta_{scatter}$, $\theta_{roll}$, $\theta_{yaw}$, and $\theta_{pol}$, respectively. The coordinates $\ell_x$ and $\ell_y$ [mm] are the horizontal and vertical distances from the optical axis on the camera sensor, respectively, and the imaging information is found in these vectors. Spectroscopy information is found in $\lambda_b$ [nm], which denotes the wavelength bands of the LEDs. The goniometric information consists of the scatter lobes in $\theta_{scatter}$ [deg], while the 3D aspect angle information of the sample is denoted in $\theta_{roll}$ and $\theta_{yaw}$ [deg]. Polarimetry is explored in the polarization-angles $\theta_{pol}$ [deg]. The performance and calibration procedures are described for each of these measurement domains in Secs. III A–III F. The range and resolution in each domain are also specified in Table I.

### A. Quantitative measurement—Intensity domain

A calibrated reflectance ($|\theta_{scatter}| > 90^\circ$) measurement can be accomplished according to

$$R_{sample} = \frac{I_{sample} - I_{dark}}{I_{ref} - I_{dark}} R_{ref}, \tag{1}$$

where $I_{sample}$ is the intensity measurement of the sample, $I_{dark}$ is the dark exposure, and $I_{ref}$ is a reference standard. $R_{\mathrm{ref}}$ is a traceable table value for the diffuse reflectance standard; in our case, Spectralon was used. Specular reflectance (where the illumination is folded into the receiver) can be calibrated with a metallic mirror instead of the diffuse standard used in Eq. (1). Forward scatter ($5^\circ < |\theta_{scatter}| < 90^\circ$) can similarly be calibrated by opal diffusers with known Lambertian transmission lobes. Finally, a measurement with a ballistic configuration ($|\theta_{scatter}| < 5^\circ$) of a transparent sample can be calibrated by an empty sample holder. Specular and ballistic measurements are generally more intense than diffuse reflectance and forward scatter. Multiple exposures may be stitched together to acquire a high dynamical range (HDR) measurement for multi-scatter angle or goniometric analysis. The dynamic range of the camera is 12-bit, which defines the full well capacity (FWC) to $2^{12}$–1 counts. The FWC per second (FWC/s) will be used throughout the paper as the intensity unit of the measurements. The level of dark exposure is highly dependent on the ambient light. It was measured in a dark room to be $10^{-3}$ FWC/s, which can be compared to a ballistic measurement of 800 FWC/s and a backscatter measurement of a diffuse white target of 40 FWC/s. These values indicate the appropriate exposure time for specific measurement configurations, e.g., a diffuse backscatter measurement should have an exposure time of less than 25 ms to avoid saturation. The dynamic resolution is given by the standard deviation of multiple acquisitions of a reference standard; it resulted in a signal-to-noise ratio of 42 dB on average over the spectral bands.

### B. Imaging—Spatial domain

The intensity measurement is extended in the spatial domain with the positional information provided by the camera configuration, which maps the object plane, $\ell_x'$, $\ell_y'$ (mm), onto the ($11.3 \times 7.1$ mm$^2$) sensor of the camera according to

$$\begin{bmatrix} \Delta\ell_x \\ \Delta\ell_y \end{bmatrix} = M \begin{bmatrix} \Delta\ell_{x'} \\ \Delta\ell_{y'} \end{bmatrix}, \tag{2}$$

where $M$ is the magnification of the system at the plane of the sensor. The magnification was calculated to be $M = 0.57$ by acquiring an image of a target with a known size while knowing the size of the imaging sensor. The image is spatially discretized by the pixel pitch of the camera sensor ($5.86 \times 5.86$ $\mu$m$^2$) into the discrete horizontal and vertical pixels ($x$, $y$). How the object maps to the sensor is described by the convolution of the light from the object, $I_{obj}(\ell_{x'}, \ell_{y'})$, and the point spread function (PSF) of the system,

$$I(x, y) = \iint I_{obj}\left(\ell_x - \ell_{x'}, \ell_y - \ell_{y'}\right) PSF_{x,y}\left(\ell_{x'}, \ell_{y'}\right) d\ell_{x'} d\ell_{y'}, \tag{3}$$

expressed in integral form.[72] This assumes that the complete FoV is illuminated.

To evaluate both the spatial resolution and the depth of field (DoF) of BIOSPACE, we imaged a Siemens star target at locations $-5$ mm $< z < +5$ mm from the focus plane of the instrument. The resolution was also evaluated for the various spectral bands to find

**TABLE I.** The measurement domains probed by BIOSPACE along with the corresponding examined features. The range and the discretization are provided for each domain. The number of measurands is reported for the relevant domains. The temporal domain could, in theory, provide an infinite number of measurands; however, this is not relevant in the samples studied, which are stationary in time. Similarly, the spatial domain has not been used for increasing the number of measurands but rather to isolate a spatial feature to study. Here, the number of sample viewing angle measurands is defined as the possible lobes in $\theta_{\mathrm{roll}}$ and $\theta_{\mathrm{yaw}}$. The resolution reported is the framerate in the temporal domain and the average spectral FWHM in the spectral domain.

| Subject/domain | Examined feature | Range | Resolution | Measurands |
|---|---|---|---|---|
| Intensity/dynamic | ⋯ | $0 \rightarrow 4095$ | 12 bit | ⋯ |
| Time/temporal | ⋯ | $1\ \mu s \rightarrow 10$ s | 164 Hz | ⋯ |
| Space/spatial | Morphology, spatial features | $19.8 \times 12.5$ mm$^2$ | 20 $\mu$m | $960 \times 600$ effective pix |
| Photon energy/spectral | Molecular composition | $365 \rightarrow 940$ nm | 25 nm | 8 bands |
| Propagation angle/goniometric | $n, g, \mu_s'$ | $-165^\circ \rightarrow 165^\circ$ | $5^\circ$ | 67 lobes |
| Polarization/polarimetric | Surface structure | $0^\circ \rightarrow 180^\circ$ | $2^\circ$ | 4 parameters |
| Sample viewing angle/angular | Iridescence, morphology | $45^\circ \rightarrow 135^\circ \times 0^\circ \rightarrow 360^\circ$ | $2^\circ$ | 45 yaw lobes<br>180 roll lobes |

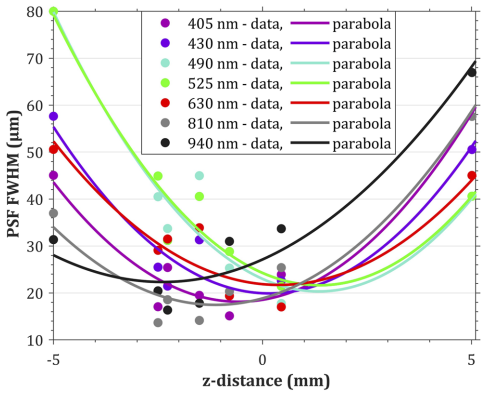


**FIG. 5.** The resolution of the imaging system for the spectral bands of BIOSPACE. The focus displacement is evident when comparing the NIR 940 nm band to the visible bands. The DoF is different for the bands and the focus displacement further reduces the combined DoF of all spectral bands. In the case of resolving a 50 $\mu$m feature in all bands, the DoF is 6 mm.

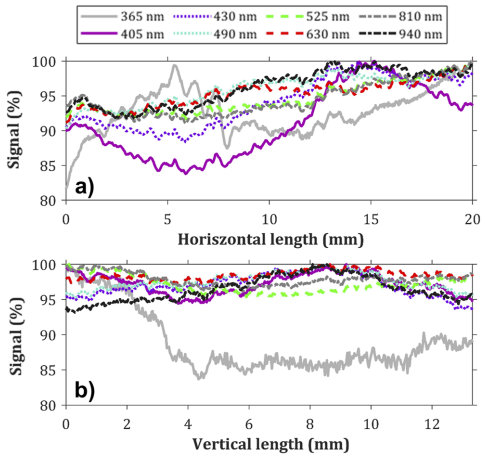


**FIG. 6.** The spatial flatness of image $I(x, y, b)$. (a) Horizontal direction. (b) Vertical direction. The signal is normalized to the highest recorded signal. All spectral bands have a high signal over the whole image; the UV 365 nm band sticks out with a slightly lower signal at some vertical positions, possibly due to contamination of the homogenizing hex rod or the reflectance standard.

the chromatic aberrations (see Fig. 5). The full width half maximum (FWHM) of the PSF was calculated for the axial positions, and the parabolic functions were fitted to the values. The resolution, depth of field, and focus displacement for each spectral band are seen in Fig. 5. The PSF FWHM represents the resolvable spot size measured at (17–23) $\mu$m for each spectral band. Our magnification and pixel size imply that the smallest resolvable features are sampled by two pixels, proving a good matching of lens and sensor resolutions according to the Nyquist–Shannon sampling theorem. However, pixel binning could be used to increase the dynamic resolution (signal-to-noise ratio).

Flat field calibration was accomplished by evaluating the spatial variation in the intensity of image $I(x, y, b)$ by acquiring images of the Spectralon standard for each spectral band. The entire image field 20 × 13 mm$^2$ was illuminated by more than 80% of the highest recorded signal (see Fig. 6).

### C. Spectroscopy–Spectral domain

The spectral intensity measurement is determined by

$$I(b) = \int E_{\lambda_b}(\lambda) I_{obj}(\lambda) S(\lambda) d\lambda, \tag{4}$$

where $E_{\lambda b}(\lambda)$ is the emitted light in the specific spectral band, $I_{obj}(\lambda)$ is the intensity of the reflected light from the object, and $S(\lambda)$ is the spectral sensitivity of the camera. White intensity calibration is accomplished according to Eq. (1). The resulting spectral shape of $E_{\lambda b}(\lambda)$ and $S(\lambda)$ was measured with the compact spectrometer (see Fig. 7), assuming similar sensitivity to the camera sensor.

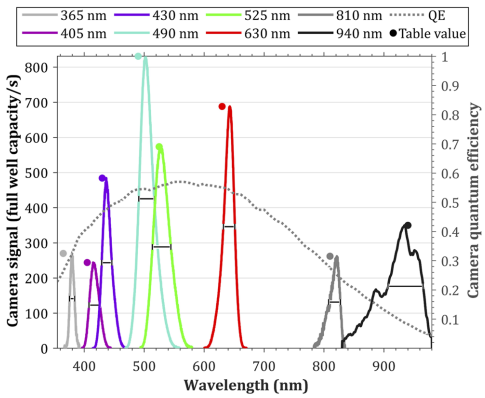


**FIG. 7.** Spectral measurement of the reference standard. The dots indicate the recorded intensity for each LED and are positioned at the peak emission wavelength according to their datasheets. The spectral shape, $E_{\lambda b}$ (λ), of the LEDs is recorded by the compact spectrometer. There is a minor overlap of the 405 and 430 nm as well as the 490 and 525 nm LEDs, but considerably less than for human color vision bands. The FWHM of the measured spectral bands ranged from 9 to 59 nm with an average of 25 nm. The bands are slightly red-shifted; however, this was deduced to be a spectrometer misalignment.

### D. Goniometry, sample rotation, and polarization state—Angular domains

The goniometric measurement $I(\theta_{scatter})$ is determined by the scatter angle between the optical axis of the illuminator and the receiver module (set by a LEGO motor). The accuracy and repeatability when performing a complete scan from −165° to 165° were measured to have a deviation of up to 2°. Potential backlash in the gears is avoided by keeping the same rotation direction throughout a measurement. The goniometric resolution of an $I(\theta_{scatter})$ measurement is limited by the angular width of the illuminator light cone convoluted with the received light cone (i.e., the goniometric instrument function). The FWHM of the goniometric resolution can be measured by scanning the scatter angle in the vicinity of ballistic mode ($\theta_{scatter} \approx 0°$), a 2D instrument scatter lobe can also be measured using side scatter mode ($\theta_{scatter} \approx 90°$), and a flat mirror in the sample holder, scanning both $\theta_{roll}$ and $\theta_{yaw}$. We estimated the goniometric resolution to 5°, indicating that the LEGO gears' hysteresis is not limiting the angular resolution. The scatter angles range from $-165° < \theta_{scatter} < 165°$, yielding up to 67 resolvable scatter lobes.

LEGO motors and gears also control the two-axis rotation of the sample with similar precision. The two axes are 45° inclined with respect to each other to allow non-obstructed goniometric scans [see Fig. 2(b) inset]. This inclination provides a 2D observational viewing angle of the sample of $45° < \theta_{yaw} < 135°$ and $0° < \theta_{roll} < 360°$. The number of unique combinations of target viewing angles depends on the angular step size for the measurement. For example, 5° steps for $\theta_{roll}$ and $\theta_{yaw}$ result in 1296 combinations of viewing angles. This is more than an adequate number to perform 3D reconstructions of, e.g., entomological museum collections.[21,73]

The polarizer is in a static angle, linearly polarizing the light illuminating the object, while the analyzer in front of the camera rotates to probe the light of specific polarization angles. The polarization information, independent of the high precision of the rotation stages, can always be reduced to four variables (called the Stokes parameters).[34]

### E. BIOSPACE performance

The combined number of measurands of a complete BIOSPACE measurement is the product of the number of measurands in each domain, which results in over $10^{13}$ 12-bit intensity values in the tensor $I(x, y, b, scatter, roll, yaw, pol)$, described in Sec. III (see Table I). This corresponds to $10^7$ unique 2-megapixel images. However, the acquisition time for complete measurement of all domains is typically unfeasible and unnecessary (e.g., at 10 ms exposure, it would take over 48 h and consume over 34 terabytes of storage). The vectors $\ell_x$, $\ell_y$, and $\lambda_b$ are generally complete in each measurement since the instrument captures multispectral images by default. However, the $\theta_{scatter}$, $\theta_{roll}$, $\theta_{yaw}$, and $\theta_{pol}$ vectors can range in length from singular to the maximum number of measurands stated in Table I. Therefore, experiments should be designed cleverly to investigate the relevant indices of $I$. In practice, only a small subset of the full capabilities of BIOSPACE is used for each experiment. What this subset contains varies on the study, and typically, some dimensions of $I$ can be singular. The huge number of possible acquirable images demonstrates the great versatility of BIOSPACE

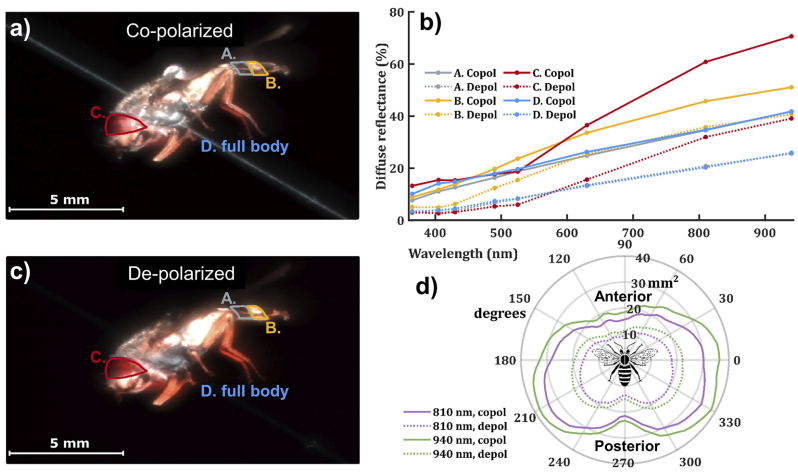


**FIG. 8.** (a) and (c) Co- and de-polarized true-color images of *Eupeodes corollae* (a species of hoverfly) acquired by BIOSPACE, respectively. Four cropped-out regions are indicated: A. dark stripe of the body; B. bright stripe of the body; C. eye; D. full-body signal from the insect. (b) Spectral responses from the different regions of the insect in both co- and de-polarized light. The de-polarized signals are noted to be weaker for all regions as expected. (d) The optical cross-section in $mm^2$ from 360° viewing angles of the full body of the insect, in the standard lidar wavelengths of 810 and 940 nm.

as a platform for pursuing unique experiments in research and education.

### F. Trade-offs between performance in optical domains

There are several design choices where trade-off effects influence the resolution in multiple dimensions, typically when one is increased and the other decreased. Such examples include spatial binning, where spatial resolution is sacrificed for a higher dynamic signal-to-noise ratio. Another example includes the F-number of the lens. A low F-number yields a high spatial resolution and a small PSF; on the other hand, it yields a short DoF. Furthermore, as the F-number affects the size of the light cone collected, it decreases the goniometric resolution, which is the convolution of the emitted light cone and the collected one. The spectral resolution is limited by the number of LEDs used, their availability in relevant peak wavelengths, and their spectral sharpness. Adding more LEDs would result in a more complex and bulky design and would lengthen the measurement durations.

## IV. EXAMPLE AREAS OF APPLICATION

### A. Entomological lidar target characterization

For *in situ* experiments in entomology and monitoring of insect biodiversity, the gold standard is manually emptied traps, often prepared with bait to attract insects.[74,75] Novel techniques such as lidar and hyperspectral imaging have emerged as complementing alternative methods for characterizing individual insect species, diversity, and behavior.[6,76,77] Automated entomological lidar measurements have the potential to improve the temporal resolution of observations while reducing the need for labor-intensive trapping. However, it is not a simple task to classify insect species using a lidar signal. A library of target properties is needed for the classification. Such properties could include the target's optical cross-section, diffuse reflectance spectrum, and the degree of polarization of the body and the wings. Note that such classification is not a biological classification.

BIOSPACE is capable of acquiring all of the aforementioned optical properties of insects. Although the optical configuration of BIOSPACE differs from lidars in terms of exposure time, spectral width, and collimation of the lasers typically used, the measurements acquired with BIOSPACE are expected to be comparable with lidar. Insect sizes fall below the laser pulse lengths and detector bandwidth encountered in lidar; therefore, steady-state spectroscopy suffices for describing the light interaction. Furthermore, the spectrally dull features in biological tissues contributed by melanin, e.g., can be sufficiently resolved by BIOSPACE. The spectrally sharpest details from insects derive from their wing interference patterns, thoroughly addressed below. An advantage of BIOSPACE is that spectral shapes arising from absorption and interference can be distinguished since the structural colors disappear with cross-polarization and shift with scatter angle $\theta_{scatter}$. Finally, the sharpest angular details arise from the wings whose surface normal distributions are comparable with the light cones employed in BIOSPACE.

The captured diffuse reflectance spectrum of a hoverfly (*Eupeodes corollae*) is shown in Fig. 8. Different parts of the body were compared in co- and de-polarized light. The sample was rotated, demonstrating the change in the optical cross-section of the insect depending on its heading direction [see Fig. 8(d)], mimicking the variation in the lidar signature of a specific insect.

The wing of a European spruce bark beetle, *Ips typographus*, was studied in a specular configuration, which can occur in lidar observations.[76] The measurements were compared to an analytical thin film equation[78,79] sampled with the spectral shape of the LED outputs according to Eq. (4). The measured thickness of the wings was around 0.5 $\mu$m and found to decrease toward the posterior end of the wing as expected.[77] Although the thickness values were found with a moderate coefficient of determination ($R^2$) values of over 0.6, this is an example where an *ex vivo* target characterization study can simplify the classification of *in vivo* lidar measurements (Fig. 9).

### B. Blood smear analysis

The study of blood with optical analysis has a long and fruitful history. One technique is spectral analysis, where, e.g., the different responses from oxygenated and deoxygenated hemoglobin have been used to determine blood oxygenation in both research and clinical settings.[47,80,81] Another technique is the visual or automated inspection of red blood cells (RBCs). RBCs are 7 $\mu$m discs; healthy cells are donut-shaped but can be inflated due to osmotic pressure.[82]

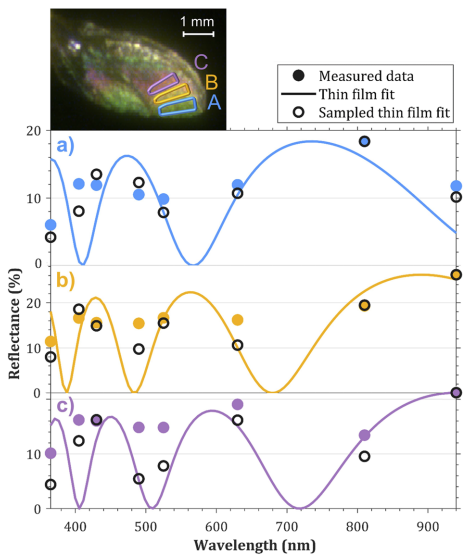


**FIG. 9.** (inset) A false-color image of the wing of a bark beetle, acquired by BIOSPACE. The crop regions A, B, and C indicate regions further away from the posterior end of the wing. The RGB color bands are represented by 940, 810, and 630 nm. (a)–(c) Reflectance measured on the specular alignment of a wing of a bark beetle on regions A, B, and C where increasing thickness is expected. The reflectance values are compared to a white diffuse reference. Fits of the thin film equation are presented for the estimated wing thicknesses for each region.

Morphological changes can occur due to diseases such as sickle cell anemia,[83] and significant changes in scattering and absorption can occur after an infection by the malaria parasites (*Plasmodium falciparum*).[43] The gold standard for blood analysis is typically to stain the blood and have a trained professional perform microscopic investigation.[84] Preliminary diagnoses without a pathologist have been explored but are not implemented clinically on a large scale. Such methods include, e.g., hyperspectral imaging, multivariate analysis,[40,85] and studying the anisotropy of the light.[86] With BIOSPACE, the magnification is insufficient to resolve the shape of individual blood cells. Instead, spectroscopic analysis is feasible as well as finding the scattering phase function and anisotropy factor of the RBCs using BIOSPACEs goniometric capabilities.

Within the framework of a study approved by the Swedish Ethical Review Authority, we obtained a blood sample from a healthy volunteer, who provided their written consent after being informed about the study and the voluntary nature of participation. The unstained blood smear was goniometrically scanned with BIOSPACE to acquire the scattering phase function (see Fig. 10). The blood smear on a microscope slide was placed in the instrument at a 45° angle from the camera. This configuration results in a specular reflection on the glass slide when the light source is at −90°, where a ballistic configuration is defined as 0°. A photograph of the mounted microscope slide and a schematic of the experimental setup are presented in Figs. 10(d) and 10(e), respectively. The blood smear measurement provides light intensity as a function of both wavelengths and scattering angles [see the heat map presented in Fig. 10(a)]. A goniometrical measurement has a large dynamic range when scanning an optically thin sample. The transmitted light intensity will typically be close to 100% of the incident light, while

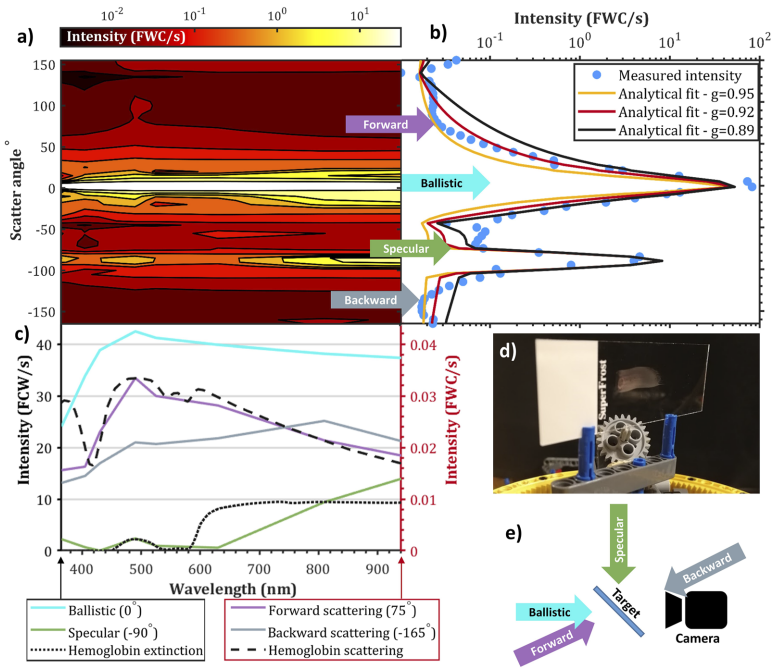


**FIG. 10.** (a) Goniometric measurement of a blood smear presented as a 2D heat map. (b) Horizontal integration of the 2D heat map yields the phase function of the blood smear in intensity over the scattering angle. A Henyey–Greenstein function multiplied with a cosine projection to compensate for the amount of light hitting the sample. Furthermore, a Gaussian function is added to account for the specular reflection at −90°. The function is fitted with anisotropy values $g = 0.89$, 0.92, and 0.95. (c) Vertical integration of the 2D heat map yields the spectral information of the different angular regions. The literature values of the extinction and scattering of hemoglobin are included.[2] The literature extinction values show similarities with the specular measurements, and similarly, the scattering values from the literature show similarities with the forward scattering region. The plots in the black boxed legend correspond to the left axis and the ones in the red boxed legend correspond to the right axis. (d) A photograph of the glass slide mounted for measurement in BIOSPACE. (e) A schematic of the different selected angular regions, where the arrows correspond to the light incidence on the target.

the scattered light can have intensities of a factor $10^4$ lower. This was the case for the blood smear measurement, as shown in Figs. 10(a) and 10(b), where the dynamic range of the measurement spans four orders of magnitude. The measurement was conducted with five different exposure times, 50 $\mu$s, 300 $\mu$s, 12.5 ms, 50 ms, and 200 ms, to resolve the large dynamic with a sufficient signal-to-noise level.

The anisotropic scatter factor ($g$) was estimated from the goniometric measurement in Fig. 10(b) by fitting a Henyey–Greenstein function to the measured scattering phase function.[42] The fit function was multiplied with a cosine projection to compensate for the fraction of light illuminating the sample for different light source angles. A Gaussian function representing the specular reflection of the light source occurring at $-90^\circ$ was also added to the fit. The anisotropic factor $g$ of the blood smear was determined to be 0.92.

### C. Tissue analysis

Skeletal muscle tissue is vital for functional anatomy, and many skeletal muscle diseases can be caused by mutations in muscles' sarcomeric proteins. The sarcomeres have a periodical fibrous structure, making them suitable for polarization analysis,[87] which is feasible with BIOSPACE.

An ~1 mm thick slice of porcine skeletal muscle tissue was mounted in BIOSPACE and analyzed for the total intensity and degree of linear polarization (DoLP) for forward- and backward-scattered light.[87] A notable contrast between different muscle tissue regions can be observed in Fig. 11. The images shown are captured from the same region of the muscle tissue. There is a substantial regional difference in the images of to what degree the light is de-polarized for the different scattering modes, as seen by comparing Figs. 11(a) and 11(b). In Fig. 11(a), a fine-striped pattern of the myosin and actin muscle-fiber arrangement is distinguishable in the co-polarized light, displayed as green in the figure. Previous research has reported backward-reflected light maintaining a higher DoLP along the axis perpendicular to muscle fiber orientation.[88] Thus, BIOSPACE enables polarization analysis to characterize tissue such as skeletal muscle.

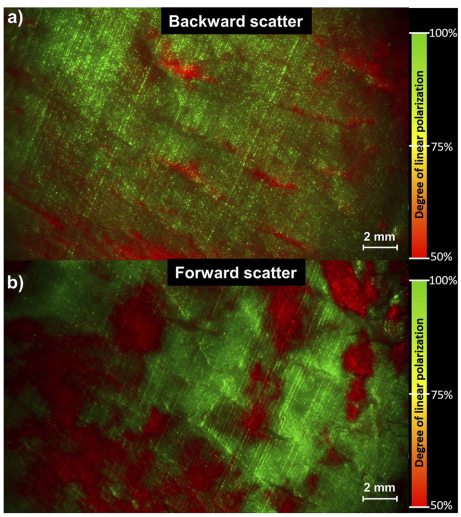


**FIG. 11.** A slice of muscle tissue in (a) backward scatter and (b) forward scatter configurations of BIOSPACE. The tissue is illuminated with 630 nm light. The DoLP is shown as green corresponding to co-polarized and red corresponding to complete de-polarization of the light.

## V. CONSTRUCTION AND UTILIZATION OF THE INSTRUMENT

The performance evaluation in this paper is based on the components listed in the bill of materials found in supplementary material Table S1. The modular design of BIOSPACE allows for easy modification with, e.g., another camera or imaging lens if there are other specific requirements on spatial resolution or FoV. BIOSPACE could be of great interest to replicate in contexts including secondary education classroom experiments or hands-on biophotonic research in low-income countries. Three copies of the instrument have been assembled and used in a biophotonics course at Lund University.[89] The project is co-funded by the International Science Program (ISP), Uppsala, in collaboration with the African Spectral Imaging Network (AFSIN). Multiple copies of BIOSPACE have been deployed in research groups at the University of Cape Coast, UCC, Ghana; Laboratory of Instrumentation Image and Spectroscopy, National Polytechnic Institute of Yamoussoukro, Ivory Coast; and Universidad Nacional de Ingeneria, Ecuador. The method is also disseminated to physics laboratories in Senegal, Togo, Mali, Burkina Faso, Cameroon, and Kenya.

Information for replicating the setup is available in supplementary files and on the software-sharing site, GitHub.[68] The available files include the acquisition/controlling software, PCB etching files, CAD files for cavity and LEGO optics adaptors, and a manual for assembly and operation.

## VI. SUMMARY AND OUTLOOK

We have presented BIOSPACE, an instrument capable of analyzing rotation aspects of a 3D target with multiple scatter angles, in different polarization modes, and with spectral sensitivity ranging from 365 to 940 nm. In total, a target can be captured by over 10 million unique images. This instrument enables automated multi-domain studies of a single sample. We have detailed the precision and calibration procedure of BIOSPACE for this paper to serve as a guide to replicate the instrument for broader use. We have shown the versatility of BIOSPACE in a few biophotonic applications involving directional dependence of an entomological lidar target, goniometric blood analysis, and polarimetric tissue analysis. The low cost and high versatility of BIOSPACE open up opportunities for research in the developing world and deployment in education even at bachelor college or high-school levels.

In analogy to the double integrating sphere method,[39,90] the scatter angle stage yields multiple potential measurement geometries. For example, ballistic transmittance, forward scattering, and

reflectance could be used to deduce the samples' optical properties (μa, μs, and g). By orientating the surface normal to intersect the median point between the illuminator and receiver, the specular reflection can be captured, and the refractive index, n, can be found by identifying the Brewster angle (refractometry). Polarimetric diagnostics is emerging with novel sensors in both medicine,[91] food inspection,[92] and vegetation analysis.[93] Our instrument could serve for feasibility studies of such applications across various domains. Envisioned applications also comprise tissue slabs,[45,90] food product inspection,[9,94] and the study of angular reflectance (BRDF) of leaves[95–97] for the diagnostics of health state or quality.

The potential applications extend beyond the examples reported in this study. One application within entomology is small animal imaging and 3D scanning of insects[21,73] and building a database of known insect species from museum collections or the wild. Similar attempts are pursued in, e.g., the oVert project,[98] where over 20 000 vertebrate species from museum collections are computer-tomography scanned and stored in a digital open-access format. Since there are over a million known insect species, a similar entomological project would need to be massively parallelized to succeed, e.g., by distribution to enthusiasts or high schools worldwide. BIOSPACE is suitable for such a project due to its low cost, use of standard components, and modular design. The extended optical capabilities of BIOSPACE could be of particular interest in such digitization projects since the insects display interesting optical phenomena such as iridescence, structural colors, ultraviolet features, and polarization-dependent reflection.[99]

## SUPPLEMENTARY MATERIAL

See supplementary material for replicating BIOSPACE. The supplementary material includes the following: S1, a bill of materials; S2, a manual for assembly and operation; and S3, files for 3D-printing the costum components needed.

## ACKNOWLEDGMENTS

This work was financed by a Uforsk Grant No. (2018-04073) from the Swedish Research Council to support realistic instrumentation and capacity building in low-income countries. The Royal Physiographical Society supported pilot studies at the Lund Laser Center (LLC). We thank the LEGO Company and colleagues at Lund University for fruitful discussions. We, therefore, extend our thanks to Olaf Diegel, David Frantz, Samuel Jansson, David Hill, David Sanned, and Andreas Johansson. We thank the staff at Laser and Fiber Optics Center (LAFOC) at the University of Cape Coast for hosting a workshop on this topic and participants from African Spectral Imaging Network (AFSIN), as well as the guest lectures Colin Sheppard, Katarina Svanberg, and Sune Svanberg. African workshops and instrument replication have been funded by the Swedish International Development Agency (SIDA) through the International Science Program (ISP, Uppsala) by a grant to the AFSIN.

## AUTHOR DECLARATIONS

### Conflict of Interest

The authors have no conflicts to disclose.

### Author Contributions

**Hampus Månefjord**: Conceptualization (equal); Formal analysis (lead); Investigation (lead); Methodology (lead); Software (lead); Visualization (lead); Writing – original draft (lead); Writing – review & editing (lead). **Meng Li** Investigation (supporting); Writing – review & editing (supporting). **Christian Brackmann**: Investigation (supporting); Supervision (supporting); Writing – review & editing (supporting). **Nina Reistad**: Funding acquisition (equal); Resources (supporting); Writing – review & editing (supporting). **Anna Runemark**: Writing – original draft (supporting); Writing – review & editing (supporting). **Jadranka Rota**: Resources (equal); Writing – original draft (supporting); Writing – review & editing (supporting). **Benjamin Andersson**: Conceptualization (supporting); Funding acquisition (equal); Writing – review & editing (supporting). **Jeremie T. Zoueu**: Conceptualization (equal); Funding acquisition (equal); Writing – review & editing (supporting). **Aboma Merdasa**: Conceptualization (equal); Methodology (equal); Project administration (equal); Supervision (supporting); Writing – review & editing (supporting). **Mikkel Brydegaard**: Conceptualization (equal); Formal analysis (equal); Funding acquisition (equal); Investigation (equal); Methodology (equal); Resources (equal); Supervision (equal); Writing – original draft (equal); Writing – review & editing (equal).

## DATA AVAILABILITY

The data that support the findings of this study are available from the corresponding author upon reasonable request.

## REFERENCES

[1]C. Boudoux, *Fundamentals of Biomedical Optics: From Light Interactions with Cells to Complex Imaging Systems* (Pollux, Montréal, 2018).
[2]J. Popp *et al.*, *Handbook of Biophotonics, Volume 3: Photonics in Pharmaceutics, Bioanalysis and Environmental Research* (John Wiley & Sons, 2012), Vol. 3.
[3]S. L. Jacques and B. W. Pogue, "Tutorial on diffuse light transport," J. Biomed. Opt. **13**(4), 041302 (2008).
[4]V. V. Tuchin, *Optical Biomedical Diagnostics* (Izdatelstvo Fizikomatematicheskoy Literaturi, Moscow, 2007), Vol. 1, p. 560.
[5]W. Turner *et al.*, "Remote sensing for biodiversity science and conservation," Trends Ecol. Evol. **18**(6), 306–314 (2003).
[6]M. Brydegaard and S. Svanberg, "Photonic monitoring of atmospheric and aquatic fauna," Laser Photonics Rev. **12**(12), 1800135 (2018).
[7]B. Park and R. Lu, *Hyperspectral Imaging Technology in Food and Agriculture* (Springer, 2015).
[8]J. M. Amigo, H. Babamoradi, and S. Elcoroaristizabal, "Hyperspectral image analysis. A tutorial," Anal. Chim. Acta **896**, 34–51 (2015).
[9]J. Qin and R. Lu, "Measurement of the optical properties of fruits and vegetables using spatially resolved hyperspectral diffuse reflectance imaging technique," Postharvest Biol. Technol. **49**(3), 355–365 (2008).
[10]S. Svanberg, "Gas in scattering media absorption spectroscopy–from basic studies to biomedical applications," Laser Photonics Rev. **7**(5), 779–796 (2013).
[11]J. G. Fujimoto and D. Farkas, *Biomedical Optical Imaging* (Oxford University Press, 2009).
[12]E. M. C. Hillman *et al.*, "*In vivo* optical imaging and dynamic contrast methods for biomedical research," Philos. Trans. R. Soc., A **369**(1955), 4620–4643 (2011).
[13]J. Michels and S. N. Gorb, "Detailed three-dimensional visualization of resilin in the exoskeleton of arthropods using confocal laser scanning microscopy," J. Microsc. **245**(1), 1–16 (2012).

[14]S. W. Hell, "Nobel Lecture: Nanoscopy with freely propagating light," Rev. Mod. Phys. **87**(4), 1169 (2015).
[15]P. Beard, "Biomedical photoacoustic imaging," Interface Focus **1**(4), 602–631 (2011).
[16]M. T. Stridh *et al.*, "Photoacoustic imaging of periorbital skin cancer *ex vivo*: Unique spectral signatures of malignant melanoma, basal, and squamous cell carcinoma," Biomed. Opt. Express **13**(1), 410–425 (2022).
[17]P. Cimalla *et al.*, "Simultaneous dual-band optical coherence tomography in the spectral domain for high resolution *in vivo* imaging," Opt. Express **17**(22), 19486–19500 (2009).
[18]O. E. Olarte *et al.*, "Light-sheet microscopy: A tutorial," Adv. Opt. Photonics **10**(1), 111 (2018).
[19]H. Jiang, *Diffuse Optical Tomography: Principles and Applications* (CRC Press, 2018).
[20]J. Sharpe, "Optical projection tomography," Annu. Rev. Biomed. Eng. **6**, 209–228 (2004).
[21]B. Strobel *et al.*, "An automated device for the digitization and 3D modelling of insects, combining extended-depth-of-field and all-side multi-view imaging," Zookeys **759**, 1–27 (2018).
[22]R. Richards-Kortum and E. Sevick-Muraca, "Quantitative optical spectroscopy for tissue diagnosis," Annu. Rev. Phys. Chem. **47**(1), 555–606 (1996).
[23]N. Reistad *et al.*, "Diffuse reflectance spectroscopy of liver tissue," Proc. SPIE **9531**, 95314E (2015).
[24]N. Gat, "Imaging spectroscopy using tunable filters: A review," Proc. SPIE **4056**, 50–64 (2000).
[25]L. L. Randeberg and J. Hernandez-Palacios, "Hyperspectral imaging of bruises in the SWIR spectral region," Proc. SPIE **8207**, 82070N (2012).
[26]E. M. Georgieva, W. Huang, and W. S. Heaps, "A new remote sensing filter radiometer employing a Fabry-Perot etalon and a CCD camera for column measurements of methane in the Earth atmosphere," in *2012 IEEE International Geoscience and Remote Sensing Symposium* (IEEE, 2012).
[27]M. W. Kudenov and E. L. Dereniak, "Compact real-time birefringent imaging spectrometer," Opt. Express **20**(16), 17973–17986 (2012).
[28]Y. Ferrec *et al.*, "Experimental results from an airborne static Fourier transform imaging spectrometer," Appl. Opt. **50**(30), 5894–5904 (2011).
[29]F. J. Bolton *et al.*, "Portable, low-cost multispectral imaging system: Design, development, validation, and utilization," J. Biomed. Opt. **23**(12), 1–11 (2018).
[30]G. ElMasry *et al.*, "Recent applications of multispectral imaging in seed phenotyping and quality monitoring—An overview," Sensors **19**(5), 1090 (2019).
[31]M. Brydegaard *et al.*, "Versatile multispectral microscope based on light emitting diodes," Rev. Sci. Instrum. **82**(12), 123106 (2011).
[32]M. Goel *et al.*, "HyperCam: Hyperspectral imaging for ubiquitous computing applications," in *Proceedings of the 2015 ACM International Joint Conference on Pervasive and Ubiquitous Computing* (Association for Computing Machinery, 2015).
[33]S. Kim *et al.*, "Smartphone-based multispectral imaging: System development and potential for mobile skin diagnosis," Biomed. Opt. Express **7**(12), 5294–5307 (2016).
[34]S. L. Jacques, "Polarized light imaging of biological tissues," in *Handbook of Biomedical Optics* (CRC Press, 2016), pp. 669–692.
[35]V. V. Tuchin, "Polarized light interaction with tissues," J. Biomed. Opt. **21**(7), 071114 (2016).
[36]H. Luo *et al.*, "Compact and miniature snapshot imaging polarimeter," Appl. Opt. **47**(24), 4413–4417 (2008).
[37]D. Rebhan *et al.*, "Principle investigations on polarization image sensors," Proc. SPIE **11144**, 111440A (2019).
[38]D. B. Murphy, *Fundamentals of Light Microscopy and Electronic Imaging* (John Wiley & Sons, 2002).
[39]J. W. Pickering, S. A. Prahl, N. van Wieringen, J. F. Beek, H. J. C. M. Sterenborg, and M. J. C. van Gemert, "Double-integrating-sphere system for measuring the optical properties of tissue," Appl. Opt. **32**, 399 (1993).
[40]A. Merdasa *et al.*, "Staining-free malaria diagnostics by multispectral and multimodality light-emitting-diode microscopy," J. Biomed. Opt. **18**(3), 036002 (2013).
[41]F. Foschum and A. Kienle, "Optimized goniometer for determination of the scattering phase function of suspended particles: Simulations and measurements," J. Biomed. Opt. **18**(8), 85002 (2013).
[42]M. L. Askoura, F. Vaudelle, and J.-P. L'Huillier, "Multispectral measurement of scattering-angular light distribution in apple skin and flesh samples," Appl. Opt. **55**(32), 9217–9225 (2016).
[43]B. K. Wilson, M. R. Behrend, M. P. Horning, and M. C. Hegg, "Detection of malarial byproduct hemozoin utilizing its unique scattering properties," Opt. Express **19**, 12190 (2011).
[44]S. Jansson *et al.*, "First polarimetric investigation of malaria mosquitoes as lidar targets," IEEE J. Sel. Top. Quantum Electron. **25**(1), 1–8 (2019).
[45]S. L. Jacques, "Optical properties of biological tissues: A review," Phys. Med. Biol. **58**(11), R37–R61 (2013).
[46]M. G. Müller *et al.*, "Intrinsic fluorescence spectroscopy in turbid media: Disentangling effects of scattering and absorption," Appl. Opt. **40**(25), 4633–4646 (2001).
[47]D. J. Faber *et al.*, "Oxygen saturation-dependent absorption and scattering of blood," Phys. Rev. Lett. **93**(2), 028102 (2004).
[48]T. Svensson *et al.*, "Near-infrared photon time-of-flight spectroscopy of turbid materials up to 1400 nm," Rev. Sci. Instrum. **80**(6), 063105 (2009).
[49]M. Burresi *et al.*, "Bright-white beetle scales optimise multiple scattering of light," Sci. Rep. **4**(1), 6075 (2014).
[50]D. Elson *et al.*, "Time-domain fluorescence lifetime imaging applied to biological tissue," Photochem. Photobiol. Sci. **3**(8), 795–801 (2004).
[51]P. Herman *et al.*, "Frequency-domain fluorescence microscopy with the LED as a light source," J. Microsc. **203**(2), 176–181 (2001).
[52]J. Borggren, "Combinatorial light path spectrometer for turbid liquids," Lund Reports in Atomic Physics, 2011.
[53]S. H. Chung *et al.*, "Macroscopic optical physiological parameters correlate with microscopic proliferation and vessel area breast cancer signatures," Breast Cancer Res. **17**(1), 72 (2015).
[54]T. Durduran *et al.*, "Diffuse optics for tissue monitoring and tomography," Rep. Prog. Phys. **73**(7), 076701 (2010).
[55]J. S. Cybulski, J. Clements, and M. Prakash, "Foldscope: Origami-based paper microscope," PLoS One **9**(6), e98781 (2014).
[56]S. Rawat *et al.*, "Compact and field-portable 3D printed shearing digital holographic microscope for automated cell identification," Appl. Opt. **56**(9), D127–D133 (2017).
[57]E. K. Grasse, M. H. Torcasio, and A. W. Smith, "Teaching UV–Vis spectroscopy with a 3D-printable smartphone spectrophotometer," J. Chem. Educ. **93**(1), 146–151 (2016).
[58]B. S. Hosker, "Demonstrating principles of spectrophotometry by constructing a simple, low-cost, functional spectrophotometer utilizing the light sensor on a smartphone," J. Chem. Educ. **95**(1), 178–181 (2018).
[59]A. Lietard *et al.*, "A combined spectrophotometer and fluorometer to demonstrate the principles of absorption spectroscopy," J. Chem. Educ. **98**(12), 3871–3877 (2021).
[60]E. Montoya-Rossi, Ó. Baltuano-Elías, and A. Arbildo-López, "A homemade cost effective Raman spectrometer with high performance," J. Lab. Chem. Educ. **3**, 67 (2015).
[61]J. Fernsler *et al.*, "A LEGO Mindstorms Brewster angle microscope," Am. J. Phys. **85**(9), 655–662 (2017).
[62]N. Haverkamp *et al.*, "Measuring wavelengths with LEGO® bricks: Building a Michelson interferometer for quantitative experiments," Phys. Teach. **58**(9), 652–655 (2020).
[63]J. M. Pearce, "Building research equipment with free, open-source hardware," Science **337**(6100), 1303–1304 (2012).
[64]X.-C. Zhang *et al.*, "Open source 3D printers: An appropriate technology for building low cost optics labs for the developing communities," in *14th Conference on Education and Training in Optics and Photonics: ETOP 2017* (SPIE, 2017).
[65]J. Larsson *et al.*, "Development of a 3-dimensional tissue lung phantom of a preterm infant for optical measurements of oxygen-laser-detector position considerations," J. Biophotonics **11**(3), e201700097 (2018).

[66]L. J. Salazar-Serrano, P. Torres, and A. Valencia, "A 3D printed toolbox for opto-mechanical components," PLoS One **12**(1), e0169832 (2017).
[67]J. P. Sharkey *et al.*, "A one-piece 3D printed flexure translation stage for open-source microscopy," Rev. Sci. Instrum. **87**(2), 025104 (2016).
[68]H. Månefjord, BIOSPACE–Github repository, 2021; Available from: https://github.com/HampusMLTH/BIOSPACE.
[69]F. Lundh, An introduction to Tkinter, URL: www.pythonware.com/library/tkinter/introduction/index.html, 1999.
[70]Stefanklug, PyPylon. 2021. p. https://github.com/basler/pypylon.
[71]Dexter Industries, BrickPi. 2021. p. https://github.com/DexterInd/BrickPi.
[72]K. Ahi, "Mathematical modeling of THz point spread function and simulation of THz imaging systems," IEEE Trans. Terahertz Sci. Technol. **7**(6), 747–754 (2017).
[73]C. V. Nguyen *et al.*, "Capturing natural-colour 3D models of insects for species discovery and diagnostics," PLoS One **9**(4), e94346 (2014).
[74]J. B. Silver, *Mosquito Ecology: Field Sampling Methods* (Springer Science & Business Media, 2007).
[75]C. A. Hallmann *et al.*, "More than 75% decline over 27 years in total flying insect biomass in protected areas," PLoS One **12**(10), e0185809 (2017).
[76]S. Jansson, Lund University, Entomological Lidar: Target Characterization and Field Applications, 2020.
[77]M. Li *et al.*, "Bark beetles as lidar targets and prospects of photonic surveillance," J. Biophotonics **14**, e202000420 (2020).
[78]H. Yin *et al.*, "Iridescence in the neck feathers of domestic pigeons," Phys. Rev. E: Stat., Nonlinear, Soft Matter Phys. **74**(5), 051916 (2006).
[79]D. G. Stavenga, "Thin film and multilayer optics cause structural colors of many insects and birds," Mater. Today: Proc. **1**, 109–121 (2014).
[80]H. Liu *et al.*, "Determination of optical properties and blood oxygenation in tissue using continuous NIR light," Phys. Med. Biol. **40**(11), 1983 (1995).
[81]A. Merdasa *et al.*, "Photoacoustic imaging of the spatial distribution of oxygen saturation in an ischemia-reperfusion model in humans," Biomed. Opt. Express **12**(4), 2484–2495 (2021).
[82]Y. Tan *et al.*, "Mechanical characterization of human red blood cells under different osmotic conditions by robotic manipulation with optical tweezers," IEEE Trans. Biomed. Eng. **57**(7), 1816–1825 (2010).
[83]H. Byun *et al.*, "Optical measurement of biomechanical properties of individual erythrocytes from a sickle cell patient," Acta Biomater. **8**(11), 4130–4138 (2012).
[84]World Health Organization, Basic malaria microscopy. Volume 2, 2010.
[85]K. R. Beebe and B. R. Kowalski, "An introduction to multivariate calibration and analysis," Anal. Chem. **59**(17), 1007A–1017A (1987).
[86]Y. Kim *et al.*, "Anisotropic light scattering of individual sickle red blood cells," J. Biomed. Opt. **17**(4), 040501 (2012).
[87]A. Shuaib, X. Li, and G. Yao, "Transmission of polarized light in skeletal muscle," J. Biomed. Opt. **16**(2), 025001 (2011).
[88]X. Li, J. C. Ranasinghesagara, and G. Yao, "Polarization-sensitive reflectance imaging in skeletal muscle," Opt. Express **16**(13), 9927–9935 (2008).
[89]H. Månefjord *et al.*, "BIOSPACE—A low-cost platform for problem-based learning in biophotonics," in *2021 Proceedings of the Teaching and Learning Conferences, 2021* (Centre for Engineering Education, Lund University, 2021), p. 11.
[90]A. ul Rehman, I. Ahmad, and S. A. Qureshi, "Biomedical applications of integrating sphere: A review," Photodiagn. Photodyn. Ther. **31**, 101712 (2020).
[91]Z. Ali *et al.*, "Assessment of tissue pathology using optical polarimetry," Lasers Med. Sci. **37**, 1907–1919 (2021).
[92]M. Peyvasteh *et al.*, "Evolution of raw meat polarization-based properties by means of Mueller matrix imaging," J. Biophotonics **14**(5), e202000376 (2021).
[93]S. N. Savenkov *et al.*, "Measurement and interpretation of Mueller matrices of barley leaves," Quantum Electron. **50**(1), 55 (2020).
[94]R. Lu *et al.*, "Measurement of optical properties of fruits and vegetables: A review," Postharvest Biol. Technol. **159**, 111003 (2020).
[95]D. Biliouris *et al.*, "A compact laboratory spectro-goniometer (CLabSpeG) to assess the BRDF of materials. Presentation, calibration and implementation on Fagus sylvatica L. leaves," Sensors **7**(9), 1846–1870 (2007).
[96]L. Lolli *et al.*, "PHYTOS: A portable goniometer for *in situ* spectro-directional measurements of leaves," Metrologia **51**(6), S309 (2014).
[97]B. Tumendemberel, "Study of spectro-polarimetric bidirectional reflectance properties of leaves," Ph.D. thesis (Hokkaido University, 2019).
[98]R. Cross, "The inside story on 20 000 vertebrates," Science **357**, 742 (2017).
[99]P. Vukusic and D. Stavenga, "Physical methods for investigating structural colours in biological systems," J. R. Soc., Interface **6**(Suppl_2), S133–S148 (2009).

# Paper VIII

INTERFACE

royalsocietypublishing.org/journal/rsif

Research

**Cite this article:** Li M, Seinsche C, Jansson S, Hernandez J, Rota J, Warrant E, Brydegaard M. 2022 Potential for identification of wild night-flying moths by remote infrared microscopy. *J. R. Soc. Interface* **19**: 20220256. https://doi.org/10.1098/rsif.2022.0256

Received: 31 March 2022
Accepted: 31 May 2022

**Subject Category:**
Life Sciences–Physics interface

**Subject Areas:**
biometeorology

**Keywords:**
Lepidoptera, remote sensing, microstructures, surface roughness, infrared spectroscopy, hyperspectral imaging

**Author for correspondence:**
Meng Li
e-mail: meng.li@forbrf.lth.se

Electronic supplementary material is available online at https://doi.org/10.6084/m9.figshare.c.6039061.

THE ROYAL SOCIETY PUBLISHING

# Potential for identification of wild night-flying moths by remote infrared microscopy

Meng Li[1], Clara Seinsche[2,3], Samuel Jansson[1,2,4], Julio Hernandez[5], Jadranka Rota[2,6], Eric Warrant[2] and Mikkel Brydegaard[1,2,4,5]

[1]Department of Physics, Lund University, Sölvegatan 14c, 22363 Lund, Sweden
[2]Department of Biology, Lund University, Sölvegatan 35, 22362 Lund, Sweden
[3]Department of Biology, University of Cologne, Zuelpicher Straße 47b, 50931 Cologne, Germany
[4]FaunaPhotonics, Støberigade 14, 2450 Copenhagen, Denmark
[5]Norsk Elektro Optikk A/S, Østensjøveien 34, 0667 Oslo, Norway
[6]Biological Museum, Department of Biology, Lund University, Sölvegatan 37, 22362 Lund, Sweden

ML, 0000-0003-4931-5647; CS, 0000-0002-0798-3367; SJ, 0000-0003-4142-6334; JR, 0000-0003-0220-3920; EW, 0000-0001-7480-7016; MB, 0000-0003-0586-664X

There are hundreds of thousands of moth species with crucial ecological roles that are often obscured by their nocturnal lifestyles. The pigmentation and appearance of moths are dominated by cryptic diffuse shades of brown. In this study, 82 specimens representing 26 moth species were analysed using infrared polarimetric hyperspectral imaging in the range of 0.95–2.5 µm. Contrary to previous studies, we demonstrate that since infrared light does not resolve the surface roughness, wings appear glossy and specular at longer wavelengths. Such properties provide unique reflectance spectra between species. The reflectance of the majority of our species could be explained by comprehensive models, and a complete parametrization of the spectral, polarimetric and angular optical properties was reduced to just 11 parameters with physical units. These parameters are complementary and, compared with the within-species variation, were significantly distinct between species. Counterintuitively to the aperture-limited resolution criterion, we could deduce microscopic features along the surface from their infrared properties. These features were confirmed by electron microscopy. Finally, we show how our findings could greatly enhance opportunities for remote identification of free-flying moth species, and we hypothesize that such flat specular wing targets could be expected to be sensed over considerable distances.

## 1. Introduction

The lives of moths (order Lepidoptera) are obscure for most people owing to their nocturnal lifestyles. Most of our encounters with these insects are limited to their erratic fluttering flights around our light bulbs at night [1], and enthusiasts and biologists attempt to understand their behaviour and diversity using moth light traps and illuminated sheets [2]. There are hundreds of thousands of species of moths—10-fold the number of butterfly species [3–5]—and include infamous agricultural pest species such as army worms [6], corn- and sugarcane borers [7] and cutworms [8], all of which are pests with an enormous potential to inflict severe economic damage [9]. Other species are beneficial, such as the silkworm moth, the edible mopane worm (the larva of a species of emperor moth) and the Bogong moth, an iconic species of immense importance to the health of Australian alpine ecosystems [10–12]. While we sleep, moths take the night shift of pollinating our crops [13], and they provide a source of food that sustains a diverse group of predators [14]. Moreover, migratory

moths transport megatons of biomass worldwide, providing a rich source of energy and nutrition for a variety of animals along the way [15].

How might we gain more insight into the fascinating lives and natural behaviours of moths? The disciplines of animal telemetry [16] and entomological radar [17] have made great progress in our understanding of moth behaviour over recent decades, and harmonic radar has been shown to track moth movements in the landscape [18], although the sample size is small in such tagging studies. The impressive dispersals of nocturnal insects have been visualized by continental networks of meteorological Doppler radars [19], with vertical polarimetric radar capable of tracking enormous numbers of untagged species above the ground clutter altitude [20]. The radar signal reflects the liquid water distribution in the moths, and the observations can be grouped by size [21], elongation [22] and, to some extent, by wingbeat frequency [23]. Despite these advances, it has not been possible to identify moths at the level of families and species with microwaves and radar.

At first glance, the coloration of moths is dull and dominated by different degrees of melanin [24,25]. Although some species display warning colours and mimic predators' eyes (e.g. the owl moth), such markings often constitute a minor fraction of the entire wings. Such markings also generally appear on the dorsal side of the wings, meaning that ground-based remote sensing technology has a limited ability to probe such spectral features [26]. The ventral sides of moth wings exhibit shades of brown [27], which is somewhat discouraging in terms of the potential for differentiating moth species remotely. The scattering phase function (the so-called bidirectional reflectance distribution function (BRDF)) recorded from the majority of moths displays a diffuse and Lambertian behaviour [28]. In other words, the ventral sides of moth wings are seldom glossy, and thus their oscillatory scattering cross-section waveform during a wingbeat does not differ more than their wingbeat dynamics [29] because of their wing shape projection throughout the wingbeat [30]. This waveform can be effectively described by only three harmonics, while a richer parameter space would yield a larger opportunity for identifying individual species.

Visual appearance and crypsis are not the only functions that could drive the evolution of wing surface morphology in moths. Other functions might include optimization of aerodynamic [31] or hydrophobic properties [32] or minimizing ultrasonic reflectance in relation to bat predation [33]. Moreover, some species possess androconial scales that produce species-specific pheromones used for mate attraction [34], while in the dot-underwing moth sexually dimorphic wing coloration might be used as a sexual signal during courtship [35]. Thus, scale morphology may also be associated with sexual selection.

While butterflies have fascinated scientists for centuries with their ability to manipulate daylight through organized nanostructures or photonic crystals [36–40], nocturnal moths have a limited benefit for such manipulations. Similarly, the relation between pigmentation and thermoregulation would therefore have little influence on the absorption of incoming visible daylight for the moth. Since thermoregulation is based on the incoming and outgoing energy balance, this leads to an intriguing thought: since butterflies manipulate visible reflectance by nanostructures, the organization of microstructures in moths might govern the thermal infrared emissivity spectrum associated with radiative cooling [41], leaving moths with a potential mechanism for adjusting thermoregulation. This idea has been proposed several times [41–43], but such functionality could not be confirmed [24]. Nonetheless, microstructures can alter infrared spectral emissivity [44] as well as angular emissivity [45]. In addition, a measure of surface roughness, which determines the specularity, depends on the wavelength of light in question [46]. Infrared waves do not resolve the smallest structures and also experience a steeper gradient of refractive index [39] within a structured surface, with the result that specularity increases towards infrared wavelengths [47–49].

It is conventional wisdom that picometre-sized atoms and molecules, too small to resolve with microscopy, can be imaged with spectral imaging [50]. Similarly, submicron-dominant spatial frequencies can be deduced from coherent tissue colours [51] or resonant thin films [39]. Even incoherent reflectance can, in some situations, reveal microscopic features, thus circumventing the imaging resolution criterion [52,53]. In this study, we demonstrate how information concerning lateral microscopic features on moth wings might be retrievable over long distances.

Here, we investigate the coherent and incoherent short-wave infrared properties of the ventral and dorsal sides of wings in 82 individuals representing 26 species of moths. We demonstrate that moth wings generally become glossier towards the infrared but that both surface roughness and the steepness of this increase consistently differ between species. We provide simple physical models and parameterization for both coherent and incoherent scattering from both the ventral and dorsal sides of moth wings. We investigate the diversity that is apparent among moths and explain the potential for remote species identification by laser radar, discussing optimal bands for specificity. Ultimately, we demonstrate how this increased flatness at infrared wavelengths can increase information richness in a lidar identification scenario.

## 2. Results

### 2.1. Infrared properties of moth wings

Hyperspectral imaging was carried out on 82 moth specimens from 26 species. Specular images of each species are presented as true-colour-visible (VIS) images and false-coloured short-wavelength infrared (SWIR) images in figure 1. Many moth wings display glossiness in the SWIR image, and some even display structural colour (figure 1$n$,$o$, $t_1$,$x$; note that gain is reduced for specular images to avoid saturation).

Hyperspectral imaging was performed for all specimens under three different illumination configurations to study coherent, incoherent and diffuse reflectance from the dorsal and ventral sides of the moth wing (see the illustration in the electronic supplementary material, figure S1). We evaluated the effective reflectance spectra integrated over the entire moth wing surface, as these are properties that can be retrieved by lidar over far distances. These effective reflectance spectra were then parameterized by several spectral reflectance models. Our models rely on parameters in SI units for intercomparability between studies (see electronic supplementary material, tables S1–S6). Co-polarized effective reflectance of 25 out of 26 species


**Figure 1.** Twenty-six moth species examined in the study are presented in both true- and false-colour images. The left halves of the moths are shown in true-colour RGB (VIS) images taken with a commercial camera with diffuse illumination. The right halves of the moths are shown in false-colour SWIR images scanned with a hyperspectral camera in specular illumination (band choices: blue at 1250 nm, green at 1700 nm and red at 2300 nm) with a gain of 40%. Species of moths: (*a*) *Tebenna bjerkandrella*, (*b*) *Meganola strigula*, (*c*) *Phiaris schulziana*, (*d*) *Agonopterix ciliella*, (*e*) *Emmelina monodactyla*, (*f*) *Crambus perlella*, (*g*) *Hypena crassalis*, (*h*) *Trichopteryx carpinata*, (*i*) *Aethalura punctulata*, (*j*) *Lygephila craccae*, (*k*) *Autographa gamma*, (*l*) *Acronicta leporina*, (*m*) *Helicoverpa armigera*, (*n*) *Phragmatobia fuliginosa*, (*o*) *Agriopis leucophaearia*, (*p*) *Apamea crenata*, (*q*) *Furcula bifida*, (*r*) *Agrotis munda*, (*s*) *Calliteara pudibunda*, ($t_1$,$t_2$) *Biston betularia*, (*u*) *Agrotis infusa*, (*v*) *Eriogaster lanestris*, (*w*) *Noctua pronuba*, (*x*) *Agrotis ipsilon*, (*y*) *Aglia tau* and (*z*) *Agrius convolvuli*.

could be explained by a long-pass function model (but seven species were out of our instrument spectral range) and de-polarized and diffused reflectance of 26 out of 26 species could be explained by a de-polarized/diffuse reflectance model. Apart from spectral parameterization, we also describe and parametrize the depolarization features of moth wings, which is another aspect that can be retrieved remotely.

The probability of correct identification of moth species based on the parametrized values was estimated for ventral remote identification. There are nine parameters for co-polarized, de-polarized and diffuse classification (see

electronic supplementary material, tables S2, S4 and S6). For each species, we produced $10^4$ synthetic data points with the corresponding median and interquartile range (IQR) for each parameter; the synthetic data were then fed into naive Bayes classifiers. The covariance between parameters was not included. The parameter overlap was estimated between species and visualized by a standard confusion matrix (see electronic supplementary material, figures S32–S37). Within the selection, several species could be distinguished with high accuracies in the range of 80–90%, even with just three parameters from either diffuse, co-polarized or de-polarized measurements (see electronic supplementary material, figures S32–S34). However, with only three parameters, the species with large parameter overlap are also the species with an asymmetric IQR caused by outliers due to wing alignments. The success of identification drastically improves when six parameters are included; for example, co-polarized parameters in conjunction with de-polarized or diffuse properties (see electronic supplementary material, figures S35 and S36). When all nine ventral parameters from co-polarized, de-polarized and diffused classification were used to identify species, the system has nearly 100% accuracy for most of the species, as shown in electronic supplementary material, figure S37. From a lidar design perspective, acquiring all nine parameters, however, implies a rather complex system. The three co-polarized parameters imply that coherent moth wing properties could be captured by a triple-band lidar system. In addition, such a system would simultaneously be able to capture the diffuse properties in between the coherent flashes in the wingbeat cycle. Band placement would need to include short bands for melanin, a long band where the infrared flatness is captured and an intermediate band in relation to the steepness coefficient, $\alpha$.

Examples of effective reflectance spectra under coherent co-polarized, incoherent de-polarized and diffuse illumination are shown for the moth *Apamea crenata* in figure 2. Apart from one species (*Agriopis leucophaearia*) displaying a fringed spectrum, the remaining moths display similar spectra to those shown in figure 2 but with distinct magnitudes, cut-on wavelengths and spectral steepness (see electronic supplementary material, tables S1 and S2). In addition, the cut-on wavelength of seven species exceeded our instrument range; thus, the cut-on wavelength could not be determined. Coherent co-polarized spectra from both the dorsal and ventral sides of the moth wings (figure 2*e*,*l*, solid black line) exceed 100% diffuse reflectance. Co-polarized coherent reflection, or the specular reflectance lobe from glossy samples, has a degree of dependence on the incidence angle and predominantly contributes to the signal in the specular imaging mode. By contrast, diffuse targets produce a Lambertian reflectance lobe where a smaller portion of the scattered light reaches the camera (see electronic supplementary material, figure S1*B*). All spectra were calibrated to a diffuse Lambertian reference, and strong specular co-polarized light reflectance exceeded Lambertian white. The coherent reflectance increases towards longer wavelengths (figure 2*e*,*l*), while the incoherent reflectance decreases with wavelength (figure 2*f*,*m*). Both these effects could be explained by the fact that long-wavelength infrared photons experience rough surfaces flatter than their short-wavelength counterparts. Thus, the rough surface features on moth wings cannot be resolved at the longer wavelengths. Consequently, wings display smoothness and glossiness towards infrared. The inverse phenomenon can also be observed in figure 2*g*,*n*, where the moth wings were under diffuse angle illumination (illustrated in the electronic supplementary material, figure S1*A*,*C*). As the moth wing surface appears smoother at longer wavelengths, the diffuse lobe gradually morphs into an elongated specular lobe along the surface normal, implying that less light reaches the camera (see light lobe shape changes from electronic supplementary material, figure S1*C*–S1*A*). The spectral increase in coherent co-polarized reflectance in figure 2*e*,*l* and the decrease in the incoherent de-polarized reflectance in figure 2*f*,*m* at a longer wavelength indicate that mainly specular-reflected photons remember their original polarization state.

Interestingly, a large proportion of the investigated species display consistently distinguishable parameters in both the spectral and polarization domains. Such a result considerably raises the prospects for remote identification of moths. To exploit the increased flatness of moth wings in the infrared regime to assist with insect species identification in lidar data, we need to understand what those extracted physical parameters in the electronic supplementary material, tables S1–S8 represent and how they are correlated to species and wing surface periodic nanostructures. All physical parameters in the electronic supplementary material, tables S1–S8 are plotted as scatter plots and are shown in the electronic supplementary material, figures S2–S21 for coherent, incoherent, diffuse and degree of linear polarization (DoLP) measurements. The data points are the median of multiple specimens of each species, and the indicated spread is by the IQR within the same species. As moth wings become glossier towards infrared wavelengths, their physical parameters consistently differ between species (see electronic supplementary material, figures S2 and S3) and, for each species, these parameters generally do not overlap with those of the majority of the remaining investigated species. This tendency also prevails in scatter plots of the rest of the optical parameter spaces (see electronic supplementary material, figures S3–S21 for both ventral and dorsal sides).

To remotely identify freely flying moths, their ventral infrared properties could be retrieved by entomological lidar [54] in vertical mode. Such lidars can be implemented with polarization sensitivity [55] and/or with dual band in the short-wave infrared [56]. Wings make the largest contribution to the backscattering, and most of the wing signal is coherent and specular. Therefore, the optical properties of moth wings from the ventral side under coherent co-polarized illumination contain the information that is useful for developing a moth-identifying vertical lidar. There are a few sources of environmental noise that may interfere with moth identification. Daylight suppression is generally a challenge in multiband atmospheric lidar but is less of an issue for monitoring nocturnal moths. Atmospheric turbulence can cause low-frequency noise that can be confused with the moth wingbeat, but this mainly occurs during the daytime. Water vapour can attenuate several bands within the infrared spectral range. On shorter ranges, e.g. a kilometer this attenuation is less severe than through the entire atmosphere.

As alluded to above, the coherent co-polarized wing reflectance can be explained by a long-pass function with three parameters: $R_{\mathrm{long}}$, the maximum reflectance for long wavelengths; $\lambda_0$, the surface roughness (the cut-on wavelength of the long-pass function in micrometres at which the surface turns from diffuse to specular); and $\alpha$, the long-pass steepness (like filter order, this is unitless). For remote lidar sensing

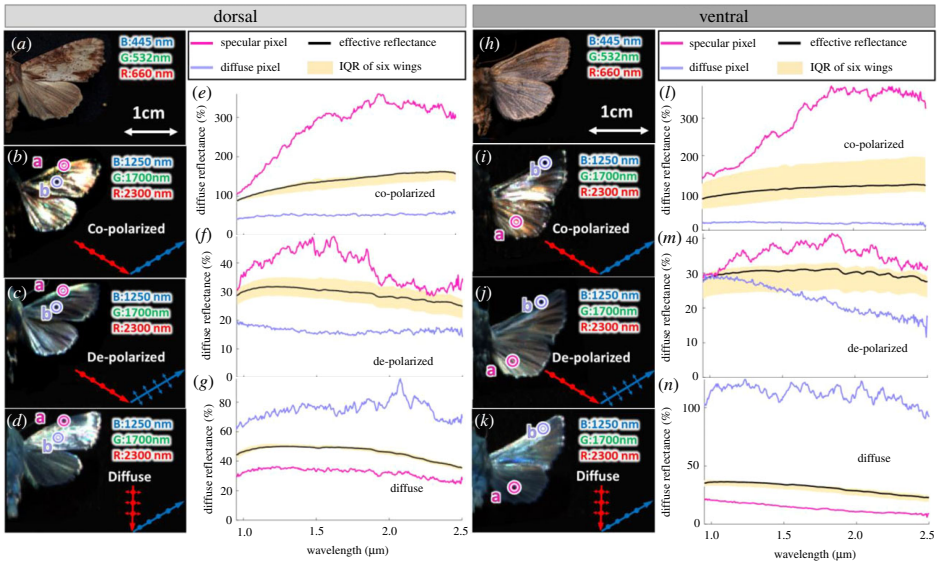


**Figure 2.** The reflectance of a specular pixel (pink circle labelled 'a'), a diffuse pixel (mauve circle labelled 'b') and entire wing pixels from the dorsal and ventral sides of the moth *A. crenata*. *Red* and *blue arrows* (in (*b–d*), (*i–k*)) indicate the illumination and detection configurations. In both (*b,i*), incident and received signals are horizontally polarized (*dots* on the *arrow* indicate that the polarization direction is perpendicular to the plane of the paper). In (*c,j*), the incident light is horizontally polarized, and the received signal is vertically polarized (the polarization direction is parallel to the plane of the paper). In (*g,n*), the incoming light is unpolarized and coincides with the surface normal, and the received signal is horizontally polarized. The *yellow area* in (*e–g*) and (*l–n*) highlights the effective reflectance (IQR spread of six individual wings of the same species).

applications, $R_{long}$ will be challenging to estimate because of the orientation of the wing as well as the position in the beam. Therefore, the surface roughness $\lambda_0$ and the steepness $\alpha$ are better candidates for remote identification. Since the spectral features $\lambda_0$ and $\alpha$ could not be associated with molecular absorption (i.e. by melanin and chitin), they necessarily relate to the microstructures of moth wings and could thus be used to differentiate species through remote microscopy. Specular wing properties are known to produce rich harmonic spectra which can be sensed remotely [57]. All spectral and polarimetry specular reflectance parameters from the moth ventral side are provided in electronic supplementary material, table S2, and a scatter plot of surface roughness $\lambda_0$ versus steepness $\alpha$ is presented in electronic supplementary material, figure S3.

Eight species (one species with two subspecies) with extreme values of surface roughness $\lambda_0$ and steepness $\alpha$ (electronic supplementary material, figure S3) are chosen and highlighted in figure 3*a*. All eight chosen species' wing surface microstructures were investigated with scanning electron microscopy (SEM) as part of this study. Two extreme cases from eight species in surface roughness and two other extreme cases in steepness are shown in figure 4 as colour-coded wing images, where $\lambda_0$ and $\alpha$ are calculated on a pixel level. The figures map out the surface roughness and steepness changes among the wings and provide a sense of which wing region has the greatest influence on the value we parametrized across the entire wing.

## 2.2. Electron microscopy of wing scale structures

The periodicity of ventral nanostructures was investigated using SEM. Moth wings are covered in scales (both ventrally and dorsally), which exhibit a periodic two-dimensional pattern on the scale surface. These structures vary in periodicity, with the coarsest feature being the ridges parallel to the scale's main growth axis. Perpendicular to the ridges, a series of more finely spaced cross-ribs can be observed, which are sometimes intersected by ripples. To quantitively assess these nanostructures, spatial frequencies of ridges, cross-ribs and ripples were measured from the SEM images to show the relationship between the different nanostructures and their spatial frequency content (figure 4). Comparing the eight extreme species, there were differences in nanostructures both qualitatively (e.g. the morphology of ridges) and quantitively (spatial frequencies); however, the orientation of scales across the wing surface was the same for all species.

The spatial periodicities of ridges and cross-ribs from the ventral wing surface in all examined species are displayed in figure 3*b*, assigning each moth a distinct position in this parameter space. Notably, periodicity or ripples did not differ significantly among species, and ripple periodicity did not scale with the ridge and rib periodicity. Most species do not overlap with the majority of the other species. Moths of the family Noctuidae and *F. bifida* (Notodontidae) account for the extreme values of $\lambda_0$, yet the within-species spread is consistent between them, reflecting their close evolutionary relatedness and thus causing them to deviate from the other species. Although the morphology differed significantly, the ridge and cross-rib periodicities resulted in a few overlapping species (figure 3*b*). The ripple spacing had a median value of 0.17 µm for all species. This might suggest that the ripples could relate to a molecular preference of the chitin polymer plane thickness [58]. Therefore, ripples could be building blocks of the wing surface structure, unrelated to both ridge

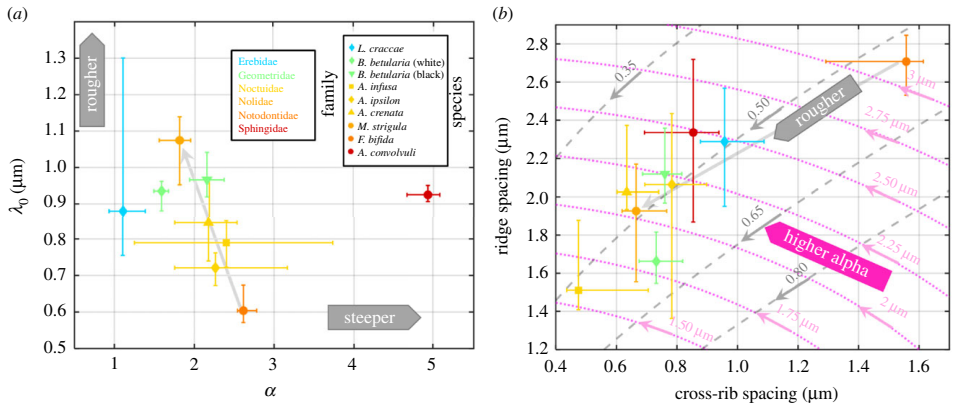


**Figure 3.** Correlation of the physical model parameters to moth wing scale nanostructures. (*a*) Scatter plot of the physical parameters, surface roughness $\lambda_0$ versus steepness $\alpha$, obtained from ventral specular reflectance spectra. (*b*) Scatter plot of ridge and cross-rib spacing from the SEM scans of moth wing scales. Bars indicate ¼ and ¾ quartiles within species variation. Grey auxiliary lines are drawn to illustrate power relations and the pink auxiliary lines are used to describe isotropic curves of periodicity in micrometres.

and cross-rib periodicity. If this is confirmed in later studies, it would imply a severe discretization of lepidopteran microstructures with large implications for both evolution and remote identification. The correlation between the periodicities of ridges, ribs and ripples is presented in the electronic supplementary material, table S9. In particular, we found a correlation of 97% in the relation $d_{Ridge}/d_{Ripple} = 5.5\ (d_{Rib}/d_{Ripple})^{½}$ among examined species. This result is used in figure 3*b* to describe the aspect ratio between ridge and ribs with a main axis having a square-root power relation (½, solid grey line in figure 3*b*).

## 2.3. Correlation between the spectral properties and moth wing nanostructure

The surface roughness $\lambda_0$ and steepness $\alpha$ are parameters that have the least sensitivity to the wing orientation and are therefore the best candidates for identifying moth species. Since these relate to the surface microstructure, we related them to the lateral periodicities observed with electron microscopy across the scale surface. The spectral long-pass function can be likened to a road coarsely paved with cobblestones (stone size of $\lambda_0$) being irradiated by ping-pong-ball-sized photons of short wavelength $\lambda$ (i.e. $\lambda < \lambda_0$). These photons would bounce off the road in random directions, whereas basketball-sized photons ($\lambda > \lambda_0$) would bounce with the memory of the incident angle. Surprisingly, we find that the species with the coarsest lateral periodicity, *F. bifida*, displays the lowest $\lambda_0$ value. Reciprocally, we find the finest lateral periodicities in *M. stigula*, which also has the largest $\lambda_0$ value (figure 3). Our interpretation is that the distribution of surface normal across the scales has a reduced spread for the coarse lateral periodicities. This could occur in a situation where the lateral periodicities scale but the depth profiles remain constant. Unfortunately, our SEM images do not yield depth profiles.

The ridge–rib aspect ratio (along the isotropic pink lines in figure 3*b*) is somewhat related to the steepness parameter, $\alpha$. For example, *B. betularia* (black) and *A. convolvuli* are both above the main square-root axis while *B. betularia* (white) and *L. craccae* are below it. However, both *A. convolvuli* and *L. craccae* display intermediate $\lambda_0$ values as well as intermediate lateral periodicities (from the SEM measurements). The black and white morphs of *B. betularia* are generally thought to differ only in melanization. Interestingly, both the structural steepness parameter $\alpha$ and the SEM images (which are blind to melanization) confirm that the scale microstructure differs significantly between the two morphs of this single species. We emphasize that there are cases where morphs and sexes differ, not only in coloration but also in the microstructure. In analogy, previous lidar studies of mosquitoes' wingbeats demonstrate high sex discrimination, whereas species can be more challenging to differentiate [54]. The expectations should thus be that differences in both coloration and microstructure only partly reflect the allocation in the phylogenetic tree and that groups and phenotypes could also be explained by other ecological factors than genetic heritage.

It is evident that the specular spectral properties $\lambda_0$ and $\alpha$ are associated with microscopic features in the SEM images. It is also evident that the ridge and rib spacing alone are not enough to precisely predict the spectral properties. Knowledge of the depth profiles of moth wing scales is likely to improve spectral prediction.

## 2.4. Implications for remote sensing of freely flying moths

With the knowledge we have gained regarding specular reflectance from moth wings, we fed the parameters of the hawk moth *A. convolvuli* into a BRDF. This model can vary continuously from diffuse Lambertian reflectance to specular reflectance. We then combined this reflectance model with the wing motion angles from a previous study on hawk moths [29]. However, such a model was constructed exclusively for Sphingidae; also fore- and hindwings of some species can conform to a wavy surface rather than a plane during flight. The simulation was intended only as an example to demonstrate the effect of infrared specularity on the scattered waveform. The wing pitch and roll angles

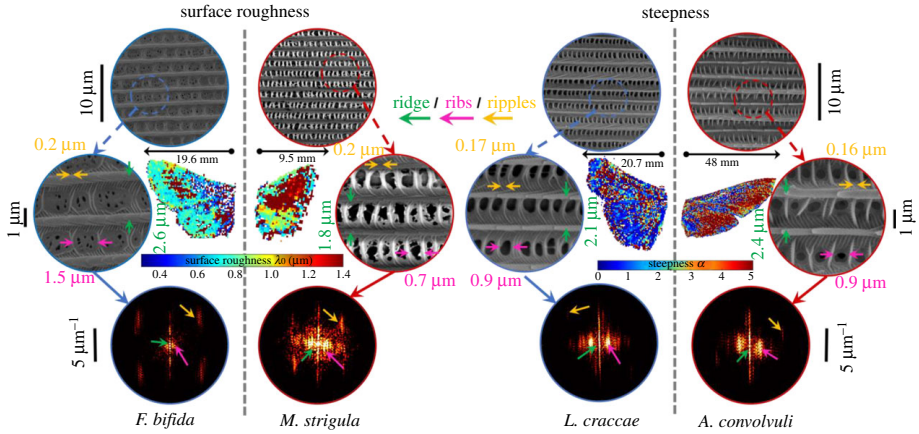


**Figure 4.** False-colour image of extreme cases of moth wings in four species in terms of surface roughness and steepness difference (*central images*) with their corresponding SEM images. Wing images are colour coded to present the pixel-wise surface roughness or steepness distribution across the entire wing. Magnified SEM images with *arrows* highlighting example spacings between ridges (*green arrows*), cross-ribs (*pink arrows*) and ripples (*yellow arrows*) for each species and where they are located in the fast Fourier transform images (*lower row*).

during one wingbeat are presented in figure 5*a*,*c*. We consider the 180° backscattered light from a vertical lidar and multiply the reflectance by the area of the projected wing shapes (figure 5*b*,*d*). Accordingly, we present the expected lidar waveform signals from flying hawk moths at two flight speeds. The dashed de-polarized diffuse Lambertian signal directly represents the projected wing area at zenith observation. The co-polarized, coherent and specular signal, on the other hand, displays a moderate flash at the instant when the wing surface normal approaches nadir (during upstrokes). This effect increases with a longer wavelength as the wing becomes glossier. At flight speeds of 5 $ms^{-1}$, the wing surface normally approaches horizontal, and the flash could even occur in horizontal lidar observation mode. Alternatively, the likelihood of observing flashes could be maximized by observing at 56° from zenith. The last two detection modes would, however, be highly sensitive to the flight direction. We conclude that infrared specular properties have a large impact on the wingbeat waveforms and are thus retrievable from far distances. The specular properties could thus be assessed by (i) a polarization-sensitive lidar, (ii) a dual-band lidar, or (iii) simply calculating the waveform skewness (see caption of figure 5*b*,*d*). Since skewness is unitless, this approach would pose a highly robust solution that is insensitive to instrument calibration.

## 3. Discussion

We have shown that moth wings become glossier towards the SWIR, that is, specularity increases with wavelength, a fact that is also reflected by their polarimetric properties. We have proposed and demonstrated reflectance models that can effectively parametrize the coherent, incoherent and diffuse effective reflectance from the dorsal and ventral surfaces of moth wings in the near-infrared (NIR)-SWIR region. Reflectance spectra from the wings of 82 specimens of 26 moth species (one species with two subspecies) are reduced to 11 non-redundant parameters (see electronic supplementary material, figure S22) in SI units for reproducibility. These spectral and polarimetric parameters differ significantly between species, a promising result for remote identification of freely flying moths with optical sensors.

We validated the idea of remote microscopy by correlating the deduced parameters from the infrared reflectance with spatial periodicities deduced in SEM scans of the ventral wing surface. Species with significantly distinct spectral parameters also showed significantly different microstructure periodicities on their wing scales, although in a non-intuitive manner. Species with rougher wing surfaces and becoming shiny at longer wavelengths had smaller spacing between ridges and cross-ribs. We speculate that a more accurate relationship between spectral properties and microstructures could be accomplished with additional measurements of the depth profiles of wing scale surfaces (using SEM). Morphological measurement precision could also be increased in future studies with additional techniques, such as micro-computed tomography.

The majority of moth species were chosen based on their abundance in the southern Swedish province of Skåne, generally with three replicates for each species to estimate variation. However, for some families, we only had one species available. Therefore, when we parameterized all reflectances and analysed how distinct each species is relative to others, we could not conclude if there is any generally applicable trend at the family level. However, the microstructure periodicities [59] and infrared properties [24] in our study compare well with previous reports on both moths and butterflies. Thus, the surface roughness assessment and model could also be applied to butterflies. Within our spectral range, we could not parametrize coherent reflectance for seven of our moth species, presumably because they had a too coarse microstructure. Further research should include more species in the same family and use a spectral system that can identify new extreme values by employing instruments in the 3–5 µm range.

By using the knowledge gained by modelling the reflectance of a hawkmoth and combining this with the wing

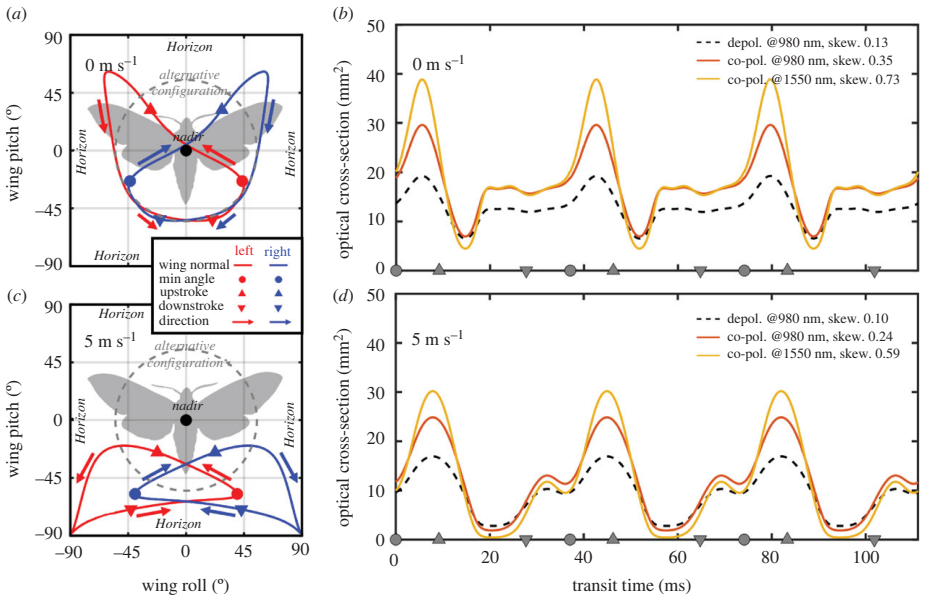


**Figure 5.** Simulated moth signals with a vertical lidar detection scheme. (*a*,*c*) Wing surface normal trajectory of a hawkmoth at two flight speeds. When the normal approaches nadir, the wings would produce a 'flash' in the vertical lidar signal. (*b*,*d*) Modelled temporal wingbeat cross-section signal from zenith. Coherent properties increase with wavelength, as does the waveform skewness.

dynamics from a previous study [29], we could simulate entomological lidar signals, and various bands and polarizations, for the purpose of remote identification of freely flying moths. Indeed, the coherent specular phenomena described in this study have a large impact on the resulting lidar signals. The infrared glossiness can be retrieved differentially with a dual-band lidar [56], through co-polarization- and de-polarization-sensitive lidar [55], or simply by calculating the waveform skewness. We thus can expect that numerous moth species can be differentiated remotely by retrieving reflected optical signals that are directly related to the microstructures of their wing scales.

## 4. Material and methods

### 4.1. Lepidoptera specimens

We included 82 individuals of 26 moth species from 13 different families representing both macro- and micromoths, provided by the Lund University Biological Museum (figure 1). As examined species show no sexual dimorphism, we do not expect any difference between males and females in the spectral and structural signatures. Most species were selected based on their abundance in the Skåne region of Sweden [60] (unpublished data based on museum material in the Biological Museum, Lund University), except for two common Australian species. The Swedish moth species included were *Agonopterix. ciliella* (Depressariidae); *Agrius convolvuli* (Sphingidae); *Apamea crenata*, *Autographa gamma*, *Agrotis ipsilon*, *Acronicta leporina*, *Helicoverpa armigera*, *Noctua pronuba* (Noctuidae); *Agriopis leucophaearia*, *Aethalura punctulata*, *Biston betularia carbonaria* (black), *Biston betularia typica* (white), *Trichopteryx carpinata* (Geometridae); *Aglia tau* (Saturniidae); *Crambus perlella* (Crambidae); *Calliteara pudibunda*, *Hypena crassalis*, *Lygephila craccae*, *Phragmatobia fuliginosa* (Erebidae); *Eriogaster lanestris* (Lasiocampidae); *Emmelina monodactyla* (Pterophoridae); *Furcula bifida* (Notodontidae); *Meganola strigula* (Nolidae); *Phiaris schulziana* (Tortricidae); and *Tebenna bjerkandrella* (Choreutidae). Two Australasian noctuids were also included in the study to increase the number of species in the genus *Agrotis* (*Agrotis infusa* and *Agrotis munda*) to test whether lidar has the potential to distinguish species within a tight taxonomic group.

Moth wings were spread and set in a horizontal plane by a skilled expert to minimize damage or wearing to the wing scales during handling. Estimation of within-species variation was allowed by at least three replicates of each species variance (except *A. munda*, a single specimen) and measurements were taken from both the left and right wings for both the dorsal and ventral sides of the body. Even if a wing should have minor damage where scales are not intact, it has minimal influence on the reported median value. In regards to the age of the specimen, a study on the wing interference pattern displayed on transparent insect wings is stable even on 100-year-old dry museum specimens [61]. Also, the nanostructures in butterflies, which produce structural colours in the visible range, are generally considered to be stable in museum collections. Our presumption is thus that the chitin microstructure on dry moth scales should also remain stable over time.

### 4.2. Hyperspectral imaging

The NIR-SWIR optical properties of moth wings were studied using a push-broom hyperspectral camera [62] (HySpex; Norsk Elektro Optikk AS, Norway). Two 150 W broadband halogen lamps were used sequentially to illuminate the sample, and two ultra-broadband polarizers [63] (Meadowlark Optics, USA) were used for polarimetric analysis. All specimens were mounted on black neoprene foam sheets to minimize

the reflection from the background. The hyperspectral camera was operated with an objective with an aperture of ø25.4 mm and a working distance of 30 cm. The push-broom scan generates a three-dimensional ($x$, $y$, $\lambda$) hyperspectral image cube, where the $\lambda$ includes 288 spectral bands ranging from 0.95 µm to 2.5 µm and a spatial resolution of 240 µm. All recorded hyperspectral data were calibrated to a target with a 50% diffuse reflectance standard (Spectralon®). The angular light distribution was captured by imaging silicon nitride spheres [64].

The hyperspectral imaging was repeated with three different configurations of illumination (electronic supplementary material, figure S1). The configurations were as follows. (i) Co-polarized specular illumination (with horizontal linear polarizers on both illumination and camera). The illumination and camera axis were at ±56° to surface normal. (ii) De-polarized illumination (with a horizontal polarizer on the light source and a vertical polarizer on the camera). Again the illumination and camera axis were at ±56° to surface normal. (iii) Diffuse illumination (illuminating with unpolarized light and capturing the horizontally polarized light). In this case, the illumination coincided with the surface normal, whereas the camera remained at 56°. Examples of reflectance spectra from a specular pixel, a diffuse pixel and the entire wing of *A. crenata* are shown in figure 2.

## 4.3. Parameterization of specular reflectance (co-polarized model)

We generally observed that the specular reflectance increased and reached a plateau towards infrared (see example in figure 2*e*,*l*). Thus, we applied a long-pass function known from electrical and photonic engineering:

$$R = R_{\text{long}} \frac{(\lambda/\lambda_0)^{\alpha}}{1 + (\lambda/\lambda_0)^{\alpha}}. \tag{4.1}$$

In this model, $R_{\text{long}}$ is the asymptotic maximum reflectance value, $\lambda_0$ is the cut-on wavelength or surface roughness and $\alpha$ is the slope steepness of the spectrum. All parameters are provided in the electronic supplementary material, tables S1 and S2. For the majority (19) of specimen explanations, grades ($R^2_{\text{adj}}$) exceed 98%. For seven species, reflectance continuously increased towards infrared without reaching a plateau within our spectral range. This does not imply that our model is inaccurate, but rather that the surface is too rough to assess with the spectral range of our instrument (0.9–2.5 µm). This also prevents us from identifying both $R_{\text{long}}$ and $\lambda_0$. The last remaining species (*A. leucophaearia*) displayed a fringy spectrum that does not comply with equation (4.1).

## 4.4. Parameterization of diffuse reflectance (de-polarized and diffuse model)

The majority of diffuse reflectance spectra decrease towards both short and long wavelengths (figure 2*f*,*g*,*m*,*n*). The decrease towards a short wavelength below 1.2 µm can be explained by eumelanin absorption [65]. The decrease in diffuse reflectance towards long wavelengths is primarily due to transmission losses owing to diffuse photon migration and random walks [66] and the increasingly specular surface (thus not contributing in diffuse mode). The mean free path increases with wavelength, and so does the chance of light escaping on the back side of the wing (and thus not contributing to reflectance). A model was developed that was inspired by the Beer–Lambert law:

$$R_{\text{diff}} \approx R_{\text{depol}} = R_0 \cdot \mathrm{e}^{-\mu_{\text{a}}\ell_{\text{mel}} - \mu_{\text{T}}\lambda}, \tag{4.2}$$

where $R_0$ is the maximum diffuse reflectance, $\ell_{\text{mel}}$ is the equivalent pathlength in pure melanin and $\mu_{\text{T}}$ is a slope coefficient arising because of transmittance. $\mu_{\text{a}}$ is pure eumelanin absorption and is also wavelength dependent [65]:

$$\mu_{\text{a}} = \varepsilon(\lambda) \cdot C = \varepsilon_0 \mathrm{e}^{-(\lambda/\lambda_{\text{m}})} \cdot C, \quad \varepsilon(\lambda) = \varepsilon_0 \mathrm{e}^{-(\lambda/\lambda_{\text{m}})}, \tag{4.3}$$

where $\varepsilon_0 = 2.45\ \mu\text{m}^{-1}\,\text{M}^{-1}$, $\lambda_{\text{m}} = 0.175$ µm and $C = 5.65\text{M}$

Increased melanin pathlength, $\ell_{\text{mel}}$, attenuates the shorter part of the reflectance spectra. An increase in the slope coefficient $\mu_{\text{T}}$ will attenuate the longer parts of the reflectance. The parameters and explanation grades are provided in electronic supplementary material, tables S3–S6.

## 4.5. Parameterization of degree of linear polarization spectrum

To investigate the feasibility of polarimetric identification of moth wings, the spectral depolarization was investigated by calculating the DoLP:

$$\text{DoLP} = \frac{I_{\text{co}}}{I_{\text{co}} + I_{\text{de}}} = \frac{1 + \mathrm{e}^{-(\lambda_{\text{p}}/\lambda)^{\gamma}}}{2}. \tag{4.4}$$

Note that there are several definitions of DoLP in the literature. The one above gives 100% for entirely co-polarized reflectance and 50% for entirely randomized reflectance. In equation (4.4), $I_{\text{co}}$ and $I_{\text{de}}$ are co-polarized and de-polarized reflected intensities, respectively, $\lambda_{\text{p}}$ is the wavelength where wings become co-polarized. The spectral dependence of DoLP is given by $\gamma$. In summary, a high $\lambda_{\text{p}}$ implies a diffuse wing, and a high $\gamma$ implies that DoLP increases with wavelength. All parameters are documented in electronic supplementary material, Tables S7 and S8, where $R^2$ indicates the fitting quality.

## 4.6. Scanning electron microscopy

Eight of 26 moth species (one species with two subspecies) were selected to investigate moth wing nanostructures using SEM. The selection was made based on the parametrization results from specular reflectance signals from the moth ventral wings (electronic supplementary material, figure S3). *A. convolvuli*, *F. bifida*, *L. craccae* and *M. strigula* were chosen because they represent the extreme values for surface roughness $\lambda_0$ and steepness $\alpha$, respectively. *A. crenata* represents the average for both parameters. *A. infusa* and *A. ipsilon* were selected to investigate the variance of nanostructures within the same genus. *B. betularia* was chosen to include another superfamily, the Geometroidea. This species inhabits a polymorphism with two different morphotypes differing in melanization. For each species, one specimen was investigated. Wings were first cut with the help of a stereomicroscope (ZEISS Stemi DV4), and three pieces of each wing were removed. Pieces were about 3 × 3 mm in size and taken from different areas of the wings. Both fore- and hindwings were inspected. The dried wings were carefully glued onto SEM stubs, air-dried and sputter-coated with gold (Cesington 108 auto, 75 s, 20 mA). Imaging was done with a scanning electron microscope (Hitachi SU3500) at 5 kV. For numerical analysis, the SEM images (of resolution 0.025 µm pixel$^{-1}$) were analysed to extract the different lateral spatial frequency components that could correlate with or account for the distinct infrared properties observed.

Each image from the samples was cropped into three windows across the scales. The windows were 20 × 20 µm. The windows were subject to Gaussian apodization, after which the two-dimensional spatial frequency power spectrum was calculated and averaged for the cropping. Three periodic structures were identified, with ridges being the coarsest (approx. 2.0 µm), cross-ribs of intermediate size (approx. 760 nm) and ripples being the finest (approx. 170 nm).

### 4.7. Bidirectional reflectance distribution function for waveform modelling

The reflected light lobe was modelled as a function of incident pitch and roll angles, $\theta$, $\varphi$. The model originated from diffuse Lambertian reflectance, $I = I_0\cos^{1/r}(\theta)$, where $r$ represents surface roughness. Here $r = 1$ is a perfect diffusor and $r = 0$ is a perfect mirror. By comparing our hawk moth recordings, we determined $r_{980\,\mathrm{nm}} = 0.53$ and $r_{1550\,\mathrm{nm}} = 0.37$ for *A. convolvuli*. To model the dependency of the specular reflectance lobes on the incident light, we introduced a symmetric link function, $F_{\mathrm{link}}(\theta,\theta_0)$, with the property $F_{\mathrm{link}}(\theta, -\theta) = 0°$ (maximum of the cosine function). This ensures that incident and reflected light angles are opposite. Furthermore, we multiply $\theta_0$ by $1 - r$; thus, the reflectance lobe of a perfect diffuser coincides with the surface normal and becomes identical to Lambertian reflectance:

$$I(\theta,\varphi) = I_0(\cos(F_{\mathrm{link}}(\theta,(1-r)\theta_0))\cos(F_{\mathrm{link}}(\varphi,(1-r)\varphi_0)))^{1/r},\quad r \in \{0\ldots1\}, \tag{4.5}$$

$$F_{\mathrm{link}}(\theta,\theta_0) = 90°\left(\left(\frac{\theta+90°}{180°}\right)^{\frac{-\log(2)}{\log\left(\frac{90°-\theta_0}{180°}\right)}} - \left(\frac{90°-\theta}{180°}\right)^{\frac{-\log(2)}{\log\left(\frac{\theta_0+90°}{180°}\right)}}\right),\quad \theta,\theta_0 \in \{-90°\ldots+90°\} \tag{4.6}$$

$$\int_{-90°}^{90°}\int I(\theta,\varphi)\,\mathrm{d}\theta\mathrm{d}\varphi = 1\,, \tag{4.7}$$

where $I$ is the light reflected in the directions $\theta$ and $\varphi$. $I_0$ is a scalar intensity, while $\theta_0$ and $\varphi_0$ are the incidence angles.

The BRDF was used to calculate the 180° backscatter from a moth using a vertical lidar. The dynamic wing roll and pitch were adopted from a previous study [29]. The backscattered reflectance during the wingbeat was multiplied by the ventral projected wing area during the wingbeat, and the optical cross-section was obtained as a function of time. The de-polarized signal is modelled with $r = 1$. We note that this model does not consider diffraction and reflectance anisotropy from the grating-like lateral periodicities on the scales. The periodic features on the scales are unlikely to be in a phase across the wing, and diffracted orders are not observable in the zeroth order, as is the case for our specular hyperspectral imaging and/or backscattering in lidar.

Data accessibility. The data are provided in the electronic supplementary material [67].

Authors' contributions. M.L.: conceptualization, data curation, formal analysis, investigation, methodology, visualization, writing—original draft; C.S.: data curation, formal analysis, investigation, visualization; S.J.: conceptualization, writing—review and editing; J.H.: conceptualization, methodology, resources, software, writing—review and editing; J.R.: conceptualization, resources, supervision, writing—review and editing; E.W.: conceptualization, funding acquisition, resources, software, supervision, writing—review and editing; M.B.: conceptualization, funding acquisition, investigation, methodology, resources, software, supervision, writing—original draft, writing—review and editing.

All authors gave final approval for publication and agreed to be held accountable for the work performed herein.

Conflict of interest declaration. The authors declare that they have no competing interests.

Funding. This project has received funding from the European Research Council (ERC) under the European Union's Horizon 2020 research and innovation programme (grant agreement nos. 850463 and 741298).

## References

1. Hölker F *et al.* 2010 The dark side of light: a transdisciplinary research agenda for light pollution policy. *Ecol. Soc.* **15**, 13. (doi:10.5751/ES-03685-150413)
2. Fry R, Waring P. 1996 *A guide to moth traps and their use*. London, UK: Amateur Entomologist's Society.
3. Kristensen N, Scoble M, Karsholt O. 2007 Lepidoptera phylogeny and systematics: the state of inventorying moth and butterfly diversity. *Zootaxa* **1668**, 699–747. See https://www.mapress.com/zootaxa/2007f/zt01668p747.pdf.
4. Mutanen M, Wahlberg N, Kaila L. 2010 Comprehensive gene and taxon coverage elucidates radiation patterns in moths and butterflies. *Proc. R. Soc. B* **277**, 2839–2848. (doi:10.1098/rspb.2010.0392)
5. Van Nieukerken EJ *et al.* 2011 Order Lepidoptera Linnaeus, 1758. *Zootaxa* **3148**, 212–221. (doi:10.11646/zootaxa.3148.1.41)
6. FAO. 2020 *The global action forfall armyworm control: action framework 2020–2022. Working together to tame the global threat*. Rome, Italy: Food and Agriculture Organization.
7. Francischini FJB *et al.* 2019 *Diatraea saccharalis* history of colonization in the Americas. The case for human-mediated dispersal. *PLoS ONE* **14**, e0220031. (doi:10.1371/journal.pone.0220031)
8. Li Y *et al.* 2016 Optical characterization of agricultural pest insects: a methodological study in the spectral and time domains. *Appl. Phys. B* **122**, 1–9. (doi:10.1007/s00340-016-6485-x)
9. Sallam MN. 1999 *Insect damage: damage on post-harvest*. Nairobi, Kenya: Food and Agriculture Organization.
10. Warrant E *et al.* 2016 The Australian Bogong moth *Agrotis infusa*: a long-distance nocturnal navigator. *Front. Behav. Neurosci.* **10**, 77. (doi:10.3389/fnbeh.2016.00077)
11. Weaver RA, Basgall ME. 1986 Aboriginal exploitation of Pandora moth larvae in east-central California. *J. Calif. Great Basin Anthropol.* **8**, 161–179.
12. Stephenson B *et al.* 2020 Year-old Bogong moth (*Agrotis infusa*) Aboriginal food remains, Australia. *Sci. Rep.* **10**, 1–10. (doi:10.1038/s41598-020-79307-w)
13. Macgregor CJ, Pocock MJ, Fox R, Evans DM. 2015 Pollination by nocturnal Lepidoptera, and the effects of light pollution: a review. *Ecol. Entomol.* **40**, 187–198. (doi:10.1111/een.12174)
14. Malmqvist E *et al.* 2018 The bat-bird-bug battle: daily flight activity of insects and their predators over a rice field revealed by high-resolution Scheimpflug Lidar. *R. Soc. Open Sci.* **2018**, 172303. (doi:10.1098/rsos.172303)
15. Holland RA, Wikelski M, Wilcove DS. 2006 How and why do insects migrate? *Science* **313**, 794–796. (doi:10.1126/science.1127272)
16. Kissling WD, Pattemore DE, Hagen M. 2014 Challenges and prospects in the telemetry of insects. *Biol. Rev.* **89**, 511–530. (doi:10.1111/brv.12065)
17. Drake VA, Reynolds DR. 2012 *Radar entomology: observing insect flight and migration*. Wallingford, UK: CABI.
18. Riley J, Valeur P, Smith A, Reynolds D, Poppy G, Löfstedt C. 1998 Harmonic radar as a means of tracking the pheromone-finding and pheromone-following flight of male moths. *J. Insect Behav.* **11**, 287–296. (doi:10.1023/A:1021004209198)
19. Westbrook JK, Eyster RS, Wolf WW. 2014 WSR-88D Doppler radar detection of corn earworm moth migration. *Int. J. Biometeorol.* **58**, 931–940. (doi:10.1007/s00484-013-0676-5)
20. Drake VA, Wang H. 2018 Ascent and descent rates of high-flying insect migrants determined with a non-coherent vertical-beam entomological radar. *Int. J. Remote Sens.* **40**, 1–22. (doi:10.1080/01431161.2018.1519283)
21. Riley JR. 1985 Radar cross section of insects. *Proc. IEEE* **73**, 228–232. (doi:10.1109/PROC.1985.13135)
22. Drake VA, Chapman JW, Lim KS, Reynolds DR, Riley JR, Smith AD. 2017 Ventral-aspect radar cross sections and polarization patterns of insects at X band and their relation to size and form. *Int. J. Remote Sens.* **38**, 5022–5044. (doi:10.1080/01431161.2017.1320453)
23. Drake V. 2016 Distinguishing target classes in observations from vertically pointing entomological

radars. *Int. J. Remote Sens.* **37**, 3811–3835. (doi:10.1080/01431161.2016.1204028)

24. Bosi SG, Hayes J, Large MC, Poladian L. 2008 Color, iridescence, and thermoregulation in Lepidoptera. *Appl. Opt.* **47**, 5235–5241. (doi:10.1364/AO.47.005235)
25. Brydegaard M (ed.). 2014 *Advantages of shortwave infrared LIDAR entomology. Imaging and applied optics*. Seattle, WA: Optical Society of America.
26. Brydegaard M, Svanberg S. 2018 Photonic monitoring of atmospheric and aquatic fauna. *Laser Photonics Rev.* **12**, 1800135–1800172. (doi:10.1002/lpor.201800135)
27. Stavenga DG, Wallace JR, Warrant EJ. 2020 Bogong moths are well camouflaged by effectively decolourized wing scales. *Front. Physiol.* **11**, 95. (doi:10.3389/fphys.2020.00095)
28. Berthier S, Charron E, Boulenguez J. 2006 Morphological structure and optical properties of the wings of Morphidae. *Insect Sci.* **13**, 145–158. (doi:10.1111/j.1744-7917.2006.00077.x)
29. Willmott AP, Ellington CP. 1997 The mechanics of flight in the hawkmoth Manduca sexta. I. Kinematics of hovering and forward flight. *J. Exp. Biol.* **200**, 2705–2722. (doi:10.1242/jeb.200.21.2705)
30. Salcedo MK, Hoffmann J, Donoughe S, Mahadevan L. 2019 Computational analysis of size, shape and structure of insect wings. *Biol. Open* **8**, bio040774. (doi:10.1242/bio.040774)
31. Warfvinge K, Johansson LC, Hedenström A. 2021 Hovering flight in hummingbird hawkmoths: kinematics, wake dynamics and aerodynamic power. *J. Exp. Biol.* **224**, jeb.230920. (doi:10.1242/jeb.230920)
32. Wang X, Cong Q, Zhang J, Wan Y. 2009 Multivariate coupling mechanism of NOCTUIDAE moth wings' surface superhydrophobicity. *Chin. Sci. Bull.* **54**, 569–575. (doi:10.1007/s11434-009-0071-0)
33. Neil TR, Shen Z, Robert D, Drinkwater BW, Holderied MW. 2020 Moth wings are acoustic metamaterials. *Proc. Natl Acad. Sci. USA* **117**, 31 134–31 141. (doi:10.1073/pnas.2014531117)
34. Simmons RB, Weller SJ, Johnson SJ. 2012 The evolution of androconia in mimetic tiger moths (Noctuoidea: Erebidae: Arctiinae: Ctenuchina and Euchromiina). *Ann. Entomol. Soc. Am.* **105**, 804–816. (doi:10.1603/AN11166)
35. Kelley JL, Tatarnic NJ, Schröder-Turk GE, Endler JA, Wilts BD. 2019 A dynamic optical signal in a nocturnal moth. *Curr. Biol.* **29**, 2919–2925. (doi:10.1016/j.cub.2019.07.005)
36. Rayleigh L. 1930 The iridescent colours of birds and insects. *Proc. R. Soc. Lond. Ser. A* **128**, 624–641. (doi:10.1098/rspa.1930.0136)
37. Vukusic P, Sambles J, Lawrence C. 2004 Structurally assisted blackness in butterfly scales. *Proc. R. Soc. Lond. B* **271**, S237–S239. (doi:10.1098/rsbl.2003.0150)
38. Ingram AL, Parker AR. 2008 A review of the diversity and evolution of photonic structures in butterflies, incorporating the work of John Huxley (The Natural History Museum, London from 1961 to 1990). *Phil. Trans. R. Soc. B* **363**, 2465–2480. (doi:10.1098/rstb.2007.2258)
39. Stavenga DG. 2014 Thin film and multilayer optics cause structural colors of many insects and birds. *Mater. Today Proc.* **1**, 109–121. (doi:10.1016/j.matpr.2014.09.007)
40. Smith GS. 2009 Structural color of morpho butterflies. *Am. J. Phys.* **77**, 1010–1019. (doi:10.1119/1.3192768)
41. Berthier S. 2005 Thermoregulation and spectral selectivity of the tropical butterfly Prepona meander: a remarkable example of temperature auto-regulation. *Appl. Phys. A* **80**, 1397–1400. (doi:10.1007/s00339-004-3185-x)
42. Tsai CC, Shi N, Pelaez J, Pierce N, Yu N (eds). 2017 Butterflies regulate wing temperatures using radiative cooling. In *Lasers and Electro-Optics (CLEO), 2017 Conf., San Jose, CA, 14–19 May 2017*. New York, NY: IEEE.
43. Herman A, Vandenbem C, Deparis O, Simonis P, Vigneron JP (eds). 2011 Nanoarchitecture in the black wings of Troides magellanus: a natural case of absorption enhancement in photonic materials. In *Nanophotonic Materials VIII. San Diego, CA, 24–25 August 2011*. Bellingham, WA: International Society for Optics and Photonics.
44. Liu X, Tyler T, Starr T, Starr AF, Jokerst NM, Padilla WJ. 2011 Taming the blackbody with infrared metamaterials as selective thermal emitters. *Phys. Rev. Lett.* **107**, 045901. (doi:10.1103/PhysRevLett.107.045901)
45. Li W, Fan S. 2018 Nanophotonic control of thermal radiation for energy applications. *Opt. Express* **26**, 15 995–16 021. (doi:10.1364/OE.26.015995)
46. Basistyy R, Genoud A, Thomas B. 2018 Backscattering properties of topographic targets in the visible, shortwave infrared, and mid-infrared spectral ranges for hard-target lidars. *Appl. Opt.* **57**, 6990–6997. (doi:10.1364/AO.57.006990)
47. Kim D, Su T, Su P, Oh CJ, Graves L, Burge J. 2015 Accurate and rapid IR metrology for the manufacture of freeform optics. *SPIE*, 9–11. See https://spie.org/news/6015-accurate-and-rapid-ir-metrology-for-the-manufacture-of-freeform-optics?SSO=1.
48. Kwon O, Wyant J, Hayslett C. 1980 Rough surface interferometry at 10.6 μm. *Appl. Opt.* **19**, 1862–1869. (doi:10.1364/AO.19.001862)
49. Munnerlyn C, Latta M. 1968 Rough surface interferometry using a $CO_2$ laser source. *Appl. Opt.* **7**, 1858–1859. (doi:10.1364/AO.7.001858)
50. Svanberg S. *Atomic and molecular spectroscopy: basic aspects and practical applications*. Berlin, Germany: Springer Science & Business Media.
51. Prum RO, Torres R. 2003 Structural colouration of avian skin: convergent evolution of coherently scattering dermal collagen arrays. *J. Exp. Biol.* **206**, 2409–2429. (doi:10.1242/jeb.00431)
52. Nolin AW, Dozier J. 2000 A hyperspectral method for remotely sensing the grain size of snow. *Remote Sens. Environ.* **74**, 207–216. (doi:10.1016/S0034-4257(00)00111-5)
53. Vukusic P, Hallam B, Noyes J. 2007 Brilliant whiteness in ultrathin beetle scales. *Science* **315**, 348. (doi:10.1126/science.1134666)
54. Brydegaard M *et al.* 2020 Lidar reveals activity anomaly of malaria vectors during pan-African eclipse. *Sci. Adv.* **6**, aay5487. (doi:10.1126/sciadv.aay5487)
55. Zhu S *et al*. 2018 Insect remote sensing using a polarization sensitive CW lidar system in Chinese rice fields. *EPJ Web Conf.* **176**, 07001. (doi:10.1051/epjconf/201817607001)
56. Brydegaard M *et al*. 2018 Short-wave infrared atmospheric Scheimpflug lidar. *EPJ Web Conf.* **176**, 01012. (doi:10.1051/epjconf/201817601012)
57. Brydegaard M, Jansson S, Schulz M, Runemark A. 2018 Can the narrow red bands of dragonflies be used to perceive wing interference patterns? *Ecol. Evol.* **8**, 5369–5384. (doi:10.1002/ece3.4054)
58. Raabe D *et al.* 2006 Microstructure and crystallographic texture of the chitin–protein network in the biological composite material of the exoskeleton of the lobster Homarus americanus. *Mater. Sci. Eng. A* **421**, 143–153. (doi:10.1016/j.msea.2005.09.115)
59. Bálint Z, Kertész K, Piszter G, Vertesy Z, Biro L. 2012 The well-tuned blues: the role of structural colours as optical signals in the species recognition of a local butterfly fauna (Lepidoptera: Lycaenidae: Polyommatinae). *J. R. Soc. Interface* **9**, 1745–1756. (doi:10.1098/rsif.2011.0854)
60. Elmquist H, Liljeberg G, Top-Jensen M, Fibiger M. 2019 *Sveriges fjärilar: en fälthandbok över sveriges samtliga dag-och nattfjärilar*. Stockholm, Sweden: Bugbook Publishing.
61. Shevtsova E, Hansson C, Janzen DH, Kjaerandsen J. 2011 Stable structural color patterns displayed on transparent insect wings. *Proc. Natl Acad. Sci. USA* **108**, 668–673. (doi:10.1073/pnas.1017393108)
62. HySpex. 2021 HySpex Classic SWIR-384. See https://www.hyspex.com/hyspex-products/hyspex-classic/hyspex-swir-384/.
63. Meadowlark Optics. 2021 Ultra Broadband Polarizer. See https://www.meadowlark.com/ultra-broadband-polarizer/.
64. Stanco F, Battiato S, Gallo G. 2017 *Digital imaging for cultural heritage preservation: analysis, restoration, and reconstruction of ancient artworks*. Boca Raton, FL: CRC Press.
65. Stavenga DG, Leertouwer HL, Hariyama T, De Raedt HA, Wilts BD. 2012 Sexual dichromatism of the damselfly *Calopteryx japonica* caused by a melanin-chitin multilayer in the male wing veins. *PLoS ONE* **7**, e49743. (doi:10.1371/journal.pone.0049743)
66. Jacques S, Pogue B. 2008 Tutorial on diffuse light transport. *J. Biomed. Opt.* **13**, 041302. (doi:10.1117/1.2967535)
67. Li M, Seinsche C, Jansson S, Hernandez J, Rota J, Warrant E, Brydegaard M. 2022 Potential for identification of wild night-flying moths by remote infrared microscopy. FigShare. (doi:10.6084/m9.figshare.c.6039061)

# Paper IX

# Feasibility of Insect Identification Based on Spectral Fringes Produced by Clear Wings

Meng Li, Anna Runemark, Noélie Guilcher, Julio Hernandez, Jadranka Rota, and Mikkel Brydegaard

***Abstract*—Due to the growing awareness that insects' diversity and populations are in decline, there is an increased need for monitoring insects. Entomological lidars and photonic sensors can monitor and remotely identify flying insects based on their backscattered signal in terms of oscillations-, polarization-, and spectral content. The backscattered light from insects is predominantly oscillatory and derives from the wings. This part of the signal is also more coherent and co-polarized than the light reflected from the insect's abdomen. Clear membranes can display soap-bubble colors due to thin-film interference, a feature that can be associated with the thickness of the wing. A hyperspectral camera can capture these wing interference patterns with hundreds of spectral bands and accurately identify the wing thickness. Here we investigate whether the spectral fringes can provide complementary information to aid remote species identification. We demonstrate that we can extract wing thickness and modulation depth information from spectral fringes of 87 species of common insect pollinators in Skåne, Sweden. The modulation depth of a fringe provides information related to insect wing thickness homogeneity, wrinkledness, or anti-reflectance features. Our results show that examined species display distinct modulation and wing thickness, and therefore such features can be used to improve the specificity of species identification of photonics sensors.**

***Index Terms*—Spectral fringe, insect, pollinator, entomological lidar, wing thickness, hyperspectral, thin-film.**

## I. Introduction

INSECT habitats and populations are adversely affected by human-driven disturbances and global warming [1], [2], [3]. Despite the fact that insects have high resilience and an incredible capacity to reproduce, there has been a decline in insect populations [4] and diversity [5], [6] over the years. Insects are essential to our ecosystems [7]. They are a key part of the food chain and play an important role in pollination. They also help to control pests and can be used as indicators of environmental health. The decrease in diversity and population of pollinators has negative effects on ecosystem functioning [8] and agricultural production [9]. To protect and manage wild pollinators, it is crucial to be able to monitor insects' diversity and distribution. Additionally, monitoring will enable predicting changes in insect population sizes in response to management strategies for the landscape [10], [11].

However, it remains a challenge to monitor insects using conventional catch-based survey methods. Adult insects, which are usually the main target for monitoring [12], [13], [14], are only present for a short period of time and appear at a specific time of the day and year. Consequently, insects captured with conventional catch-based methods come with strong biases [15]. Baits or pheromones used in traps are also generally designed to attract certain species. Methods based on catching and identifying species of insects are also very labor-intensive and require an experienced taxonomist. Genetic methods have recently been used to identify trapped insect species, but they could not report values in insect abundance [16].

Compared to conventional trap-based methods, laser remote sensing [17], [18] can provide unbiased data on insect activity and flux in situ with very high spatial and temporal resolution [19]. Such information could be used to monitor pests [20], track the spread of disease vectors [21], and monitor and manage agricultural pests or pollinators [22]. Machine vision and imaging-based techniques have been reported in combination with traps [23], [24], but focusing challenges imply that recognition of anatomical details is difficult for free-flying insects [25]. Fortunately, methods based on wing beat oscillation-, polarization- and spectral- features of the insects can retrieve signals regardless of focus on insects appearing sparsely in time and space [17], [21].

Insect species have distinct wing beat frequencies and distinct compositions of overtones. These signals have been demonstrated to enable species discrimination in flight chambers [26], [27], and multiple groups of insects have been differentiated in the field based on their oscillatory properties [10], [28].

In complement to oscillation signatures of detected insects, we explore if multiple polarization- or spectral bands could increase the number of discernable species. Detailed spectral information from insect bodies can be used to differentiate insect species, sex, and age [29], [30]. Oscillatory signals from free-flying insects can be expanded to discriminate co- and

Manuscript received 26 August 2022; revised 6 October 2022; accepted 27 October 2022. Date of publication 31 October 2022; date of current version 10 November 2022. This work was supported by the European Research Council under through the European Union's Horizon 2020 Research and Innovation Programme under Grant 850463. *(Corresponding author: Meng Li.)*

Meng Li and Anna Runemark are with the Department of Physics and Department of Biology, Lund University, 22363 Lund, Skåne, Sweden (e-mail: meng.li@forbrf.lth.se; anna.runemark@biol.lu.se).

Noélie Guilcher is with the Department of Biology, Polytech Clermont Ferrand 63170 Aubiére, France (e-mail: noelie.guilcher@gmail.com).

Julio Hernandez is with the Norsk Elektro Optikk A/S, Norway (e-mail: julio@neo.no).

Jadranka Rota is with the Biological Museum, Department of Biology, Lund University, 22362 Lund, Skåne, Sweden (e-mail: jadranka.rota@biol.lu.se).

Mikkel Brydegaard is with the Department of Physics and Department of Biology, Lund University, 22363 Lund, Skåne, Sweden, and also with Norsk Elektro Optikk A/S 0667 Oslo, Norway (e-mail: mikkel.brydegaard@fysik.lth.se).

Color versions of one or more figures in this article are available at https://doi.org/10.1109/JSTQE.2022.3218218.

Digital Object Identifier 10.1109/JSTQE.2022.3218218

de-polarized backscatter both in caged environments [20], [26], [27] and in situ [31]. This allows for the discrimination of coherent specular and incoherent diffuse scattering. If the wavelength resonates with the wing membrane thickness, rapid specular flashes appear on the scattered waveform, and consequently, a large number of harmonics appear. Both polarized recordings with photonic sensor environments on insects in cages [20], [26], [27] and lidar field recordings [31] show that most of the scattered signals from insects is oscillatory and specular, and WIPs account for most of the optical signature ($\sim$80%) of free-flying clear winged insects [31]. Flat clear wings of insects can exhibit reflectance 50 times more than a diffuse white at the resonant wavelength [31]. This is far brighter than any diffuse light reflected from vegetation or the sky background. Insect sensors [18], [19], [32] or lidars [20], [31], [33] with dual- or multiple wavelength bands are, therefore highly sensitive to Wing Interference Patterns (WIPs) and could potentially distinguish species based on wing thickness. Like some polarimetric insect vision systems, polarimetric lidars can also further enhance contrast for resonant backscatter from WIPs against the natural environment [31].

For clear-winged insect pollinators, a dominant spectral feature is thus the spectral fringe produced from their thin wing membrane associated with the wing thickness, also known as WIPs. This feature is stable over time and generations, according to studies on museum specimens [34]. Studies on WIPs suggest that the variation is low within species but high among species [35], [36]; thus, wing thickness could be the ideal parameter for discerning species.

Morphological data of insects could improve the interpretation of oscillatory signals [37], whereas differences in nano- and micro-surface structures could improve specificity in multispectral systems [38]. Allometric relationships between insect size and the morphology of their wings are known for a range of species [39], [40], [41], and allometric relationships are typically hard to alter. However, the relationship between wing area and wing thickness is not well studied. It is interesting to study allometry to understand how insects make morphological changes in order to maintain the same performance despite their size differences and whether wing thickness scales allometrically with wing size for biomechanical reasons or if it is locked by species interactions or sexual selection.

In this study, we investigated if spectral fringes could provide information complementary to improving remote insect identification in optical sensing. Specifically, we captured the spectral fringes and measured the wing thickness of 87 species belonging to the most important groups of distinct insect pollinators: bees, wasps, and flies. The aim was to examine the feasibility of using fringe information to improve the remote identification of more species with lidar or other optical techniques by recording both wing-beat modulation and spectral information simultaneously.

## II. Materials and Methods

The Lund University Biological Museum provided 87 species of pollinators representing 8 families from two insect orders (Hymenoptera and Diptera) with 1 specimen of each. These species of bees, wasps, and flies were selected as they are important pollinators and are difficult to identify for amateurs. They also have clear and flat wings, increasing the feasibility of using spectral fringes for identification. The species included in this study are presented in Table I.

The experimental setup is shown in Fig. 1. A hyperspectral camera with 288 spectral bands from 0.95 $\mu$m to 2.5 $\mu$m was used to capture the spectral fringes from the wings [42]. Melanin contribution from the wings can be neglected in this wavelength region. A 150 W broadband halogen lamp was used to illuminate the wings, and two ultra-broadband polarizers [43] were used to capture co- and de-polarized reflectance. The angle of incidence and observation were $\pm 56^{\circ}$. The objective of the camera had an aperture of Ø20 mm, and a working distance of 30 cm (forming a light cone of 3.8°). Mirrored spheres were used to image the size and position of the light source [44], [45]; the reflection of the light source on the spheres provides information on the convolution of the light cone from the source (15°) and cone received by the camera. All hyperspectral data were calibrated to a diffused grey reflectance standard with 50% reflectance (Spectralon); a specular pixel calibrated to such a diffused standard will exceed 100% diffuse reflectance. All samples were mounted on black neoprene with horizontal wing surfaces. Black neoprene was used to reduce the background light. One wing of each specimen was scanned, and sexual dimorphism was not taken into consideration in this study. We only scanned one wing because most specimens did not have both their wings spread, as it is not a common procedure in preparing and storing specimens of Hymenoptera and Diptera orders of insect specimens.

## III. Results

When a clear insect wing is illuminated by a white light source, different wavelengths of light are attenuated or resonant depending on the membrane thickness, which results in the soap bubble color patterns appearing on the wing that are visible in both RGB and false-color images shown in Fig. 2(a), (b). The red and blue arrows in Fig. 2(b), (c) illustrate the incident- and captured ray paths and polarizations. Dots on the red and blue arrows in Fig. 2(b) indicate that incident and capture light are both horizontally polarized, whereby an co-polarized image is acquired. The dots and smaller arrows on the red and blue arrows in Fig. 2(c) show the incident light is horizontally polarized, and the captured light is vertically polarized, as the polarization directions are perpendicular, the signal captured by the camera is de-polarized. Specular pixels from the wings are only present in the co-polarized false-color image shown in Fig. 2(b), not in the de-polarized image shown in Fig. 2(c), which indicates the light reflected from the wing membrane is a coherent phenomena.

As different wavelengths either resonate in forward- or backscattering depending on the wing thickness, the spectral profile of each wing pixel display a spectral fringe [46]. Examples of a thicker and a thinner wing pixel highlighted by two arrows in Fig. 2(b) have corresponding spectral fringes shown in Fig. 2(d). The effective fringe shown in Fig. 2(d) of the entire wing acquired by spatially averaging all wing pixels. Wing thickness is calculated for all 3 fringes shown in Fig. 2(d) by a

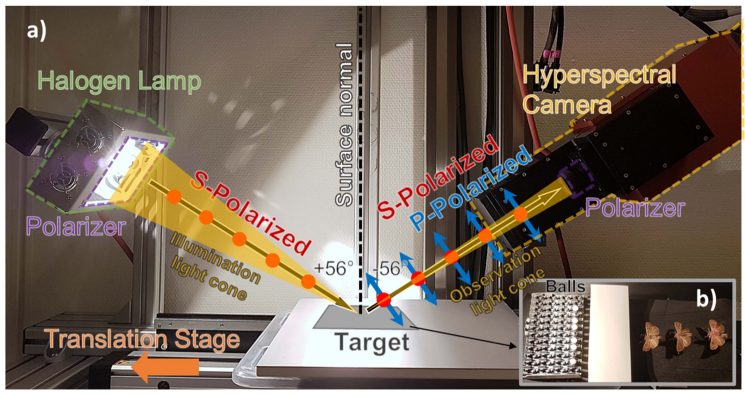


Fig. 1. (a) The experimental configuration used for hyperspectral imaging. The illuminator was equipped with a large wire grid polarizer, and another linear polarizer was placed in front of the camera. This analyzer can be rotated to alternate between capturing co- and de-polarized reflectance. (b) The order of objects included in each scan were: Chrome spheres, teflon spheres, a flat grey diffuse standard, and insects mounted on black neoprene.

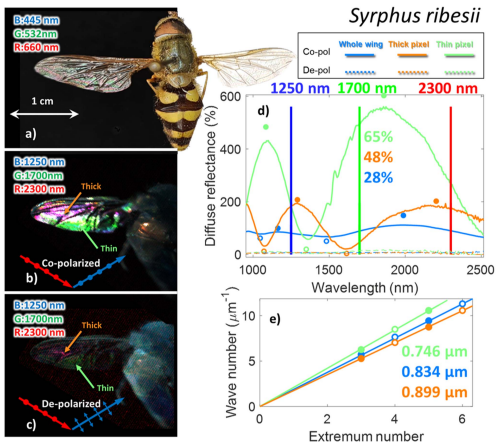


Fig. 2. (a) Soap bubble colors on the wing are more visible when the insect wing is placed against a black background. (b-c) Two false-color images were generated for co- and de-polarizations. The orange and green circles in (b-c) correspond to two wing pixels from a thicker and thinner region of the wing; Blue colored reflectance spectrum in (d) corresponds to the effective wing reflectance integrated over the whole wing. Value 28, 48, and 65% describe how modulated its corresponding fringe. (e) Reflectance maxima are illustrated with closed circles, and minima are illustrated with open circles from (d).

linear fitting method with extremum numbers (Fig. 2(e)) [46]. The two selected pixels in Fig. 2(b), (c) with different thicknesses display different colors (thicker: pink, thinner: green, in this particular false color visualization); the thin pixel fringe has a larger modulation depth than thick pixel (see Fig. 2(d)), and the thick fringe is more fringed than the thin fringe in the spectral window. Modulation depth ($M$) measures how pronounced the fringe effect is for a given wing. If modulation depth approach zero, the accuracy of wing thickness estimation would vanish. The mean- and standard deviation of reflectance are considered in the spectral domain. The modulation depth is expressed as:

$$M = \frac{\sigma(R_\lambda) \cdot \mu(F_\lambda)}{\sigma(F_\lambda) \cdot \mu(R_\lambda)} \tag{1}$$

where $R$ is measured reflectance and $F$ is computed fringe, $\lambda$ is the wavelength, $\sigma$ is the standard deviation, and $\mu$ is the mean of the sample. Based on the Fresnel equation and thin-film physics, its reflectance fringe $F(\lambda)$ can be expressed as [47],

$$F(\lambda, d) = \frac{4R_s \sin^2\left(2\pi d\sqrt{n^2 - \sin^2\theta}/\lambda\right)}{(1 - R_s)^2 + 4R_s \sin^2\left(2\pi d\sqrt{n^2 - \sin^2\theta}/\lambda\right)} \tag{2}$$

where $n$ is the refractive index of the chitin, $d$ is the thickness of the wing, $\theta$ is the incident angle to the wing membrane, $\lambda$ is the wavelength, and $r$ is the reflection coefficient by Fresnel equations. The refractive index of the cuticle is expressed as [46]:

$$n = k_0 + k_1/\lambda^2 \tag{3}$$

where $k_0 = 1.517$ and $k_1 = 8800$ nm$^2$. For S-polarization (electric field is perpendicular to the plane of incidence), the reflection coefficient $R_s$ is expressed as:

$$R_s = \left(\frac{\cos\theta - \sqrt{n^2 - \sin^2\theta}}{\cos\theta + \sqrt{n^2 - \sin^2\theta}}\right)^2 \tag{4}$$

The reflectance from P-polarization should be absent in our case since we measure at the Brewster angle. The crossed de-polarized P-polarized signal thus only captures multiple scattered lights from veins; as can be seen in Fig. 2(c), (d) this contribution is minimal compared to the fringed coherent reflectance. Thus fringes are horizontally co-polarized (S-polarization) as

TABLE I
LIST OF THE 87 SPECIES OF INSECT POLLINATORS STUDIED

| Family | Genus | Specie | $d_{eff}$ (μm) | M (%) | A (mm$^2$) |
|---|---|---|---|---|---|
| Andrenidae | *Andrena* | *barbilabris* | 0.95 | 36 | 28.4 |
| | | *carantonica* | 1.23 | 21 | 32.2 |
| | | *cineraria* | 1.49 | 14 | 31.2 |
| | | *clarkella* | 1.00 | 22 | 39.0 |
| | | *denticulata* | 1.10 | 24 | 15.9 |
| | | *flavipes* | 0.94 | 15 | 18.9 |
| | | *fucata* | 1.13 | 23 | 19.3 |
| | | *fulva* | 0.74 | 27 | 28.8 |
| | | *fuscipes* | 1.05 | 21 | 15.8 |
| | | *haemorrhoa* | 0.82 | 22 | 24.9 |
| | | *hattorfiana* | 1.02 | 17 | 37.4 |
| | | *helvola* | 0.66 | 31 | 30.4 |
| | | *lapponica* | 1.10 | 16 | 12.7 |
| | | *lathyri* | 1.30 | 17 | 24.7 |
| | | *minutula* | 0.49 | 47 | 8.69 |
| | | *nigroaenea* | 0.74 | 20 | 25.7 |
| | | *praecox* | 0.79 | 38 | 24.7 |
| | | *ruficrus* | 0.39 | 49 | 12.4 |
| | | *semilaevis* | 0.57 | 22 | 9.57 |
| | | *subopaca* | 0.45 | 45 | 10.8 |
| | | *tibialis* | 1.21 | 18 | 51.0 |
| | | *vaga panzer* | 1.43 | 28 | 32.3 |
| | | *wilkella* | 0.79 | 32 | 18.5 |
| Apidae | *Apis* | *mellifera* | 1.07 | 14 | 28.9 |
| | *Bombus* | *bicornis* | 0.98 | 20 | 17.8 |
| | | *bohemicus* | 1.86 | 11 | 68.3 |
| | | *campestris* | 1.98 | 10 | 45.7 |
| | | *distinguendus* | 2.33 | 12 | 55.9 |
| | | *hortorum* | 1.79 | 12 | 69.6 |
| | | *humilis* | 2.67 | 11 | 51.6 |
| | | *hypnorum* | 1.24 | 11 | 38.7 |
| | | *jonellus* | 0.94 | 16 | 20.7 |
| | | *lapidarius* | 2.49 | 9 | 81.2 |
| | | *magnus* | 1.86 | 9 | 66.9 |
| | | *muscorum* | 2.31 | 8 | 81.3 |
| | | *pascuorum* | 1.54 | 9 | 49.1 |
| | | *pratorum* | 2.29 | 15 | 50.8 |
| | | *ruderarius* | 2.35 | 11 | 51.5 |
| | | *rupestris* | 3.79 | 18 | 117 |
| | | *soroeensis* | 2.63 | 14 | 69.9 |
| | | *sporadicus* | 1.28 | 11 | 78.8 |
| | | *terrestris* | 2.37 | 10 | 51.7 |
| | | *veteranus* | 1.32 | 6 | 51.0 |
| Colletidae | *Hylaeus* | *annulatus* | 0.69 | 10 | 6.65 |
| | | *brevicornis* | 0.73 | 18 | 6.36 |
| | | *communis* | 1.42 | 11 | 7.09 |
| | | *confusus* | 1.02 | 41 | 6.86 |
| | | *gibbus* | 0.50 | 37 | 10.0 |
| | | *hyalinatus* | 0.62 | 35 | 5.01 |
| Halictidae | *Lasioglossum* | *fulvicorne* | 0.49 | 36 | 9.99 |
| | | *leucopus* | 0.41 | 17 | 6.31 |
| | | *morio* | 0.48 | 25 | 12.8 |
| | | *quadrinotatum* | 0.60 | 56 | 10.9 |
| | | *sexstrigatum* | 0.51 | 35 | 3.04 |
| | | *villosulum* | 0.82 | 22 | 10.4 |
| Megachilidae | *Megachile* | *centuncularis* | 1.16 | 14 | 21.6 |
| | | *circumcincta* | 1.56 | 20 | 32.0 |
| | | *lagopoda* | 1.99 | 17 | 39.2 |
| | | *lapponica* | 1.14 | 18 | 15.9 |
| | | *versicolor* | 1.25 | 16 | 22.2 |
| | | *willughbiella* | 1.44 | 16 | 25.9 |
| | *Osmia* | *caerulescens* | 1.34 | 13 | 10.3 |
| | | *leaiana* | 0.96 | 24 | 12.5 |
| Syrphidae | *Episyrphus* | *balteatus* | 0.94 | 12 | 19.3 |
| | *Eupeodes* | *corollae* | 0.81 | 18 | 22.7 |
| | *Melanostoma* | *mellinum* | 0.52 | 39 | 12.0 |
| | *Scaeva* | *pyrastri* | 1.17 | 15 | 49.1 |
| | *Sphaerophoria* | *scripta* | 0.57 | 41 | 11.4 |
| | *Syrphus* | *ribesii* | 0.85 | 30 | 15.8 |
| | | *vitripennis* | 0.87 | 18 | 27.3 |
| Tabanidae | *Tabanus* | *bovinus* | 1.13 | 7 | 98.8 |
| Vespidae | *Ancistrocerus* | *claripennis* | 0.93 | 31 | 16.7 |
| | | *nigricornis* | 1.07 | 15 | 25.8 |
| | | *oviventris* | 1.39 | 16 | 17.4 |
| | | *parietinus* | 1.08 | 18 | 26.8 |
| | | *parietum* | 0.75 | 15 | 26.1 |
| | | *trifasciatus* | 1.02 | 18 | 31.8 |
| | *Dolichovespula* | *saxonica* | 1.61 | 16 | 48.5 |
| | *Eumenes* | *coronatus* | 1.19 | 18 | 28.3 |
| | | *notatus* | 1.09 | 20 | 17.9 |
| | *Odynerus* | *spinipes* | 1.45 | 20 | 25.9 |
| | *Symmorphus* | *allobrogus* | 0.83 | 29 | 13.1 |
| | | *bifasciatus* | 0.35 | 26 | 9.08 |
| | *Vespa* | *crabro* | 2.18 | 18 | 65.4 |
| | *Vespula* | *germanica* | 1.20 | 23 | 32.7 |
| | | *rufa* | 1.44 | 15 | 59.0 |
| | | *vulgaris* | 1.42 | 16 | 47.2 |

shown in Fig. 2(b), (c), (d); therefore, only reflection coefficient $r_s$ was used in developing the fringe model in (2).

The modulation depth was calculated for 3 example fringes shown in Fig. 2(d) with their values shown in the same plot; the effective fringe (whole wing) has the lowest modulation, and it is attenuated towards the shorter wavelengths. To investigate the reasons for the decrease in the modulation depth of the effective fringe compared to individual specular wing pixels (for example, thick and thin fringes), the wing thickness and modulation depth were calculated and documented for all wing pixels for the same wing shown in Fig. 2(b) and in Table I. Instead of the peak-valley fitting in Fig. 2(e) [46], the fringe model *F(λ)* in (2) was used to determine wing thickness for all wing pixels. Fringe model *F(λ,d)* was first used to generate multiple (1000) computed fringes with wing thicknesses 0.35 $\mu$m$<d<4$ $\mu m$, the modulation of *F(λ,d)* is always 100% because it lacks bias terms. Each computed fringe *F(λ,d)* was then compared to the measured fringe *R(λ)* from a wing pixel, according to the correlation, *C*, in (5). We then introduced a fit quality parameter, *Q* in (6):

$$C\ (R, F\,(d)) = \frac{\int_{0.35}^{4} \left(F_{\lambda,d} - \mu\left(F_{\lambda,d}\right)\right)\left(R_{\lambda} - \mu\left(R_{\lambda}\right)\right)}{\sqrt[2]{\int_{0.35}^{4} \left(F_{\lambda,d} - \mu\left(F_{\lambda,d}\right)\right)^2 \partial\lambda \int_{0.35}^{4} \left(R_{\lambda} - \mu\left(R_{\lambda}\right)\right)^2 \partial\lambda}} \tag{5}$$

$$Q\,(d)\ =\ C\,(R, F)\left(C\left(\frac{\partial R}{\partial \lambda}, \frac{\partial F}{\partial \lambda}\right)\right)^2 \tag{6}$$

Here the spectral derivatives are used to ignore slope differences. The squared power is needed to avoid double negative correlation coefficients.

Wing thickness and modulation of all wing pixels from the example wing shown in Fig. 2 were estimated and presented as a wing thickness map, and a wing modulation depth map in Fig. 3(a). The wing thickness map example shows that wings are generally thicker around the frontal edges (costal margin) and thinner near the rear edge (anal margin). It is important to note that the membrane thickness in Fig. 3 is based on the thin film principle and does not describe vein thicknesses. However, vein pixels also have very low modulation depth, as shown in Fig. 3(a), and their influence on the effective fringe is relatively small.

The density plot of thicknesses and modulation in Fig. 3(b) shows that there is a large variation in wing thickness across the wing. The thickness histogram reveals specific thickness preferences; for example, thickness at 1.0 $\mu$m and 1.2 $\mu$m is more dominant than wing thickness at 1.1 $\mu$m. A relevant question is if these nanoscale thicknesses are quantized. Studies of chitin polymers in lobster's exoskeletons [48] displayed specific folding and curling preferences of the chitin polymer.

The density plot in Fig. 3(b) also shows that the fringes of a large amount of wing pixels display high modulation depths. The fringes with high modulation also correspond to specific prominent wing thicknesses (see Fig. 3(a)). Thicker wing pixels produce narrow spectral fringes than thin wing pixels. Thus,

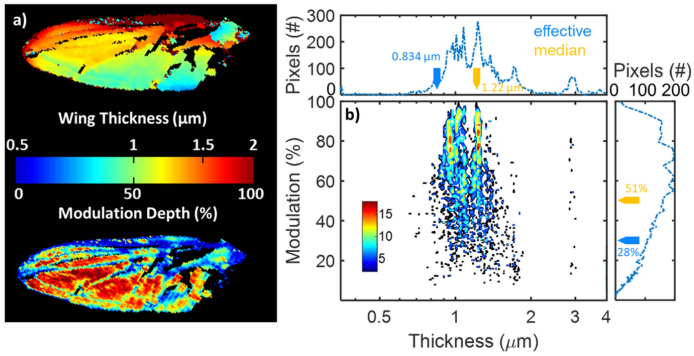


Fig. 3. (a) Wing thickness and modulation depth maps of the same example wing shown in Fig. 2. (b) Wing thickness and modulation distribution and histograms. Yellow arrows indicate the location of medians in both wing thickness and modulation. Blue arrows indicate the position of effective wing thickness and modulation calculated and presented in Fig. 2. The effective fringe modulation is lower than the median of all fringes.

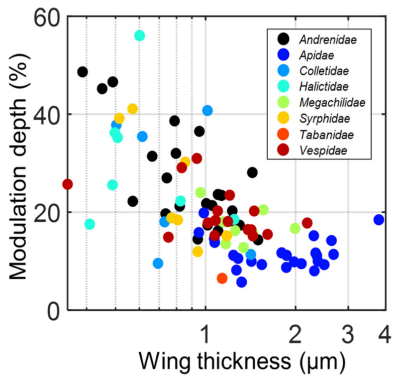


Fig. 4. Effective wing thickness and modulation depth were investigated for a large selection of insect species while each family of insects is color-coded.

fringes across the wing surface are more likely to interfere constructively with thin wings and for long wavelengths. Examples where fringe resonance modes are out of phase are shown in Fig. 2(d) with thick and thin fringes. Consequently, the effective modulation is reduced.

The effective wing thickness, $d_{eff}$, and modulation were then estimated for 87 species of Hymenoptera (bees and wasps) and Diptera (mainly hover flies), see Table I. This estimation was based on the effective fringe from their entire wings (the effective fringe for *S. ribesii* is shown in Fig. 2(d). All 87 studied individuals were museum specimens, each representing a different species, belonging to 8 different families. The effective modulation depth was investigated for all specimens and color-coded at the family level (not spread of individual species). Note that modulation values are valid only for the spectral window of our instrument. In Fig. 4, it can be seen that the insect family Apidae, which includes, for example, honeybees and bumblebees, and the family Megachilidae, which includes mason bees and leafcutter bees, display a wide variation in wing thickness and low modulation. We find that Vespidae, the family comprising wasps, has a wide wing thickness distribution and a medium degree of modulation depth among all studied species. Only one specimen of Tabanidae, a horsefly, was investigated, and it displayed a low degree of modulation depth. The rest of the insect families display a high degree of modulation depth.

All scatter points in Fig. 4 show a trend that thin wings display higher modulation depths; this could be explained by three reasons: 1) the modulation could be damped due to wrinkled wings, 2) nanostructures on some wings can induce anti reflectance effect by gradient refractive index interfaces [46], 3) fringes from a thicker wing are narrow in the spectral domain, thus more likely to get out of phase due to thickness heterogeneity causing the reduction in modulation depth, whereas fringes from a thin wing are less sensitive to phase displacement. This can also explain why the effective fringe modulation is getting higher in the longer wavelengths (see Fig. 2(d) effective fringe). We found the last explanation most plausible.

The relation between wing thickness and wing area was investigated for all species and presented in Fig. 5. A squared power relation of wing area, $A$ (mm$^2$), and effective wing thickness $d_{eff.}$ ($\mu$m) indicate allometric scaling, which is illustrated with a grey line in Fig. 5, with a scaling factor of 17 [16–19, confidence interval]. However, the relationship is better described by the relation colored in red, with a scaling factor of 23 [21–26, confidence interval] and a power relation of 1.2 [1.0–1.3] instead of squared. The result in Fig. 5 shows there is a 74% $R^2_{\text{adj.}}$ correlation between wing area and wing thickness (described by the power relation), the correlation described by the squared relation is only 41% $R^2_{\text{adj.}}$; the thickness is not scaling allometrically with wing area. Moreover, the power relation seemingly fails to describe all families; for example, the family Colletidae displays a range of thicknesses with a negligible change in wing areas. This means the scaling relation between wing area and thickness could be family specific, and despite the correlation area alone could not

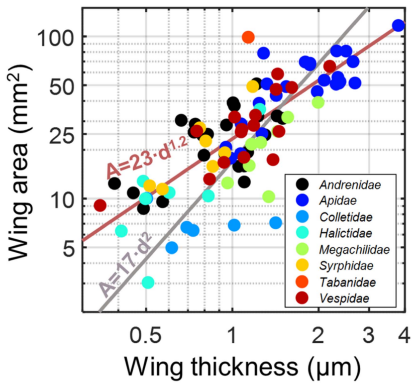


Fig. 5. Effective wing thickness and wing area relation was investigated, they show a strong correlation.

explain thickness variations. This encourages improved specificity by acquiring fringes.

## IV. Discussion

Our results suggest that the wing thickness of these groups of pollinators ranges from ∼0.5 to 2 $\mu$m. We found that some insect families do produce strong modulated effective fringes even when the signals from the whole wings are integrated, in particular when the wing membrane is thin. This effect could yield complementary information in addition to wing beat modulation, or it could be used to employ strategically resonant wavelengths in order to improve detection range or signal-to-noise. We also found that pixel modulation depth for examined insects is always lower than 100%, which implies that accurate thickness assessment is not possible by Newton rings color-coding and RGB imaging in previous studies (computer generated newton series scale of two-beam interference colors), thus multi- or hyperspectral methods are needed.

For many species of Apidae, especially species of bumblebees (genus *Bombus*), the wing segments are not in a single plane and display a large thickness variation across the wings, and this attenuates modulation depth. The species in the families Andrenidae (e.g., ground-nesting bees), Colletidae (e.g., plasterer bees), Halictidae (e.g., sweat bees), and Syrphidae (e.g., hover flies) displayed high modulation depth. Insect species with thin wings (∼0.5 to 1 $\mu$m) will have a higher potential to be detected from a long distance with its relatively high modulation depth, as fringes of thin membranes are also less sensitive to the damping of modulation due to the resonance modes getting out of phase. Effective fringes also become broader at longer wavelength regions and become hard to get out of phase, resulting in an increase in the effective modulation depth. This motivates infrared methods to capture this effect. The wing thickness strongly (74% $R^2_{\mathrm{adj}}$) correlated to wing area, but such relation scaling can differ between families.

During this initial survey, we only measured 1 specimen of each species, and we did not study the sexual dimorphism among species. WIPs play a role in the mating choice for some species [36], [49], [50]. Hence, sexual selection based on WIPs might prevent wing thickness from scaling allometrically with wing size. In the future, we will assess within-species variation by measuring multiple specimens of each species, sex, and distinct size. Despite our small sample size, we have provided realistic expectations of the thickness and effective modulation of examined 87 species of insect pollinators. Effective wing thickness, together with the fringe model, provide essential information to assist the development of photonics sensors; by placing sensors' laser band at the resonant wavelength of WIPs to maximize the retrieved signal magnitude and contrast for targeted insect specie. Our data will prove crucial for designing optical sensors for insect monitoring. Distinctness of wing thickness and modulation between insect families opens up the possibility for remote species identification using WIPs.

## Acknowledgment

We gratefully acknowledge the fruitful discussion and comments from Benjamin Thomas.

## Materials & Correspondence

Correspondence and requests for materials should be addressed to ML.

## References

[1] A. Holzschuh, I. Steffan-Dewenter, and T. Tscharntke, "How do landscape composition and configuration, organic farming and fallow strips affect the diversity of bees, wasps and their parasitoids?," *J. Animal Ecol.*, vol. 79, no. 2, pp. 491–500, 2010.

[2] C. Robinet and A. Roques, "Direct impacts of recent climate warming on insect populations," *Integrative Zoology*, vol. 5, pp. 132–142, Jun. 2010.

[3] T. Tscharntke et al., "Insect conservation in agricultural landscapes," *Insect Conservation Biol.*, vol. 16, pp. 383–404, 2007.

[4] C. A. Hallmann et al., "More than 75 percent decline over 27 years in total flying insect biomass in protected areas," *PLoS One*, vol. 12, no. 10, 2017, Art. no. e0185809.

[5] M. L. Forister, E. M. Pelton, and S. H. Black, "Declines in insect abundance and diversity: We know enough to act now," *Conservation Sci. Pract.*, vol. 1, no. 8, 2019, Art. no. e80.

[6] R. van Klink et al., "Meta-analysis reveals declines in terrestrial but increases in freshwater insect abundances," *Science*, vol. 368, no. 6489, pp. 417–420, 2020.

[7] J. C. Miller, "Insect natural history, multi-species interactions and biodiversity in ecosystems," *Biodiversity Conservation*, vol. 2, no. 3, pp. 233–241, 1993.

[8] B. J. Brosi and H. M. Briggs, "Single pollinator species losses reduce floral fidelity and plant reproductive function," *Proc. Nat. Acad. Sci.*, vol. 110, no. 32, pp. 13044–13048, 2013.

[9] M. A. Aizen and L. D. Harder, "The global stock of domesticated honey bees is growing slower than agricultural demand for pollination," *Curr. Biol.*, vol. 19, no. 11, pp. 915–918, Jun. 2009.

[10] M. Brydegaard et al., "Lidar reveals activity anomaly of malaria vectors during pan-African eclipse," *Sci. Adv.*, vol. 6, no. 20, May 2020, Art. no. eaay5487.

[11] N. M. A. El-Ghany, S. E. A. El-Aziz, and S. S. Marei, "A review: Application of remote sensing as a promising strategy for insect pests and diseases management," *Environ. Sci. Pollut. Res.*, vol. 27, no. 27, pp. 33503–33515, Sep. 2020.

[12] D. L. Kline, "Traps and trapping techniques for adult mosquito control," *J. Amer. Mosquito Control Assoc.*, vol. 22, no. 3, pp. 490–496, 2006.

[13] E. M. Raebel, T. Merckx, P. Riordan, D. W. Macdonald, and D. J. Thompson, "The dragonfly delusion: Why it is essential to sample exuviae to avoid biased surveys," *J. Insect Conservation*, vol. 14, no. 5, pp. 523–533, Oct. 2010.

[14] S. D. Wratten, A. J. White, M. H. Bowie, N. A. Berry, and U. Weigmann, "Phenology and ecology of hoverflies (Diptera: Syrphidae) in New Zealand," *Environ. Entomology*, vol. 24, no. 3, pp. 595–600, 1995.
[15] R. Muirhead-Thompson, "Trap responses of flying insects: The influence of trap design on capture efficiency," *Bull. Entomological Res.*, vol. 82, no. 3, pp. 433–434, Sep. 1992.
[16] R. Meier, W. Wong, A. Srivathsan, and M. Foo, "$1 DNA barcodes for reconstructing complex phenomes and finding rare species in specimen-rich samples," *Cladistics*, vol. 32, no. 1, pp. 100–110, 2016.
[17] M. Brydegaard and S. Svanberg, "Photonic monitoring of atmospheric and aquatic fauna," *Laser Photon. Rev.*, vol. 12, no. 12, 2018, Art. no. 1800135.
[18] K. Rydhmer et al., "Automating insect monitoring using unsupervised near-infrared sensors," *Sci. Rep.*, vol. 12, no. 1, pp. 1–11, 2022.
[19] A. Genoud, G. Williams, and B. Thomas, "Continuous monitoring of aerial density and circadian rhythms of flying insects in a semi-urban environment," *PLoS One*, vol. 16, Nov. 2021, Art. no. e0260167.
[20] M. Li et al., "Bark beetles as lidar targets and prospects of photonic surveillance," *J. Biophotonics*, vol. 14, no. 4, 2020, Art. no. e202000420.
[21] S. Jansson et al., "Real-time dispersal of malaria vectors in rural Africa monitored with lidar," *PLoS One*, vol. 16, no. 3, 2021, Art. no. e0247803.
[22] K. Rydhmer et al., "Scheimpflug lidar range profiling of bee activity patterns and spatial distributions," *Animal Biotelemetry*, vol. 10, no. 1, pp. 14–27, Apr. 2022.
[23] K. Bjerge et al., "An automated light trap to monitor moths (Lepidoptera) using computer vision-based tracking and deep learning," *BioRxiv*, 2020, Art. no. 2020.03.18.996447.
[24] L. Wührl et al., "DiversityScanner: Robotic handling of small invertebrates with machine learning methods," *Mol. Ecol. Resour.*, vol. 22, no. 4, pp. 1626–1638, 2022.
[25] S. Butail et al., "Reconstructing the flight kinematics of swarming and mating in wild mosquitoes," *J. Roy. Soc. Interface*, vol. 9, no. 75, pp. 2624–2638, 2012.
[26] A. Gebru et al., "Multiband modulation spectroscopy for determination of sex and species of mosquitoes in flight," *J. Biophotonics*, vol. 11, no. 8, 2018, Art. no. e201800014.
[27] A. Genoud, Y. Gao, G. Williams, and B. Thomas, "Identification of gravid mosquitoes from changes in spectral and polarimetric backscatter cross-sections," *J. Biophotonics*, vol. 12, Jun. 2019, Art. no. e201900123.
[28] B. K. Kouakou, S. Jansson, M. Brydegaard, and J. T. Zoueu, "Entomological scheimpflug lidar for estimating unique insect classes in-situ field test from Ivory Coast," *OSA Continuum*, vol. 3, no. 9, pp. 2362–2371, Jul. 2020.
[29] M. T. Sikulu, "Non-destructive near infrared spectroscopy for simultaneous prediction of age and species of two major African malaria vectors: An. gambiae and an. arabiensis," *NIR News*, vol. 25, no. 5, pp. 4–6, 2014.
[30] M. T. Sikulu-Lord et al., "Near-infrared spectroscopy, a rapid method for predicting the age of male and female wild-type and Wolbachia infected Aedes aegypti," *PLoS Neglected Trop. Dis.*, vol. 10, no. 10, 2016, Art. no. e0005040.
[31] M. Brydegaard, S. Jansson, M. Schulz, and A. Runemark, "Can the narrow red bands of dragonflies be used to perceive wing interference patterns?," *Ecol. Evol.*, vol. 8, no. 11, pp. 5369–5384, 2018.
[32] A. Gebru, M. Brydegaard, E. Rohwer, and P. Neethling, "Probing insect backscatter cross-section and melanization using kHz optical remote detection system," *J. Appl. Remote Sens.*, vol. 9975, pp. 23–39, 2016.
[33] M. Brydegaard and S. Jansson, "Advances in entomological laser radar," *J. Eng.*, vol. 2019, no. 21, pp. 7542–7545, 2019.
[34] E. Shevtsova, C. Hansson, D. H. Janzen, and J. Kjaerandsen, "Stable structural color patterns displayed on transparent insect wings," *Proc. Nat. Acad. Sci.*, vol. 108, no. 2, pp. 668–673, Jan. 2011.
[35] E. Shevtsova and C. Hansson, "Species recognition through wing interference patterns (WIPs) in Achrysocharoides Girault (Hymenoptera, Eulophidae) including two new species," *Zookeys*, vol. 2011, no. 154, pp. 9–30, 2011.
[36] N. J. Butterworth, T. E. White, P. G. Byrne, and J. F. Wallman, "Love at first flight: Wing interference patterns are species-specific and sexually dimorphic in blowflies (Diptera: Calliphoridae)," *J. Evol. Biol.*, vol. 34, no. 3, pp. 558–570, 2021.
[37] C. Kirkeby, M. Wellenreuther, and M. Brydegaard, "Observations of movement dynamics of flying insects using high resolution lidar," *Sci. Rep.*, vol. 6, no. 1, pp. 1–11, 2016.
[38] M. Li et al., "Potential for identification of wild night-flying moths by remote infrared microscopy," *Roy. Soc. Interface*, vol. 19, no. 191, 2022, Art. no. 20220256.
[39] R. Sacchi and S. Hardersen, "Wing length allometry in Odonata: Differences between families in relation to migratory behaviour," *Zoomorphology*, vol. 132, no. 1, pp. 23–32, 2013.
[40] D. L. Stern and D. J. Emlen, "The developmental basis for allometry in insects," *Development*, vol. 126, no. 6, pp. 1091–1101, 1999.
[41] C.-A. Darveau, P. W. Hochachka, K. C. Welch Jr., D. W. Roubik, and R. K. Suarez, "Allometric scaling of flight energetics in Panamanian orchid bees: A comparative phylogenetic approach," *J. Exp. Biol.*, vol. 208, no. 18, pp. 3581–3591, 2005.
[42] HySpex, "HySpex classic SWIR-384," Accessed: Jun. 7, 2021. [Online]. Available: https://www.hyspex.com/hyspex-products/hyspex-classic/hyspex-swir-384/
[43] MeadowlarkOptics, "Ultra broadband polarizer," Accessed: Jun. 7, 2021. [Online]. Available: https://www.meadowlark.com/ultrabroadband-polarizer/
[44] P. Debevec et al., "Estimating surface reflectance properties of a complex scene under captured natural illumination," *ACM Trans. Graph.*, vol. 1, pp. 1–11, Jan. 2004.
[45] F. Stanco, S. Battiato, and G. Gallo, *Digital Imaging for Cultural Heritage Preservation: Analysis, Restoration, and Reconstruction of Ancient Artworks*. Boca Raton, FL, USA: CRC, 2017.
[46] D. G. Stavenga, "Thin film and multilayer optics cause structural colors of many insects and birds," *Mater. Today: Proc.*, vol. 1, pp. 109–121, 2014.
[47] H. Yin et al., "Iridescence in the neck feathers of domestic pigeons," *Phys. Rev. E*, vol. 74, no. 5, 2006, Art. no. 051916.
[48] D. Raabe et al., "Microstructure and crystallographic texture of the chitin–protein network in the biological composite material of the exoskeleton of the lobster Homarus americanus," *Mater. Sci. Eng.: A*, vol. 421, no. 1, pp. 143–153, Apr. 2006.
[49] N. Katayama, J. K. Abbott, J. Kjærandsen, Y. Takahashi, and E. I. Svensson, "Sexual selection on wing interference patterns in Drosophila melanogaster," *Proc. Nat. Acad. Sci.*, vol. 111, no. 42, pp. 15144–15148, 2014.
[50] M. F. Hawkes et al., "Sexual selection drives the evolution of male wing interference patterns," *Proc. Roy. Soc. B: Biol. Sci.*, vol. 286, no. 1903, 2019, Art. no. 20182850.

**Meng Li** was born in Kunming, China in 1993. She received the M.Sc. degree in photonics in 2018 from Lund University, Lund, Sweden, where she is currently working toward the Ph.D. degree in biophotonics and remote sensing, with special focus on specular flashes from insect wings. In particular, using thin-film membrane thickness assessment as a tool to identify and monitor the diversity of insects.

**Anna Runemark** was born in Ronneby, Sweden in 1982. She received the M.Sc. degree in biology from Uppsala University, Uppsala, Sweden, and the Ph.D. degree in evolutionary animal ecology from Lund University, Lund, Sweden. She is currently working toward the Postdoctoral degree with the Centre for Ecological and Evolutionary Synthesis, University of Oslo, Oslo, Norway. She is also an Associate Senior Lecturer with the Department of Biology, Lund University.

**Noélie Guilcher** was born in Rennes, France in 1998. She received the M.Sc. degree in biological engineering from the Polytech Clermont-Ferrand School of Engineering, Aubière, France, in 2021. She completed Internship with Lund University, Lund, Sweden, in 2021.

**Julio Hernandez** was born in Mexico. He received the B.Sc. degree in physics from the National Autonomous University of Mexico, UNAM, Mexico City, Mexico and the M.Sc. degree in nanotechnology from the Chalmers University of Technology, Göteborg, Sweden. He is/was a Senior Research Scientist with Hyspex, Norsk Elektro Optikk AS in Oslo, Norway. He develops hyperspectral cameras and applications for remote sensing, defence and biomedical research in academia and industry.

**Jadranka Rota** was born in Zagreb, Croatia in 1976. She received the M.Sc. and Ph.D. degrees in entomology from the University of Connecticut, Storrs, CT, USA. She is/was a Postdoctoral Researcher with Smithsonian Institution, Washington, DC, USA, and Natural History Museum of Denmark, Copenhagen, Denmark. She is currently an insect Curator with Biological Museum, Department of Biology, Lund University, Lund, Sweden.

**Mikkel Brydegaard** was born in Copenhagen, Denmark in 1980. He received the M.Sc. degree in electrical Engineering in 2007, and the Ph.D. degree in atomic physics, biophotonics and remote sensing from Lund University, Lund, Sweden, in 2012. He is/was a Postdoctoral Research with Stellenbosch University, Stellenbosch, South Africa, and Norsk Elektro Optikk, Oslo, Norway. He was the recipient of the Inaba prize 2014, Docent 2016, a Senior Lecturer, in 2021 with Lund University, also ERC awardee 2018, and Co-Founder of the African Spectral Imaging Network and FaunaPhotonics, Denmark.

# Paper X

Vol. 10 • No. 34 • December 6 • 2023

# ADVANCED SCIENCE

Open Access

WILEY VCH

www.advancedscience.com

ADVANCED SCIENCE Open Access
www.advancedscience.com

# Discrimination of Hover Fly Species and Sexes by Wing Interference Signals

*Meng Li,* Anna Runemark, Julio Hernandez, Jadranka Rota, Rune Bygebjerg, and Mikkel Brydegaard*

**Remote automated surveillance of insect abundance and diversity is poised to revolutionize insect decline studies. The study reveals spectral analysis of thin-film wing interference signals (WISs) can discriminate free-flying insects beyond what can be accomplished by machine vision. Detectable by photonic sensors, WISs are robust indicators enabling species and sex identification. The first quantitative survey of insect wing thickness and modulation through shortwave-infrared hyperspectral imaging of 600 wings from 30 hover fly species is presented. Fringy spectral reflectance of WIS can be explained by four optical parameters, including membrane thickness. Using a Naïve Bayes Classifier with five parameters that can be retrieved remotely, 91% is achieved accuracy in identification of species and sexes. WIS-based surveillance is therefore a potent tool for remote insect identification and surveillance.**

## 1. Introduction

Insect diversity and abundance have been significantly reduced by anthropogenic changes,[1–3] such as habitat loss driven by agricultural intensification, pollution, and global warming, with insects experiencing significant declines even within protected areas.[4] Insects have important ecological roles, crucial not only for natural ecosystems but also for agriculture.[5,6] For instance, pollination is necessary for the majority of the food crops produced today.[7] Efficient pollinator groups include bees and bumblebees[8,9] (Hymenoptera), butterflies and moths[10,11] (Lepidoptera), and flies[12] (Diptera), including hover flies[13,14] (Syrphidae). Different groups of pollinators may respond differently to anthropogenic change, with specialist insects typically showing higher sensitivity to habitat alterations.[15,16] Therefore, understanding the responses of single species and groups is important. Hover flies are considered the second most important pollinators after wild bees,[17] and hover fly pollination is thought to be relatively resistant to fluctuating environmental conditions.[13] To understand the impact of diversity and abundance of pollinators in ecosystems, it is necessary to efficiently assess all important pollinator groups, including hover flies. However, monitoring insect abundance and diversity remains a challenge for researchers.

Conventional methods for surveillance of insect diversity and abundance are time-consuming and do not efficiently monitor all free-flying insects. Malaise traps are considered to capture the least biased species composition of flying insects[18] and pan-traps are used to monitor the Hymenoptera and Diptera pollinators.[19] These methods are labor-intensive and require taxonomic expertise for insect identification.[20,21] Environmental DNA (eDNA) monitoring[22–24] does not provide abundance estimates or insights into activity patterns. Machine vision approaches can provide species-level identification, but only of caught insects[24] and pollinating visitors in the field,[8,25] as free-flying insects cause focus and motion blur issues. Thus, current image recognition approaches rely on trap designs and baits, and they yield a low number of observations to resolve weather and hourly niches.

To improve species identification of free-flying insects, the frequency-, polarimetric- and spectral domains have been explored,[26] and real-time field sensors that discriminate free-flying insect species based on wing beat frequencies (WBFs) and harmonic overtones developed.[27–30] WBF and harmonic spectrum depend on both the wing dynamics,[31] wing surface roughness,[11] and wing membrane thickness[32–34] in relation to the wavelength. The WBFs of hover flies are in the

M. Li, M. Brydegaard
Department of Physics
Lund University
Sölvegatan 14c, Lund 22363, Sweden
E-mail: meng.li@forbrf.lth.se
A. Runemark, M. Brydegaard
Department of Biology
Lund University
Sölvegatan 35, Lund 22362, Sweden
J. Hernandez, M. Brydegaard
Norsk Elektro Optikk
Østensjøveien 34, Oslo 0667, Norway
J. Rota, R. Bygebjerg
Biological Museum, Department of Biology
Lund University
Sölvegatan 37, Lund 22362, Sweden
M. Brydegaard
FaunaPhotonics
Støberigade 14, Copenhagen 2450, Denmark

The ORCID identification number(s) for the author(s) of this article can be found under https://doi.org/10.1002/advs.202304657



**DOI: 10.1002/advs.202304657**

150–300 Hz range,[35] which is between the WBFs of bees[36] and mosquitoes.[35] However, the WBF depend on environment temperature,[29,36,37] humidity,[36] and body mass.[9,38] Even for a constant temperature, the relative spread of the WBF[37,39] for a single species and sex is typically 25%, in the best case this would leave room to distinguish 3–4 species or sex of hover flies (log(300 Hz/150 Hz)/25%). Therefore, utilizing WBF alone does not enable differentiation among the hundreds of coexisting species of syrphid flies.

In order to improve the discrimination of free-flying species of insects, photonic modulation methodology can be expanded in dimensionality by adding polarimetric- and spectral bands. The polarimetric domain provides sensitivity to microstructural features,[34,40] whereas different spectral bands[41] may yield molecular or nanoscopic information on the wing membrane thickness.[32,33] Importantly, most of the light backscattered by insects is oscillatory and contributed by insect wings,[39,42] and most of that light is scattered by specular reflections in insect wings. Thus, specular flashes can be observed by insects in flight.[34] Spectrally, this wing flash is dominated by fringy thin-film interference resonances[32,34] referred to as a wing interference signal (WIS) in this study. The flash instances represent the rare occasions when the wing orientation is entirely known and the reflectance spectra[34,43] may provide the quantitative information to determine the species and sex. Existing literature on wing interference patterns (WIPs) includes comparative studies[44,45] with RGB color cameras or spectroscopic case studies for single insect specimens.[34,46] WIPs are reported as species-specific, sexually dimorphic in blow flies,[47] and stable over time.[44] However, no literature provides quantitative estimates of the thicknesses, statistics across the entire wings, or any clues on how the differences between species compare to the within-species variation. We previously reported values for membrane thickness for various families,[33] but that study did not include replicates within species, and the significance of species contrast could therefore not be evaluated.

Here, we address how the nanoscopic features extracted from WIS can improve the species and sex identification of hover flies. We used infrared hyperspectral imaging and scanned a total of 600 wings from 30 species of pinned hover flies, including five replicates of each sex, and both the left-right wings. To our knowledge, no studies quantitatively determined membrane thickness or its within-species variation and how it can be used for differentiating insect species. Here, we ask to what extent the membrane thickness differs within wings and if wing thickness and variation in thickness differ among species and sexes. We assess how the membrane thickness scales with wing area and test if genetic divergence or ecological niche explains the variation in wing thickness and modulation. A challenge for interpreting signals is to document how fringe modulation depth and fringe heterogeneity vary across and within species and sexes. This determines the applicability of WIS for species identification and signaling. Based on thin-film theory, we explain WIS by four parameters (membrane thickness, thickness heterogeneity, fringe amplitude, and -bias). We uncover that wings as a whole produce fringy spectra, that the thickness differs significantly among species and sexes, and ecological traits explain variation in WIS better than genetic distance. This paves the way for improved specificity and species identification of insects using photonic entomological sensors with spectral sensitivity. This can imply the applicability of insect monitoring techniques across species and could greatly improve our understanding of the factors affecting insect diversity and abundance.

## 2. Results and Discussion

### 2.1. Wing Interference Fringes Survive Spatial Averaging over the Wing Surfaces

A polarimetric shortwave infrared hyperspectral camera ($0.95<\lambda<2.5$ μm, details see Section 4.4) was used to capture the WIS from the entire wings of the mounted individuals. Each pinned individual was scanned by a polarimetric shortwave infrared hyperspectral imager by specular illumination configurations (see example in **Figure 1**). The visual appearance of the broad spectral bands of the ordinary RGB color camera (Figure 1A) fails to resolve the narrow interference fringes spectrally, and consequently, the wings appear whitish. In contrast, a false color image based on selected narrow infrared bands results in soap bubble colors over the wing surface (Figure 1B). These WIPs are highly coherent, directional, and thus co-polarized as illustrated by the negligible de-polarized light (Figure 1C). Spectral fringes, caused by thin film interference,[33,46,48] differ between thick and thin wing sections (Figure 1F). The WIPs (as shown in Figure 1B) are reflected from the chitin membrane, whose structure remains unchanged from living adult flies to pinned museum specimens.[44] As the specular WIS is highly directional, the resonant reflectances exceed the white Lambertian reference (100% diffuse reflectance). This implies that WIS could be detectable over extended distances with a considerable contrast against background,[32,34] with consequences both for visual ecology and the prospects for detection and monitoring. The spectra obtained from an individual pixel exhibit significant fluctuations, reaching up to 88% modulation (Figure 1F, orange solid line, see also Section 4.5). In contrast, the de-polarized contribution shows minimal reflectance of a few percent, (See Figure 1F orange dash line). By averaging the reflectance across the entire wing, the spectral modulation decreases to 23% (Figure 1F, blue solid line). We conclude that the reduced spectral modulation for whole wings is due to the dephasing of fringes from distinct membrane thicknesses across the wing surface. As a result, thinner wings and longer wavelengths generally exhibit higher levels of spectral modulation. However, fringy properties are still detected in all species examined, enabling the estimation of effective thickness for the whole wings (Figure 1D). Generally, clear insect wings are thick toward the anterior edge and thin toward the posterior edge. The left-right discrepancy of the effective thickness is just 10 nm, values are shown in Figure 1D for the examined individual, similar to the precisions achieved by lidar estimates on free-flying insects.[32] The spectral modulation depth varies across the wing surface (Figure 1E), implying that all parts of the wing surfaces does not contribute equally to the effective fringe. In particular, the wing veins do not produce spectral fringes and display low modulation, as illustrated by the histogram of wing thicknesses in individual pixels (Figure 1G). The histograms from the right and left wings are highly consistent. Finally, the effective thickness of 1.15 μm is somewhat thinner than the

 

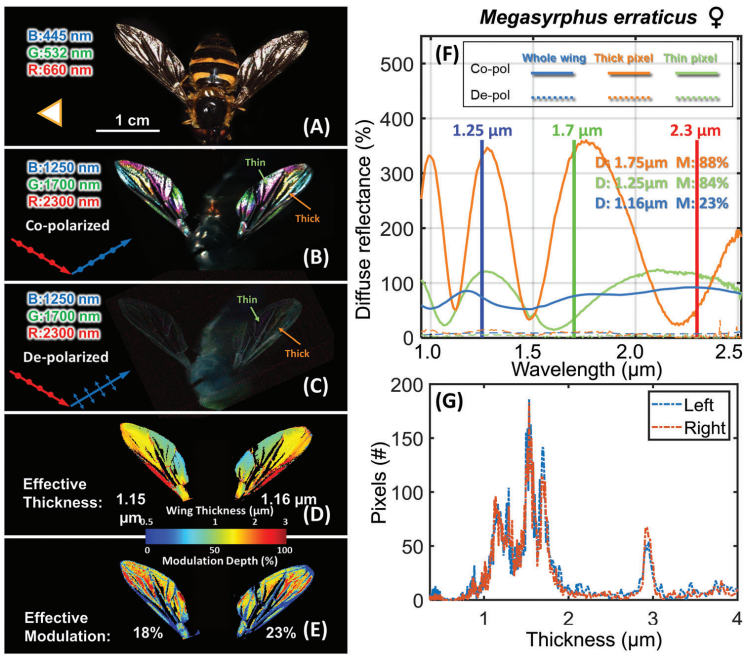


**Figure 1.** RGB and false color images of the hover fly *M. erraticus*. A) A photo of female *M.erraticus*. B,C) Two false color images were generated for co- and depolarizations with false color bands chosen according to the hyperspectral data cube (band choices: blue @ 1250 nm, green @ 1700 nm, and red @ 2300 nm) with a gain of 80%. D,E) Membrane thickness and modulation depth maps, showing the reflectance of the selected thick and thin wing pixels in (B,C). The blue colored reflectance spectrum in (F) corresponds to the effective wing reflectance integrated over the whole left wing. The orange and green reflectance spectra corresponding to the fringes form the thick and thin wing pixels. *D*: thickness, *MD*: modulation depth. G) Histograms of the wing thickness distributions of all left- and right-wing pixels.

most common thicknesses encountered on the same wing. This is because the thinner areas of the wing have higher modulation values and fringes from thinner membranes are more prone to interfere constructively.

### 2.2. Wing Interference Signals are Species- and Sex-Specific

Wings from five individuals of each sex from 30 hover fly species were analyzed. The wing surfaces were spatially averaged, and effective fringes were obtained (Figure 1). The effective fringes or WIS (**Figure** 2A) can be explained by a spectral model with four degrees of freedom; an effective thickness, $d_{wing}$, the thickness heterogeneity across the wing surface, $\lambda_0$, a fringe amplitude, $\alpha$, and a bias term, $\beta$. For convenience, we also measure the spectral modulation depth, $M$, within the spectral window of our instrument. Determining the effective thicknesses and modulations for each sex and species, we find that thickness ranged between 0.4 and 2.2 µm (Figure 2A; Figures S1 and S2, Supporting Information), and effective modulation depth in the short-wave infrared varied from 10 to 70%. Thicker wings are not highly modulated, whereas some thin-winged species display a variety of modulation depths.

In contrast to the frequency domain,[35] we found that among species differences were more pronounced than differences within species and between sexes. While many species overlap with their neighbors in this 2D scatterplot, most species do not have any overlap with the majority of the other 29 examined species. Species- and sex differences were apparent in both the effective membrane thickness, $d_{wing}$, and effective fringe modulation depth, $M$ (Figure 2A). We also observed differences in the other WIS properties such as effective fringe heterogeneity, $\lambda_0$, effective fringe amplitude, $\alpha$, and bias $\beta$ (see Figures S3–S5, Supporting Information). The differences have interesting implications, primarily for the feasibility of using spectral technology to differentiate free-flying species but also for signaling in visual ecology. As indicated by the resemblance of species with similar color codes, more closely related species across tribes and genera have more similar WIS properties. However, there is no obvious pattern of thickness across the entire hover fly family. To illustrate the substantial variation in membrane thickness and modulation across species (Figure 2A), we selected nine representative cases and presented their membrane thickness maps and corresponding modulation maps (Figure 2B). Generally, insect wings are thinner toward the rear edge, which also primarily contributes to the effective fringe and modulation. We found this

 

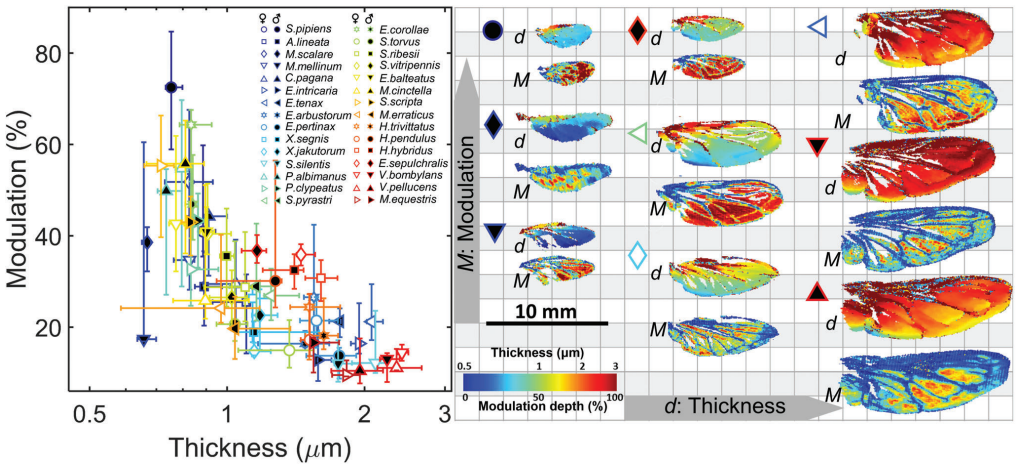


**Figure 2.** Membrane thickness and fringe modulations scatter plot. A) Effective membrane thickness versus spectral fringe modulation depth. The markers indicate median values and the bars indicate the ¼ and ¾ quartiles of the within-species and sex variation. The full name of the species in the legend is listed in Table S1 (Supporting Information). The species color coding is sorted by minimizing genetic distance with their neighbors in Figure S1 (Supporting Information). B) Nine representative cases showing the membrane thickness and modulation depth maps.

pattern to hold true across both species and sexes, but different species and sexes displayed different degrees of gradient changes in thickness and modulation variation (Figure 2B). Finally, our results showed that thin-winged species are more likely to produce WISs with strong modulation depths (Figure 2A; Figure S6, Supporting Information).

One study[49] suggested that subwavelength gradient refractive indices on wing surfaces reduce modulation depths of fringes and WISs, and others have suggested that wrinkled wings distribute interference signals spherically.[44] To uncover the main limiting factor for the effective modulation of hover fly wing fringes, we introduced the mean broadband reflectance, $\mu(R_\lambda)$, for the wings and calculated the broadband reflectance spatial standard deviation reflectance, $\Delta R_{pix}$, as a measure of wrinkles. We correlated the modulation depth $M$ with the wing heterogeneity, $\Delta d_{pix}$, fringe heterogeneity, $\lambda_0$, broadband reflectance, $\mu(R_\lambda)$, and degree of wrinkling, $\Delta R_{pix}$. We employed the Pearson correlation coefficient, and positive definite quantities were logarithmized prior to correlation (marked in gray in **Figure 3**). Our study incorporated all 30 species, and distinctions were made solely when correlating males and females individually, as represented by the respective sex symbols in the figure. We found that modulation was primarily related to membrane thickness heterogeneity $\Delta d_{pix}$ and $\lambda_0$, and less to $\mu(R_\lambda)$ and $\Delta R_{pix}$ (Figure 3). Modulation damping by thickness heterogeneity takes effect when widely distinct membrane thicknesses across the surface are averaged and interfere destructively. This effect predominantly damps the WISs toward shorter wavelengths because thin-film WISs are chirped, and the higher-order modes toward shorter wavelengths are more sensitive to dephasing. Thus, we concluded that the effective fringe modulation depth is primarily influenced by the heterogeneity in wing thickness compared to other nano features such as wrinkles and anti-reflective gradient refractive indices.

### 2.3. The Allometric Relationship between Wing Area and Membrane Thickness is Not Isometric

Projected wing- and body-area are available for both machine vision, wingbeat sensors, and lidars. To assess whether the membrane thickness provides complementary information or scales with wing area, we investigated the relationship in the examined hover flies (**Figure 4**A,B). We found the relationship to be described by a power relation of the form $A_{wing} = G_{all}\, \bar{d}_{wing}{}^{\gamma}$, where $\gamma = 1.3$ [1.2–1.4] and the *aspect ratio* $G_{all} = 15$ (14–16, 95% confidence interval, and $R^2_{adj}$ of 80%; Figure 4A). This relationship is significantly different from isometric scaling with the form $A_{wing} = G\, \bar{d}_{wing}{}^{2}$, where $G = 10$ (9–11, 95% confidence, and $R^2_{adj}$ of only 56%; Figure 4A). Despite the strong covariance between wing area and thickness, many species deviate from the allometric expectation providing additional species-specific signals. Notably, some larger flying insects, such as dragonflies,[34] have wing areas of 700 mm$^2$ but similar wing thicknesses of 2–3 µm. Another study found submicron thicknesses of equally large grasshopper wings.[32] These examples illustrate how thickness-to-area aspect ratio and allometric relation can be entirely different for other orders and families.[33] Our study highlights the diversity of membrane thickness maps in relation to wing sizes (Figure 4B).

Interestingly, although wing area and membrane thickness covary, the two parameters also hold complementary species-specific information as illustrated by the correlation matrix including WIS parameters to wing- and body area (Figure 3). The wing membrane thickness $\bar{d}_{wing}$ correlates with both the wing area $A_{wing}$ and body area $A_{body}$ (Figure 3). Furthermore, the wing membrane thickness is anti-correlated with the modulation depth, $M$, and estimated WBF, $f^*$, (Figure 3; Figure S7, Supporting Information). The WBF, $f^*$, was estimated based on hover flies body mass and wing area (details are reported in the

 

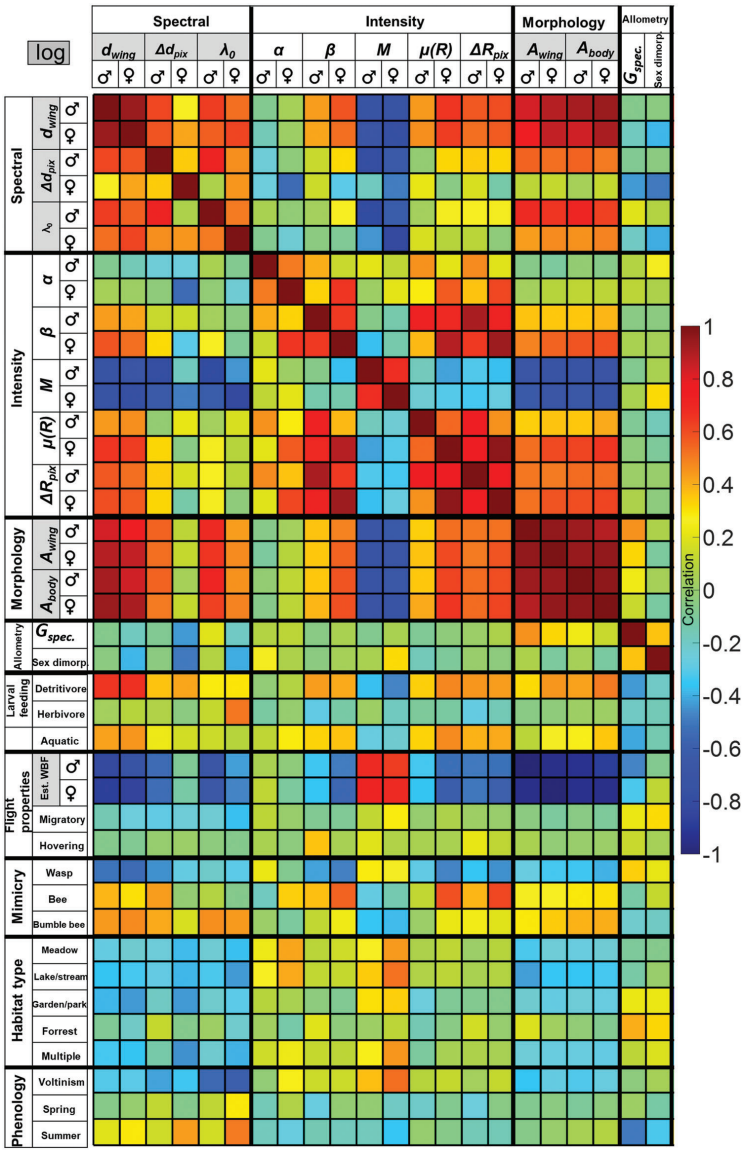


**Figure 3.** A correlation coefficient matrix of WIS parameters with ecological traits (cropped version, full matrix is shown in Figure S7, Supporting Information). The maximum positive correlation is 1, the maximum negative correlation is −1 and the minimum correlation is 0. Definition of abbreviations; $d_{wing:}$ membrane thickness $\Delta d_{pix:}$ wing heterogeneity, $\lambda_0$: fringe heterogeneity, $\alpha$:effective fringe amplitude, $\beta$: effective fringe bias, $M$: fringe modulation depth, $\mu(R)$: broadband reflectance, $\Delta R_{pix}$: degree of wrinkling, $A_{wing}$: wing area, $A_{body}$: body area, $\gamma$: allometric power relation, Est.WBF: estimated wing beat frequency.

 

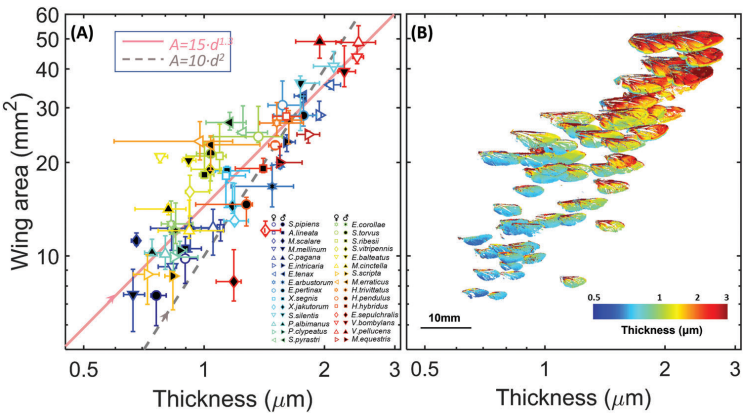


**Figure 4.** Wing area and membrane thickness are not isometrically related. A) Effective membrane thickness versus wing area. The power relation $A_{wing} = 15 \cdot d_{wing}^{1.3}$ represents the allometric relationship between the wing area and thickness better than $A_{wing} = 10 \cdot d_{wing}^{2}$. B) Wing thickness map for each species and sex based on their medians in (A). The scale bar is for the scaling of wing thickness maps.

Experimental Section). Overall, the correlations between WIS parameters, wing, and body area suggest hover flies with large bodies are more prone to have larger and thicker wings, a lower WBF, and weak WIS modulation.

Our results demonstrate that the membrane thickness, heterogeneity, and modulation provide complementary information on wing area. The wing and body area can be retrieved from free-flying insects with existing photonic sensors[50] and lidar technique[51] (as projected scattering cross-section in mm$^2$). Therefore, it is feasible to expand the capability of lidar to capture the membrane thickness of in-flight insects and use it as complementary information to significantly improve species identification. Although this study reports measurements from mounted individuals with known illumination geometry, the results can be translated to field observations. This is because backscattered signals from clear-winged insects are dominated by the specular WIS flash[34] and because the wing surface orientation is known in the instance a WIS flash occurs. In a recent report,[32] we demonstrated that such signals can be retrieved remotely in the field, that the membrane thickness can be estimated, and that this thickness is consistent with laboratory recordings. This implies that any photonic device measuring backscattering from insects would favor the detection of species with resonant wings for the employed wavelength bands.

### 2.4. Classification Accuracies Based on Interference Signals

We concluded that the light reflected by insect wings is sensitive to the membrane thickness and that this thickness differs greatly between species. Moreover, most hover fly species exhibit sexually dimorphic WIS properties (Figures 3 and 4; Figures S3–S5, Supporting Information). Interestingly, this also holds true for species where sex determination based on morphology and size is known to be challenging (Table S1, Supporting Information).

We evaluated the benefit of including spectral information for species- and sex-specificity of photonic-based sensors. We combined thickness $d_{wing}$ and $\lambda_0$ with several features, including the WBF, $f^{\wedge}$, wing area $A_{wing,}$ and modulation depth $M$ (see methods). We included $f^{\wedge}$ and $A_{wing}$ because they are common features for insect identification with photonic sensors,[52–55] the spectral parameters $d_{wing}$ and $\lambda_0$ can potentially be determined with great accuracy,[32] and the modulation, $M$, is a unitless feature that can be extracted from a WIS. In addition, a WIS with a low $M$ implies great uncertainty of the fringe parameters. We applied a Naïve Bayesian Classifier (NBC), a classification method simply estimating the overlap of groups in an N-dimensional parameter space on these parameters, specified in metric units. We show that the successful identification rate based on the WBF, $f^{\wedge}$, alone was only 13%, but 91% when all four features were considered (**Table 1**). We note that $\lambda_0$ and $M$ could not be estimated without simultaneously estimating $d_{wing}$ This improve-

**Table 1.** Accuracy of identifying the correct species and sex of hover flies based on one or several chosen parameters, more details see Figures S12–S20 (Supporting Information). WBF: wing beat frequency, $d_{wing}$: effective membrane thickness, $M$: fringe modulation depth, $\lambda_0$: fringe heterogeneity, $A_{wing}$: wing area.

| Accuracy [%] | *WBF* [Hz] | $d_{wing}$ [μm] | $\lambda_0$ [μm] | $A_{wing}$ [mm$^2$] | $M$ [%] |
|---|---|---|---|---|---|
| 13 | ✓ | | | | |
| 22 | | ✓ | | | |
| 35 | | ✓ | | | ✓ |
| 40 | | ✓ | ✓ | | |
| 63 | ✓ | ✓ | | | |
| 74 | ✓ | ✓ | ✓ | | |
| 75 | ✓ | ✓ | | | ✓ |
| 85 | ✓ | ✓ | | ✓ | ✓ |
| 91 | ✓ | ✓ | ✓ | ✓ | ✓ |

 

ment demonstrates that the deduced spectral information, such as the membrane thickness $d_{wing}$ and modulation depth $M$, is complementary and could revolutionize remote species identification using WISs. Several studies have explored the discrimination of free-flying insects by their oscillatory properties using a single band,[54,56–59] and our findings show that specificity can be strongly improved by adding up to four spectral bands according to the fringe model. For single-band instruments, our findings imply increased signal-noise-ration or detection range for species with resonant wings for the particular wavelength. The resonant condition is given by $\lambda_{max} = 2nd_{wing}/(m\text{-}½)$, $m \in \mathbb{N}$, as an example, the most brilliant of our hoverflies *Syritta pipiens* has $d_{wing}$ of 762 nm and resonant backscatter at 670, 925, and 1546 nm wavelength. The half mode term in the equation derives from the 180° phase shift from the first air-chitin reflection (this flip is absent from the backside chitin-air reflection).

### 2.5. Nanoscopic Features, Genetic Distance, Species Ecology, and Morphology

Using correlation analyses, we found that genetic distance between species only explained 29% and 26% of the variation in wing thickness, $d_{wing}$, for males and females respectively. The genetic distance explained 31% of the variation in spectral modulation, $M$, for males, but just 8% for females. For comparison, the group of detritivorous larvae explained 35% and 37% of the difference in wing thickness for males and females respectively. Grouping the species into wasp- and bumblebee mimicking explained equally much of wing thickness variation as genetic relatedness, with correlation coefficients between 22 and 29% (Figures S9 and S10, Supporting Information). We also tested if differences in wing thickness-area aspect ratios, $G_{spec.}$, and differences in sexual dimorphism in different species were significantly correlated with genetic distance, but found that this was not the case. There are two potential caveats to our approach. One is that we used a short fragment of the mitochondrial DNA (the DNA barcode) for estimating genetic distance, and the other is that we have only sampled a small percentage of the known hover fly species. To test a more complicated relationship between thickness and genetic relatedness, we plotted wing thickness against cumulative genetic distance from the two extreme species *S. pipiens* to *Merodon equestris* (Figure S11, Supporting Information). The analysis revealed that the wing thickness parameter folds twice across the hover fly family (a third-order polynomial yielded 36% and 41% $R^2_{adj}$. for males and females, respectively). This confirms our observation that thicknesses are similar on the genus level but not on the family level (Figure 2A).

In addition, we tested whether ecological niche, phenology, or morphological differences influenced the nanoscopic properties or biomechanical structure of hover fly wings, which would increase the ability to interpret signals from unknown taxa in field studies. Hover flies are often generalist or broad-spectrum flower visitors,[60,61] but differ in phenology, habitat use, larval diet,[62] and morphology. For instance, some hover fly species mimic bumble bees, whereas others mimic wasps, with considerably distinct wings and WISs. The larval diets of Syrphidae span carnivore aphid predators, aquatic detritus feeders, and herbivores. Moreover, hover fly sexes exhibit distinct behaviors, with females collecting more pollen-containing proteins for egg production and males establishing territories and fiercely defending them from intruders[63] through hoovering. To understand how the species morphology and ecology predict WIS parameters, we investigated the relationship between larval feeding habits, larval habitats, flight properties, mimicry, habitat type, and phenology of the focal species to our four WIS parameters (Figure 3; the full matrix is shown in Figure S7, Supporting Information). We found that hover flies with thicker wings are: a) more likely to be mimics of bees and bumble bees (rather than wasps), b) less likely to be found near lakes/streams or gardens/parks, c) more likely to have detritivorous larvae, and d) tend to be more active during summer than during other seasons. Since thinner wings are more strongly modulated, we generally encountered anticorrelations between these ecological traits and spectral modulation, $M$. Hover flies with higher spectral modulation, are a) more likely to mimic wasps, b) prefer diverse habitats, including meadows, c) are more likely to have terrestrial and carnivorous larvae, and d) have more generations within a year and less active during summer. These findings can potentially provide clues about the traits of the hover fly species observed based on WIS observations. For instance, if larval feeding habits are reflected by membrane thickness, it could have applications for sensors in agriculture.

Finally, we addressed if species deviated from the general allometric relation by estimating a species-specific wing thickness-area aspect ratio, $G_{spec.} = Ad^{-\gamma}$ (Figure 4; Figure S8, Supporting Information). We found that large-winged species with thinner wings than expected by the allometric relationship have a tendency to be more sexually dimorphic (36% of the variation is explained by this correlation), and males generally have larger wings than females with sex explaining 46% of the within-species variation in data (Figure 4A). This could potentially be due to selection for sexually selected visual signaling, as proposed in earlier work,[45] or reflect sex-specific behaviors or morphology. Hover flies with large thin wings prefer forest habitats (40%), whereas hover flies with thick small wings are more likely to have detritivorous (43%) or aquatic larvae (41%), and be active during the summer month (50%; Figure 3 row $G_{spec}$; see also Figures S7–S8, Supporting Information).

## 3. Conclusion

We presented a new and innovative approach that could revolutionize our ability to remotely identify species and sex of flying hover flies. We can explain wing interference signals by four parameters, including membrane thickness and thickness heterogeneity. Using these parameters, we successfully distinguished 30 different species of hover flies and could discriminate between sexes. The proposed scheme achieves an identification accuracy of up to 91% on mounted hover flies. Similar signals can be captured from free-flying insects in the field,[32] and hence discrimination can be greatly improved by additional spectral bands in photonic insect sensors. The implications of this work are that 1) single-band photonic sensors[29] or lidars[28] have preferences for species with resonant wings for the employed wavelength, 2) dual-band systems[30,41,43] could differentiate species according to wing thicknesses although thickness would be ambiguous, 3) unique determination of wing thickness would require minimum four spectral bands, however hyperspectral monitoring[32]

 

of insect could prove excessive and benefit from speed rather than spectral bands.

Wing features were correlated with hover fly morphology and ecology, including habitat use and larval ecology, which potentially could help classify signals from field observation from hover fly species not included in the study in the future. Our novel method for identifying hover flies is expected to make a significant contribution to the development of remote monitoring sensors for flying insects. The ability to accurately identify species and sexes of hover flies will greatly enhance our understanding of their abundance and distribution as well as habitat-specific diversity, which ultimately can inform the development of more effective strategies for protecting these important pollinators and their habitats.

## 4. Experimental Section

*Hover Fly Specimens*: A total of 300 individual hover flies from 30 hover fly species (five replicates of each sex) were provided by the Lund University Biological Museum, and both the right and left wings of each specimen were studied. While hover flies (Syrphidae) are challenging for amateur entomologists to identify, the flat and clear wings of hover flies are ideal targets for identification over long distances using photonic sensors based on spectral WISs. The 30 hover fly species were chosen based on their abundance in Sweden and wing size: species with wingspans between 15 and 40 mm were chosen to fit within the field of view of the instrument. The 30 hover fly species included in this study are listed in Table S1 (Supporting Information). The males and females of some hover fly species (e.g., *Episyrphus balteatus*), are similar in size and form.[20,21] These are marked gray in Table S1 (Supporting Information).

*Ecological Traits*: The 30 species studied here were categorized according to the following traits covering different aspects of the hover fly biology: larval feeding habits (herbivores, carnivores, or detritivores), larval habitats (terrestrial or aquatic), flight properties (WBF, migratory and hovering), mimicry (wasp, bee, or bumblebee), habitat type (meadow, lake/stream, garden/park, forest or multiple), and phenology (voltinism, spring, or summer). Information about the ecological traits was provided by Rune Bygebjerg from the Lund University Biological Museum (see Supplementary Spreadsheet, *Hover fly listRB2.xlsx*).

*Genetic Pairwise Distance*: The genetic distance between the 30 species of Syrphidae was calculated using the publicly available sequences and tools in The Barcode of Life Data System tools.[64] The K2P distance model was applied on the sequences that were aligned using the BOLD Aligner. The DNA barcodes for *Anasimyia lineata* and *Cheilosia pagana* could not be found in the BOLD databases; thus, they were replaced by proxy congener species (*Anasimyia lunulata* and *Cheilosia albipila*) to complete the pairwise distance comparisons. The result of these pairwise genetic distances is visualized in Figure S1 (Supporting Information), where the species are sorted by maximizing neighbor similarity. It is noted that the use of a proxy species could weaken the strength of the genetic results.

*Capturing Spectral WISs with a Hyperspectral Camera*: A polarimetric Short-wave infrared (SWIR) hyperspectral imaging system (HySpex: SWIR-384, Norsk Elektro Optikk AS, Norway) similar to that used in previous studies[11,33,65] was used to image the hover fly wings. The hyperspectral camera covered the shortwave infrared wavelength range from 0.95 to 2.5 µm and a spatial resolution of 240 µm/pix, with 288 spectral bands. A broadband halogen-tungsten lamp (150 W) placed 30 cm away from the sample was used for illumination (impinging on the pixel footprints in a ±8° light cone). The camera and light source were arranged in a specular condition with ±56° (Brewster angle of chitin) to the hover fly wing surface. This angle was taken into account when calculating membrane thickness, but similar fringes can be measured at any backscatter angle. In fact, smaller incidence angles as in lidar[32] ease the constraints for flat wings. Two ultra-broadband polarizers[66] were used to capture the co- and de-polarized reflectance. The objective of the camera had an aperture of Ø20 mm and a working distance of 8 cm (numerical aperture of ±7° imaging cone). The swath width was 40 mm for the imaged specimen. All hyperspectral images were calibrated to a Lambertian gray standard reference (Spectralon®) of 50% reflectance. Calibrating the shiny wings to a diffused Lambertian standard implies that the specular reflectance of the wings can exceed 100% diffuse reflectance. All hover flies had their wings spread and were mounted on black neoprene, resulting in a horizontal wing surface. Black neoprene was used to reduce the amount of background light.

*Parametrizing Spectral Fringes with the Modulation and Fringe Model*: The reflectance of clear insect wings can be explained by thin film interference.[46] According to this, light may resonate in backscatter or transmission depending on the wavelength, membrane thickness, refractive index, and incident angle. For the case of coaxial lidar, resonant backscatter is achieved at the wavelengths $\lambda_{\mathrm{Rmax}} = 2nd/(m\text{-}½)$ where as no resonance is observed at $\lambda_{\mathrm{Rmin}} = 2nd/m$, where $n$ is the refractive index, $d$ membrane thickness and $m \in \mathbb{N}$. For all wavelengths, each wing pixel in the hyperspectral images had a corresponding spectral profile referred to as a fringe; thick and thin wing pixel examples are shown in Figure 1F, and their corresponding spectral fringes are shown in Figure 1F. The effective fringe was acquired by spatially integrating all wing pixel spectral profiles. All three example fringes shown in Figure 1F show different degrees of modulation, which can be described by the modulation depth $M$ with the following equation:

$$M = \frac{\sigma_\lambda(R_\lambda) \cdot \mu_\lambda(F_\lambda)}{\sigma_\lambda(F_\lambda) \cdot \mu_\lambda(R_\lambda)} \tag{1}$$

where $R$ denotes measured reflectance, $F$ denotes the computed fringe, $\lambda$ is the wavelength, $\sigma_\lambda$ denotes standard deviation in the spectral domain, and $\mu_\lambda$ is the spectral mean value. The computed fringe $F(\lambda, d_{\mathrm{pix}})$ can be calculated[48] according to the membrane thickness $d_{\mathrm{pix}}$ as follows:

$$F(\lambda, d_{pix}) = \frac{4R_s \sin^2\left(2\pi d_{pix}\sqrt{n^2 - \sin^2\theta}/\lambda\right)}{(1-R_s)^2 + 4R_s \sin^2\left(2\pi d_{pix}\sqrt{n^2 - \sin^2\theta}/\lambda\right)} \tag{2}$$

where $n$ is the refractive index of chitin, $\theta$ is the light incident angle on the membrane, which was 56° in the recordings, and $R_s$ is the reflectance coefficient, which can be determined with the Fresnel equations. Only the S-polarization reflectance $R_s$ was included in the fringe model, as the P-polarization reflectance $R_p$ was absent when measuring specular light at the Brewster angle. The reflection coefficient $R_s$ is expressed as:

$$R_s = \left(\frac{\cos\theta - \sqrt{n^2 - \sin^2\theta}}{\cos\theta + \sqrt{n^2 - \sin^2\theta}}\right)^2 \tag{3}$$

The refractive index of chitin $n$ at a given wavelength $\lambda$ can be calculated[46] as:

$$n = k_0 + k_1/\lambda^2 \tag{4}$$

where $k_0 = 1.517$ and $k_1 = 8800\ \mathrm{nm}^2$. It is noted that the refractive index is generally given by the density of the medium[67] and further by spectral dispersion described by the Kramers–Kronig relation. Since the SWIR range is far from chitin's main absorption band at 280 nm, the refractive index only varies between 1.527 and 1.518 (<1% change). No differences are expected in refractive index between living- and preserved specimens. The modulation depth $M$ was calculated for all three fringe examples shown in Figure 1F, and the values are shown in the same figure. The fringe model $F(\lambda, d_{\mathrm{pix}})$ shown in Equation (2) was used to determine the membrane thickness for fringes in all pixels. This was done by computing 1000 fringes by using the fringe model $F(\lambda, d_{\mathrm{pix}})$ for membrane thicknesses ranging from 0.35 to 4 µm. The thinnest observable fringes are given by the instrument's spectral range and the thickest observable fringes by the in-

 

strument's spectral resolution. For robust numerical fitting to signals with noise, the search range should be reduced to realistic values. The range was chosen to cover the predominant thicknesses of all species and sexes (See Figure S2, Supporting Information). Minor features are also seen in Figure S2 (Supporting Information), they arise from vein pixels, which are poorly described by the fringe model. However, veins have low reflectance and thus a minimal contribution to the WIS from the whole wing.

The modulation of the fringe model $F(\lambda, d_{pix})$ is 100% across all wavelengths, but the factor is included in Equation (1) to compensate for the arbitrary number of fringes covered by the spectral range of the instrument. The measured fringes, $R(\lambda)$, in each pixel was then matched with the computed fringe $F(\lambda, d_{pix})$ based on the correlation coefficient, $C$, and fitting quality parameter, $Q$:

$$C\ (R, F) = \frac{\int_{0.95}^{2.5}\left(F_{\lambda,d_{pix}} - \mu_\lambda\left(F_{\lambda,d_{pix}}\right)\right)\left(R_\lambda - \mu_\lambda\left(R_\lambda\right)\right)}{\sqrt[2]{\int_{0.95}^{2.5}\left(F_{\lambda,d_{pix}} - \mu_\lambda\left(F_{\lambda,d_{pix}}\right)\right)^2 \partial\lambda \int_{0.95}^{2.5}\left(R_\lambda - \mu_\lambda\left(R_\lambda\right)\right)^2 \partial\lambda}} \quad (5)$$

$$Q\left(d_{pix}\right) = C\left(R, F\right)\left(C\left(\frac{\partial R}{\partial\lambda}, \frac{\partial F}{\partial\lambda}\right)\right)^2 \quad (6)$$

The derivatives of the fitting quality parameter Q were used to neglect the slopes and the squared factor void sign flipping. The membrane thicknesses of three example WISs shown in Figure 1F were calculated, and the same model was then used to calculate the membrane thickness and modulation for each specular wing pixel in Figure 1B. The membrane thicknesses and modulation depths are presented in Figure 1D,E. Histograms of the membrane thicknesses for all wing pixels from left and ring wings are shown in Figure 1G, which demonstrates the precision of the method. The fringe model $F(\lambda, d_{pix})$ in Equation (2) was applied to parametrize the effective fringes of the whole wings and wings with a single thickness $d_{wing}$. Since fringe modulation increases toward infrared wavelengths and decreases toward visible wavelengths, a longpass function was used to describe the amplitude, whereas a shortpass function was used to describe the bias:

$$F_{eff}\left(\lambda, d_{wing}\right) = \frac{\alpha \cdot F\left(\lambda, d_{wing}\right) \cdot \lambda^k + \beta \cdot \lambda_0^k}{\left(\lambda_0^k + \lambda^k\right)} \quad (7)$$

where $k$ is the slope of the long- and shortpass functions, and the best value to describe all effective fringes was $k = e = 2.71$. The remaining parameters are amplitude, $\alpha$, bias, $\beta$, and heterogeneity, $\lambda_0$. These parameters were fitted to all recordings by a numerical search algorithm (Curve fitting toolbox, MATLAB, MathWorks, USA).

Because damaged, folded, or misaligned wings cause outliers, precision weight factor was introduced based on the left–right symmetry of each individual:

$$\varepsilon_{LR} = \left(1 - \frac{\left|d_{left} - d_{right}\right|}{d_{left} + d_{right}}\right) \quad (8)$$

where $d_{left}$ and $d_{right}$ are the effective membrane thicknesses of the left and right wings of the same specimen. This weight factor, $\varepsilon_{LR}$, was used when calculating the medians and interquartile ranges (IQRs) of all WIS parameters (modulation depth $M$, membrane thickness $d_{wing}$, fringe amplitude $\alpha$, WIS bias $\beta$, and fringe heterogeneity $\lambda_0$) for each species and sex. The weighted medians and IQRs of the WIS parameters are presented in Figure 2A, Figures S3–S5 and Tables S2–S3 (Supporting Information).

More wing surface structure information can be deduced from the hyperspectral data outside the effective spectral WISs. The wrinkling measure $\Delta R_{pix}$ and wing heterogeneity $\Delta d_{pix}$ of the wing surface were determined by measuring the standard deviation of the broadband reflectance $R_{pix}$ or membrane thickness $d_{pix}$ of all wing pixels of a given species:

$$\Delta\ R_{pix} = \sigma_{pix}\ \left(\int_{0.95}^{2.5} R_{pix}\partial\lambda\right) \quad (9)$$

$$\Delta\ d_{pix} = \sigma_{pix}\ \left(d_{pix}\right) \quad (10)$$

The mean reflectance $\mu(R_\lambda)$ of the wing surface was calculated by averaging the reflectance of all wing pixels:

$$\mu\ \left(R_\lambda\right) = \mu_{pix,\lambda}\ \left(\int_{0.95}^{2.5} R\partial\lambda\right) \quad (11)$$

It was noted that these three parameters could only be measured from the hyperspectral data because they required spatial information, which was not included in the effective spectral WISs. These parameters are measued although they are not applicable for remote discrimination of insects. This is done to increase the understanding of the mechanisms affecting spectral modulation. All parameters are provided in Tables S2–S3 (Supporting Information).

*Estimating the Wing Beat Frequency of the Examined Species*: The relationship between wing beat frequency, body mass, and wing area has been studied extensively and provides valuable insights into insect flight dynamics.[35,38] However, the literature lacks information on the wingbeat frequencies of most species and sexes of the studied hover flies. Therefore, the wingbeat frequency was estimated based on the hover fly body mass and wing area. Because the specimens were dried museum specimens, the body masses of all specimens were approximated based on their body area and wing area and correlated to the Syrphidae body mass values provided in the literature.[35] The predicted wing beat frequency $\hat{f}$ for Syrphidae is calculated as[35,38]:

$$\hat{f} = f_0 \frac{\sqrt{m}}{A_{wing}} \quad (12)$$

where $f_0$ is 386.9 Hz mg$^{-½}$mm$^2$, $m$ is the approximated body mass and $A_{wing}$ is the wing area measured according to the hyperspectral images. These values can be found in Tables S2–S3 (Supporting Information).

*The Success Rate of Identifying the Correct Hover Fly Species and Sex Based on the WISs*: In addition to the spatial and frequency information, the spectral domain was considered to greatly enhance the species specificity of the photonic sensors. One hundred synthetic data points for each of the 30 species were produced for both sexes (resulted in 6000 generated data points) based on the medians and interquartile ranges (IQRs) of the membrane thickness $d_{wing}$, modulation $M$, estimated WBF $\hat{f}$ and wing area (all values are shown in Tables S2–S3, Supporting Information). The 100 synthetic data points were then input into NBC without including the covariance between parameters. The classification accuracy and overlap between the species were visualized with standard confusion matrices, as shown in Figures S12–S20 (Supporting Information).

*Allometry*: A power relation formula was used to describe how wing area $A_{wing}$ and membrane thickness $d$ are related in hover flies.

$$A_{wing} = G_{all} d_{wing}^{\gamma} \quad (13)$$

The constant factor $G_{all}$ and the exponent $\gamma$ in the formula were specific to examined hoverflies and describe how changes in wing area affect membrane thickness. When the wing area to wing thickness relation was isometric, $\gamma$ would be expected to equal 2. However, the analysis showed that the best fit for all data points occurred when $\gamma$ was 1.3 [with a range of 1.2–1.4], indicating that the scaling relationship between wing area and membrane thickness was not isometric in these hoverflies.

 

*Sexual Dimorphism in WISs*: The sexual dimorphism was calculated as the membrane thickness of males divided by that of females for each species.

$$\Delta_{sex} = \frac{d_{wing\,♂}}{d_{wing\,♀}} \quad (14)$$

## Supporting Information

Supporting Information is available from the Wiley Online Library or from the author.

## Acknowledgements

This project was funded by the European Research Council (ERC) under the European Union's Horizon 2020 Research and Innovation Program (Grant Agreement No. 850463).

## Conflict of Interest

The authors declare no conflict of interest.

## Author Contributions

M.B., A.R., J.R., and M.L. conceptualized the idea. M.B., J.H., and M.L. designed the methodology. M.B., A.R., J.R., R.B., and M.L. performed investigation. M.B. and M.L. visualized the idea. M.B. performed funding acquisition. M.B., A.R., and J.R. performed project administration. M.B., A.R., J.R., and R.B. performed supervision. M.L. and M.B. wrote the original draft. M.B., A.R., J.R., J.H., M.L., and R.B. wrote, reviewed, and edited the final manuscript.

## Data Availability Statement

The data that support the findings of this study are available in the supplementary material of this article.

## Keywords

biodiversity, hover fly, hyperspectral, insect wing, wing interference signals (WISs)

Received: July 10, 2023
Revised: September 8, 2023
Published online: October 17, 2023

[1] J. C. Habel, A. Segerer, W. Ulrich, O. Torchyk, W. W. Weisser, T. Schmitt, *Conserv Biol* **2016**, *30*, 754.
[2] J. C. Biesmeijer, S. P. M. Roberts, M. Reemer, R. Ohlemu?Ller, M. Edwards, T. Peeters, A. P. Schaffers, S. G. Potts, R. Kleukers, C. D. Thomas, J. Settele, W. E. Kunin, *Science* **2006**, *313*, 351.
[3] G. D. Powney, C. Carvell, M. Edwards, R. K. A. Morris, H. E. Roy, B. A. Woodcock, N. J. B. Isaac, *Nat. Commun.* **2019**, *10*, 1018.
[4] E. Mathieu-Bégné, G. Loot, M. Chevalier, I. Paz-Vinas, S. Blanchet, *Oikos* **2019**, *128*, 196.
[5] J. E. Losey, M. Vaughan, *Bioscience* **2006**, *56*, 311.
[6] T. D. Schowalter, *Insects and Sustainability of Ecosystem Services*, CRC Press, Boca Raton, FL **2013**.
[7] A.-M. Klein, B. E. Vaissière, J. H. Cane, I. Steffan-Dewenter, S. A. Cunningham, C. Kremen, T. Tscharntke, *Proc. Royal Soc. B: Biol. Sci.* **2007**, *274*, 303.
[8] T. T. Høye, J. Ärje, K. Bjerge, O. L. P. Hansen, A. Iosifidis, F. Leese, H. M. R. Mann, K. Meissner, C. Melvad, J. Raitoharju, *Proc. Natl. Acad. Sci. USA* **2021**, *118*, e2002545117.
[9] K. Rydhmer, J. Prangsma, M. Brydegaard, H. G. Smith, C. Kirkeby, I. Kappel Schmidt, B. Boelt, *Anim. Telem.* **2022**, *10*, 14.
[10] K. Bjerge, M. V. Sepstrup, J. B. Nielsen, F. Helsing, T. T. Hoye, *bioRxiv* **2020**, *03*, 996447.
[11] M. Li, C. Seinsche, S. Jansson, J. Hernandez, J. Rota, E. Warrant, M. Brydegaard, *J. R. Soc., Interface* **2022**, *19*, 20220256.
[12] P. Goldblatt, J. C. Manning, *Ann. Mo. Bot. Gard.* **2000**, *87*, 146.
[13] F. Jauker, V. Wolters, *Oecologia* **2008**, *156*, 819.
[14] M. Solomon, D. Kendall, **1970**, *101*, 101.
[15] F. Sánchez-Bayo, K. A. G. Wyckhuys, *Biol. Conserv.* **2019**, *232*, 8.
[16] M. S. Warren, J. K. Hill, J. A. Thomas, J. Asher, R. Fox, B. Huntley, D. B. Roy, M. G. Telfer, S. Jeffcoate, P. Harding, G. Jeffcoate, S. G. Willis, J. N. Greatorex-Davies, D. Moss, C. D. Thomas, *Nature* **2001**, *414*, 65.
[17] B. M. H. Larson, P. G. Kevan, D. W. Inouye, *Can. Entomol.* **2001**, *133*, 439.
[18] D. Karlsson, E. Hartop, M. Forshage, M. Jaschhof, F. Ronquist, *Biodivers Data J* **2020**, *8*, e47255.
[19] SPRING, Strengthening Pollinator Recovery through INdicators and monitorinG, (accessed: March **2023**).
[20] H. Bartsch, Tvåvingar : blomflugor del 1, Nationalnyckeln, **2009**.
[21] H. Bartsch, Tvåvingar : blomflugor del 2, Nationalnyckeln, **2009**.
[22] C. S. Svenningsen, T. G. Frøslev, J. Bladt, L. B. Pedersen, J. C. Larsen, R. Ejrnæs, C. Fløjgaard, A. J. Hansen, J. Heilmann-Clausen, R. R. Dunn, A. P. Tøttrup, *Biol Lett* **2021**, *17*, 20200833.
[23] R. Meier, W. Wong, A. Srivathsan, M. Foo, *Cladistics* **2016**, *32*, 100.
[24] L. Wührl, C. Pylatiuk, M. Giersch, F. Lapp, T. Von Rintelen, M. Balke, S. Schmidt, P. Cerretti, R. Meier, *Mol. Ecol. Resour.* **2022**, *22*, 1626.
[25] K. Bjerge, J. Alison, M. Dyrmann, C. E. Frigaard, H. M. R. Mann, T. T. Høye, *PLOS Sustainability and Transformation* **2023**, *2*, e0000051.
[26] M. Brydegaard, S. Svanberg, *Laser Photonics Rev.* **2018**, *12*, 1800135.
[27] Y. Li, K. Wang, R. Quintero-Torres, R. Brick, A. V. Sokolov, M. O. Scully, *Opt. Express* **2020**, *28*, 21891.
[28] S. Jansson, E. Malmqvist, Y. Mlacha, R. Ignell, F. Okumu, G. Killeen, C. Kirkeby, M. Brydegaard, *PLoS One* **2021**, *16*, e0247803.
[29] A. P. Genoud, G. M. Williams, B. P. Thomas, *PLoS One* **2021**, *16*, e0260167.
[30] K. Rydhmer, E. Bick, L. Still, A. Strand, R. Luciano, S. Helmreich, B. D. Beck, C. Grønne, L. Malmros, K. Poulsen, F. Elbæk, M. Brydegaard, J. Lemmich, T. Nikolajsen, *Sci. Rep.* **2022**, *12*, 2603.
[31] R. J. Bomphrey, T. Nakata, N. Phillips, S. M. Walker, *Nature* **2017**, *544*, 92.
[32] L. Müller, M. Li, H. Månefjord, J. Salvador, N. Reistad, J. Hernandez, C. Kirkeby, A. Runemark, M. Brydegaard, *Adv. Sci.* **2023**, *10*, 2207110.
[33] M. Li, A. Runemark, N. Guilcher, J. Hernandez, J. Rota, M. Brydegaard, *IEEE J. Sel. Top. Quantum Electron.* **2022**, *29*, 1.
[34] M. Brydegaard, S. Jansson, M. Schulz, A. Runemark, *Ecol Evol* **2018**, *8*, 5369.
[35] D. N. Byrne, S. L. Buchmann, H. G. Spangler, *J Exp Biol* **1988**, *135*, 9.
[36] A. R. S. Parmezan, V. M. A. Souza, I. Zliobaite, G. E. A. P. A. Batista, *Apidologie* **2021**, *52*, 731.
[37] D. M. Unwin, S. A. Corbet, *Physiol Entomol* **1984**, *9*, 115.
[38] M. A. B. Deakin, *J Insect Sci* **2010**, *10*, 96.
[39] M. Li, S. Jansson, A. Runemark, J. Peterson, C. T. Kirkeby, A. M. Jönsson, M. Brydegaard, *J Biophotonics* **2020**, *14*, e202000420.
[40] A. P. Genoud, Y. Gao, G. M. Williams, B. P. Thomas, *J Biophotonics* **2019**, *12*, e201900123.

 

[41] V. Santos, C. Costa-Vera, P. Rivera-Parra, S. Burneo, J. Molina, D. Engalada, J. Salvador, M. Brydegaard, *Opt. Express* **2022**, *77*, 593.
[42] S. Jansson, P. Atkinson, R. Ignell, M. Brydegaard, *IEEE J. Sel. Top. Quantum Electron.* **2018**, *25*, 7201808.
[43] A. Gebru, S. Jansson, R. Ignell, C. Kirkeby, J. C. Prangsma, M. Brydegaard, *J Biophotonics* **2018**, *11*, e201800014.
[44] E. Shevtsova, C. Hansson, D. H. Janzen, J. Kjærandsen, *Proc. Natl. Acad. Sci. USA* **2011**, *108*, 668.
[45] N. Katayama, J. K. Abbott, J. Kjærandsen, Y. Takahashi, E. I. Svensson, *Proc. Natl. Acad. Sci. USA* **2014**, *111*, 15144.
[46] D. G. Stavenga, *Mater Today Proc* **2014**, *1*, 109.
[47] N. J. Butterworth, T. E. White, P. G. Byrne, J. F. Wallman, *J Evol Biol* **2021**, *34*, 558.
[48] H. Yin, L. Shi, J. Sha, Y. Li, Y. Qin, B. Dong, S. Meyer, X. Liu, L. Zhao, J. Zi, *Phys Rev E* **2006**, *74*, 051916.
[49] D. G. Stavenga, H. L. Leertouwer, T. Hariyama, H. A. De Raedt, B. D. Wilts, *PLoS One* **2012**, *7*, e49743.
[50] A. P. Genoud, T. Saha, G. M. Williams, B. P. Thomas, *Appl. Phys. B* **2023**, *129*, 26.
[51] M. Brydegaard, B. Kouakou, S. Jansson, J. Rydell, J. Zoueu, *IEEE J. Sel. Top. Quantum Electron.* **2021**, *27*, 6900711.
[52] M. Brydegaard, *Imaging and Applied Optics*, Optical Society of America, Washington **2014**.
[53] M. Brydegaard, A. Gebru, C. Kirkeby, S. Åkesson, H. Smith, *EPJ Web Conf. EDP Sci.* **2016**, *119*, 22004.
[54] C. Kirkeby, M. Wellenreuther, M. Brydegaard, *Sci. Rep.* **2016**, *6*, 29083.
[55] S. Jansson, PhD Thesis, Lund University, **2020**.
[56] M. J. Tauc, K. M. Fristrup, J. A. Shaw, in Lidar Remote Sensing for Environmental Monitoring 2017 International Society for Optics and Photonics, SPIE, Bellingham, WA **2017**, 104060G.
[57] S. Zhu, E. Malmqvist, W. Li, S. Jansson, Y. Li, Z. Duan, K. Svanberg, H. Feng, Z. Song, G. Zhao, M. Brydegaard, S. Svanberg, *Appl. Phys. B* **2017**, *123*, 211.
[58] M. Brydegaard, S. Jansson, E. Malmqvist, Y. P. Mlacha, A. Gebru, F. Okumu, G. F. Killeen, C. Kirkeby, *Sci. Adv.* **2020**, *6*, eaay5487.
[59] B. K. Kouakou, S. Jansson, M. Brydegaard, J. T. Zoueu, *OSA Continuum* **2020**, *3*, 2362.
[60] J. Klecka, J. Hadrava, P. Biella, A. Akter, *PeerJ* **2018**, *6*, e6025.
[61] A. Lucas, O. Bodger, B. J. Brosi, C. R. Ford, D. W. Forman, C. Greig, M. Hegarty, P. J. Neyland, N. De Vere, *J Anim Ecol* **2018**, *87*, 1008.
[62] G. E. Rotheray, F. Gilbert, *The Natural History of Hoverflies*, Forrest Text, Scotland **2011**.
[63] T. S. Collett, M. F. Land, *J. Comp. Physiol.* **1975**, *99*, 1.
[64] R. Sujeevan, P. Hebert, *Mol. Ecol. Notes* **2007**, *7*, 355.
[65] L. L. Randeberg, E. Catelli, J. Hernandez, *Short-Wavelength Infrared Windows for Biomedical Applications*, SPIE, Bellingham, WA **2021**, Ch. 5.
[66] MeadowlarkOptics, Ultra Broadband Polarizer, https://www.meadowlark.com/ultrabroadband-polarizer/, (accessed: June **2021**).
[67] S. L. Jacques, *Phys Med Biol* **2013**, *58*, R37.

 

# Paper XI

# The deadliest animals with the thinnest wings – near infrared properties of tropical mosquitoes.

Hampus Månefjord[†], Meng Li[†], Julio Hernandez, Lauro Müller, Christian Brackmann, Aboma Merdasa, Carsten Kirkeby, Mengistu Dawit Bulo, Rickard Ignell, Mikkel Brydegaard[*]

[*]Correspondance, E-mail: mikkel.brydegaard@fysik.lth.se

[†]Equal contributors

Lecturer, M. Brydegaard

Dept. of Physics, Lund University, Sölvegatan 14C, 22362 Lund, Sweden

Dept. of Biology, Lund University, Sölvegatan 37, 22362 Lund, Sweden

Norsk Elektro Optikk, Østensjøveien 34, 0667 Oslo, Norway

Ph.D. cand. M. Li, Dr. H. Månefjord, Lauro Müller, Dr. Christian Brackmann

Dept. of Physics, Lund University, Sölvegatan 14C, 22362 Lund, Sweden

Eng. Julio Hernandez

Norsk Elektro Optikk, Østensjøveien 34, 0667 Oslo, Norway

Dr. Aboma Merdasa

Dept. Biology, Dept. Ophthalmology, Lund University, Lund, Sweden

Dr. Carsten Kirkeby

Dept. of Veterinary and Animal Sciences, University of Copenhagen, Copenhagen, Denmark.

Dr. Mengistu Dawit Bulo, Prof. Rickard Ignell

Dept. Plant Protection Biology, Swedish Agricultural University, Alnarp, Sweden.

Keywords: mosquito, biophotonics, thin-film, tissue spectroscopy, ballistic light, small animal imaging, hyperspectral, lidar, remote microscopy

# Abstract

Tropical mosquitoes transmit diseases like malaria, yellow fever, and Zika. Classifying mosquitoes by species, sex, age, and gravidity offers vital insights for assessing transmission risk and effective mitigations. Photonic monitoring for mosquito classification can be used in distributed sensors or lidars on longer ranges. However, a reflectance model and its parameters are lacking in current literature. This study investigates mosquitoes of different species, sexes, age groups, and gravidity states, and reports metric pathlengths of wing chitin, body melanin, and water. We use hyperspectral push-broom imaging and laser multiplexing with a rotation stage to measure near-infrared spectra from different angles and develop simple models for spectral reflectance, including wing thickness and equivalent absorption path lengths for melanin and water. We demonstrate wing thickness of 174 (±1) nm – the thinnest wings reported to our knowledge. Water and melanin pathlengths are determined with ~10 µm precision, and spectral models achieve adjusted $R^2$ values exceeding 95%. While mosquito aspect angle impacts the optical cross-section, it alters shortwave infrared spectra minimally (~2%). These results demonstrate the potential for remote retrieval of micro- and nanoscopic mosquito features using spectral sensors and lidars irrespective of insect body orientation. Improved specificity of vector monitoring can be foreseen.

# 1. Introduction

Mosquitoes are the deadliest animals on our planet due to their role in transmitting vector-borne diseases[1]. Human diseases, such as malaria, dengue, yellow fever, and Zika, as well as livestock diseases, including West Nile fever, bluetongue, and the Schmallenberg virus (transmitted by midges), have significant impacts globally. Many of these diseases affect rural populations in tropical regions with poor housing quality[2,3], leading to reduced life expectancy, higher stillbirth rates, poverty, and hindrance to development[4]. Outbreaks also occur in North America following

the socioeconomic crisis[5, 6], and global warming is expanding the range of vectors and pathogens into northern Europe[7].

Despite continuous public monitoring and reporting of environmental risk factors, such as ozone, $NO_2$, $SO_2$, air quality[8], and birch pollen[9], the monitoring of deadly vectors lags behind[10,11]. Mosquito populations can fluctuate dramatically over seasons [12], and strategically timed elimination can locally eradicate transmission for years[13]. Accurate species identification is crucial for risk assessment, as not all mosquitoes pose a threat to humans. Many species do not blood-feed on humans and only older, previously blood-fed females transmit diseases. Moreover, sub-species can have distinct feeding timings and preferences[14, 15]. For example, the size of *Aedes aegypti* correlates with blood meals from multiple hosts, increasing infection risk[16]. Therefore, effective public monitoring of vector-borne disease risk requires identification of mosquito species, sex, size, and life stage.

Wingbeat frequency (WBF) is a key feature for monitoring mosquitoes in flight. Mosquitoes can be distinguished from other insects by their high WBF, a characteristic partly linked to acoustic sexual attraction for mating in darkness[17]. Various studies have proposed mosquito sensing by WBF, including acoustic sensing via smartphones in bedrooms[18, 19] and optical sensors using transmittance[20] or backscatter[21, 22]. These methods have shown success in classifying a limited set of species and sexes in controlled[20, 21, 22] and semi-wild environments[23]. However, in situ identification by WBF alone is impractical. Males have significantly higher WBFs than females, but WBF can overlap between sexes of co-existing species. Additionally, WBF increases with gravidity[24] and air temperature[25]. Although some species exhibit statistically different WBFs[26], the intra-species variation is about 25% even under constant conditions. This variability limits the differentiation of species based solely on WBF, especially in habitats with multiple mosquito species.

Harmonic overtone analysis of time series signals[27, 28] and spectral analysis of signals from the wings and bodies of insects [29, 30, 31] have been shown to improve species specificity beyond WBFs. However, the physical mechanisms behind these improvements, the origin of harmonic overtones, and the factors governing reflectance from mosquito bodies remain unclear. This study aims to bridge these gaps by providing physical models for optical scattering by wings and bodies from several species of tropical disease vectors, including variations in sex, age, and gravidity. We demonstrate that microscopic and nanoscopic pathlengths of melanin, water, and chitin can be extracted from optical signals. We showcase spectral variations depending on the aspect angles of mosquitoes. Additionally, we provide the first quantitative values for the parameters governing the spectral reflectance of mosquitoes and show that these parameters significantly differ among species, sex, age, and gravidity.

# 2. Optical backscattering signatures of mosquitoes

The study of optical backscattering signatures, specifically through the wavelength and angle-dependent backscatter ($\sigma_{BS}$) and extinction ($\sigma_{Ext}$) cross-sections, offers a powerful method for the optical sensing of mosquitoes. Dedicated optical systems, such as entomological lidars[32], the Electronic Backscatter Optical Scanning System (EBOSS)[33], and various e-trap systems[34, 35], use single-band[36] or multiband[37, 38] illumination and detection to study the interactions of light with mosquitoes. These systems enable detailed analysis of species composition and activity patterns.

The backscatter cross-section ($\sigma_{BS}$) quantifies the amount of light reflected towards the sensor. It depends on the mosquito's projected area $A(\psi, \phi)$, which varies with its orientation (yaw and pitch angles, $\psi$ and $\phi$, relative to the source and detector), and its reflectance ($R(\lambda)$), the wavelength-dependent ratio of reflected incident light. The extinction cross-section ($\sigma_{Ext}$) provides a complementary perspective by measuring the total attenuation of light due to both scattering and absorption as it passes through a mosquito. This attenuation depends on the mosquito's size, shape, and tissue composition (through its projected area, $A(\psi,\phi)$), and its wavelength-dependent optical properties ($\lambda$). The $\sigma_{Ext}$ offers insights into a mosquito's interaction with light beyond direct backscatter, making it valuable in environments where backscatter signals might be weak or difficult to isolate.

To gain even greater insights, both $\sigma_{BS}$ and $\sigma_{Ext}$ can be decomposed into envelope ($\sigma_{body}$) and oscillatory ($\sigma_{wing}$) components[32, 39]. The envelope component reflects the mosquito path through the beam profile and the body size, while the oscillatory components capture the wing dynamics and their bidirectional reflectance distribution function (BRDF). This distinction is key for identifying species-specific characteristics and flight behaviors. To increase measurement precision, techniques, such as sliding min/max windows adjusted to wingbeat frequency (WBF), have been developed[31, 32, 40]. These methods separate the scattering contribution from the wings and body, enabling differentiation of species by wing interference[30, 41] or deducing information from the abdomen, such as gravidity[24], biomass[42], or pathogen content[43].

While a simplified model approximates the mosquito body as a volumetric ellipsoid and the wings as flat ellipses, the intricate microstructures of mosquito anatomy introduce complexities to real-world scatter. Importantly, the scattered light from the elliptical mosquito body exhibits omnidirectional characteristics resembling the Henyey-Greenstein scattering phase function dominated by forward scatter[44]. In contrast, the flat wings scatter light directionally, similar to falling ice flakes[45, 46]. This specular property, in combination with wing dynamics, produces flashes[47] and harmonic overtones, which can differentiate closely related mosquito subspecies[21]. This differentiation is crucial for the development of optical mosquito sensing systems.

**Table 1. Optical Properties and Physical Characteristics of Mosquito Anatomy:** A concise overview highlighting the distinct anatomical features of mosquito bodies and wings, their spatial and temporal properties, and the underlying optical and physical mechanisms.

| Anatomy | Spatial shape [µm] | Temporal [µm] | Frequency [kHz] | Goniometric [°] | Polarimetric [% DoLP] | Spectral [nm] | Physics |
|---|---|---|---|---|---|---|---|
| Body [a)] | Ellipsoid | Envelope | Low-pass convolution | Henyey-Greenstein, Omnidirectional | Partial co-polarized | Absorption by melanin and $H_20$ | Ballistic tissue transport |
| Wings | Two elliptical planes | Waveforms and flashes | Wingbeats harmonics | Specular, Directional | Co-polarized | Interference in chitin | Thin film |

# 2.1 Specular wing scattering provides species contrast due to nano-features

## 2.1.1. Background

The BRDF for clear mosquito wings is close to specular, resulting in flashes when the surface normal of the wings coincides with the light source-detector midpoint. The two wings have four surface normals, which, when convoluted by the wing flatness and illumination and detection aperture, cover a large fraction of the unit sphere, creating a high likelihood of a specular flash for each wingbeat of the mosquito. The dynamical wing orientation can be accurately described by just three harmonics[48, 49]. Consequently, the geometrical cross-section of mosquitoes can also be described by three harmonics.

Mosquito wingbeats have a period of 1-3 ms, during which the observed flashes of backscattered light can contain at least 30 overtones[47]. These flashes are commonly observed and have been previously extracted as signal features[21, 28]. The flashes typically constitute the largest fraction of the total light scattering by insects[39] and can be retrieved over distances of at least a hundred meters by entomological lidars[41, 47]. The flash duration, limited by the wing flatness and numerical aperture of the source and detector, can be as short as 50 µs. The flash is particularly pronounced for wavelengths matching the criterion for resonant back-scattering according to the thin-film interference between reflection from the front and back surface of the chitin wing membrane, see Equation 1.

**Eq.1**

$$\lambda_{Rmax} = \frac{2dn_{chi}}{m - ½}\sqrt{1 - \frac{sin^2\theta}{n_{chi}^2}} \quad , m \in \mathbb{N}$$

here $\lambda_{Rmax}$ are wavelengths with resonant backscatter, $d$ is the thickness of the wing, $n_{chi}$ is the refractive index of chitin, $\theta$ is the light incidence angle, and m is the mode number. For backscattering instruments, such as lidar, $\theta$ is zero and the square root term can be omitted.

Numerous studies of wing interference patterns (WIPs) have indicated great species contrast and sexual dimorphism. Studies include large sample sizes[50, 51, 52, 53, 54, 55, 56] surveyed by simple RGB imagers, which cannot quantitatively determine membrane thickness. Spectral case studies [47, 57] describe the relation to the membrane thickness. Non-imaging studies in flight chambers[21] or with lidar[Error! Bookmark not defined.] indicate that spectral flash properties, and thus effective thickness differ between closely related subspecies[21], which cannot be differentiated without genetics. Hyperspectral imaging of insect wings[30, 58, 59, 60] can provide quantitative thickness maps of wing membranes. It is conceivable that such quantitative hyperspectral images, capturing both wing shape[61], vein structure, melanization, and membrane thickness, provide enough quantitative information to classify each individual to species and even subspecies level.

## 2.1.2. Methods

Mosquito specimens were reared at the Swedish University of Agricultural Sciences (SLU), Alnarp, Sweden[21, 62, 63]. A total of 428 wings from dead male and female mosquitoes from four species: *Anopheles stephensi* (110 wings), *Culex pipiens* Biotype *Molestus* (hereafter *Cx. p. molestus*; 106 wings), *Culex pipiens* biotype *Pipiens* (hereafter *Cx. p. pipiens*; 110 wings), and *Culex quinquefasciatus* (102 wings) were detached and glued on a black edge of neoprene foam using a stereo microscope. The wings were mounted 20 mm above a black neoprene background, see Fig.1a. The mounted wings were brought to Norsk Elektro Optikk's laboratories in Oslo, Norway, for hyperspectral imaging.

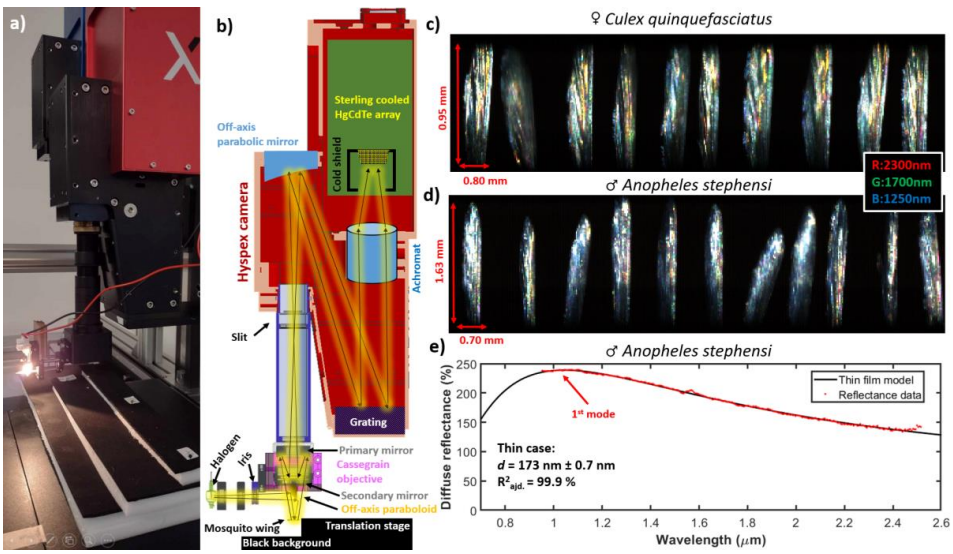


***Figure 1.*** *Hyperspectral imaging of mosquito wings. a) Picture of the setup at Norsk Elektro Optikk, Oslo, Norway. b) Approximate ray diagram for the setup, including the custom-made objective made for the purpose. c,d) False-color short-wave infrared images of mosquito wings.*

*e) An example of fitting the thin film model to measured reflectance data. In this case, the first interference mode is on the edge of the spectral range of the instrument.*

To obtain adequate magnification, a custom microscope objective was 3D printed, see Fig.1b. The setup includes a 10 W halogen-tungsten filament, which is imaged onto the object plane by a 90° off-axis parabolic gold mirror. The backscattered light is collected by a reflective gold objective (Edmund Optics), which images the wings onto the slit of a hyperspectral camera (Hyspex SWIR, Norsk Elektro Optikk). The off-axis paraboloid and reflective objective are in a coaxial configuration. Spatial calibration was done by imaging a ruler. The hyperspectral camera provides 288 bands covering 900-2500 nm. Second-order diffractions are rejected by a coating on the HgCdTe imager.

Hyperspectral images were calibrated to diffuse reflectance by a grey standard. Multiple scans with different focuses were made, and the sharpest wing was cropped out by a custom Matlab script (MathWorks, USA). The area of the wings was extracted from the masks. Each wing image was averaged spatially, and reflectance spectra, $R_{wing}(\lambda)$, were calculated. The measured reflectance spectra were fitted to a thin film model, see Fig.1e and previous thin-film work[30, 41, 59, 64].

**Eq.2**

$$F_{(\lambda,d)} = \frac{4R_{Fresnel}\sin^2\left(\frac{2\pi d n_{chi}}{\lambda}\right)}{(1-R_{Fresnel})^2 + 4R_{Fresnel}\sin^2\left(\frac{2\pi d n_{chi}}{\lambda}\right)} \quad , R_{Fresnel} = \left(\frac{n_{air}-n_{chi}}{n_{air}+n_{chi}}\right)^2 \quad , n_{chi} = 1.517 + \frac{8800nm^2}{\lambda^2}$$

$$\hat{R}_{wing(\lambda)} = \frac{aF(\lambda,d)\lambda^k + b\lambda_0^k}{\lambda_0^k + \lambda^k}$$

Here, the variable $\lambda$ is the wavelength of light that interacts with the mosquito wing, and $d$ is the wing's chitin layer thickness. $R_{Fresnel}$ is the reflectance based on the refractive indexes of air, $n_{air}$, and chitin, $n_{chi}$. $n_{air}$ is almost always considered as 1, and $n_{chi}$ changes with $\lambda$. The coefficients $a$ and $b$ are used to adjust the model. The exponent $k$ influences how reflectance changes with wavelength.

In a previous study, the spatial thickness heterogeneity was evaluated over each wing by letting fringe bias and amplitude depend on a cut wavelength, $\lambda_0$, as short- and long-pass functions, respectively[30]. This is not possible in this study, because we only observe a single fringe period within the spectral range of the short-wave infrared instrument due to thinner wings than previously reported. Consequently, $k$ is set to zero and $\lambda_0$ is indeterminable. To resolve more fringes, future hyperspectral imaging of mosquito wings should be carried out by instruments based on

conventional Si CMOS image sensors in the visible to near-infrared regime. These image sensors also feature better resolution and reduced cost.

### 2.1.3. Results

The wing reflectance model explained 97% [94…99%] (median $R^2_{adj.}$ and IQR respectively) of the measured reflectance yielded wing thickness confidence intervals (CI) of ±1.0 nm or ±0.4% relative precision.

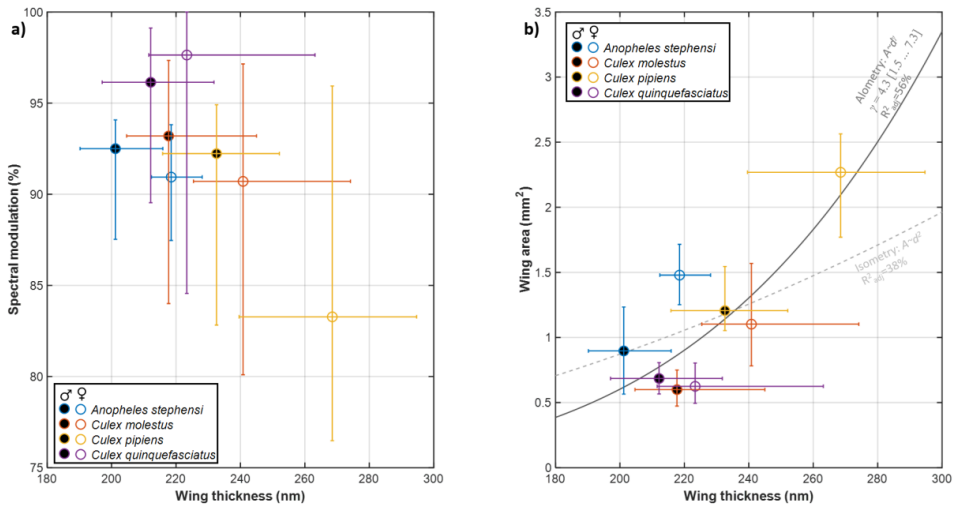


***Figure 2.*** *Measured specular properties of mosquito wings. a) Median overall wing thickness for the investigated species of both males and females. The bars indicate within-species and -sex spread by IQR. The spectral modulation depth, a/(a+b) from Eq.2, is very high, exceeding 90% for most cases. b) Wing membrane thickness correlates weakly with the area.*

The reflectance measurements indicate that the first interference mode for resonant backscattering is captured within the shortwave infrared range. Consequently, the spectral modulation depth is extremely high with most of the specimens exceeding 90%. This implies that photonic sensors[37, 65, 66] and lidars[32, 67, 68], retrieving backscattered wingbeat waveforms from mosquitoes, will be extremely sensitive to the choice of wavelength in relation to the wing thicknesses. This is the case for single-band systems[32], whereas dual-band[38] or hyperspectral systems[41] would have an increased likelihood of capturing flashes and harmonics in one or another band.

The effective wing thickness ranges from ~200 to ~300 nm, see Fig. 1a. To our knowledge, these are the thinnest wings reported in the literature. A thickness of 358 nm was previously reported from a much larger mosquito species[69]. Insect wings are always thinner on the hind edge[30,

[41], thus wings are locally thinner than the effective thicknesses in Fig.2. Chitin polymer chains are spaced by 1 nm, but the hierarchical preferences form nanofibrils of 3 nm and larger nanofibers with 20 nm spacing[70]. Therefore, mosquito wings are quite close to the quantized world of molecular sizes. Quantum entomology, in which wing membranes vary discretely is thus possible.

Specificity: The intraspecies- and intrasexual variations were estimated by interquartile ranges (IQRs) indicated in Fig.2. The spread was as small as ±10 nm or ± 5% for *An. stephensi*. Although many of the groups overlap there are also cases with significant discrepancies in wing thickness between sexes, *e.g.*, *An. stephensi*, and between species, *e.g.*, *An. stephensi* vs. *Cx. p. pipiens*.

Allometry: The wing thickness of the investigated species only correlated with the wing area by 56% across species and sexes, see Fig.2b, and the allometric relation exponent, $\gamma$, is uncertain and isometry cannot be excluded ($\gamma$=2). Previous studies showed that wing thickness and area can deviate significantly from isometry[30, 41, 47, 59].

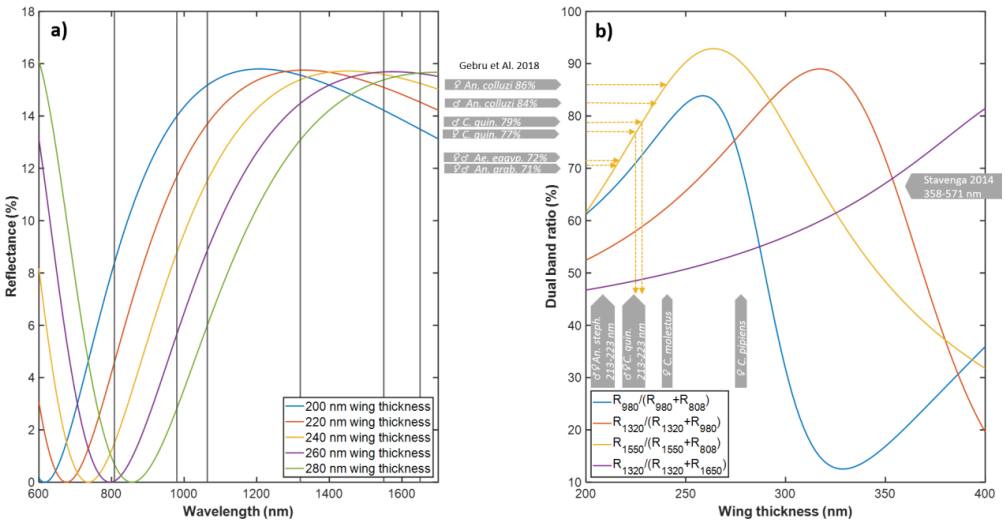


***Figure 3.*** *Effect of observed range of wing thicknesses on specular reflectance responsible for wing beat flashes. a) Modelled reflectance of the thickness spans observed in this study in the near- and short-wave infrared range. The black lines indicate common laser bands previously used in entomological sensing. b) Dual-band ratios modeled between common laser bands. Our current recordings match ratios from a previous study within 10 nm.*

We compared observed mosquito wing membrane thickness ranges against common laser wavelengths, previously used in entomological sensors[22, 31, 71] and lidars[38], see Fig.3. In particular, near-infrared bands (NIR, 808-980 nm) display great sensitivity to the wing membrane thickness.

Several dual-band sensors and lidars have been reported, Fig.3b, to display the dual-band ratio for specular wing beat flashes as a function of membrane thickness. In one case, we can compare this ratio to 10-year-old recordings from our laboratory[21]. At that time, the thicknesses could not be uniquely determined but it was pointed out as a means to distinguish between related species, which are almost impossible to differentiate by microscopy by taxonomists. We can here verify that *Cx. quinquefasciatus* wing membranes are 213-223 nm, with a discrepancy of just 10 nm to the previous study[21]. Additionally, both studies show that female wings are generally thicker than male wings

## 2.2 Quantitative microscopic features retrieved from diffuse body reflectance

### 2.2.1. Background

Light transport in scattering media, such as biological tissue, is governed by absorption- and reduced scattering coefficients, $\mu_a$ and $\mu'_s$, in metric units[72]. Light diffusion[73] and photon migration[74] theories were developed on macro scales of centimeters for biomedical[75] and life science[76] applications. Mosquitoes are over a thousand times smaller than humans, but $\mu_a$ for water and melanin remain constant. Although the highest $\mu'_s$ is reported in insects[77], the scattering mean-free-path is bound by the wavelength of light. Consequently, near-infrared light interaction with mosquitoes is ballistic, similar to x-ray imaging of humans - or optical clearing scenarios[78, 79], where scattering is low compared to the organism sizes[80].

As opposed to diffuse light transport, ballistic interrogation implies that most photons inside mosquitoes keep their initial propagation direction, polarization state, and phase. It also implies that the interrogation pathlength of backscattered light is longer than the pathlength for transmitted or forward-scattered light[44]. Consequently, backscatter can display larger depolarization and equivalent water absorption pathlength than transmitted light. Melanized cuticles are mainly transparent for short-wave infrared light ($\lambda$>1μm), and thus this light interrogates the entire body of mosquitoes. This has multiple applications for detailed mosquito diagnostics[43], for example, classification of species[29] and sexes[21], estimation of age[81], detection of gravidity by depolarization[24], or even detection of pathogens by the tissues-spectral scatter coefficients[82].

### 2.2.2. Method

Several species of mosquitoes, reared at SLU, including *Aedes aegypti*, *Anopheles coluzzii*, *Anopheles gambiae*, and *Culex quinquefasciatus*, were brought alive to a hyperspectral imager at the eye clinic at Lund University hospital. Both sexes, of all species, ranging from 2 to 5 days post-adult emergence, were represented. The specimens were immobilized by rapid chilling and immediately scanned, to avoid changes in the body structure after death and desiccation. Spectral imaging included whole mosquitoes with both body and wings towards a black background. The spectral imager[83] (by Norsk Elektro Optikk) is based on a visible extended InGaAs camera by

down conversion. For our experiment, the visible range (and thus their second-order refractions) was blocked by a RG780 long-pass filter. Hence, the usable spectral range was 382 spectral bands from 900 to 1600 nm. Two ultra-broadband wire grid linear polarizers (Medowlark, USA) were used to capture both co- and de-polarized images. The incidence angle of the light was 45°. The spectral imager was positioned at 0° with a working distance of 80 mm. The spatial resolution was 33 μm/pix. The hyperspectral image cube was white calibrated and flat field calibrated by a Lambertian grey standard, thereby obtaining an image calibrated to diffuse reflectance for both co- and de-polarized light. Each specimen was initially cropped out by hand from the hyperspectral image, and then a mask was automatically applied to exclude background pixels. The area of the mosquito was calculated by the number of pixels in the mask times their physical size in the object plane. The mean reflectance over the mosquito pixels was calculated for both polarizations, $R_{copol}(\lambda)$ and $R_{depol}(\lambda)$, see Fig.4ad. The signal-to-noise ratio (SNR) of the average reflectance of this experimental setup was not great. However, the SNR resembles what can currently be retrieved by hyperspectral lidar[41] of free-flying insects *in situ*. This instrument lacks second-order rejection filters on the imager, thus the long end of the spectrum cannot be used.

Reflectance can be split into two parts[84]: specular reflectance, $R_{spec}$, and diffuse reflectance, $R_{diff}$. Specular reflectance is often thought to be spectrally flat since it is caused by a mismatch in refractive index $(n_1\text{-}n_2)^2/(n_1\text{+}n_2)^2$ since the refractive indices of tissues are simply given by the density[72]. These statements are truths with modifications; biological interfaces are not step-changes from $n_1$ to $n_2$ but can have protruding subwavelength features causing gradient indices[69], also known as anti-reflectance features. For mosquito bodies, these features can comprise nanoscopic hairs or scales[85]. In addition, the refractive index can deviate due to strong absorption bands, as described by the Kramer-Kronig relation. For mosquitoes, the near-infrared absorption is dominated by melanin and water, and their refractive indices do not change noteworthy in the near-infrared range. We estimated the wavelength-independent specular reflectance by the difference of co- and de-polarized reflectance across the spectral range of our instrument:

**Eq.3**

$$R_{spec.} = \left| R_{copol.(\lambda)} - R_{depol.(\lambda)} \right|_{median}$$

There are multiple approaches for modeling light transportation in scattering media, and their usefulness depends entirely on the application. Our aim was to deduce microscopic metric features from the backscattering cross-section or spectral reflectance of free-flying mosquito bodies. The theory for diffuse reflectance that we found adequate for our purpose is the Kubelka-Munck theory[86]. This was developed to estimate the reflectance from slabs or paper and paint in the 1930th Czechoslovakia. Specifically, we adopt Equation #44, which estimates diffuse reflectance by 'thin specimens of poorly scattering material'. Kubelka-Munck state that the scattering- and absorption mean-free-path, and the sample thickness, control the diffuse reflectance and transmittance of a sample, but since reflectance is dimensionless, metric factors must be

relative to each other. Such metric coefficients are possible to quantify and compare between studies.

With knowledge about the spectral dependence of scattering and absorption, we can deduce metric features from reflectance in multiple spectral bands. We introduce the term *scatterance*, $S(\lambda)$, and *absorbance*, $A(\lambda)$. The spectral scatterance can in principle display complicated structures[87], but for the short-wave infrared region a simple power law suffices[76, 88] for biological tissue. Diffuse reflectance, $R_{diff}$, must converge to 100% when $S \rightarrow \infty$ and 0% when $A \rightarrow \infty$. Further, $R_{diff}=0$ when $S=0$. The following equation fulfills this:

**Eq.4**

$$\hat{R}_{body}(\lambda) = R_{spec.} + R_{diff}\,(\lambda) = R_{spec.} + \frac{S}{1+S+A}$$

$$S(\lambda) = \left(\frac{D_{½}}{\lambda}\right)^{\alpha} \quad , \quad A(\lambda) = \ell_{H_20}\mu_{H_20} + \ell_{mel.}\mu_{mel.}$$

$$\hat{R}_{body}(\lambda) = R_{spec.} + \frac{\left(\frac{D_{½}}{\lambda}\right)^{\alpha}}{1 + \left(\frac{D_{½}}{\lambda}\right)^{\alpha} + \ell_{H_20}\mu_{H_20(\lambda)} + \ell_{mel}\mu_{mel(\lambda)}}$$

Here, $D_{½}$ is the wavelength where half of the light is reflected without absorption or transmission. This parameter acts as a gain for diffuse reflectance. $\alpha$, representing the spectral dependence of the scattering, is unitless, and can tilt the spectra, for example as a result of pathogens[82]; $\ell_{H2O}$ and $\ell_{mel}$ are the equivalent absorption pathlengths in water and melanin, respectively; and $\mu_{H2O}(\lambda)$ and $\mu_{mel}(\lambda)$ are the absorption coefficients for pure water[89] and melanin[49]. The coefficients, $D_{½}$, $\alpha$, $\ell_{H2O,}$ and $\ell_{mel}$ were fitted to the measured diffuse reflectance $R_{copol}$-$R_{spec}$ and $R_{depol}$ by a numerical search algorithm (Curvefit toolbox, Matlab, MathWorks, USA).

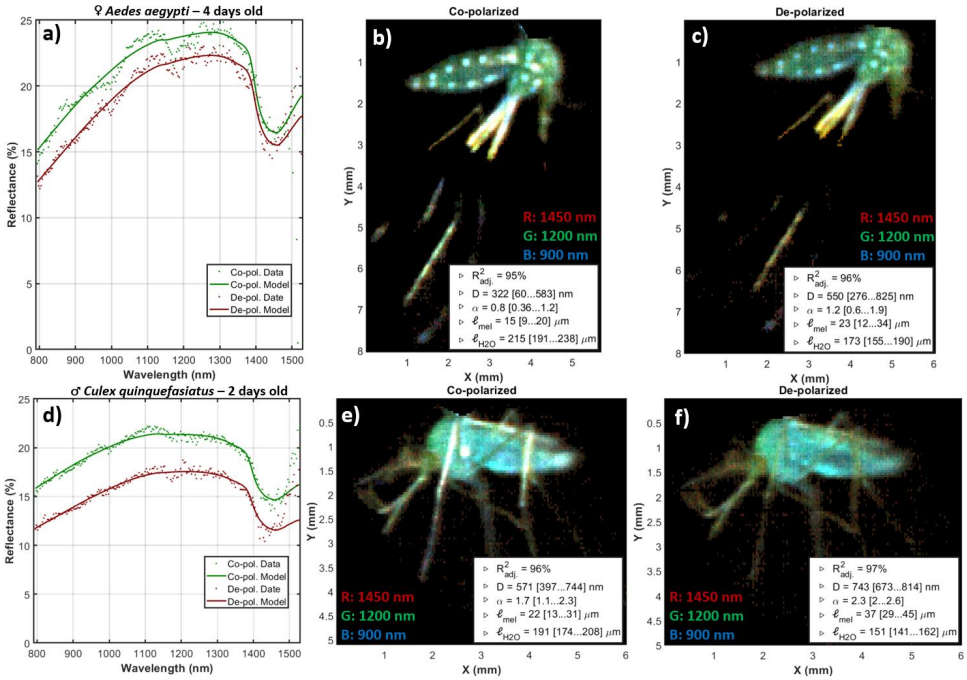


***Figure 4.*** *Hyperspectral short-wave infrared imaging of whole mosquitoes. a,d) Co- and de-polarized reflectance for two mosquitoes. The spectra are offset by a flat specular contribution to the co-polarized image. b,c,e,f) False-color infrared images of the same two mosquitoes. The blue color represents 900 nm, and is diminished by melanin. The green color represents 1200 nm and is insensitive to melanin and water, whereas the red color represents 1450 nm and is diminished by water. The model parameters are indicated with model explanation grade and 95% confidence intervals. Note how the white spots on the* Aedes aegypti *diminish for de-polarized light, also note the absence of leg gloss in the depolarized image of the* Culex quinquefasciatus.

## 2.2.3. Results

The median specular reflectance was 3% (±1% IQR) for the 82 specimens. The model for diffuse reflectance achieved a median explanation grade, $R^2_{adj}$, of 96% (95…97 % IQR). However, the lower confidence bound of all four coefficients, $D_{½}$, $\alpha$, $\ell_{H2O}$, and $\ell_{mel}$, was only distinct from zero in 46 cases of co-polarized reflectances, and 49 cases of de-polarized reflectance. Since the cases with insignificant coefficients showed strong preference for a specific group we chose to include them on the axis of Fig.5 with a note.

The median water pathlength across all samples was 51 μm for co-polarized reflectance and 61 μm for de-polarized reflectances. The confidence was ±12 μm (±20% relative error) for co-polarized reflectance and ±13 μm (±17% relative error) for de-polarized reflectance. The

equivalent water absorption pathlength only covaried slightly (21% $R^2_{adj.}$) with the area, $\ell_{H2O} \sim A^{\gamma}$, in which $\gamma$=1.3 (0.4…1.8 CI).

The median melanin pathlength across all samples was 25 µm for co-polarized reflectance and 32 µm for de-polarized reflectances. The confidence was ±11 µm (±27% relative error) for co-polarized reflectance and ±10 µm (±36% relative error) for de-polarized reflectance. The scattering parameter $D_{½}$ was estimated with confidences of ±90 nm (±27% relative error). The scatterance, $S \sim D_{½}\alpha$, scaled slightly (9% $R^2_{adj}$) with the area, $A$, with $D_{½}\alpha \sim A^{\gamma}$, in which $\gamma$=0.34 (0.23…0.44 CI). This gives a small indication that reflectance is contributed by the volume and depth.

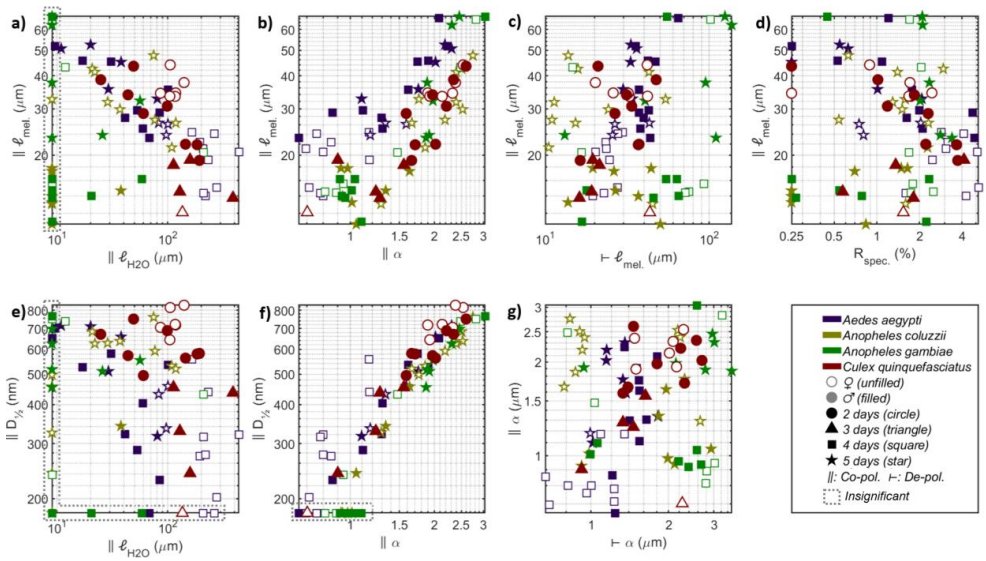


***Figure 5.*** *Mosquito body reflectance parameters among the investigated groups. a) Co-polarized water versus melanin pathlength. Melanin pathlength anticorrelates with water pathlength. Females display stronger absorption than males. b) Melanin pathlength versus spectral tilt, α. Despite a covariance, new groups are differentiated, see for instance male* Aedes aegypti *and female* Anopheles*. c) The melanization can be entirely distinct for co- and de-polarized reflectance, presumably because of the micro-organization of the pigment.* Anopheles coluzzii *and* Anopheles gambiae *occupy opposite corners of this parameter space, even though they are closely related. d) Despite the high refractive index of melanin, the specular reflectance vary independently, since subwavelength structures and gradients have a greater impact. e) The total tissue scatter does not increase with the water pathlength. f) Spectral tilt, α, and total scatter, $D_{½}$, covary but sexes protrude from the diagonal. g) The spectra tilt differently for co- and de-polarized light, with the larger* Aedes aegypti *having the flattest spectra. The two* Anopheles *species display opposite spectral tilt for co- and de-polarized light, which is of interest as these highly related species are not possible to differentiate through microscopy.*

We made a separate analysis of the white spots on *Ae. aegypti* in Fig.4bc. White color is rare in thin objects due to photon escape before multiple scattering[77, 85]. In addition, nanostructures with extreme scatter coefficients in the visible region have reduced scattering toward infrared when the structures are subwavelength. Indeed, the reflectance of the white spots on the *Ae. aegypti* abdomen could be explained by a short-pass function:

**Eq.5**

$$R_{spot(\lambda)} = \frac{1}{1 + \left(\frac{\lambda}{D_{½}}\right)^{\alpha}}$$

where $D_{½}$ is 1215 nm (1204…1226 nm CI) and $\alpha$ is 4.2 (3.9 … 4.5 CI). This confirms that the spots are white in the visible range below 600 nm, but steadily decrease in reflectance for longer wavelengths, supposedly since near-infrared wavelengths fail to resolve scattering nanostructures. It is noteworthy that previous studies[77, 85] could not display such a decrease of reflectance towards infrared wavelengths.

## 2.3 Aspect dependence of mosquito lidar targets

### 2.3.1. Background

Similar to radar cross sections[90], lidar cross sections, $\sigma_{BS}$, also depend on observational aspect angles of pitch and yaw. This poses both a challenge and an opportunity for assessing heading directions. The spherical geometrical cross-section of dried or immobilized insects could be calculated from 3D models of insects from photogrammetry[44, 48, 91, 92]. The wings can be detached from the body for independent measurements[58, 93], since the body and wing scatter contributions can later be separated in the frequency domain for free-flying specimens. By combining kHz wing beat sensing and stereo vision[21, 31], both body- and wing cross sections can be acquired simultaneously as the heading direction. Despite the complicated anatomy of insects, their elongated bodies can be approximated as an ellipsoidal spherical cross-section. Multiple symmetries (left/right, dorsal/ventral) apply to mosquito bodies, and measured cross sections at various aspects can be projected to a low number of polar or spherical harmonics[44, 58]. As it has been proposed that spectral- or polarimetric band ratios could prove more stable for varying observation angles[21, 24], this would be reasonable for the ballistic regime of small insects where the backscatter intensity is scaling with insect volume rather than cross-section.

### 2.3.2. Materials and method

We imaged six groups of mosquitoes, comprising male, as well as female virgin and gravid *An. coluzzii*. In addition, young and old *Cx. quinquefasciatus* females and males were imaged.

A multispectral multi-aspect imaging instrument was used for the analysis[92, 94]. The instrument was upgraded with an InGaAs camera (C-RED3, FirstLight, France), and laser diode multiplexing, to acquire multispectral images in seven shortwave infrared wavelengths spanning

from 1000-1640 nm. The instrument has a rotation stage to rotate targets to various angles, analyzing different aspect angles, see Fig.6. Compared to previously[92], the target stage was flipped upside down for suspended mounting.

The wings were removed from freshly killed mosquitoes, following rapid chilling, and their bodies glued with their legs on pins. The pins were thereafter mounted onto the mounting stage of the instrument, with the mosquitoes hanging from the pins. The mosquito bodies were rotated 360° with 15° steps. For each aspect, a multispectral image was acquired. The images were flat field- and white calibrated by a diffuse grey reference. The precise laser diode emissions deviate from the specifications but were measured by an InGaAs spectrometer (Stellanet).

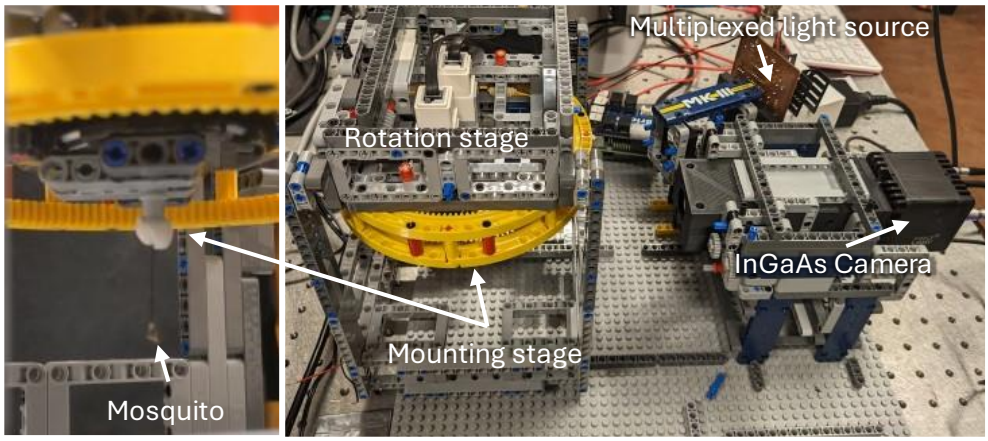


***Figure 6.*** *The instrumentation used for studying aspect angles of mosquito bodies with multispectral short-wave infrared images. An infrared version of the versatile Biophotonic, Imaging, Optical, Spectral, Polarimetric, Angular, and Compact Equipment (BIOSPACE).*

## 2.3.3. Results

The multispectral images reveal different spectral features of the mosquitoes. False-color images were formed by combining images of 1463 nm, 1291 nm, and 1002 nm as red, green, and blue, respectively, see Fig.7. In the images, the bodies show a blue-cyan color, while the eyes appear green, and the limbs appear red.

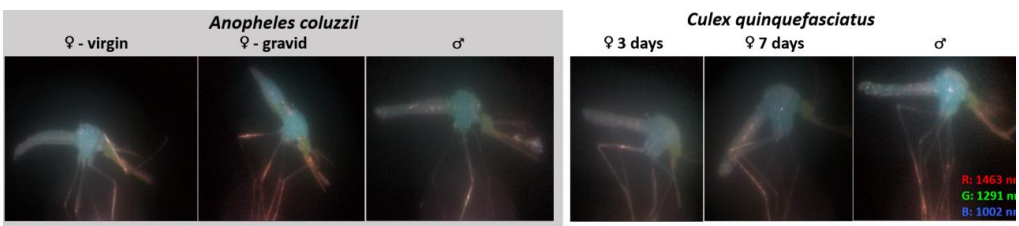

***Figure 7.*** *The six groups of mosquitoes visualized as false color infrared images. Anatomical features display distinct spectral contributions; the body primarily scatter short wavelengths (displayed in blue), since water attenuate the longer bands, the eyes display green tones since both melanin and water decrease eyeshine. Legs and antennae scatter long waved light, and are seen as red.*

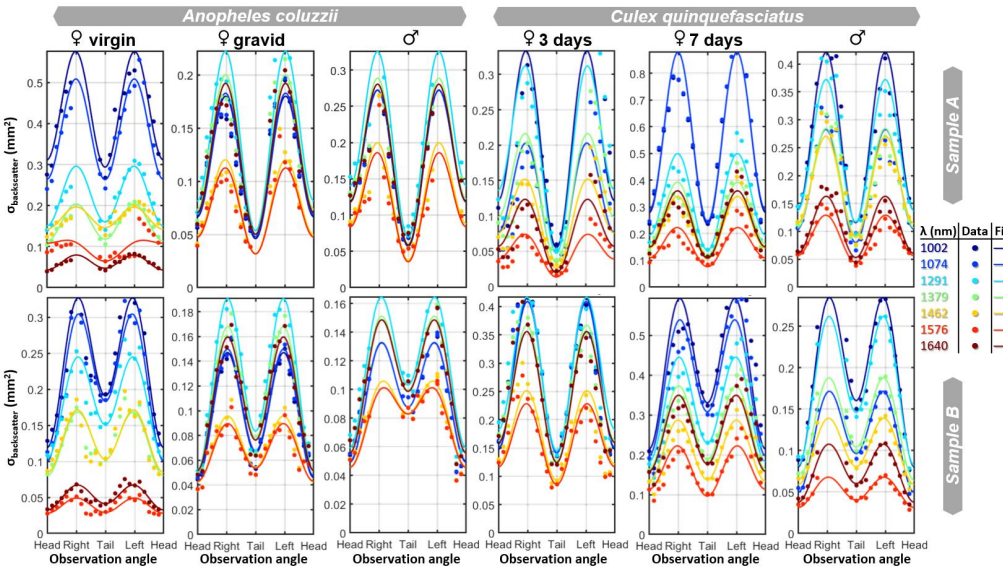


***Figure 8.*** *The measured cross section for two replicas from each of the 6 groups of mosquitoes, as a function of observation angle (yaw) and wavelength. The cross-section can be described by three polar harmonics. The spectral composition displays minimal dependence on the observation angle and replicate, however, spectral differences are pronounced between the groups.*

Aspect angles; The yaw observation angle, $\psi$, foremost affects the cross-section regardless of the spectral band. The relation is adequately described by:

**Eq.6**

$$\hat{\sigma}(\lambda,\psi) = k_0(\lambda) - k_1(\lambda)\cos(\psi) - k_2(\lambda)\cos(2\psi)$$

where $\sigma$ is the backscatter cross-section as a function of wavelength and observation angle, $\psi$, (yaw). The head is in the direction where $\psi$=0. $k_0$ is the average cross-section from all angles; $k_1$ is the reduction of the cross-section in the direction of the head; and $k_2$ is the increase of cross-section from the sagittal plane. Here, *elongation* is given by $k_2/(k_2+k_0)$ and the head/tail asymmetry is given by $k_1/(k_1+k_0)$. These dimensionless parameters are mainly constant across spectral bands, see Fig.9.

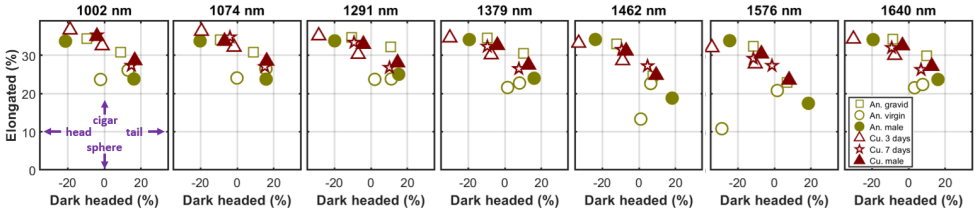


***Figure 9.*** *The elongation ($k_2/(k_2+k_0)$) and the head/tail asymmetry: dark headed ($k_1/(k_1+k_0)$) are shown for the 12 samples in all seven bands. The gravid anophelines display greater elongation than their virgin counterparts. The eye melanization shows surprisingly little reduction of the frontal cross-section, however, we note that* Culex *males and the older* Culex *females show a slightly dark frontal cross-section compared to the younger* Culex *females.*

We analyzed the spectral composition within the aspect scans in Fig.8 by singular value decomposition (SVD). Across the specimens, the trend is that the 1st spectral component explains 91% of the spectra observed from all angles, the 2nd component explains 5% of the variance and the 3rd component explains just 2%. The 2nd and 3rd spectral components could not be associated with melanin or water, rather the specular reflections from the legs and abdomen produce a strong glittering, see animated GIFs in supplementary materials, S1. Mosquitoes have relatively small eyes, and eye melanization could be more pronounced for other more visual vectors, such as horseflies[95]. Differentiation of head and tail could also be more feasible with shorter bands, where melanin absorption is stronger.

# 3. Conclusion

This study presents measured near-infrared optical properties of mosquitoes with metric values and high precision, focusing on species, age, sex, and gravidity states. Our results demonstrate the thinnest (174 nm) insect wing in literature, to our knowledge, with a high precision (~1 nm), as well as water and melanin pathlengths (~10 µm precision). The spectral models derived from these measurements, with adjusted $R^2$ values over 95%, show a contrast between species, age, sex, and gravidity states of the mosquitoes. Moreover, our investigation reveals that, while the aspect angle of mosquitoes significantly influences their optical cross-section, the spectral variations in the shortwave infrared remain minimal (~5%).

The methods have room for improvement; the spatial resolution of the hyperspectral imaging was marginal. We could extract some anatomical features, such as the spots on the yellow fever mosquito but could not provide a wing thickness map as reported in previous studies[30, 58]. A cheaper CMOS hyperspectral camera could be preferable to the infrared setup used in this study.

The CMOS camera could capture more interference fringes in the visible regime compared to the infrared, which struggled to estimate thickness heterogeneity as previously achieved[30].

The experimental VIS extended InGaAs hyperspectral camera only has a limited spectral range and suffers from 2nd diffraction orders. The robustness of numerical fitting and the accuracy of the estimated reflectance parameters would greatly improve if reflectance could be measured on both sides of the 1450 nm water absorption band, and in particular if the 1940 nm water absorption bands could also be covered. The illumination of the fresh mosquitoes was suboptimal and signal-to-noise ratio (SNR) could have been better. On the other hand, the noisy reflectance spectra resemble those retrieved from free-flying insects by hyperspectral lidar[41].

The ability to remotely retrieve micro- and nanoscopic features of mosquitoes using multispectral lidars presents a powerful tool for vector surveillance. By accurately distinguishing mosquito species, age, sex, and gravidity, targeted and efficient control strategies could be developed. This, in turn, could lead to improved management of mosquito-borne diseases, such as malaria, dengue, Zika, and others, directly enhancing global health outcomes. Further research could expand this work with more replicates and a wider range of mosquito species, incorporating additional variables, such as feeding status. Developing robust spectral libraries of mosquito optical properties would facilitate advanced classification algorithms for remote sensing applications. Ultimately, this research has laid a foundation for optical analysis to combat mosquito-borne diseases, which could in extension improve global health.

# Supporting Information

Supplementary information is available from the Wiley Online Library or from the author.

# Conflict of Interest

Authors have no conflict of interest.

# Acknowledgements

This work was supported by the Swedish Research Council, the European Research Council (Grant Agreement No. 850463), and by Norsk Elektro Optikk, Norway. We thank Malin Malmsjö for the work carried out in her laboratory. We thank Trond Løke, Lars Lierstuen, and Fredrike Körting for hosting experiments in Oslo. We are grateful to the staff at SLU Alnarp for providing live-bred tropical mosquito specimens.

# References

[1] I. Statista. (2022, 2024-03-12). *Deadliest Animals Globally by Annual Number of Human Deaths 2022*. Available: https://www.statista.com/statistics/448169/deadliest-creatures-in-the-world-by-number-of-human-deaths/

[2] A. H. M. Chastonay and O. J. Chastonay, "Housing Risk Factors of Four Tropical Neglected Diseases: A Brief Review of the Recent Literature," *Trop Med Infect Dis,* vol. 7, Jul 21 2022.

[3] A. Nigusie, Z. Gizaw, M. Gebrehiwot, and B. Destaw, "Vector-Borne Diseases and Associated Factors in the Rural Communities of Northwest Ethiopia: A Community-Based Cross-Sectional Study," *Environ Health Insights,* vol. 15, p. 11786302211043049, 2021.

[4] A. R. Magalhães, C. T. Codeço, J.-C. Svenning, L. E. Escobar, P. Van de Vuurst, and T. Gonçalves-Souza, "Neglected tropical diseases risk correlates with poverty and early ecosystem destruction," *Infectious Diseases of Poverty,* vol. 12, p. 32, 2023/04/10 2023.

[5] D. R. Thompson, M. de la Torre Juárez, C. M. Barker, J. Holeman, S. Lundeen, S. Mulligan, T. H. Painter, E. Podest, F. C. Seidel, and E. Ustinov, "Airborne imaging spectroscopy to monitor urban mosquito microhabitats," *Remote sensing of environment,* vol. 137, pp. 226-233, 2013.

[6] E. Hernandez, *Environmental and Socioeconomic Factors Associated with Dengue, and the Mosquito Vector Aedes aegypti*: University of California, Merced, 2021.

[7] M. Rudolf, C. Czajka, J. Börstler, C. Melaun, H. Jöst, H. von Thien, M. Badusche, N. Becker, J. Schmidt-Chanasit, A. Krüger, E. Tannich, and S. Becker, "First Nationwide Surveillance of Culex pipiens Complex and Culex torrentium Mosquitoes Demonstrated the Presence of Culex pipiens Biotype pipiens/molestus Hybrids in Germany," *PLOS ONE,* vol. 8, p. e71832, 2013.

[8] L. Han, W. Zhou, W. Li, and L. Li, "Impact of urbanization level on urban air quality: A case of fine particles (PM2. 5) in Chinese cities," *Environmental Pollution,* vol. 194, pp. 163-170, 2014.

[9] M. Berger, K. Bastl, M. Bastl, L. Dirr, H.-P. Hutter, H. Moshammer, and W. Gstöttner, "Impact of air pollution on symptom severity during the birch, grass and ragweed pollen period in Vienna, Austria: Importance of O3 in 2010–2018," *Environmental pollution,* vol. 263, p. 114526, 2020.

[10] A. L. Wilson, O. Courtenay, L. A. Kelly-Hope, T. W. Scott, W. Takken, S. J. Torr, and S. W. Lindsay, "The importance of vector control for the control and elimination of vector-borne diseases," *PLoS neglected tropical diseases,* vol. 14, p. e0007831, 2020.

[11] M. Brydegaard, R. D. Pedales, V. Feng, A. S. D. Yamoa, B. Kouakou, H. Månefjord, L. Wührl, C. Pylatiuk, D. D. S. Amorim, and R. Meier. "Towards global insect biomonitoring with frugal methods." *Philosophical Transactions of the Royal Society B* 379, no. 1904 (2024): 20230103.

[12] A. Dao, A. S. Yaro, M. Diallo, S. Timbine, D. L. Huestis, Y. Kassogue, A. I. Traore, Z. L. Sanogo, D. Samake, and T. Lehmann, "Signatures of aestivation and migration in Sahelian malaria mosquito populations," *Nature,* vol. 516, pp. 387-390, 2014.

[13] A. Björkman, Shakely D, Ali AS, Morris U, Mkali H, Abbas AK, Al-Mafazy AW, Haji KA, Mcha J, Omar R, Cook J. From high to low malaria transmission in Zanzibar—challenges and opportunities to achieve elimination. BMC medicine, 17, pp.1-15, 2019.

[14] S. Boyer, B. Durand, S. Yean, C. Brengues, P.-O. Maquart, D. Fontenille, and V. Chevalier, "Host-feeding preference and diel activity of mosquito vectors of the Japanese encephalitis virus in rural Cambodia," *Pathogens,* vol. 10, p. 376, 2021.

[15] W. Takken and N. O. Verhulst, "Host preferences of blood-feeding mosquitoes," *Annual review of entomology,* vol. 58, pp. 433-453, 2013.

[16] Farjana T, Tuno N. “Multiple blood feeding and host-seeking behavior in Aedes aegypti and Aedes albopictus (Diptera: Culicidae),” *Journal of medical entomology*. 2013 Jul 1;50(4):838-46.

[17] G. Gibson, B. Warren, and I. J. Russell, "Humming in tune: sex and species recognition by mosquitoes on the wing," *J. Assoc. Res. Otolaryngol.,* vol. 11, pp. 527-40, Dec 2010.

[18] H. Mukundarajan, F. J. H. Hol, E. A. Castillo, C. Newby, and M. Prakash, "Using mobile phones as acoustic sensors for high-throughput mosquito surveillance," *elife,* vol. 6, p. e27854, 2017.

[19] M. E. Sinka, D. Zilli, Y. Li, I. Kiskin, D. Kirkham, W. Rafique, L. Wang, H. Chan, B. Gutteridge, and E. Herreros-Moya, "HumBug–An Acoustic Mosquito Monitoring Tool for use on budget smartphones," *Methods in Ecology and Evolution,* vol. 12, pp. 1848-1859, 2021.

[20] I. Potamitis and I. Rigakis, "Measuring the fundamental frequency and the harmonic properties of the wingbeat of a large number of mosquitoes in flight using 2D optoacoustic sensors," *Applied Acoustics,* vol. 109, pp. 54-60, 2016.

[21] A. Gebru, S. Jansson, R. Ignell, C. Kirkeby, J. Prangsma, and M. Brydegaard, "Multiband modulation spectroscopy for determination of sex and species of mosquitoes in flight," *J. Biophotonics,* vol. 11, 2018.

[22] A. P. Genoud, R. Basistyy, G. M. Williams, and B. P. Thomas, "Optical remote sensing for monitoring flying mosquitoes, gender identification and discussion on species identification," *Applied Physics B,* vol. 124, p. 46, February 17 2018.

[23] B. J. Johnson, M. Weber, H. M. Al-Amin, M. Geier, and G. J. Devine, "Automated differentiation of mixed populations of free-flying female mosquitoes under semi-field conditions," *Scientific Reports,* vol. 14, p. 3494, 2024.

[24] A. P. Genoud, Y. Gao, G. M. Williams, and B. P. Thomas, "Identification of gravid mosquitoes from changes in spectral and polarimetric backscatter cross-sections," *Journal of biophotonics,* p. e201900123, 2019.

[25] S. M. Villarreal, O. Winokur, and L. Harrington, "The Impact of Temperature and Body Size on Fundamental Flight Tone Variation in the Mosquito Vector Aedes aegypti (Diptera: Culicidae): Implications for Acoustic Lures," *Journal of Medical Entomology,* vol. 54, pp. 1116-1121, 2017.

[26] D. Kim, T. J. DeBriere, S. Cherukumalli, G. S. White, and N. D. Burkett-Cadena, "Infrared light sensors permit rapid recording of wingbeat frequency and bioacoustic species identification of mosquitoes," *Scientific Reports,* vol. 11, p. 10042, 2021.

[27] A. Moore and R. H. Miller, "Automated identification of optically sensed aphid (*Homoptera: Aphidae*) wingbeat waveforms," *Ann. Entomol. Soc. Am.,* vol. 95, pp. 1-8, 2002.

[28] K. Rydhmer, S. Jansson, L. Still, B. D. Beck, V. Chatzaki, K. Olsen, B. Van Hoff, C. Grønne, J. K. Meier, M. Montoro, I. Kappel Schmidt, C. Kirkeby, H. G. Smith, and M. Brydegaard, "Photonic sensors reflect variation in insect abundance and diversity across habitats," *Ecological Indicators,* vol. 158, p. 111483, 2024.

[29] M. Sikulu, G. F. Killeen, L. E. Hugo, P. A. Ryan, K. M. Dowell, R. A. Wirtz, S. J. Moore, and F. E. Dowell, "Near-infrared spectroscopy as a complementary age grading and species identification tool for African malaria vectors," *Parasit. Vectors,* vol. 3, p. 49, 2010.

[30] M. Li, A. Runemark, J. Hernandez, J. Rota, R. Bygebjerg, and M. Brydegaard, "Discrimination of Hover Fly Species and Sexes by Wing Interference Signals," *Advanced Science,* vol. 10, p. 2304657, 2023.

[31] Y. Li, Z. Han, R. Nessler, Z. Yi, P. Hemmer, R. Brick, A. V. Sokolov, and M. O. Scully, "Optical multiband polarimetric modulation sensing for gender and species identification of flying native solitary pollinators," *Iscience,* vol. 26, 2023.

[32] S. Jansson, E. Malmqvist, Y. Mlacha, R. Ignell, F. Okumu, G. Killeen, C. Kirkeby, and M. Brydegaard, "Real-time dispersal of malaria vectors in rural Africa monitored with lidar," *PLOS ONE,* vol. 16, p. e0247803, 2021.

[33] T. Saha, A. P. Genoud, G. M. Williams, and B. P. Thomas, "Monitoring the abundance of flying insects and atmospheric conditions during a 9-month campaign using an entomological optical sensor," *Scientific reports,* vol. 13, p. 15606, 2023.

[34] I. Potamitis, I. Rigakis, and N.-A. Tatlas, "Automated Surveillance of Fruit Flies," *Sensors,* vol. 17, p. 110, 2017.

[35] I. Potamitis, I. Rigakis, and K. Fysarakis, "The electronic McPhail trap," *Sensors,* vol. 14, pp. 22285-22299, 2014.

[36] M. Brydegaard, S. Jansson, E. Malmqvist, Y. Mlacha, A. Gebru, F. Okumu, G. Killeen, and C. Kirkeby, "Lidar reveals Activity Anomaly of Malaria Vectors during Pan-African Eclipse," *Science Advances,* 2020.

[37] A. Genoud, Y. Gao, G. Williams, and B. Thomas, "Identification of gravid mosquitoes from changes in spectral and polarimetric backscatter cross-sections," *Journal of Biophotonics,* vol. 12, p. e201900123, 06/18 2019.

[38] V. Santos, C. Costa-Vera, P. Rivera-Parra, S. Burneo, J. Molina, D. Encalada, J. Salvador, and M. Brydegaard, "Dual-Band Infrared Scheimpflug Lidar Reveals Insect Activity in a Tropical Cloud Forest," *Applied Spectroscopy,* vol. 77, pp. 593-602, 2023.

[39] M. Brydegaard and S. Svanberg, "Photonic monitoring of atmospheric and aquatic fauna," *Laser & Photonics Reviews,* 2018.

[40] E. Malmqvist, S. Jansson, S. Török, and M. Brydegaard, "Effective parameterization of laser radar observations of atmospheric fauna," *IEEE Journal of Selected Topics in Quantum Electronics,* vol. 22, pp. 327-334, 2015.

[41] L. Müller, M. Li, H. Månefjord, J. Salvador, N. Reistad, J. Hernandez, C. Kirkeby, A. Runemark, and M. Brydegaard, "Remote Nanoscopy with Infrared Elastic Hyperspectral Lidar," *Advanced Science,* vol. 10, p. 2207110, 2023.

[42] A. P. Genoud, T. Saha, G. M. Williams, and B. P. Thomas, "Insect biomass density: measurement of seasonal and daily variations using an entomological optical sensor," *Applied Physics B,* vol. 129, p. 26, 2023.

[43] B. Goh, K. Ching, R. J. Soares Magalhães, S. Ciocchetta, M. D. Edstein, R. Maciel-de-Freitas, and M. T. Sikulu-Lord, "The application of spectroscopy techniques for diagnosis of malaria parasites and arboviruses and surveillance of mosquito vectors: A systematic review and critical appraisal of evidence," *PLoS neglected tropical diseases,* vol. 15, p. e0009218, 2021.

[44] S. Jansson, P. Atkinson, R. Ignell, and M. Brydegaard, "First Polarimetric Investigation of Malaria Mosquitos as Lidar Targets," *IEEE JSTQE Biophotonics,* vol. 25, pp. 1-8, 2018.

[45] M. Vollmer and J. A. Shaw, "Brilliant colours from a white snow cover," *Physics Education,* vol. 48, p. 322, 2013.

[46] M. Goerke, Z. Ulanowski, G. Ritter, E. Hesse, R. Neely, L. Taylor, R. Stillwell, and P. Kaye, "Characterizing ice particles using two-dimensional reflections of a lidar beam," *Applied optics,* vol. 56, pp. G188-G196, 2017.

[47] M. Brydegaard, S. Jansson, M. Schulz, and A. Runemark, "Can the narrow red bands of dragonflies be used to perceive wing interference patterns?," *Ecology and evolution,* vol. 8, pp. 5369-5384, 2018.

[48] R. J. Bomphrey, T. Nakata, N. Phillips, and S. M. Walker, "Smart wing rotation and trailing-edge vortices enable high frequency mosquito flight," *Nature,* vol. 544, p. 92, 03/29/online 2017.

[49] M. Li, C. Seinsche, S. Jansson, J. Hernandez, J. Rota, E. Warrant, and M. Brydegaard, "Potential for identification of wild night-flying moths by remote infrared microscopy " *Royal Society Interface,* vol. 19, p. 20220256, 2022.

[50] E. Shevtsova, C. Hansson, D. H. Janzen, and J. Kjaerandsen, "Stable structural color patterns displayed on transparent insect wings," *PNAS,* vol. 108, pp. 668-73, Jan 11 2011.

[51] N. Katayama, J. K. Abbott, J. Kjærandsen, Y. Takahashi, and E. I. Svensson, "Sexual selection on wing interference patterns in *Drosophila melanogaster*," *PNAS,* vol. 111, pp. 15144-15148, October 21, 2014 2014.

[52] A. Pielowska-Ceranowska and J. Szwedo, "Wing Interference Patterns in patterned wings of Culicoides Latreille, 1809 (Diptera: Ceratopogonidae)—exploring potential identification tool," *Zootaxa,* vol. 4868, pp. 389-407, 2020.

[53] M. Hawkes, E. Duffy, R. Joag, A. Skeats, J. Radwan, N. Wedell, M. Sharma, D. Hosken, and J. Troscianko, "Sexual selection drives the evolution of male wing interference patterns," *Proceedings of the Royal Society B,* vol. 286, p. 20182850, 2019.

[54] N. J. Butterworth, T. E. White, P. G. Byrne, and J. F. Wallman, "Love at first flight: wing interference patterns are species-specific and sexually dimorphic in blowflies (Diptera: Calliphoridae)," *Journal of Evolutionary Biology,* vol. 34, pp. 558-570, 2021.

[55] A. Cannet, C. Simon-Chane, M. Akhoundi, A. Histace, O. Romain, M. Souchaud, P. Jacob, D. Sereno, K. Mouline, and C. Barnabe, "Deep learning and wing interferential patterns identify Anopheles species and discriminate amongst Gambiae complex species," *Scientific Reports,* vol. 13, p. 13895, 2023.

[56] A. Cannet, C. Simon-Chane, M. Akhoundi, A. Histace, O. Romain, M. Souchaud, P. Jacob, P. Delaunay, D. Sereno, and P. Bousses, "Wing interferential patterns (WIPs) and machine learning, a step toward automatized tsetse (Glossina spp.) identification," *Scientific Reports,* vol. 12, p. 20086, 2022.

[57] P. Vukusic and D. G. Stavenga, "Physical methods for investigating structural colours in biological systems," *J. R. Soc. Interface,* vol. 6 Suppl 2, pp. S133-48, Apr 6 2009.

[58] M. Li, S. Jansson, A. Runemark, J. Peterson, C. Kirkeby, A. M. Jönsson, and M. Brydegaard, "Bark beetles as lidar targets and prospects of photonic surveillance," *Journal of Biophotonics,* 2020.

[59] M. Li, A. Runemark, N. Guilcher, J. Hernandez, J. Rota, and M. Brydegaard, "Feasibility of Insect Identification Based on Spectral Fringes Produced by Clear Wings," *IEEE journal of quantum electronics,* vol. 29, pp. 1-8, 2022.

[60] K. H. Takahashi, "Quantitative analysis of wing interference patterns in Drosophila spp. using hyperspectral images," *Physiological Entomology,* vol. 48, pp. 83-89, 2023.

[61] M. K. Salcedo, J. Hoffmann, S. Donoughe, and L. Mahadevan, "Computational analysis of size, shape and structure of insect wings," *Biology open,* vol. 8, 2019.

[62] S. Jansson, P. Atkinson, R. Ignell, and M. Brydegaard, "First polarimetric investigation of malaria mosquitoes as lidar targets," *IEEE Journal of Selected Topics in Quantum Electronics,* vol. 25, pp. 1-8, 2018.
[63] A. Gebru, S. Jansson, R. Ignell, C. Kirkeby, J. Prangsma, and M. Brydegaard, "Remote species and sex determination of disease vector mosquitoes using multispectral polarimetric techniques," *2017 Conference on Lasers and Electro-Optics (CLEO)*, pp. 1-2. IEEE, 2017.

[64] H. Yin, L. Shi, J. Sha, Y. Li, Y. Qin, B. Dong, S. Meyer, X. Liu, L. Zhao, and J. Zi, "Iridescence in the neck feathers of domestic pigeons," *Phys. Rev. E,* vol. 74, p. 051916, 2006.

[65] K. Rydhmer, E. Bick, L. Still, A. Strand, R. Luciano, S. Helmreich, B. D. Beck, C. Grønne, L. Malmros, K. Poulsen, F. Elbæk, M. Brydegaaard, J. Lemmich, and T. Nikolajsen, "Automating insect monitoring using unsupervised near-infrared sensors," *Scientific Reports,* vol. 12, pp. 1-11, 2022.

[66] A. P. Genoud, R. Basistyy, G. M. Williams, and B. P. Thomas, "Optical remote sensing for monitoring flying mosquitoes, gender identification and discussion on species identification," *Applied Physics B,* vol. 124, pp. 1-11, 2018.

[67] B. K. Kouakou, S. Jansson, M. Brydegaard, and J. T. Zoueu, "Entomological Scheimpflug lidar for estimating unique insect classes in-situ field test from Ivory Coast," *OSA Continuum,* vol. 3, 07/22 2020.

[68] M. Brydegaard, S. Jansson, E. Malmqvist, Y. Mlacha, A. Gebru, F. Okumu, G. Killeen, and C. Kirkeby, "Lidar reveals activity anomaly of malaria vectors during pan-African eclipse," *Science Advances,* vol. 6, 05/13 2020.

[69] D. G. Stavenga, "Thin film and multilayer optics cause structural colors of many insects and birds," *Materials Today: Proceedings,* vol. 1, pp. 109-121, 2014/01/01 2014.

[70] S. Nikolov, M. Petrov, L. Lymperakis, M. Friák, C. Sachs, H.-O. Fabritius, D. Raabe, and J. Neugebauer, "Revealing the design principles of high-performance biological composites using ab initio and multiscale simulations: the example of lobster cuticle," *Advanced Materials,* vol. 22, p. 519, 2010.

[71] K. Rydhmer, E. Bick, L. Still, A. Strand, R. Luciano, S. Helmreich, B. D. Beck, C. Grønne, L. Malmros, K. Poulsen, F. Elbæk, M. Brydegaard, J. Lemmich, and T. Nikolajsen, "Automating insect monitoring using unsupervised near-infrared sensors," *Scientific Reports,* vol. 12, pp. 1-11, 2022.

[72] S. L. Jacques, "Optical properties of biological tissues: a review," *Physics in medicine and biology,* vol. 58, p. R37, 2013.

[73] S. L. Jacques and B. W. Pogue, "Tutorial on diffuse light transport," *J. Biomed. Opt.,* vol. 13, p. 041302, 2008.

[74] S. L. Jacques, "Tutorial on Monte Carlo simulation of photon transport in biological tissues," *Biomedical Optics Express,* vol. 14, pp. 559-576, 2023.

[75] S. Fantini and A. Sassaroli, "Near-Infrared Optical Mammography for Breast Cancer Detection with Intrinsic Contrast," *Ann. Biomed. Eng.,* vol. 40, pp. 398-407, Feb 2012.

[76] J. Qin and R. Lu, "Measurement of the optical properties of fruits and vegetables using spatially resolved hyperspectral diffuse reflectance imaging technique," *Postharvest Biol. Tech.,* vol. 49, pp. 355-365, 2008.

[77] M. Burresi, L. Cortese, L. Pattelli, M. Kolle, P. Vukusic, D. S. Wiersma, U. Steiner, and S. Vignolini, "Bright-White Beetle Scales Optimise Multiple Scattering of Light," *Scientific Reports,* vol. 4, p. 6075, 08/15/online 2014.

[78] D. Zhu, K. V. Larin, Q. Luo, and V. V. Tuchin, "Recent progress in tissue optical clearing," *Laser & photonics reviews,* vol. 7, pp. 732-757, 2013.

[79] I. Costantini, R. Cicchi, L. Silvestri, F. Vanzi, and F. S. Pavone, "In-vivo and ex-vivo optical clearing methods for biological tissues," *Biomedical optics express,* vol. 10, pp. 5251-5267, 2019.
[80] M. Bernardello, M. Marsal, E. J. Gualda, and P. Loza-Alvarez, "Light-sheet fluorescence microscopy for the in vivo study of microtubule dynamics in the zebrafish embryo," *Biomedical optics express,* vol. 12, pp. 6237-6254, 2021.

[81] B. Lambert, M. T. Sikulu-Lord, V. S. Mayagaya, G. Devine, F. Dowell, and T. S. Churcher, "Monitoring the age of mosquito populations using near-infrared spectroscopy," *Scientific reports,* vol. 8, p. 5274, 2018.

[82] J. N. Fernandes, L. M. Dos Santos, T. Chouin-Carneiro, M. G. Pavan, G. A. Garcia, M. R. David, J. C. Beier, F. E. Dowell, R. Maciel-de-Freitas, and M. T. Sikulu-Lord, "Rapid, noninvasive detection of Zika virus in Aedes aegypti mosquitoes by near-infrared spectroscopy," *Science advances,* vol. 4, p. eaat0496, 2018.

[83] L. L. Randeberg and J. Hernandez-Palacios, "Hyperspectral imaging of bruises in the SWIR spectral region," in *Photonic Therapeutics and Diagnostics VIII*, San Francisco, CA, USA, 2012, p. 82070N.

[84] S. L. Jacques, "Polarized Light Imaging of Biological Tissues," in *Handbook of biomedical optics*, D. A. Boas, C. Pitris, and N. Ramanujam, Eds., ed Boca Raton, FL, USA: CRC press, 2016, pp. 649-669.

[85] M. Rebora, G. Salerno, S. Piersanti, A. Kovalev, and S. N. Gorb, "The origin of black and white coloration of the Asian tiger mosquito Aedes albopictus (Diptera: Culicidae)," *Beilstein Journal of Nanotechnology,* vol. 14, pp. 496-508, 2023.

[86] P. Kubelka, "New contributions to the optics of intensely light-scattering materials. Part I," *Josa,* vol. 38, pp. 448-457, 1948.

[87] D. Faber, M. Aalders, E. Mik, B. Hooper, M. van Gemert, and T. van Leeuwen, "Oxygen saturation-dependent absorption and scattering of blood," *Phys. Rev. Lett.,* vol. 93, 2004.

[88] T. Svensson, E. Alerstam, D. Khoptyar, J. Johansson, S. Folestad, and S. Andersson-Engels, "Near-infrared photon time-of-flight spectroscopy of turbid materials up to 1400 nm," *Rev. Sci. Instr.,* vol. 80, p. 063105, 2009.

[89] G. M. Hale and M. R. Querry, "Optical Constants of Water in the 200-nm to 200-□m Wavelength Region," *Appl. Opt.,* vol. 12, pp. 555-563, 1973.

[90] J. Riley, "Angular and temporal variations in the radar cross-sections of insects," in *Proceedings of the Institution of Electrical Engineers*, 1973, pp. 1229-1232.

[91] B. Ströbel, S. Schmelzle, N. Blüthgen, and M. Heethoff, "An automated device for the digitization and 3D modelling of insects, combining extended-depth-of-field and all-side multi-view imaging," *ZooKeys,* p. 1, 2018.

[92] H. Månefjord, M. Li, C. Brackmann, N. Reistad, A. Runemark, J. Rota, B. Anderson, J. T. Zoueu, A. Merdasa, and M. Brydegaard, "A biophotonic platform for quantitative analysis in the spatial, spectral, polarimetric, and goniometric domains," *Review of Scientific Instruments,* vol. 93, p. 113709, 2022.

[93] J. A. Shaw, N. L. Seldomridge, D. L. Dunkle, P. W. Nugent, and L. H. Spangler, "Polarization lidar measurements of honey bees in flight for locating land mines," *Opt. Expr.,* vol. 13, pp. 5853-5863, 2005.

[94] H. Månefjord, M. Li, C. Brackmann, N. Reistad, A. Merdasa, and M. Brydegaard. "BIOSPACE–A low-cost platform for problem-based learning in biophotonics." In *11: e Pedagogiska inspirationskonferensen*. 2021.

[95] M. W. Service, "Introduction to the order Diptera — mosquitoes, horseflies, houseflies, tsetse flies etc.," in A Guide to Medical Entomology, Palgrave, London, pp. 20-21, 1980

# Paper XII

ADVANCED SCIENCE
Open Access
www.advancedscience.com

# Remote Nanoscopy with Infrared Elastic Hyperspectral Lidar

*Lauro Müller,* Meng Li, Hampus Månefjord, Jacobo Salvador, Nina Reistad, Julio Hernandez, Carsten Kirkeby, Anna Runemark, and Mikkel Brydegaard*

**Monitoring insects of different species to understand the factors affecting their diversity and decline is a major challenge. Laser remote sensing and spectroscopy offer promising novel solutions to this. Coherent scattering from thin wing membranes also known as wing interference patterns (WIPs) have recently been demonstrated to be species specific. The colors of WIPs arise due to unique fringy spectra, which can be retrieved over long distances. To demonstrate this, a new concept of infrared (950–1650 nm) hyperspectral lidar with 64 spectral bands based on a supercontinuum light source using ray-tracing and 3D printing is developed. A lidar with an unprecedented number of spectral channels, high signal-to-noise ratio, and spatio-temporal resolution enabling detection of free-flying insects and their wingbeats. As proof of principle, coherent scatter from a damselfly wing at 87 m distance without averaging (4 ms recording) is retrieved. The fringed signal properties are used to determine an effective wing membrane thickness of 1412 nm with ±4 nm precision matching laboratory recordings of the same wing. Similar signals from free flying insects (2 ms recording) are later recorded. The accuracy and the method's potential are discussed to discriminate species by capturing coherent features from free-flying insects.**

## 1. Introduction

Insects decline, in both abundance and diversity, at alarming rates.[1–4] This loss of insect poses a major threat to the ecosystem services they provide, including crop pollination.[5] The main reasons have been identified as habitat loss and the use of pesticides.[6] Conventional insect inventorying is accomplished by trapping,[1,7] and the subsequent analysis is both time-consuming and expensive. To speed up this process, innovative approaches are needed for insect surveillance. Machine vision has been applied in field,[8] on traps,[9] and for trap catch analysis.[10] Distributed sensors picking up the wingbeat oscillations from insects are also reported.[11,12] The fact that free-flying insects appear sparsely in time and space,[13] implies that insect monitoring becomes particularly efficient when the probe-volume is elongated over hundreds of meters and trans-illuminated by a laser beam.[14,15] Hereby, an enormous amount of insects can be observed daily using only a couple watts of light as opposed to hyperspectral push broom imaging,[16] where hundreds of Watts illumination is split up between every pixel footprint. Hyperspectral lidar can be implemented with only a few Watts of illumination as the same laser light is recycled from one pixel footprint to the next one until it intercepts an insect or the end of the transect. The wide range of detection distances and the rapid movements of free flying insects, however, cause focus challenges and motion blur in spatial domain imaging. Alternatively, insects can be classified in the frequency domain by their wingbeat frequency and overtone spectra[17,18] which is not subject to optical defocusing. Wingbeats range from 10 to 1000 Hz, but the relative frequency spread within a single species and sex are generally some

L. Müller, M. Li, H. Månefjord, J. Salvador, N. Reistad, M. Brydegaard
Department of Physics
Lund University
Sölvegatan 14c, Lund 22363, Sweden
E-mail: lauro.muller@forbrf.lth.se
N. Reistad
Centre for Environmental and Climate Science
Lund University
Sölvegatan 37, Lund SE-223 62, Sweden

The ORCID identification number(s) for the author(s) of this article can be found under https://doi.org/10.1002/advs.202207110



**DOI: 10.1002/advs.202207110**

J. Hernandez, M. Brydegaard
Norsk Elektro Optikk A/S
Østensjøveien 34, Oslo 0667, Norway
C. Kirkeby
Department of Veterinary and Animal Sciences
Copenhagen University
Frederiksberg 1870, Denmark
C. Kirkeby, M. Brydegaard
FaunaPhotonics
Støberigade 14, Copenhagen 2450, Denmark
A. Runemark, M. Brydegaard
Department of Biology
Lund University
Sölvegatan 35, Lund 22362, Sweden

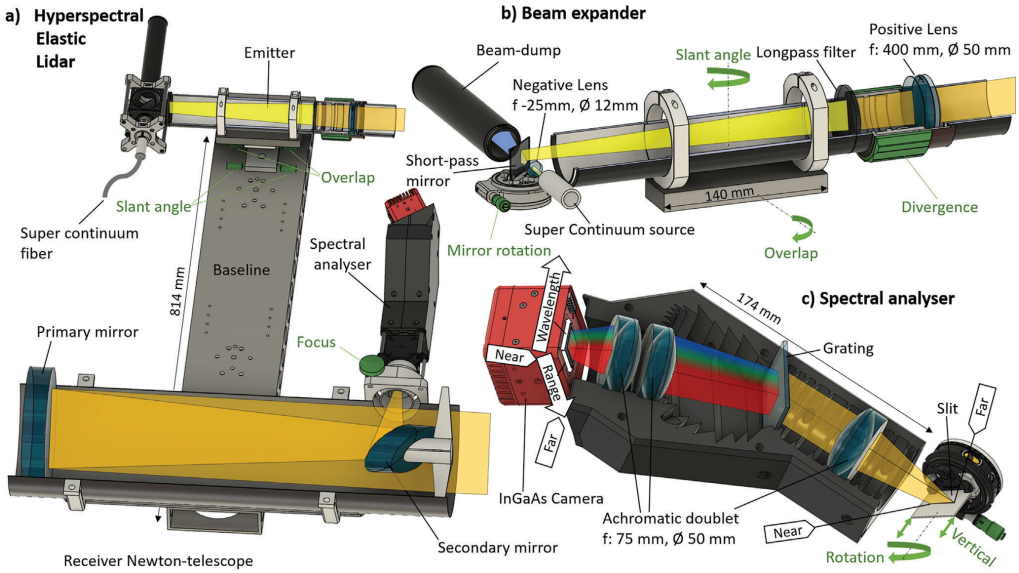


**Figure 1.** Elastic hyperspectral Scheimpflug lidar (EHSL). Color coding; gray: optomechanics, green: degrees of freedom for alignment, yellow: broadband light cones. a) The beam expander and receiver mounted on a Scheimpflug lidar base of 81 cm. b) Light from a supercontinuum source is stripped from visible light, expanded and collimated. c) Retrieved light is dispersed in photon energy perpendicular to the slit. Both the slit and the 2D InGaAs array are tilted according to the Scheimpflug condition and the hinge rule.

20–40% broad[19] and depends on temperature[15] and body mass variations[20,21] (e.g., age, reproductive stage, or pollen payload). In particular, the 100–200 Hz region is crowded with species, and the frequency domain alone is unlikely to be able to differentiate the thousands of species in a single habitat.

Adding spectroscopy to lidar allows retrieval of tiny features over far distances; for example, picometer spacings between electron shells in atoms[22] or molecules.[23] Micrometer features such as snow grain size or eggs inside a mosquito abdomen can be deduced from incoherent scattering by measuring the equivalent water absorption pathlength[24] or depolarization ratio.[20] Insects have either two or four wings, which constitute thin films,[25,26] and depending on the membrane thickness, the wings can exhibit resonant backscatter for specific wavelengths. These wing interference patterns (WIPs) have been proposed to be important for mate choice.[27,28] Such mate choice signals are expected to be highly species-specific.[29] The spectral fringes from wings can be preserved during spatial integration across the wing, producing a fringed spectrum from the whole wing.[30] The two or four wing surface normal visits a large fraction of the hemispheres during each wingbeat, and when a wing surface normal coincides with the source-detector midpoint, a coherent flash appears. This microsecond instance represents one of the rare occasions where the orientation of the insect's wing is known, and an accurate assessment of area, thickness, and reflectance can be done. In a previous study, two closely related mosquito species could be differentiated by such flash chromaticity,[19] although the species were impossible to differentiate by morphology in the microscope. Wing flashes have previously been retrieved remotely by polarization lidar[28] and dual-band lidar.[31] These studies have eluded on the existence of coherent scattering, but until now no remote instrumentation has allowed to capture such flashes, resolve them spectrally and uniquely determine the wing thickness.

In this work, we demonstrate a new elastic hyperspectral Scheimpflug lidar (EHSL) that can simultaneously resolve flashes from insect wings in range, time, and wavelength. The approach is based on continuous wave Scheimpflug lidar[23,32] and its inelastic hyperspectral variety, which was previously developed in fluorescence mode.[33–35]

## 2. Results

### 2.1. EHSL

Based on previous Scheimpflug lidars, we developed a system with sufficient sensitivity, range resolution, spectral range as well as the necessary speed to potentially capture a flash from a free flying insect wing. Here, a baseline bar (**Figure 1**a) separates the beam expander and receiver. In order to vastly increase the number of spectral bands, a broadband supercontinuum light source (stripped from its visible emission) is used, expanded and transmitted to the atmosphere (Figure 1b). In the tilted focal plane of the receiving telescope, backscattered light passes a slit and is dispersed in photon energy by a 3D printed spectral analyzer (Figure 1c). The backscattered and dispersed light is projected on

 

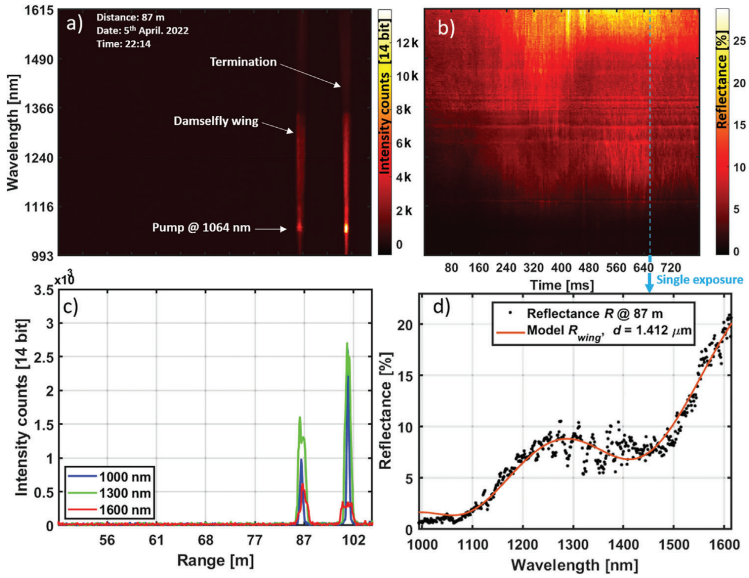


**Figure 2.** Remote Nanoscopy. a) Instantaneous lidar range-wavelength map (light distribution on the 2D InGaAs array), the signal is uncalibrated intensity counts and the Nd:YAG supercontinuum pump laser is seen. b) Calibrated lidar time-wavelength reflectance map at 87 m range made from 200 consecutive exposures. A single, representative, exposure/echo (marked by blue arrow) is selected for further inspection. c) This lidar echo at three selected wavelength bands, the wing displays distinct chromaticity compared to the spectrally flat neoprene termination. d) Retrieved reflectance spectrum from a damselfly wing at 87 m range acquired during 4 ms compared to a thin film model. At this instance and wing orientation, the thickness is estimated to 1412 ± 4 nm (95% confidence interval and 96% $R^2_{adj}$).

a 2D InGaAs camera where 1D represents target distance and the other dimension represent wavelength.

### 2.2. Retrieved Spectral Fringe

To demonstrate the capacity of rapid retrieval and resolving an insect wing and quantifying the thickness, we inserted a forewing of a female damselfly, *Calopteryx virgo*, into the lidar transect at 87 m range (**Figure 2**a). The echo from the beam termination on a black neoprene target is also seen at 100 m range. The data were collected at a pace of 200 Hz and exposure times of 4 ms (Figure 2b). When the wing surface orientation is in specular conditions, high signal magnitude is observed. Such single unfiltered exposure from the lidar is displayed in Figure 2c. The hyperspectral echo from the delicate wing displays a spectral fringe Figure 2d. We could accurately model the remotely retrieved fringe by thin film theory[26] and determine the thickness with an astonishing accuracy of a few nanometers corresponding to less than 1% relative error.

### 2.3. Hyperspectral Imaging

To validate the thickness value and the precision, we analyzed the same wing (**Figure 3**a) in detail in the laboratory by polarimetric hyperspectral imaging[36] (Figure 3b,c). A spectral fringe model[26] was applied to the individual pixels, and the thicknesses were estimated across the wing surface (Figure 3d). The wing contains cells with thin and thick membranes but also an effective fringe for the wing as a whole (Figure 3e). The absence of fringes in the depolarized recordings verifies that the phenomena are coherent, and a high degree of collimation from the backscattered light can be expected. Thus, values exceed 100% compared to a diffuse Lambertian reflectance standard. The encountered thickness across the wing is displayed in Figure 3f. The remotely retrieved fringe was recorded without the knowledge of the orientation of the wing (as would be the case for free-flying insects). Thus, only a specific part of the wing could fulfill the specular reflection criterion in the field experiment. However, the remotely measured thickness of 1.41 μm closely resembles the effective thickness which is 1.69 μm and falls within the thickness encountered across the wing.

### 2.4. Lidar Signals from Free Flying Insects

After the initial test described above, the lidar was deployed again at the same location and the experiment was left unperturbed to capture free flying insects. Numerous hyperspectral lidar observations were captured during an evening. Two representative examples are displayed in **Figure 4**. In the left figures, the

 

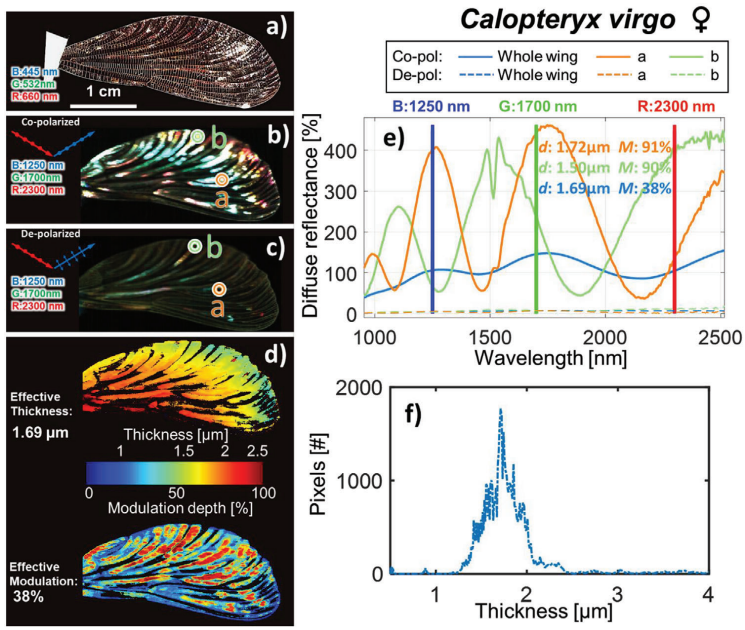


**Figure 3.** Laboratory recordings. a) A damselfly wing appears glossy under a specular illumination; structural colors can be seen on some wing spots. b,c) False color image of the same wing in co- and depolarization (band choices: blue @ 1250 nm, green @ 1700 nm, and red @ 2300 nm) by infrared hyperspectral imaging. d) Map of the wing thickness and modulation depth. e) Examples of fringes of selected orange and green circled wing pixel from the thin and thick region as well as the effective fringe (blue line) from the whole wing. The thickness, *d*, and the modulation depth, *M*, is indicated. The absence of depolarized reflectance indicates that the phenomenon is highly coherent. f) Histogram of thicknesses across the examined wing.

total backscattered intensity is plotted over time. Two instances of specular flashes from the wings were selected for spectral analysis. We also present a negative control in-between the flashes, this signal arises from the insect body and should not display thin-film fringes.

The first example in Figure 4ac was detected after sunset at 85 m distance. Multiple signals of this type were recorded with very low wing beat frequencies in the range 16–22 Hz (indicating a large insect). Further, the waveform in Figure 4a displays narrow spikes and consequently high intensity skewness. This indicates an insect species with clear, glossy wings, and a wing membrane thickness fulfilling resonant backscatter. This wing membrane is very thing and indeed the two consecutive flashes for the first example show a discrepancy of only 13 nm, see Figure 4b. The spectra from the insect body are characterized by melanin absorption toward the shorter wavelengths.

The second selected example in Figure 4c,d, is also nocturnal but a much smaller insect (intensity counts are lower despite closer range). The wingbeat of 150 Hz is marginally resolved in time, it is therefore not possible to deduce exactly how rapid and how intense the flashes are. Even so, spectral fringes could be retrieved, see Figure 4d. Despite the smaller size, the wing is three times thicker than in the previous case, however, the discrepancy is now 430 nm which is considerable. Also, the body contribution shows traces of fringed properties, this points to the fact that neither the peaks nor the valleys in the backscattered waveform were resolved properly in time.

### 2.5. Hyperspectral Lab Inspection of Possible Candidates

We speculated on several insect species- or family candidates which could account for the free flight lidar recordings in Figure 4ab. The candidate is probably a large nocturnal insect species with ultrathin clear wings and wing beats of 16–22 Hz. Crane flies, grasshoppers, and beetles were spotted at the field site during our lidar work. From these groups, three locally common species were selected from the zoological museum. Hyperspectral image analysis was carried out as previously, **Figure 5**. There are ≈60 insect families present at the ecological field station in late summer and much more species. Although, we encountered both crane flies and grasshoppers with similar submicron effective wing thicknesses, none of the selected species matches the recording exactly.

## 3. Discussion

This progress and the EHSL method open up for a new and complementary domain for detecting and classifying free-flying

 

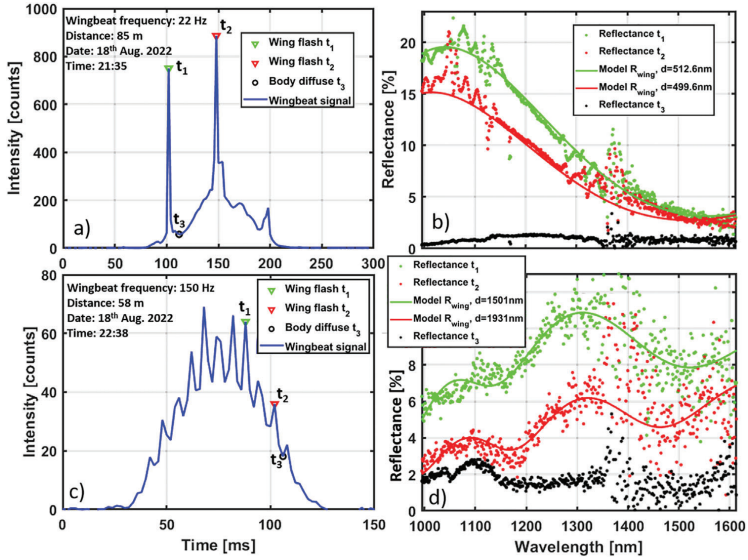


**Figure 4.** Examples of hyperspectral lidar signals from unknown free flying insects. a) Average intensity of all spectral bands versus time from an insect at 85 m range. The spiky and asymmetric waveform indicates clear glossy wings and the low wingbeat frequency is typical for large insects. b) Spectral reflectance from the observation in 4a at the three indicated instances. The fringe model attained $R^2_{adj.}$ of 97% and thickness certainly of ± 2 nm (95% confidence intervals). Similarly, the consecutive flashes display 13 nm discrepancy, the body reflectance between the flashes displays a characteristic attenuation by melanin toward the shorter wavelengths. c) Another and smaller insect observed at 58 m distance where wing beat flashes are barely resolved. d) For the case in (c), the fringe model attained $R^2_{adj.}$ of only 80% and thickness certainty of ±10 nm, but the two fringes display discrepancy of 430 nm, even the body spectrum displays traces of fringed properties.

insects in situ, namely the remote acquisition of wing thicknesses with nanometers precision. We have demonstrated that the method can be deployed in field and capture signals from insects in flight. We have shown the potential in terms of precision and also that the technique could benefit from increased sample rates. Although we could not find a perfect match to our field recordings, lidar signals could in principle be compared to pinned specimens from ecological museums. Until now, lidar techniques for detecting free-flying insects have relied mostly on frequency analysis of wingbeat patterns, which requires multiple wingbeats during the beam transit. The EHSL technique could in principle determine the wing thickness from a single microsecond flash. This could ease constrains on beam width and power allowing to detect smaller insects at further distances, however, with a reduced probe volume. The fact that spectral fringes from insect wings exist, that they can be retrieved over distance and that these fringes are highly copolarized, specular, and coherent—also implies that their backscatter is collimated to some extent. Therefore, the range attenuation of fringed signals is likely to be weaker than the ordinary square factor known from aerosol and molecular lidar.[37] Rather related studies suggest that flat lidar targets can cause back-propagating laser light which is partially collimated.[38] This could imply considerable advantages in signal-to-noise ratio if the sample rate increases (despite less illumination energy per exposure).

The presented recordings were carried out at night as our current supercontinuum source does not allow modulation. However, inelastic hyperspectral lidar has been demonstrated in sunlight[35] (despite the weaker target interaction), thus this elastic method can be expected to work in sunlit conditions if modulation technicalities are overcome. The thin-film effect does generally not apply to the important and large order of *Lepidoptera* (Greek: scale wings) comprising butterflies and moth. However, species in this order can be classified in the shortwave infrared region according to the surface roughness of the microstructures on their wing scales.[36] The same instrument presented here also enables quantification of such scale microstructures and also the equivalent absorption path lengths of melanin[36] and liquid water[39] in the body. Resulting parameters from scale microstructures and equivalent absorption path lengths can also be determined quantitatively and reported in microns for inter-comparability between studies. In fact, the detailed shortwave infrared reflectance of insect bodies can potentially enable differentiating insect species, sexes, age groups, life stage, and infection status.[40–43] Therefore, the described technique has the potential to revolutionize insect surveillance. We foresee that other disciplines of optical remote sensing and environmental monitoring also could benefit from the outlined hyperspectral lidar method. For example, hyperspectral lidar for vegetation canopies[34,44] could improve tree species classification and report on leaf moisture, fertilization, or internal leaf structures.

 

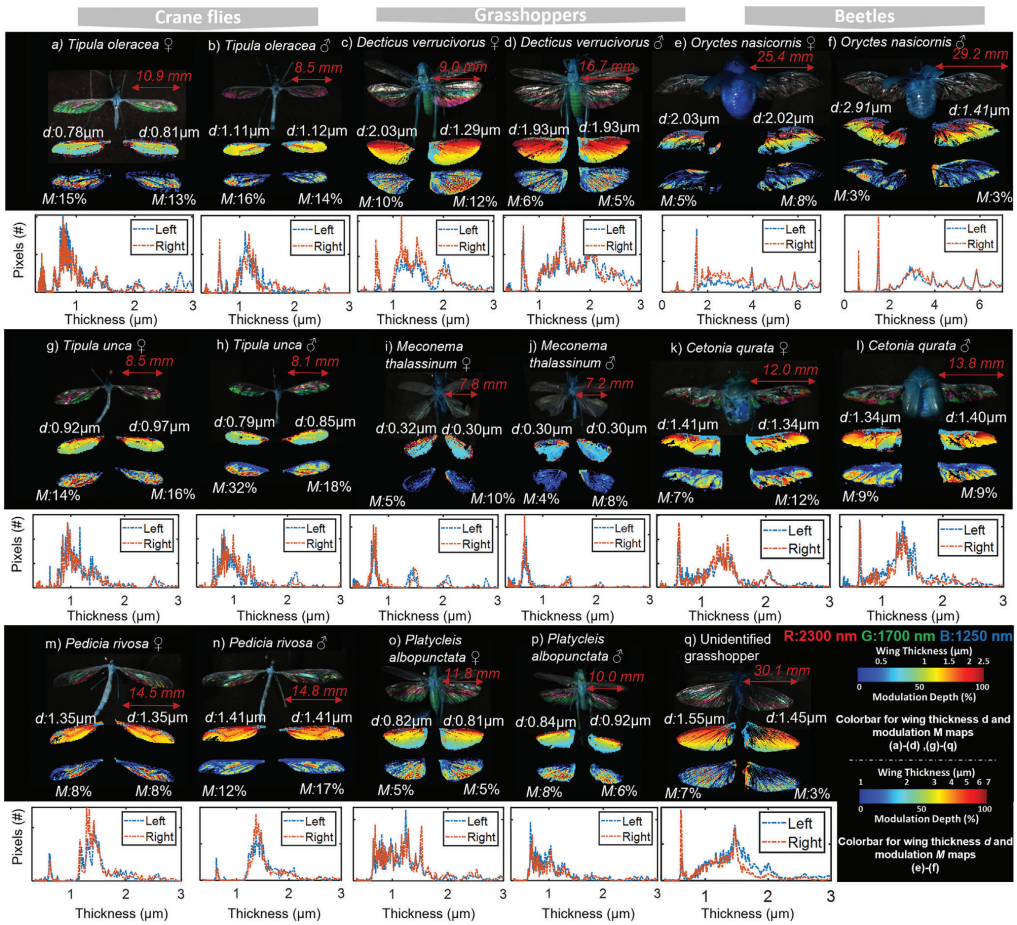


**Figure 5.** Small survey of species groups; crane flies, grasshoppers, and beetles which could possibly account for lidar signals in Figure 4. For each species and sex; top: Short-wave infrared false color images ($R$ = 2300 nm, $G$ = 1700 nm, $B$ = 1250 nm), middle: thickness distributions across left and right wings. The numbers, $d$, indicate the effective wing thicknesses for left- and right wings, bottom: wing maps indicating spectral modulation, $M$ indicates fringe modulation from the entire wings. The thickness distributions for left and right wings are displayed under each specimen. (The narrow spikes in the thickness distributions should be disregarded, since these are from the veins where the algorithm could not identify a fringe).

The method could also be employed in atmospheric sensing of particles[45,46] and gasses such as $CH_4$, $O_2$, $H_2O$,[47] and $CO_2$.[23]

## 4. Experimental Section

*Field Measurements*: An initial field campaign was conducted at Stensoffa field station[48] in southern Sweden (55°41′44″N 13°26′50″E) on the 5th of April 2022 to test the hyperspectral lidar. A map of the experimental site is shown in Figure S1 (Supporting Information). The lidar was mounted on a tripod, pointing at a neoprene termination at 100 m distance. A near infrared silicon monitor camera was used to align and verify the broad infrared beam which is invisible to the human eye. The measurements were conducted during the night to reduce background illumination. The acquisition rate was set to 200 Hz with maximal laser power. During that measurement, a single damselfly wing was held in the beam on a blackened wire at 87 m distance. The surface orientation was varied randomly, while the system was collecting the data.

In 18th August 2022, the same site was returned for the purpose of collecting signals from free flying insects. The lidar transect was identical, but the acquisition rate was set to 500 Hz again with the maximal available power.

*Instrumentation*: The lidar in this work is based on the Scheimpflug method, applying the Scheimpflug and Hinge rules which are described and developed.[49–51] Mathematical derivations of the Scheimpflug principle are found.[52,53] In hyperspectral lidar, the Scheimpflug and

 

Hinge rules are applied twice since not only range but also spectrum has to be determined. This concept was derived from previous studies.[33–35]

The lidar setup is shown in Figure 1 and consist of several elements described below:

Baseline: The receiver telescope and the beam expander are mounted on a baseline with 814 mm separation (Figure 1a). The length of the baseline, together with the angle between beam expander and telescope, and the orientation of the slit, determine the first Scheimpflug and Hinge rule.

Super continuum light source: Supercontiuum light is broadband light that is generated from picosecond pulses from a mode-locked, diode-pumped solid-state laser (DPSS) that propagates through a single mode nonlinear fiber.[54] The source used in this work is a Supercontiuum fiber laser (SC400 Fianium, Nordiske Kabel og Trådfabriker, Denmark) with a spectral range from 400 to 2400 nm. The wavelength of the pump is at 1064 nm, generated by a DPSS Nd:YAG laser with a repetition rate of 80 MHz, a pulse duration of 400 fs and a max pulse energy of 50 nJ. The output collimator of the supercontinuum fiber is connected to the beam expander (Figure 1a,b).

Beam expander: The purpose of the beam expander (Figure 1b) is to expand the beam of the supercontinuum source and strip off the visible part of the spectrum. The beam expander is designed with a Galilean telescope composition where first a negative lens ($f = -25$ mm, Ø = 12 mm, LC1054-B-ML, Thorlabs, USA) is used to expand the beam and afterward collimate it with a positive lens ($f = 400$ mm, Ø = 50 mm, ACT508-400-B-ML, Thorlabs, USA). The visible part is stripped off with a dichroic mirror (SP 650 nm, 25 × 36 mm$^2$ Thorlabs, USA) and a long-pass filter (RG850 Schott, Ø = 50 mm, Edmund Optics, UK), resulting in an emitted spectral range of 850–2400 nm and an average power of ≈3 W. The beam expander is mounted on a tangential stage (Stronghold, Baader Planetarium, Germany) with which the slant- and overlap angles[55] can be adjusted. The supercontinuum light beam is eye-safe for aerofauna but not for humans, the experiment area was restricted for public access.

Receiver: The backscattered light is collected with a $f = 800$ mm, Ø = 200 mm Newton telescope (Quattro, SkyWatcher, China) mounted on the lidar baseline. The collected light is then focused onto the 45° tilted entrance slit of the spectral analyzer which is directly mounted in the focal stage (Figure 1ac). This fulfills the first Scheimpflug condition (Beam-Newton-Slit). Furthermore, the focuser of the Newton telescope can be adjusted to fulfill the hinge rule, see Figure 1a.

Spectral analyzer: The purpose of the spectral analyzer (Figure 1c) is to disperse light from the slit according to photon energy and project it on a 2D detector array, while keeping the range information along the slit intact. The aperture of the slit is 20 mm × 200 µm. A second set of Scheimpflug condition and hinge rule is considered (Slit-Grating-Array). The Scheimpflug condition and the hinge rule is based on simple geometrical optics considerations and assume thin optics with large F/# and no aberrations. The optics is F/4, matching the receiving Newton telescope, therefore it includes 3 lenses with several centimeters path lengths in solid glass. Because of this, the Scheimpflug condition and hinge rule can only be used as a first order approximation for the design. The optical system needs refinement by raytracing (Zemax, Ansys, USA) see Figures S2 and S3 (Supporting Information) and is described in more detail in the section *Raytracing*. This double Scheimpflug design process is also described.[35] The optical elements in the spectral analyzer include 3 identical SWIR achromatic lenses, focal length $f = 75$ mm, diameter Ø = 50 mm (AC508- 075-C, Thorlabs, USA), and a 300 groove mm$^{-1}$ transmission grating (GTI50-03A, Thorlabs, USA). The first achromat, collimates the received light cone, thereafter the grating disperses the light by photon energy. The dispersed light is reimaged onto the camera with the two remaining achromats. The distance between grating and focusing lens is chosen such that the 0th diffraction order can be separated for beam dumping. The axial magnification from slit to camera is 2:1.

The effective magnification of the spectral analyzer unit is 2:1 from slit to 2D detector array. With the raytraced optical system, an opto-mechanical system was designed with CAD (fusion 360, Autodesk, USA) see Figure S4 (Supporting Information). This is discussed in the below section. The opto-mechanical system was 3D-printed in black Polyactic acid (PLA-DF = 02, Dremel, USA) with a commercial 3D-printer (3D45, Dremel, USA).

Camera: The camera utilized in the spectral analyzer (Figure 1c) is a 640 × 512 pixel InGaAs camera (C-RED3, FirstLight, France), with a pixel pitch of 15 × 15 µm and a dynamic range of 14 bit. The spectral range of the sensor is $\Delta\lambda \approx 800$ nm (900–1700 nm), with a max framerate of 600 fps. The output of the camera is a USB 3.1 Gen 1 port.

Data storage: The hyperspectral lidar is recording backscattered light intensity, $I(pix_r, pix_\lambda)$, (14 bit) as a function of range ($1 \leq pix_r \leq 640$ pixels) and photon energy ($1 \leq pix_\lambda \leq 512$ pixels) in single exposures of the 2D-camera detector. The time is recorded by stacking consecutive exposures. The acquisition rate for the free flying insect signals was 90 GB h$^{-1}$, the temporal fill factor was 8% (time gaps between datafiles are caused by real time visualization and saving to hard drives). The hyperspectral images are stored in data cubes where the axes are range, wavelength, and time, respectively. The data are transferred from the camera to a computer by USB 3.1 where an acquisition script (LabView, National Instruments) visualizes the hyperspectral data real time and stores them as raw files with a time stamp.

*Raytracing Design*: Raytracing is a numerical simulation of light rays for optimizing performance and optical systems. Raytracing features a merit function tool that allowed optimizing the system with the goal of achieving the smallest spot size in range-, $\delta r$, and spectral, $\delta\lambda$, domain. The parameters that were adjusted by the merit function are lens separations, position and 2 axis tilt of the detector. A weight function was introduced to optimize the system to perform better in the far range since the pixel footprints increase with range, and thus the impact of a large spot size is greatest at far distances. The result of the optimization can be observed in the spot-diagram in Figures S2a and S3a,b (Supporting Information) where the root-mean-square (RMS, $\delta r$, $\delta\lambda$) is plotted as a function of wavelength for three different range positions. The raytracing predicts a spot size in the spectral domain of ≈40 µm for mid- and far range, whereas the spectral spot size at near range is close to the 100 µm image of the demagnified slit (by which the PSF will be convolved with). Thus, raytracing suggests that spectral resolution is constrained by the slit width. The demagnified image of the slit fits ≈76 times across the chip, consequently 76 independent lidar spectral bands can be expected between 1000 and 1600 nm and accordingly a spectral resolution of 8 nm. In addition, binning several spectral pixels would not deteriorate the spectral resolution. In the range domain (Figure S3a, Supporting Information), spot sizes are ≈80 µm for close range and <30 µm (2 pixels) for far ranges. This gives 0.4% relative range accuracy. In practice, the range inaccuracy also depends on the lidar beam width, and the precision in field indicates 1%, which is somewhat better than previous Scheimpflug lidars.[53]

*CAD-Design*: The opto-mechanical system of the spectral analyzer was designed with CAD (Fusion 360, Autodesk, USA) see Figure S4 (Supporting Information). The unit is based on a 3D-printed sandwich structure[35] combined with cage system elements. Four rods (ERx, Ø = 6 mm, Thorlabs, USA) connect the 3D-printed structure with the cage cube (CW4, 30 mm, Thorlabs, USA) using two cage plate adapters (LCP4S, 30–60 mm, Thorlabs, USA). The tilted slit is mounted on a rotation stage (B4CRP M, Thorlabs, USA) with a filter holder (FFM1, Thorlabs, USA). The angle of the slit can be adjusted with the rotation stage. In addition to the angle, three adjustment screws allow vertical positioning. Furthermore, the spacing between the cage cube with the slit and the 3D-printed part can be adjusted to ensure sharp focus from slit to InGaAs camera. When focus is achieved, the rods can be locked with three lateral screws. The two 3D-printed parts are held together with bolts, combined with threaded brass inserts. This allows disassembling and reassembling the plastic material. The bolts and the rods furthermore act as a reinforcement structure to avoid deformation of the 3D-printed material. The camera is attached to the 3D-printed structure with a milled aluminum camera adapter plate. Baffles are included in the design at different positions along the optical path to reduce stray light. Baffles block forward scattered light (snake light), which becomes more significant at grazing angles. Moreover, horn-like structures[56] were included to absorb the light from diffraction orders other than the first. Light from the 0th, 2nd, and −1st-diffraction order will be trapped in the beam-dumps and

 

eventually absorbed. The spectral analyzer is installed on the focus stage of the receiver telescope with a cylindrical aluminum adapter.

*Spectral Analyzer Alignment and Characterization*: The system is aligned and characterized using a halogen tungsten light bulb as well as a low-pressure spectral Xenon lamp to illuminate the slit of the spectral analyzer. An integrating sphere coated with $BaSO_4$ (Ø = 200 mm, Oriel, USA) was used to uniformly illuminate the entrance slit.[35]

First, the system was aligned using the halogen light bulb as a light source. The spectral analyzer can be focused by adjusting the spacing between 3D-print and cage-cube (see Figure S4, Supporting Information). A transparent plastic foil with a line pattern was placed in the plane of the entrance slit[57,58] and the spacing was adjusted until the black lines were sharpest. Figure S5 (Supporting Information) a) shows the black lines of such line pattern. In Figure S5b (Supporting Information), the intensity is plotted along the range, featuring the line pattern. The line pattern in Figure S5ab, Supporting Information) moreover illustrates the optimization of the far range performance where modulation depth is highest. As in all triangulation approaches to ranging, the observation angle (position along the slit, $pix_r$) relates to distance tangentially. More details on Scheimflug range calibration can be found in literature.[52,53]

Such relation was used and Scheimpflug range calibration for the case of 2D detectors of the hyperspectral variety was expanded. The estimated range becomes

$$\hat{r}\left(p_r, p_\lambda\right) = \ell_{BL}\cot\left(\Phi_{slant} + \theta_{FoV}p_r + \varphi_{shift}p_\lambda + \varphi_{fan}p_\lambda p_r\right) \quad (1)$$

here, $p_r$ and $p_\lambda$ denote the chip normalized pixel positions (values from 0 to 1 across the array detector chip), $\ell_{BL}$ is the length of the baseline (0.814 m), $\Phi_{slant}$ is the angle between the optical axis of the beam expander and receiver, $\theta_{FoV}$ is the field of view (±) of the receiver, whereas $\varphi_{shift}$ and $\varphi_{fan}$ denote undesirable wavelength dependent artifacts. The rulings across the slit in Figure S5a (Supporting Information) is used to select 21 pairs of $p_r$ and $p_\lambda$ across the detector array, and fitted the four coefficients; $\Phi_{slant}$, $\theta_{FoV}$, $\varphi_{shift}$, and $\varphi_{fan}$. Equation (1) explained the pairs with an $R^2_{adj}$: = 99.99%. The coefficients are provided in Figure S5d (Supporting Information) along with the 95% confidence interval. As the table indicates, the artifacts are less than 1% across the chip and not significantly different from zero (indicative that artefacts are absent in the ranging domain). More information regarding keystone and smile artifacts in hyperspectral instruments is provided.[59]

In Figures S6 and S7 (Supporting Information), the halogen tungsten filament lamp was also used as a light source to characterize the spectral sensitivity and flat-field of the system. The light bulb is presumed to be a blackbody radiator at 3000 K. In Figure S6 (Supporting Information), the measured spectrum of the halogen filament is divided by Plank's radiation spectrum of a 3000 K radiation, resulting in the instrument spectral sensitivity curve. The decrease in sensitivity for longer wavelengths is due to the decrease in the efficiency of the diffraction grating. The camera responsivity slightly attenuate shorter wavelengths. Moreover, dips at ≈1200 and ≈1400 nm are present in the sensitivity curve. The dip around 1400 nm is caused by the $BaSO_4$ coating of the integrating sphere which exhibits a dip in reflectance at ≈1400 nm, whereas residual OH ions in the quartz envelope of the halogen bulb account for absorption around both 1200 and 1400 nm. Hence, the dips arose during the calibration and will not limit the performance of the system in field.

In Figure S7a (Supporting Information), the spectral sensitivity is plotted at three different range positions. Figure S7b (Supporting Information) shows a detector exposure with the slit uniformly illuminated. The flat-field plot in Figure S7c (Supporting Information) describes the sensitivity as a function of range. In practice, the lidar sensitivity range dependence, known as the form factor,[60,61] is a complicated matter of overlap between beam and field-of-view as well as the environmental conditions (humidity and atmospheric attenuation coefficients). The lower sensitivity at far and near might be caused by partly shielding, because the illumination cone from the integrating sphere is wider than the F/4 cone from the Newton receiver. Therefore, this effect does not necessarily affect field performance.

In Figure S8 (Supporting Information) a low-pressure spectral Xenon lamp was used to calibrate the system. Figure S8a (Supporting Information) shows a single exposure of the Xenon emission lines recorded with the spectral analyzer. The visibility is enhanced by a high-pass image filter (Matlab, MathWorks, USA). Figure S8c (Supporting Information) displays the Xenon's atomic emission lines as a function of $pix_\lambda$ around $pix_r = 50$. Several lines could be identified and literature values were assigned.[62] The spectral lines display some artifacts but as in Equation (1), the wavelength can be estimated accordingly

$$\hat{\lambda}\left(p_r, p_\lambda\right) = \lambda_0 + \lambda_{span}p_\lambda + \delta_{bend}p_r^2 + \delta_{fan}p_\lambda p_r \quad (2)$$

here $p_r$ and $p_\lambda$ again denote the chip normalized pixel positions, $\lambda_0$ is the shortest spectral band, $\lambda_{span}$ is the spectral range of the instrument and $\delta_{bend}$ and $\delta_{fan}$ are undesired artifacts. The $\delta_{bend}$ and $\delta_{fan}$ parameters describe the spectral misregistration caused by the smile effect.[59] 17 pairs of $p_r$ and $p_\lambda$ were selected across the chip, and the hyperplane was fitted to the table values ($R^2_{adj}$ = 99.99%). The fitted parameters are given in Figure S8d (Supporting Information) along with the confidence intervals. In terms of spectral calibration, the two artifacts constitute 2% and 4% across the whole chip. The linewidth (FWHM) in Figure S8c (Supporting Information) of the spectral line at 1473.3 nm is 8 pixels which corresponds to a spectral resolution of $\Delta\lambda \approx 9.5$ nm. This implies 64 independent effective spectral bands of the system which is much beyond any other elastic lidar system reported.

*Field Calibration of Reflectance*: With the collected backscattered light, $I(pix_r, pix_\lambda)$, the reflectance of the target, $R$, was calculated (Figure 2d) as follows

$$R\left(p_{r\_target}, p_\lambda\right) = R_{term}\frac{\left[\left(I_{target}\left(p_{r\_target}, p_\lambda\right) - I_{dark}\left(p_{r\_target}, p_\lambda\right)\right)\right.}{\left.\hat{r}^2\left(p_{r\_target}, p_\lambda\right)S\left(p_{r\_term}, p_\lambda\right)\right]}$$
$$\frac{\left[\left(I_{term}\left(p_{r\_term}, p_\lambda\right) - I_{dark}\left(p_{r\_term}, p_\lambda\right)\right)\right.}{\left.\hat{r}^2\left(p_{r\_term}, p_\lambda\right)S\left(p_{r\_target}, p_\lambda\right)\eta\right]} \quad (3)$$

here $R$ is the reflectance of a target at pixel position $p_r$ and $p_\lambda$ (associated with the range and photon energy given by Equations (1) and (2). $R_{term}$ is the reflectance of the beam termination, which in the case is a black Neoprene foam sheet with a spectrally flat reflectance of 2%. $I_{target}$ denotes the measured backscattered intensity from a target at $p_{r\_target}$ in a spectral band at $p_\lambda$. $I_{dark}$ is the background intensity. Due to environmental structures and structured dark current, $I_{dark}$ is pixel specific. $I_{dark}$ was measured by manually blocking the beam, this was done several times during the evening since both ambient light and dark current decreases (due to falling temperatures). $I_{term}$ is the backscattered light from the beam termination with known reflectance. $S$ denotes the instrument sensitivity as a function of range and photon energy. This factor could compensate for distinct spectral sensitivities at the target- and termination ranges, but as seen in Figure S7a (Supporting Information), the spectral sensitivity does not change noteworthy. Regarding range dependent sensitivity, the form factor can be expected to be comparable to similar single band systems.[61] In addition, InGaAs sensors can suffer from a structured pixel specific gain pattern which is also included in $S$. For the purpose, it is assumed that $S$ = 1. Omitting the form factor can imply that the absolute reflectance value is inaccurate. However, as it can be understood from the squared range factors in Equation (3), the expression is valid for diffuse targets, whereas a specular target is presented. Studies of specular lidar targets are rare[38] and would require a detailed description of the scattering phase function. The last parameter, $\eta$, denotes the beam-target overlap. This factor can be estimated by the relative reduction of the termination echo when the target is in the beam. In the case $\eta \approx 11\%$. With these arguments, it is understood that the absolute reflectance value cannot be expected to be accurate.

*Hyperspectral Imaging*: A reference hyperspectral measurement[16] of the same damselfly wing was carried out in a laboratory with a polarimetric short-wave infrared (SWIR) camera (HySpex, Norsk Elektro Optikk

 

AS, Norway) with 288 spectral bands (from 0.95 to 2.5 μm). A 150 W broadband halogen lamp was used to illuminate the wing in a specular condition (the illumination and camera axis were at ±56° to wing surface normal), the light was horizontally polarized with an ultra-broadband polarizer (Meadowlark Optics, USA). A second ultra-broadband polarizer was used to select and capture the polarimetric properties of the wing. The camera objective had an aperture of Ø = 25.4 mm and a working distance of 8 cm. The damselfly wing was taped to an index card paper (taped near the axillary area of the wing, see Figure 3a. The wing was then mounted on a black neoprene sheet during the hyperspectral imaging to reduce the background reflection. The captured hyperspectral image of the wing was then calibrated to a diffused reflectance standard with 50% reflectance (Spectralon, LabSphere Inc., USA).

*Fringe Model Hyperspectral Imaging*: A fringe model was developed based on the Fresnel equations and thin-film physics[26] to estimate the wing thickness of captured fringes from both EHSL and hyperspectral imaging

$$F(\lambda, d) = \frac{4R_s \sin^2\left(2\pi d\sqrt{n^2 - \sin^2\theta}/\lambda\right)}{(1-R_s)^2 + 4R_s \sin^2\left(2\pi d\sqrt{n^2 - \sin^2\theta}/\lambda\right)} \tag{4}$$

where $\lambda$ is the wavelength, $d$ is the thickness of the wing, $\theta$ is the incident angle to the membrane (56° for laboratory recordings and 0.25° for EHSL). $R_s$ is the reflection coefficient according to Fresnel equations, and $n$ is the refractive index of the wing membrane

$$R_s = \left(\frac{\cos\theta - \sqrt{n^2 - \sin^2\theta}}{\cos\theta + \sqrt{n^2 - \sin^2\theta}}\right)^2 \tag{5}$$

and the refractive index of the chitin in the wing membrane is expressed as[25]

$$n = A + B/\lambda^2 \tag{6}$$

where $A = 1.517$ and $B = 8800\ \text{nm}^2$.

For the hyperspectral imaging (Figure 2), the fringe model $F(\lambda,d)$ was used to generate multiple (1000x) computed fringes with wing thickness in between range 0.35–4 $\mu$m. The modulation of computed fringes $F(\lambda,d)$ are always 100% since there are no bias terms. To determine the thickness of the captured fringe with the reflectance $R(\lambda)$ from the hyperspectral imaging, each computed fringe $F(\lambda,d)$ was then compared to the captured fringe $R(\lambda)$ based on correlation, $C$ in Equation (7) with a fitting quality parameter, $Q$ in Equation (8)

$$C(R, F(d)) = \frac{\int_{0.35}^{4}\left(F_{\lambda,d} - \mu\left(F_{\lambda,d}\right)\right)\left(R_\lambda - \mu\left(R_\lambda\right)\right)}{\sqrt[2]{\int_{0.35}^{4}\left(F_{\lambda,d} - \mu\left(F_{\lambda,d}\right)\right)^2 \partial\lambda \int_{0.35}^{4}\left(R_\lambda - \mu\left(R_\lambda\right)\right)^2 \partial\lambda}} \tag{7}$$

$$Q(d) = C(R, F)\left(C\left(\frac{\partial R}{\partial\lambda}, \frac{\partial F}{\partial\lambda}\right)\right)^2 \tag{8}$$

where $R$ is the measured reflectance and $F$ is the computed fringe. Here, the spectral derivatives are used to ignore slope differences. The squared power is needed to avoid double negative correlation coefficients. The modulation depth of the captured fringe can be determined by

$$M = \frac{\sigma(R_\lambda)\cdot\mu(F_\lambda)}{\sigma(F_\lambda)\cdot\mu(R_\lambda)} \tag{9}$$

$\sigma$ is the standard deviation, and $\mu$ is the mean of the spectra. As the examples in Figure 3e show, effective fringe amplitudes increase by wavelength because the narrower fringes at shorter wavelengths are more prone to dephase and interfere destructively due to thickness heterogeneities across the wing surface.

**Table 1.** Fitting parameters for thin-film model.

| Parameter | Value | Confidence interval | Unit |
|---|---|---|---|
| $d$ | 1412 | [1408, 1416] | nm |
| $\lambda_0$ | 1419 | [1370, 1469] | nm |
| $\alpha$ | 7.7 | [7.0, 8.4] | |
| $R_{bias}$ | 14 | [12, 15] | % |
| $R_{fringe}$ | 111 | [99, 123] | % |

*Fringe Model Hyperspectral Lidar*: In order to match the increasing amplitude of the hyperspectral lidar measurements, the fringe model $F(\lambda,d)$ with a long pass function is multiplied to obtain a wing reflectance model

$$R_{wing}(d) = \frac{\left(\frac{\lambda}{\lambda_0}\right)^\alpha}{1+\left(\frac{\lambda}{\lambda_0}\right)^\alpha}\cdot\left(R_{bias} + R_{fringe}\cdot F(\lambda, d)\right) \tag{10}$$

here $\lambda_0$ is the cut-on wavelength for the long pass function and $\alpha$ is the long pass steepness. Since thickness heterogeneities across the wing damp the effective wing fringe toward shorter wavelengths, $\lambda_0$ is expected to scale with this heterogeneity. Other phenomena, such as gradient refractive coatings in damselflies could also contribute to this effect.[25] $R_{bias}$ is a scalar indicating a nonfringy bias of the spectrum. $R_{fringe}$ is a scalar indicating the amplitude of the effective fringe.

The parameters; $\lambda_0$, $\alpha$, $R_{bias}$, $R_{fringe}$, and $d$ were fitted to the measured and calibrated reflectance from the damselfly wing target, $R$, from Equation (3). The fit was done using a numerical search algorithm (Curve Fitting Toolbox, Matlab, MathWorks, USA), and ended at $R^2_{adj}$ 96% with the following values (**Table 1**).

## Supporting Information

Supporting Information is available from the Wiley Online Library or from the author.

## Acknowledgements

This project has received funding from the European Research Council (ERC) under the European Union's Horizon 2020 research and innovation program (Grant Agreement No. 850463 Bug-Flash). The authors thank Norsk Elektro Optikk A/S, for the continuous support and support measurements. They also thank Lund Laser Centre for access to the super continuum light source, Jadranka Rota for input and assistance with the entomological collections at Lund's zoological museum, and Paul Travers for assistance. The authors are grateful to Rachel Muheim and the Department of Biology in Lund for hosting the experiments at the Stensoffa ecological field station.

## Conflict of Interest

The authors declare no conflict of interest.

## Author Contributions

M.B. and N.R. acquired grants for salaries and materials, L.M., M.L., A.R., and M.B., conceived and designed study, A.R. selected species, M.L. prepared specimen, L.M., H.M., J.S., and M.B. designed, and built the lidar,

 

L.M., M.L., H.M., J.S., N.R., C.K., A.R., and M.B. participated in field work, M.L., J.H., M.B. contributed hyperspectral laboratory recordings, L.M., M.L., and M.B. analysis code, L.M. produced all graphics with M.B. supervision. L.M., M.L., and M.B. drafted the manuscript, all authors contributed to the manuscript.

## Data Availability Statement

The data that support the findings of this study are available from the corresponding author upon reasonable request.

## Keywords

biophotonics, hyperspectral imaging, infrared spectroscopy, lidar, supercontiuum, thin film physics, insects

Received: December 2, 2022
Revised: February 17, 2023
Published online: March 25, 2023

[1] C. A. Hallmann, M. Sorg, E. Jongejans, H. Siepel, N. Hofland, H. Schwan, W. Stenmans, A. Müller, H. Sumser, T. Hörren, D. Goulson, H. De Kroon, *PLoS One* **2017**, *12*, e0185809.
[2] S. Seibold, M. M. Gossner, N. K. Simons, N. Blüthgen, J. Müller, D. Ambarlı, C. Ammer, J. Bauhus, M. Fischer, J. C. Habel, K. E. Linsenmair, T. Nauss, C. Penone, D. Prati, P. Schall, E.- D. Schulze, J. Vogt, S. Wöllauer, W. W. Weisser, *Nature* **2019**, *574*, 671.
[3] R. Van Klink, D. E. Bowler, K. B. Gongalsky, A. B. Swenge, A. Gentile, J. M. Chase, *Science* **2020**, *368*, 417.
[4] D. L. Wagner, E. M. Grames, M. L. Forister, M. R. Berenbaum, D. Stopak, *Proc. Natl. Acad. Sci. USA* **2021**, *118*, e2023989118.
[5] J. Ollerton, R. Winfree, S. Tarrant, *Oikos* **2011**, *120*, 321.
[6] F. Sánchez-Bayo, K. A. G. Wyckhuys, *Biol. Conserve.* **2019**, *232*, 8.
[7] C. S. Svenningsen, T. G. Frøslev, J. Bladt, L. B. Pedersen, J. C. Larsen, R. Ejrnæs, C. Fløjgaard, A. J. Hansen, J. Heilmann-Clausen, R. R. Dunn, A. P. Tøttrup, *Biol. Lett.* **2021**, *17*, 20200833.
[8] S. Butail, N. Manoukis, M. Diallo, J. M. Ribeiro, T. Lehmann, D. A. Paley, *J. R. Soc., Interface* **2012**, *9*, 2624.
[9] T. T. Høye, J. Ärje, K. Bjerge, O. L. P. Hansen, A. Iosifidis, F. Leese, H. M. R. Mann, K. Meissner, C. Melvad, J. Raitoharju, *Proc. Natl. Acad. Sci. USA* **2021**, *118*, e2002545117.
[10] L. Wührl, C. Pylatiuk, M. Giersch, F. Lapp, T. Von Rintelen, M. Balke, S. Schmidt, P. Cerretti, R. Meier, *Mol. Ecol. Resour.* **2022**, *22*, 1626.
[11] M. E. Sinka, D. Zilli, Y. Li, I. Kiskin, D. Msaky, J. Kihonda, G. Mkandawile, E. Kaindoa, G. Killeen, J. Zanga, E. Metelo, D. Kirkham, P. Mansiangi, E. Herreros-Moya, W. Rafique, T. Chareonviriyaphap, R. Tisgratog, L. Wang, H. Chan, B. Gutteridge, H. Portwood, S. Roberts, K. J. Willis, *Methods Ecol. Evol.* **2021**, *12*, 1848.
[12] K. Rydhmer, E. Bick, L. Still, A. Strand, R. Luciano, S. Helmreich, B. D. Beck, C. Grønne, L. Malmros, K. Poulsen, F. Elbæk, M. Brydegaard, J. Lemmich, T. Nikolajsen, *Sci. Rep.* **2022**, *12*, 2603.
[13] M. Brydegaard, S. Svanberg, *Laser Photonics Rev.* **2018**, *12*, 1800135.
[14] S. Jansson, E. Malmqvist, Y. Mlacha, R. Ignell, F. Okumu, G. Killeen, C. Kirkeby, M. Brydegaard, *PLoS One* **2020**, *14*, e0247803.
[15] A. P. Genoud, G. M. Williams, B. P. Thomas, *PLoS One* **2021**, *16*, e0260167.
[16] L. L. Randeberg, J. Hernandez-Palacios, *Proc. SPIE* **2012**, *8207*, 129.
[17] M. Brydegaard, S. Jansson, E. Malmqvist, Y. P. Mlacha, A. Gebru, F. Okumu, G. F. Killeen, C. Kirkeby, *Sci. Adv.* **2020**, *6*, eaay5487.
[18] B. K. Kouakou, S. Jansson, M. Brydegaard, J. T. Zoueu, *OSA Continuum* **2020**, *3*, 2362.
[19] A. Gebru, S. Jansson, R. Ignell, C. Kirkeby, J. C. Prangsma, M. Brydegaard, *J. Biophotonics* **2018**, *11*, 201800014.
[20] A. P. Genoud, Y. Gao, G. M. Williams, B. P. Thomas, *J. Biophotonics* **2019**, *12*, 201900123.
[21] K. Rydhmer, J. Prangsma, M. Brydegaard, H. G. Smith, C. Kirkeby, I. Kappel Schmidt, B. Boelt, *Anim. Biotelemetry* **2022**, *10*, 14.
[22] G. Zhao, W. Zhang, Z. Duan, M. Lian, N. Hou, Y. Li, S. Zhu, S. Svanberg, *Sci. Rep.* **2020**, *10*, 10414.
[23] J. Larsson, J. Bood, C. T. Xu, X. Yang, R. Lindberg, F. Laurell, M. Brydegaard, *Opt. Express* **2019**, *27*, 17348,.
[24] A. W. Nolin, J. Dozier, *Remote Sensing Environ.* **2000**, *74*, 207.
[25] D. G. Stavenga, *Mater. Today Proc.* **2014**, *1*, 109.
[26] H. Yin, L. Shi, J. Sha, Y. Li, Y. Qin, B. Dong, S. Meyer, X. Liu, L.i Zhao, J. Zi, *Phys. Rev. E* **2006**, *74*, 051916.
[27] N. Katayama, J. K. Abbott, J. Kjærandsen, Y. Takahashi, E. I. Svensson, *Proc. Natl. Acad. Sci. USA* **2014**, *111*, 15144.
[28] M. Brydegaard, S. Jansson, M. Schulz, A. Runemark, *BMC Ecol. Evol.* **2018**, *8*, 5369.
[29] N. J. Butterworth, T. E. White, P. G. Byrne, J. F. Wallman, *J. Evol. Biol.* **2020**, *34*, 558.
[30] M. Li, S. Jansson, A. Runemark, J. Peterson, C. T. Kirkeby, A. M. Jönsson, M. Brydegaard, *J Biophotonics* **2020**, *14*, e202000420.
[31] M. Brydegaard, S. Jansson, *J. Eng.* **2019**, *2019*, 7542.
[32] G. Zhao, M. Ljungholm, E. Malmqvist, G. Bianco, L.-A. Hansson, S. Svanberg, M. Brydegaard, *Proc. SPIE* **2017**, *10406*, 104.
[33] G. Zhao, J. Li, S. He, *Laser Photonics Rev.* **2016**, *10*, 807.
[34] X. Wang, Z. Duan, M. Brydegaard, S. Svanberg, G. Zhao, *Appl. Phys. B* **2018**, *124*, 207.
[35] H. Manefjord, L. Muller, M. Li, J. Salvador, S. Blomqvist, A. Runemark, C. Kirkeby, R. Ignell, J. Bood, M. Brydegaard, *IEEE J. Sel. Top. Quantum Electron.* **2022**, *28*, 1.
[36] M. Li, C. Seinsche, S. Jansson, J. Hernandez, J. Rota, E. Warrant, M. Brydegaard, *J. R. Soc., Interface* **2022**, *19*, 20220256.
[37] V. A. Kovalev, W. E. Eichinger, *Elastic Lidar: Theory, Practice, and Analysis Methods*, John Wiley & Sons, Hoboken, NJ **2004**.
[38] M. Goerke, Z. Ulanowski, G. Ritter, E. Hesse, R. R. Neely, L. Taylor, R. A. Stillwell, P. H. Kaye, *Appl. Opt.* **2017**, *56*, G188.
[39] S. Jansson, *Ph.D. Thesis*, Lund University **2020**.
[40] H. M. Ferguson, G. F. Killeen, K. Michel, R. A. Wirtz, M. Q. Benedict, F. E. Dowell, V. S. Mayagaya, *Am. J. Trop. Med. Hyg.* **2009**, *81*, 622.
[41] W. C. Aw, F. E. Dowell, J. W. O. Ballard, *G3: Genes, Genomes, Genet.* **2012**, *2*, 1057.
[42] B. Lambert, M. T. Sikulu-Lord, V. S. Mayagaya, G. Devine, F. Dowell, T. S. Churcher, *Sci. Rep.* **2018**, *8*, 5274.
[43] M. F. Maia, M. Kapulu, M. Muthui, M. G. Wagah, H. M. Ferguson, F. E. Dowell, F. Baldini, L. Ranford-Cartwright, *Malar. J.* **2019**, *18*, 85.
[44] S. Kaasalainen, *Laser Scanning*, CRC Press, London **2019**, p. 5.
[45] NATO. Laser Based Stand-Off Detection of Biological Agents. Report No. SET-098/RTG-55, (North Atlantic Treaty Organisation, 2010).
[46] O. Shoshanim, A. Baratz, *J. Environ. Chem. Eng.* **2020**, *8*, 104392.
[47] S. M. Spuler, M. Hayman, R. A. Stillwell, J. Carnes, T. Bernatsky, K. S. Repasky, *Atmos. Meas. Tech.* **2021**, *14*, 4593.
[48] C. Kirkeby, M. Wellenreuther, M. Brydegaard, *Sci. Rep.* **2016**, *6*, 29083.
[49] J. Carpentier, *British Patent, GB 1139*, **1901**.
[50] T. Scheimpflug, *British Patent, GB 1196*, **1904**.
[51] H. Mayer, *Ophthalmic. Res.* **1994**, *26*, 3.
[52] L. Mei, M. Brydegaard, *Opt. Express* **2015**, *23*, A1613.
[53] E. Malmqvist, M. Brydegaard, M. Aldén, J. Bood, *Opt. Express* **2018**, *26*, 14842.
[54] N. Photonics, *NKT Photonics–Blokken* **2009**, *84*, 3460.
[55] E. Malmqvist, *Ph.D. Thesis*, Lund University, **2019**.
[56] P. C. Hobbs, *Building Electro-Optical Systems: Making It All Work*, John Wiley & Sons, New York **2022**.

 

[57] G. Høye, A. Fridman, *Opt. Express* **2013**, *21*, 11057.
[58] E. Kristensson, J. Bood, M. Alden, E. Nordström, J. Zhu, S. Huldt, P.-E. Bengtsson, H. Nilsson, E. Berrocal, A. Ehn, *Opt. Express* **2014**, *22*, 7711.
[59] G. Høye, T. Løke, A. Fridman, *Opt. Eng.* **2015**, *54*, 053102.
[60] K. Stelmaszczyk, M. Dell'aglio, S. Chudzyński, T. Stacewicz, L. Wöste, *Appl. Opt.* **2005**, *44*, 1323.
[61] M. Brydegaard, B. Kouakou, S. Jansson, J. Rydell, J. Zoueu, *IEEE J. Sel. Top. Quantum Electron.* **2021**, *27*, 1.
[62] J. E. Sansonetti, W. C. Martin, *J. Phys. Chem. Ref. Data* **2005**, *34*, 1559.

 

# Paper XIII

# Resolving fast Wingbeat Flashes *in situ* with Entomological Lidar

Meng Li[1]*, Hampus Månefjord[1], Mikkel Brydegaard[1,2,3]
1 Dept. Physics, Lund University, Sölvegatan 14c, 22363 Lund, Sweden
2 Dept. Biology, Lund University, Sölvegatan 35, 22362 Lund, Sweden
3 Norsk Elektro Optikk, Østensjøveien 34, 0667 Oslo, Norway
*Correspondence: meng.li@fysik.lu.se

***Abstract*—Specular flashes from insect wings are useful for remote diversity assessment, yet their duration limits and constraining factors remain unknown. We studied this using sampling rates in entomological lidar system up to 40 kHz, resolving quick wing flashes down to 130µs duration from 40 m.**

***Keywords — insects, lidar, environmental monitoring, biodiversity, biophotonics, remote sensing, modulation spectroscopy.***

## I. Introduction

Insects play a vital role in ecosystems, influencing pollination and pest control[1, 2]. Understanding their populations and species compositions is essential for safeguarding environmental and agricultural health. Conventional methods for studying insects can be time-consuming, expensive, and potentially disruptive to insect populations[3]. To address these limitations, our group developed a kHz entomological lidar system for rapid, non-invasive assessment of insect populations and activity[4, 5]. This system utilizes laser light to detect and identify insects based on wing modulations, polarization, and spectral content. We previously operated the systems at a 8 kHz shared sampling rate (2.66 kHz after demultiplexing)[6]. However, this sampling rate was insufficient to capture higher-order wing beat harmonics, especially for male mosquitoes with fundamental tones of 600-800 Hz. This limits the number of observable harmonic tones, induce sampling artifacts such as beating and folding and reduce accuracy of wing thicknesses assessment[7].

To improve understanding of the speed of wing flashes across all insect species, we push the sampling frequency to new extremes over a short test range of 100 m to investigate the impact on data quality.

## II. Material and Methods

In August 2022, a field campaign was carried out at Stensoffa ecological field station (55°41′44”N 13°26′50″E) in southern Sweden, to evaluate the performance of our entomological lidar system operating at three different acquisition rates, including 8kHz, 20kHz, and 40kHz. The experimental site was mapped and illustrated in Fig.1. The lidar instrument was mounted to a tripod and aimed along a transect stretching over a meadow and terminated at a neoprene-covered board located 100 meters away (The diffuse reflectance was 1.8%). The laser wavelength is 808nm. The measurements were conducted within from 18:00 to 24:00 local hour and repeated for each respective acquisition rate. In this study, the laser module was operated in continuous wave mode and was not modulated as in previous studies[6].

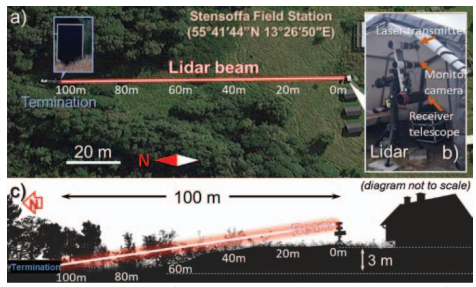


Fig. 1: Experimental site for measurements. a) Detection range and top-down aerial view of the site. b) Illustration of the Scheimpflug lidar with constituent components. The CMOS camera is tilted 37° relative to the optical axis (according to the Scheimpflug criterion) for an extended depth of field. c) The lidar system transmits light over a meadow, terminated at a black neoprene-covered board. The vegetation the beam passes through changes along its path: 0-40m (grass only), 40-100m (salix- and raspberry bushes), surrounded by deciduous forests and swamps.

## III. Results & Discussion

The insect activity patterns and distributions for all three measurement days, captured at different sampling frequencies, are shown in Fig. 2. Two significant areas of high insect activity near 50m and 80m appear consistently across these measurements. Based on Fig. 1, these hotspots are in closer vicinity to taller trees and vegetation compared to the more open parts of the transect. These hotspots also display peak activity occurring slightly before sunset in each instance. This consistent timing suggests species with a certain light level niche. When comparing the activity distributions between the 8kHz and 20kHz configurations (where pre-amp and gain settings remain identical), a reduced number of insects are observed at 20kHz. Due to the faster sampling rate; less laser energy falls into the shorter exposures, diminishing the lidar sensitivity. Consequently, less insects' signals exceed the noise levels and thus detection threshold.

However, at 40kHz, where both gain and preamp settings are doubled, there is a noticeable increase in observations. This suggests that enhanced electronic gain can compensate for the shorter exposure times of high sample rates. The lidar observations featured in Fig. 3 were specifically chosen because

This project has received funding from the European Research Council (ERC) under the European Union's Horizon 2020 research and innovation program (grant agreement no. 850463 Bug-Flash). In additional the FORMAS, Swedish Research Council (2018-01061).

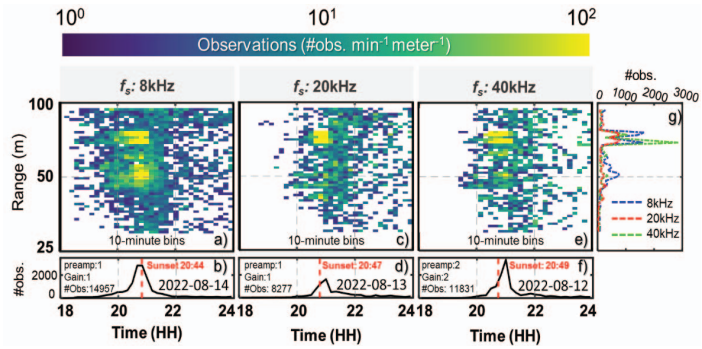


Fig. 2: Activity pattern recorded with different sampling frequency. a, c, e) Range-time distribution maps of detected insects at different sampling frequencies. b, d, f) Corresponding histograms of insect count over time. g) Histograms of observed insect range distribution for all three sampling frequencies.

they share similar detection ranges and exceptionally high wingbeat frequencies (above 600 Hz), indicative of male mosquitoes. This selection allows for a direct comparison of how effectively different sampling frequencies resolve the same wingbeat signals. The 20kHz and 40kHz data samples the flash

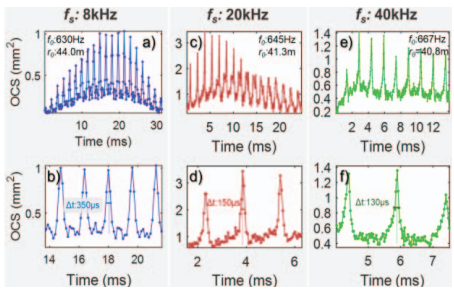


Fig. 3: Example of lidar observations under three different sampling frequencies. a, b): a lidar observation sampled with 8kHz sampling frequency, with b) showing a zoomed-in view of a). c, d): d) is a zoomed-in version of c), sampled at 20 kHz. e, f): Sampled at 40 kHz, with f) being a zoomed-in version of e). Note: this depicts the fastest wing flash observed during this measurement campaign.

by multiple exposures. The single flash per wing beat period is likely to occur at anterior or posterior aspect of observation during upstroke[8]. The wing rotation amplitude is 90°, thus the angular speed is 4·667 Hz·90°= 240.000 °/s and a 130µs flash imply that specular reflection is obtained from a 31° cone from the wing. In comparison, the diffraction limit forms a perfectly plane 1 mm target over 40 m, would result in an 808 nm light cone of only 0.06° and the Ø150 mm receiver collects a 0.2°. The flash duration is thus constrained by the wing flatness in this scenario. Other species have flatter wings, still the implications are that faster flashes cannot be expected at further ranges. Also, fast specular flashes can be expected at much shorter ranges of other insect sensors[9] .

## IV. Conclusion

This study demonstrates the fastest entomological lidar and flashes to date of just 130 µs . Two consistent hotspots and distant insects could be detected despite reduced laser energy per exposure. While a high sampling frequency can reduce signal intensity, the sensitivity at a higher sampling frequency can provide more detailed observations especially for wing flashes. Flash duration is predominantly constrained by the flatness of insect wings.

## Acknowledgment

We thank Rachel Muheim for receiving us at the Stensoffa ecological field station.

## References

[1] P. Goldblatt, and J. C. Manning, “The long-proboscid fly pollination system in southern Africa,” Annals of the Missouri Botanical Garden, pp. 146-170, 2000.

[2] M. A. Jervis, G. E. Heimpel, P. N. Ferns, J. A. Harvey, and N. A. C. Kidd, “Life-history strategies in parasitoid wasps: a comparative analysis of ‘ovigeny’,” Journal of Animal Ecology, vol. 70, no. 3, pp. 442-458, 2001.

[3] Y. Basset, B. Corbara, H. Barrios, P. Cuénoud, M. Leponce, H.-P. Aberlenc, J. Bail, D. Bito, J. R. Bridle, and G. Castano Meneses, “IBISCA-Panama, a large-scale study of arthropod beta-diversity and vertical stratification in a lowland rainforest: rationale, study sites and field protocols,” Bulletin de L'Institut Royal des Sciences Naturelles de Belgique Entomologie, 2007.

[4] M. Brydegaard, S. Jansson, E. Malmqvist, Y. Mlacha, A. Gebru, F. Okumu, G. Killeen, and C. Kirkeby, “Lidar reveals activity anomaly of malaria vectors during pan-African eclipse,” Science Advances, vol. 6, 05/13, 2020.

[5] M. Li, S. Jansson, A. Runemark, J. Peterson, C. T. Kirkeby, A. M. Jönsson, and M. Brydegaard, “Bark beetles as lidar targets and prospects of photonic surveillance,” Journal of Biophotonics, vol. 14, no. 4, pp. e202000420, 2021.

[6] H. Chen, M. Li, H. Månefjord, P. Travers, J. Salvador, L. Müller, D. Dreyer, J. Alison, T. T. Høye, H. Gao, E. Warrant, and M. Brydegaard, “Lidar as a potential tool for monitoring migratory insects,” iScience, vol. 27, no. 5, pp. 109588, 2024/05/17/, 2024.

[7] L. Müller, M. Li, H. Månefjord, J. Salvador, N. Reistad, J. Hernandez, C. Kirkeby, A. Runemark, and M. Brydegaard, “Remote Nanoscopy with Infrared Elastic Hyperspectral Lidar,” Advanced Science, vol. 10, no. 15, pp. 2207110, 2023.

[8] R. J. Bomphrey, T. Nakata, N. Phillips, and S. M. Walker, “Smart wing rotation and trailing-edge vortices enable high frequency mosquito flight,” Nature, vol. 544, no. 7648, pp. 92-95, 2017/04/01, 2017.

[9] K. Rydhmer, E. Bick, L. Still, A. Strand, R. Luciano, S. Helmreich, B. D. Beck, C. Grønne, L. Malmros, K. Poulsen, F. Elbæk, M. Brydegaaard, J. Lemmich, and T. Nikolajsen, “Automating insect monitoring using unsupervised near-infrared sensors,” Scientific Reports, vol. 12, no. 1, pp. 1-11, 2022.














Printed by Media-Tryck, Lund 2024
NORDIC SWAN ECOLABEL 3041 0903

LUND UNIVERSITY

Department of Physics

LRCP 257
ISBN 978-91-8104-153-8
ISSN 1102-8718
ISRN LUTFD2/TFCP-257-SE